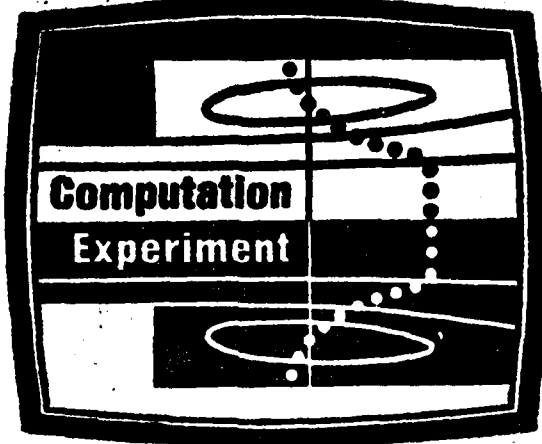


MICROCOPY RESOLUTION TEST CHART
NATIONAL BUREAU OF STANDARDS-1963-A

2

Complex Turbulent Flows



AD-A236034

Volume III

Comparison of Computation with
 Experiment, and Computers'
 Summary Reports

DTIC
 ELECTE
 DEC 19 1983
 S D

DTIC FILE COPY

Edited by
 S. J. Kline,
 B. J. Cantwell,
 G. M. Lilley

DISTRIBUTION STATEMENT A
 Approved for public release;
 Distribution Unlimited

83 12 18 131

UNCLASSIFIED

SECURITY CLASSIFICATION OF THIS PAGE (When Data Entered)

REPORT DOCUMENTATION PAGE		READ INSTRUCTIONS BEFORE COMPLETING FORM	
1. REPORT NUMBER AFOSR-TK- 88-1003	2. GOVT ACCESSION NO. ADA 136034	3. RECIPIENT'S CATALOG NUMBER	
4. THE 1980-81 AFOSR-HTM-STANFORD CONFERENCE ON COMPLEX TURBULENT FLOWS: COMPARISON OF COMPUTATION AND EXPERIMENT-VOLUME-3		5. TYPE OF REPORT & PERIOD COVERED INTERIM	
		6. PERFORMING ORG. REPORT NUMBER	
7. AUTHOR(S) S J KLINE B J CANTWELL G M LILLEY		8. CONTRACT OR GRANT NUMBER(s) F49620-80-C-0027	
9. PERFORMING ORGANIZATION NAME AND ADDRESS STANFORD UNIVERSITY MECHANICAL ENGINEERING DEPARTMENT STANFORD, CA 94305		10. PROGRAM ELEMENT, PROJECT, TASK AREA & WORK UNIT NUMBERS 61102F 2307/A1	
11. CONTROLLING OFFICE NAME AND ADDRESS AIR FORCE OFFICE OF SCIENTIFIC RESEARCH/NA BOLLING AFB, DC 20332		12. REPORT DATE September 1981	
		13. NUMBER OF PAGES 1552	
14. MONITORING AGENCY NAME & ADDRESS (if different from Controlling Office)		15. SECURITY CLASS. (of this report) Unclassified	
		15a. DECLASSIFICATION/DOWNGRADING SCHEDULE	
16. DISTRIBUTION STATEMENT (of this Report) Approved for Public Release; Distribution Unlimited.			
17. DISTRIBUTION STATEMENT (of the abstract entered in Block 20, if different from Report)			
18. SUPPLEMENTARY NOTES Proceedings of the 1980-81 AFOSR-HTM-Stanford Conference on Complex Turbulent Flows: Comparison of Computation and Experiment, Stanford, CA, 14-18 September 1981, Stanford University 1982			
19. KEY WORDS (Continue on reverse side if necessary and identify by block number) COMPLEX TURBULENT FLOWS THREE-DIMENSIONAL FLOW EXPERIMENTAL DATA ATTACHED BOUNDARY LAYERS SEPARATED FLOWS TWO-DIMENSIONAL FLOW			
20. ABSTRACT (Continue on reverse side if necessary and identify by block number) Volumes II and III together give an overview of the state of the art in Computing Complex Turbulent Flows in 1981 using the data base established for this purpose in Volume I. The materials are intended to be complete in the sense of providing all elements necessary for understanding the state of the art. Thus, Volumes II and III include: (i) taxonomies that organize the flows, methods of modeling, numerics; (ii) comments by non-computors (the reporters) on results for each class of flows; (iii) discussions carried through to closure and carefully edited (see Discussion Procedures in Volume I);			

DD FORM 1473
1 JAN 73

EDITION OF 1 NOV 65 IS OBSOLETE

UNCLASSIFIED

SECURITY CLASSIFICATION OF THIS PAGE (When Data Entered)

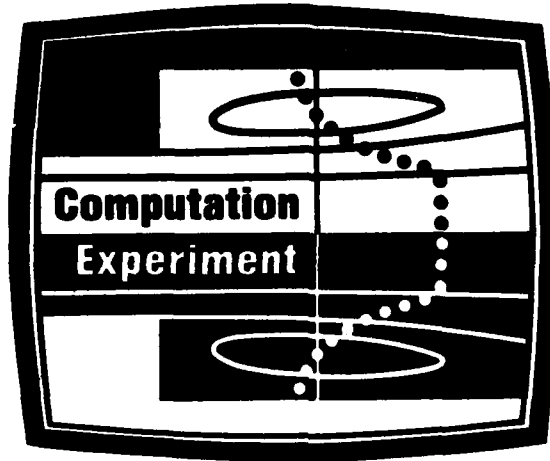
(iv) samples of recent high-level research computations that are currently beginning to provide information of aid to turbulence modelers; (v) an overall evaluation of the state of the art by a distinguished committee of nine workers in the field; (vi) an opinion by the leading editor on the question of "universality" of turbulence models, potential roads toward further progress, and discussion thereof by others; (vii) all computer output compared with data, case by case; (viii) comments by the computer groups on experiences and problems; (ix) several cross indexes to aid readers.

Accession For	
NTIS GRA&I	<input checked="" type="checkbox"/>
DTIC TAB	<input type="checkbox"/>
Unannounced	<input type="checkbox"/>
Justification	
By	
Distribution/	
Availability Codes	
Dist	Avail and/or Special
A/1	



AFOSR-TR. 83-1003

COMPLEX TURBULENT FLOWS



**THE 1980-81 AFOSR-HTTM-STANFORD CONFERENCE ON COMPLEX TURBULENT FLOWS:
COMPARISON OF COMPUTATION AND EXPERIMENT**

VOLUME III

**COMPARISON OF COMPUTATION WITH EXPERIMENT,
AND COMPUTERS' SUMMARY REPORTS**

**Proceedings of the 1981 Conference
Stanford University, Stanford, California
September 14-18, 1981**

**DTIC
ELECTE
S DEC 19 1983 D
D**

Edited by S. J. Kline, B. J. Cantwell, and G. M. Lilley

**Published and Distributed by
Thermosciences Division
Mechanical Engineering Department
Stanford University
Stanford, California
1982**

**Approved for public release;
distribution unlimited.**

Editors Stephen J. Kline
Mechanical Engineering Department
Stanford University
Stanford, CA 94305, USA

Brian J. Cantwell
Department of Aeronautics and Astronautics
Stanford University
Stanford, CA 94305, USA

Geoffrey M. Lilley
Department of Aeronautics and Astronautics
University of Southampton
Southampton SO9 5NH, England

Production Editor
Ditter Peschcke-Koedt
Palo Alto, CA 94301, USA

ISBN. 0-9607348-2-1 (Volume III)
0-9607348-3-X (3-Volume Set)

(c) 1982 by the Board of Trustees of the Leland Stanford Junior University.

All rights reserved. Printed in the United States of America.

L.C. 81-84184

Stanford, California, USA 94305, 1982.
(First Printing)

ACKNOWLEDGMENTS

The 1981 Conference, together with the 1980 Conference, is best viewed as a cooperative learning process within the research community. To achieve the aims of the Conference with impartiality, the fullest cooperation of the scientific and engineering communities was sought and generously given. Our special thanks are extended to all the Computers and Computer Groups, Technical Recorders, whose names appear in the List of Participants to the 1981 Conference in Volume II. The 1981 Conference was attended by approximately 190 invited participants from 18 countries (Australia, Brazil, Canada, Chile, England, France, Hong Kong, India, Iran, Israel, Italy, Japan, Netherlands, South Africa, Switzerland, United States of America, West Germany, and Yugoslavia).

The principal financial sponsorship for the work of this conference was supplied by the U.S. Air Force Office of Scientific Research under contract AF F49620-80-C-0027 and a predecessor grant. Added support for work on data processing of compressible flow cases was supplied by the NASA Ames Research Center under Grant NAG 2-79. Contributions were also made by the Langley and Lewis Research Centers of NASA, by the U.S. Office of Naval Research and by the National Science Foundation. The specific assistance of Dr. Morris Rubesin and Dr. Dannis Bushnell of NASA with regard to funding is gratefully acknowledged. The steadfast support of Dr. James Wilson of AFOSR was critical to the success of the Conference. When the volume of cases found to be useful grew far beyond the initial estimates, with a resulting and considerable increase in cost, Dr. Wilson spent much effort to organize the concerned government agencies and thereby secure the funds to complete the work. Funds for some special purposes were also supplied from the Heat Transfer and Turbulence Mechanics (HTTM) Program of the Industrial Affiliates Program of the Stanford Thermosciences Division. Funds to cover an overdraft in the base contract were generously supplied by the Stanford School of Engineering.

Special thanks are accorded the Organizing Committee: S. J. Kline (Chairman, P. Bradshaw, B. J. Cantwell, B. E. Launder, E. Reshotko, M. W. Rubesin, and G. Sovran, who worked long and thoughtfully beginning in 1977 on the plans, organization, and personnel problems. The continuing confidence and enthusiasm of the members of this committee were important ingredients in the success of the Conference.

The unenviable task of judging the comparison between data and computer output fell to the Evaluation Committee: H. W. Emmons (Chairman), D. R. Chapman, P. G. Hill, G. H. Lilley, M. Lubert, M. V. Morkovin, W. C. Reynolds, P. J. Roache, and J. Steger. Professor Emmons had also been the Chairman of the Evaluation Committee for the 1968 AFOSR-IFP-Stanford Conference on the Computation of Turbulent Boundary Layers. The

work of the Evaluation Committee was greatly appreciated and their conclusions set out in Vol. II provide important guidelines for further effort in work on Complex Turbulent Flows.

The critical task of summarizing results of computation in each class of flows was assumed by the eleven "Reporters" shown in the program, p. xiii, Vol. II. This allowed the attendees and the Evaluation Committee to obtain a clear picture of the large, heterogeneous mass of results that otherwise would not have been possible within a few days. The reporters did this task on very short time scales in a highly responsible manner and with great clarity. None of the eleven persons asked to be a reporter, declined the task, and hence each represents the expert best qualified to discuss the given class of flows in the opinion of the Organizing Committee.

Responsibility for the important task of creating, ad novo, a taxonomy of turbulence modeling methods and also of numerical procedures was assumed by Prof. J.H. Ferziger. He was very ably assisted by Jorge Bardina on turbulence modeling and by Gary Allen on numerical procedures.

Special thanks are also due to Brian Launder and Wolfgang Rodi for several tasks including: organizing groups of computers thus giving a wide comparison of related k- ϵ methods for various numerical methods; carrying out full computations on predictive cases; organizing the computers during the meeting to insure maximum learning from their experiences; and much effort with K. Hanjalić on studying and describing all the methods employed.

No conference of this sort would have been held without the willing help of the Host Committee, who made all the local arrangements, and the many Stanford graduate students who served as Technical Recorders and Aides; to all these we add our grateful thanks. Special appreciation is given to Profs. J. P. Johnston and J. H. Ferziger for important assistance in studying data and closing many special gaps. Roger Strawn and Ranga Jayaraman organized the aides and supervised all physical arrangements in an excellent fashion. Professors W. C. Reynolds and R. J. Moffat lent the support of the Thermosciences Division and the Department of Mechanical Engineering at important points. Professor M. V. Morkovin acted as a senior advisor on many issues.

The arduous and critical task of transferring the output from the computer groups on to the poster boards was expertly handled by a dedicated cadre of Stanford graduate students and others working under the direction of B. J. Cantwell. They included: Jorge Bardina, Juan Bardina, Jalal Ashjee, Ken Schultz, Jim Talleghani, and Priscilla Spolyar. Special thanks are due to Juan Bardina and Jalal Ashjee for many late nights in the computer center writing plot routines to make the standard plotting windows with experimental results displayed.

The Conference was fortunate in having the aid of a very able secretarial staff. Particular praise is needed for both Ditter Peschcke-Koedt, who was responsible for typing of the indexes and manuscript organization, and to Pauline Polen, the Conference Secretary, who organized the paperwork system, including finances, travel, filing, and programs in a highly independent and responsible fashion. Thanks are also due to Priscilla Spolyar and Gerda Dewerk who spent long hours preparing the plates of computed output for final copy.

PREFACE

This is the third of the three volumes of Proceedings of the 1980-81 AFOSR-HTTM-Stanford Conference on Complex Turbulent Flows: Comparison of Computation and Experiment.

In this volume are included: (i) Several cross indexes of the flows, cases, and methods used by the various Computer Groups; (ii) The comprehensive results of the computation output and their comparison with the experimental data; these results are presented in Plates 1 through 187; (iii) Brief commentaries by each Computer Group on methods used and experiences gained in performing the computations.

This volume forms a set with Volumes I and II. The use of this volume is explained in the Preface to Volume II and, in particular, in the "Reader's Guide" (pp. xx, Vol. II), which suggests various parts of the three volumes that are useful for particular purposes. Reference should be made also to the "Introduction to Summaries by Technical Reporters" (p. 725, Vol. II).

The overall conclusions of the 1980-81 AFOSR-HTTM-Stanford Conference on Complex Turbulent Flows are presented at the end of Volume II along with recommendations for further work and a follow-on conference in the next few years.

The editors will welcome notification concerning any errors in this or other volumes. Such notices can be sent to any of the editors at the addresses listed.

S. J. Kline
B. J. Cantwell
G. M. Lilley
July 1982

TABLE OF CONTENTS

	<u>Page</u>
Acknowledgments	111
Preface	vi
General Nomenclature	x

TAXONOMIES

PICTORIAL SUMMARY	1049
CLASSIFICATION OF FLOWS	1073
TAXONOMY OF METHODS	1074
CLASSIFICATION OF INTEGRAL METHODS	1078
CLASSIFICATION OF ONE-POINT CLOSURE	1079
CLASSIFICATION OF TWO-POINT CLOSURE	1080
TAXONOMY OF NUMERICAL METHODS	1081

INDEXES TO PLOTTED OUTPUTS

SUMMARY OF METHODS AND NUMERICS EMPLOYED ALPHABETIC BY GROUP COORDINATOR . .	1085
INDEX OF COMPUTER GROUPS BY GROUP NUMBER	1095
INDEX BY METHOD	1099
INDEX OF PLATES BY PLATE NUMBER AND CASE NUMBER	1102

PLATES 1 THROUGH 187

(Comparison of Computation Output with Experimental Data)

SUMMARY REPORTS OF COMPUTER GROUPS	1302
---	------

Group No.	Coordinator or Lead Author [*]	Cases	
50	Bailey, H.E.	8621, 8623, 8691	1303
24	Birch, S.F.	0311, 0381	1305
52	Cambon, C.	0371, 0372, 0373, 0374, 0375, 0376	1307
23 ¹	Chow, W.L.	0111	1312
23 ²	Chow, W.L.	0441	1318
22	Cousteix, J.	0111, 0141, 0142, 0143, 0211, 0231, 0232, 0233, 0261, 0381, 0382, 0371, 0374, 0375, 0376, 0431, 0471, 0511, 0512, 0612, 8101, 8201, 8411, 8621	1326
47	Deiwert, G.S.	8621, 8623	1337

^{*}An alphabetic list of all members of the Computer Groups follows the Summary Reports on p. 1550.

Group No.	Coordinator or Lead Author	Cases	
21	Donaldson, C.duP.	0141, 0241, 0242, 0244, 0311, 0371, 0373, 0374, 0375, 0376, 0421, 0422, 0612, 8101, 8201, 8301, 8403, 8411	1342
46	Dvorak, F.A.	0441	1346
45	Fersiger, J.H.	0141, 0142, 0143, 0431, 0612	1353
19	Hah, C.	0331	1358
18	Hanjalić	0141, 0142, 0143, 0241, 0244, 0371, 0373, 0374, 0375, 0376, 0612	1364
43	Hung, C.	8101, 8201, 8631	1372
17 ¹	Chang, S.M.*	0512	1375
17 ²	Demirdzic, A.D.*	0421, 0422, 0423	1383
17 ³	Lauder, B.E.*	0142, 0143, 0211, 0231, 0232, 0233, 0261, 0263, 0311, 0331, 0375, 0376, 0381, 0382, 0421, 0422, 0424, 0612	1390
17 ⁴	Bonnet, J.P.*	8501	1408
42	La Balleur	0441, 8621, 8623, 8631, 8691	1411
02	Mansour, M.N.	0331, 0421	1418
41	McDonald, H.	0441, 0512, 8601, 8641	1424
14	Mellor, G.L.	0331, 0421, 0431	1428
39	Melnick, R.E.	8621	1438
44 ¹	Ha Minh, H.	8101, 8201, 8612	1443
44 ²	Ha Minh, H.	0421	1449
01	Moore, J.	0141, 0142, 0143, 0512, 0612	1453
27	Moses, H.L.	0141, 0142, 0421, 0431, 0441, 0612	1459
28	Murphy, J.D.	0141, 0431, 0612	1464
04	Nagamatsu, T.	0141, 0231, 0232, 0233, 0612	1468
05	Orlandi, P.	0141, 0231, 0232, 0233, 0141, 0242, 0244, 0281, 0612	1472
30	Fletcher, R.H.	0141, 0241, 0242, 0421, 0424, 0431, 0612	1479
06	Pollard, A.	0421	1486
31	Rakich, J.V.	8101, 8201, 8661, 8671	1491
07	Rodi, W.	0111, 0112, 0113, 0141, 0142, 0143, 0211, 0231, 0232, 0233, 0241, 0242, 0244, 0261, 0263, 0281, 0311, 0331, 0371, 0372, 0373, 0374, 0375, 0376, 0381, 0382, 0421, 0422, 0423, 0471, 0511, 0512, 0612	1495

*Computer Groups 17 were coordinated by B.E. Lauder and appear here and in other alphabetic listings under "Lauder".

Group No.	Coordinator or Lead Author	Cases	
32	Smith, P.D.	0141, 0231, 0232, 0233, 0612, 8101, 8411, 8621	1517
33	Spalding, D.B.	0141, 0142, 0143, 0421, 0512, 0612	1521
09	Tassa, Y.	8621	1527
35	Vandromme, D.D.	0381, 0382, 0471	1532
36	Viegas, J.	0471, 8101, 8201, 8403, 8601, 8611, 8631, 8632, 8641, 8651, 8661, 8663	1535
12	Whitfield, D.	0141, 0612, 8621	1540
37	Wilcox, D.C.	0141, 0142, 0143, 0241, 0242, 0244, 0311, 0371, 0372, 0374, 0376, 0421, 0612, 8101, 8201, 8403, 8411, 8501, 8621, 8623	1544

#####

COMPUTOR GROUP MEMBERS IN ALPHABETIC ORDER	1550
LOCATION OF THE CONCLUSIONS AND GENERAL COMMENTS IN THESE PROCEEDINGS	1551

GENERAL NOMENCLATURE

Computer	Conventional	Meaning	S.I. Units
BETA	β	$(dp/dx) \delta^*/\tau_w$	-
DEL	δ_{995}	Boundary-layer thickness to $0.995 U_e$	m
DELS	δ^*	Displacement thickness = $\int_0^\delta (1 - \frac{\rho U}{\rho_e U_e}) dy$	m
ENTH	δ^{**}	Energy thickness = $\int_0^\delta \frac{\rho U}{\rho_e U_e} (1 - \frac{U^2}{U_e^2}) dy$	m
CLTH	Δ	Clouser thickness = $\int_0^\delta \frac{\rho_e U_e - \rho U}{\rho_w U_*} dy$	m
EPSILON	ϵ	Dissipation function	$m^2 \text{ sec}^{-3}$
THETA	θ	Momentum thickness = $\int_0^\delta \frac{\rho U}{\rho_e U_e} (1 - \frac{U}{U_e}) dy$	m
XNU	ν	Kinematic viscosity	$m^2 \text{ sec}^{-1}$
RO	ρ	Density	$kg \text{ m}^{-3}$
TAU	τ	Shear stress	$N \text{ m}^{-2}$
PHIL	ϕ_L	Left-hand side of momentum integral equation balance	-
PHIR	ϕ_R	Right-hand side of momentum integral equation balance	-
CD	C_D	Drag coefficient	-
CL	C_L	Lift coefficient	-
CF	C_f	Skin-friction coefficient = $\tau_w / (\frac{1}{2} \rho_e U_e^2)$	-
CFE	C_f	C_f as reported by originator	-
CFLT	C_f	C_f according to Ludwig-Tillmann formula	-
CFPT	C_f	Measured using Preston tube	-
CP	C_p	Pressure coefficient	-
G	G	Equilibrium shape factor = $\int_0^\delta \left(\frac{\rho_e U_e - \rho U}{\rho_w U_*} \right)^2 d(y/\Delta)$	-
H	H	Shape factor = δ^*/θ	-
HS	H^*	δ^{**}/θ	-
KAY	K	$(\overline{u^2} + \overline{v^2} + \overline{w^2})$	-
-	k	Turbulence kinetic energy (K/2)	-
LREF	L_{ref}	Reference length	m
XM	M	Mach number	-

Symbol

Computer	Conventional	Meaning	S.I. Units
XMREF	M_{ref}	Reference Mach number	-
P	p	Pressure	$N m^{-2}$
PR	Pr	Prandtl number	-
PREF	P_{ref}	Reference pressure	$N m^{-2}$
PIU1	\overline{pU}	Pressure-velocity covariance	-
QREF	q_{ref}	Reference dynamic pressure	$N m^{-2}$
RE	Re	Reynolds number based on reference values $Re = \frac{U_{ref} L_{ref}}{\nu_{ref}}$	-
RDELS	R_{δ^*}	Reynolds number = $U_e \delta^* / \nu$	-
ROIU1	$\overline{\rho U}$	Density-velocity covariance	-
RTHETA	R_{θ}	Reynolds number = $U_e \theta / \nu$	-
ST	St	Stanton number	-
STR	Str	Strouhal number	-
-	T	Temperature	-
-	t	Time	-
TENTH	t^+	Thermal energy thickness $\frac{\sqrt{C_f}/2}{St} \left(\frac{T_w - T}{T_w - T_e} \right)$	m
XS	s	Coordinate tangent to an arc	m
XN	n	Coordinate normal to an arc	m
U	U	Mean streamwise velocity	$m sec^{-1}$
V	V	Mean transverse velocity	$m sec^{-1}$
W	W	Mean spanwise velocity	$m sec^{-1}$
UDEF	-	Defect velocity = $(U_e - U)/U_*$	$m sec^{-1}$
UE	U_e	Velocity external to boundary layer	$m sec^{-1}$
UI	U_{∞}	Free-stream velocity	$m sec^{-1}$
UREF	U_{ref}	Reference velocity	$m sec^{-1}$
US	U_*	Wall shear velocity = $\sqrt{\tau_w / \rho_w}$	$m sec^{-1}$
UPLUS	U^+	U/U_*	-
U2	$\overline{u^2}$	Reynolds stress	$m^2 sec^{-2}$
V2	$\overline{v^2}$	Reynolds stress	$m^2 sec^{-2}$
W2	$\overline{w^2}$	Reynolds stress	$m^2 sec^{-2}$

Computer	Conventional	Symbol	Meaning	S.I. Units
U1V1	\overline{uv}		Reynolds shear stress	$m^2 \text{ sec}^{-2}$
U1W1	\overline{uw}		Reynolds shear stress	$m^2 \text{ sec}^{-2}$
V1W1	\overline{vw}		Reynolds shear stress	$m^2 \text{ sec}^{-2}$
UaVm	$\overline{u^a v^m}$		Higher-order velocity covariance	-
	ω		Frequency (also c/k)	sec^{-1}
X	x		Streamwise coordinate	m
Y	y		Transverse coordinate	m
Z	z		Spanwise coordinate	m
X	x or s		Streamwise coordinate on curved surface	m
Y	y or n		Direction normal to curved surface	m
Z	z		Spanwise coordinate	m
YPLUS	y^+		yU_* / ν	-

Subscript "w" denotes wall value.

Subscript "e" denotes conditions external to boundary layer.

$$\phi_L^*(x) = \frac{U_w^2}{(U_e^2)_0} - 1 + \frac{1}{2} \int_{x_0}^x \frac{\delta^*}{\theta} d\left(\frac{U_w^2}{(U_e^2)_0}\right) .$$

$$\phi_k^*(x) = \int_{x_0}^x \left(\frac{U_*}{(U_e)_0}\right)^2 d\left(\frac{x}{\theta_0}\right) .$$

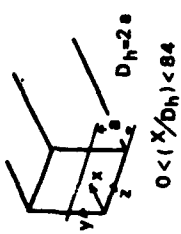
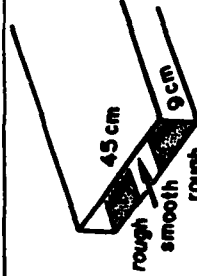
PICTORIAL SUMMARY

The initial version of the pictorial and tabular presentation of all the "Flows" used in the 1981 Conference was prepared by Professor S. Honami. The initial version was modified and edited for these Proceedings. All the major features of the flows which appeared as "Specifications" for the 1981 Conference are included. They are given here in the numerical order of the "Flows." Each individual chart was also included within the relevant "Case" in Volume I and with each Technical Reporter's Summary in Volume II.



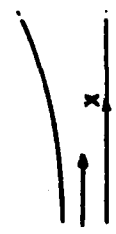


S. Honami

PICTORIAL SUMMARY
 Flow 0110. Data Evaluator: F. Gessner. "Corner Flow (Secondary Flow of the Second Kind)."

Case Data Taker	Test Rig Geometry	dp/dx or C _p	Number of Stations Measured							Re	Ini- tial Condi- tion	Other Notes
			Mean Velocity		Turbulence Profiles							
			U	V or W	$\overline{u^2}$	$\overline{v^2}$	$\overline{w^2}$	Others	C _f			
Case 0111 J. Fo E. Lund F. Gessner	 $0 < (x/D_h) < 84$	34 sta- tions on walls A and B	17	5	-	-	3	3 pro- files of K	1	2.5 $\times 10^5$ (based on bulk velocity and D_h)	sym- etric inlet flow	C, vs x data for laminar flow (Beavers, Goldstein) included with data file. Goldstein's laminar velocity data also included. Nominally uniform, low turbulence level flow at inlet ($x/D_h = 0$).
Case 0112 J. Hinze			1		1	1	1	1	1	1.5 $\times 10^5$ (based on hy- draulic diam and U_{max})	One wall rough with smooth center- strip	All measurements were made at $x/D_h = 126$. Data include viscous dissipation.

PICTORIAL SUMMARY

Flow 0140. Data Evaluated: E. Simpson. "Diffuser Flows (unoperated)."

Case No.	Investigator	Test Rig Geometry	$\frac{dp}{dx}$ or C_p	Number of Stations Measured						Initial Condition	Other Notes			
				Mean Velocity		Turbulence Profiles								
				\bar{V}	\bar{w}	\bar{u}	\bar{v}	\bar{w}	Other			C_f		
Case 0141	A. Samuel P. Jobert		$\frac{dp}{dx} > 0$ $\frac{d^2p}{dx^2} > 0$	6	6	6	6	6	6	6	Floating balance, Preston tube, pressure plots	1.76×10^6 per m	Turbulence intensity 0.3%	Two-dimensionality was checked.
Case 0142	R. Pessorini	 1/4 = 4.5; Area Ratio 4; Cone Angle 6°	> 0	12	12	12	12	12	12	-	Pressure plots, Preston tube	2.54×10^5 (based on inlet pipe radius)	Turbulence intensity 0.31%	Conical diffuser—core (low turbulence).
Case 0143	R. Pessorini	 1/4 = 7.25; Area Ratio 4; Cone Angle 6°	> 0	6	6	6	6	6	6	-	Pressure plots, Preston tube	1.27×10^5 (based on inlet pipe radius)	Turbulence intensity 1%	Conical diffuser—core (high turbulence).


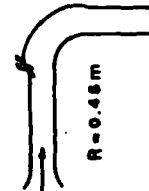
PICTORIAL SUMMARY

Flow 0210. Data Evaluator: P. Bradshaw. "Effect of Free-Stream Turbulence on Boundary Layers."

Case Data Taker	Test Rig Geometry	dp/dx or C _f ^p	Number of Stations Measured							Re	Ini- tial Condi- tion	Other Notes
			Mean Velocity		Turbulence Profiles							
			U	V or W	u ²	v ²	w ²	uv	Others			
Case 0211 P. Hancock and others			Smoothed curve of $\frac{AC_f}{C_f^0} \text{ vs } \left(\frac{U}{V}\right)_0 / \left(\frac{L}{\delta_{995}} + 2\right) \text{ given}$									

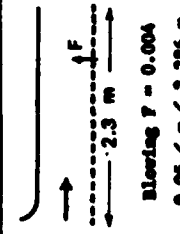
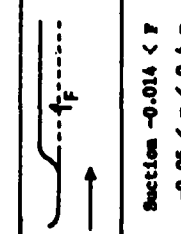
PICTORIAL SUMMARY

Flow 0230. Data Evaluator: I. Simon and S. Kozumi. "Boundary Layer Flows with Streamline Curvature."


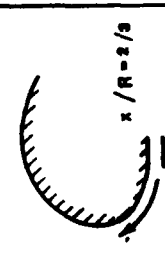
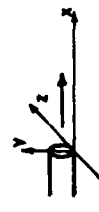
Case Data Taker	Test Rig Geometry	dp/dx or C _f ^p	Number of Stations Measured							Re	Ini- tial Condi- tion	Other Notes	
			Mean Velocity		Turbulence Profiles								
			U	V or W	u ²	v ²	w ²	uv	Others				C _f
Case 0231-convex Case 0232-concave P. Hoffmann & P. Bradshaw		12	5	-	5	-	5	v ²	5	u ³⁻⁵ v ³⁻⁵ w ²⁻⁵ uv ²⁻⁵ v ³⁻⁵	5 ^a	5.2 x 10 ⁴ (based on 6 at be- ginning of curve)	6/R = 0.01 Mild Curvature.
Case 0233 J. Gillis & J. Johnston		24	11	-	12	12	12	12	12	24 ^a	4.6 x 10 ⁴ (based on 6 at be- ginning of curve)	0.10 Strong Curvature with Recovery.	

^a Clauser Plot Method.



Flow 0240. Data Evaluator: L. Squire. "Turbulent Boundary Layers with Section or Blowing."
 PICTORIAL SUMMARY

Case Data Table	Test Rig Geometry	dp/dx or Cp	Number of Stations Measured					Re	Initial Condition	Other Notes
			Mean Velocity		Turbulence Profiles					
			U	V or W	$\overline{u^2}$	$\overline{v^2}$	Other			
Case 0241 P. Anderson V. Keys E. Moffat		0	9	-	-	-	-	9	M=0	No turbulence data.
Case 0242 P. Anderson V. Keys E. Moffat	As Case 0241 Section F = -0.004 0.05 < x < 2.286 m	Adverse $U_x \sim x^{-0.15}$	9	-	1	1	1	9	0	Turbulence data available at initial station.
Case 0244 A. Favre E. Demas E. Verollet M. Comtic		0	1	-	1	1	1	9	0	Data available for 4 section rates: F = -0.002, -0.0053, -0.0100, -0.0144. Velocity and turbulence data restricted to one streamwise station.

PICTORIAL SUMMARY
Flow 0260. Data Evaluators: B. Launder and V. Modi. "Turbulent Wall Jet."

Case Data Taker	Test Rig Geometry	dp/dx or Cp	Number of Stations Measured							Initial Condition	Other Notes	
			Mean Velocity		Turbulence Profiles							
			U	V or W	$\overline{u^2}$	$\overline{v^2}$	$\overline{w^2}$	\overline{uv}	Others			Cf
Case 0261 Various data takers		> 0	Yes	-	Yes	Yes	Yes	Yes	Yes	Intermittency. Razon triple, blade quadruple velocity correlations	4×10^3 to 5×10^4	Equilibrium wall jet in adverse pressure gradient.
Case 0263 D. Gaitton B. Newman		-	Yes	-	Yes	-	Yes	-	K	7×10^3 to 5×10^4 (based on slot height)	Self-preserving wall jet on logarithmic spiral surface.	
Case 0264 Various Data Takers		-	Yes	-	-	-	-	-	-	> 10^4	3D wall jet in still air on plane surface. No output plots required.	

PICTORIAL SUMMARY
 Flow 0290. Data Evaluator: K. R. Sreenivasan. "Re-laminarizing Flows."

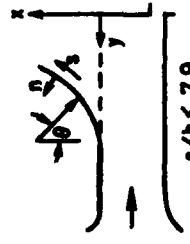
Case Data Taker	Test Rig Geometry	dp/dx or C _p	Number of Stations Measured				Re	Initial Condi- tion	Other Notes
			Mean Velocity		Turbulence Profiles				
			U	V or W	$\overline{u^2}$	$\overline{v^2}$ or $\overline{w^2}$			
Case 0281 R. Simeon D. Wallace		-	15	-	-	-	15	2342 (based on δ^* at inlet)	Boundary layer developing under mild adverse pres- sure gradient upstream of contraction.
Case 0282 J. Laufer (V. Patel & M. Head)		-	6	5	-	-	1725 (based on radius at inlet)	Initial mean velocity data taken from Patel and Head (1969).	

PICTORIAL SUMMARY
 Flow 0310. Data Evaluator: S. Birch. "Planar Mixing Layer."

Case Data Taker	Test Rig Geometry	dp/dx or C _p	Number of Stations Measured				Re	Initial Condi- tion	Other Notes
			Mean Velocity		Turbulence Profiles				
			U	V or W	$\overline{u^2}$	$\overline{v^2}$ or $\overline{w^2}$			
Case 0311 Data combined from several sources.	L/θ_1 vs x/θ_1								Initial development of the $\theta_2 = 0$ plane mixing layer.

PICTORIAL SUMMARY

Flow 0330. Data Evaluator: P. Bradshaw. "Free-Shear Layer with Streamwise Curvature."

Case Data Taker	Test Rig Geometry	dp/dx or Cp	Number of Stations Measured						Initial Condition	Other Notes
			Mean Velocity		Turbulence Profiles					
			U	V or W	u ²	v ²	uv	Others Cf		
Case 0331 I. Castro P. Bradshaw	 s/h < 7.9		17*	17*	17*	17*	17*	17*	2.55 x 10 ⁵ (based on nozzle opening h)	Tabulated data are in a mix of x, y, or r, θ coordinates. Digital processing techniques are used.

*Results are plotted in semi-curved linear (θ, n) coordinates; the n = 0 line being a nominal curved centerline of the mixing layer.

PICTORIAL SUMMARY

Flow 0360. Data Evaluator: V. Patel. "Wakes of Round Bodies (Axisymmetric Wakes)."

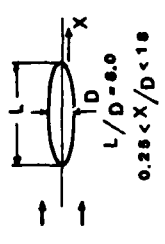
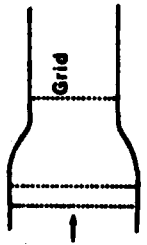
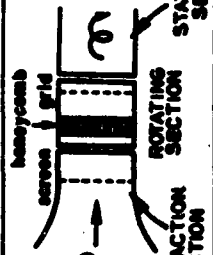
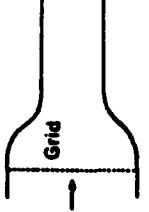
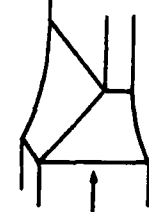
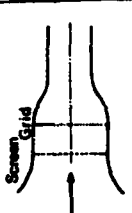

Case Data Taker	Test Rig Geometry	dp/dx or Cp	Number of Stations Measured						Initial Condition	Other Notes
			Mean Velocity		Turbulence Profiles					
			U	V or W	u ²	v ²	uv	Others Cf		
Case 0361 R. Chevray	 L/D = 8.0 0.28 < X/D < 1.8 L = 1.52 m	Magi- sible tunnel block- age effect	12	5	12	12	12	12	2.75 x 10 ⁶ (based on L)	Model 1.52 m long, 0.254 m maximum diam. spheroid. Static pressure distribution across wake is provided. Model surface pressure not measured.

FIGURE 1. SUMMARY
Flow 0370. Data Evaluators: J. Persinger. "Homogeneous Turbulent Flows."

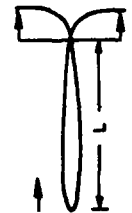

Case Name	Test Rig Geometry	dp/dx or C _p	Number of Stations Measured						Re	Ini- tial Condi- tion	Other Notes
			Mean Velocity		Turbulence Profiles						
			U	V or W	$\overline{v^2}$	$\overline{w^2}$	Others	C _f			
Case 0371 G. Gault-Bullet S. Corrales		zero	Yes	-	Yes	Yes	-	-	1600 3200 (based on M)	-	Homogeneous isotropic turbulence. Grid 3 cases
Case 0372 R. Wigland H. Magib (0372A,B,C)		-	Yes	-	Yes	Yes	-	-	-	-	Rotating homogeneous turbulence.
Case 0373 M. Uberoi (0373A,B,C,D)		zero	Yes	-	Yes	Yes	Yes	-	3710 (based on M)	-	Return to isotropy. Contraction 3 cases.
H. Tcher A. Reynolds (0373E)								Spec- tra of $\frac{u', v', w'}{u', v', w'}$			
Case 0374 A. Townsend (0374A) H. Tcher A. Reynolds (0374B)		-	Yes	-	Yes	Yes	Yes	-	-	-	Plane strained homo- geneous turbulence.

Flow 0370 continued

Flow 0370. Data Evaluator: J. Fersiger. "Homogeneous Turbulent Flows." (continued)


Case Data Taker	Test Rig Geometry	dp/dx or Cp	Number of Stations Measured							Initial Condition	Other Notes
			Mean Velocity		Turbulence Profiles						
			U	V or W	u ²	v ²	w ²	Others	C _f		
Case 0375 J. Tharstichat (0375A, B, C, D, E)		-	Yes	-	Yes	Yes	-	-	-	270 to 8100 (based on M)	Asymmetric strained homogeneous turbulence. Grid 6 cases. Contraction 7 cases.
Case 0376 F. Champagne V. Harris S. Corrales (0376A) V. Harris J. Graham S. Corrales (0376B)		zero	Yes	-	Yes	Yes	Yes	-	-	-	Sheared homogeneous turbulence.

Flow 0380. Data Evaluator: V. C. Patel. "Wakes of Two-Dimensional Bodies."

Case Data Taker	Test Rig Geometry	dp/dx or Cp	Number of Stations Measured							Initial Condition	Other Notes	
			Mean Velocity		Turbulence Profiles							
			U	V or W	u ²	v ²	w ²	Others	C _f			
Case 0381 J. Andreopoulos			10		4	4	-	4	-	-	6.8 x 10 ⁶ (based on L)	Symmetrical Case. Conditional averages to study the mixing in the central part of wake.
Case 0382 J. Andreopoulos			6		4	4	-	4	-	-	6.8 x 10 ⁶ (based on L)	Asymmetrical Case. Conditional averages to study the mixing in the central part of wake.

PICTORIAL SUMMARY

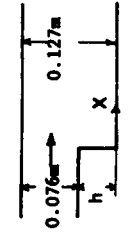
Flow 0410. Data Evaluator: B. Cantwell. "Evaluation of Bluff-Body, Near-Wake Flow."

Case Data Taker	Test Rig Geometry	dp/dx or C _p	Number of Stations Measured						Initial Condi- tion	Other Notes		
			Mean Velocity		Turbulence Profiles							
			U	V or W	$\overline{u^2}$	$\overline{v^2}$	$\overline{w^2}$	\overline{uv}			Others C _f	
Case 0411 B. Cantwell D. Coles	 <p>$-3.0 < x/D < 3.0$ $-0.5 < z/D < 8.0$</p>	Mean sur- face pres- sure	U	V or W	Yes ^a	Yes ^a	Yes ^a	Yes ^a	Yes ^a	Yes ^a u ³ , v ³ , w ³ , uv, vw, uw, u ² v, uv ²	Free stream turb. on level < 0.6% (based on cylin- der dia.)	Flying hot-wire data. Large body of data field. Unsteady data included.

^aLocation: $x/D = -3.0 + 0.1(i-1)$, $1 \leq i \leq 61$; $x/D = -0.5 + 0.1(j-1)$, $1 < j \leq 86$.


PICTORIAL SUMMARY

Flow 0420. Data Evaluators: J. Eaton and J. Johnston. "Backward-Facing Step Flow."

Case Data Taker	Test Rig Geometry	dp/dx or C _p	Number of Stations Measured						Initial Condi- tion	Other Notes		
			Mean Velocity		Turbulence Profiles							
			U	V or W	$\overline{u^2}$	$\overline{v^2}$	$\overline{w^2}$	\overline{uv}			Others C _f	
Case 0421 J. Kin S. Kline J. Johnston	 <p>$X/h < 16$</p>	Wall pres- sure	U	V or W <td>6</td> <td>6</td> <td>6</td> <td>6</td> <td>6</td> <td>Reattach- ment length $\times 10^4$ about 7h</td> <td>6/h = 0.3</td> <td>Aspect ratio 16. Data inadequate in zones of high turbulence and oscillating flow. Laser data needed. Reattached layer wall documented. Pressure on upper and lower walls available.</td>	6	6	6	6	6	Reattach- ment length $\times 10^4$ about 7h	6/h = 0.3	Aspect ratio 16. Data inadequate in zones of high turbulence and oscillating flow. Laser data needed. Reattached layer wall documented. Pressure on upper and lower walls available.

PICTORIAL SUMMARY

Flow 0430. Data Evaluator: R. Simpson. "Diffuser Flow (Separated)."


Case Data Taker	Test Rig Geometry	dp/dx or Cp	Number of Stations Measured							Initial Condition	Other Notes
			Mean Velocity		Turbulence Profiles			Cf	Re		
			U	V or W	$\overline{u^2}$	$\overline{v^2}$	$\overline{w^2}$				
Case 0431 R. Simpson Y. Chew B. Shivaprasad		< 0 up-stream of throat > 0 down-stream	11†	11†	21*	11*	6*	11*	Pres-ton tube	1.07 x 10 ⁶ per m	Turbulence intensity 0.1% Two-dimensionality was checked. Position of an inviscid streamline near the upper wall is given.

*Hot-wire measurement.

†Laser Doppler measurement.

PICTORIAL SUMMARY

Flow 0440. Data Evaluator: A. Wedcock. "Two-Dimensional Stalled Airfoil."

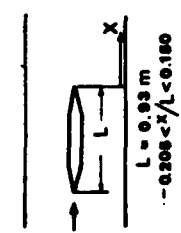
Case Data Taker	Test Rig Geometry	dp/dx or Cp	Number of Stations Measured							Initial Condition	Other Notes
			Mean Velocity		Turbulence Profiles			Cf	Re		
			U	V or W	$\overline{u^2}$	$\overline{v^2}$	$\overline{w^2}$				
Case 0441 D. Coles A. Wedcock		Mean sur-face pres-sure	125	125	125	125	-	125	Inter-stit-ency	1.5 x 10 ⁶ (based on air-foil chord)	Aspect ratio = 2. Probe interference present for attached boundary layer data--separated zone and wake is interference-free.

$$0.62 \leq \alpha/c \leq 2.00$$

$$\Delta x/c = 0.0111$$

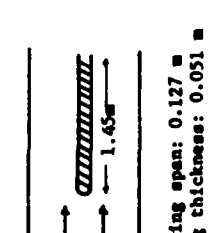
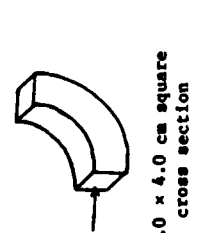
PICTORIAL SUMMARY

Flow 0470. Data Evaluator: P. Drecher. "Flow over the Trailing Edge of Blades and Airfoils."

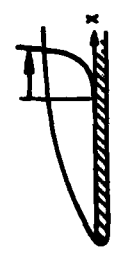
Case Data Taker	Test Rig Geometry	dp/dx or Cp	Number of Stations Measured							Re	K ₀	Other Notes
			Mean Velocity		Turbulence Profiles							
			U	V or W	$\overline{u^2}$	$\overline{v^2}$	$\overline{w^2}$	Others	C _f			
Case 0471 P. Vignasch J. Cleary E. Seegmiller C. Horstman		Surfaces and wake pressure	9	-	7	7	-	7	-	2.4 to 3.7 x 10 ⁵ (based on chord)	0.4 and 0.7	Subsonic trailing edge flow, variable flap angle. Symmetric and unsymmetric cases.

PICTORIAL SUMMARY

Flow 0510. Data Evaluator: R. Dean. "Turbulent Secondary Flows of the First Kind."

Case Data Taker	Test Rig Geometry	dp/dx or Cp	Number of Stations Measured							Re	Initial Condition	Other Notes		
			Mean Velocity		Turbulence Profiles									
			U ₀	U _t	$\overline{u_0^2}$	$\overline{u_t^2}$	$\overline{w^2}$	\overline{uv}	Others				C _f	
Case 0511 I. Shabaka		Measured	3	Secondary flow vectors at 3 stations	3	3	3	3	3	7	1.1 x 10 ⁵ (based on wing thickness)	BL thickness at the leading edge was about 0.025 m	Wing-body junction. Calculations should be started downstream of leading edge.	
Case 0512 J. Humphrey		Not recorded in bend	7	U ₀	2	7	2	2	2	-	2	4 x 10 ⁴ (based on duct height)	Nearly fully developed	Curved rectangular duct. Calculations should be started 8.2 duct dia. upstream of bend using Melling's (1975) data.

PICTORIAL SUMMARY
 Flow 0610. Data Evaluator: D. E. Coles. "Attached Boundary Layers ('68 Conference)."

Case Data Taker	Test Rig Geometry	dp/dx or C _p	Number of Stations Measured						Initial Condi- tion	Other Notes	
			Mean Velocity		Turbulence Profiles						
			U	V or W	$\overline{u^2}$	$\overline{v^2}$	$\overline{w^2}$	Others			C _f
Case 0612 K. Wieghardt		0	23	-	-	-	-	-	-	2.2 x 10 ⁶ Clouser per m plots < 0.25%	Data include computed values of boundary layer integral parameters.

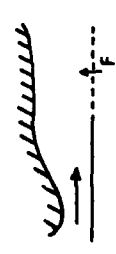
PICTORIAL SUMMARY
 Flow 8100. Data Evaluators: H. Rubesin and C. Horstman. "Supersonic Flow Over a Flat Plate (Insulated Wall)."

Case Data Taker	Test Rig Geometry	dp/dx or C _p	Number of Stations Measured						Initial Condi- tion	Other Notes			
			Mean Velocity		Turbulence Profiles								
			U	V or W	$\overline{u^2}$	$\overline{v^2}$	$\overline{w^2}$	Others			C _f	Re	
Case 8101 Various data takers												C _f /C _{f0} vs. H	Effect of compressibility on skin friction.

FIGURIAL SUMMARY
 Flow 8200. Data Evaluator: H. Babasin and C. Borstman. "Supersonic Flow Over a Flat Plate (Cooled Wall)."

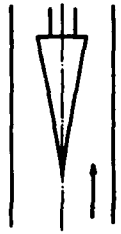
Case Data Taker	Test Rig Geometry	dp/dx or Cp	Number of Stations Measured					Initial Condition	Other Notes
			Mean Velocity		Turbulence Profiles				
			U	V or W	$\overline{u^2}$	$\overline{v^2}$	Others C_f		
Case 8201 Various data takers									
C_f/C_{f0} vs. x/L									
Effect of surface cooling on skin friction.									

FIGURIAL SUMMARY
 Flow 8300. Data Evaluator: L. Equire. "Turbulent Boundary Layers with Section or Blowing at Supersonic Speeds."

Case Data Taker	Test Rig Geometry	dp/dx or Cp	Number of Stations Measured					Initial Condition	Other Notes
			Mean Velocity		Turbulence Profiles				
			U	V or W	$\overline{u^2}$	$\overline{v^2}$	Others C_f		
Case 8301 G. Thomas		< 0	11	-	-	-	-	M (2.53 to 2.87)	M, P, θ , δ^* vs x data available on file. No turbulence data.
Blowing $0.02 < F < 0.0028$ $0 < x < 0.127$ m									


PICTORIAL SUMMARY

Flow 8400. Data Evaluators: M. Rubesin and C. Horstman. "Boundary Layers in an Adverse Pressure Gradient in an Axisymmetric Internal Flow."

Case Data Tabar	Test Rig Geometry	dp/dx or C _p	Number of Stations Measured							Re	M _∞	Other Notes
			Mean Velocity		Turbulence Profiles							
			U	V or W	$\overline{u^2}$	$\overline{v^2}$	$\overline{w^2}$	\overline{uv}	Others			
Case 8403 M. Kussow C. Horstman N. Acharya		> 0	8	-	8	8	8	8	8	1.6 x 10 ⁵ to 4.32 x 10 ⁶ (based on δ ₀)	2.3	Axisymmetric. Profile data for 2 pres- sure gradients. Skin friction data for 6 pres- sure gradients, each at 4 Reynolds numbers.

PICTORIAL SUMMARY

Flow 8410. Data Evaluators: M. Rubesin and C. Horstman. "Boundary Layers in an Adverse Pressure Gradient in 2-Dimensional Flow."

Case Data Tabar	Test Rig Geometry	dp/dx or C _p	Number of Stations Measured							Re	M _∞	Other Notes
			Mean Velocity		Turbulence Profiles							
			U	V or W	$\overline{u^2}$	$\overline{v^2}$	$\overline{w^2}$	\overline{uv}	Others			
Case 8411 P. Zwarts		> 0	6	-	-	-	-	-	-	3.5 x 10 ⁴ (based on θ ₀)	4	

PICTORIAL SUMMARY

Flow 8500. Data Evaluator: P. Bradsher. "Compressible Effects on Free Shear Layers."

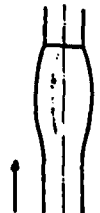
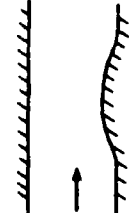
Case Data Taker	Test Rig Geometry	dp/dx or C _p	Number of Stations Measured						Initial Condi- tion	Other Notes
			Mean Velocity		Turbulence Profiles					
			U	V or W	$\overline{u^2}$	$\overline{v^2}$	$\overline{w^2}$	Other C _f		
Case 8501 Various data takers			Smoothed curve of ds/dx vs. M given.							Shear layer spreading rate vs Mach number.

PICTORIAL SUMMARY

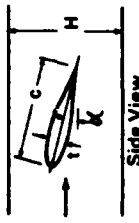

Flow 8600. Data Evaluator: M. Babesin and C. Horstman. "Impinged Normal Shock Wave-Boundary Layer Interaction at Transonic Speeds."

Case Data Taker	Test Rig Geometry	dp/dx or C _p	Number of Stations Measured						Re	Other Notes
			Mean Velocity		Turbulence Profiles					
			U	V or W	$\overline{u^2}$	$\overline{v^2}$	$\overline{w^2}$	Other C _f		
Case 8601 G. Mateer A. Broth J. Viegas			8	-	-	-	8		3x10 ⁵ to 6x10 ⁶ (based on δ_0)	Axisymmetric profile data for one test condition. Skin friction data for several test conditions varying M and Re .

PICTORIAL SUMMARY
 Flow 8610. Data Evaluators: N. Rubesin and C. Horstman. "Transonic Flow over a Bump."



Case Data Taker	Test Rig Geometry	dp/dx or C _p	Number of Stations Measured							M _∞	Re	Other Notes
			Mean Velocity			Turbulence Profiles						
			U	V or W	U ²	V ²	W ²	uv	Others			
Case 8611 W. Bachalo D. Johnson			12	12	12	12	12	12	-	-	1.4 x 10 ⁵ (based on δ ₀)	Axisymmetric. Complete LDV data.
Case 8612 J. Delery P. Le Dizet			28	28	28	28	28	28	28	-	7x10 ⁴ (based on δ)	Complete LDV data. Top wall is important in solving problem.

PICTORIAL SUMMARY
Flow 8620. Data Evaluator: R. E. Melnik: "Transonic Airfoils."

Case Data Taker	Test Rig Geometry	dp/dx or C _p	Number of Stations Measured						M _∞	Re	Other Notes
			Mean Velocity		Turbulence Profiles						
			U	V or W	$\overline{u^2}$	$\overline{v^2}$	\overline{uv}	Others C _f			
Case 8621 P. Cook M. McDonald M. Firmin	RAE 2822 Airfoil 	Air-foil upper & lower surface pressure	9	-	-	-	-	-	5.7 to 6.5 x 10 ⁶ Law of (based on Wall chord)	0.676 to 0.730	RAE 8x6 ft. transonic tunnel. Data include computed values of boundary-layer integral parameters.
Case 8623 F. Spald L. Stivers, Jr.	DERA 523, Airfoil 	Air-foil upper & lower surface pressure	7	-	-	-	-	Law of Wall by trans-formed velocity (based on chord)	0.6 to 0.8	MASA-Ames 2x2 ft. transonic tunnel.	


PICTORIAL SUMMARY

Flow 8630. Data Evaluators: M. Rubesin and C. Horstman. "Compressible Flow over Deflected Surfaces."

Case Data Taker	Test Rig Geometry	dp/dx or Cp	Number of Stations Measured							M _∞	Other Notes	
			Mean Velocity		Turbulence Profiles				C _f			
			U	V or W	u ²	v ²	w ²	uv				Others
Case 8631 G. Settles T. Fitzpatrick S. Bogdanoff		> 0	9	-	-	-	-	-	Pres-ton tube M and p/p _∞	8x10 ⁵ to 7.6 x 10 ⁶ (based on δ ₀)	2.85	θ = 8, 16, 20 and 24°. Wall pressure also available.
Case 8632 J. Dussange J. Caviglio		< 0	23	-	2	-	-	-	Tu	5x10 ³ (based on δ ₀)	1.76	Prandtl Meyer expansion. Wall pressure also available.

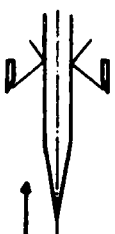
PICTORIAL SUMMARY

Flow 8640. Data Evaluators: M. Rubesin and C. Horstman. "Compressible Flow over Compression Corner with Reattaching Planar Shear Layer."

Case Data Taker	Test Rig Geometry	dp/dx or Cp	Number of Stations Measured							M _∞	Other Notes	
			Mean Velocity		Turbulence Profiles				C _f			
			U	V or W	u ²	v ²	w ²	uv				Others
Case 8641 G. Settles B. Beca D. Williams S. Bogdanoff		> 0	11	-	-	-	-	-	M _∞ Pres-ton probe 11	2.2 x 10 ⁵ (based on δ ₀)	2.8	Combines three problems: Free-shear layer development, reattachment, and downstream development.

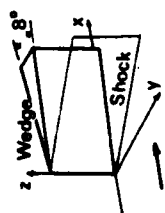
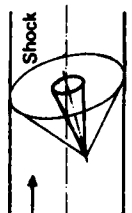
PICTORIAL SUMMARY

Flow 8650. Data Evaluators: M. Rubesin and C. Horstman. "Axisymmetric Shock Impingement (Supersonic)."

Case Data Taker	Test Rig Geometry	dp/dx or Cp	Number of Stations Measured							Re	M _∞	Other Notes
			Mean Velocity		Turbulence Profiles							
			U	V or W	$\overline{u^2}$	$\overline{v^2}$	$\overline{w^2}$	Others	C _f			
Case 8651 M. Kussey C. Horstman		various	10	-	-	4	-	-	PR 4	3.6 x 10 ⁵ (based on δ ₀)	7.2	Axisymmetric. Two cases - one attached and one separated. Most transfer measure- ments included.


PICTORIAL SUMMARY

Flow 8660. Data Evaluators: M. Rubesin and C. Horstman. "Three-Dimensional Shock Impingement (Supersonic)."

Case Data Taker	Test Rig Geometry	dp/dx or Cp	Number of Stations Measured							Re	M _∞	Other Notes
			Mean Velocity		Turbulence Profiles							
			U	V or W	$\overline{u^2}$	$\overline{v^2}$	$\overline{w^2}$	Others	C _f			
Case 8661 D. Peake			5	5*	-	-	-	-	-	1.5 x 10 ⁵ (based on δ ₀)	2	3D planar shock inter- action. *V known in terms of U and flow angle.
Case 8663 M. Kussey J. Viegas C. Horstman			5	Flow angle at various stations around cone	5	5	5	5	PR 5	1.0 x 10 ⁶ (based on δ ₀)	2.17	3D curved shock inter- action. Turbulence measurements limited to windward and leeward planes.


PICTORIAL SUMMARY

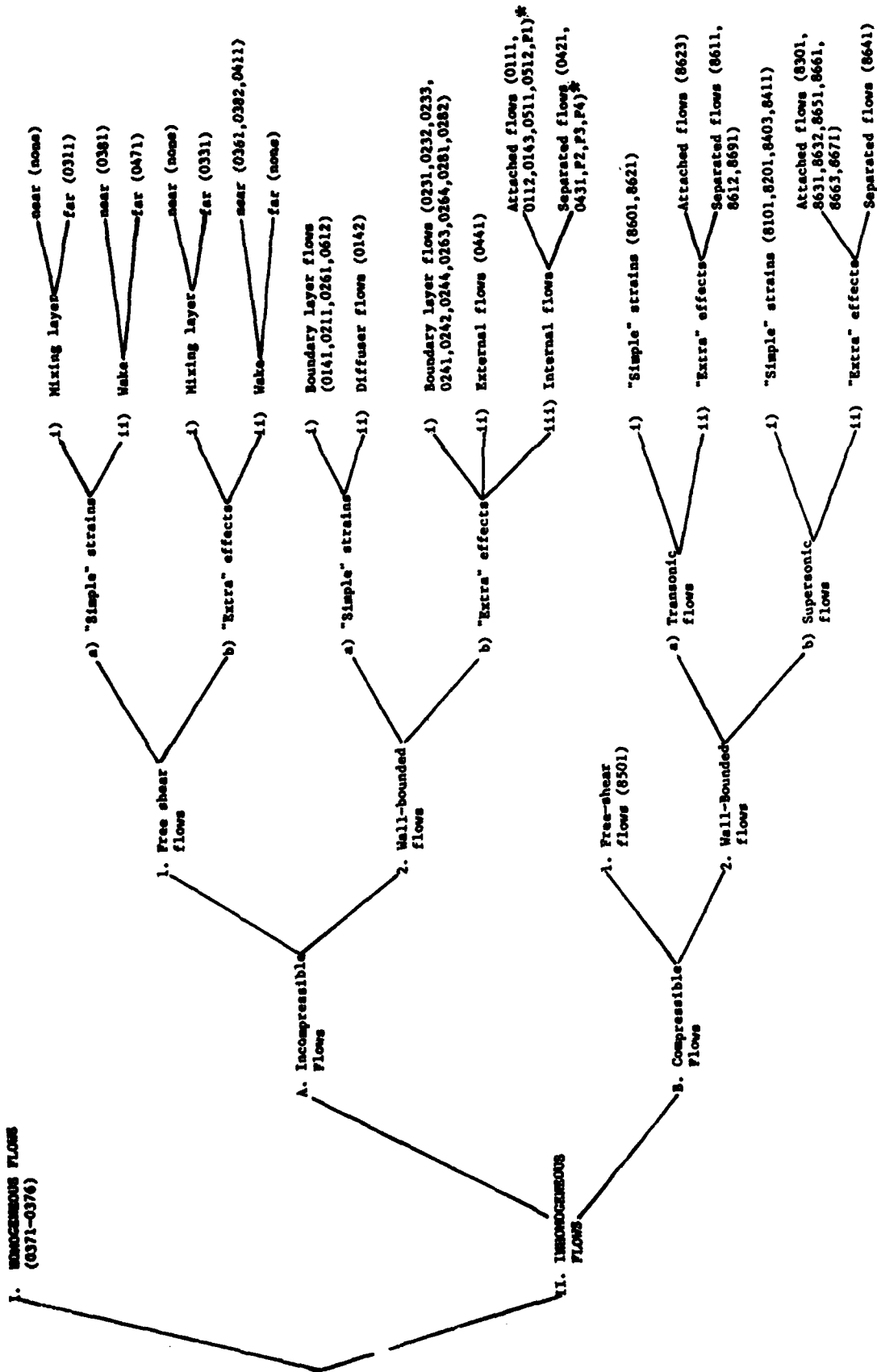
Flow 8670. Data Evaluators: D. Peake (D. J. Cockrell). "Pointed Axisymmetric Bodies at Angle of Attack (Supersonic)."

Case Data Taker	Test Rig Geometry	dp/dx or C _p	Number of Stations Measured							M _∞	Other Notes	
			Mean Velocity	Turbulence Profiles				C _f	Re			
				U	V	W	uv					Others
Case 8671 V. Rainbird			1	-	-	-	-	Sur- face pres- sure	Pres- ton tubes and oil flow visual- ization (length)	2.5 3.4 x 10 ⁷ (based on cone length)	1.8	Free-stream turbulence ~ 0.2%. Data at two angles of attack. Measurements at one axial station x/L = 0.85.

PICTORIAL SUMMARY

Flow 8690. Data Evaluators: M. Rubesin and C. Horstman. "Non-Lifting, Transonic Airfoil with Shock-Separation."

Case Data Taker	Test Rig Geometry	dp/dx or C _p	Number of Stations Measured							M _∞	Other Notes	
			Mean Velocity	Turbulence Profiles				C _f	Re			
				U	V	W	uv					Others
Case 8691 J. McDevitt A. Okuno H. Seegmiller			7	7	7	7	7	Surfac pres- sure	Buried wire	1.1 x 10 ⁷ (based on chord)	0.785	Circular arc airfoil with large separation.



* Flows designated P1, etc., were predictive cases. Following the 1980 meeting, these flows were assigned permanent numbers as follows: P1 = 0113; P2 = 0422; P3 = 0423; P4 = 0424.

CLASSIFICATION OF FLOWS

TAXONOMY OF METHODS

<u>Level</u>	<u>Method</u>
1	Correlations
2	Integral Methods
3	One-Point Closures
4	Two-Point Closures
5	Large-Eddy Simulation
6	Full Simulation

TAXONOMY OF METHODS

1. CORRELATIONS

No descriptors

2. INTEGRAL METHODS

- (EE) Energy Integral Equation
- (ML) Moment of Momentum Equation
- (HN) Entrainment Correlation--Shape Factor, No Lag
- (HG) Entrainment Correlation--Shape Factor, Lag
- (SN) Entrainment Correlation--Shear Stress, No Lag
- (SG) Entrainment Correlation--Shear Stress, Lag

3. ONE-POINT CLOSURE

TREATMENT OF REYNOLDS STRESSES

	<u>Examples</u>
(B) <u>Boussinesq</u> (eddy viscosity)	
(A) <u>Algebraic</u>	
OP Prescribed	
OL l from ODE	(BOP-)
1K k equation, l prescribed	
1L k equation, l from ODE	(A1W-)
1W l prescribed, ω equation	
 <u>Two-equation model</u>	
KE k, ϵ	
KW k, ω	(AKE-)
KL k, l	
QE $k^2 l, \epsilon$	
 <u>Differential</u>	
D { 4E $k, \epsilon, \overline{uv}, \overline{uw}$	(D5E-)
5E $\epsilon, \overline{uv}, \overline{u^2}, \overline{v^2}, \overline{w^2}$	
5Q $k^2 l, \overline{uv}, \overline{u^2}, \overline{v^2}, \overline{w^2}$	
 <u>Reynolds Stress</u>	
RS { T No additional PDE	(RSE-)
E Additional PDE for ϵ	
L Additional PDE for l	

SPECIAL EFFECTS

1. Treatment Near Solid Walls

X	No slip--Explicit Damping	(BOPX)
N	No slip--No Explicit Damping	(AKEZ)
Y	Law of the wall--Explicit Damping	(D5EC)
Z	Law of the wall--No Explicit Damping	(RSEZ)
C	Not applicable (free shear flows)	
O	Other	

2. Extra Rates of Strain

Curvature
 Lateral Divergence
 Rotation
 Roughness
 Blowing
 Suction
 Pressure Gradient
 Other

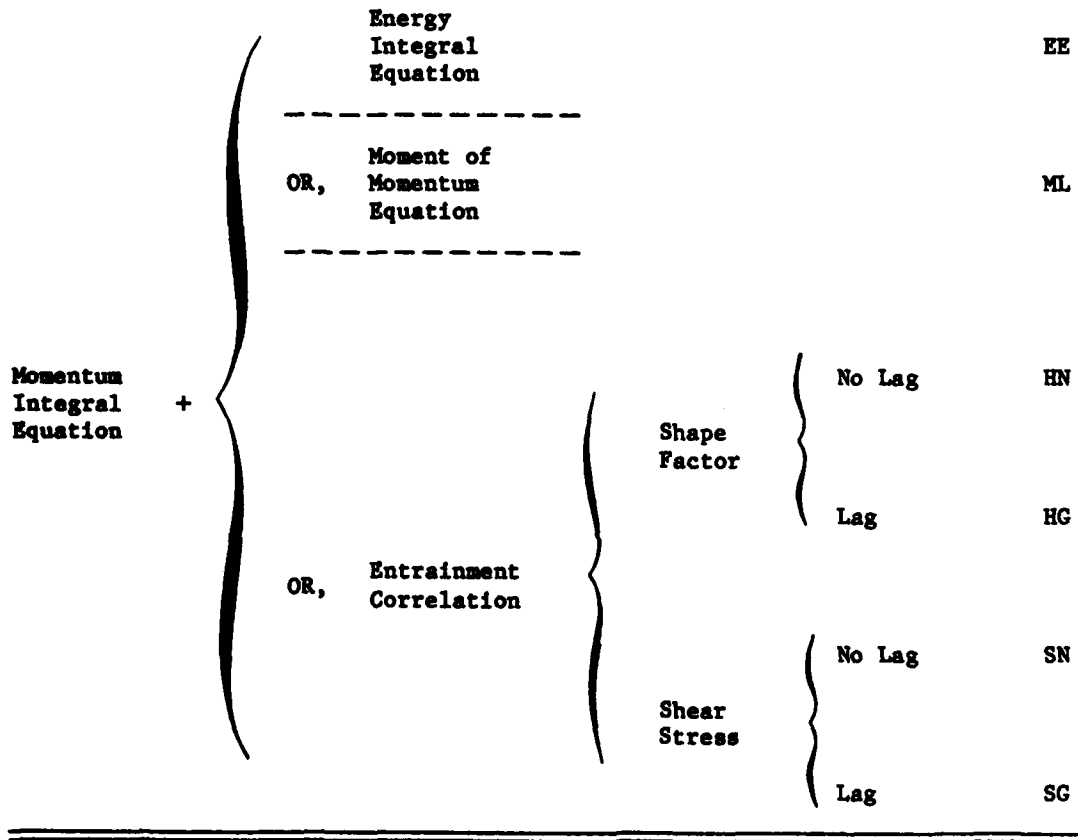
4. TWO-POINT CLOSURES

- (2DI) Direct Interaction Approximation
- (2ED) Eddy Damped Quasi-Natural Hypothesis

5. LARGE-EDDY SIMULATION

6. FULL SIMULATION

CLASSIFICATION OF INTEGRAL METHODS



CLASSIFICATION OF ONE-POINT CLOSURES

Method	Reynolds Stress	n-Equation Model	Wall Treatment
AOPX	Algebraic	0-Equation Eddy Viscosity Prescribed	No Slip Damped Eddy Viscosity
AKEC	"	2-Equation k, ε	Not Applicable
AKEX	"	"	No Slip Damped Eddy Viscosity
AKEY	"	"	Law of Wall "
AKEZ	"	"	" No Special Treatment
AKWC	"	"	Not Applicable
AKWX	"	" k, ω	No Slip Damped Eddy Viscosity
AKWY	"	"	Law of Wall "
BOPX	Boussinesq	0-Equation Eddy Viscosity Prescribed	No Slip Damped Eddy Viscosity
BKEC	"	2-Equation k, ε	Not Applicable
BKEX	"	"	No Slip Damped Eddy Viscosity
BKEY	"	"	Law of Wall "
BKEZ	"	"	" No Special Treatment
BKWX	"	" k, ω	No Slip Damped Eddy Viscosity
BKWY	"	"	Law of Wall "
BOLX	"	0-Equation l from ODE	No Slip "
BILX	"	l from ODE k-Equation	No Slip "
BIKX	"	l Prescribed	" "
RSTC	Reynolds Stress	No Additional PDE	Not Applicable
RSTZ	"	"	Law of Wall No Special Treatment
RSTO	"	"	Other
RSEC	"	Additional PDE for ε	Not Applicable
RSEN	"	Additional PDE for ε	No Slip No Special Treatment
D5QZ	Differential	Several Equations	Law of Wall No Special Treatment

CLASSIFICATION OF TWO-POINT CLOSURES

Method

2DI	Direct Interaction Approximation
2ED	Eddy Damped Quasi-Normal Hypothesis

**TAXONOMY OF
NUMERICAL METHODS**

TAXONOMY OF NUMERICAL METHODS

- (1) Overall Strategy
- Zonal (separate methods in different regions; matched or patched) Z
 Global (single method for entire flow) G
- Note: If zonal, it is assumed that there is a turbulent region and a potential flow region. Where possible a separate numerical taxonomy is given for each region.
- (2) Governing Equation
- Parabolic (equations solved by marching in streamwise direction) P
 Elliptic (iterative method required) E
 Hyperbolic Y
 Mixed (specify) M
- (3) Type of Discretization
- Finite difference--regular grid R
 Finite difference--staggered grid T
 Finite volume--regular grid V
 Finite volume--staggered grid S
 Finite element L
 Hybrid H
 Other (specify) O
- (4) Differencing of Convective Terms
- Central C
 Upwind standard U
 Upwind--skewed K
 Rotated A
 Explicit artificial viscosity D
 Hybrid (specify) H
 Other (describe) O
- (5) Formal Order of Accuracy (convective terms)
- First 1
 Second 2
 Third 3
 Fourth 4
 Mixed (specify) M
 Other (specify) O
- (6) Formally Conserve Quantities
- Mass only Q
 Mass and momentum N
 Mass, momentum, and kinetic energy J
 Mass, momentum, and total energy W
 Other (specify) O

(7) Treatment of Difficult Boundary Geometries

Asymmetric stars	X
Boundary-fitted coordinates	B
Coordinate transformations	F
Non-applicable (simple geometry only)	*
Other (specify)	O

(8) Flow Type

Compressible	C
Incompressible	I

(9) Strategy

Explicit, time-like	X
Explicit, not time-like	E
Implicit, time-like	T
Implicit, not time-like	M
Semi-implicit	S
Other (specify)	O

(10) Tactics

Point substitution	P
Line substitution	L
Direct matrix inversion	D
Split (ADI-like)	A

IF METHOD IS FOR COMPRESSIBLE FLOWS, SKIP TO SECTION 13.

(11) Pressure (Incompressible only)

Poisson equation	Q
Artificial compressibility	F
Other form of pressure correction	O

(12) Relaxation (Incompressible only)

Under-relaxation throughout	U
Over-relaxation throughout	R
Variable relaxation	V
Other (specify)	O

(13) General

Computer used	_____
Approximate time per iteration per point	_____

(14) Specifics

For each flow solved, the following information (where possible) is given in the index below.

<u>Flow</u>	<u>Number of Grid points in x and y directions or x,y or z directions</u>	<u>First y⁺</u>
-------------	---	--------------------------------

INDEXES TO
PLOTTED OUTPUTS

**SUMMARY OF METHODS
AND
NUMERICS EMPLOYED
ALPHABETIC BY GROUP COORDINATOR**

SUMMARY OF METHODS AND NUMERICS EMPLOYED ALPHABETIC BY GROUP COORDINATOR

Code to "Taxonomy of Numerical Methods" see pp. 1082-1083

Group Coordinator [Number]	Method	Case	(1)	(2)	(3)	(4)	(5)	(6)	(7)	(8)	(9)	(10)	(11)	(12)	Comp. Used	Time/Iter- ation/ Point [sec]	No. of Grid Points			Comments (see p.1094)
																	x	y	z	
Bailey [50]	BOPK	8621	G	E	R	C	2	W	B	C	T	A			ILLIAC	0.00013	128	60	90	
		8623																		
		8691																		
Birch [24]	BKNC	0381	G	F	S	U,H	I,M	Q	*	C	M				CDC 6600	0.0002	93	40	40	
	BKXZ	0311	G	P	S	U,H	I,M	Q	*	C	M				CDC 6600	0.0002	194	20-40	20-40	
	2ED	0371																		
		0372ABC	G	P	T	J	*	I	X				0		PRIME 550	1	60	30	30	(spectral space)
Cambon [52]		0374AB															75	30	30	
		0375ABCDE															60	30	30	
		0376AB																		
	2ED(A)	0371	G	P		J	*	I	X				0		PRIME 550	600	18 spheres	radius k		
		0373E	G	P		J	*	I	X				0		PRIME 550	600	38 points	per sphere		
		0374AB																		
		0376AB																		
	2ED(B)	0376B	G	P		J	*	I	X				0		PRIME 550	600	3D non-linear	term done on 4 spheres		
Chow [23]	AKXZ	0111	G	E	S	H	M	J	B	I	M	A	0	U	CYBER 175		30	9	9	
	BKXZ	0441	G	E	V	H	M	J	B	I	M	A	0	U	CYBER 175	0.0083	95	31	31	
Constaix [22]	AOPK	0111	G	P	V	U	1	N	B	I	L				IRIS 80	0.01	500	24	24	
		0511													IRIS 80		200	40	40	2-3
		0512															200	45	23	
		BKXZ	0141																	
		BKXZ(A)	0141																	
		0211																		
		0231		G	P	V	U	1	N	*	I	D			IRIS 80	0.00025		50-60	50-60	< 2
		0232																		
		0233																		
		0612																		
		BKXZ(B)	0231	P	S	U	1	N	*	I	T	D			IRIS 80	0.28	3000	60	60	
			0233																	
		BKXZ(C)	0141	P	V	U	1	N	*	I	T	D			IRIS 80	0.28	5400	65	65	< 2
		BKXZ(D)	0261	P	S	U	1	N	*	I	T	D	0		IRIS 80	0.28	2000	60	60	
		0381															2000	100	100	
		0382																		
		0471																		
		BK(A)	0142	Z	P	R	U	1	V	*	C	D	0		IRIS 80	0.01				b
		0143																		

SUMMARY OF METHODS AND NUMERICS EMPLOYED ALPHABETIC BY GROUP COORDINATOR

Code to "Taxonomy of Numerical Methods" see pp. 1082-1083

Group Coordinator [Number]	Method	Case	(1)	(2)	(3)	(4)	(5)	(6)	(7)	(8)	(9)	(10)	(11)	(12)	Comp. Used	Time/Iter- ation/ Point [sec]	No. of Grid Points				Comments (see p.1094)		
																	x	y	z	s			
Covataix cont. [22]	MM(B)	0141	G	P	R	U	1	W	*	C	D	D	0	IRIS 80	0.01					< 2	b		
	MM(C)	0141																					
			0211																				
			0231																				
			0232																				
			0233	G	P	R	U	1	W	*	C	D	D	0	IRIS 80	0.01					< 2	b	
			0431																				
			0612																				
			8101																				
			8201																				
			8411																				
			8621																				
Delwert [47]	MSBC	0371																					
		0374AB																					
		0375B	G	P	R	U	1	*	I	X	D	D		IRIS 80									
		0376AB																					
		MSBC(B)	0371																				
		0374AB	G	P	R	U	1	*	I	X	D	D		IRIS 80									
Donaldson [21]	MSBC	8621	G	E	V	C	2	W	B	C	X	A		CDC 7600	0.0005	107	107			37-47			
		8623																			37		
		MSLC	0371																				
		0373ABCDE	G																				
		0374AB																					
		0375ABCDE	G																				
		0376AB																					
		MSLC(A)	0376B	G																			
		MSLC	0421	G	E	R	C	1	*	I	T	A	Q	0	VAX	0.025	40	63			30		
			P2(0422)																				
		MSTC	0311	G	P	R	C	1	*	C	T	D	D		VAX	0.1	100-200	30-50					
	MSTW	0141																					
		0241																					
		0242																					
		0244																					
		0612	G	P	R	C	1	P	C	T	D	D		VAX	0.1	100-200	30-50						
		8101																					
		8201																					
		8301																					
		8403																					
		8411																					

SUMMARY OF METHODS AND NUMERICS EMPLOYED ALPHABETIC BY GROUP COORDINATOR

Code to "Taxonomy of Numerical Methods" see pp. 1062-1083

Group Coordinator [Number]	Method	Case	(1) (2) (3) (4) (5) (6) (7) (8) (9) (10) (11) (12)	Inter- gral	D	Q	Comp. Used	Time/Iter- Point [sec]	No. of Grid Points			Comments (see p.1094)
									x	y	z	
Brewer [46]	ML	0441	Z E O O 2 N O I	176	15-20							d
Forsiger [45]	BS	0141										
	BN	0142										
		0143										
		0431										
		0612										
Ruh [19]	AKEC	0331	Z P R U L N B I M D	Q	U	IMH	4033					
Manjelić [18]	AKEX	0142	G P S U 1 N * I H L O	V			CDC		300-600	30		
		0143					CYNER 72					
	AKEX	0142	G P S U 1 N * I H L O	V			CYNER 72		300	33		e
		0143										
		0371										
Lauder [17 ³]		0373ABCDE										
		0374AB	G P R U 4 N * I X P				CDC					f
		0375ABCDE										
		0376AB										
		0141										
Huang [43]		0241	G P S U 1 N * I H L O				CDC		300-500	33		
		0244										
		0612										
		0101										
		8201										
Chang [17 ¹]		8631	G E R C 2 W F C T A				CDC	7600	0.00044	77	42	2
		0512	G E T K 2 N * I T A Q	U			CDC	7600	3.6×10^{-5}	14	10	37 (upstream)
		0512	G E T H 1 N * I T A Q	U			CDC	7600	3.6×10^{-5}	14	10	17 (downstream)
										14	10	37 (upstream)
										14	10	17 (downstream)
Demirdöğ [17 ²]		0375ABCDE										
		0376AB										
		0375BDE										
		0421	G E S H 1 N * I S L O	U			CDC	7600		28	28	8
		0422(F2)										
Lauder [17 ³]		0423(F3)										
		0261										
		0262										
		0375ABCDE										
		0376AB										
AKEX(C)		0331	G E S C U 1 N * I S L O	U			CDC	7600	0.5	27	31	1
		0421								42	42	

Summary of Methods and Metrics Employed Algebraic by Group Coordinator

Code to "Taxonomy of Numerical Methods" see pp. 1082-1083

Group Coordinator [Number]	Method	Case	(1)	(2)	(3)	(4)	(5)	(6)	(7)	(8)	(9)	(10)	(11)	(12)	Comp. Used	Time/Iteration/ Point [sec]	No. of Grid Points			Comments (see p. 1094)		
																	x	y	z			
Lauder [173]	AKKZ(D)	0142																				
		0143																				
		0231																				
		0232																				
		0233		G	P	S	C,U	L	M	B	I	M	L	O	O	CDC	0.001					1
		0311																				
		0381																				
		0382																				
		0612																				
		AKKZ(D)	0231																			
			0331																			
		AKKZ(E)	0421																			
	AKKZ(C)	0331																				
		0421																				
	AKKZ(B)	0142																				
		0143																				
		0211																				
		0231																				
		0232																				
		0233																				
		0311																				
		0382																				
		0612																				
	AKKZ(D)	0331																				
	RSTC(A)	8501																				
	RSTC(A)	8501																				
Bonnet [174]	SC	0441																				
		8621																				
		8623																				
		8631																				
		8691																				
Le Bailleur [42]	SC	0441																				
		8621																				
		8623																				
		8631																				
		8691																				
Manour [02]	AKKZ	0331																				
		0421																				
McDonald [41]	AKKZ	8601																				
	B1EX	0441																				
		0512																				
		8641																				
Mellor [39]	D5QZ	0331																				
		0421																				
		0431																				

SUMMARY OF METHODS AND NUMERICS EMPLOYED ALPHABETIC BY GROUP COORDINATOR

Code to "Taxonomy of Numerical Methods" see pp. 1082-1083

Group Coordinator [Number]	Method	Case	(1)	(2)	(3)	(4)	(5)	(6)	(7)	(8)	(9)	(10)	(11)	(12)	Comp. Used	Time/Iteration/ Point [sec]	No. of Grid Points				Comments (see p. 1094)
																	x	y	z	r	
Melnik [39]	SC	8621	Z	R	O	A	O	1	4	H	O	B	C	O	IBM 370-168		160	32		n	
Mc Nish [44]	MKKX	8101	G	E	V	K	Z	V	B	C	S	D			CDC 7600	0.00012	32	32			
		8201																			
	BOFX	8612	G	E	V	K	Z	V	B	C	S	D			CDC 7600	0.00009	32	32			
	MKKX	0421	Z	E	S	C	Z	N	I	S	L	F	U	VAX 11/780	0.0027	40	40				
Moore [01]	MKKX(A)	0421															40	40			
	BOFX	0141															13	10			
		0142															13	12			
		0143	Z	P	R	C	N	B	I	E	A	Q	O				13	12			
		0312															13	7			
	0612															13	12				
Moses [27]	KE	0141															50				
		0142															100	6	100		
		0421	Z	P	R	C	U	I	J	X	I	L	O		IBM 370	0.001-	100	6		o	
		0431														0.002	50	1			
		0441															40	40			
		0612															50				
Murphy [28]	MKKX	0141	G	E	H	H	M	O	*	M	D	Q	V		CDC 7600		22	31	1	P	
		0612															30	25			
	MKKX	0141	G	E	H	H	M	O	*	M	D	Q	V		CDC 7600		22	31	1	P	
		0612															30	25			
	BOFX	0141															22	31			
		0431	G	E	H	H	M	O	*	M	D	Q	V		CDC 7600		30	27	1	P	
		0612															30	25			
	BIKX	0141	G	E	H	H	M	O	*	M	D	Q	V		CDC 7600		22	31	1	P	
	0612															30	25				
Magamatsu [04]	BOFX	0141															59	32	2.37		
		0231															65	30	3.75		
		0232	G	P	T	C	Z	N	B	I	M	D	O	O	UNITVAC		65	30	3.73	q	
		0233															99	30	2.53		
	0612															23	32	1.25			
Orlandi [05]	BIKX	0141																			
		0142																			
		0143																			
		0241	G	P	R	C	Z	*	I	T	D				UNITVAC	0.008	40	40	0.7	r	
		0242													1100/22						
		0244																			
	0281																				
	0612																				

SUMMARY OF METHODS AND NUMERICS EMPLOYED ALPHAMETRIC BY GROUP COORDINATOR
 Code to "Taxonomy of Numerical Methods" see pp. 1082-1083

Group Coordinator [Number]	Method	Case	(1)	(2)	(3)	(4)	(5)	(6)	(7)	(8)	(9)	(10)	(11)	(12)	Comp. Used	Time/Iter- ation/ Point [sec]	No. of Grid Points			First y ⁺	Comments (see p. 1094)
																	x	y	z		
Fletcher [30]		0424(P4)																			
	BOLX	0141	G	P	R	X	Z	Q	*	I	M	L			MAS-AS6		300-400	90		0.6-1.2	
		0241																			
		0242																			
		0612																			
	BOLX(A)	0421	Z	P	R	H	1	Q		I	M	A	Q	V	MAS-AS6		104	130		1.2	t
	BOPZ	0421	Z	P	R	H	1	H	*	I	M	L,A		V	MAS-AS6		104	130		1.2	t
	BIEK	0421	Z	P	R	H	1	H	*	I	M	L,A			MAS-AS6		104	130		1.2	t
		0431																			
	BILZ	0431	G	P	R	H	1	Q	*	H	L				MAS-AS6		298	100		0.3	u
	BILX(A)	0421	Z	P	R	H	1	Q	*	I	M	A	Q	V	MAS-AS6	9.7	104	130			
		0431														per sweep	298	35-110		0.3	v
Pollard [06]	BKEZ	0421	G	E	T	H	1	H	*	I	S	A	O	U	Honey- well		34	24		40	
																	58	24			
																	87	38			
Bakich [31]	BOPX	8101	G	P	C	O	W			C	H	A			CDC 7600	0.0015		50		< 1.5	
		8201																50			< 1.5
		8661																30	45		< 3
		8671																47	50		< 4-9
Boadi [07]	AKBC	037AAB	G												Burroughs D7700						
		0375AC																			
		0376AB																			
	AKEX	0231	G	P	V	C	2	H	B	I	M	L			Burroughs D7700	0.0016	Ax =	100		0.5	
		0232															0.258				0.5
		0233																			0.5
	AKXZ	0231	G	P	V	C	2	N	B	I	M	L			Burroughs D7700		Ax =	0.58	40		
		0232																			0.58
		0233																			0.58
		0261																			0.057 1/2
		0263																			0.057 1/2
		0331																			0.28
	AKXZ(A)	0111	G	P	S	H	M	N	*	I	S	L	O		UNIVAC			20	20	Ax =	0.025H 89.5
		0112																15	20	Ax =	0.025H 52.3
		0113(P1)													1108			20	20	Ax =	0.05H 84
	BKXX	0141																			
		0211	G	P	V	C	2	N	B	I	M	L			Burroughs D7700	0.0015	Ax =	100		0.5	
		0241																			
		0242																			
		0244																			
		0281																			
		0612																			

SUMMARY OF METHODS AND NUMERICS EMPLOYED ALPHABETIC BY GROUP COORDINATOR

Code to "Taxonomy of Numerical Methods" see pp. 1082-1083

Group Coordinator [Number]	Method	Case	(1) (2) (3) (4) (5) (6) (7) (8) (9) (10) (11) (12)										Comp. Used	Time/Iter- ation/ Point [sec]	No. of Grid Points			Comments (see p. 1094)			
			G	P	S	H	M	N	*	I	S	L			O	Univac 1108	x		y	z	
Baddi (cont.) [07]	HEEZ	0311	G	P	S	H	M	N	*	I	S	L	O	Univac 1108	16	16	16	As = 0.05H	46.2		
	HEEZ(A)	0141																			
		0142																			
		0143																			
		0211	G	P	V	C	2	H	B	I	M	L	Burrroughs D7700	0.001	40	40	30				
		0381																			
		0382																			
		0471																			
		0612																			
		HEEZ(B)	0421	G	E	S	H	M	N	*	I	S	L	O	UNIVAC 1108	0.0035	32	32	49	x	
Baddi (cont.) [07]	HEEZ(C)	0312	G	E	S	H	M	N	*	I	S	L	O	U							
	HEEZ(D)	0422(P2)	G	E	S	H	M	N	B	I	T	A	O	U		17	14	71			
	HEEZ(E)	0423(P3)	G	E	S	H	M	N	B	I	T	A	O	U		35	23				
	HEEZ(F)	0142	G	P	R	C	2	H	F	I	N	P	O	Burrroughs B7700	0.001	As = 0.05H	41	50	y		
Smith [32]	HEEZ(G)	0143																			
	HEEZ(H)	0371																			
	HEEZ(I)	0372ABC																			
	HEEZ(J)	0373ABCDE	G											UNIVAC 1108						v	
	HEEZ(K)	0374AB																			
	HEEZ(L)	0376AB																			
Spalding [33]	HEEZ(M)	0141																			
	HEEZ(N)	0142																			
	HEEZ(O)	0143	G	P	E	T	U	I	W	O	C	I	N	P	Q	V	Perkin- Elmer 7-32	0.04			
	HEEZ(P)	0421																			
	HEEZ(Q)	0512																			
	HEEZ(R)	0612																			
Tases [09]	HEEZ(S)	0621	G	R	C	D	2	W	B	C	H	A					VAX	0.013	81	35	
	HEEZ(T)	0471	G	P	V	U	2	W	*	C	M	D					VAX 11/780		4000	200	
Vandromme [35]	HEEZ(U)	0381	G	P	V	U	2	N	*	C	N	D					VAX 11/780		4000	200	
	HEEZ(V)	0382																			

SUMMARY OF METHODS AND SERVICES EMPLOYED ALPHABETIC BY GROUP COORDINATOR

Code to "Taxonomy of Numerical Methods" see pp. 1082-1083

Group Coordinator [Number]	Method	Case	(1)	(2)	(3)	(4)	(5)	(6)	(7)	(8)	(9)	(10)	(11)	(12)	Comp. Used	Time/Iter- ation/ Point [sec]	No. of Grid Points			First y [*]	Comments (see p. 1094)			
																	x	y	z					
Viegas [36]	MKX	0471																60	50	100				
		8101																	80	36				
		8201																	80	36				
		8403																	27	44				
		8601	G	E	V	O	2	W	B	C	O	A				CDC 7600	0.001		38, 76	40, 40				
		8611																	129	50			< 0.2	
		8631																	80, 160	36, 40				
		8632																	100	40				
		8641																	85	82				
		8651																	89	50				
Whitfield [12]	MKX	8651																24	30	20				
		8663																24	30	20				
		8101	G	E	V	O	2	W	B	C	O	A				CDC 7600	0.0005		80	33			< 4	
		8201																	21	30	28		< 4	
Whitecox [37]	MKX	8661	G	E	V	O	2	W	B	C	O	A				CDC 7600	0.0005		24	30	20			
		8663																24	30	20				
		0141	Z	E	E	T	S	C	2	2	W	B	C	X			CRAY-1S	0.0055		500	32			
		0612																500						
		8621																126						
		0372ABC	G	E	C													100						
		0374AB																180	80					
		0376AB																170	85					
		0141																170	85					
		0142																190	85					
0143																170	85							
0241																170	85							
0242																50	80							
0244																100	70							
0311	G	P	T	U	2	W	B	C	H	D	O	U			URIVAC			250	280					
0371																300	225							
0612																300	225							
8101																300	225							
8201																50	230							
8403																50	230							
8411																1000	70							
8501																250	230							
8621																30	29							
8623																								
0421	G	E	R	H	I	W	*	I	M	D	F	U			URIVAC			30	29					
																1108								

KEY TO COMMENTS FOLLOW:

SUMMARY OF METHODS AND NUMERICS EMPLOYED ALPHAMETRIC BY GROUP COORDINATOR
KEY TO COMMENTS

Symbol	Meaning
a	$\Delta x = 0.1 \delta$.
b	Δx on the order of δ .
c	Same as MSLC but with different initial conditions.
d	75 panels to describe airfoil.
e	MEKZ used for comparison with ANKZ.
f	Standard Mangou-Katts fourth-order with adjustable step; approximately 100 steps in x-direction.
g	All other Cases/Method submitted by Group [17 ³].
h	Refer to Computer Summary (page 1399) for a discussion of methods applied to Cases 0261 and 0263.
i	Call Peclet Number.
j	Similar to ANKZ.
k	Upwind for integral thickness, sized for pressure.
l	28 streamwise, 13 half-planes symmetry.
m	Only vorticity conserved, only stream function solved using ADI.
n	Mixed elliptic/hyperbolic hybrid SLOW/direct iteration, forward marching.
o	One-dimensional pressure.
p	3-4 points $y^+ < 10$.
q	Constant pressure normal to wall, Keller box method. Step size $\eta = (U_0/vx)^{1/2} y = 0.05$.
r	Linearized in the streamwise direction.
s	Refer to Computer Summary (page 1484) for a discussion of method applied to Case 0424. See end of Summary for Table of Output.
t	Inviscid grid 51 x 51.
u	Inviscid region grid 51 x 51.
v	Inviscid region grid 51 x 48.
w	Simple Euler method.
x	First-order in regions of upwind differencing; second-order in regions of central differencing.
y	Numerical methods similar to MEKZ(A) with changed initial conditions.
z	Two-step predictor corrector, mixed implicit-explicit hybrid, time-like.

**INDEX OF
COMPUTOR GROUPS
BY GROUP NUMBER**

INDEX OF COMPUTER GROUPS BY GROUP NUMBER

Computer Group Number	Computer Group Coordinator	Other Members of Computer Group	Method	Cases
01	Moore, J.	J.G. Moore	BOPX	0141, 0142, 0143, 0512, 0612
02	Mansour, N.N.	T. Morel	BKEZ	0331, 0421
04	Nagamatsu, T.	-	BOPX	0141, 0231, 0232, 0233, 0612
05	Orlandi, P.	-	B1KX	0141, 0142, 0143, 0241, 0242, 0244, 0281, 0612
06	Pollard, A.	-	BKEZ	0421
07	Rodi, W.	I. Celik, A.O. Demuren, G. Scheurer, E. Shirani M.A. Leschziner, A.K. Rastogi	AKEC AKEK AKEZ AKEZ(A) BKEK BKEZ BKEZ(A) BKEZ(B) BKEZ(C) BKEZ(D) BKEZ(E) RSEC	0374AB, 0375AC, 0376AB 0231, 0232, 0233 0231, 0232, 0233, 0261, 0263, 0331 0111, 0112, 0113(P1) 0141, 0211, 0241, 0242 0244, 0281, 0612 0511 0141, 0142, 0143, 0211, 0311, 0381, 0382, 0471, 0612 0421 0512 0422(P2) 0142, 0143 0371, 0372ABC, 0373ABCDE, 0374AB, 0375ABCDE, 0376AB
09	Tassa, Y.	-	BOPX	8621
12	Whitfield, D.	A. Jameson, W. Schmidt	EE	0141, 0612, 8621
14	Mellor, G.L.	M.C. Celenligil	D5QZ	0331, 0421, 0431
17	Lauder, B.E.	S.M. Chang, T. Han, J.A.C. Humphrey I. Demirdzic, A.D. Gosman, R.I. Issa M.A. Leschziner, M. Sindir, A. Barba, R.W. Johnson, J.M. MacInnes, R.J. Mjolsness, N.G. Teku	BKEZ(G) BKEZ(I) BKEZ(F) BKEZ(H) AKEC(A) AKEC(C) AKEZ(B) AKEZ(D) AKEZ(E) BKEC(C) BKEZ(B) BKEZ(D) RSEC(A) RSEC(B) RSTC(A) RSTC(B)	0512 0512 0421 0422(P2), 0423(P3) 0375ABCDE, 0376AB 0331, 0421 0142, 0143, 0231, 0232, 0233, 0311, 0381, 0382, 0612 0231, 0331 0421 0331, 0421 0142, 0143, 0211, 0231, 0232, 0233, 0311, 0382, 0612 0331 0375ABCDE, 0376AB 0375BDE 8501 8501
17 ¹				
17 ²				
17 ³				
17 ⁴		J.P. Bonnet		

INDEX OF COMPUTER GROUPS BY GROUP NUMBER (cont.)

Computer Group Number	Computer Group Coordinator	Other Members of Computer Group	Method	Cases
18	Hanjalić, K.	M. Ivanović, R. Selimović, N. Stosić, S. Vasić	AKEZ BKEZ RSEC RSEN	0142, 0143 0142, 0143 0371, 0373ABCDE, 0374AB, 0375ABCDE, 0376AB 0141, 0241, 0244, 0371, 0612
19	Hah, C.	B. Lakshminarayan	AKEC	0331
21	Donaldson, C.duP.	B. Quinn, W.S. Lewellyn R.D. Sullivan R.I. Sykes, A.K. Varma	RSLC RSLC(A) RSLZ RSTC RSTN	0371, 0373ABCDE, 0374AB, 0375ABCDE, 0376AB 0376B 0421, 0422(P2) 0311 0141, 0241, 0242, 0244, 0612, 8101, 8201, 8301, 8403, 8411
22	Cousteix, J.	R. Houdeville D. Arnal	AOPX BKEK BKEK(A) BKEK(B) BKEK(C) BKEK(D) HN(A) HN(B) HN(C) RSEC RSEC(B)	0111, 0511, 0512 0141 0141, 0211, 0231, 0232, 0233, 0612 0231, 0232, 0233 0141 0261, 0381, 0382, 0471 0142, 0143 0141 0141, 0211, 0231, 0232, 0233, 0431, 0612, 8101, 8201, 8411, 8621 0371, 0374AB, 0375B, 0376AB 0371, 0374AB, 0375BDE, 0376AB
23 ¹ 23 ²	Chow, W.L.	A. Nakayama, D. Sharma C.M. Rhie, D. Sharma	AKEZ BKEZ	0111 0441
24	Birch, S.F.	-	BKEC BKEZ	0381 0311
27	Moses, H.L.	S.B. Thompson, J.M. Hill, R.R. Jones III	EE	0141, 0142, 0421, 0431, 0441, 0612
28	Murphy, J.D.	-	BKEK BKWX BOPX BIKK	0141, 0612 0141, 0612 0141, 0431, 0612 0141, 0612
30	Fletcher, P.H.	O.K. Kwon	BOLX BOLX(A) BOPX BIKK BILX BILX(A)	0141, 0241, 0242, 0612 0421 0421 0421, 0431 0431 0421, 0431

INDEX OF COMPUTER GROUPS BY GROUP NUMBER (cont.)

Computer Group Number	Computer Group Coordinator	Other Members of Computer Group	Method	Cases
31	Rakich, J.V.	J.C. Tannehill, I.K. Tree	BOPX	8101, 8201, 8661, 8671
32	Smith, P.D.	-	SG	0141, 0231, 0232, 0233, 0612, 8101, 8411, 8621
33	Spalding, D.B.	A.M. Abdelmeguid S.Y. Goh, J. Ilegbusi	BKEY	0141, 0142, 0143, 0421, 0512, 0612
35	Vandromme, D.D.	-	BKEX RSEC	0471 0381, 0382
36	Viegas, J.	C.C. Horstman, C. Hung	BOPX(A) BOPX(B) BKWX	8101, 8201 8661, 8663 0471, 8101, 8201, 8403 8601, 8611, 8631, 8632, 8641, 8651, 8663
37	Wilcox, D.C.	-	AKWC AKWX BKWY	0372ABC, 0374AB, 0376AB 0141, 0142, 0143, 0241, 0242, 0244, 0311, 0371, 0612, 8101, 8201, 8403, 8411, 8501, 8621, 8623 0421
39	Melnik, R.E.	-	SG	8621
41	McDonald, H.	-	BKEX BKX	8601 0441, 0512, 8641
42	LeBalleur, J.C.	-	SG	0441, 8621, 8623, 8631 8691
43	Hung, C.	-	BOPX	8101, 8201, 8631
44	Ha Minh, H.			
44 ¹		D.D. Vandromme, R.W. MacCormack	BKEX BOPX	8101, 8201 8612
44 ²		P. Chassaing, D.D. Vandromme	BKEZ BKEZ(A)	0421 0421
45	Ferziger, J.H.	J.G. Bardina A.A. Lyrio, R.C. Strawn	HG HN SG	0141 0142, 0143, 0431 0612
46	Dvorak, F.A.	B. Maskev	ML	0441
47	Deiwert, G.S.	-	BOPX	8621, 8623
50	Bailey, H.E.	-	BOPX	8621, 8623, 8691
52	Cambon, C.	J.P. Bertoglio D. Jeandel	2ED 2ED(A) 2ED(B)	0371, 0372ABC, 0373ABCDE 0374AB, 0375ABCDE, 0376AB 0371, 0373E, 0374AB, 0376AB 0376B

**INDEX
BY
METHOD**

INDEX BY METHOD

<u>Method</u>	<u>Case</u>	<u>Method</u>	<u>Case</u>
Integral Methods:			
2ED 52	0371, 0372ABC, 0373ABCDE, 0374AB, 0375ABCDE, 0376AB	AKWX 37	0141, 0142, 0143, 0241, 0242, 0244, 0311, 0371, 0612, 8101, 8201, 8403, 8411, 8501, 8621, 8623
2ED 52A	0371, 0373E, 0374AB, 0376AB	BOLX 30	0141, 0241, 0242, 0612
2ED 52B	0376B	BOLX 30A	0421
EE 12	0141, 0612, 8621	BOPX 01	0141, 0142, 0143, 0512, 0612
EE 27	0141, 0142, 0421, 0431, 0441, 0612	BOPX 04	0141, 0231, 0232, 0233, 0612
EG 45	0141	BOPX 09	8621
HN 22A	0142, 0143	BOPX 28	0141, 0431, 0612
HN 22B	0141	BOPX 30	0421
HN 22C	0141, 0211, 0231, 0232, 0233, 0431, 0612, 8101, 8201, 8411, 8621	BOPX 31	8101, 8201, 8661, 8671
HN 45	0142, 0143, 0431	BOPX 36A	8101, 8201
ML 46	0441	BOPX 36B	8661, 8663
SG 32	0141, 0231, 0232, 0233, 0612, 8101, 8411, 8621	BOPX 43	8101, 8201, 8631
SG 39	8621	BOPX 44	8612
SG 42	0441, 8621, 8623, 8631, 8691	BOPX 47	8621, 8623
SG 45	0612	BOPX 50	8621, 8623, 8691
Differential Methods:		BILX 30	0431
AOPX 22	0111, 0511, 0512	BILX 30A	0421, 0431
AKEC 07	0374AB, 0375AC, 0376AB	BIKX 05	0141, 0142, 0143, 0241, 0242, 0244, 0281, 0612
AKEC 17A	0375ABCDE, 0376AB	BIKX 28	0141, 0612
AKEC 17C	0331, 0421	BIKX 30	0421, 0431
AKEC 19	0331	BIKX 41	0441, 0512, 8641
AKEK 07	0231, 0232, 0233	BKEC 17C	0331, 0421
AKEZ 07	0231, 0232, 0233, 0261, 0263, 0331	BKEC 24	0381
AKEZ 07A	0111, 0112, 0113(P1)	BKEK 07	0141, 0211, 0241, 0242, 0244, 0281, 0612
AKEZ 17B	0142, 0143, 0231, 0232, 0233, 0311, 0381, 0382, 0612	BKEK 22	0141
AKEZ 17D	0231, 0331	BKEK 22A	0141, 0211, 0231, 0232, 0233, 0612
AKEZ 17E	0421	BKEK 22B	0231, 0232, 0233
AKEZ 18	0142, 0143	BKEK 22C	0141
AKEZ 23	0111	BKEK 22D	0261, 0381, 0382, 0471
AKWC 37	0372ABC, 0374AB, 0376AB	BKEK 28	0141, 0612
		BKEK 35	0471
		BKEK 41	8601

INDEX BY METHOD (cont.)

Method	Case	Method	Case
BKEY 44	8101, 8201	BKWX 28	0141, 0612
BKEY 33	0141, 0142, 0143, 0421, 0512, 0612	BKWX 36	0471, 8101, 8201, 8403, 8601, 8661, 8631, 8632, 8641, 8651, 8663
BKEY 02	0331, 0421	BKWX 37	0421
BKEY 06	0421	D5QZ 14	0331, 0421, 0431
BKEY 07	0511	RSEC 07	0371, 0372ABC, 0373ABCDE, 0374AB, 0375ABCDE, 0376AB
BKEY 07A	0141, 0142, 0143, 0211, 0311, 0381, 0382, 0471, 0612	RSEC 17A	0375ABCDE, 0376AB
BKEY 07B	0421	RSEC 17B	0375 BDE
BKEY 07C	0512	RSEC 18	0371, 0373ABCDE, 0374AB, 0375ABCDE, 0376AB
BKEY 07D	0422(P2)	RSEC 22	0371, 0374AB, 0375B, 0376AB
BKEY 07E	0142, 0143	RSEC 22B	0371, 0374AB, 0375BDE, 0376AB
BKEY 17B	0142, 0143, 0211, 0231, 0232, 0233, 0311, 0382, 0612	RSEC 35	0381, 0382
BKEY 17D	0331	RSEN 18	0141, 0241, 0244, 0612
BKEY 17F	0421	RSLC 21	0371, 0373ABCDE, 0374AB, 0375ABCDE, 0376AB
BKEY 17G	0512	RSLC 21A	0376B
BKEY 17H	0422(P2), 0423(P3)	RSLZ 21	0421, 0422(P2)
BKEY 17I	0512	RSTC 17A	8501
BKEY 18	0142, 0143	RSTC 17B	8501
BKEY 23	0441	RSTC 21	0311
BKEY 24	0311	RSTN 21	0141, 0241, 0242, 0244, 0612, 8101, 8201, 8301, 8403, 8411
BKEY 44	0421		
BKEY 44A	0421		

**INDEX OF PLATES
BY PLATE NUMBER
AND
CASE NUMBER**

INDEX TO PLATES BY PLATE NUMBER AND CASE NUMBER

Plate Number	Case No.	Plot No. (Vol. I)	Method	Page Number
1	0111	1	AOPX 22, AKEZ 07A, AKEZ 23	1115
		2	AOPX 22, AKEZ 07A, AKEZ 23	
		3	AOPX 22, AKEZ 07A, AKEZ 23	
2		4	AOPX 22, AKEZ 07A, AKEZ 23	1116
		5	AOPX 22, AKEZ 07A, AKEZ 23	
3		6	AOPX 22, AKEZ 07A, AKEZ 23	1117
		7	AOPX 22, AKEZ 07A, AKEZ 23	
		8	AOPX 22, AKEZ 07A, AKEZ 23	
4		9	AOPX 22, AKEZ 07A, AKEZ 23	1118
		10	AOPX 22, AKEZ 07A, AKEZ 23	
		11	AOPX 22, AKEZ 07A, AKEZ 23	
5		12	AOPX 22, AKEZ 07A, AKEZ 23	1119
		13	AOPX 22, AKEZ 07A, AKEZ 23	
		14	AOPX 22, AKEZ 07A, AKEZ 23	
6		15	AOPX 22, AKEZ 07A, AKEZ 23	1120
		16	AOPX 22, AKEZ 07A, AKEZ 23	
		17	AOPX 22, AKEZ 07A, AKEZ 23	
7		18	AOPX 22, AKEZ 07A, AKEZ 23	1121
		19	AOPX 22, AKEZ 07A, AKEZ 23	
See also Plate 187				
8	0112	1	AKEZ 07A	1122
		2	AKEZ 07A	
		3	AKEZ 07A	
		4	AKEZ 07A	
		5	AKEZ 07A	
		6	AKEZ 07A	
		7	AKEZ 07A	
		8	AKEZ 07A	
		9	AKEZ 07A	
Pl(0113) See Plate 179				
9	0141	1	HN 22B, HN 22C, SG 32, AKWX 37, BOLX 30, BOPX 28, B1KX 05, BKEZ 22A, BKEY 22C, BKEY 33	1123
10			EE 12, EE 27, HG 45, BOPX 01, BOPX 04, B1KX 28, BKEY 07, BKEY 28, BKEZ 07A, BKWX 28, RSEN 18, RSTN 21,	1124
11		2	AKWX 37, BOLX 30, B1KX 05, BKEY 33	1125
12			BOPX 28, B1KX 28, BKEZ 22A, BKEY 28, BKEZ 07A, BKWX 28	1126
13			EE 12, BOPX 01, BOPX 04, B1KX 05, BKEY 07, BKEY 22, RSEN 18, RSTN 21,	1127
14		3	EE 12, BOPX 28, B1KX 05, B1KX 28, BKEY 28, BKEY 33, BKWX 28	1128
15			BOPX 01, BOPX 04, BKEY 07, BKEY 22A, BKEY 22C, BKEZ 07A, RSEN 18, RSTN 21,	1129
16			AKWX 37, BOLX 30, B1KX 05,	1130

INDEX TO PLATES BY PLATE NUMBER AND CASE NUMBER (cont.)

Plate Number	Case No.	Plot No. (Vol. I)	Method	Page Number
17		4	AKWX 37, BOLX 30, BOPX 01, BOPX 04, BOPX 28, BIKX 28, BKEK 22C, BKEK 28, BKEY 33, BKWX 28	1131
18	0141	4	EE 12, EE 27, HG 45, HN 22B, HN 22C, BIKX 05, BKEK 07, BKEK 22A, BKEZ 07A, RSEN 18, RSTN 21	1132
19	0142	1	EE 27, HN 22A, HN 45, AKEZ 17B, AKEZ 18, AKWX 37, BOPX 01, BIKX 05, BKEY 33, BKEZ 07A, BKEZ 07E, BKEZ 17B, BKEZ 18,	1133
20		2	EE 27, HN 22A, HN 45, AKEZ 17B, AKEZ 18, BOPX 01, BIKX 05, BKEY 33, BKEZ 07A, BKEZ 17B	1134
21		3	EE 27, HN 45, AKEZ 17B, AKEZ 18, AKWX 37, BOPX 01, BIKX 05, BKEY 33, BKEZ 07A, BKEZ 17B, BKEZ 18	1135
22		4	AKEZ 17B, AKEZ 18, AKWX 37, BOPX 01, BIKX 05, BKEY 33, BKEZ 07A, BKEZ 18	1136
23	0143	1	HN 22A, HN 45, AKEZ 17B, AKEZ 18, AKWX 37, BOPX 01, BIKX 05, BKEY 33, BKEZ 07A, BKEZ 07E, BKEZ 17B	1137
24		2	HN 22A, HN 45, AKEZ 17B, AKEZ 18, BOPX 01, BKEY 33, BKEZ 07A, BKEZ 17B	1138
25		3	HN 45, AKEZ 17B, AKEZ 18, AKWX 37, BOPX 01, BIKX 05, BKEY 33, BKEZ 07A, BKEZ 17B, BKEZ 18	1139
26		4	AKEZ 17B, AKEZ 18, AKWX 37, BOPX 01, BIKX 05, BKEY 33, BKEZ 07A, BKEZ 18	1140
27	0211	1	HN 22C, BKEK 07, BKEK 22A, BKEZ 07A, BKEZ 17B	1141
28	0231	1	HN 22C, SG 32, AKEK 07, AKEZ 07, AKEZ 17B, BOPX 04, BKEK 22A, BKEK 22B, BKEZ 17B	1142
29		2	HN 22C, SG 32, AKEK 07, AKEZ 07, AKEZ 17B, BOPX 04, BKEK 22A, BKEK 22B, BKEZ 17B	1143
30		3	HN 22C, SG 32, AKEK 07, AKEZ 07, AKEZ 17B, BOPX 04, BKEK 22A, BKEK 22B	1144
31		4	HN 22C, AKEK 07, AKEZ 07, AKEZ 17B, BOPX 04, BKEK 22A, BKEK 22B	1145
32		5	AKEZ 07, AKEZ 17B	1146
		6	AKEZ 07B, AKEK 07, AKEZ 17B, BOPX 04, BKEK 22A, BKEK 22B	
33	0232	1	HN 22C, SG 32, AKEK 07, AKEZ 07, AKEZ 17B, BOPX 04, BKEK 22A, BKEK 22B, BKEZ 17B	1147
34		2	HN 22C, SG 32, AKEK 07, AKEZ 07, AKEZ 17B, BOPX 04, BKEK 22A, BKEK 22B, BKEZ 17B	1148
35		3	HN 22C, SG 32, AKEK 07, AKEZ 07, AKEZ 17B, BOPX 04, BKEK 22A, BKEK 22B, BKEZ 17B	1149
36		4	HN 22C, AKEK 07, AKEZ 07, AKEZ 17B, BOPX 04, BKEK 22A, BKEK 22B	1150
		5	AKEZ 07B, AKEZ 17B	

INDEX TO PLATES BY PLATE NUMBER AND CASE NUMBER (cont.)

Plate Number	Case No.	Plot No. (Vol. I)	Method	Page Number
37		6	AKEX 07, AKEZ 07, AKEZ 17B, BOPX 04, BKEK 22A, BKEK 22B	1151
38	0233	1	HN 22C, SG 32, AKEX 07, AKEZ 07, AKEZ 17B, BOPX 04, BKEK 22A, BKEK 22B, BKEZ 17B	1152
		2	HN 22C, SG 32, AKEX 07, AKEZ 07, AKEZ 17B, BOPX 04, BKEK 22A, BKEK 22B, BKEZ 17B	
39		3	HN 22C, AKEX 07, AKEZ 07, AKEZ 17B, BOPX 04, BKEK 22A, BKEK 22B	1153
40		4	AKEZ 07, AKEZ 17B, BOPX 04	1154
		5	AKEZ 07	
41		6	AKEZ 07	1155
		7	AKEX 07, AKEZ 07B, AKEZ 17B, BOPX 04, BKEK 22A, BKEK 22B	
42	0241	1	AKWX 37, BOLX 30, B1KX 05, BKEK 07, RSEN 18, RSTN 21	1156
		2	AKWX 37, BOLX 30, B1KX 05, BKEK 07, RSEN 18, RSTN 21	
43		3	AKWX 37, BOLX 30, B1KX 05, BKEK 07, RSEN 18, RSTN 21	1157
		4	AKWX 37, BOLX 30, B1KX 05, BKEK 07, RSEN 18, RSTN 21	
44	0242	1	AKWX 37, BOLX 30, B1KX 05, BKEK 07, RSTN 21	1158
		2	AKWX 37, BOLX 30, B1KX 05, BKEK 07, RSTN 21	
45		3	AKWX 37, BOLX 30, B1KX 05, BKEK 07, RSTN 21	1159
		4	AKWX 37, BOLX 30, B1KX 05, BKEK 07, RSTN 21	
46	0244	1	AKWX 37, B1KX 05, BKEK 07, RSEN 18, RSTN 21	1160
		2	AKWX 37, B1KX 05, RSEN 18, RSTN 21	
47		3	AKWX 37, RSEN 18, RSTN 21	1161
		4	AKWX 37, B1KX 05, BKEK 07, RSEN 18, RSTN 21	
48	0261	1	AKEZ 07, BKEK 22D	1162
		2	AKEZ 07, BKEK 22D	
		3	AKEZ 07, BKEK 22D	
		4	AKEZ 07, BKEK 22D	
49		6	AKEZ 07	1163
		11	AKEZ 07	
50	0263	1	AKEZ 07	1164
		2	AKEZ 07	
		5	AKEZ 07	
51	0281	1	B1KX 05, BKEK 07	1165
		2	B1KX 05, BKEK 07	
		3	BKEK 07	
		4	B1KX 05, BKEK 07	
		5	B1KX 05, BKEK 07	
		6	B1KX 05	
52	0311	1	AKEZ 17B, AKWX 37, BKEC 24, BKEZ 07A, BKEZ 17B, RSTC 21	1166
53	0331	1	AKEC 17C, AKEC 19, AKEZ 07, AKEZ 17D, BKEC 17C, BKEZ 02, BKEZ 17D, D5QZ 14	1167

INDEX TO PLATES BY PLATE NUMBER AND CASE NUMBER (cont.)

Plate Number	Case No.	Plot No. (Vol. I)	Method	Page Number
54		2	AKEC 17C, AKEC 19, AKEZ 07, AKEZ 17D, BKEZ 02, D5QZ 14	1168
55	0331	3	AKEC 17C, AKEC 19, AKEZ 07, AKEZ 17D, BKEZ 02, D5QZ 14	1169
56		4	AKEC 17C, AKEC 19, AKEZ 07, AKEZ 17D, BKEC 17C, BKEZ 02, BKEZ 17D, D5QZ 14	1170
57		5	AKEC 17C, AKEC 19, AKEZ 07, AKEZ 17D, BKEZ 02, D5QZ 14	1171
58		6 7	AKEC 17C, AKEC 19, AKEZ 07, AKEZ 17D, BKEZ 02, D5QZ 14	1172
59	0371	1	2ED 52, 2ED 52A, AKWC 37, RSEC 18, RSEC 07, RSEC 22, RSEC 22B, RSLC 21	1173
60	0372A	1	2ED 52, AKWC 37, RSEC 07	1174
61	0372B	1 2	2ED 52, AKWC 37, RSEC 07 2ED 52, AKWC 37, RSEC 07	1175
62	0372C	1 2	2ED 52, AKWC 37, RSEC 07 2ED 52, AKWC 37, RSEC 07	1176
63	0373A	1 2	2ED 52, RSEC 07, RSEC 18, RSLC 21 2ED 52, RSEC 07, RSEC 18, RSLC 21	1177
64	0373B	1 2	2ED 52, RSEC 07, RSEC 18, RSLC 21 2ED 52, RSEC 07, RSEC 18, RSLC 21	1178
65	0373C	1	2ED 52, RSEC 07, RSEC 18, RSLC 21	1179
66		2	2ED 52, RSEC 07, RSEC 18, RSLC 21	1180
67	0373D	1 2	2ED 52, RSEC 07, RSEC 18, RSLC 21 2ED 52, RSEC 07, RSEC 18, RSLC 21	1181
68	0373E	1	2ED 52, 2ED 52A, RSEC 07, RSEC 18, RSLC 21	1182
69		2	2ED 52, 2ED 52A, RSEC 07, RSEC 18, RSLC 21	1183
70		3	2ED 52, 2ED 52A, RSEC 07, RSEC 18, RSLC 21	1184
71	0374A	1	2ED 52, 2ED 52A, AKEC 07, AKWC 37, RSEC 07, RSEC 18, RSEC 22, RSEC 22B, RSLC 21	1185
72		2	2ED 52, 2ED 52A, AKEC 07, AKWC 37, RSEC 07, RSEC 18, RSEC 22, RSEC 22B, RSLC 21	1186
73		3	2ED 52, 2ED 52A, AKEC 07, AKWC 37, RSEC 07, RSEC 18, RSEC 22, RSEC 22B, RSLC 21	1187
74	0374B	1	2ED 52, 2ED 52A, AKEC 07, AKWC 37, RSEC 07, RSEC 18, RSEC 22, RSEC 22B, RSLC 21	1188
75		2	2ED 52, 2ED 52A, AKEC 07, AKWC 37, RSEC 07, RSEC 18, RSEC 22, RSEC 22B, RSLC 21	1189
76		3	2ED 52, 2ED 52A, AKEC 07, AKWC 37, RSEC 07, RSEC 18, RSEC 22, RSEC 22B, RSLC 21	1190
77	0375A	1	2ED 52, AKEC 07, AKEC 17A, RSEC 07, RSEC 17A, RSEC 18, RSLC 21	1191

INDEX TO PLATES BY PLATE NUMBER AND CASE NUMBER (cont.)

Plate Number	Case No.	Plot No. (Vol. I)	Method	Page Number
78		2	2ED 52, AKEC 07, AKEC 17A, RSEC 07, RSEC 17A, RSEC 18, RSLC 21	1192
79	0375B	1	2ED 52, AKEC 17A, RSEC 07, RSEC 17A, RSEC 17B, RSEC 18, RSEC 22, RSEC 22B, RSLC 21	1193
80		2	2ED 52, AKEC 17A, RSEC 07, RSEC 17A, RSEC 17B, RSEC 18, RSEC 22, RSEC 22B, RSLC 21	1194
81	0375C	1	2ED 52, AKEC 07, AKEC 17A, RSEC 07, RSEC 17A, RSEC 18, RSLC 21	1195
82		2	2ED 52, AKEC 07, AKEC 17A, RSEC 07, RSEC 17A, RSEC 18, RSLC 21	1196
83	0375D	1	2ED 52, AKEC 17A, RSEC 07, RSEC 17A, RSEC 17B, RSEC 18, RSEC 22A, RSEC 22B, RSLC 21	1197
84		2	2ED 52, AKEC 17A, RSEC 07, RSEC 17A, RSEC 17B, RSEC 18, RSEC 22A, RSEC 22B, RSLC 21	1198
85	0375E	1	2ED 52, AKEC 17A, RSEC 07, RSEC 17A, RSEC 17B, RSEC 18, RSEC 22A, RSEC 22B, RSLC 21	1199
86		2	2ED 52, AKEC 17A, RSEC 07, RSEC 17A, RSEC 17B, RSEC 18, RSEC 22A, RSEC 22B, RSLC 21	1200
87	0376A	1	2ED 52, 2ED 52A, AKEC 07, AKEC 17A, AKWC 37, RSEC 07, RSEC 17A, RSEC 18, RSEC 22, RSEC 22B, RSLC 21	1201
88		2	2ED 52, 2ED 52A, AKEC 07, AKEC 17A, AKWC 37, RSEC 07, RSEC 17A, RSEC 18, RSEC 22, RSEC 22B, RSLC 21	1202
89		3	2ED 52, 2ED 52A, AKEC 07, AKEC 17A, AKWC 37, RSEC 07, RSEC 17A, RSEC 18, RSEC 22, RSEC 22B, RSLC 21	1203
90		4	2ED 52, 2ED 52A, AKEC 07, AKEC 17A, AKWC 37, RSEC 07, RSEC 17A, RSEC 18, RSEC 22, RSEC 22B, RSLC 21	1204
91	0376B	1	AKEC 07, AKEC 17A, RSEC 07, RSEC 17A, RSEC 18, RSEC 22, RSEC 22B, RSLC 21	1205
92		2	2ED 52, 2ED 52A, 2ED 52B, AKWC 37, RSLC 21A 2ED 52, 2ED 52A, 2ED 52B, AKWC 37, RSLC 21A	1206
93			AKEC 07, AKEC 17A, RSEC 07, RSEC 17A, RSEC 18, RSEC 22, RSEC 22B, RSLC 21	1207
94		3	AKEC 07, AKEC 17A, RSEC 07, RSEC 17A, RSEC 18, RSEC 22, RSEC 22B, RSLC 21	1208
95		4	2ED 52, 2ED 52A, 2ED 52B, AKWC 37, RSLC 21A 2ED 52, 2ED 52A, 2ED 52B, AKWC 37, RSLC 21A	1209
96			AKEC 07, AKEC 17A, RSEC 07, RSEC 17A, RSEC 18, RSEC 22, RSEC 22B, RSLC 21	1210
97	0381	1	AKEZ 17B, BKEC 24, BKEX 22D, BKEZ 07A, RSEC 35,	1211
		2	AKEZ 17B, BKEC 24, BKEX 22D, BKEZ 07A, RSEC 35	
98		3	AKEZ 17B, RSEC 35	1212
		4	AKEZ 17B, RSEC 35	
		5	RSEC 35	
		6	RSEC 35	

INDEX TO PLATES BY PLATE NUMBER AND CASE NUMBER (cont.)

Plate Number	Case No.	Plot No. (Vol. I)	Method	Page Number
99	0382	1	AKEZ 17B, BKEK 22D, BKEZ 07A, BKEZ 17B, RSEC 35	1213
		2	AKEZ 17B, BKEK 22D, BKEZ 07A, BKEZ 17B, RSEC 35	
100		3	AKEZ 17B, RSEC 35	1214
		4	AKEZ 17B, RSEC 35	
		5	RSEC 35	
		6	RSEC 35	
101	0421	1	EE 27, BOLX 30A, BOPX 30, B1KX 30, B1LX 30A, BKEY 33, BKEZ 02, BKEZ 06, BKEZ 07B, BKEZ 44, D5QZ 14	1215
102			AKEC 17C, AKEZ 17E, BKEC 17C, BKEZ 17F, BKEZ 44A, BKWY 37	1216
103		2	AKEC 17C, AKEZ 17E, B1KX 30, B1LX 30A, BKEZ 02, BKEZ 07B, BKEZ 17C, BKEZ 44, BKEZ 44A, BOLX 30A, BOPX30	1217
104		2B	BOLX 30A, BOPX 30, B1KX 30, B1LX 30A, BKEY 33, BKEZ 02, BKEZ 06, BKEZ 07B, BKEZ 17F, BKWY 37, D5QZ 14	1218
105		3	EE 27, BOLX 30A, BOPX 30, B1KX 30, B1LX 30A, BKEY 33, BKEZ 02, BKEZ 06, BKEZ 07B, BKEZ 44, D5QZ 14, RSLZ 21	1219
106			AKEZ 17C, AKEZ 17E, BKEZ 17C, BKEZ 17F, BKEZ 44A, BKWY 37	1220
107		4	AKEZ 17C, AKEZ 17E, BKEZ 17C, BKEZ 17F, BKEZ 44A, BKWY 37	1221
108			BOLX 30A, B1KX 30, B1KX 30A, B1LX 30A, BKEY 33, BKEZ 02, BKEZ 06, BKEZ 07B, BKEZ 44, D5QZ 14, RSLZ 21	1222
	P2(0422)		See Plate 180	
	P3(0423)		See Plate 184	
109	0431	1	EE 27, HN 22C, HN 45, BOPX 28, B1LX 30, B1LX 30A, D5QZ 14	1223
110		2	HN 22C, BOPX 28, B1LX 30, B1LX 30A, D5QZ 14	1224
111		3	EE 27, HN 22C, HN 45, BOPX 28, B1LX 30, B1LX 30A, D5QZ 14	1225
112		4	EE 27, HN 22C, HN 45, BOPX 28, B1LX 30, B1LX 30A, D5QZ 14	1226
		5	D5QZ 14	
113		6	BOPX 28, B1LX 30, B1LX 30A, D5QZ 14	1227
		7	D5QZ 14	
114	0441	1	EE 27, ML 46, SG 42, B1KX 41, BKEZ 23	1228
		2	B1KX 41, BKEZ 23	
115			EE 27, SG 42	
		3	B1KX 41, BKEZ 23	1229
		4	BKEZ 23	
		5	BKEZ 23	
116		6	SG 42, B1KX 41, BKEZ 23	1230

INDEX TO PLATES BY PLATE NUMBER AND CASE NUMBER (cont.)

Plate Number	Case No.	Plot No. (Vol. I)	Method	Page Number
117	0471	1	BKEX 22D, BKEX 35, BKEZ 07A, BKWX 36	1231
		2	BKEX 22D, BKEX 35, BKEZ 07A, BKWX 36	
118		3	BKEX 22D, BKEX 35, BKEZ 07A, BKWX 36	1232
		4	BKEX 35, BKEZ 07A, BKWX 36	
119	0471	5	BKEX 35, BKEZ 07A, BKWX 36	1233
		6	BKEX 35, BKEZ 07A, BKWX 36	
		7	BKEX 35, BKEZ 07A, BKWX 36	
120		8	BKEX 35, BKEZ 07A, BKWX 36	1234
		9	BKEX 35, BKEZ 07A, BKWX 36	
		10	BKWX 36	
		11	BKWX 36	
		12	BKWX 36	
121	0511	1	AOPX 22, BKEZ 07	1235
		2	AOPX 22, BKEZ 07	
		3	AOPX 22, BKEZ 07	
122		4	AOPX 22, BKEZ 07	1236
		5	AOPX 22, BKEZ 07	
		6	AOPX 22, BKEZ 07	
123		7	AOPX 22, BKEZ 07	1237
		8	AOPX 22, BKEZ 07	
		9	AOPX 22, BKEZ 07	
124		10	AOPX 22, BKEZ 07	1238
		11	AOPX 22, BKEZ 07	
		12	AOPX 22, BKEZ 07	
125		13	AOPX 22, BKEZ 07	1239
		14	AOPX 22, BKEZ 07	
126	0512	1	AOPX 22, BOPX 01, B1KX 41, BKEY 33, BKEZ 07C, BKEZ 17G, BKEZ 17I	1240
127		2	AOPX 22, BOPX 01, B1KX 41, BKEY 33, BKEZ 07C, BKEZ 17G, BKEZ 17I	1241
128		3	AOPX 22, BOPX 01, B1KX 41, BKEY 33, BKEZ 07C, BKEZ 17G, BKEZ 17I	1242
129		4	AOPX 22, BOPX 01, B1KX 41, BKEY 33, BKEZ 07C, BKEZ 17G, BKEZ 17I	1243
130		5	AOPX 22, BOPX 01, B1KX 41, BKEY 33, BKEZ 07C, BKEZ 17G	1244
131		6	AOPX 22, BOPX 01, B1KX 41, BKEY 33, BKEZ 07C, BKEZ 17G	1245
132		7	AOPX 22, BOPX 01, B1KX 41, BKEY 33	1246
		8	AOPX 22, BOPX 01, B1KX 41, BKEY 33	
133	0612	1	EE 12, EE 27, HN 22C, SG 32, SG 45, AKEZ 17B, B1KX 28, RSEN 18, RSTN 21,	1247
134			AKWX 37, BOLX 30, BOPX 01, BOPX 04, BOPX 28, B1KX 05, BKEX 07, BKEX 22A, BKEX 28, BKEY 33, BKEZ 07A, BKWX 28	1248
135		2	AKWX 37, BOLX 30, BOPX 01, BOPX 04, BOPX 28, B1KX 05, BKEX 07, BKEX 22A, BKEX 28, BKEY 33, BKEZ 07A, BKWX 28	1249

INDEX TO PLATES BY PLATE NUMBER AND CASE NUMBER (cont.)

Plate Number	Case No.	Plot No. (Vol. I)	Method	Page Number
136			EE 12, EE 27, HN 22C, SG 32, SG 45, AKEZ 17B, BIKX 28, BKEZ 17B, RSEN 18, RSTN 21	1250
137		3	EE 27, HN 22C, SG 32, SG 45, AKEZ 17B, BKEZ 17B, RSEN 18, RSTN 21	1251
138			EE 12, AKWX 37, BOLX 30, BOPX 01, BOPX 04, BOPX 28, BIKX 05, BIKX 28, BKEK 07, BKEK 22A, BKEK 28, BKEY 33, BKEZ 07A, BKWX 28	1252
139	8101	1	HN 22C, SG 32, AKWX 37, BOPX 31, BOPX 36A, BOPX 43, BKWX 36, RSTN 21	1253
140		2 A	AKWX 37, BOPX 31, BOPX 36A, BKWX 36 BOPX 43, BKEK 44, RSTN 21	1254
141		B 3	AKWX 37, BOPX 36A, BOPX 43, BKWX 36 BKEK 44, RSTN 21	1255
142	8201	1 2	HN 22C, AKWX 37, BOPX 31, BOPX 36A, BOPX 43, BKEK 44 BKWX 36, RSTN 21 BKEK 44	1256
143		A	AKWX 37, BOPX 36A, BOPX 43, BKWX 36, RSTN 21	1257
144	8301	1 2 3	RSTN 21 RSTN 21 RSTN 21	1258
145	8403	1 2 3	AKWX 37, BKWX 36, RSTN 21 AKWX 37, BKWX 36, RSTN 21 AKWX 37	1259
146		4 5 6	AKWX 37, BKWX 36, RSTN 21 AKWX 37, BKWX 36, RSTN 21 AKWX 37, BKWX 36, RSTN 21	1260
147		7 8 9	AKWX 37, BKWX 36, RSTN 21 AKWX 37, BKWX 36, RSTN 21 AKWX 37, BKWX 36, RSTN 21	1261
148		10 11	AKWX 37, BKWX 36, RSTN 21 AKWX 37, BKWX 36, RSTN 21	1262
149	8411	1 2 3	HN 22C, SG 32, AKWX 37, RSTN 21 HN 22C, SG 32, AKWX 37, RSTN 21 HN 22C, SG 32, AKWX 37, RSTN 21	1263
150		4	AKWX 37, RSTN 21	1264
151	8501	1	AKWC 37, RSTC 17A, RSTC 17B	1265
152	8601	1 2 3 4 5 6 7 8	BKEK 41, BKWX 36 BKWX 36 BKWX 36 BKWX 36 BKWX 36 BKWX 36 BKWX 36 BKEK 41, BKWX 36	1266

INDEX TO PLATES BY PLATE NUMBER AND CASE NUMBER (cont.)

Plate Number	Case No.	Plot No. (Vol. I)	Method	Page Number
153	8601	9	BKWX 36	1267
		10	BKWX 36	
		11	BKWX 36	
153		12	BKWX 36	
		13	BKWX 36	
		14	BKWX 36	
		15	BKEX 41, BKWX 36	
154		16	BKEX 41, BKWX 36	
155	8611	1	BKWX 36	1268
		2	BKWX 36	
		3	BKWX 36	
		4	BKWX 36	
156	8612	1	BOPX 44	1269
		2	BOPX 44	
		3	BOPX 44	
		4	BOPX 44	
157	8621	1	EE 12, HN 22C, SG 32, SG 39, SG 42, AKWX 37, BOPX 50	1270
158		2	EE 12, HN 22C, SG 32, SG 39, SG 42, AKWX 37, BOPX 47, BOPX 50	1271
159		3	EE 12, HN 22C, SG 32, SG 39, SG 42, AKWX 37, BOPX 09, BOPX 47, BOPX 50	1272
160		4	SG 32, SG 39, SG 42, BOPX 09, BOPX 47, BOPX 50	1273
161		5	EE 12, SG 32, SG 39, SG 42, BOPX 47, BOPX 50	1274
162		6	BOPX 50	1275
163			SG 32, SG 39, SG 42, BOPX 47	1276
164		7	EE 12, SG 32, SG 39, SG 42, BOPX 47, BOPX 50	1277
165		8	SG 32, SG 39, SG 42, BOPX 09, BOPX 47, BOPX 50	1278
166	8623	1	SG 42, AKWX 37, BOPX 47, BOPX 50	1279
		2	SG 42, AKWX 37, BOPX 47, BOPX 50	
		3	SG 42, AKWX 37, BOPX 47, BOPX 50	
167		4	SG 42, AKWX 37, BOPX 47, BOPX 50	1280
		5	AKWX 37, BOPX 47, BOPX 50	
		6	AKWX 37, BOPX 47, BOPX 50	
168		7	SG 42, BOPX 47, BOPX 50	1281
169	8631	1	SG 42, BOPX 43, BKWX 36	1282
		2	SG 42, BOPX 43, BKWX 36	1283
		3	BKWX 36, BOPX 43	
170		4	SG 42, BOPX 43, BKWX 36	1284
		5	BKWX 36, BOPX 43	
171	8632	1	BKWX 36	1285
		2	BKWX 36	
		3	BKWX 36	

INDEX TO PLATES BY PLATE NUMBER AND CASE NUMBER (cont.)

Plate Number	Case No.	Plot No. (Vol. I)	Method	Page Number
172	8641	1	B1KX 41, BKWX 36	1286
		2	BKWX 36	
		3	B1KX 41, BKWX 36	
		4	B1KX 41, BKWX 36	
173	8651	1	BKWX 36	1287
		2	BKWX 36	
		3	BKWX 36	
		4	BKWX 36	
174	8661	1	BOPX 31, BOPX 36B	1288
		2	BOPX 31, BOPX 36B	
		3	BOPX 31, BOPX 36B	
		4	BOPX 31, BOPX 36B	
		5	BOPX 31, BOPX 36B	
175	8663	1	BOPX 36B, BKWX 36	1289
		2	BOPX 36B, BKWX 36	
		3	BOPX 36B, BKWX 36	
		4	BOPX 36B, BKWX 36	
		5	BOPX 36B, BKWX 36	
		6	BOPX 36B, BKWX 36	
		7	BOPX 36B, BKWX 36	
176	8671		BOPX 31	1290
177			BOPX 31	1291
178	8691	1	SG 42, BOPX 50	1292
		2	SG 42, BOPX 50	
		4	SG 42	
179	P1(0113)	1	AKEZ 07A	1293
		2	AKEZ 07A	
		3	AKEZ 07A	
		4	AKEZ 07A	
		5	AKEZ 07A	
		6	AKEZ 07A	
		7	AKEZ 07A	
		8	AKEZ 07A	
		9	AKEZ 07A	
		10	AKEZ 07A	
180	P2(0422)	1	BKEZ 07D, BKEZ 17H	1294
		2	BKEZ 07D, BKEZ 17H	
		3	BKEZ 07D, BKEZ 17H	
181		4	BKEZ 07D, BKEZ 17H	1295
		5	BKEZ 07D, BKEZ 17H	
		6	BKEZ 17H, RSLZ 21	
182		7	BKEZ 07D, BKEZ 17H, RSLZ 21	1296
		8	BKEZ 07D, BKEZ 17H, RSLZ 21	
		9	BKEZ 17H, RSLZ 21	
183		10	BKEZ 17H, RSLZ 21	1297
		11	BKEZ 17H, RSLZ 21	

INDEX TO PLATES BY PLATE NUMBER AND CASE NUMBER (cont.)

Plate Number	Case No.	Plot No. (Vol. I)	Method	Page Number
184	P3(0423)	1	BKEZ 07D, BKEZ 17H	1298
		2	BKEZ 07D, BKEZ 17H	
		3	BKEZ 07D, BKEZ 17H	
		4	BKEZ 07D, BKEZ 17H	
185		5	BKEZ 17H	1299
		6	BKEZ 17H	
		7	BKEZ 17H	
		8	BKEZ 17H	
		10	BKEZ 07D, BKEZ 17H	
		11	BKEZ 07D, BKEZ 17H	
186		9	BKEZ 07D, BKEZ 17H	1300
		12	BKEZ 17H	
187	0111		AOPX 22 (supplementary—laminar flow)	1301

PLATES 1 THROUGH 187

(COMPARISON OF COMPUTATION OUTPUT WITH EXPERIMENTAL DATA)

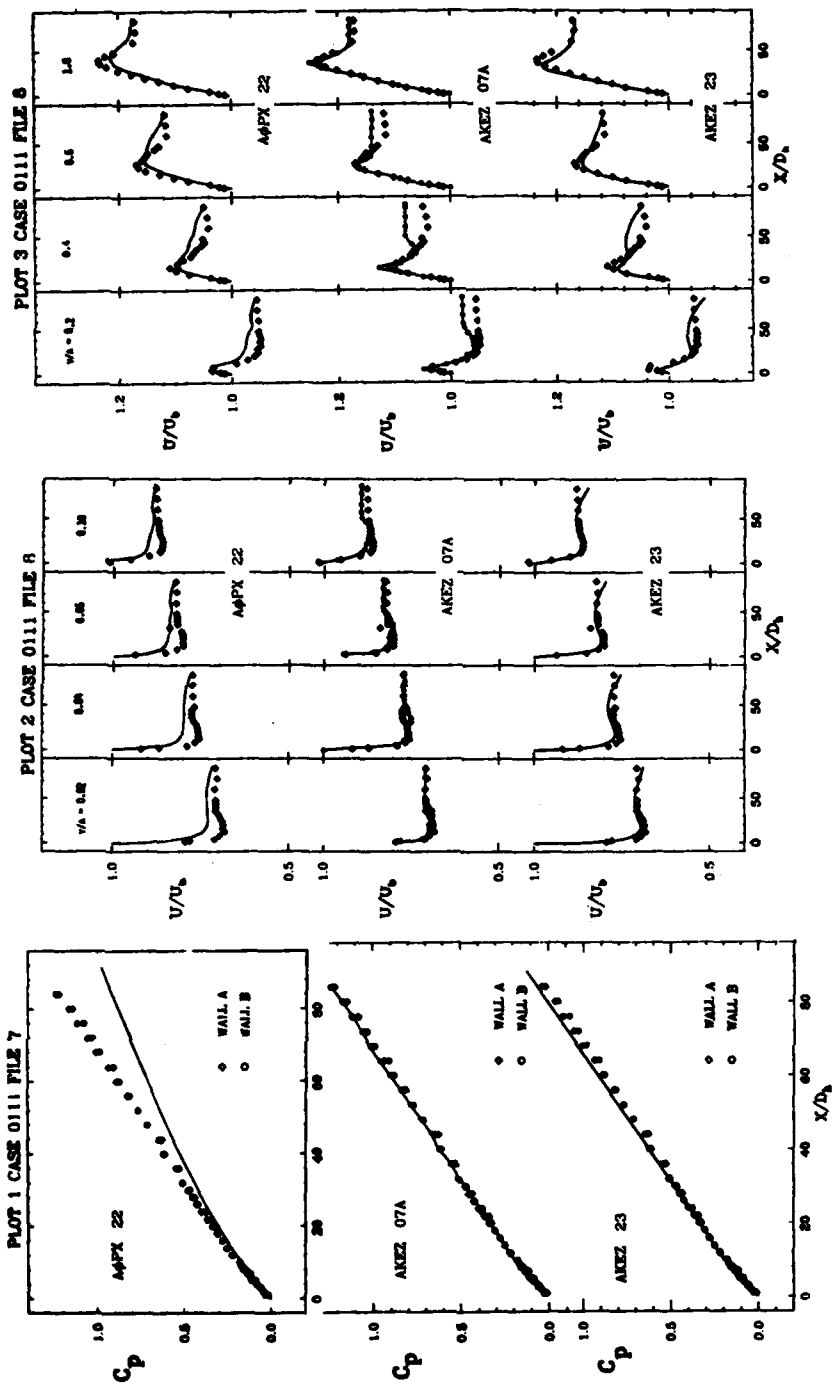
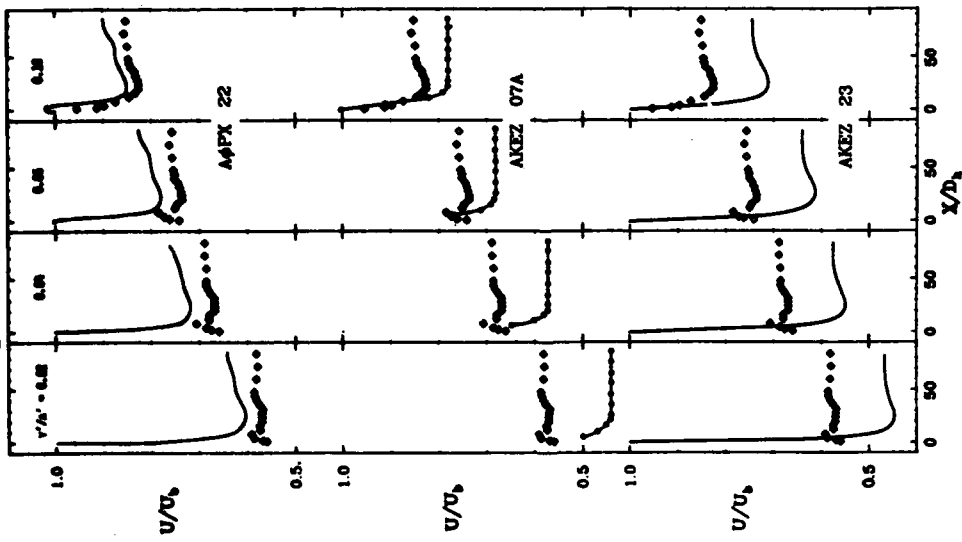


PLATE 1

PLOT 4 CASE 0111 FILE 9



PLOT 5 CASE 0111 FILE 9

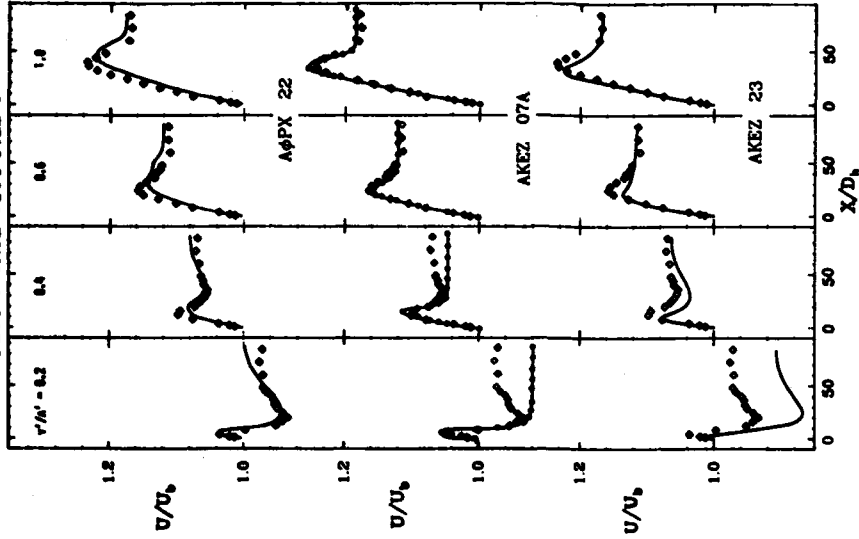


PLATE 2

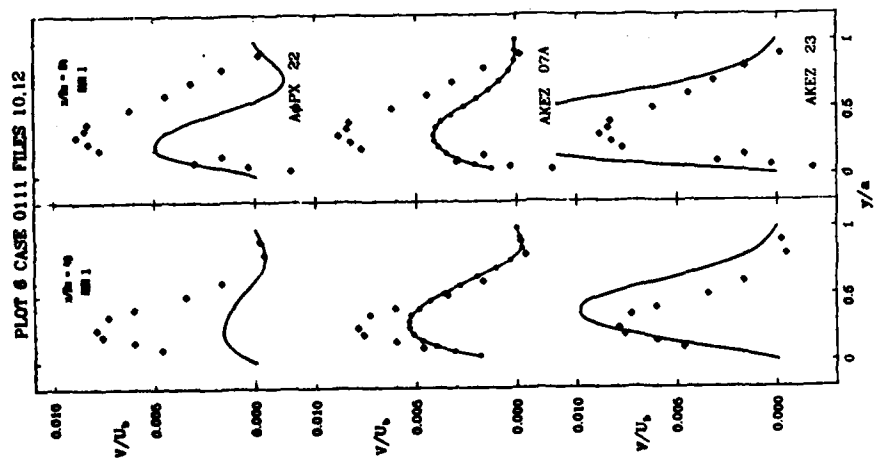
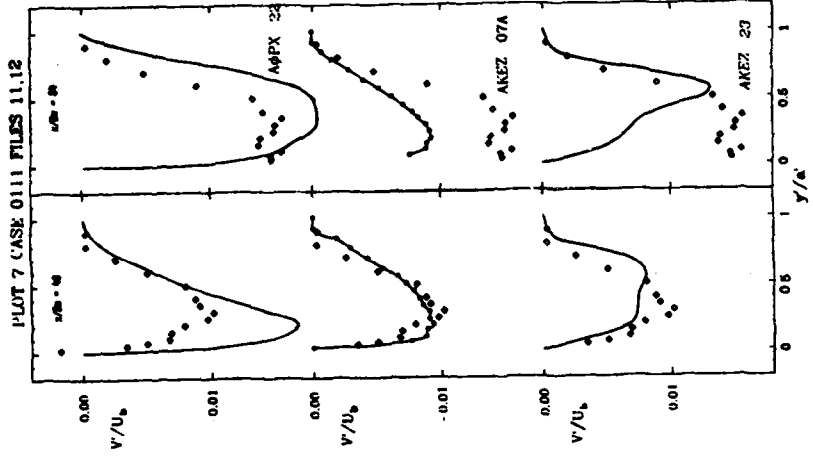
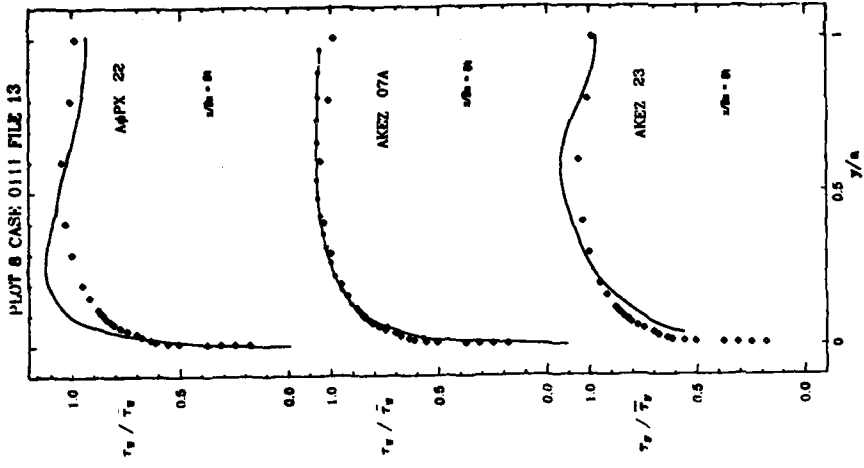


PLATE 3

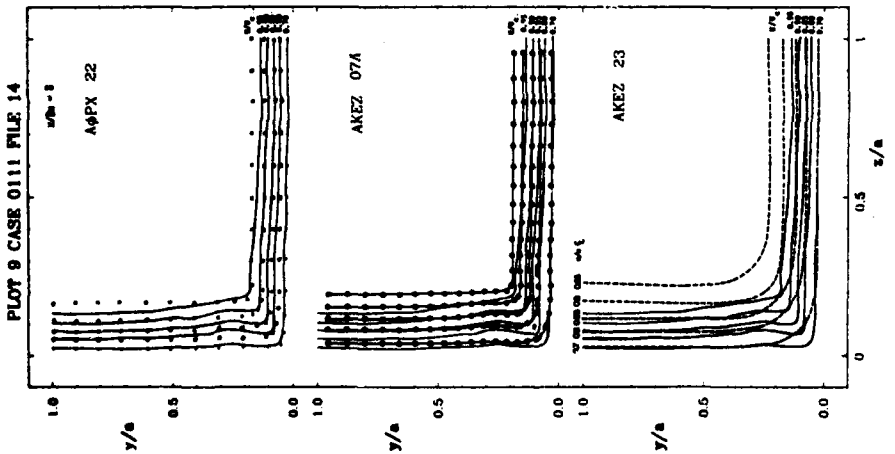
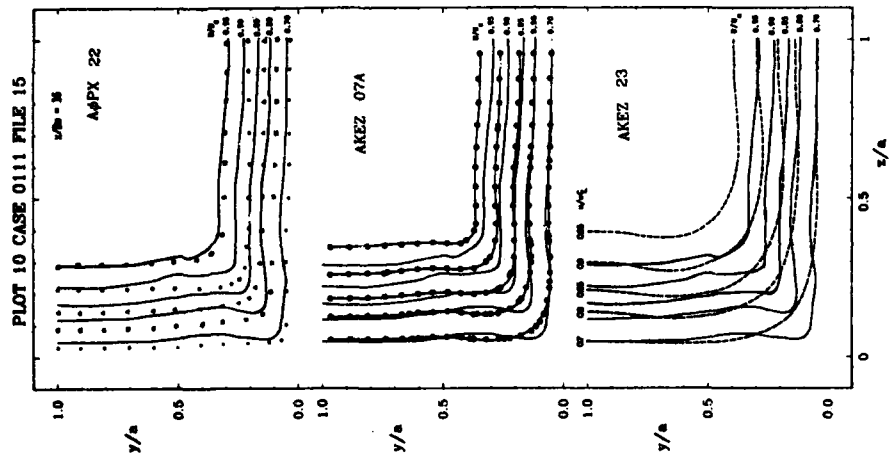
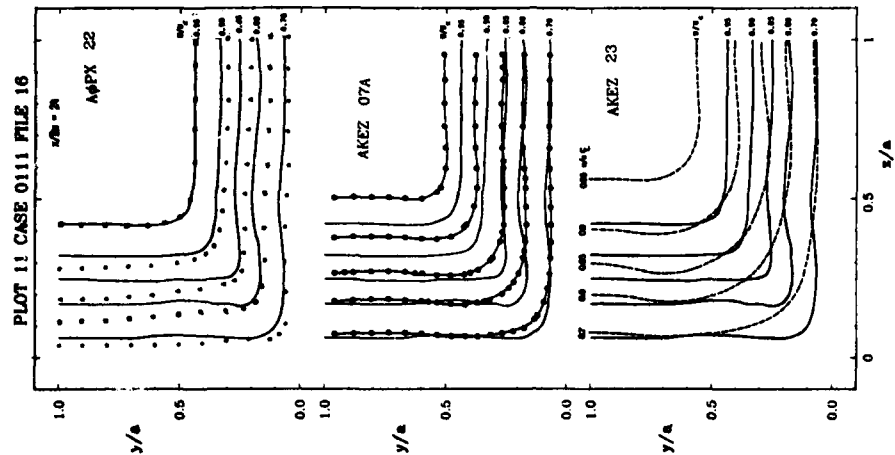


PLATE 4

(Full lines - data)

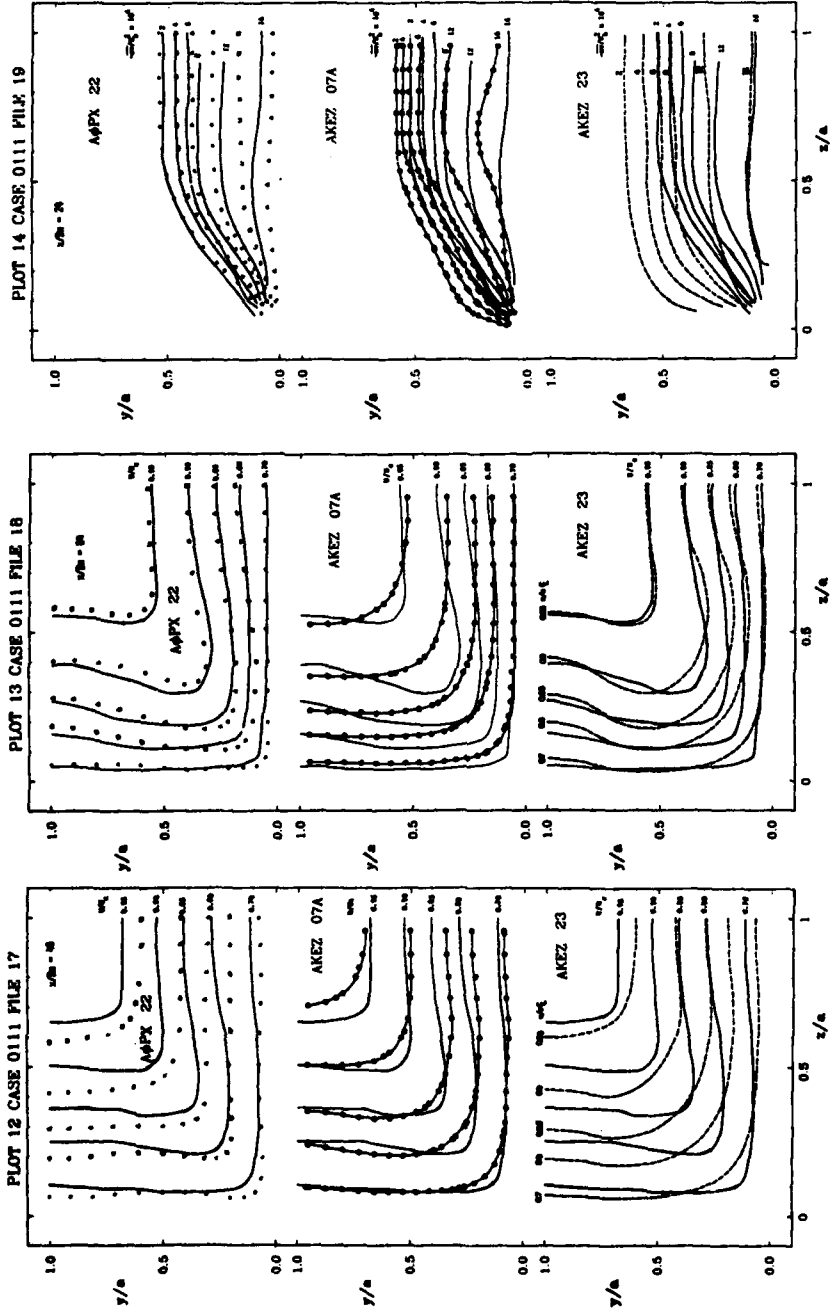


PLATE 5
 (Full lines - data)

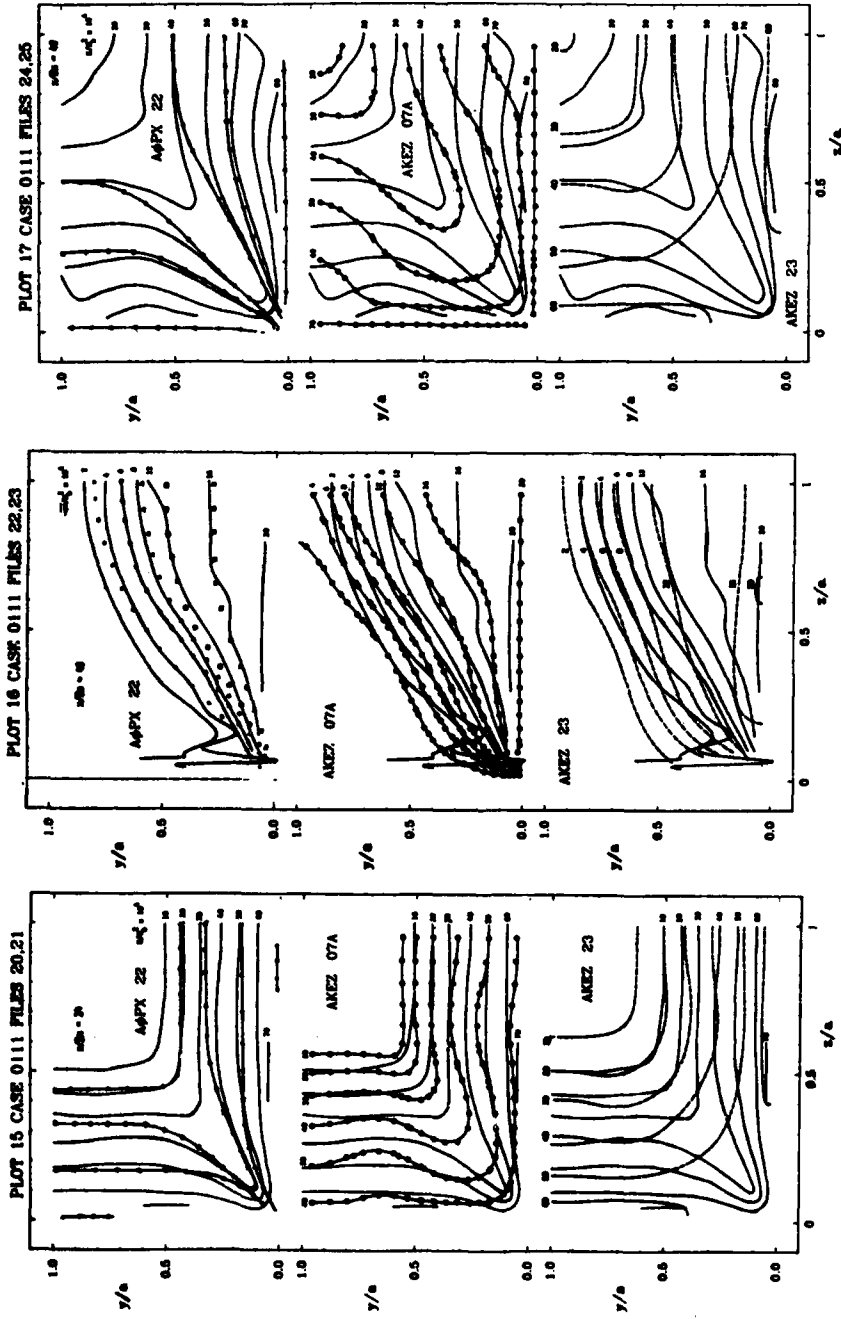


PLATE 6

(Full lines - data)

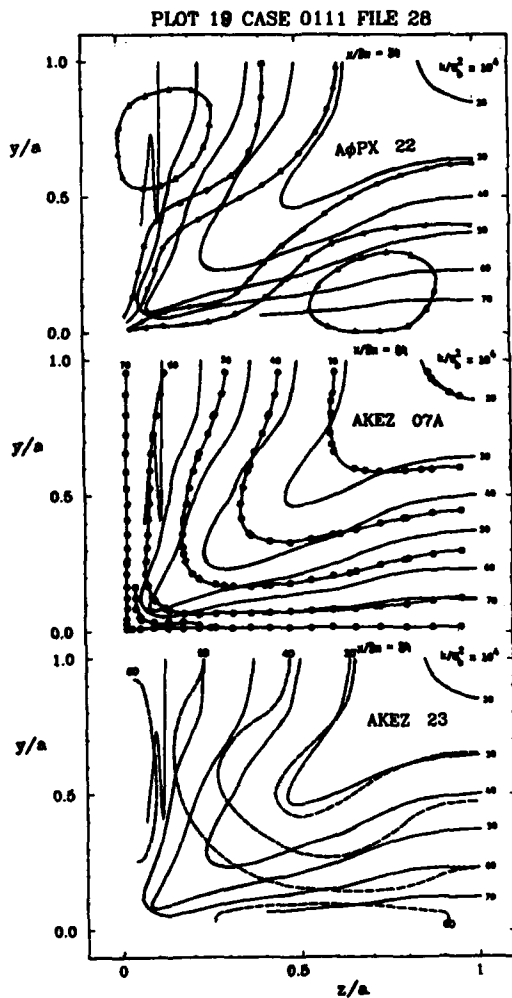
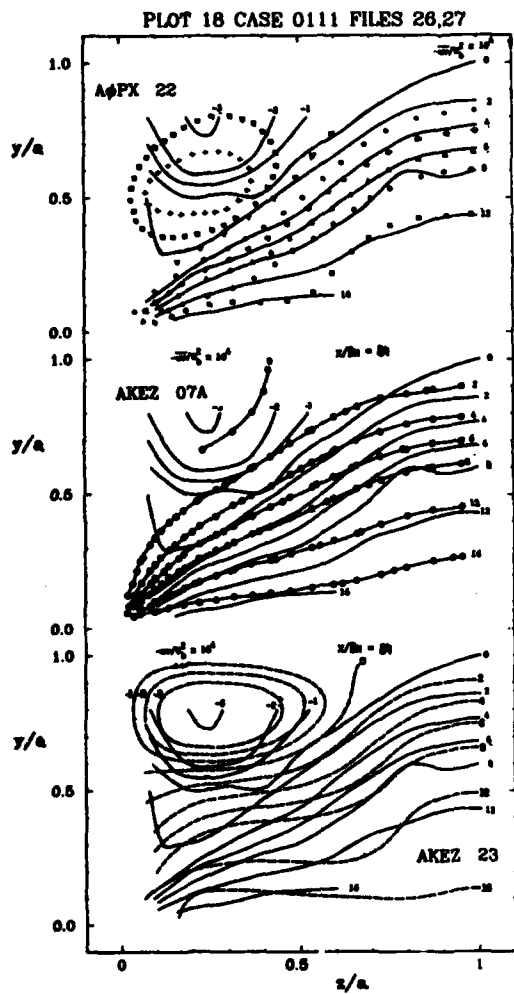


PLATE 7

(Full lines - data)

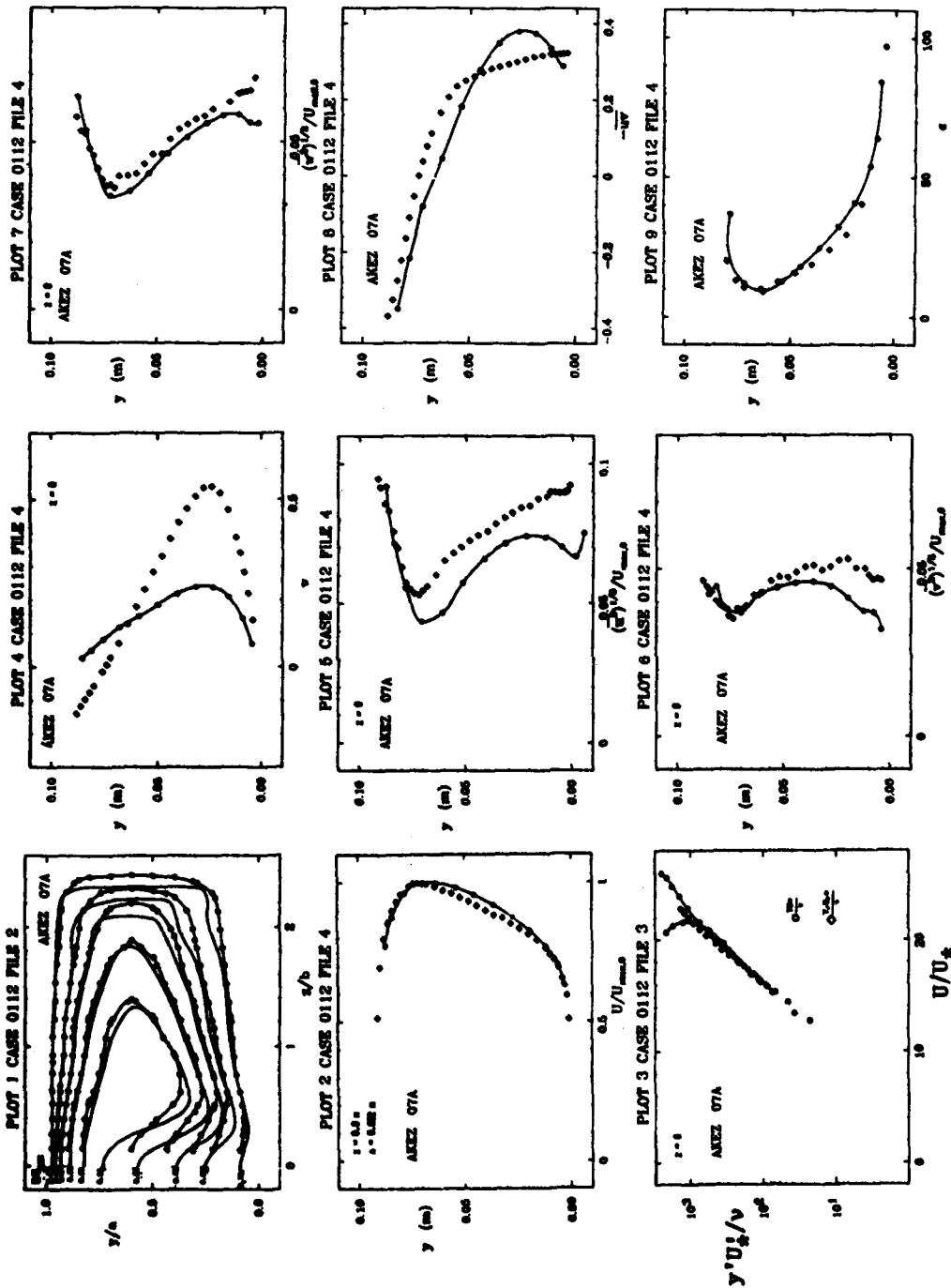
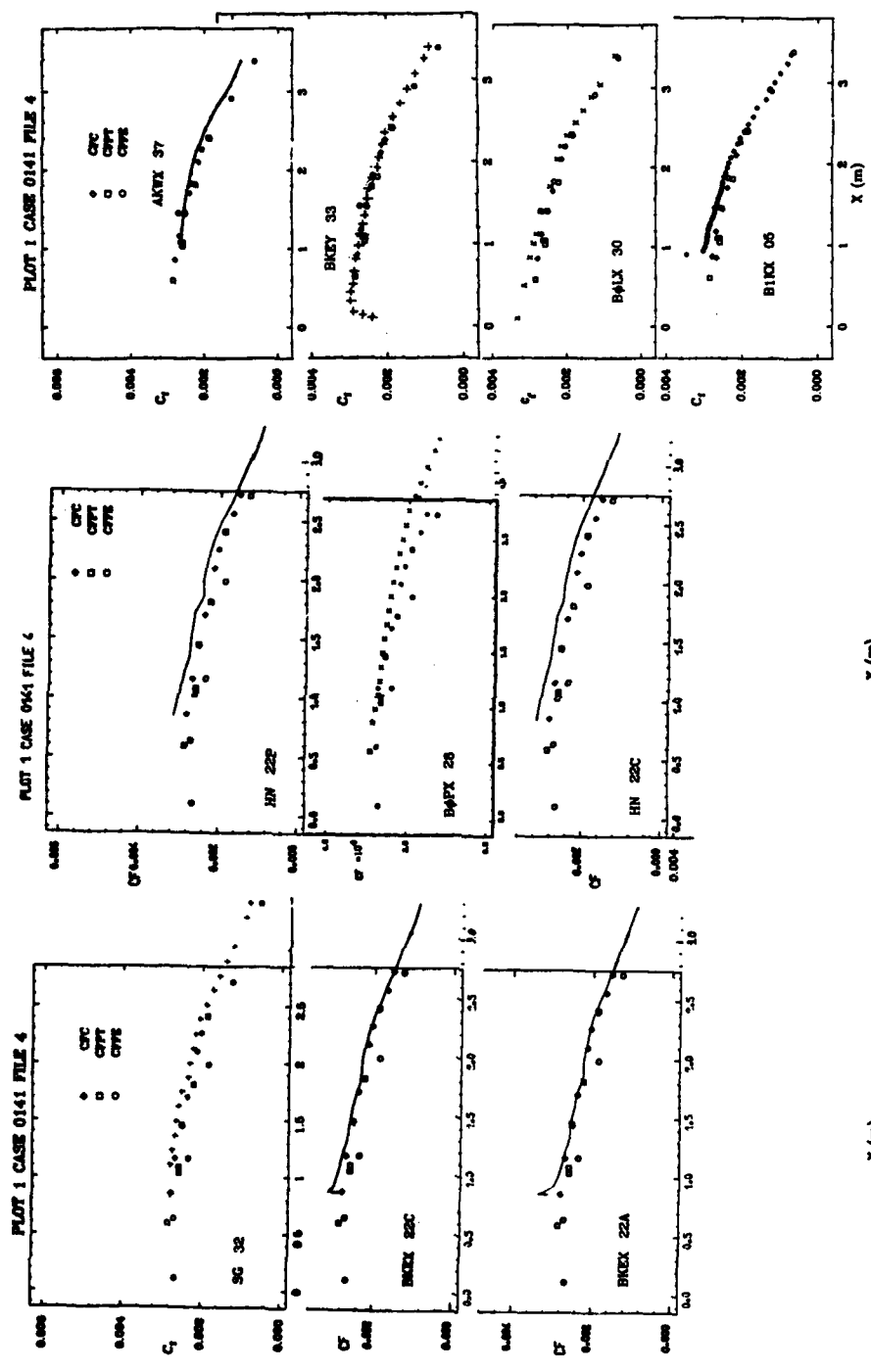


PLATE 8

(Full lines in Plot 1 - data)



X (m)

X (m)

PLATE 9

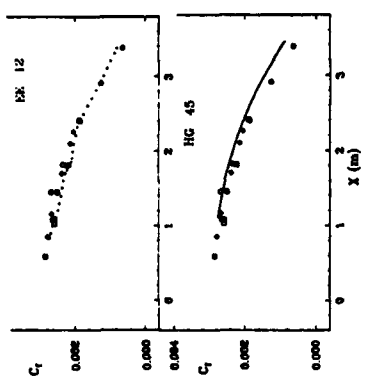
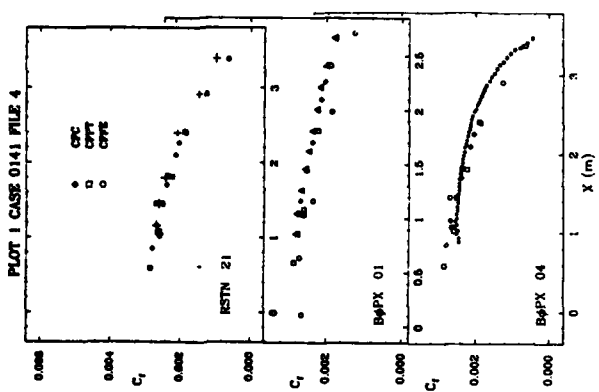
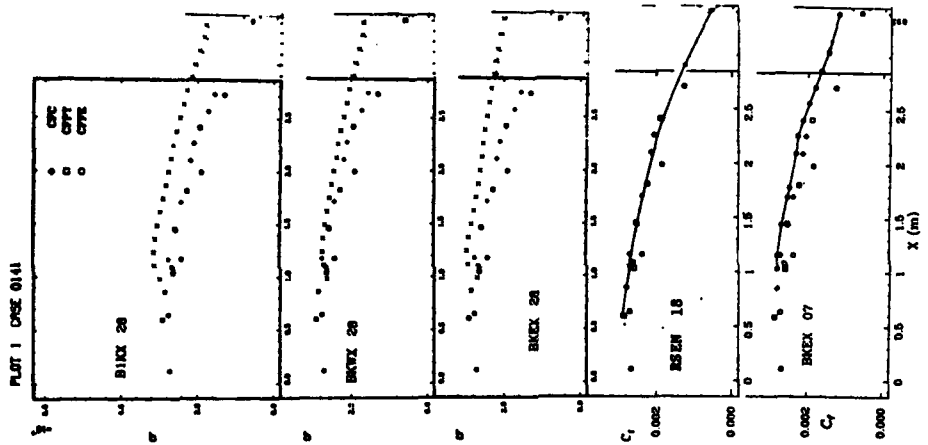
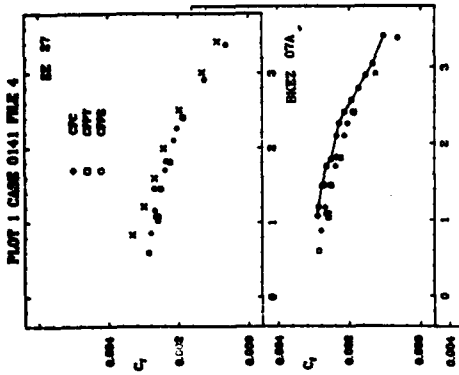


PLATE 10

PLOT 2 CASE 0141 FILE 25,26,27

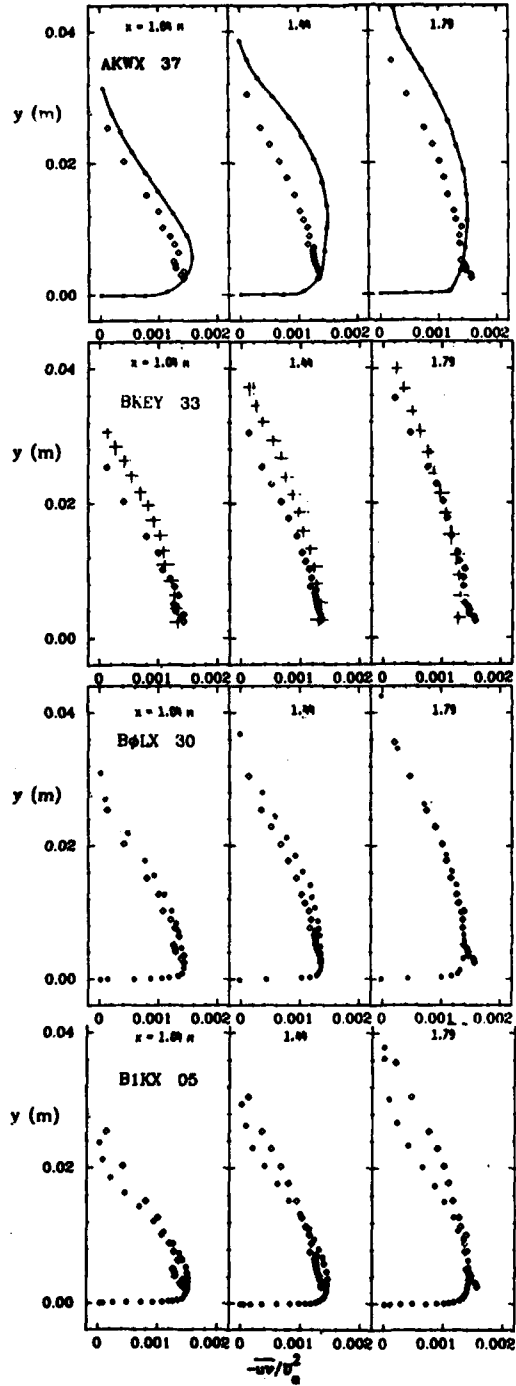
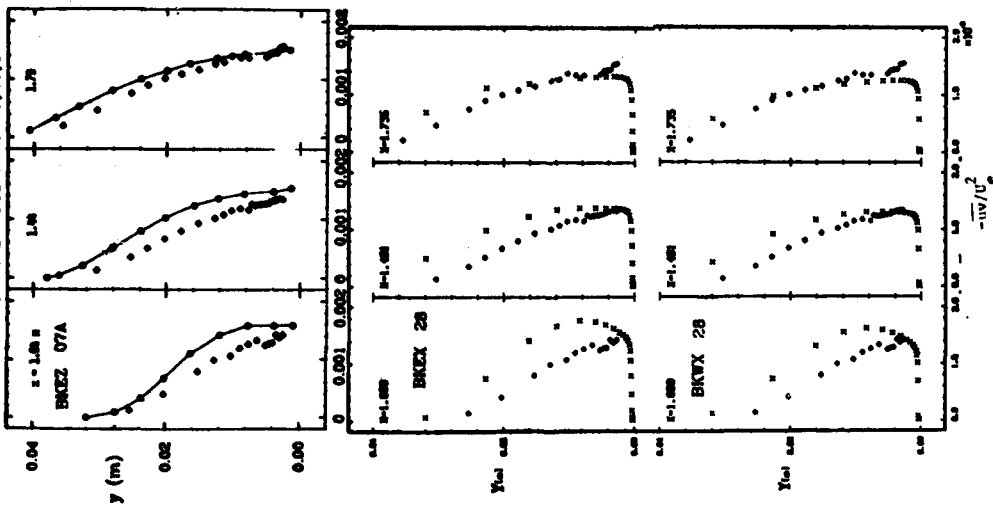


PLATE 11

PLOT 2 CASE 0141 FILE 25.26.27



PLOT 2 CASE 0141 FILE 25.26.27

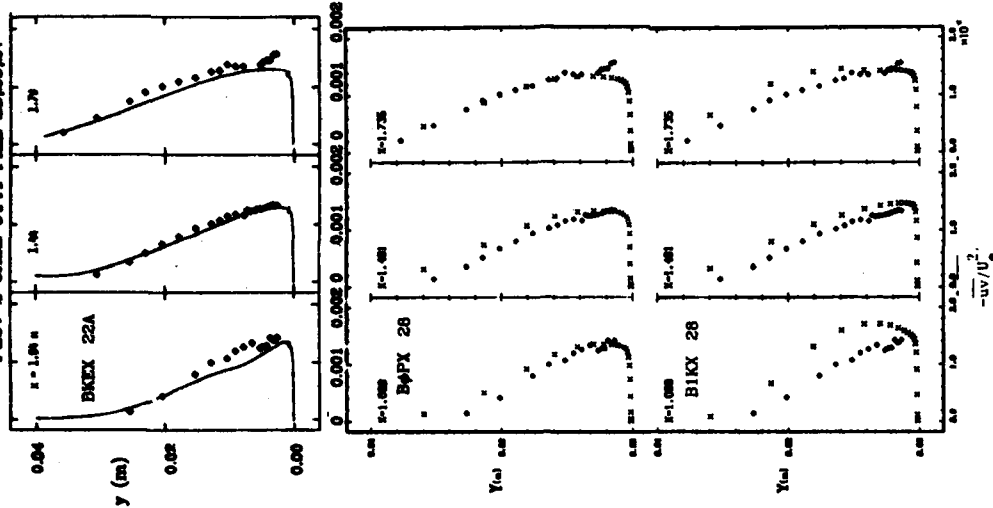


PLATE 12

PLOT 2 CASE 0141 FILES 25.26.27

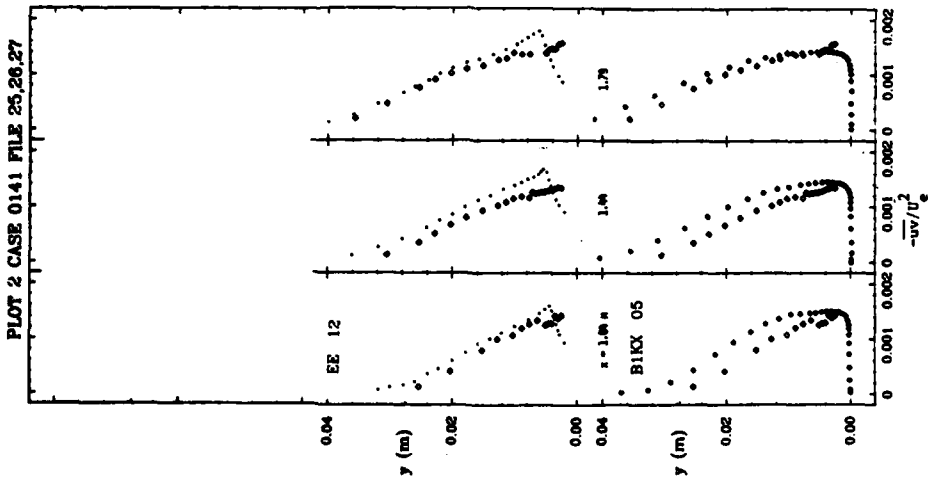
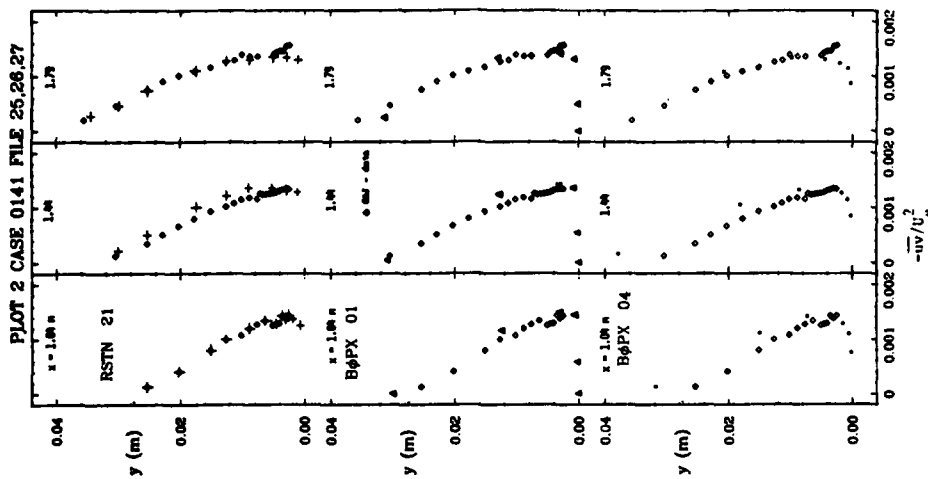
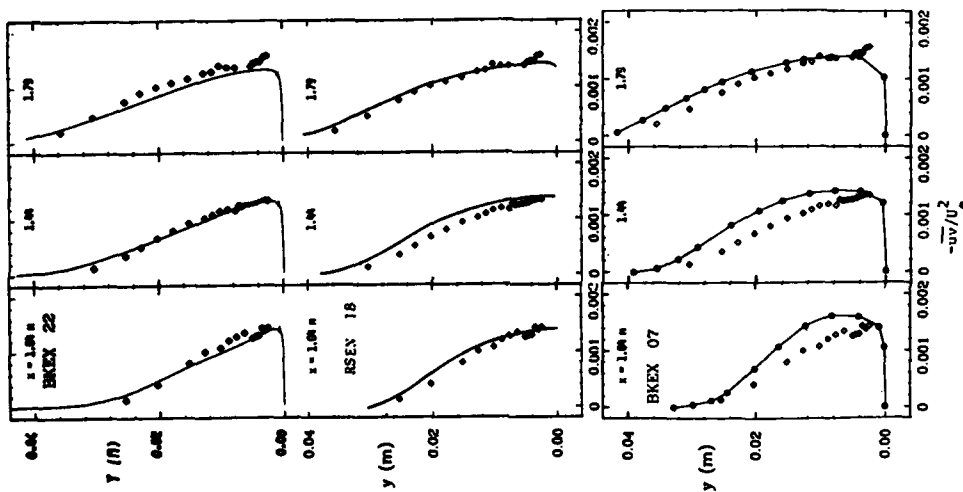
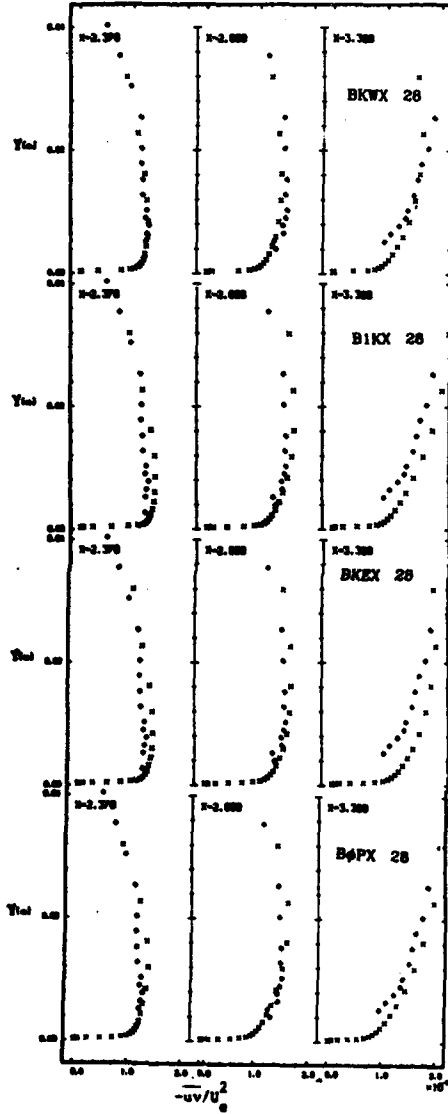


PLATE 13

PLOT 3 CRSE 0141



PLOT 3 CASE 0141 FILE 28,29,30

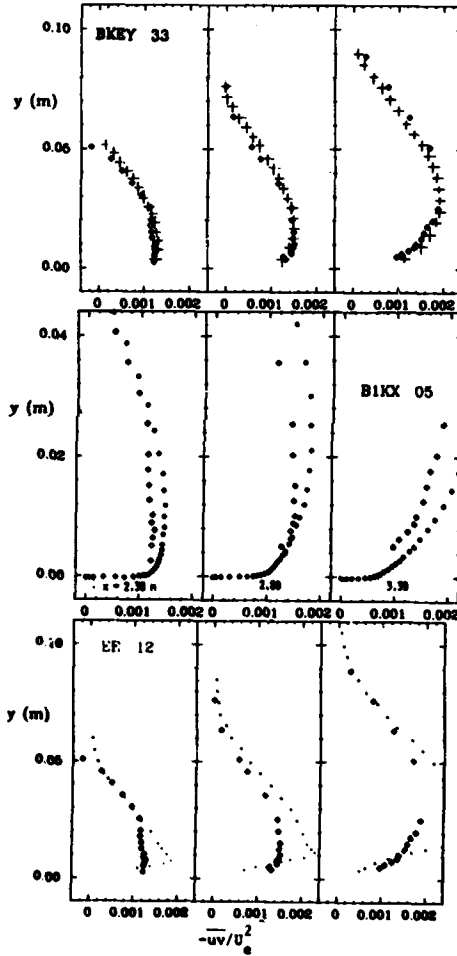
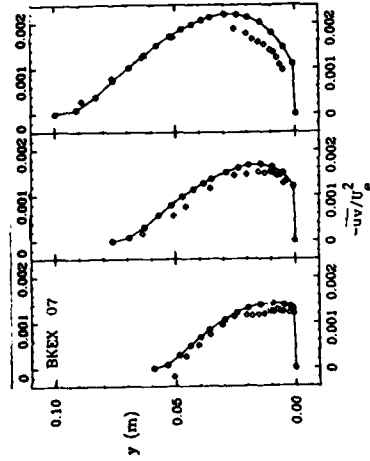
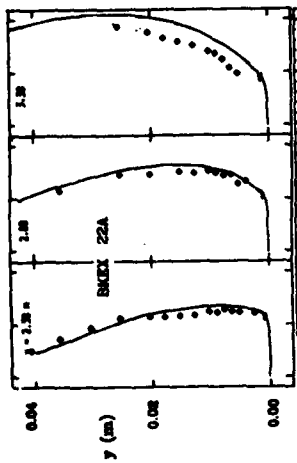
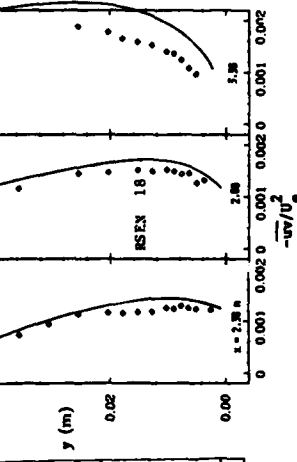
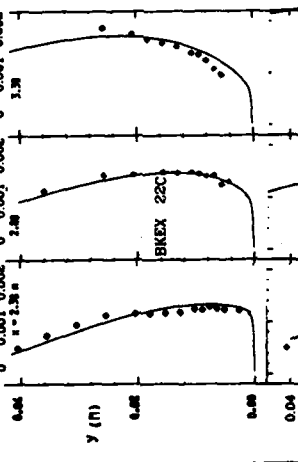
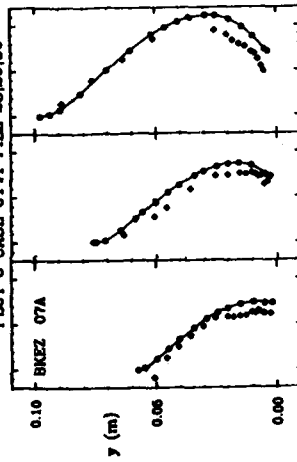


PLATE 14

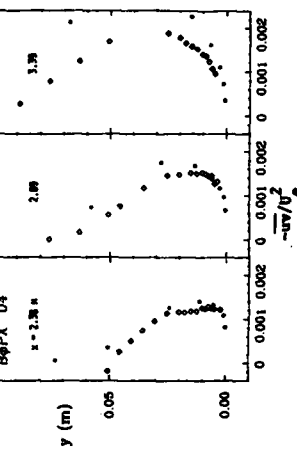
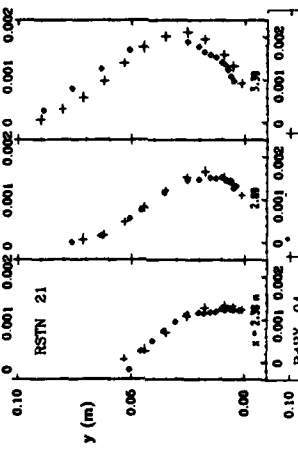
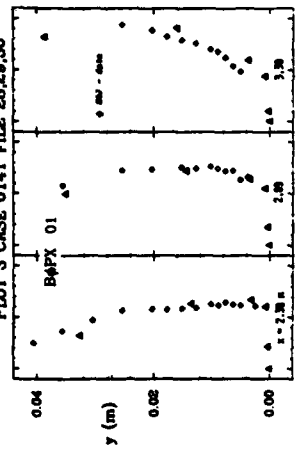
PLOT 3 CASE 0141 FILE 26,29,30



PLOT 3 CASE 0141 FILE 28,29,30



PLOT 3 CASE 0141 FILE 28,29,30



PLOT 3 CASE 0141 FILE 28,29,30

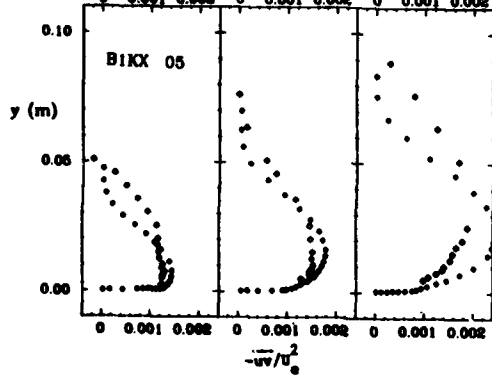
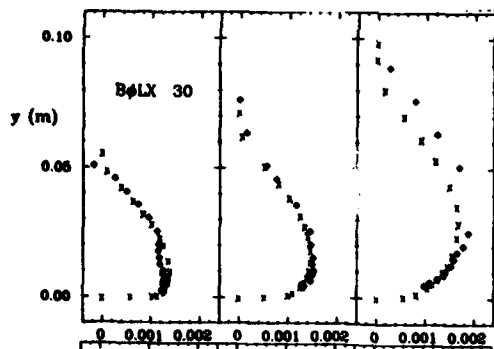
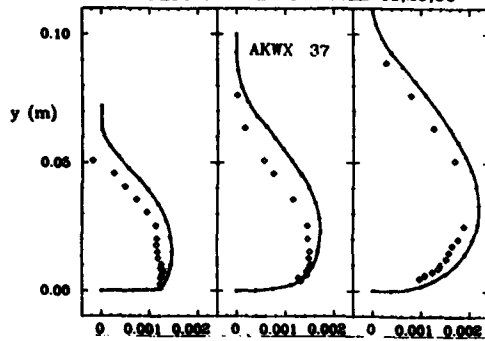


PLATE 16

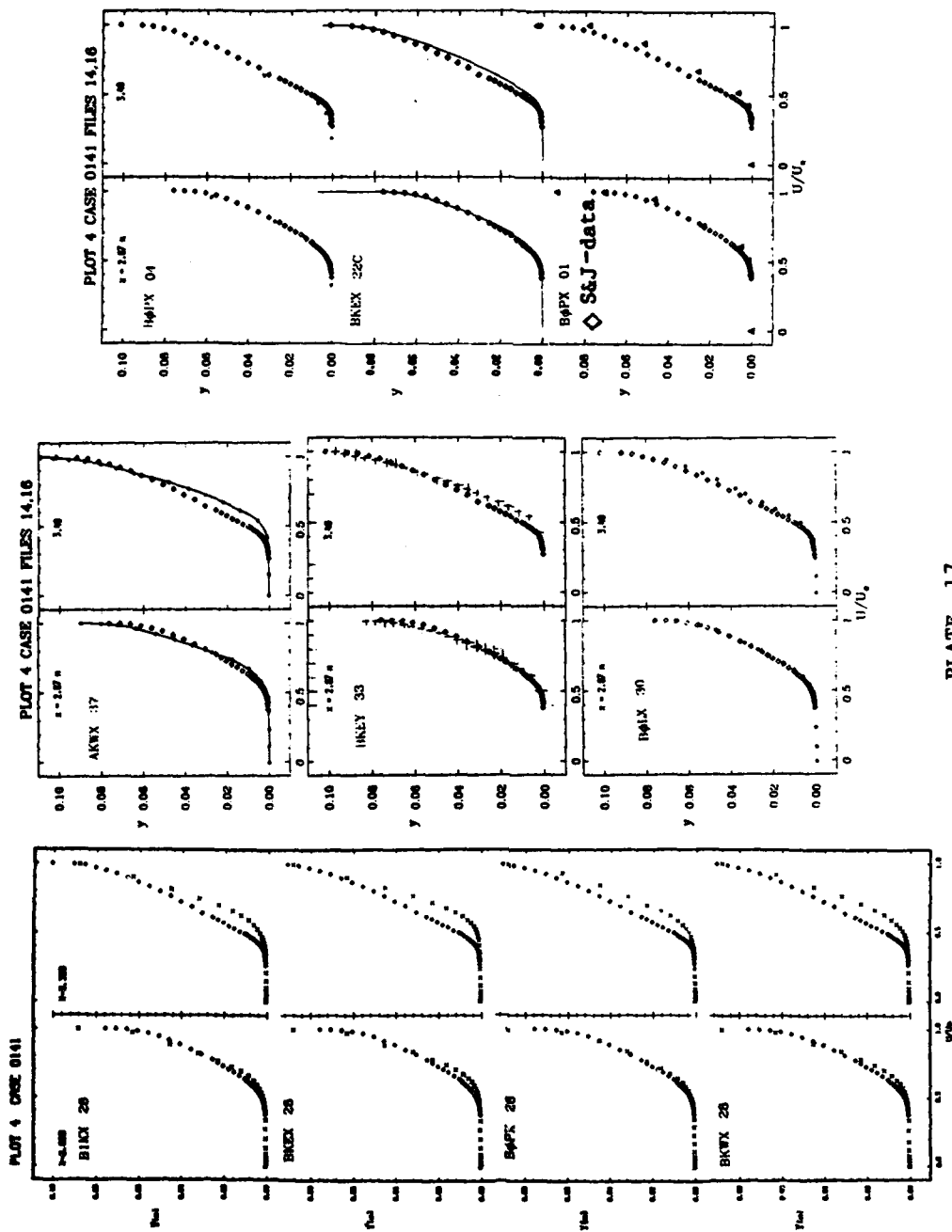


PLATE 17

AD-A136 034

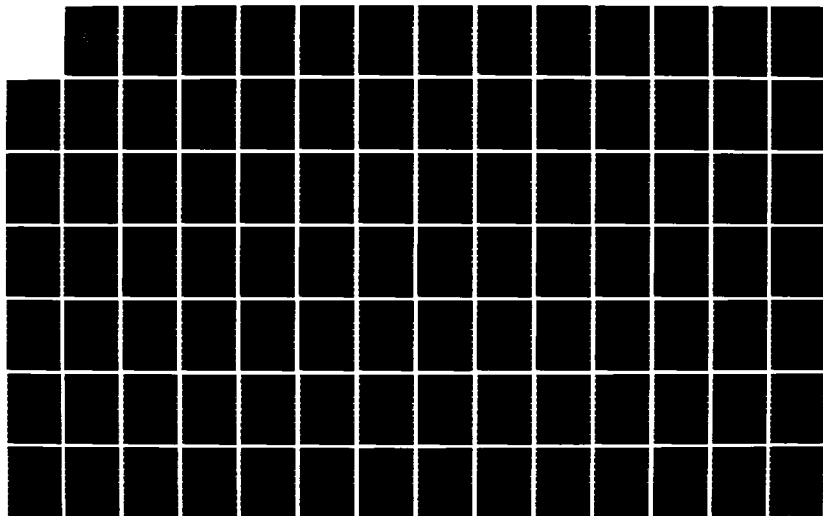
THE 1980-81 AFOSR (AIR FORCE OFFICE OF SCIENTIFIC
RESEARCH)-HTM (HEAT TR. (U) STANFORD UNIV CA DEPT OF
MECHANICAL ENGINEERING S J KLINE ET AL. SEP 81
AFOSR-TR-83-1003 F49620-80-C-0027

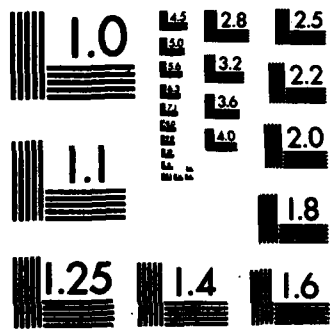
2/6

UNCLASSIFIED

F/G 20/4

NL





MICROCOPY RESOLUTION TEST CHART
NATIONAL BUREAU OF STANDARDS-1963-A

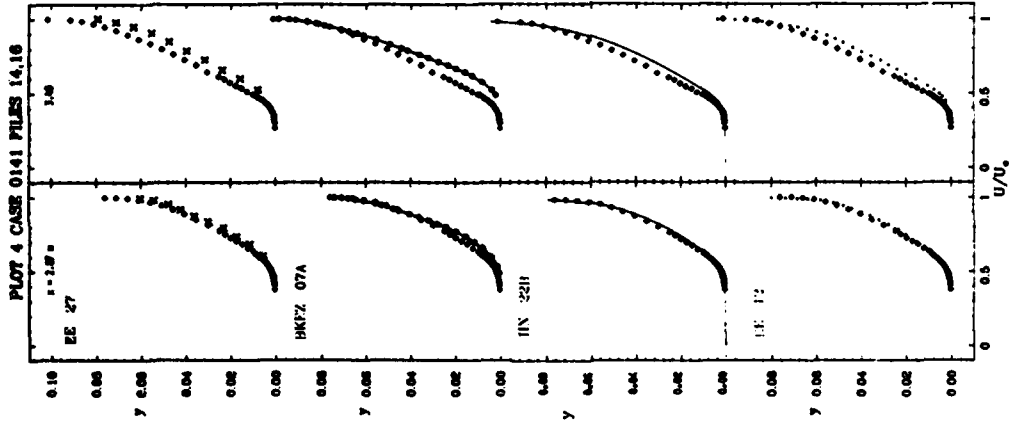
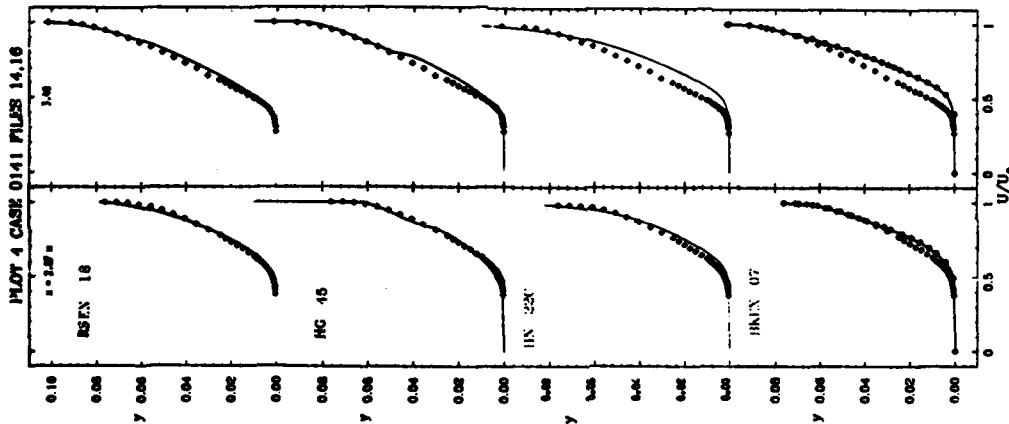
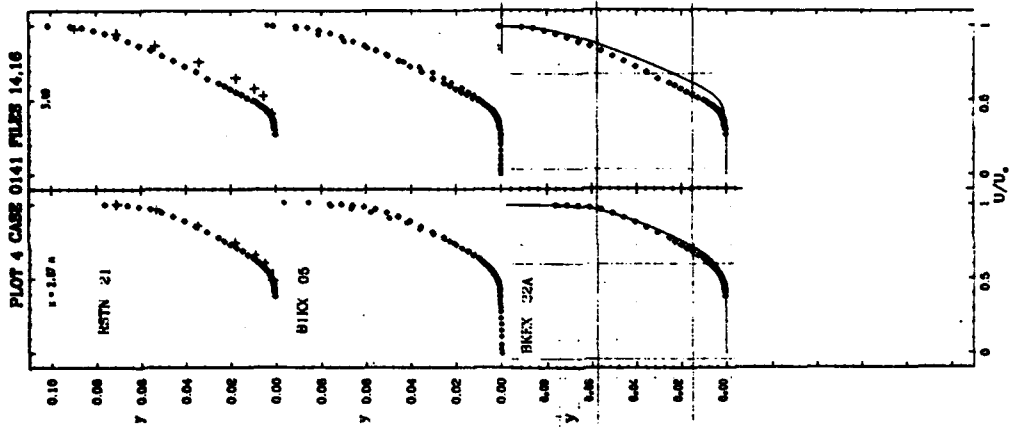


PLATE 18

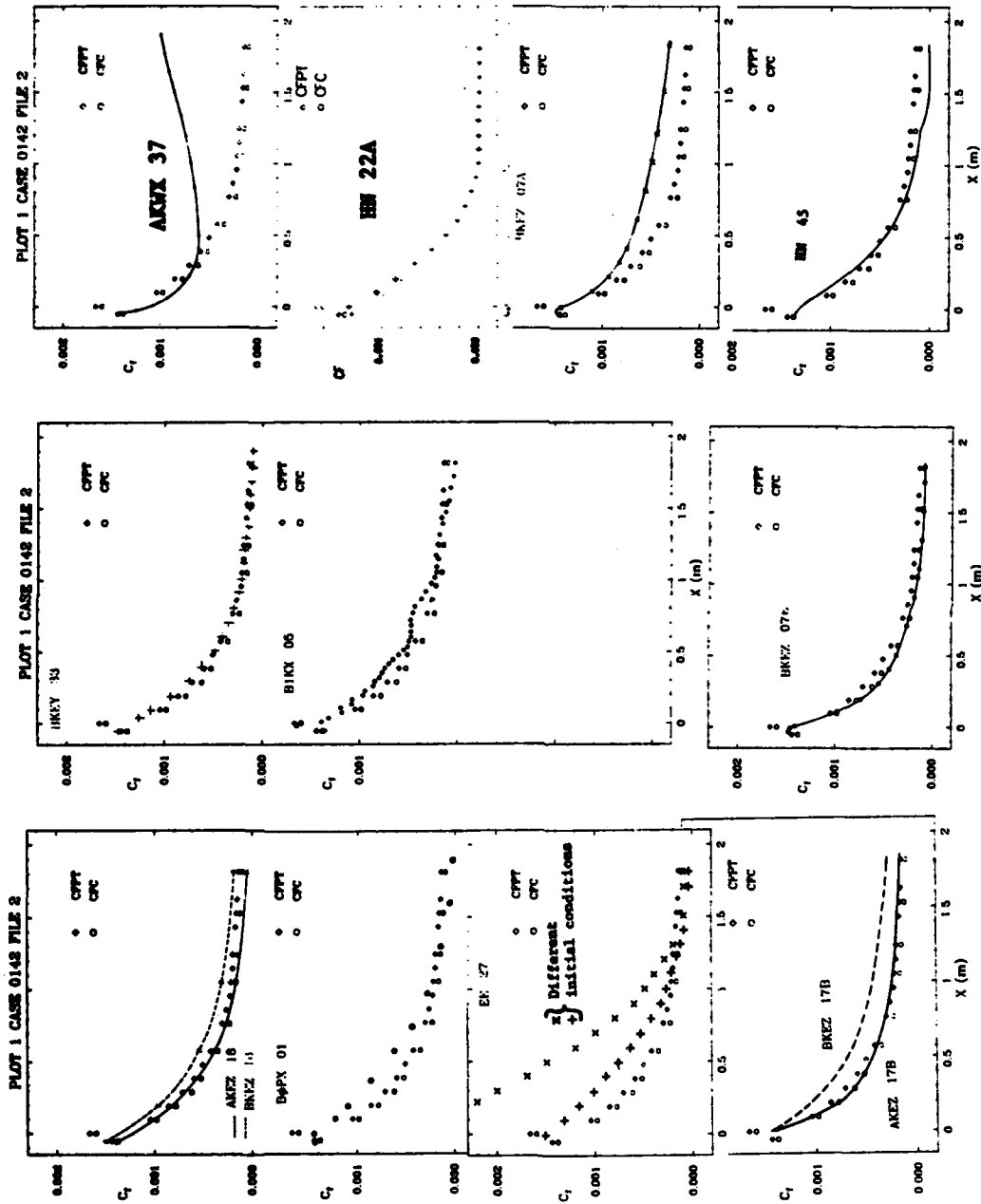


PLATE 19

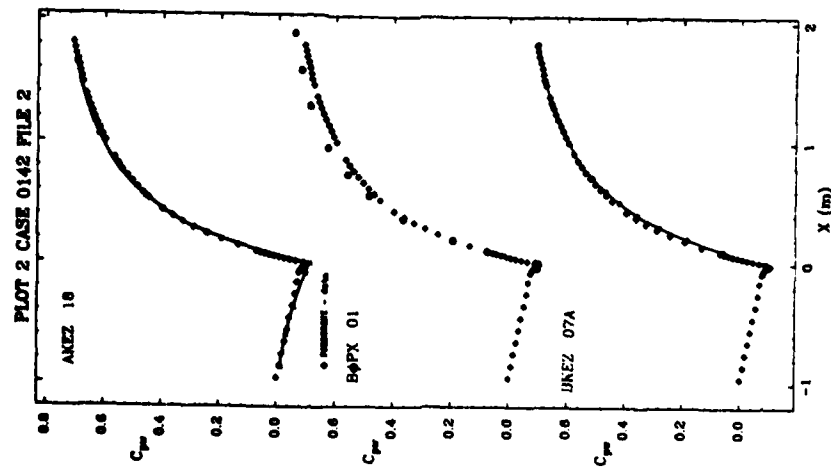
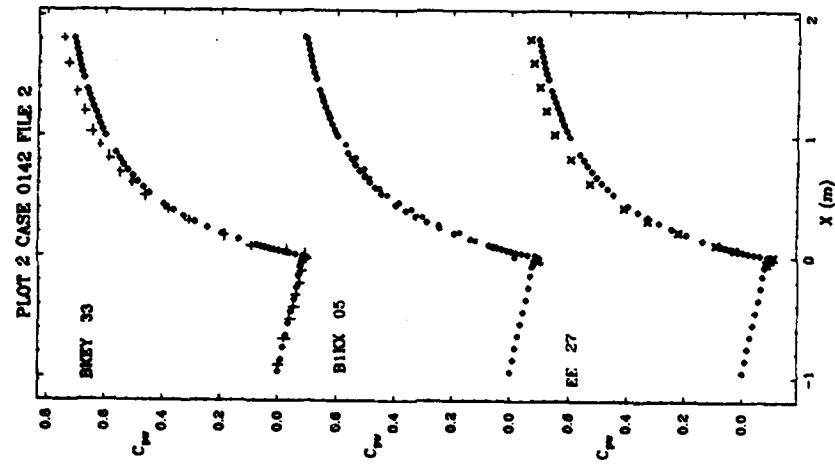
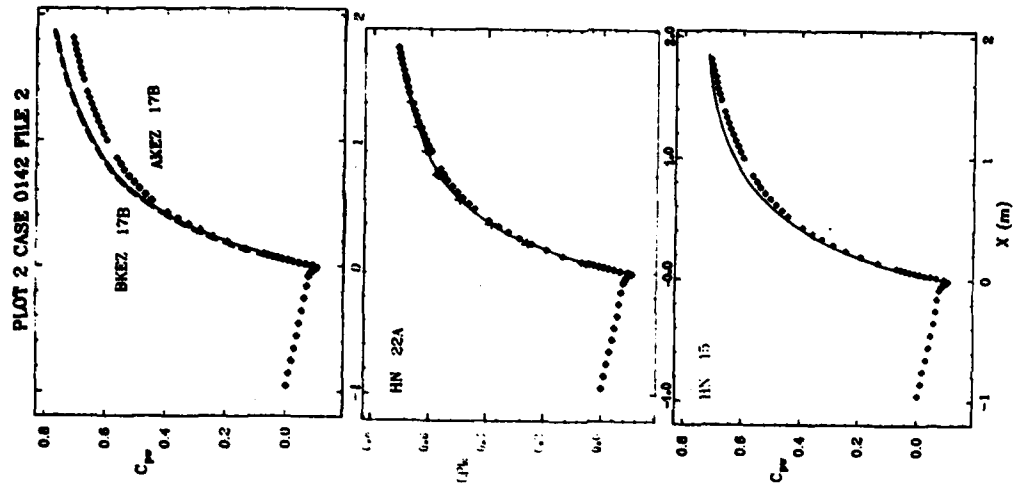


PLATE 20

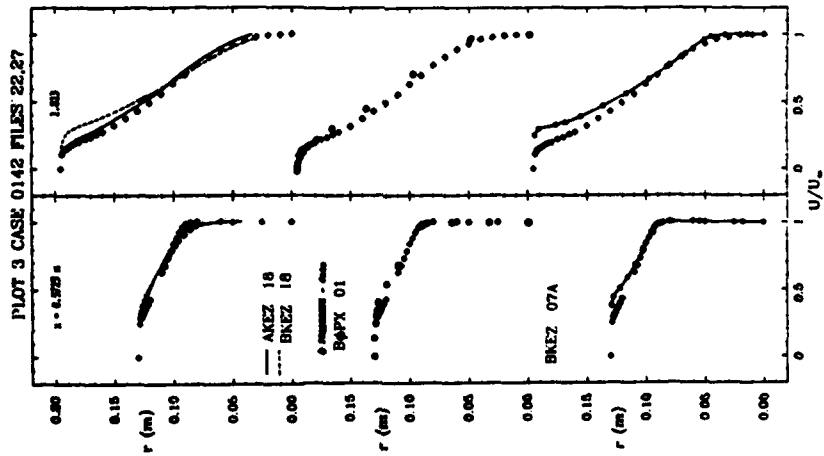
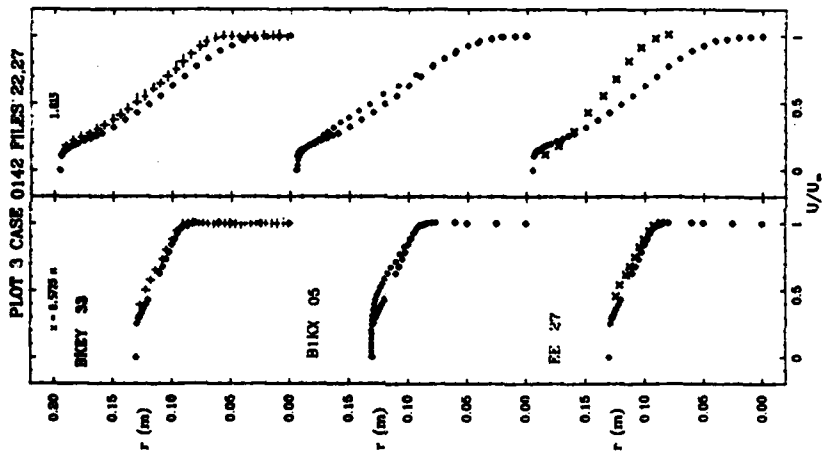
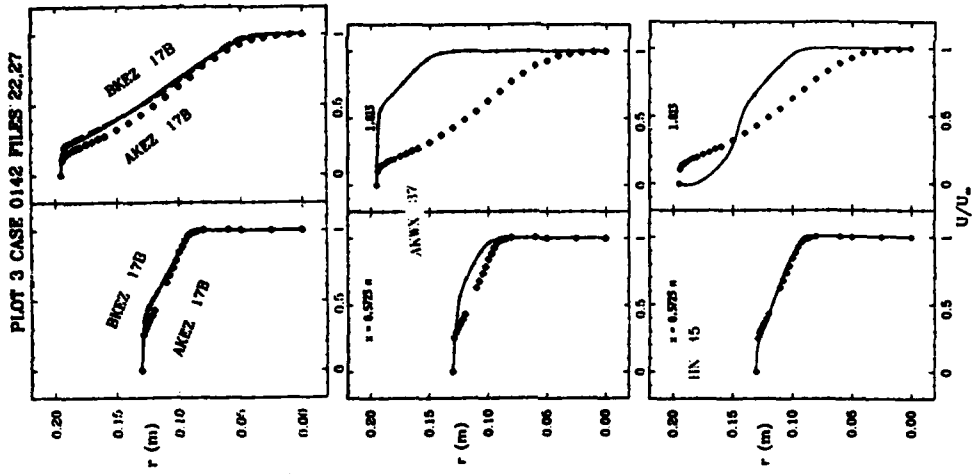


PLATE 21

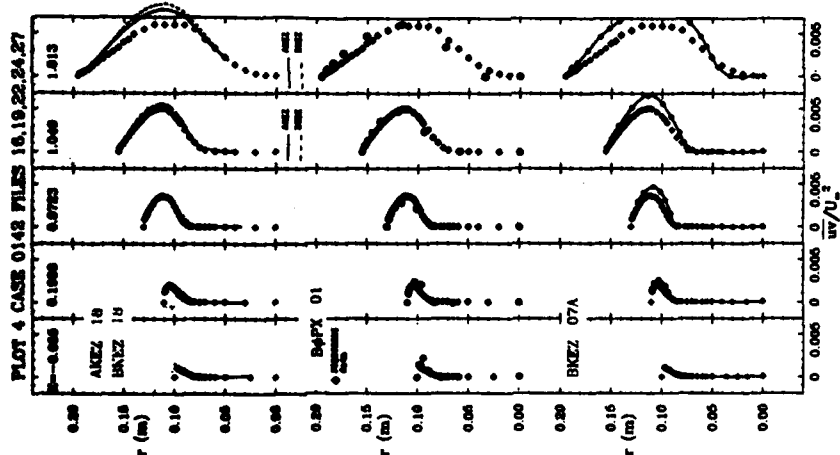
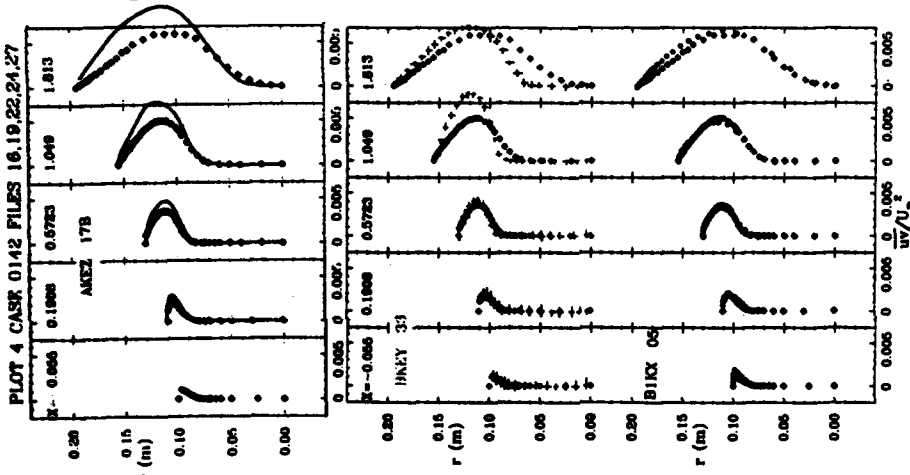
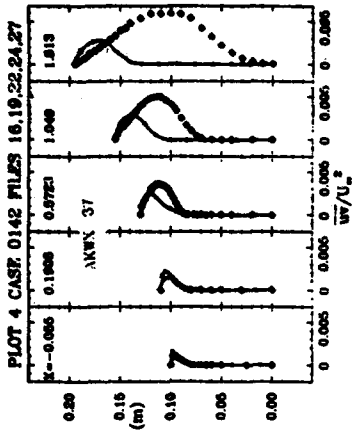


PLATE 22

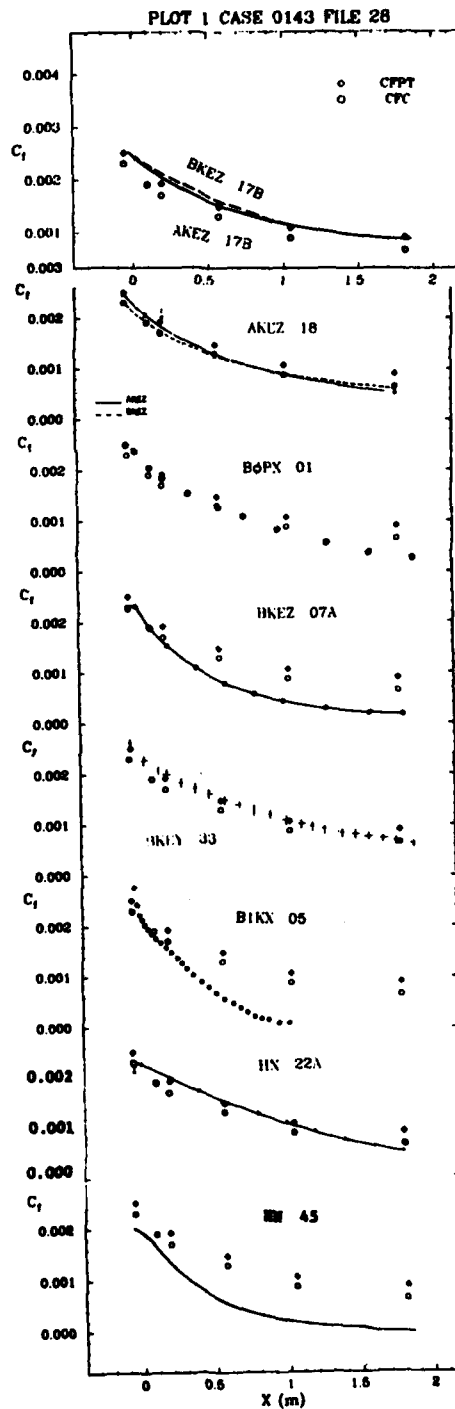
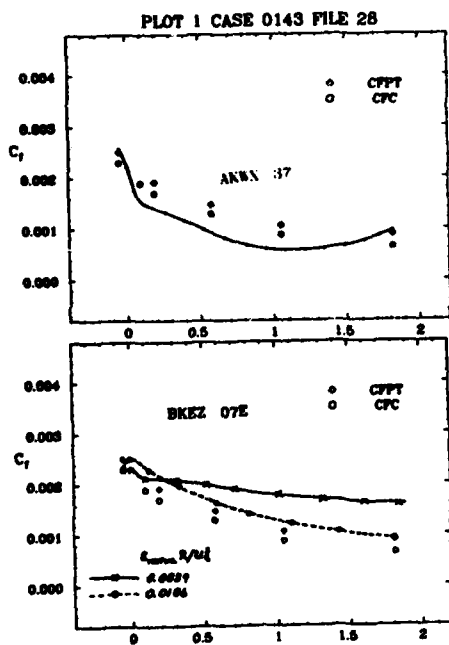


PLATE 23

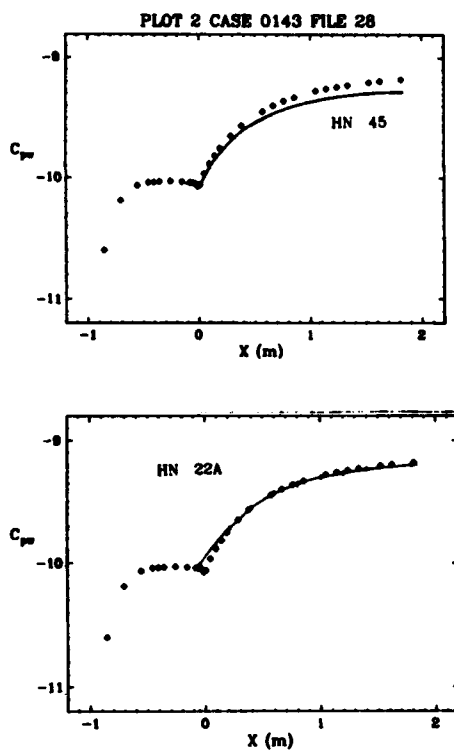
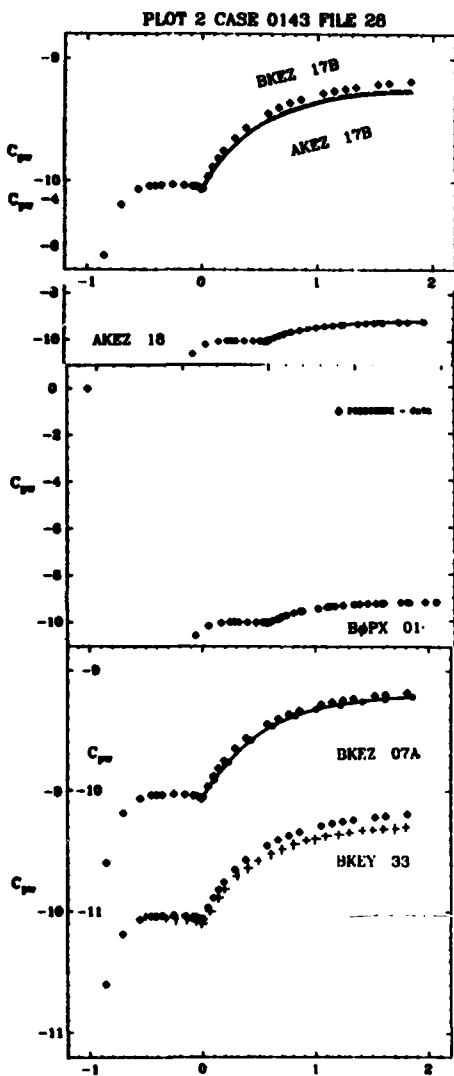


PLATE 24

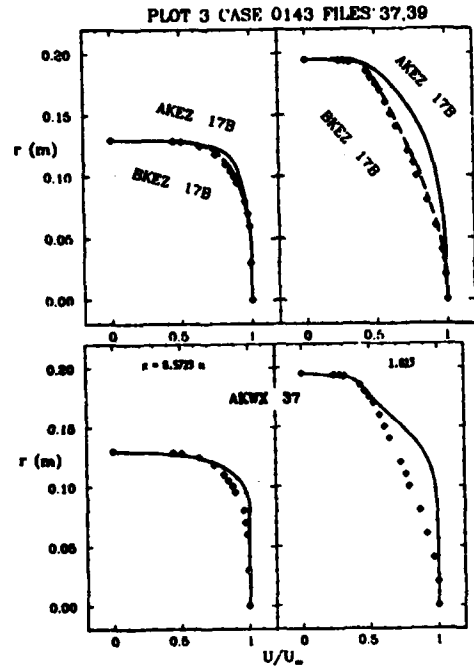
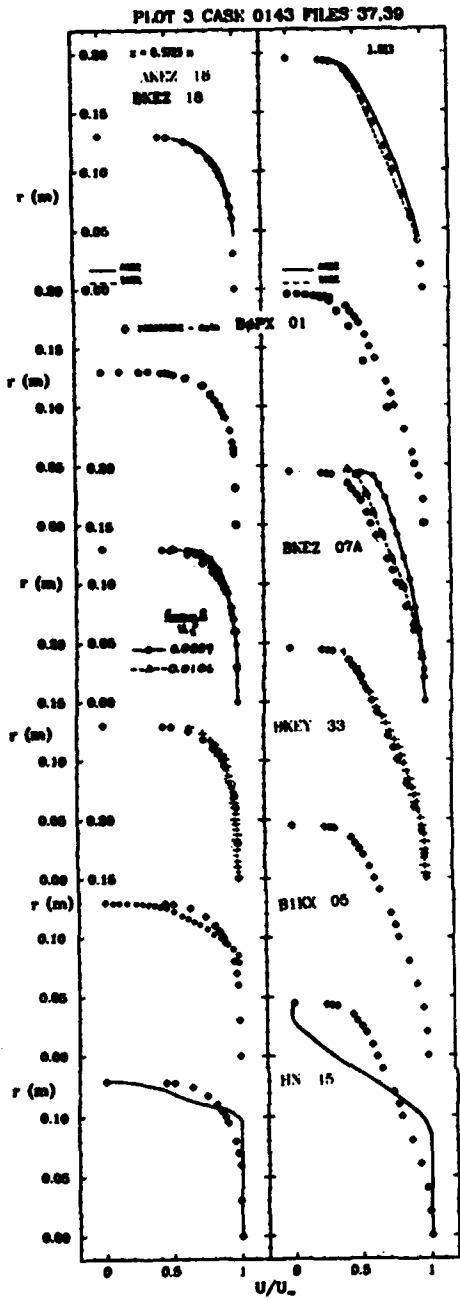
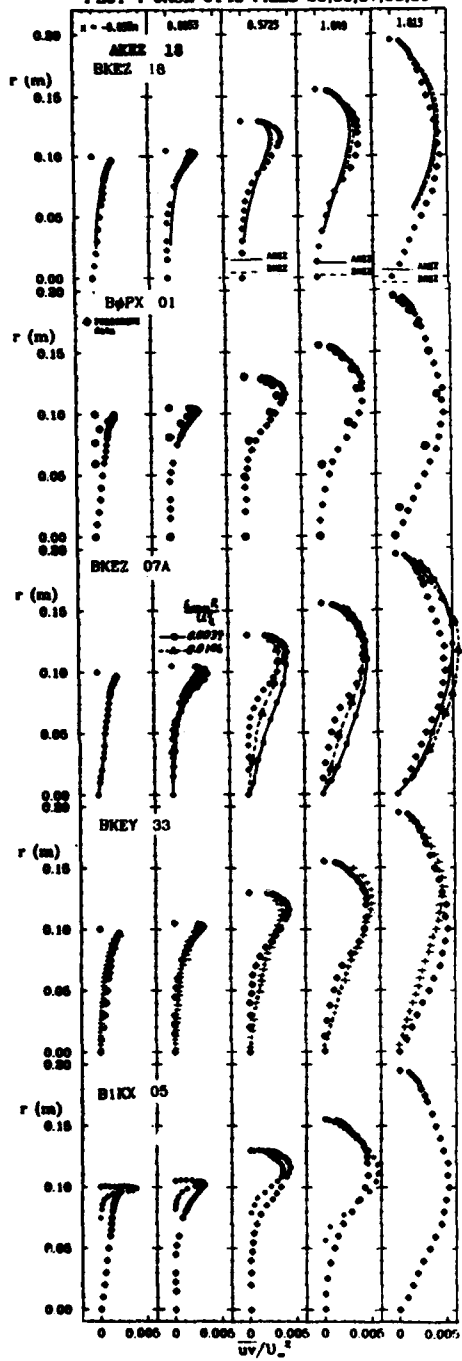
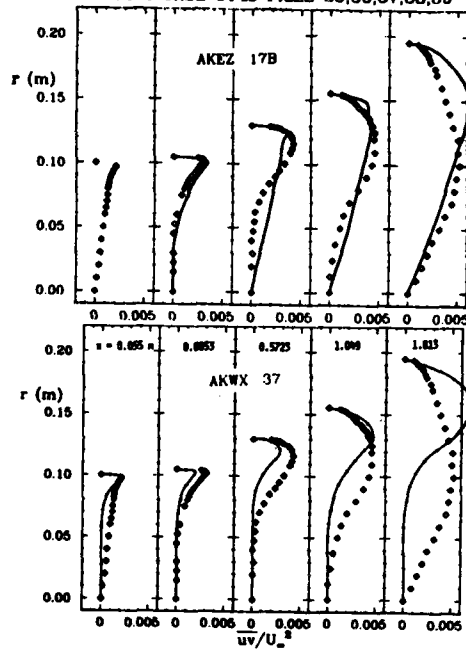


PLATE 25

PLOT 4 CASE 0143 FILES 35,36,37,38,39



PLOT 4 CASE 0143 FILES 35,36,37,38,39



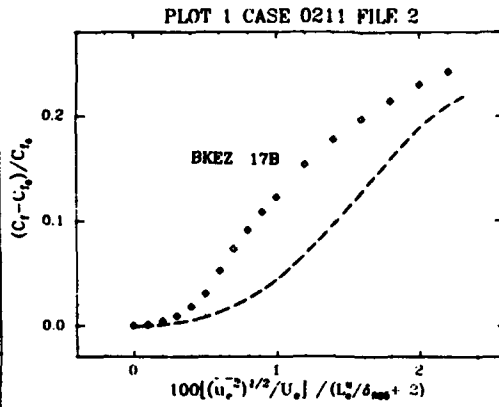
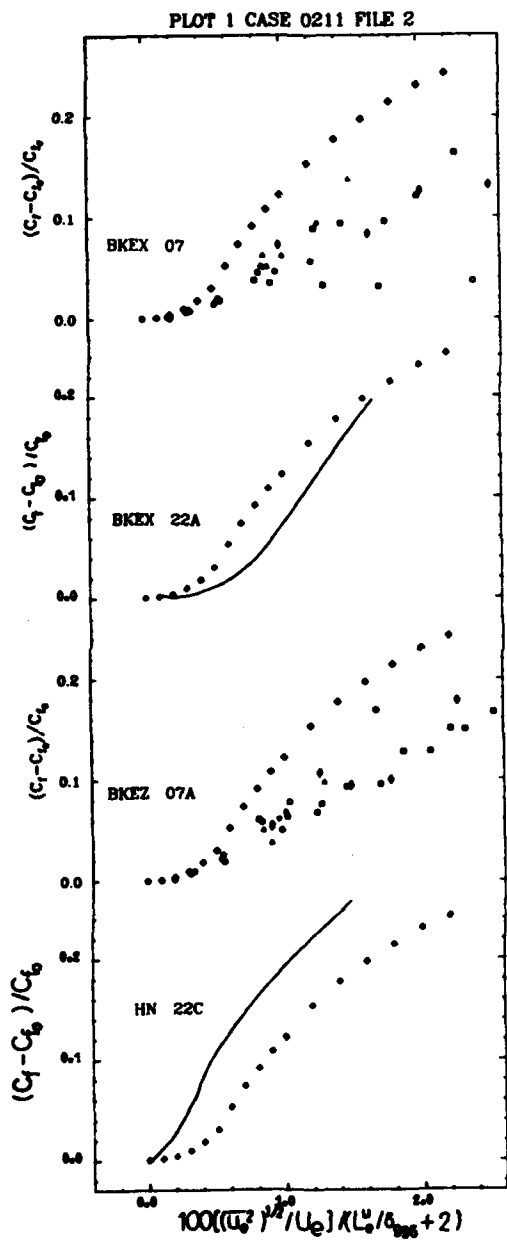


PLATE 27

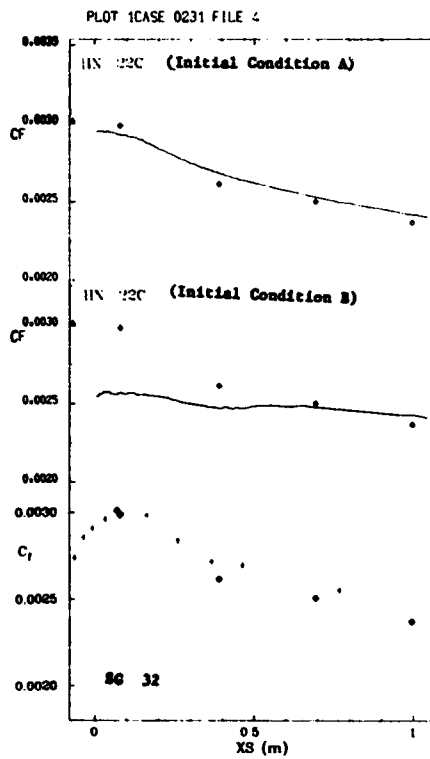
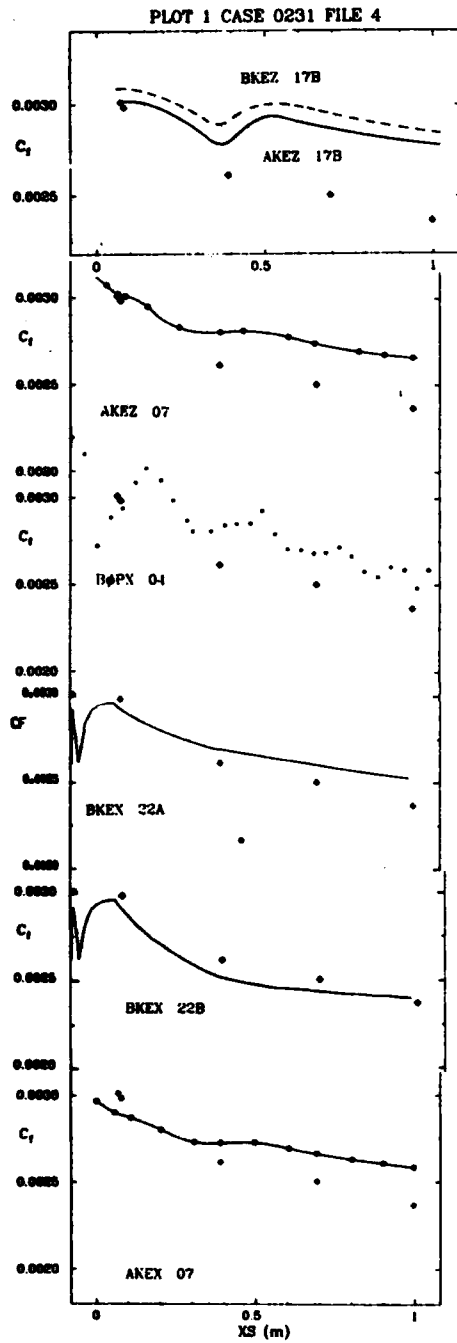


PLATE 28

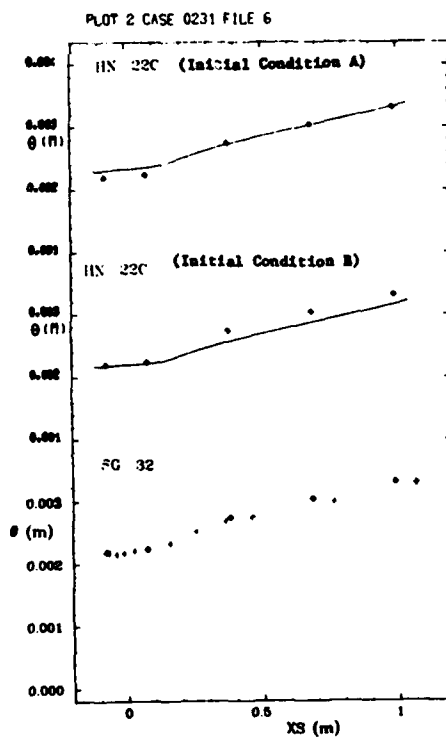
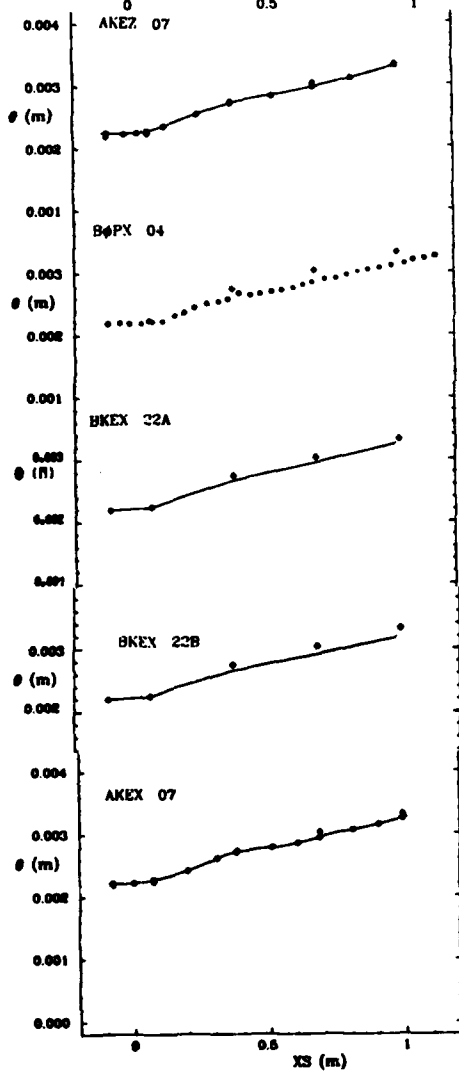
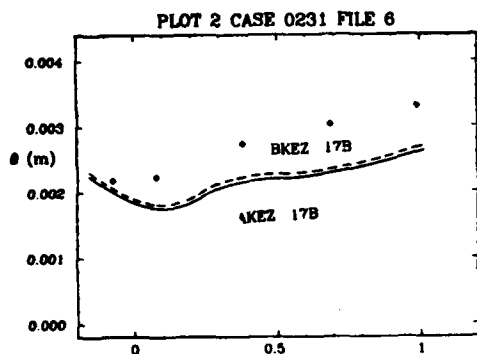


PLATE 29

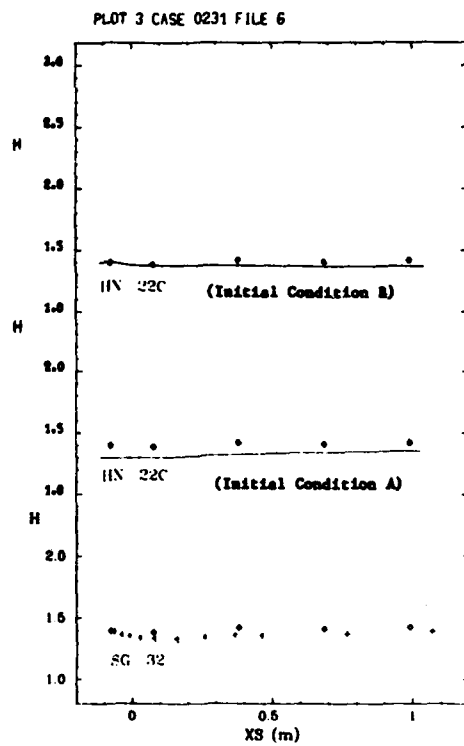
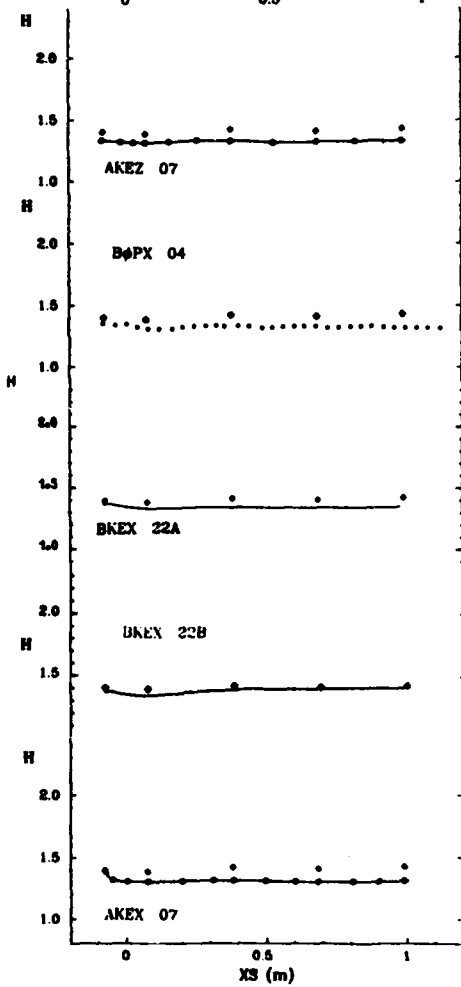
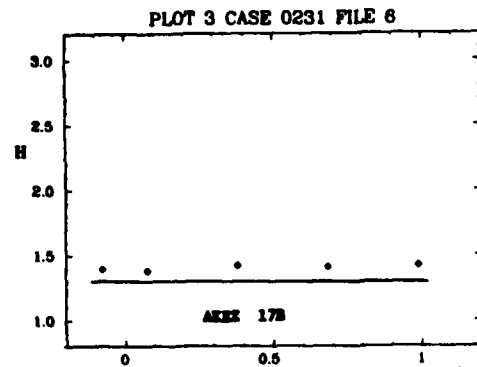


PLATE 30

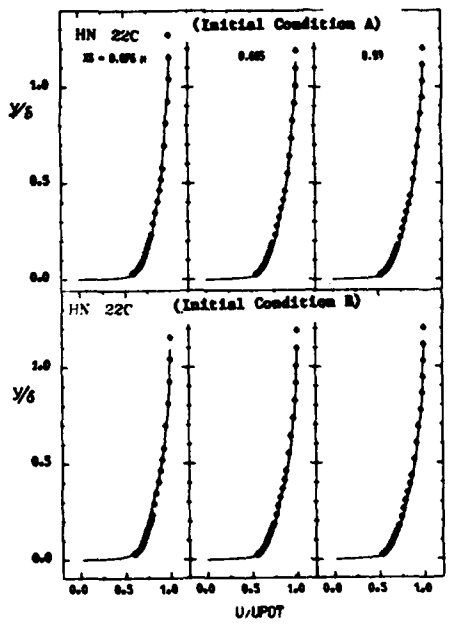
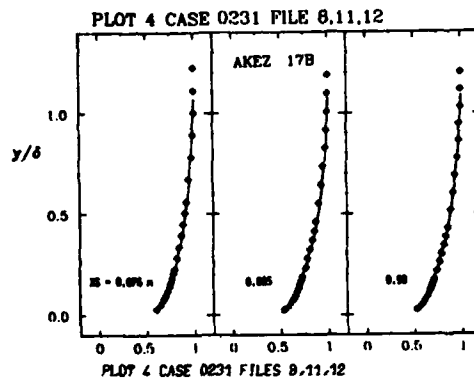
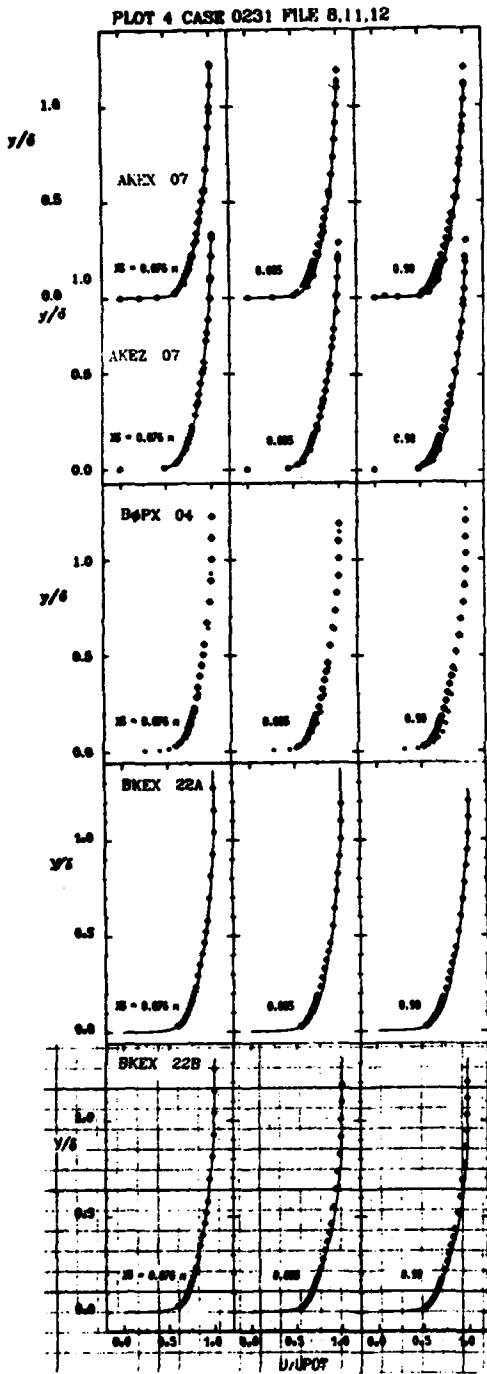
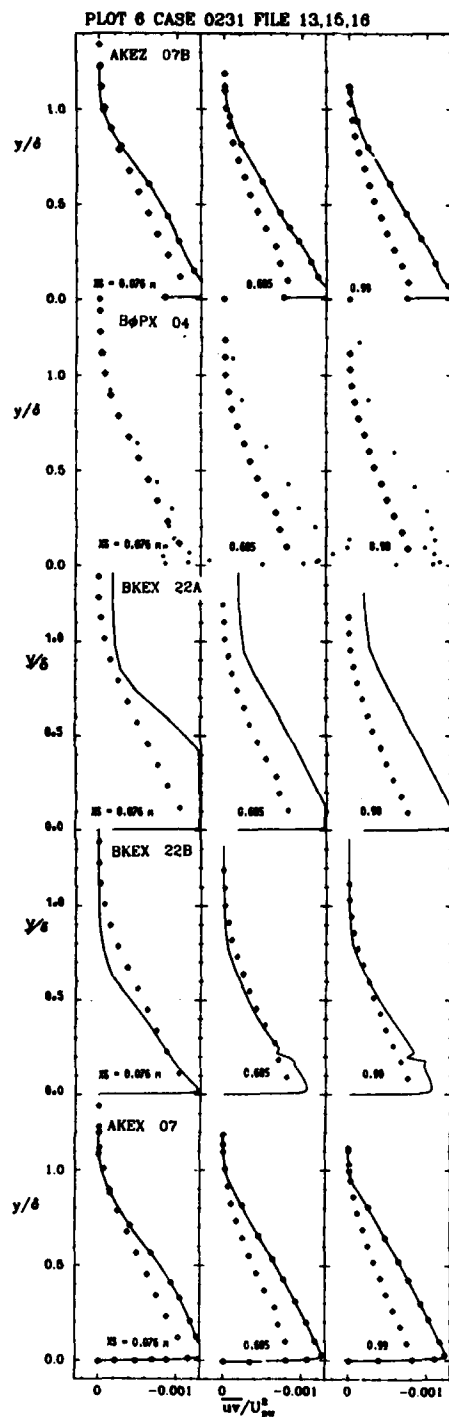
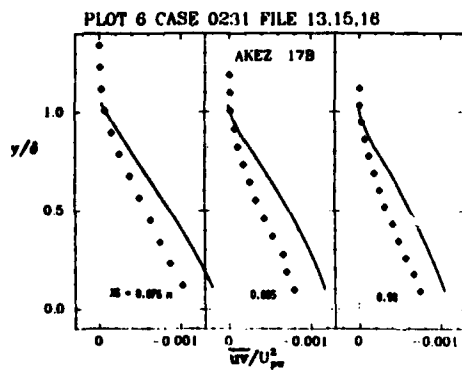
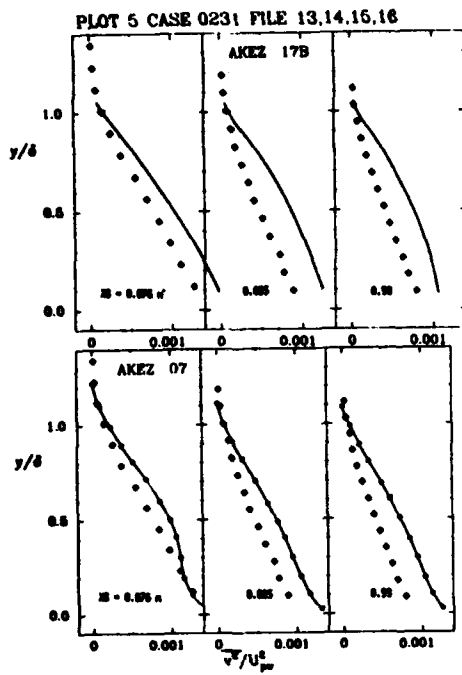


PLATE 31



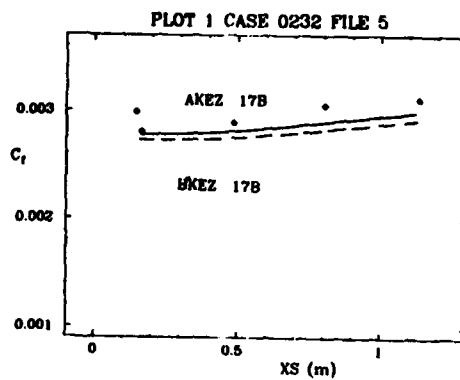
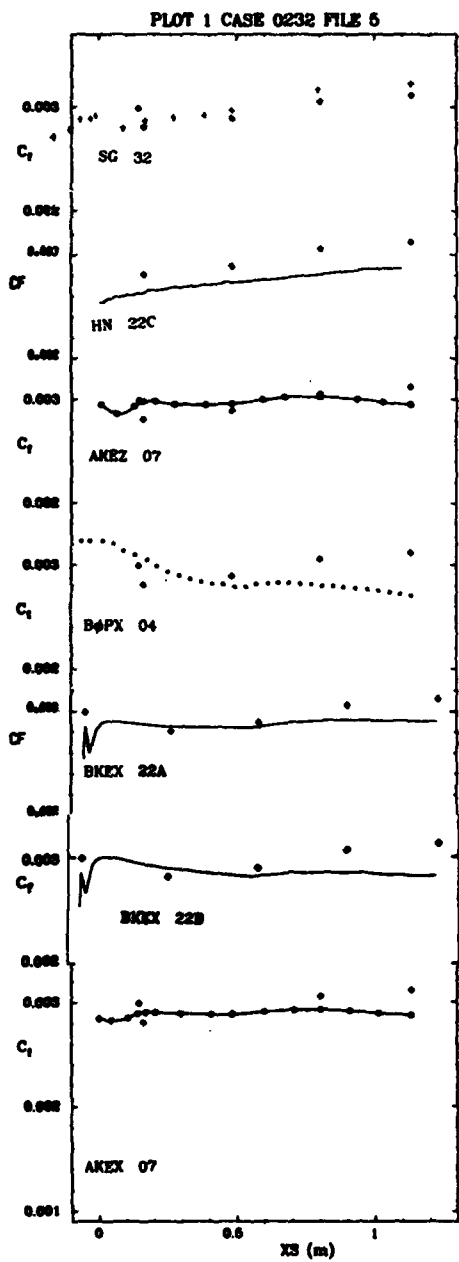


PLATE 33

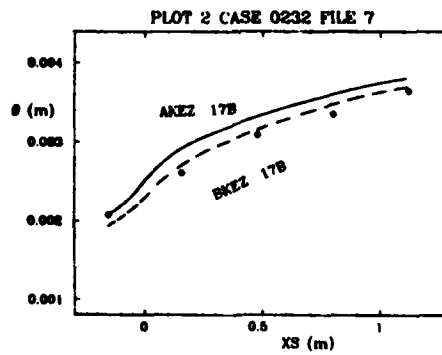
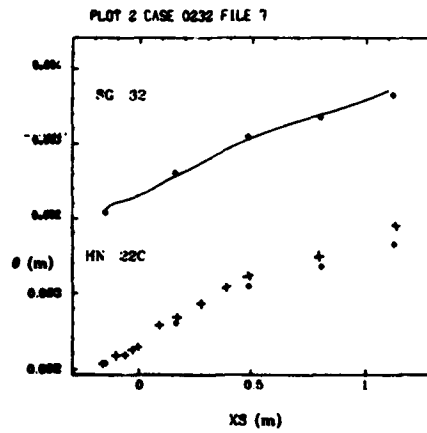
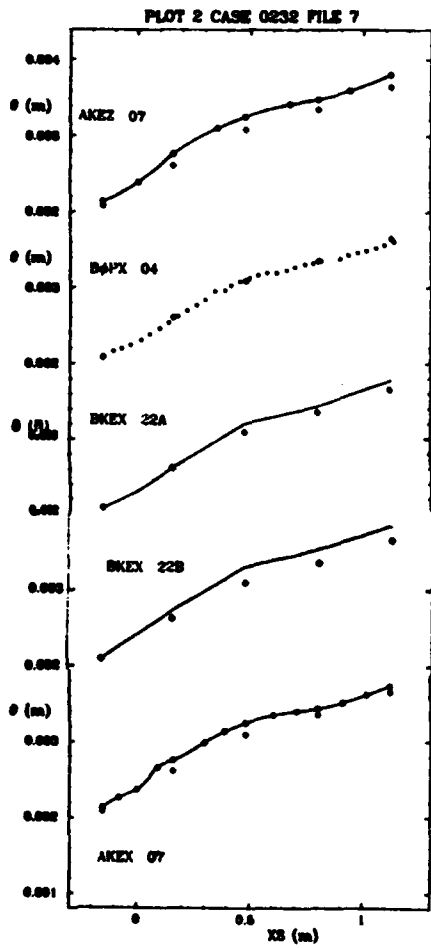


PLATE 34

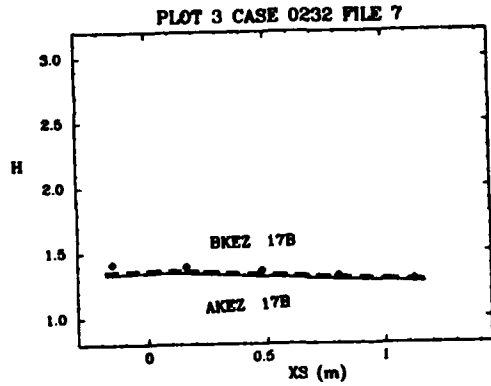
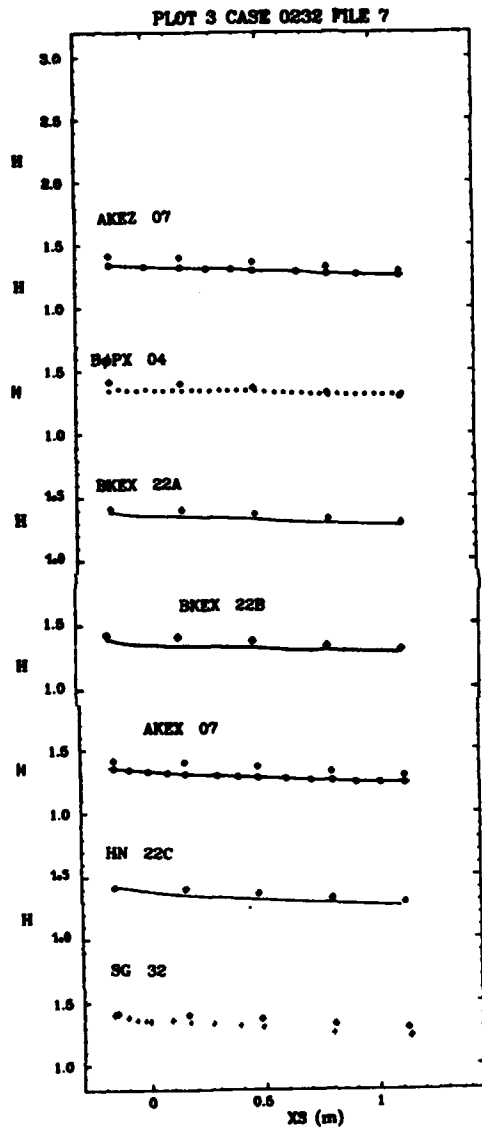
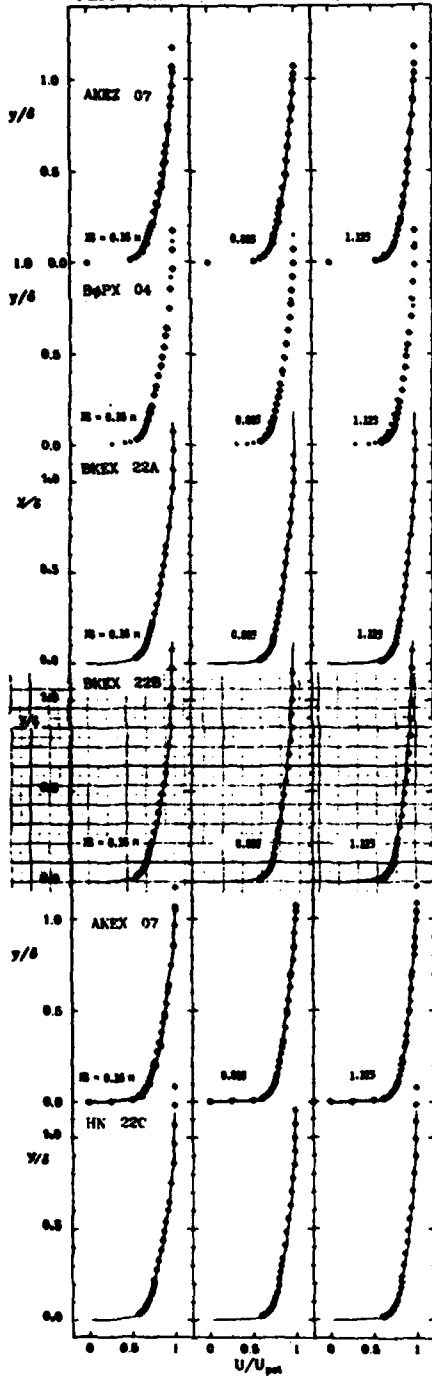
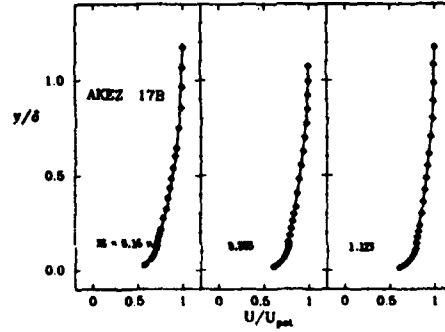


PLATE 35

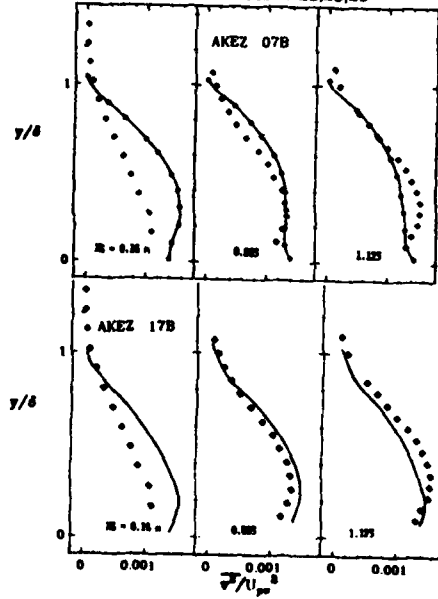
PLOT 4 CASE 0232 FILES 18,20,21



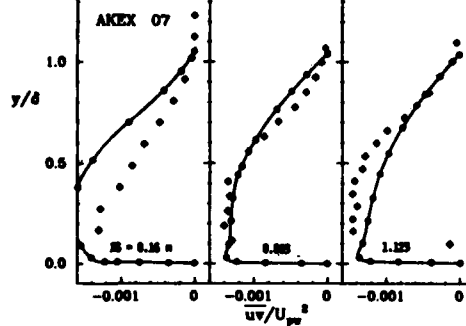
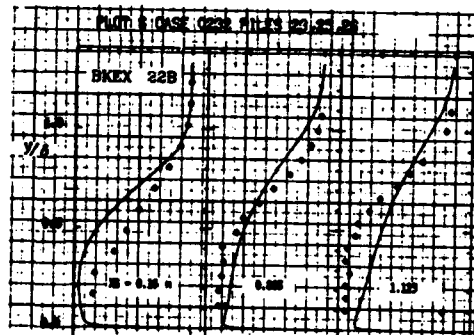
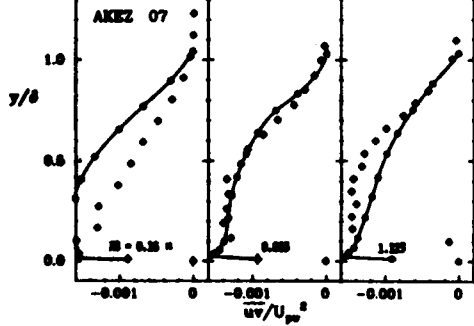
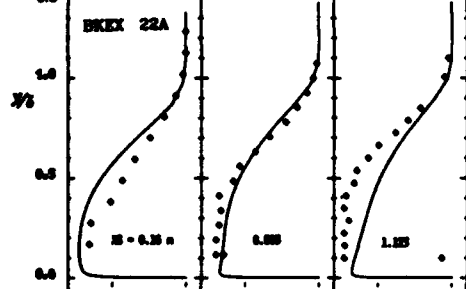
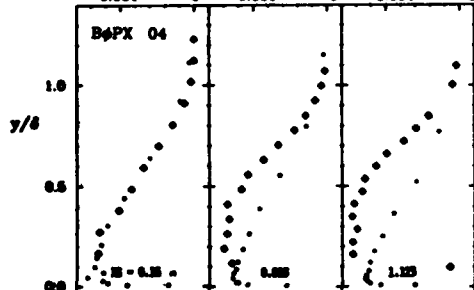
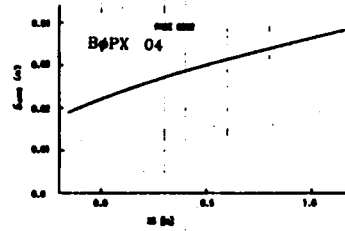
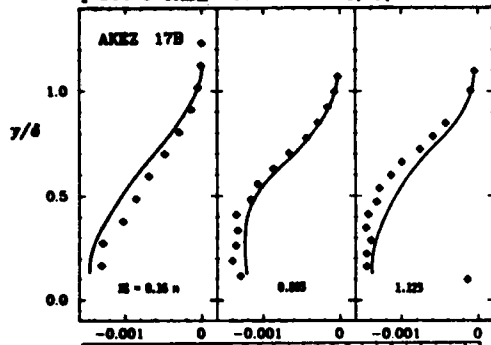
PLOT 4 CASE 0232 FILES 18,20,21



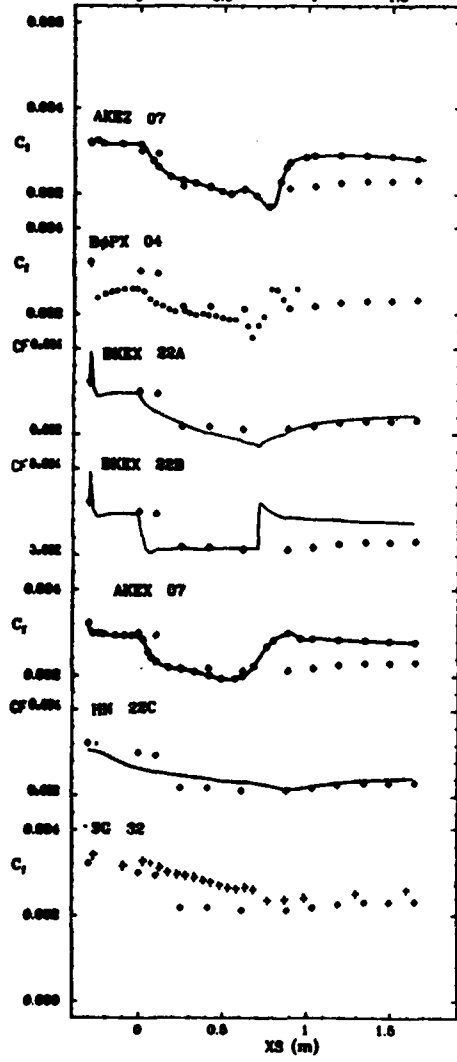
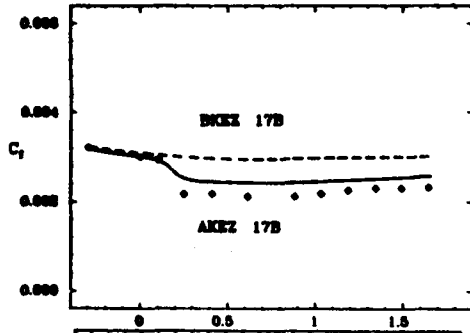
PLOT 5 CASE 0232 FILES 23,25,26



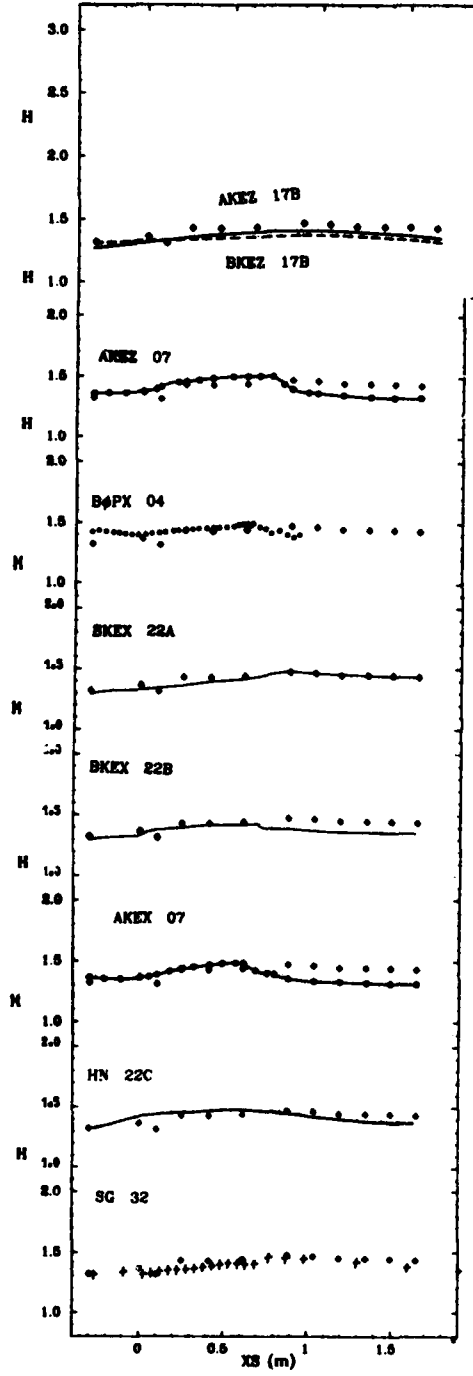
PLOT 6 CASE 0232 FILES 23,25,26



PLOT 1 CASE 0233 FILE 3



PLOT 2 CASE 0233 FILE 3



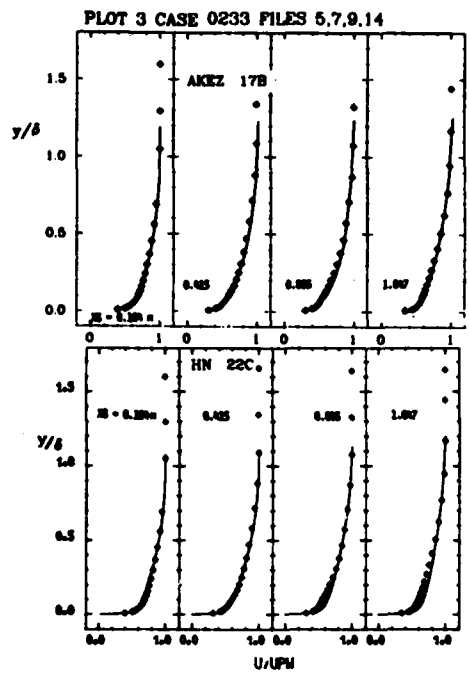
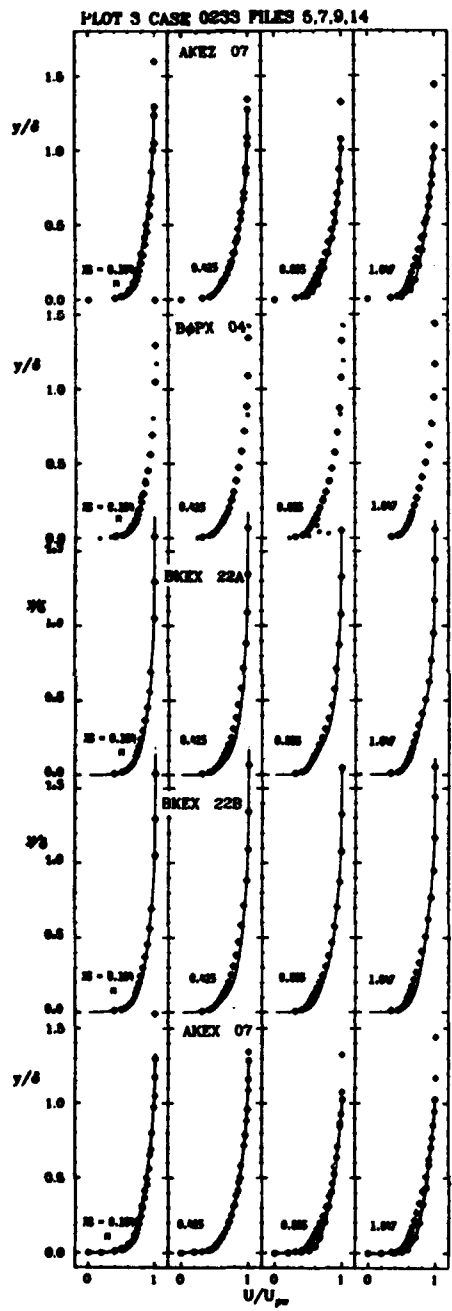
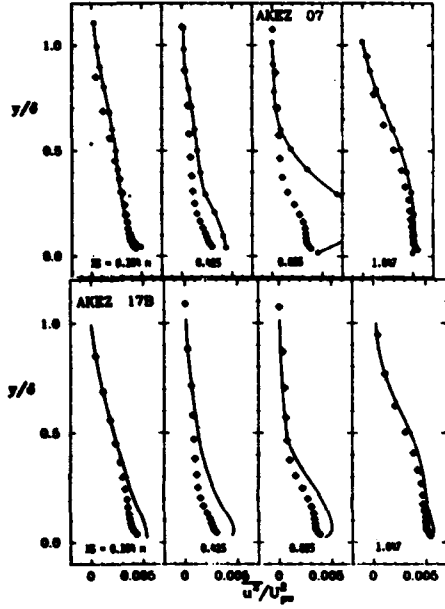


PLATE 39

PLCT 4 CASE 0233 FILES 17,19,21,26



PLCT 5 CASE 0233 FILES 17,19,21,26

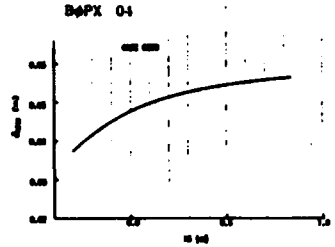
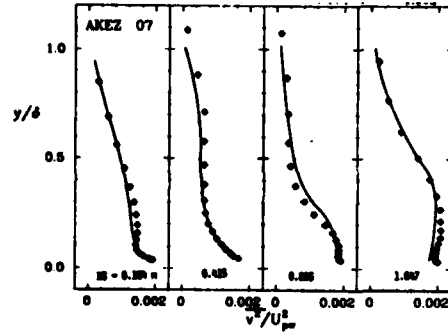


PLATE 40

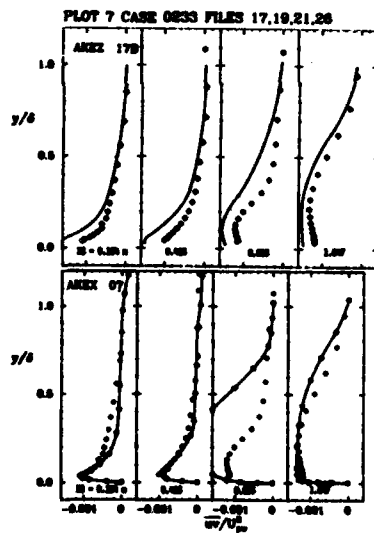
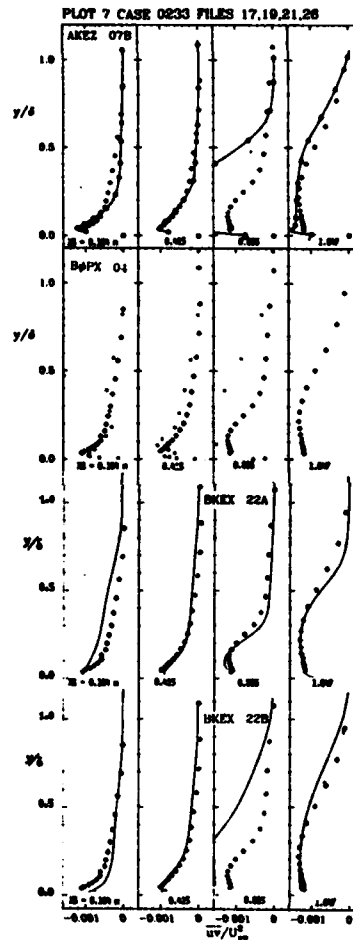
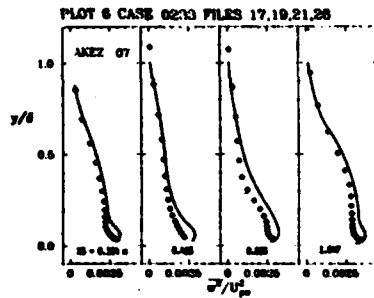
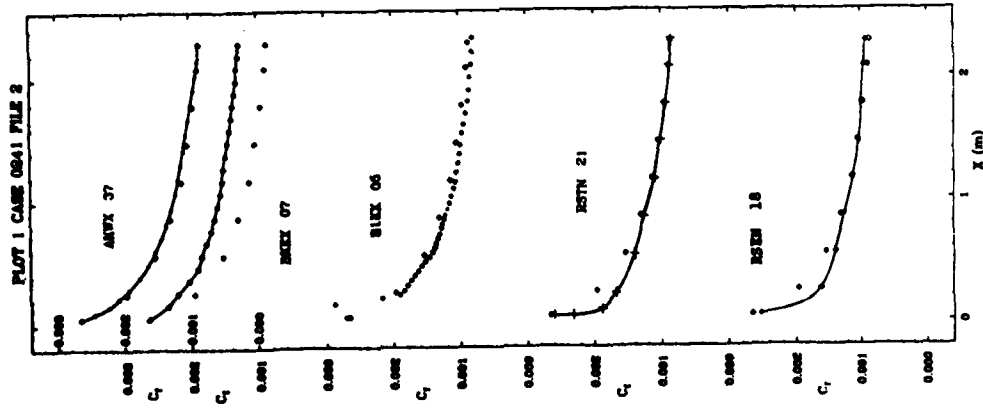
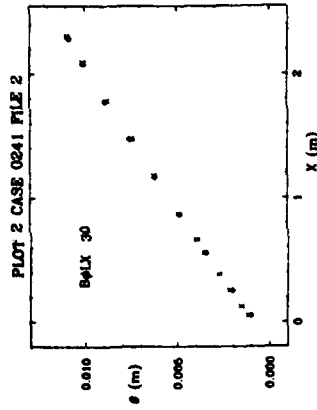
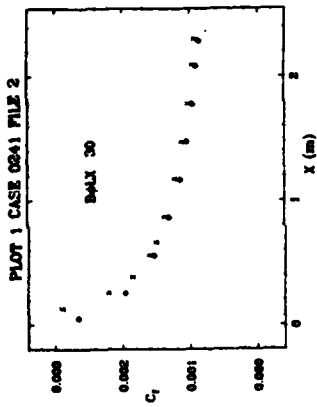
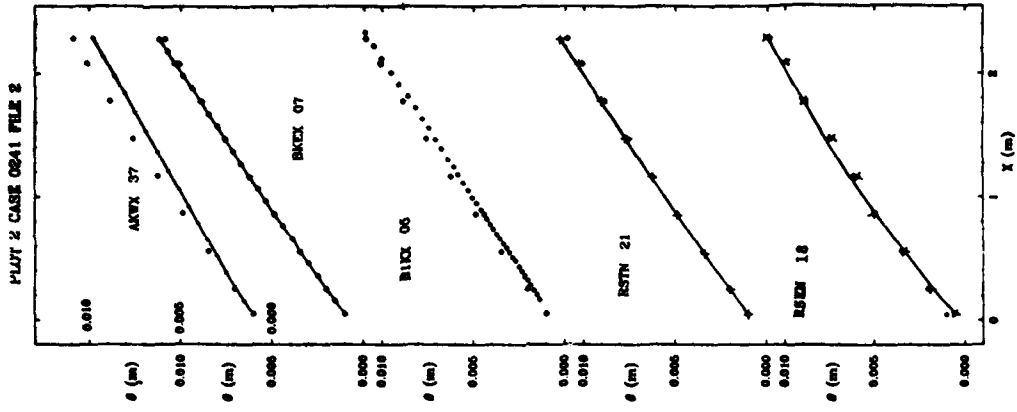


PLATE 41



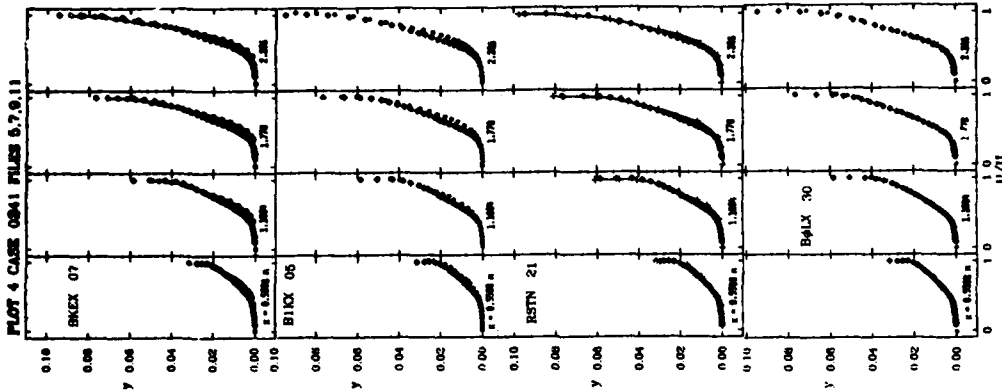
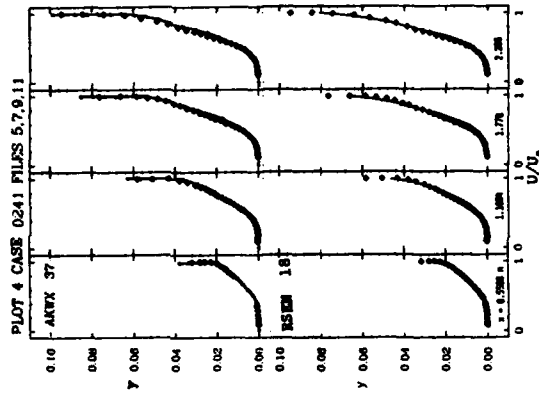
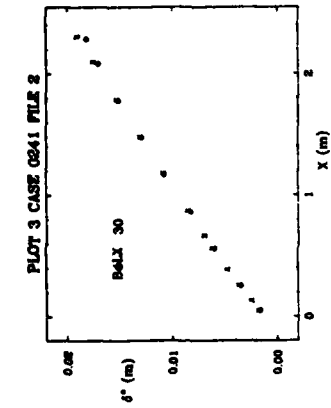
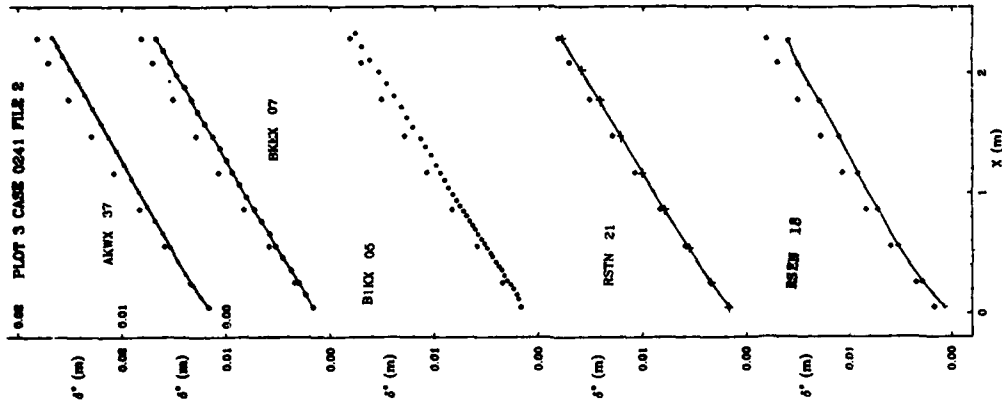
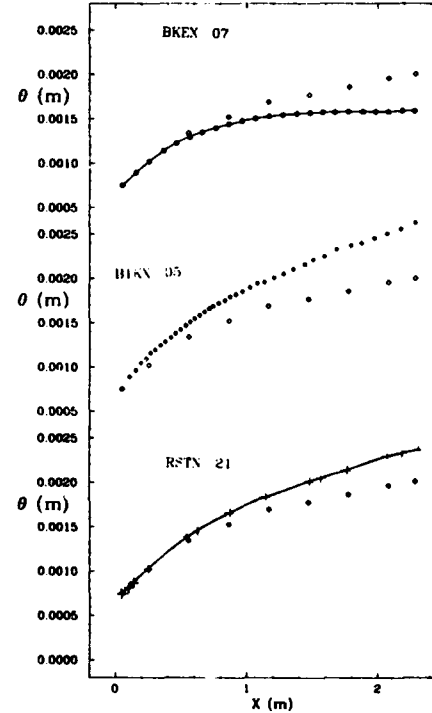
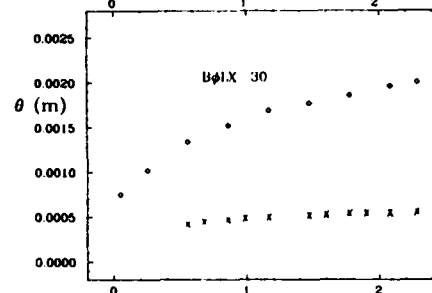
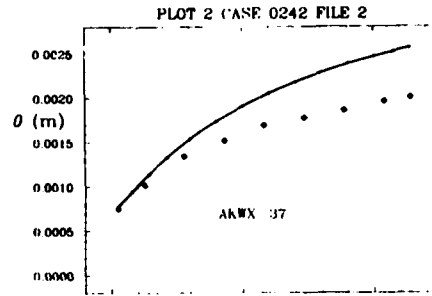
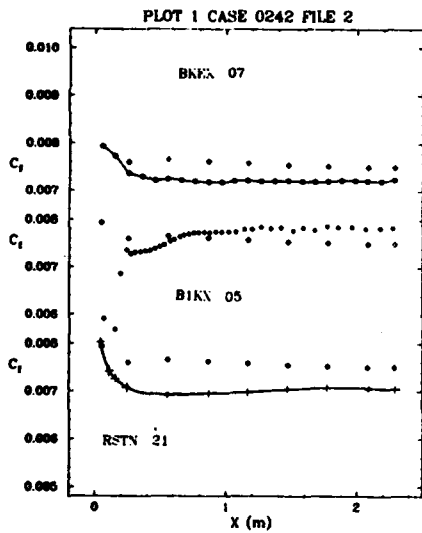
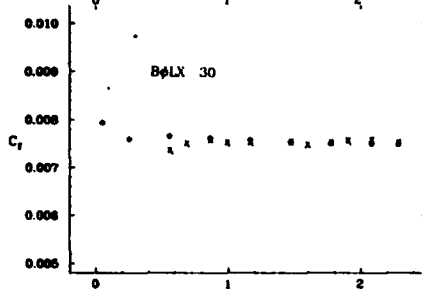
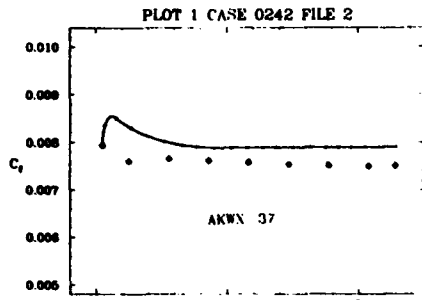


PLATE 43



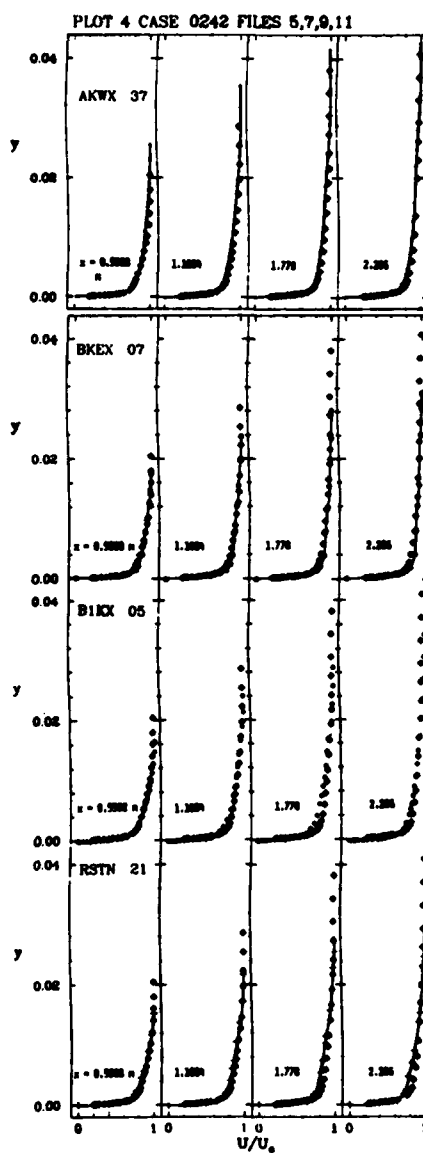
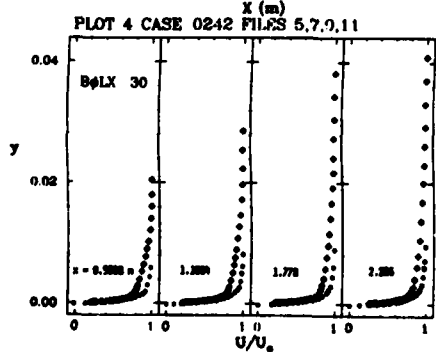
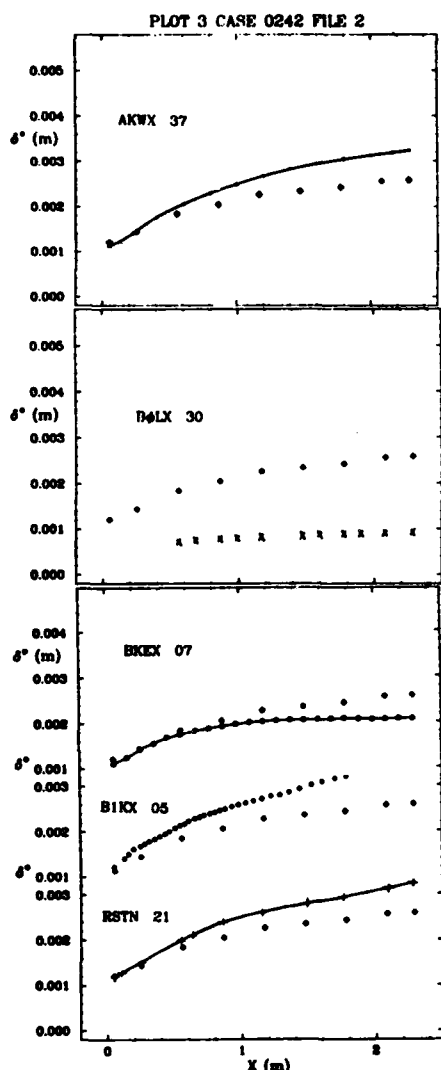


PLATE 45

$\bullet - (\sqrt{y})^{1/2}/\mu_0$
 $\circ - \epsilon^{1/2}/\mu_0$

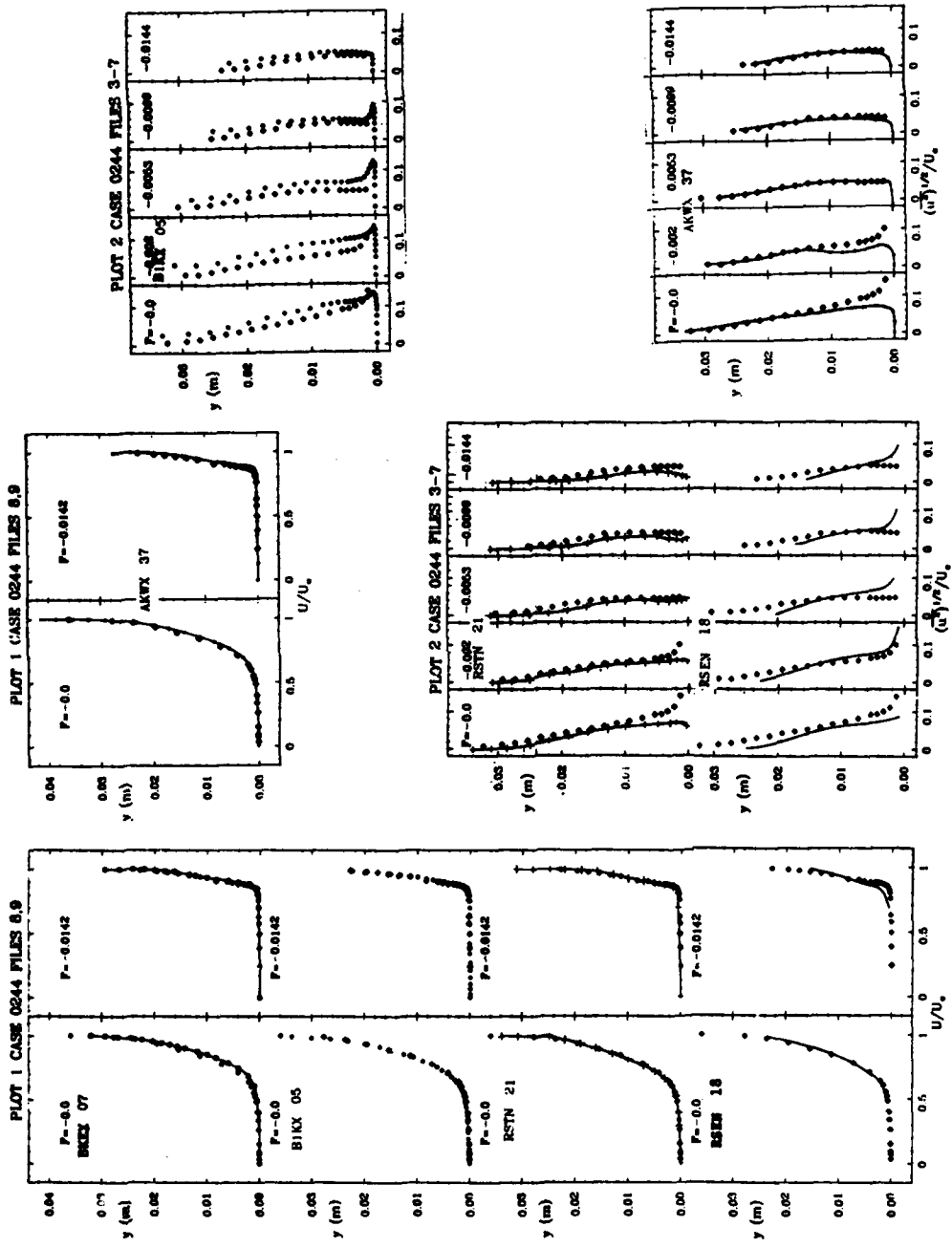


PLATE 46

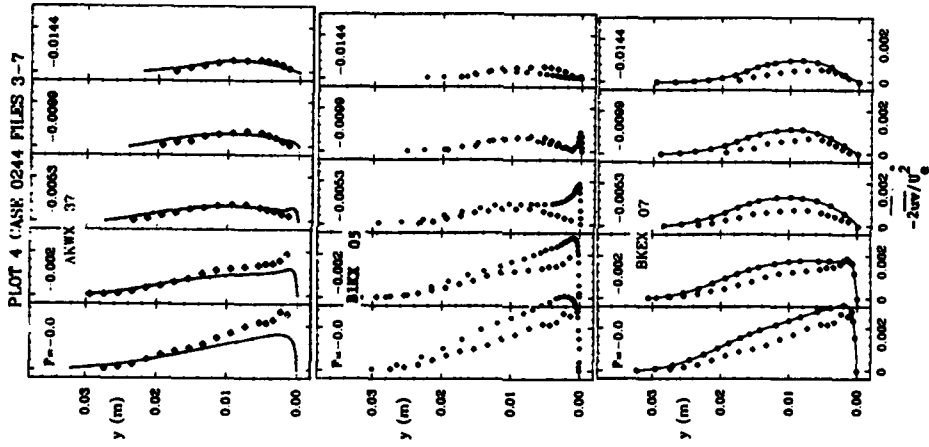
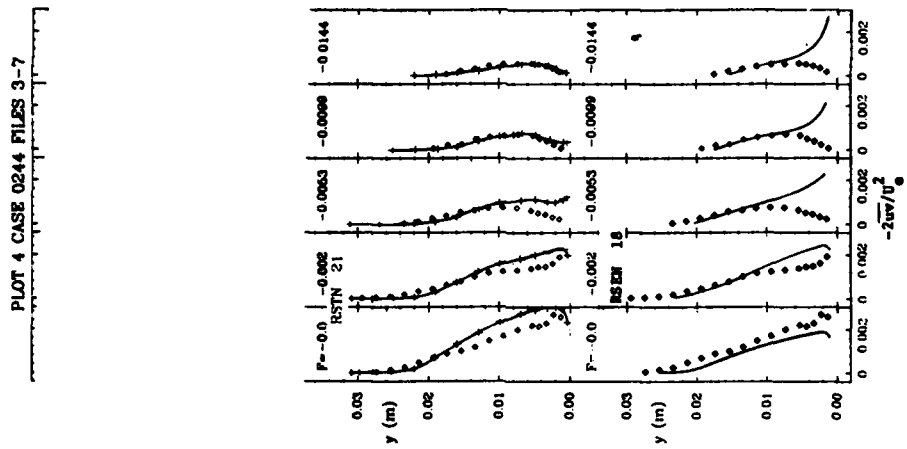


PLATE 47

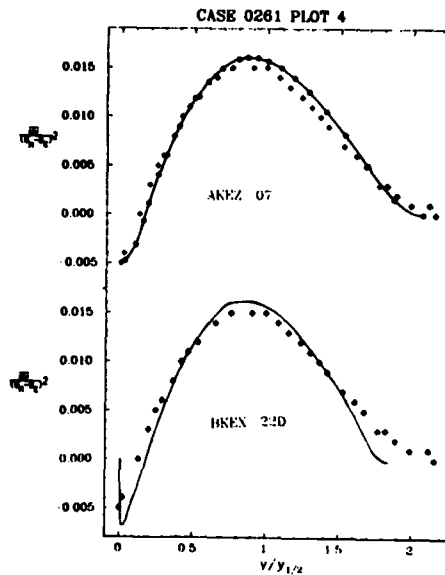
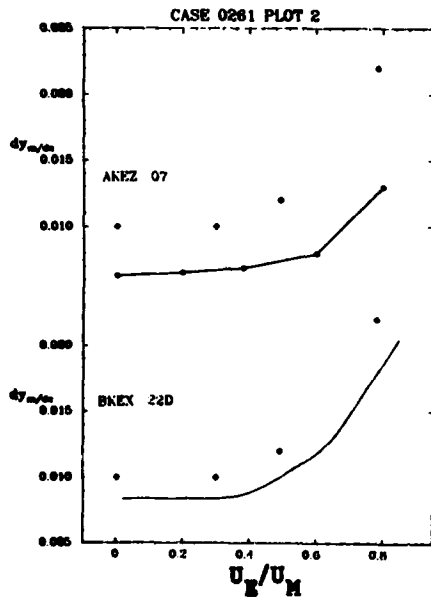
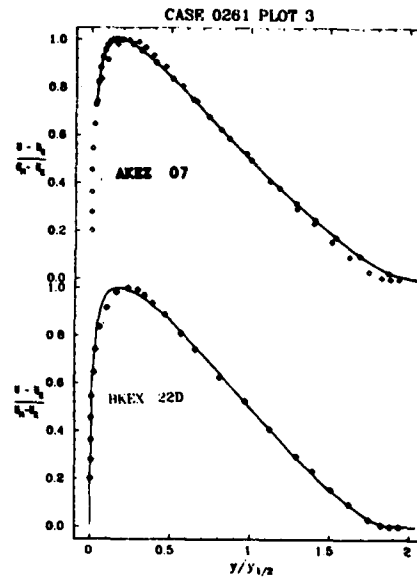
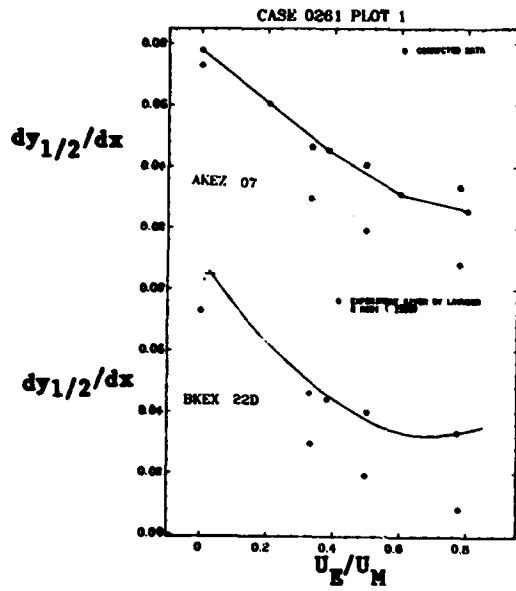
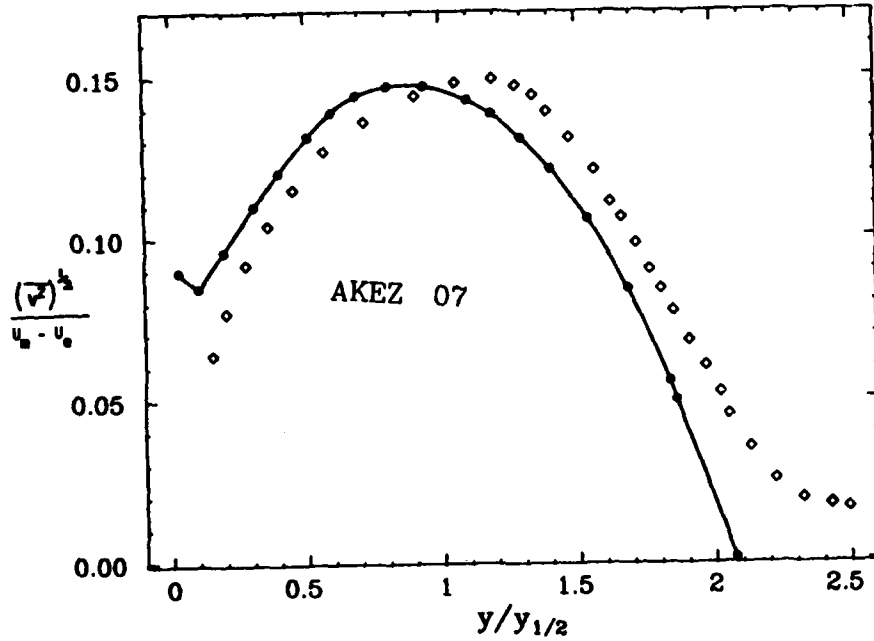


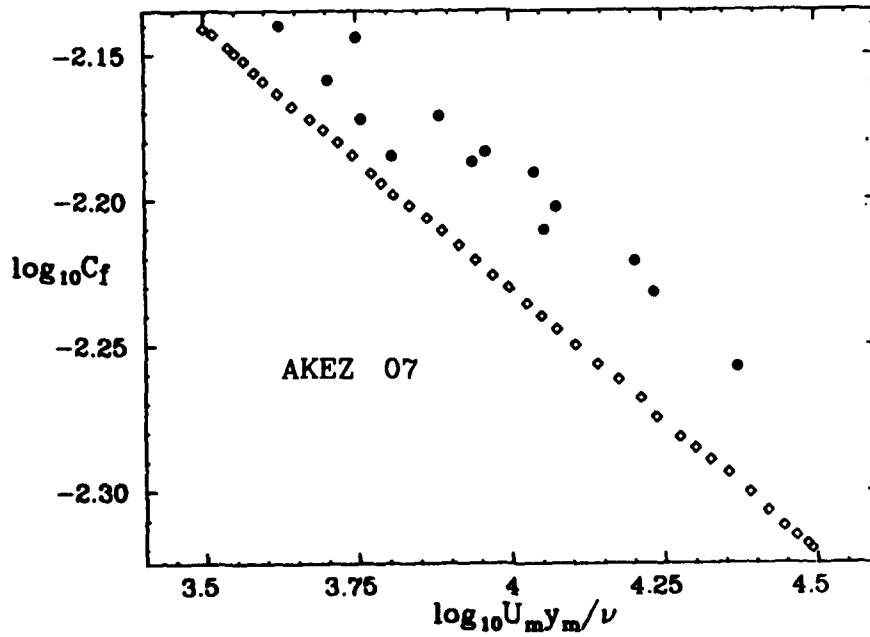
PLATE 48

See further output by Group 17³, pp. 1405-7.

CASE 0261 PLOT 6



PLOT 11 CASE 0261



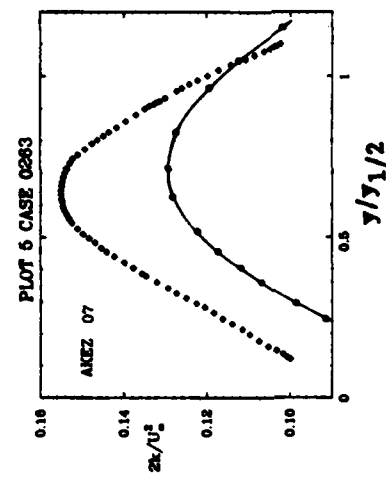
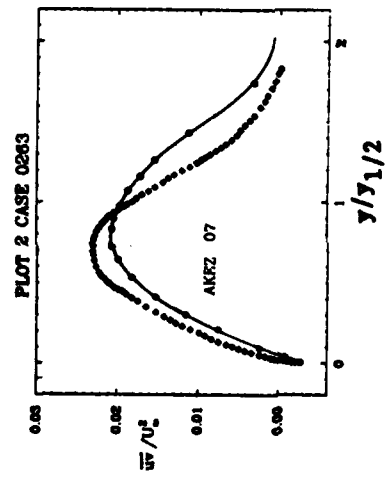
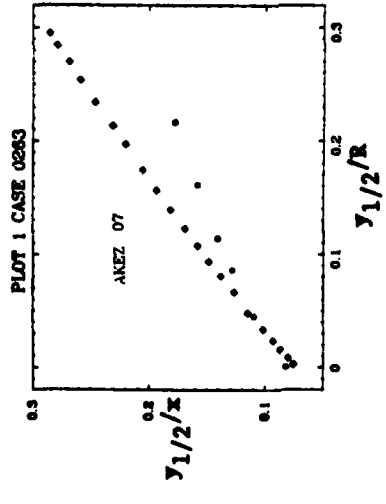
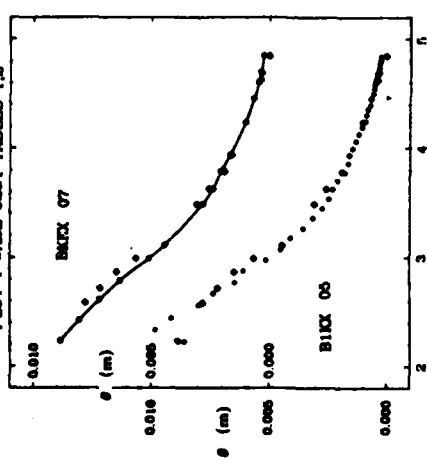


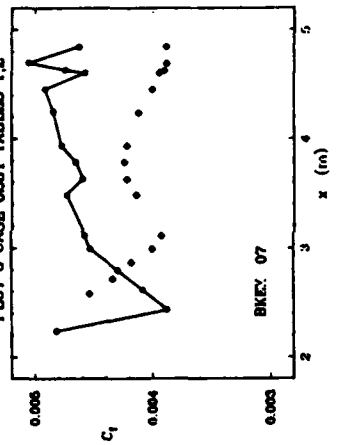
PLATE 50

See further output by Group 173, pp. 1405-7.

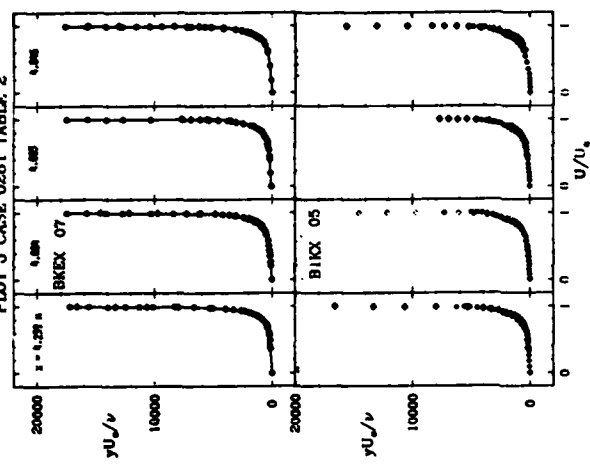
PLOT 1 CASE 0281 TABLES 1,2



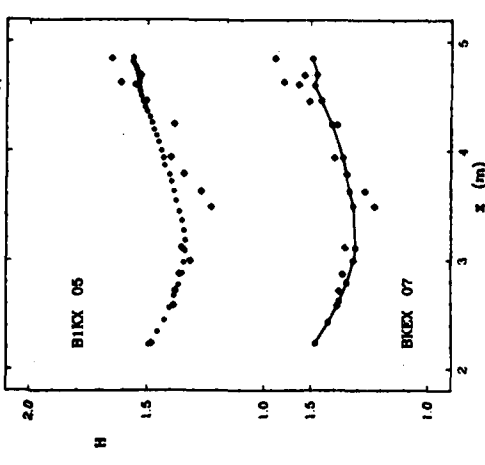
PLOT 3 CASE 0281 TABLES 1,2



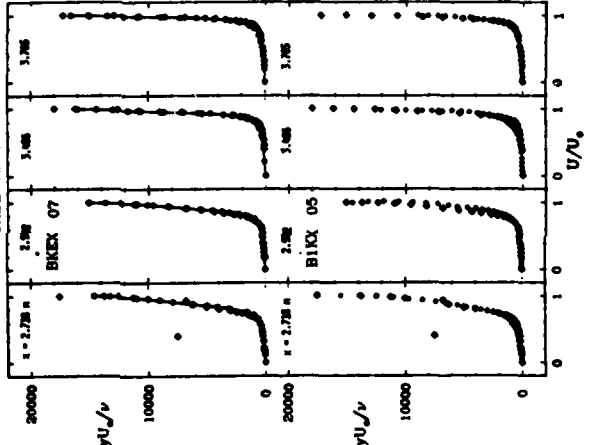
PLOT 5 CASE 0281 TABLE 2



PLOT 2 CASE 0281 TABLES 1,2



PLOT 4 CASE 0281 TABLE 2



PLOT 6 CASE 0281 TABLE 2

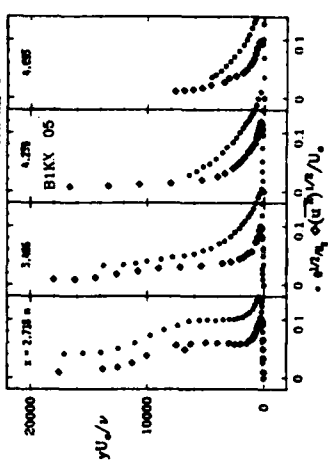
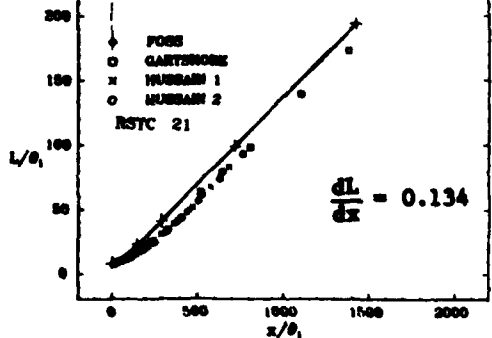
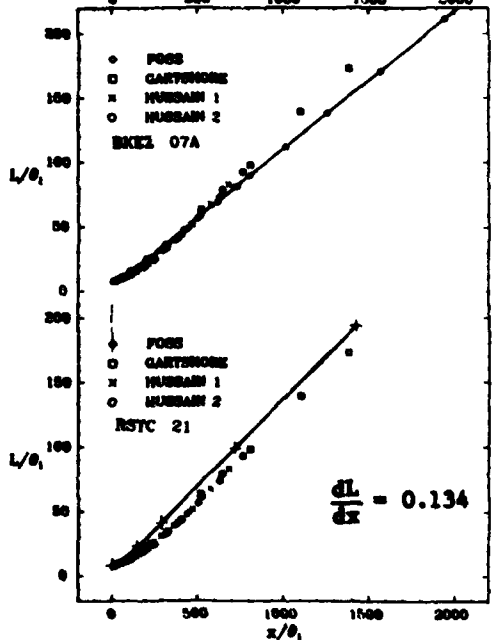
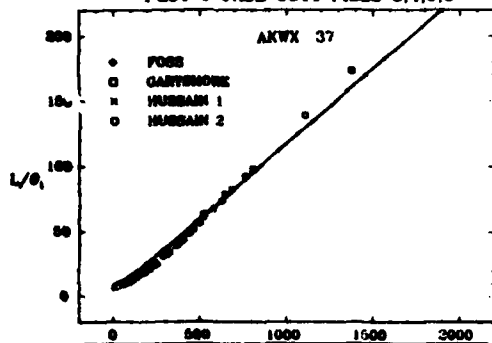
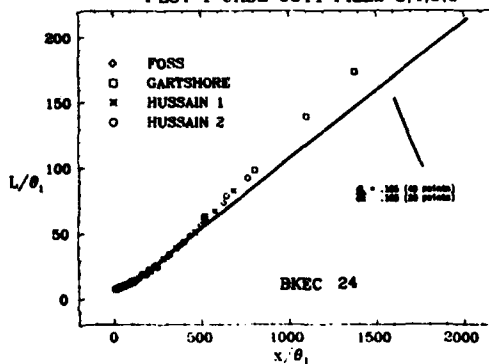


PLATE 51

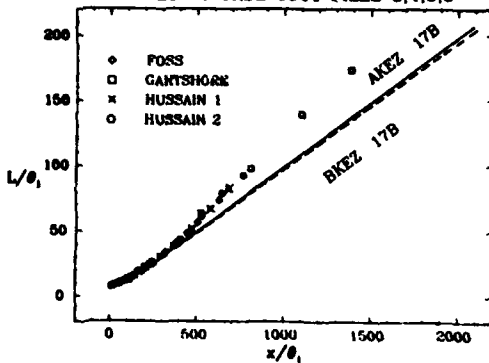
PLOT 1 CASE 0311 FILES 3,4,5,6



PLOT 1 CASE 0311 FILES 3,4,5,6



PLOT 1 CASE 0311 FILES 3,4,5,6



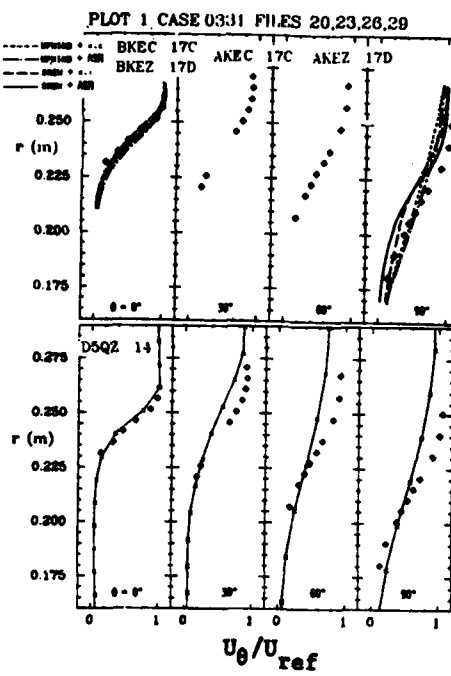
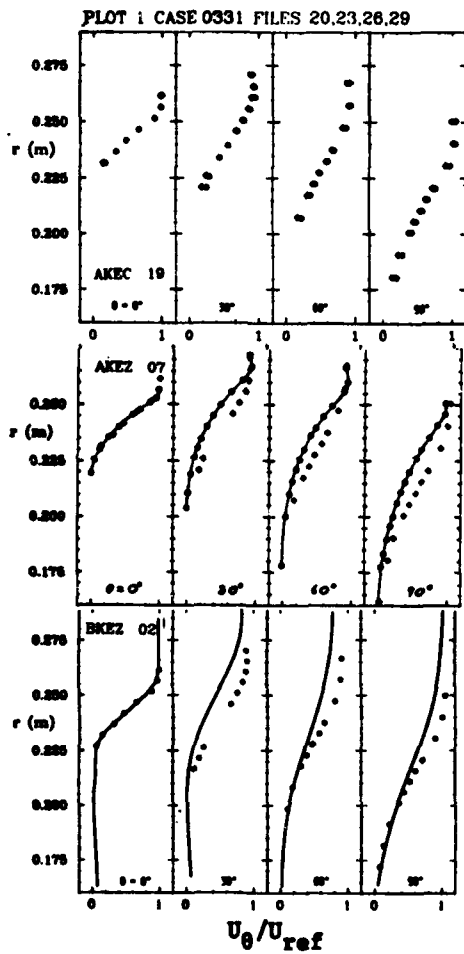


PLATE 53

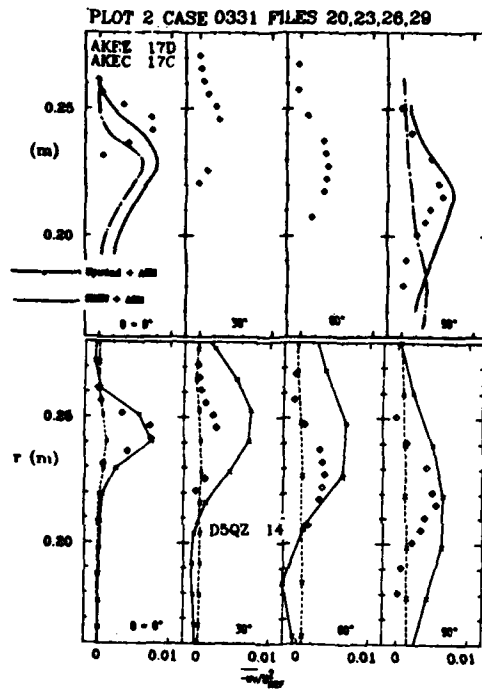
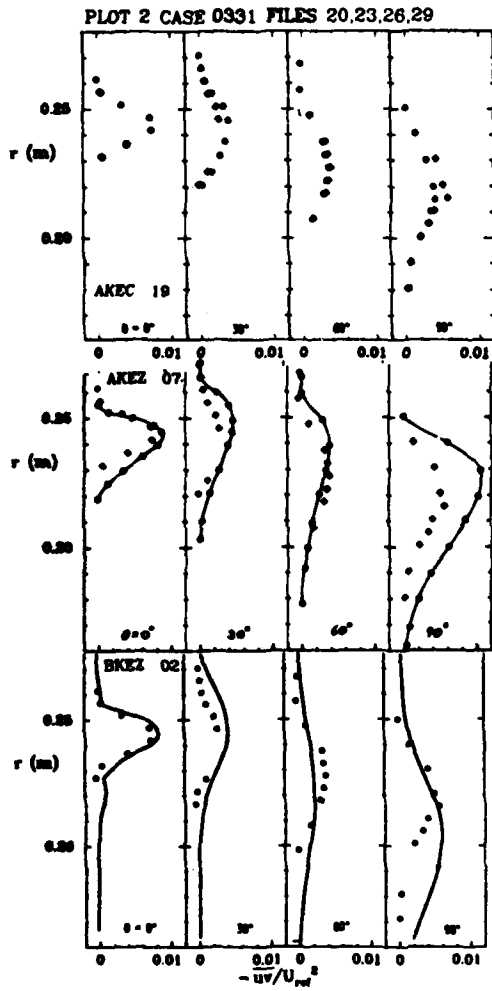


PLATE 54

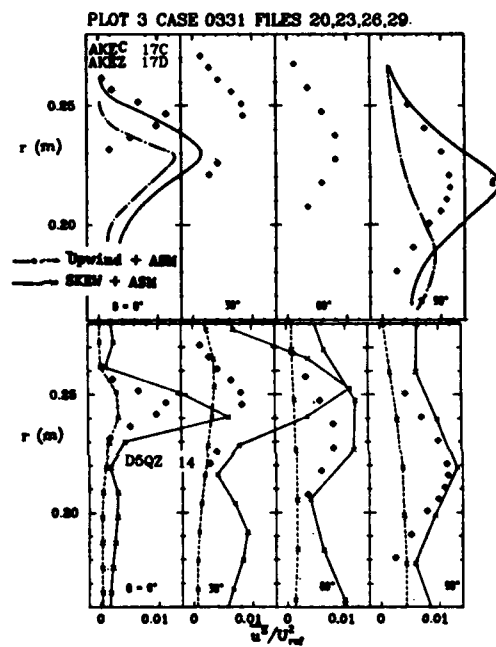
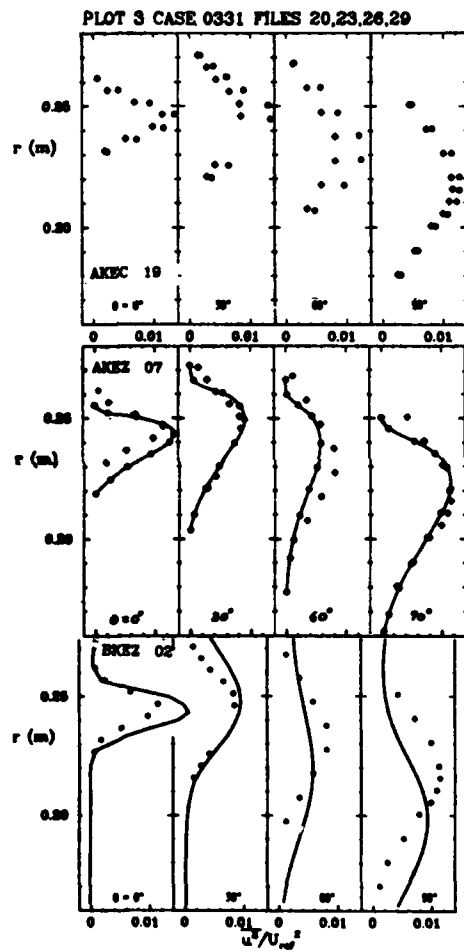


PLATE 55

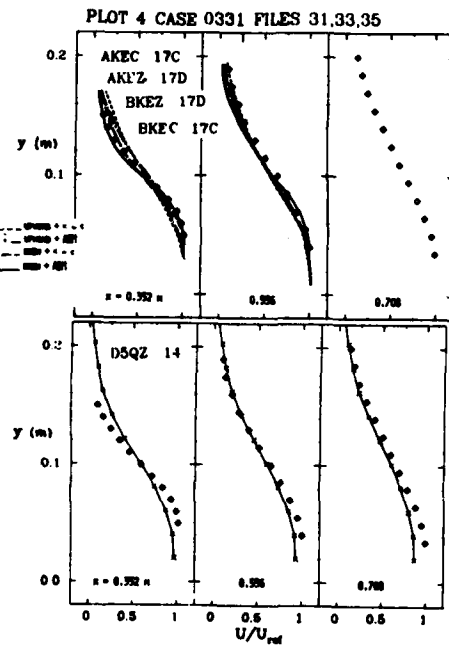
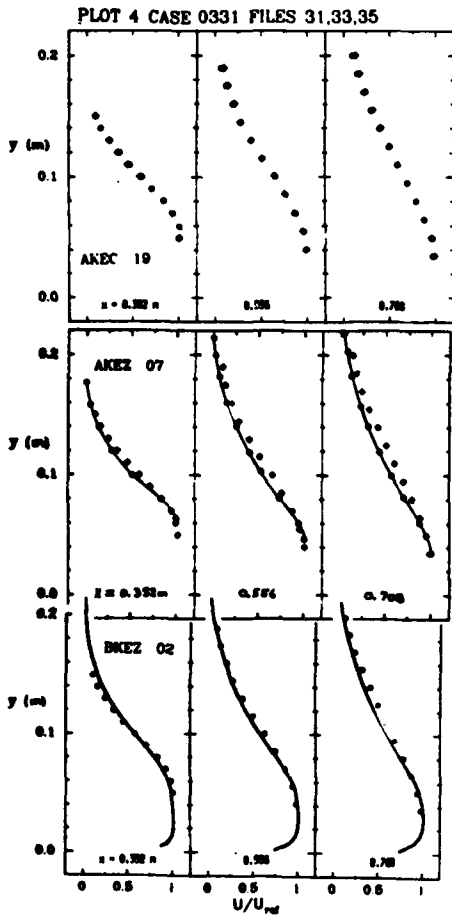


PLATE 56

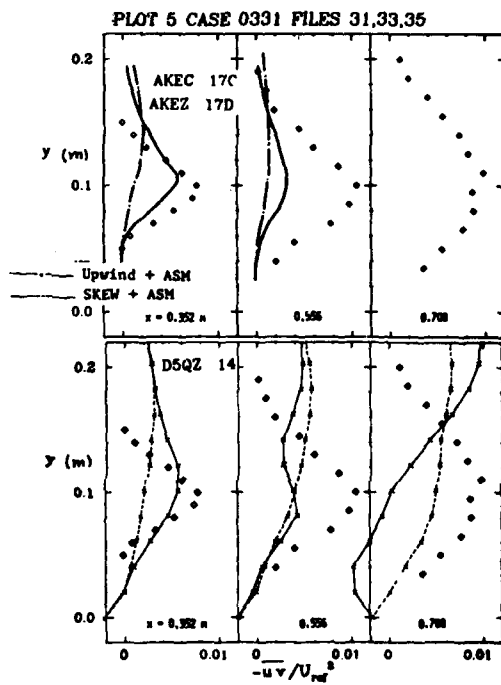
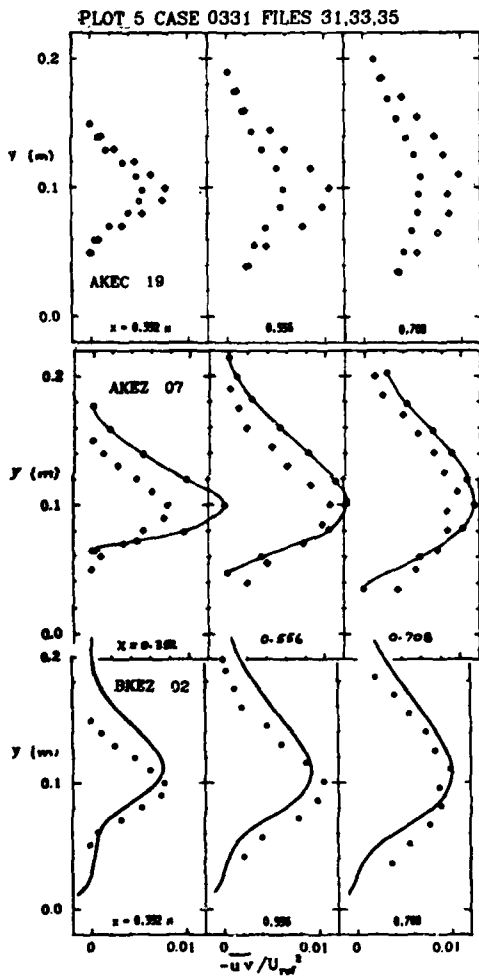


PLATE 57

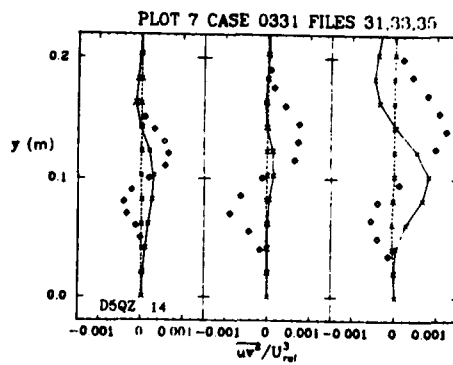
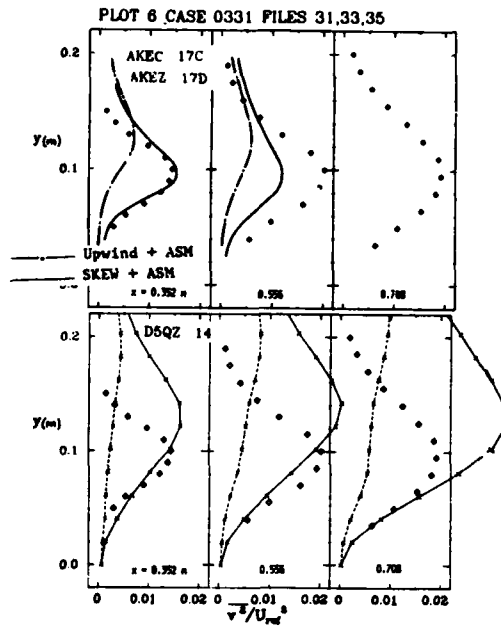
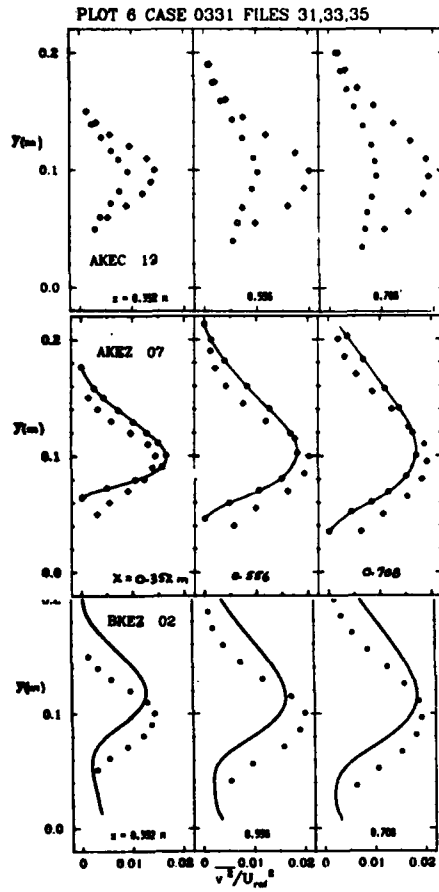


PLATE 58

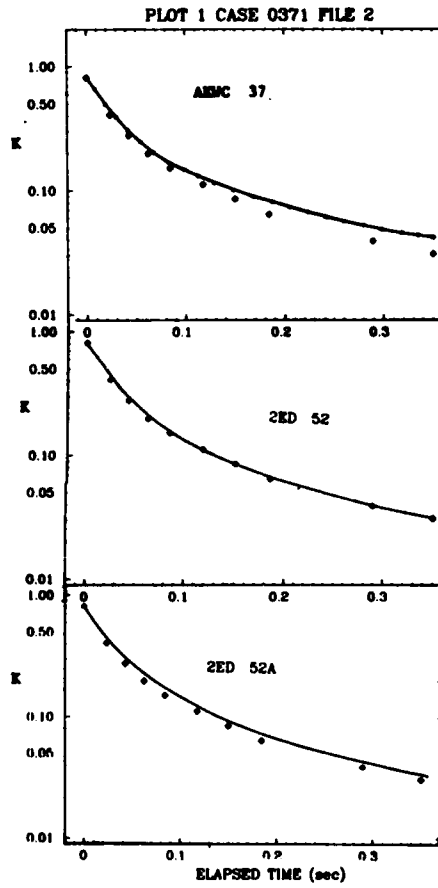
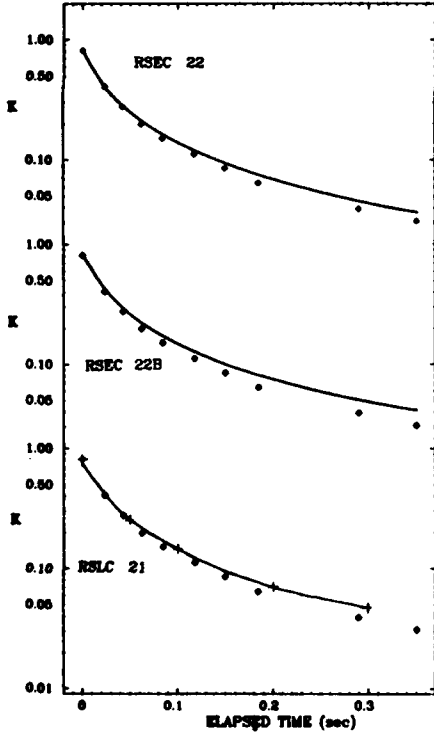
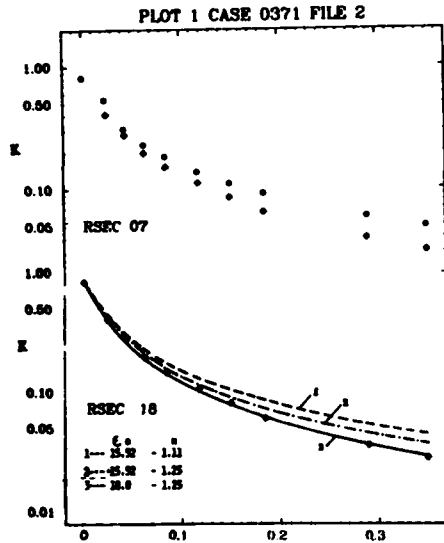


PLATE 59

PLOT 1 CASE 0372A FILE 3

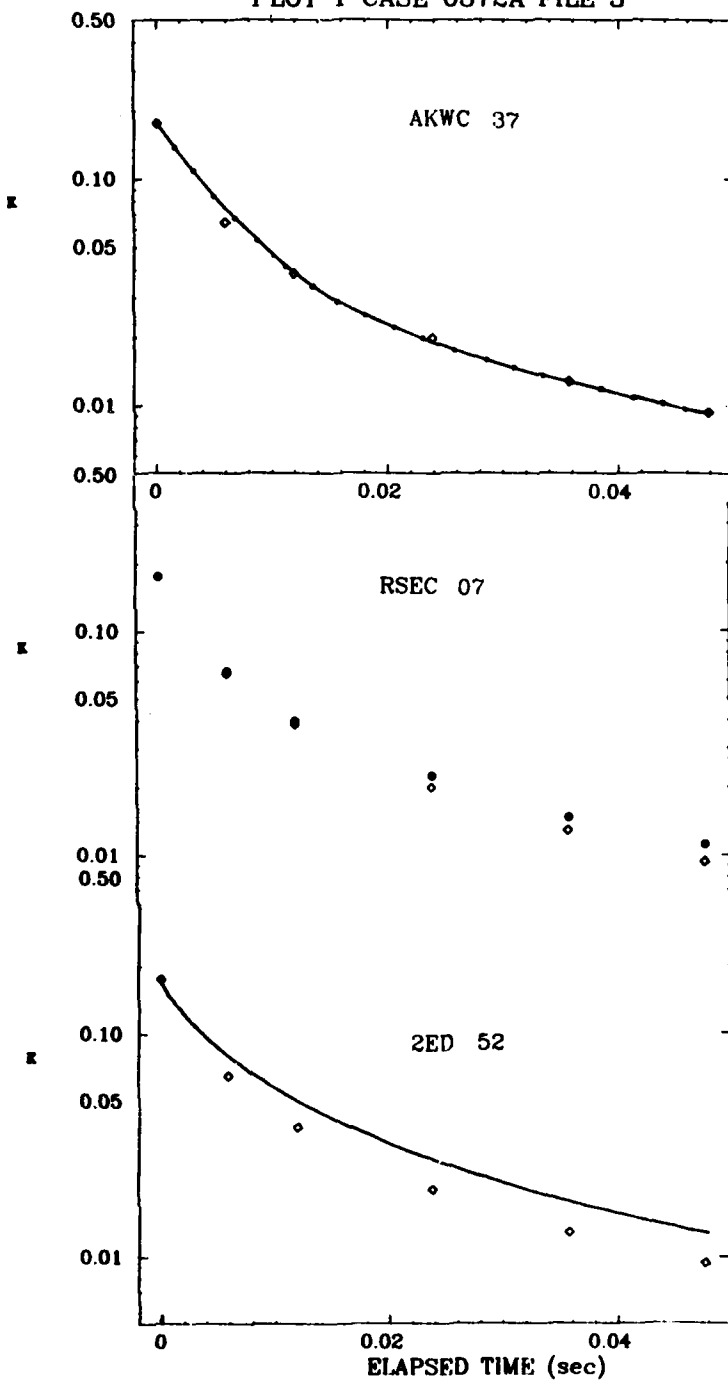


PLATE 60

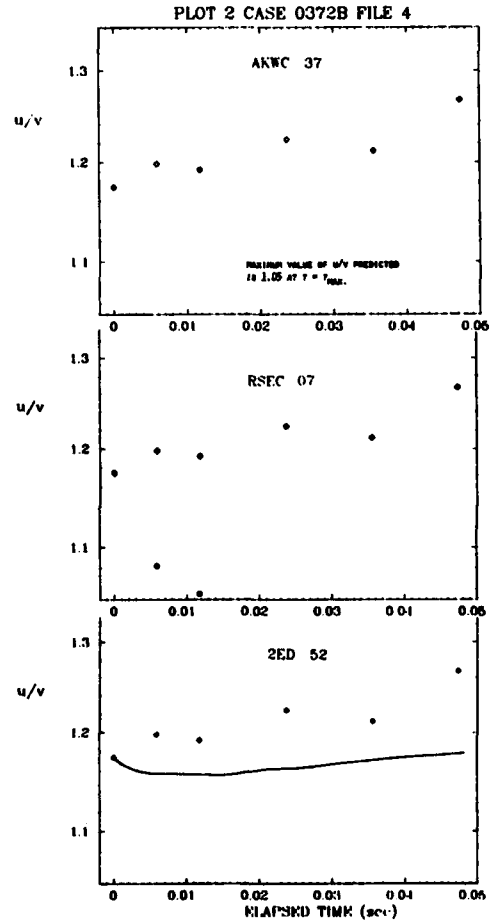
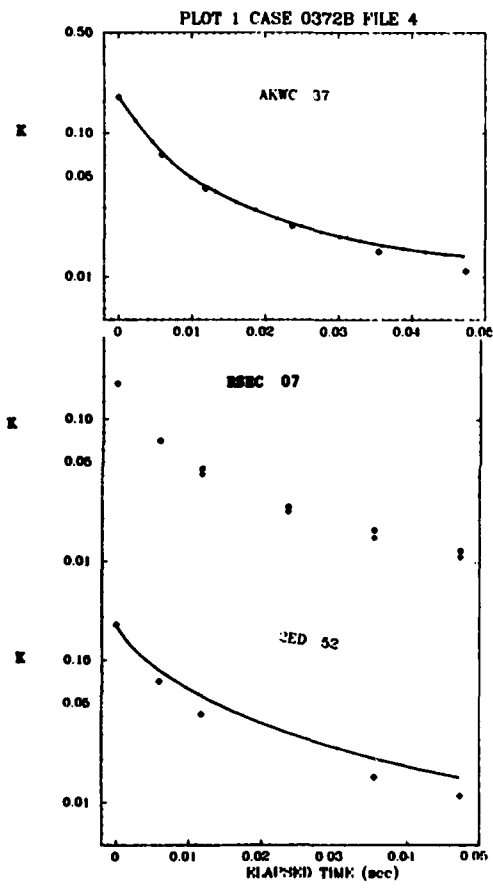


PLATE 61

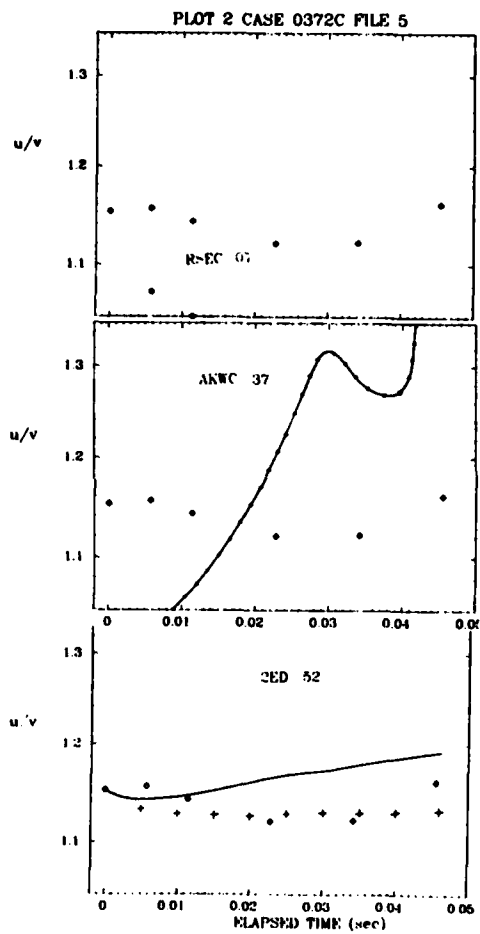
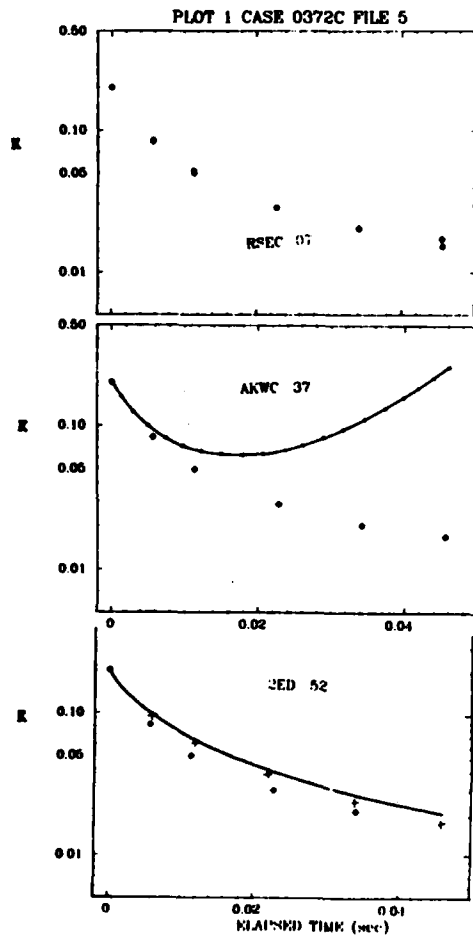
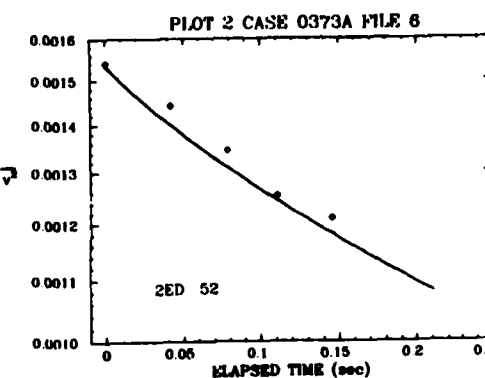
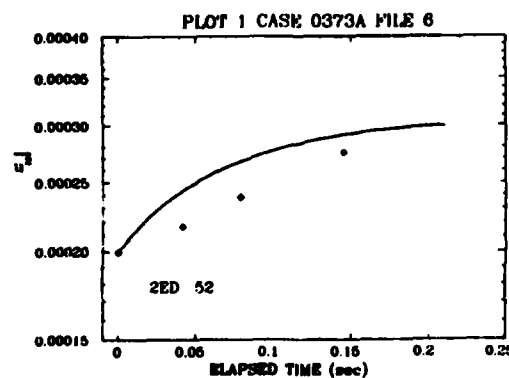
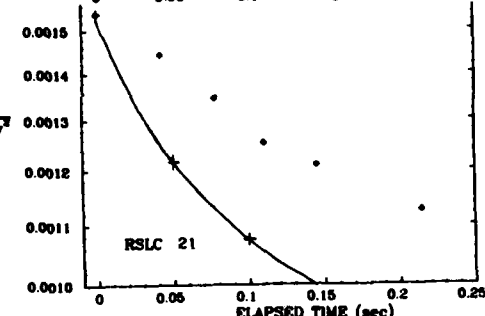
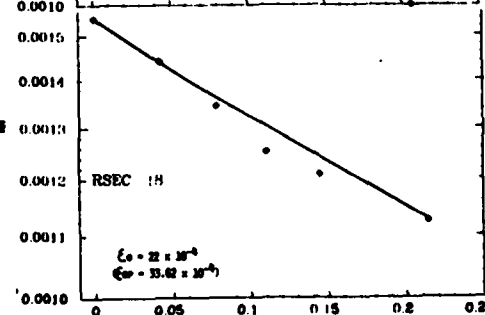
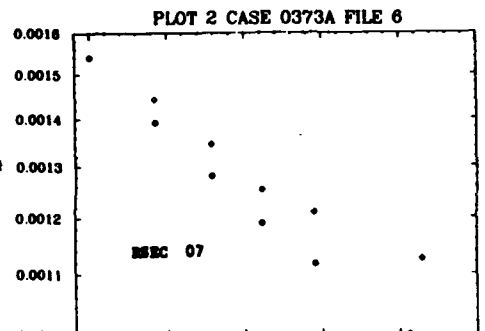
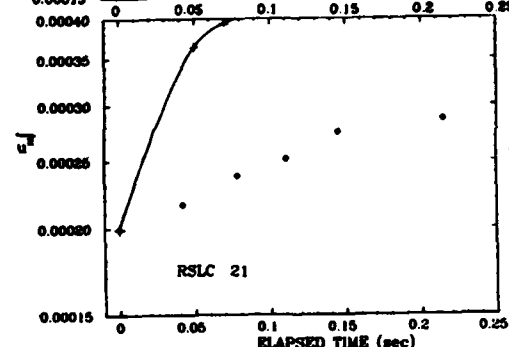
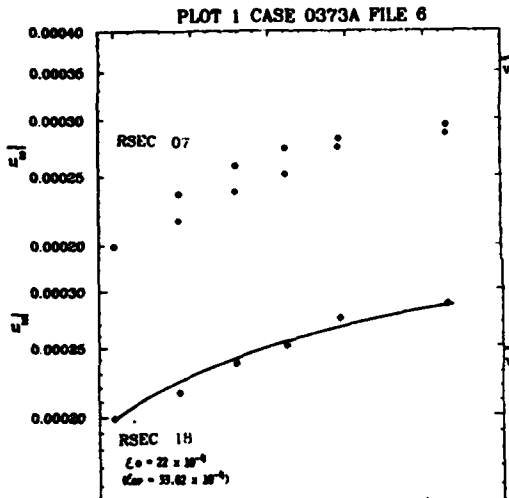
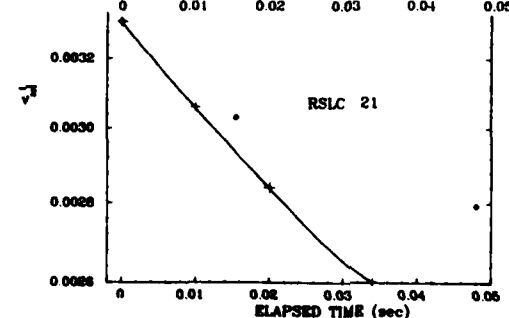
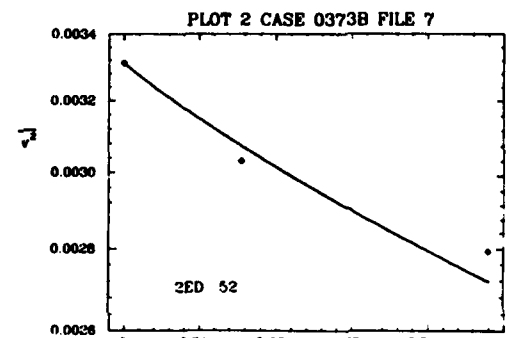
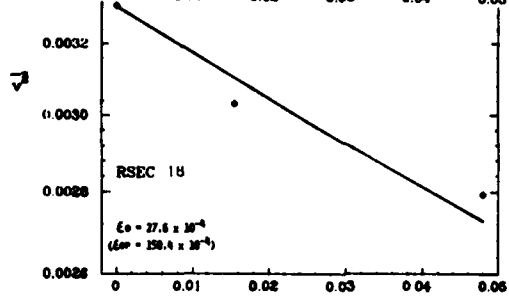
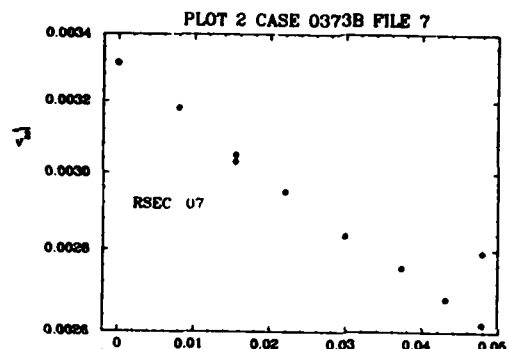
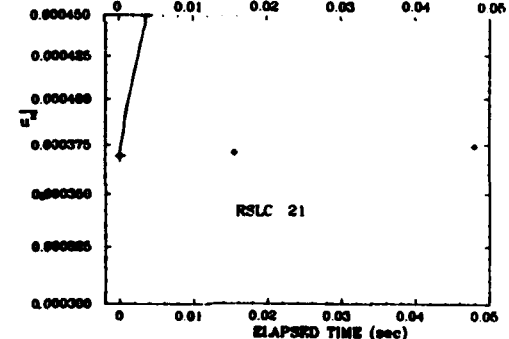
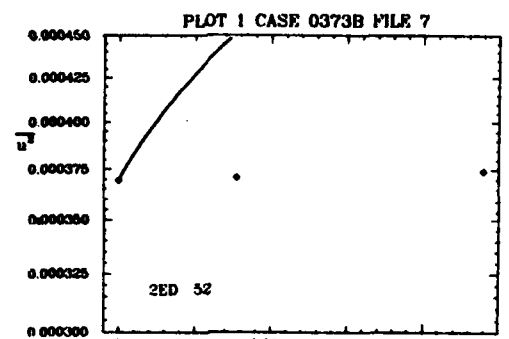
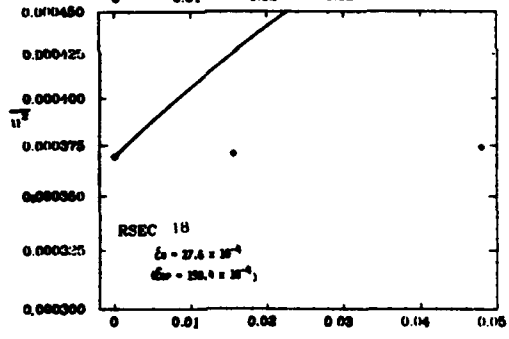
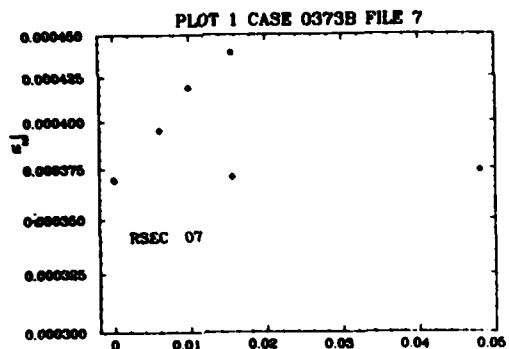


PLATE 62





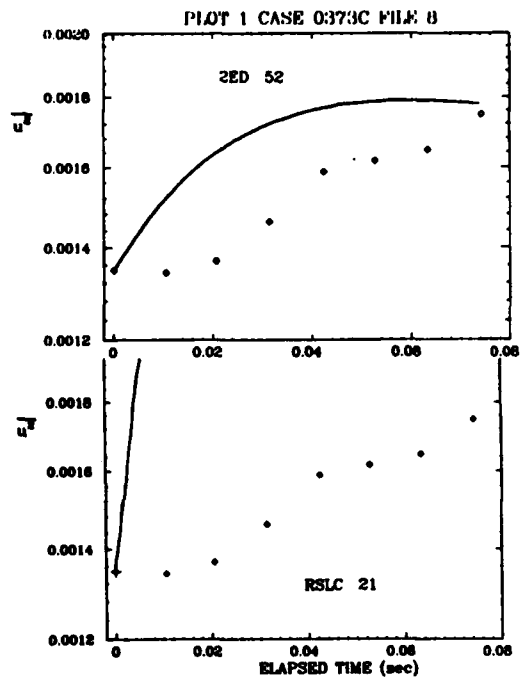
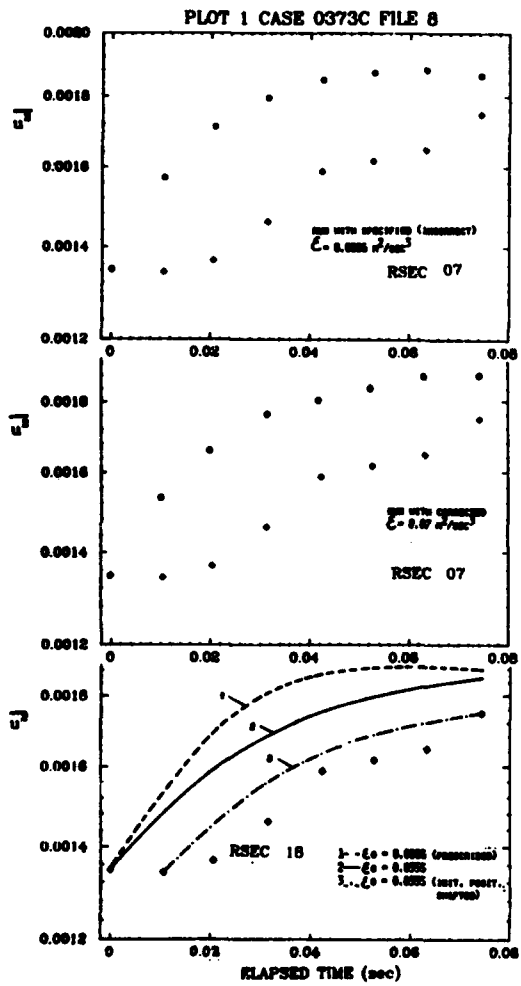


PLATE 65

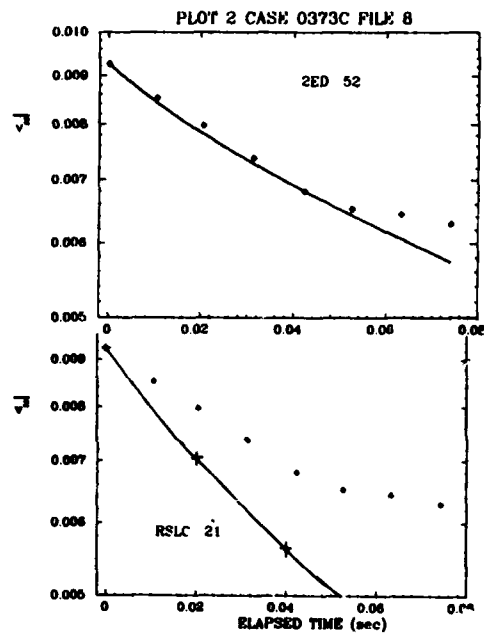
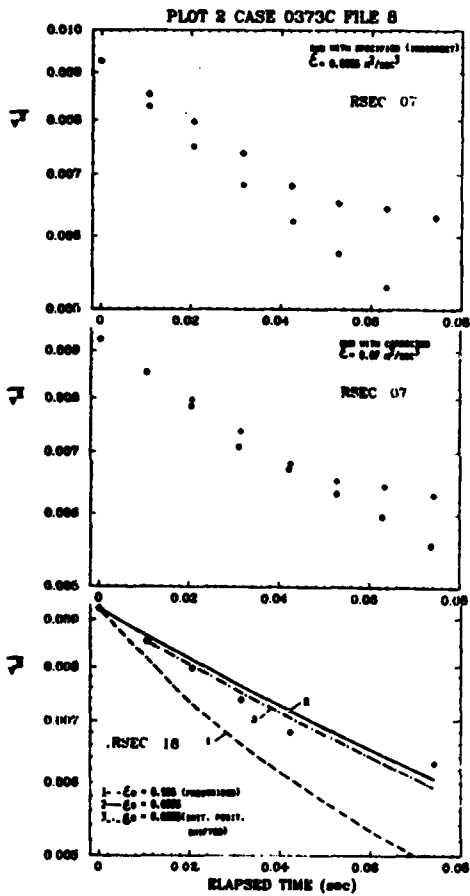


PLATE 66

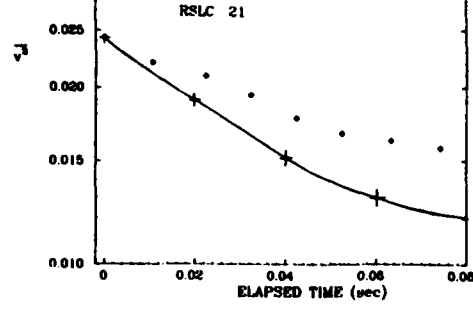
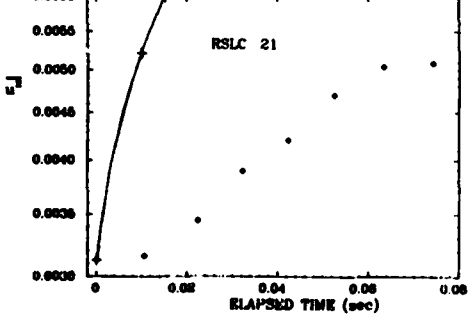
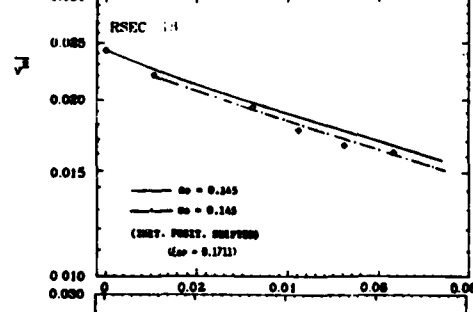
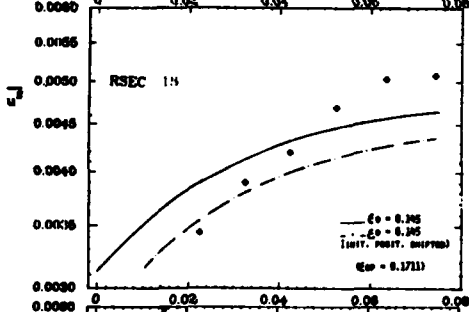
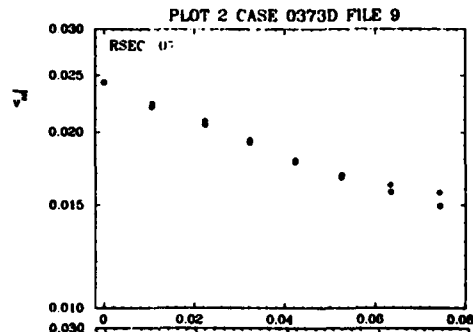
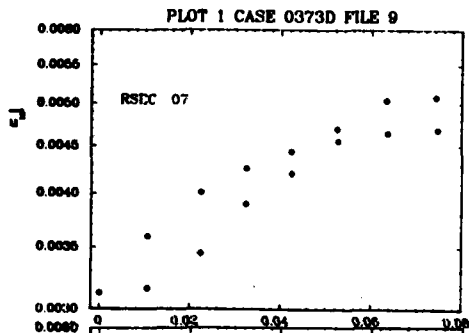
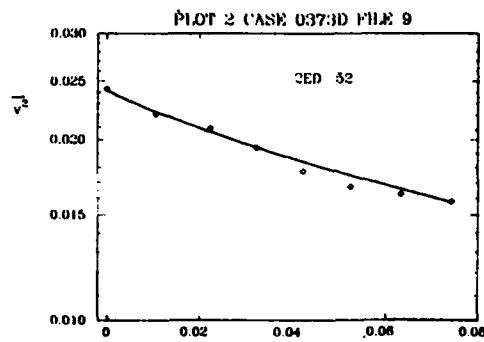
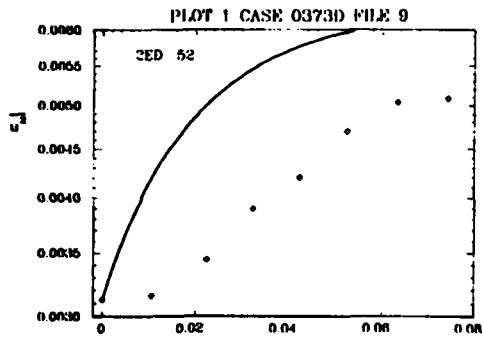


PLATE 67

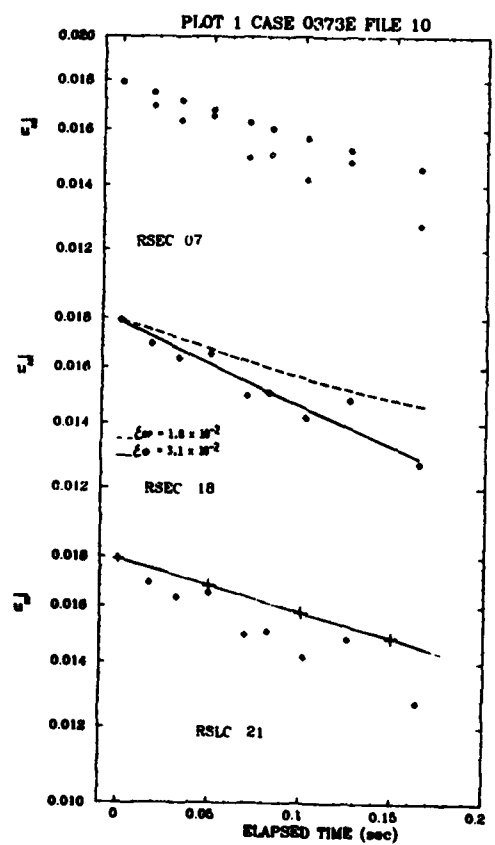
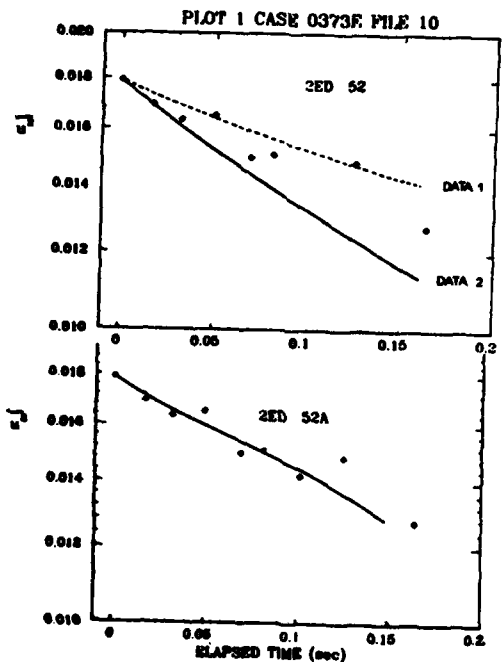


PLATE 68

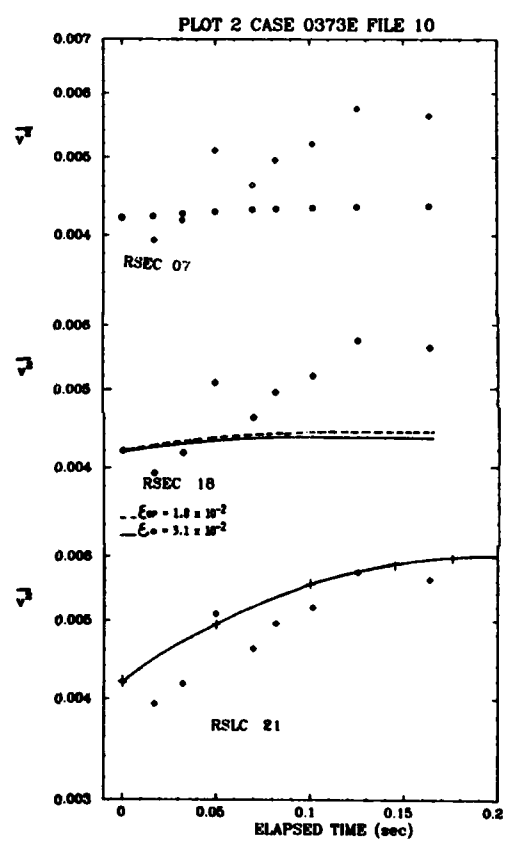
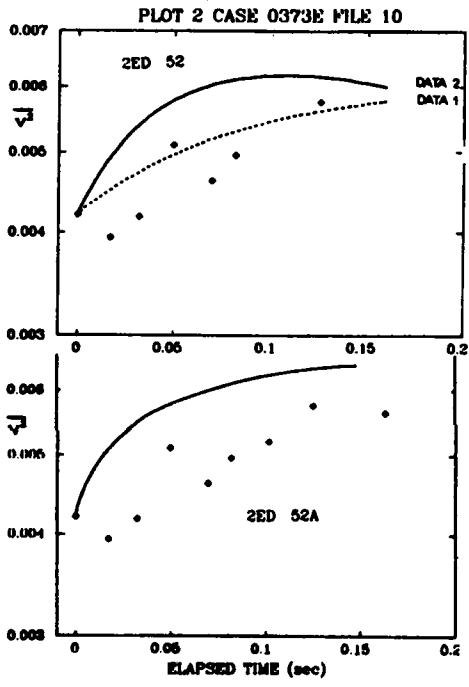


PLATE 69

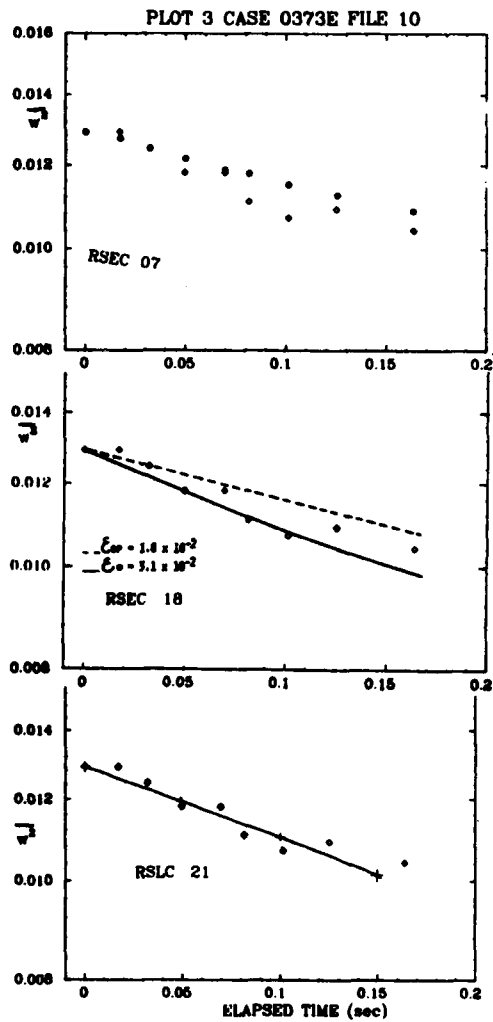
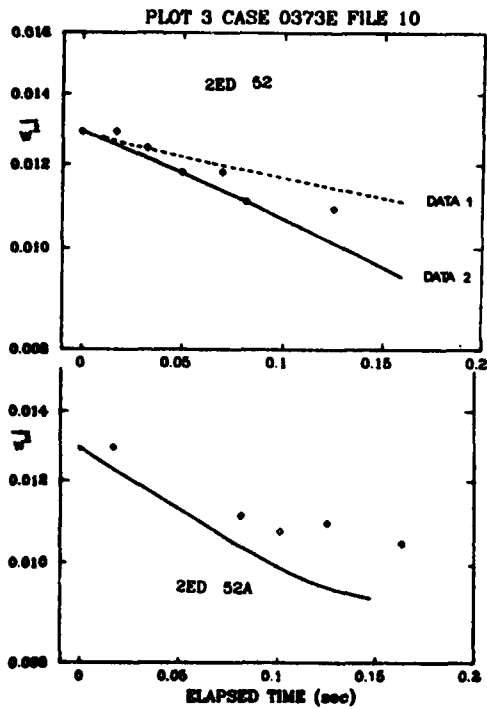


PLATE 70

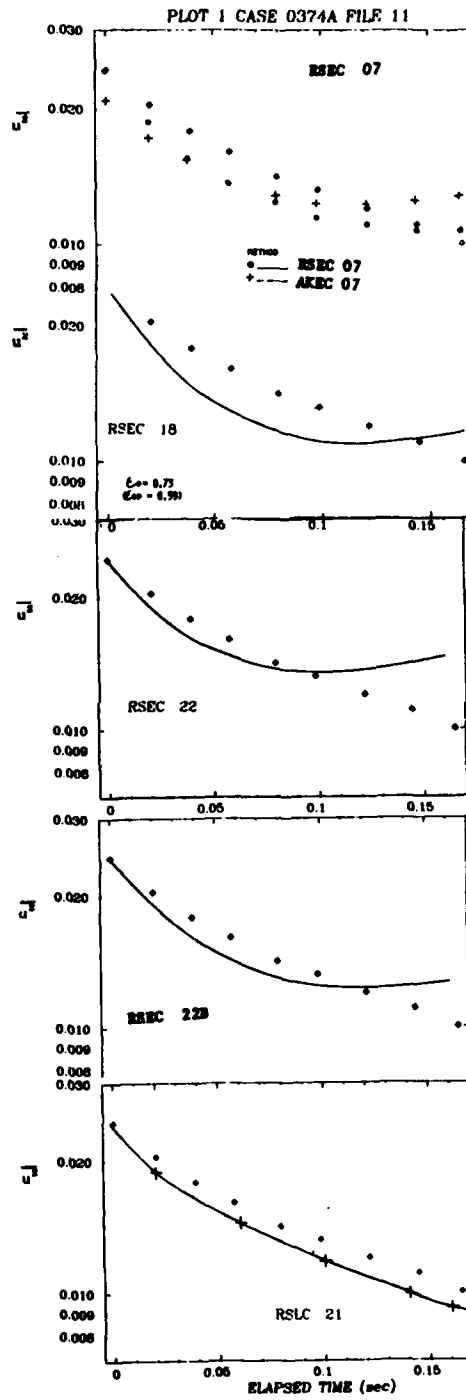
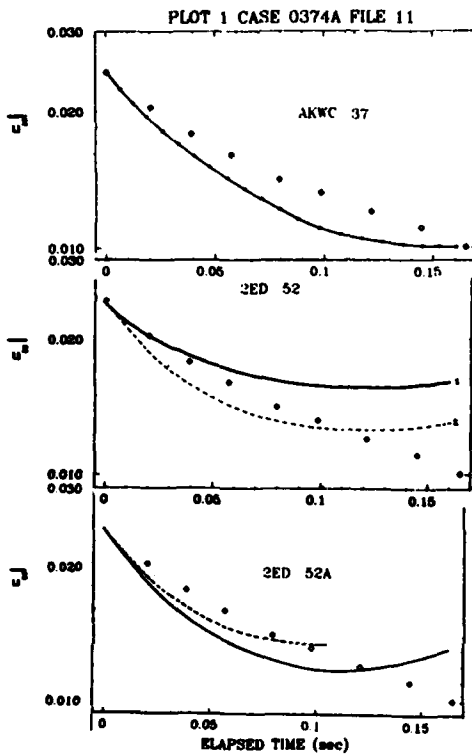


PLATE 71

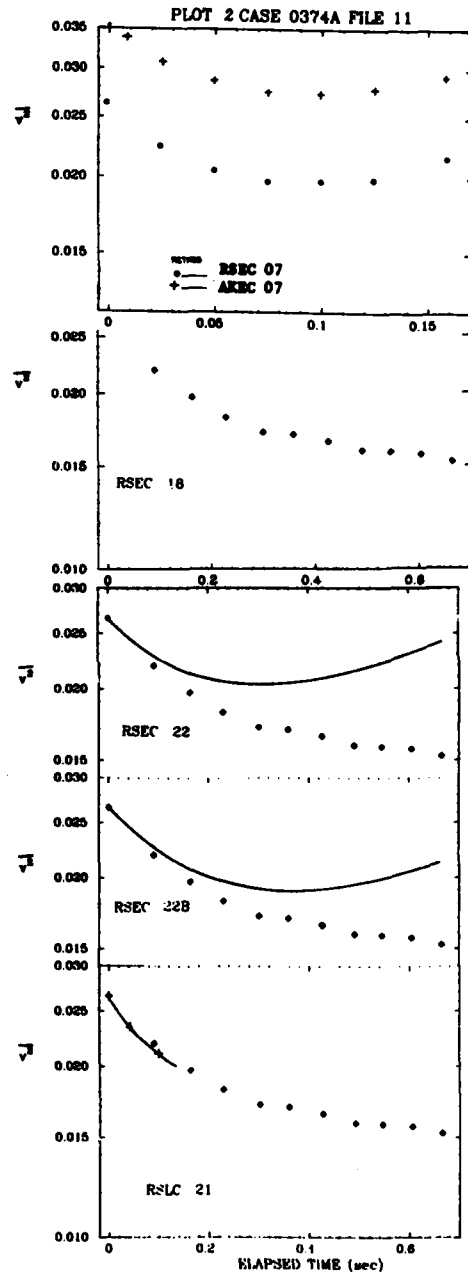
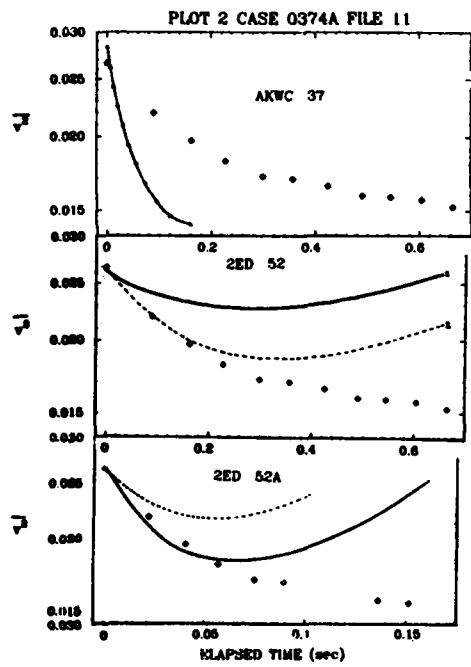


PLATE 72

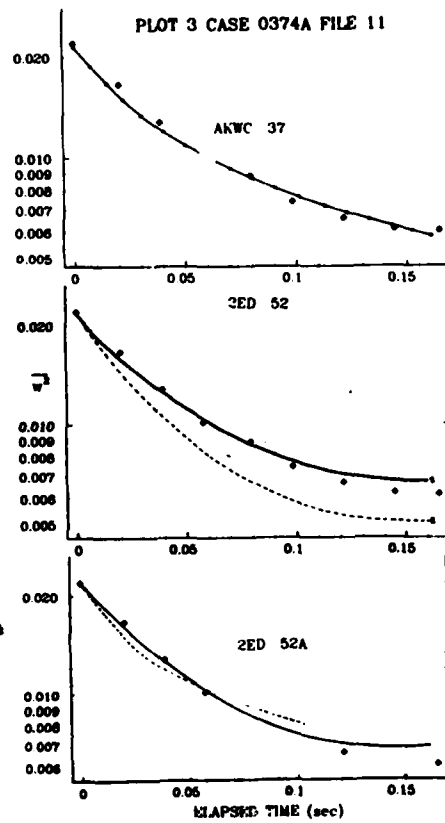
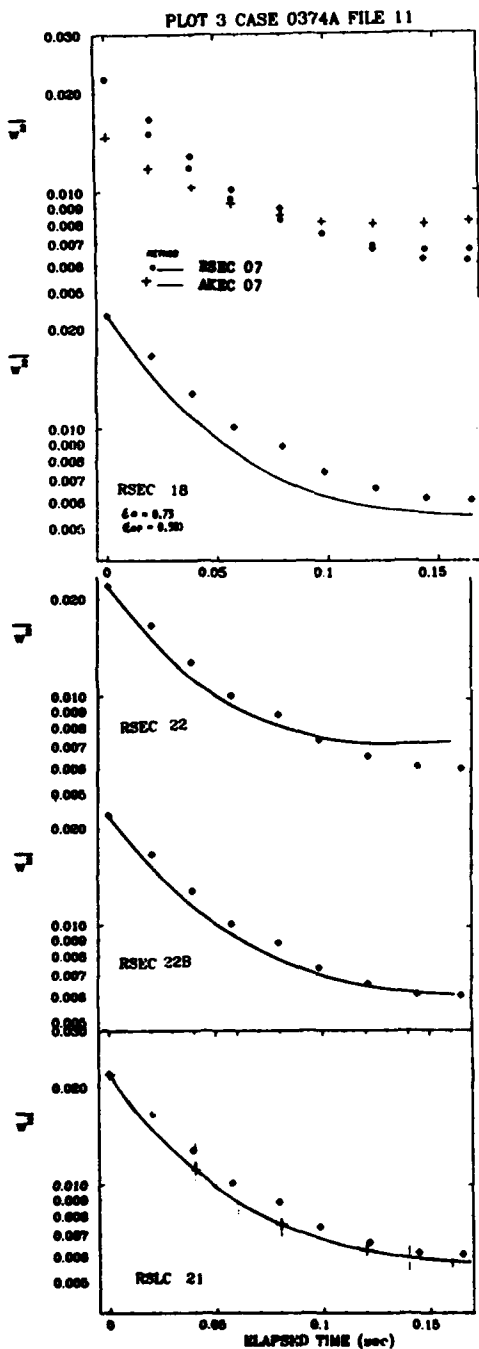


PLATE 73

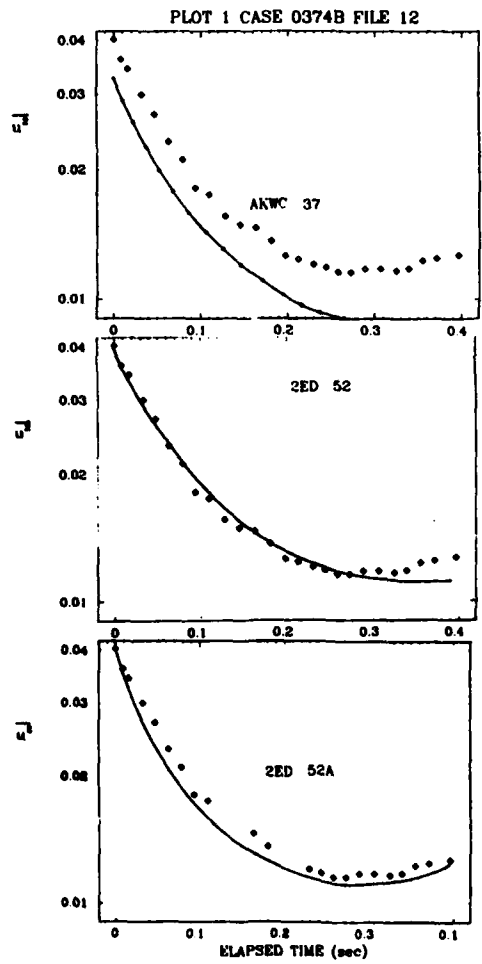
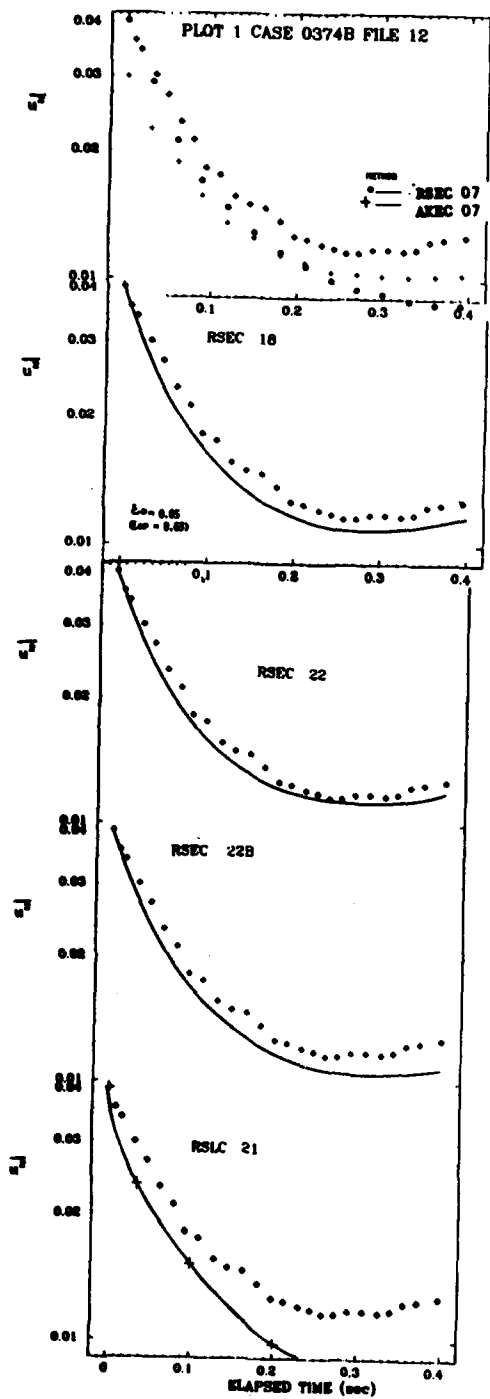


PLATE 74

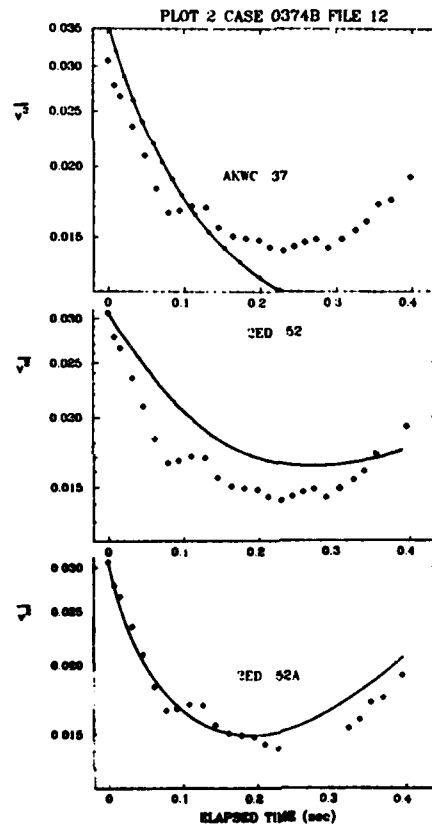
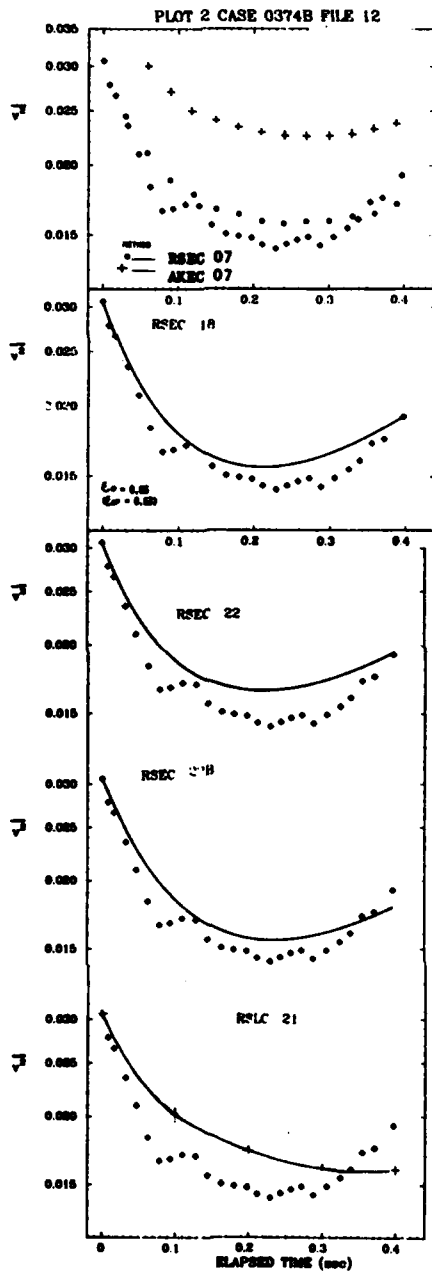


PLATE 75

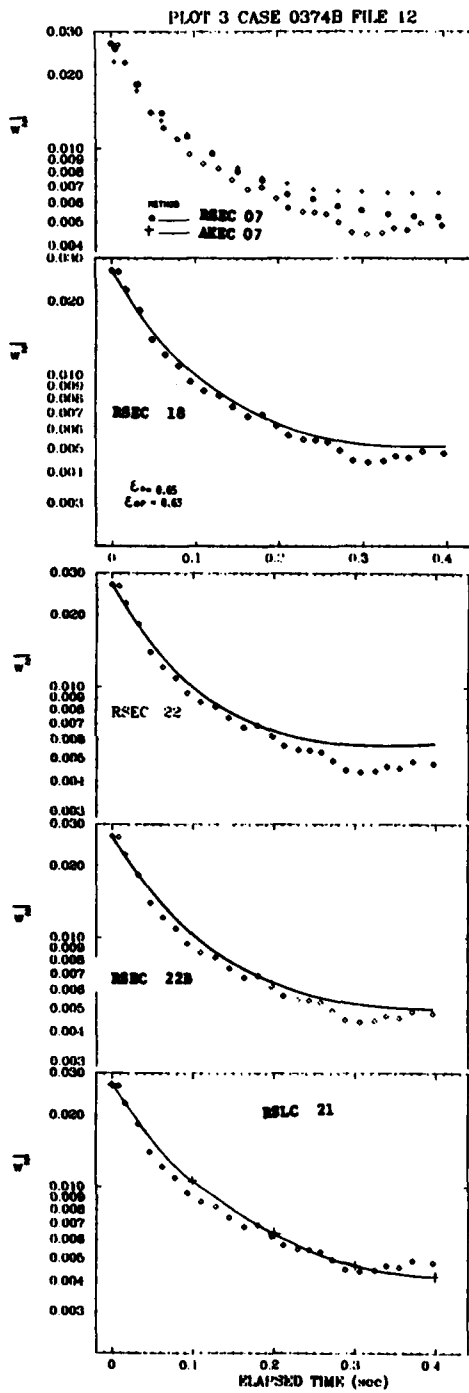
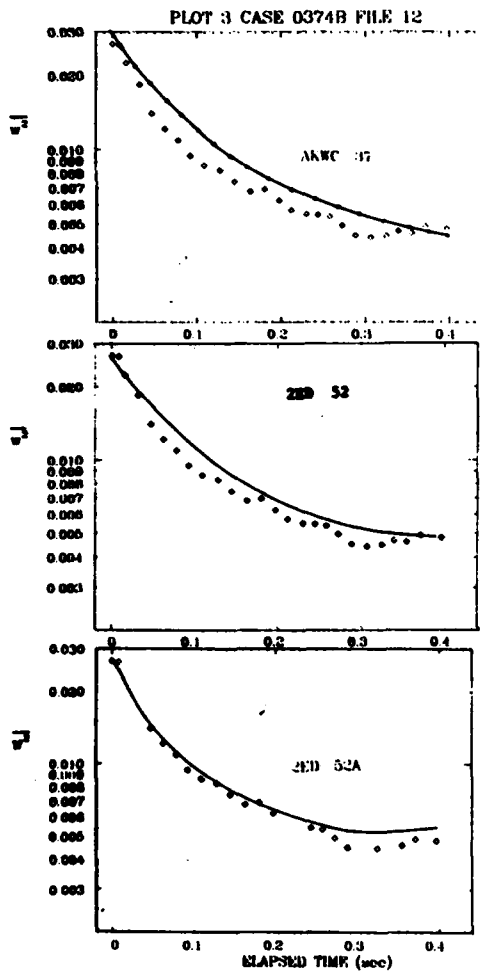


PLATE 76

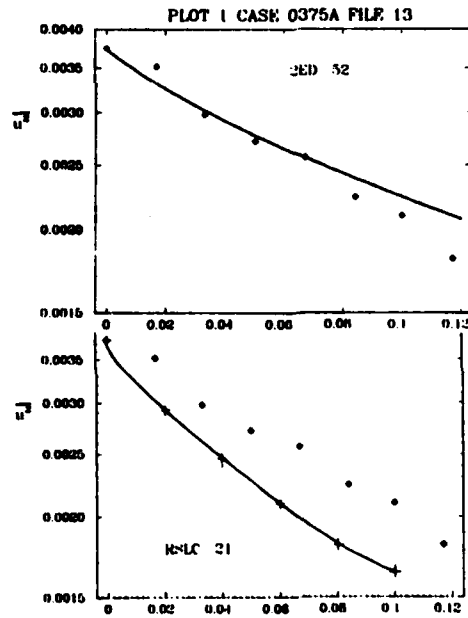
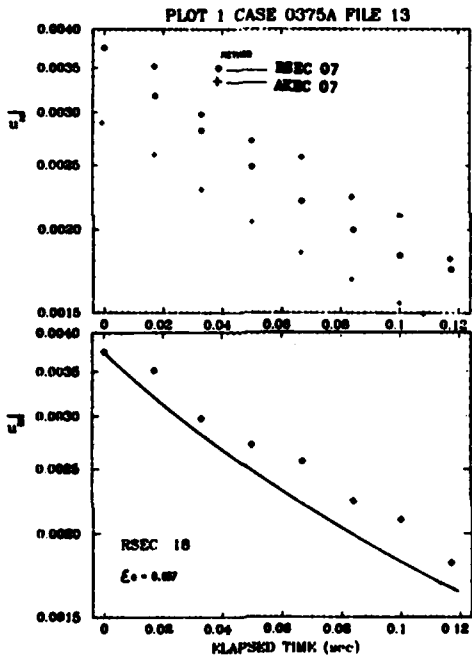
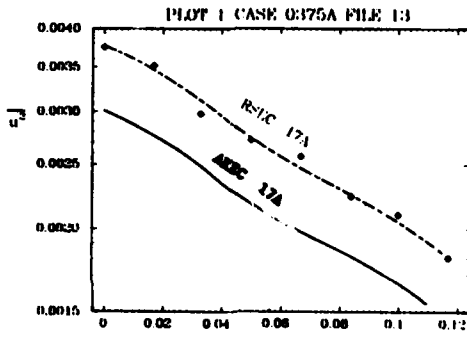


PLATE 77

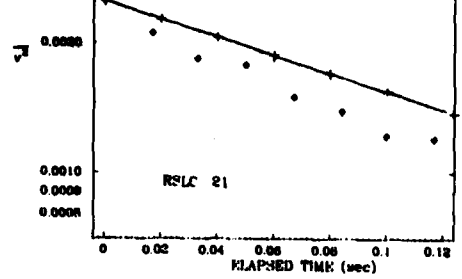
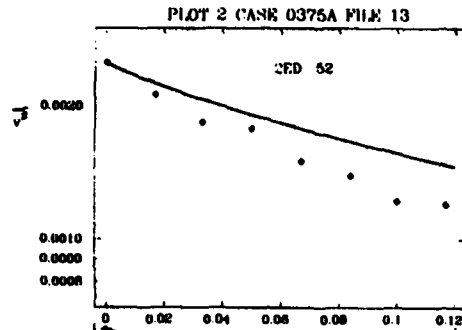
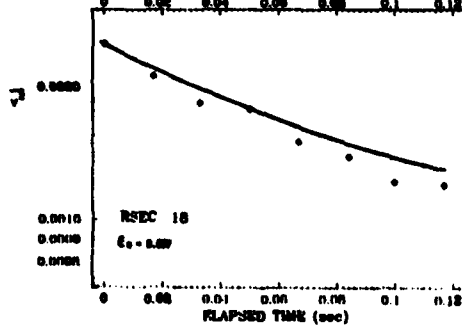
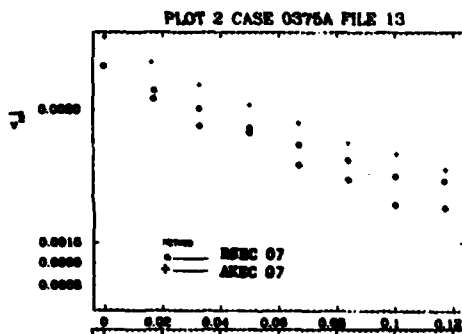
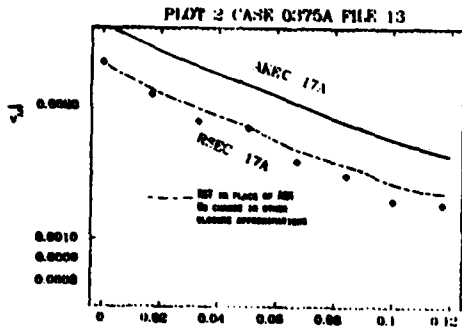
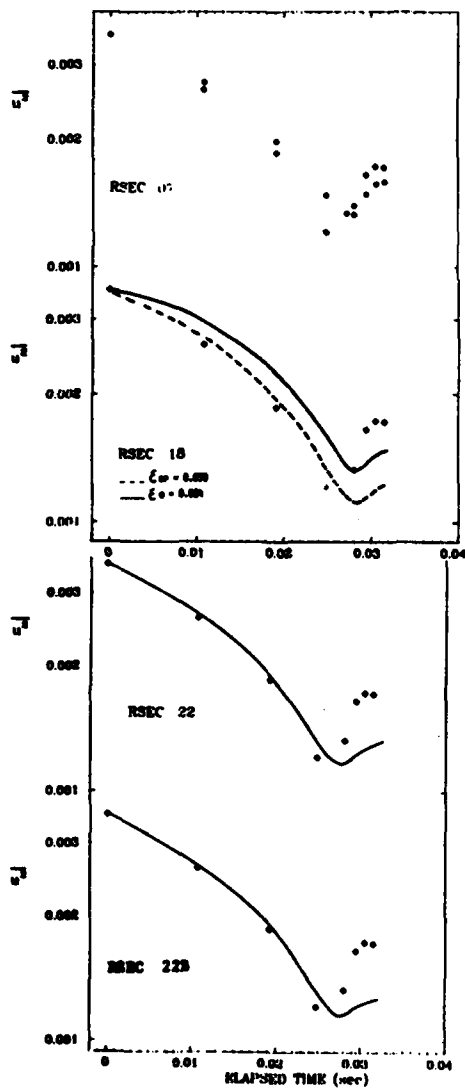
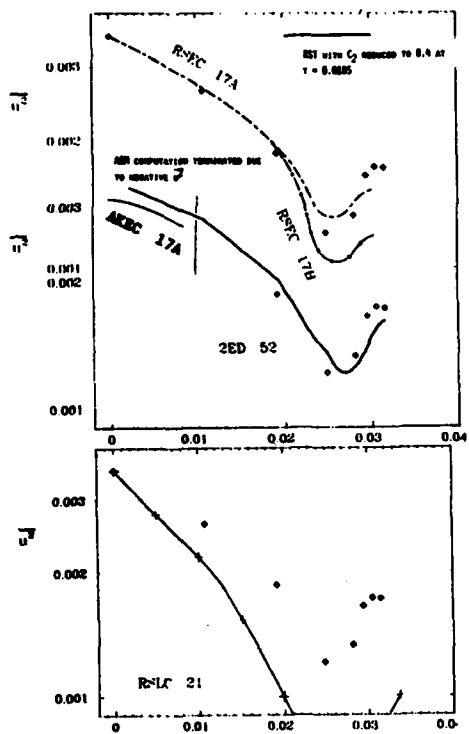


PLATE 78

PLOT 1 CASE 0375D FILE 14



PLOT 1 CASE 0375D FILE 14



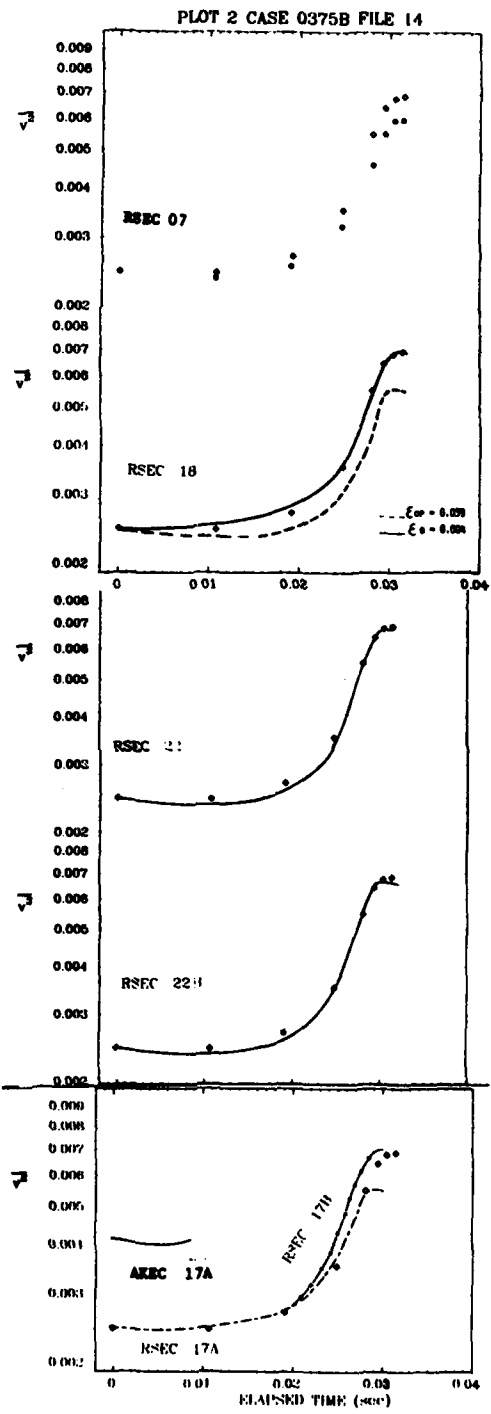
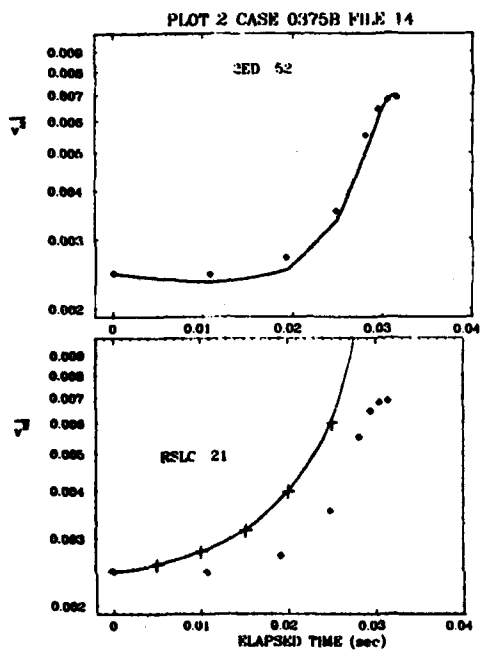


PLATE 80

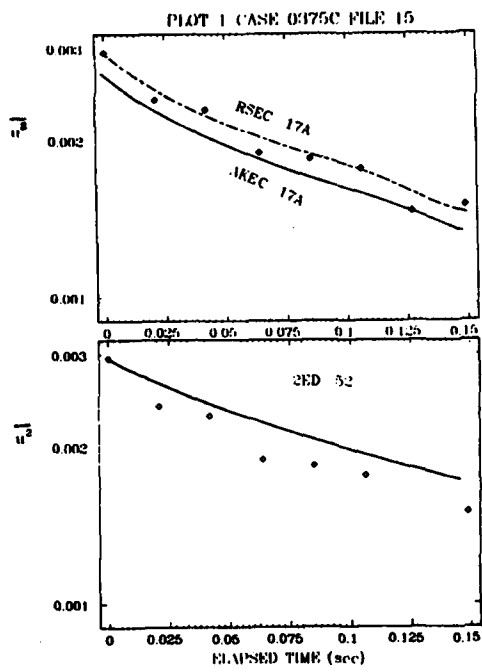
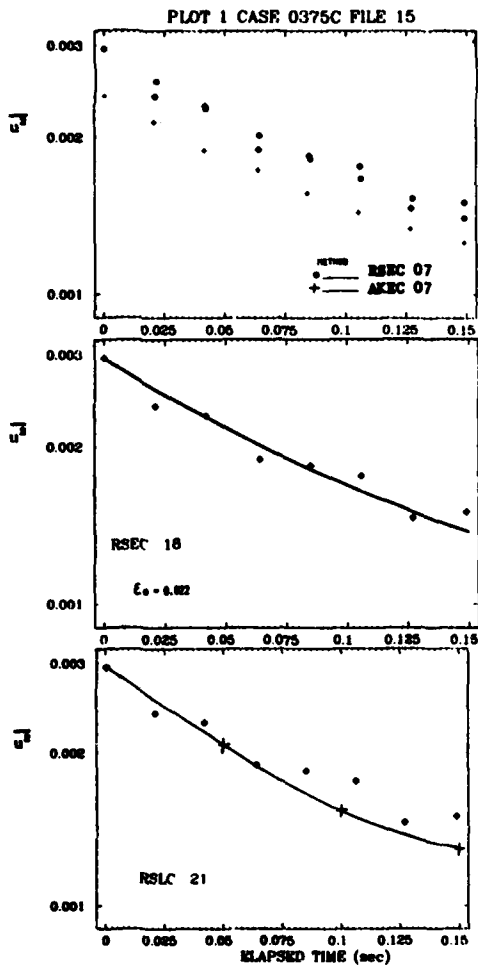


PLATE 81

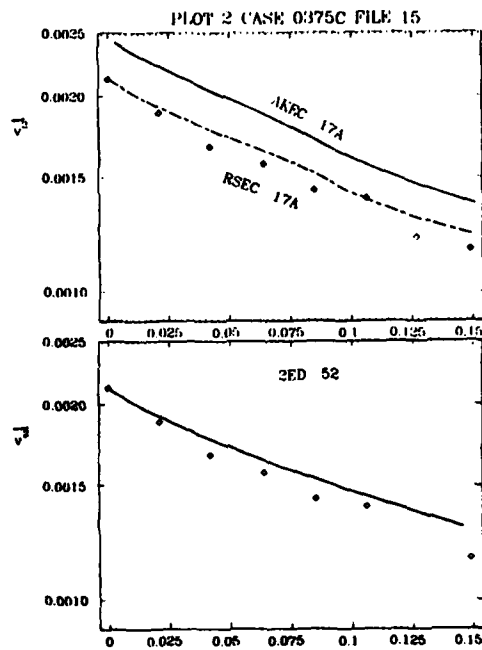
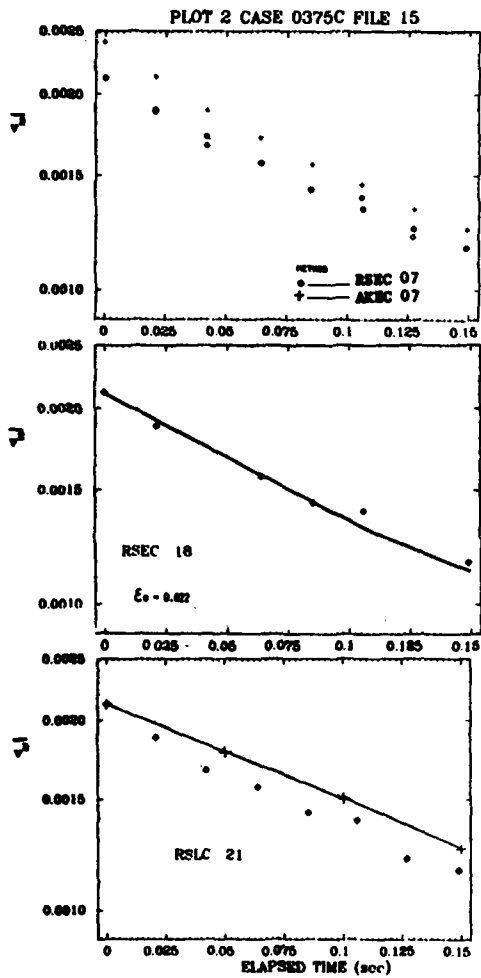


PLATE 82

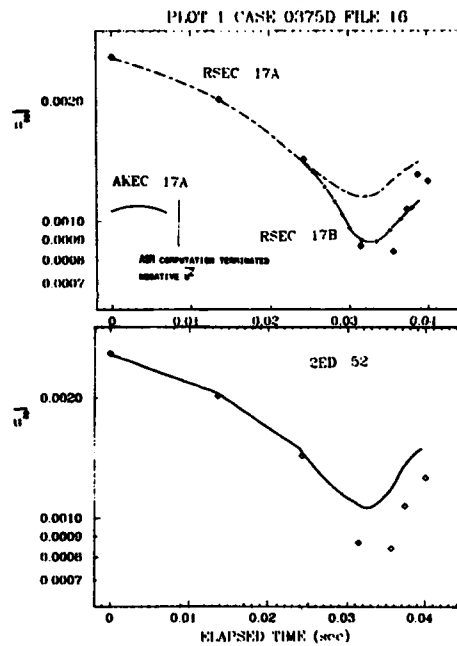
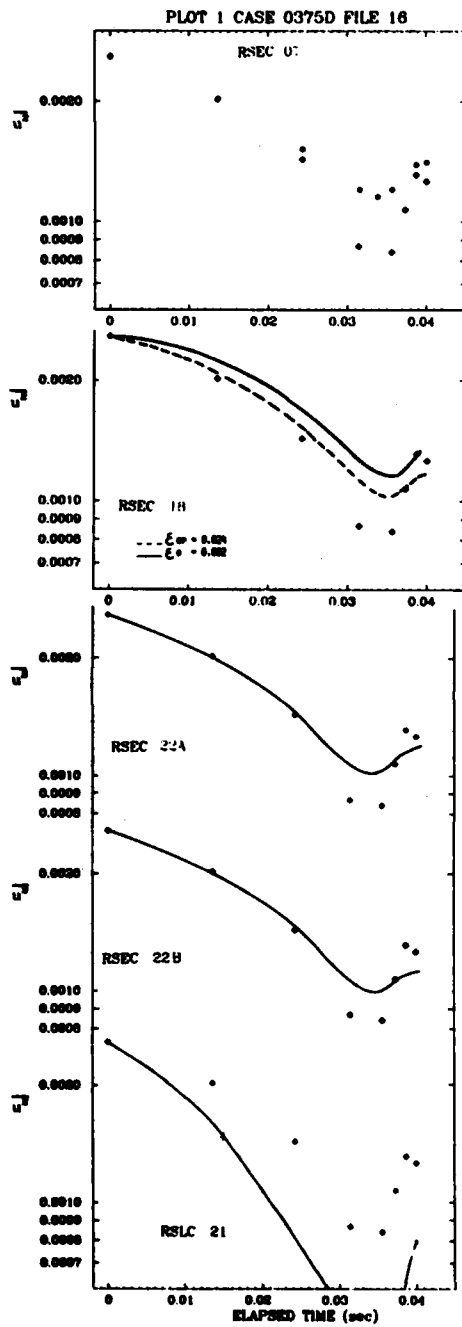
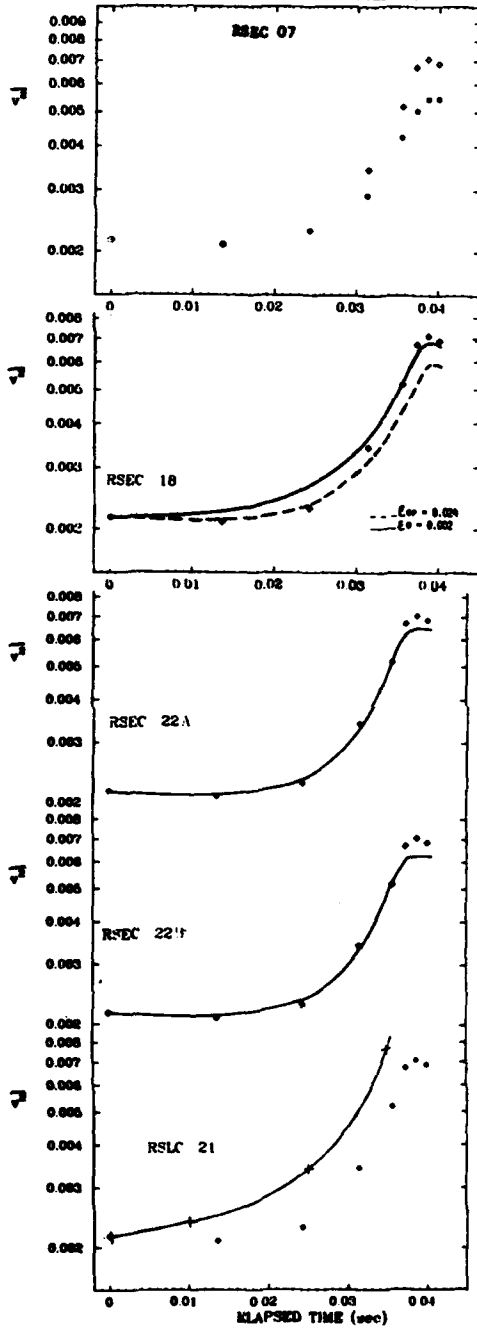
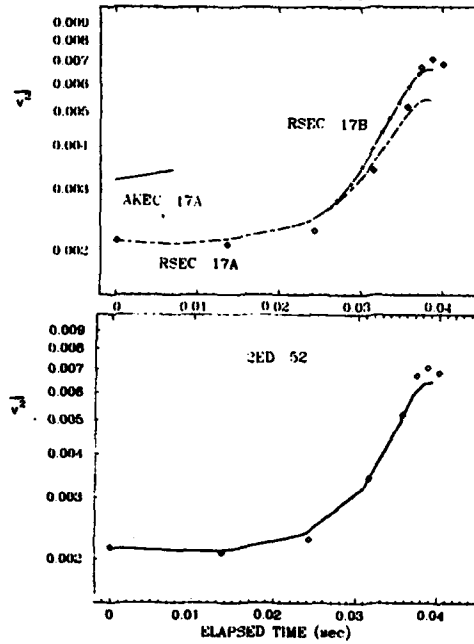


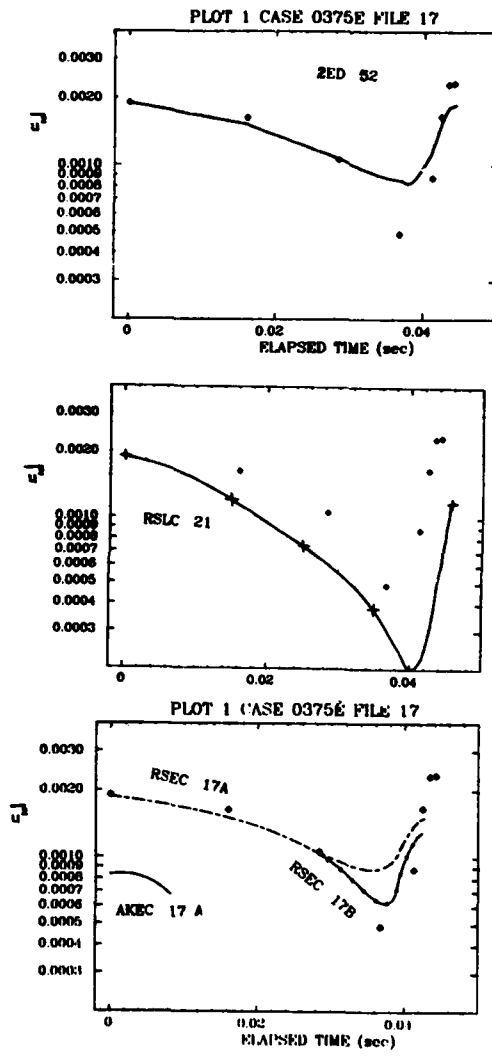
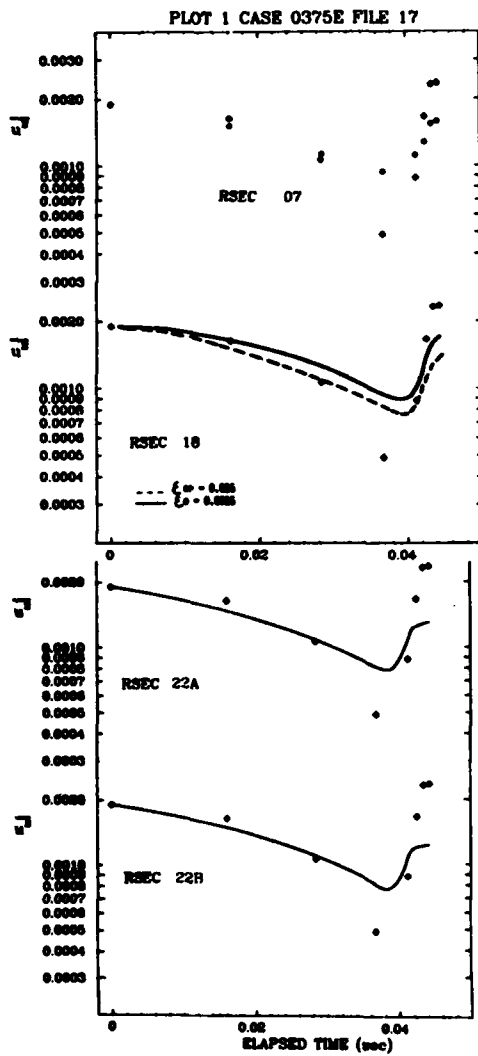
PLATE 83

PLOT 2 CASE 0375D FILE 16



PLOT 2 CASE 0375D FILE 16





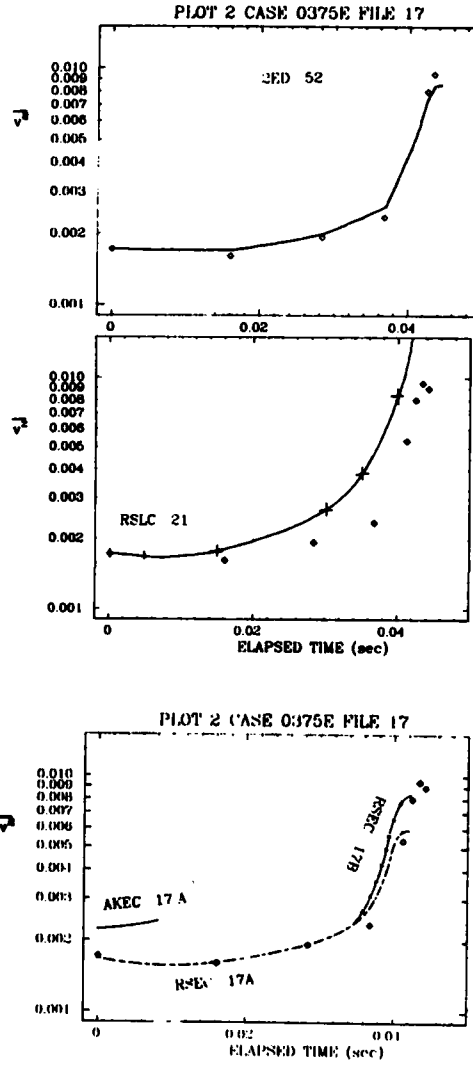
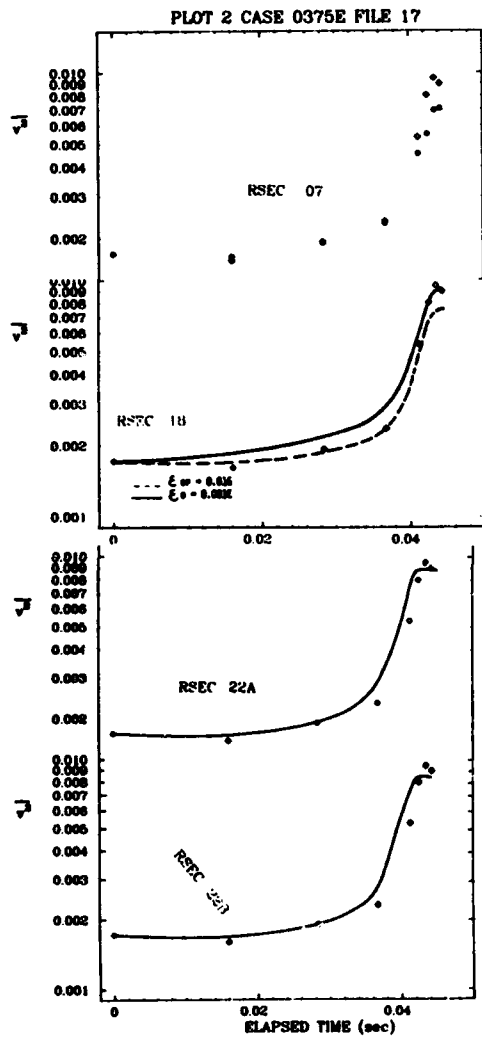


PLATE 86

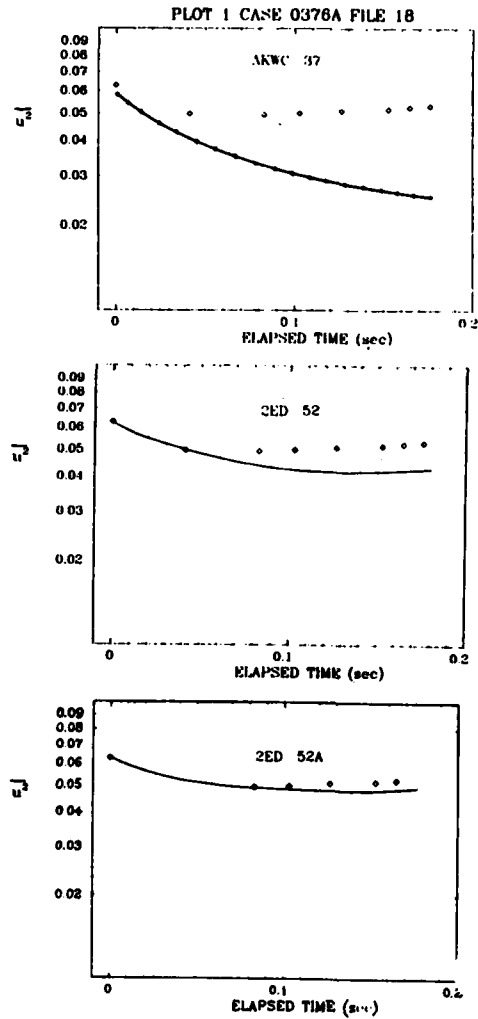
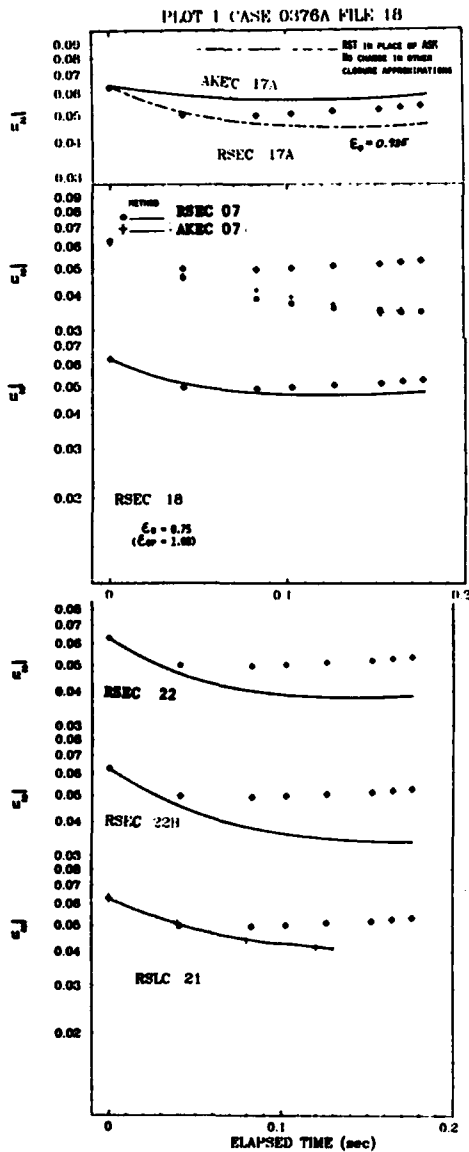
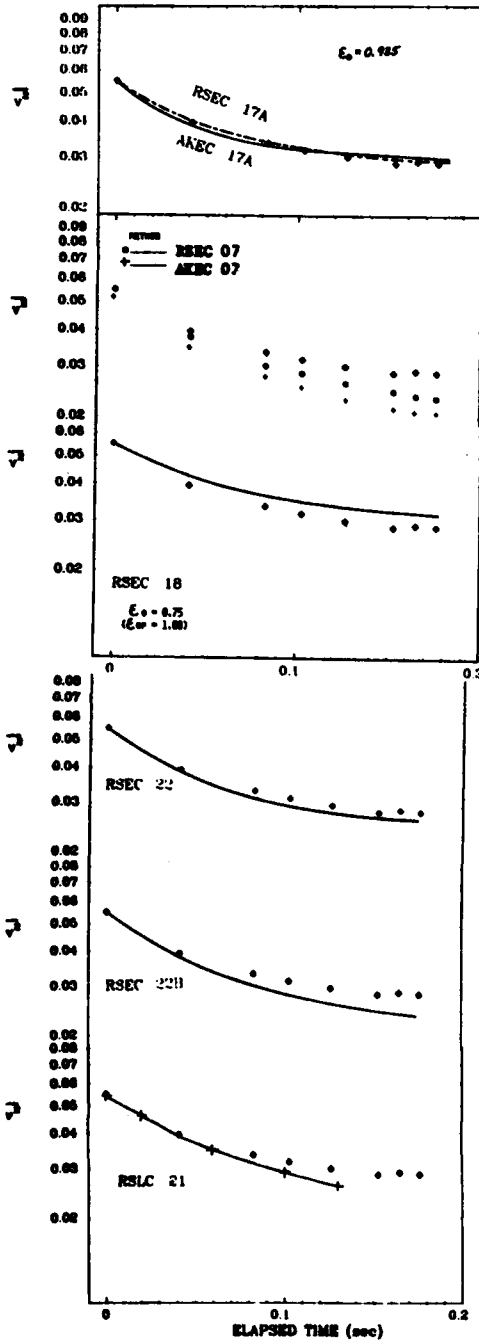


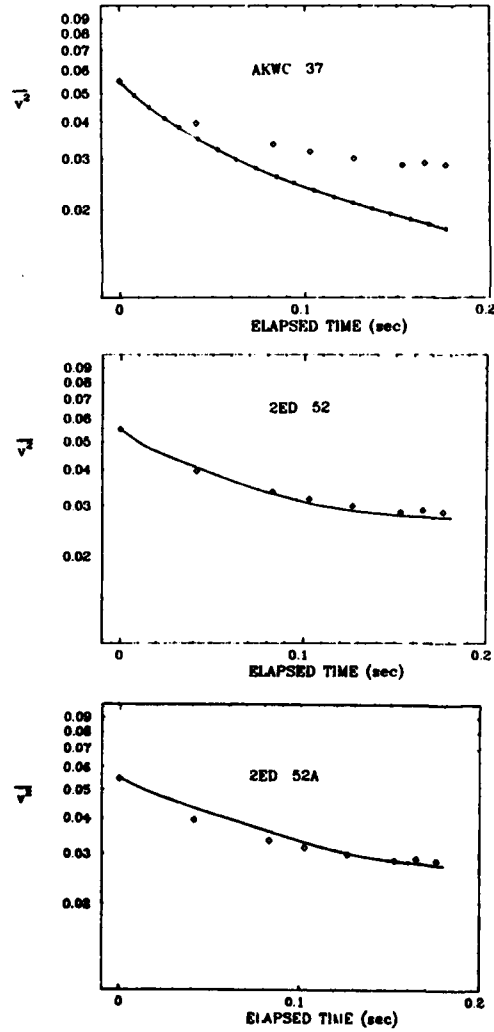
PLATE 87

1201

PLOT 2 CASE 0376A FILE 18



PLOT 2 CASE 0376A FILE 18



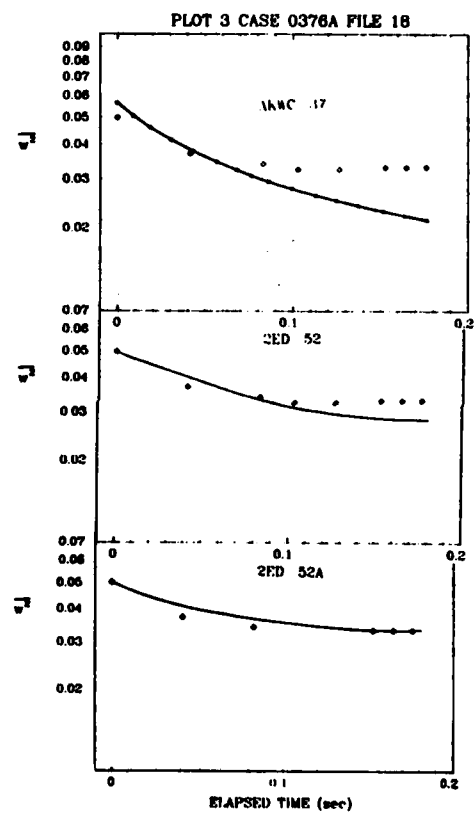
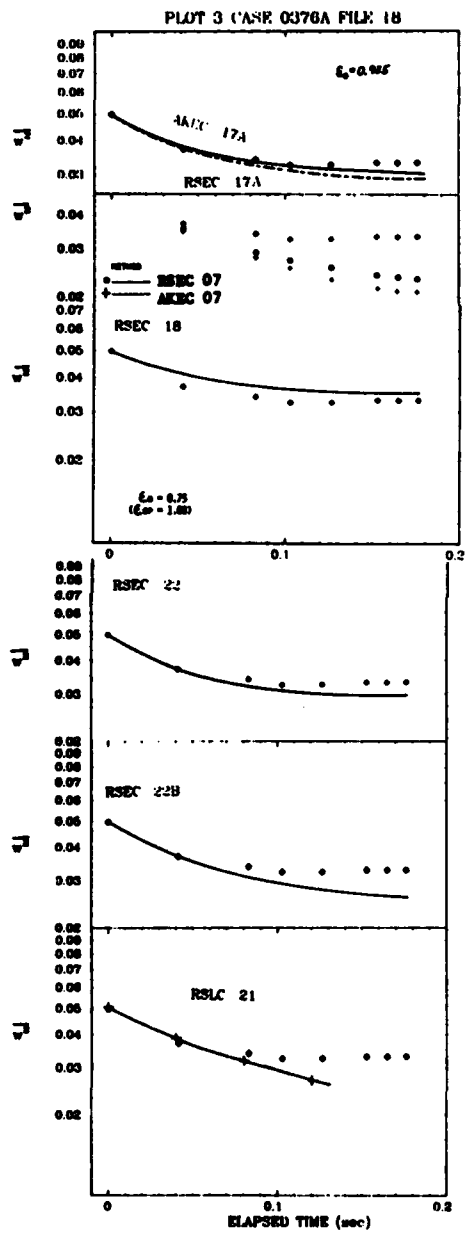
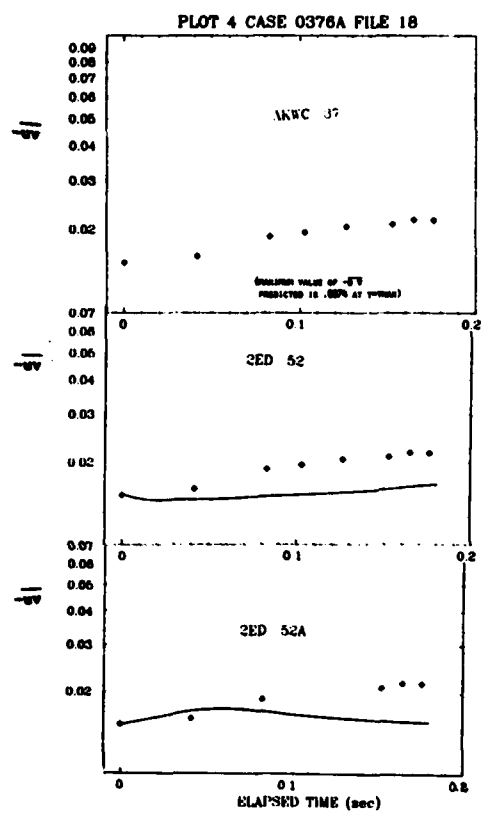
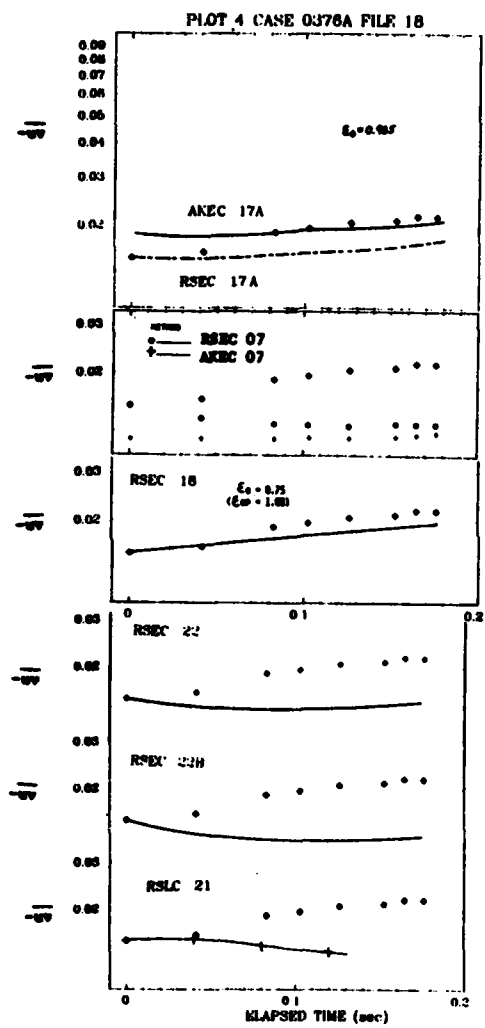
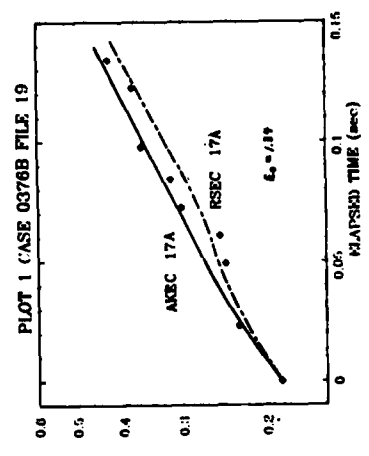
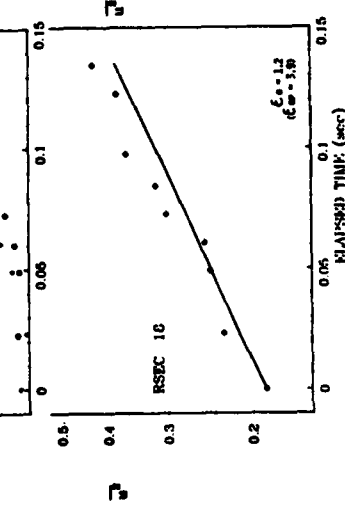
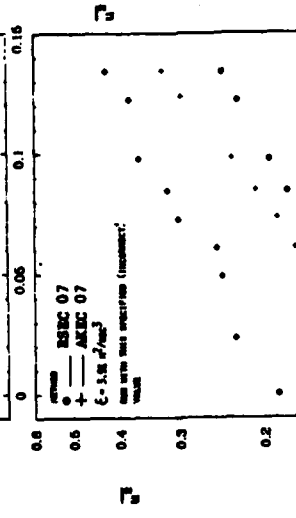
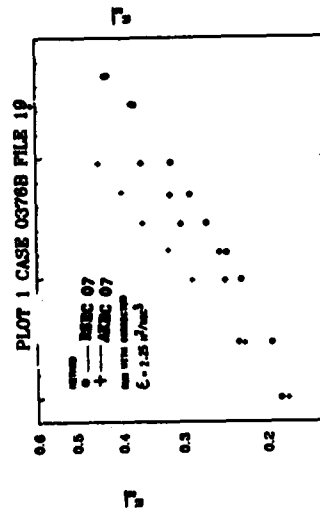
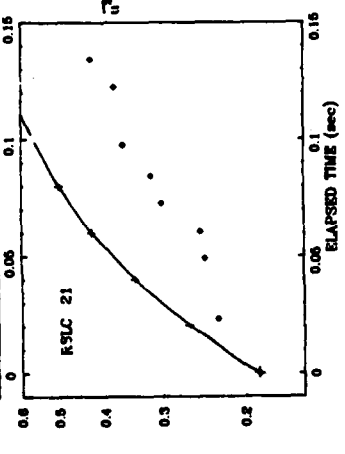
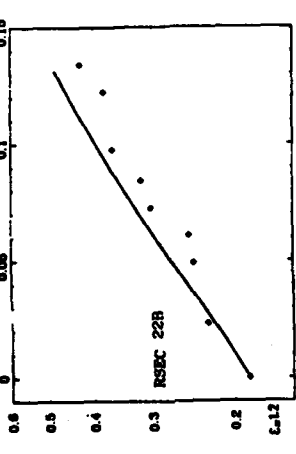
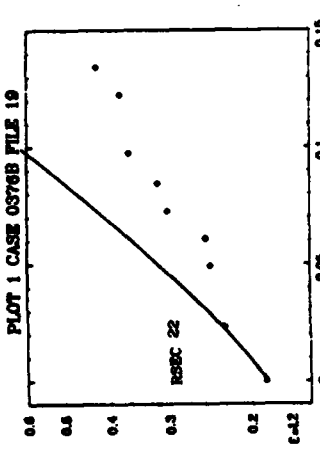


PLATE 89





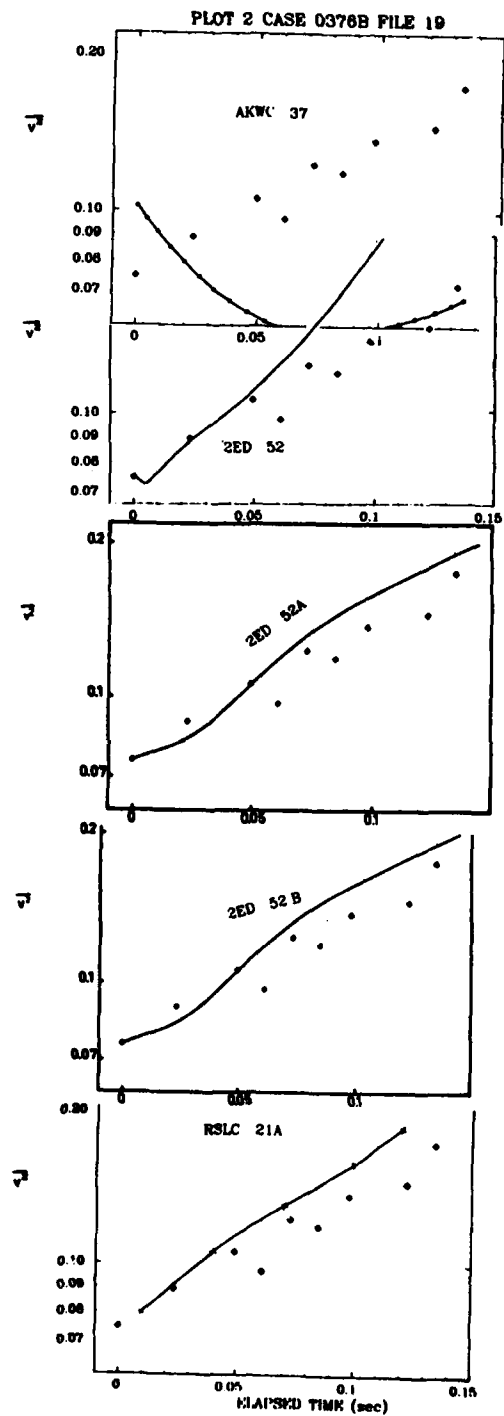
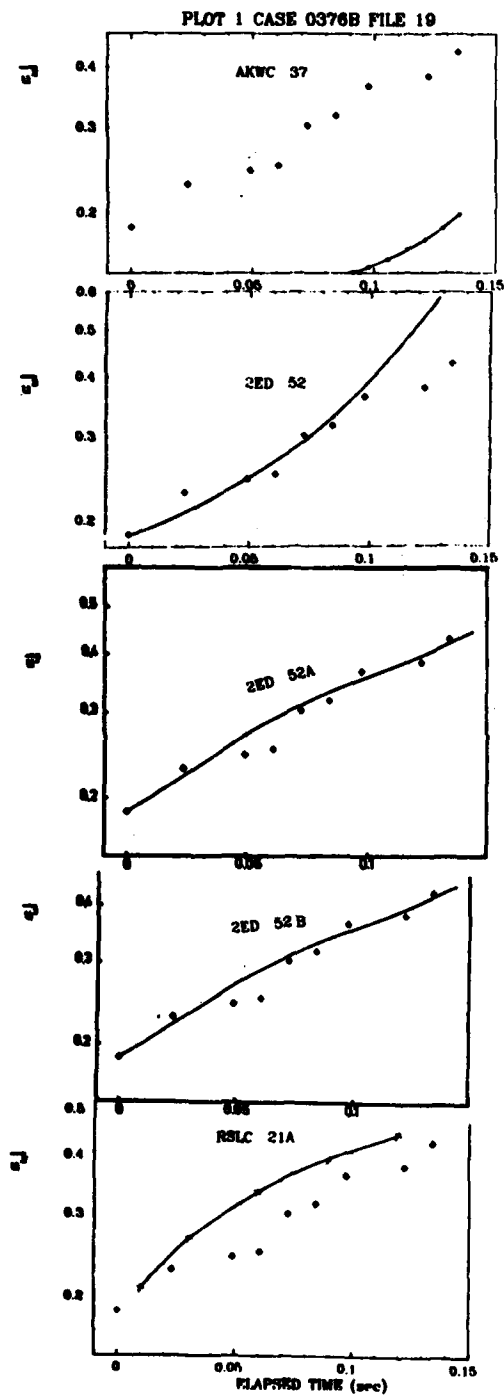


PLATE 92

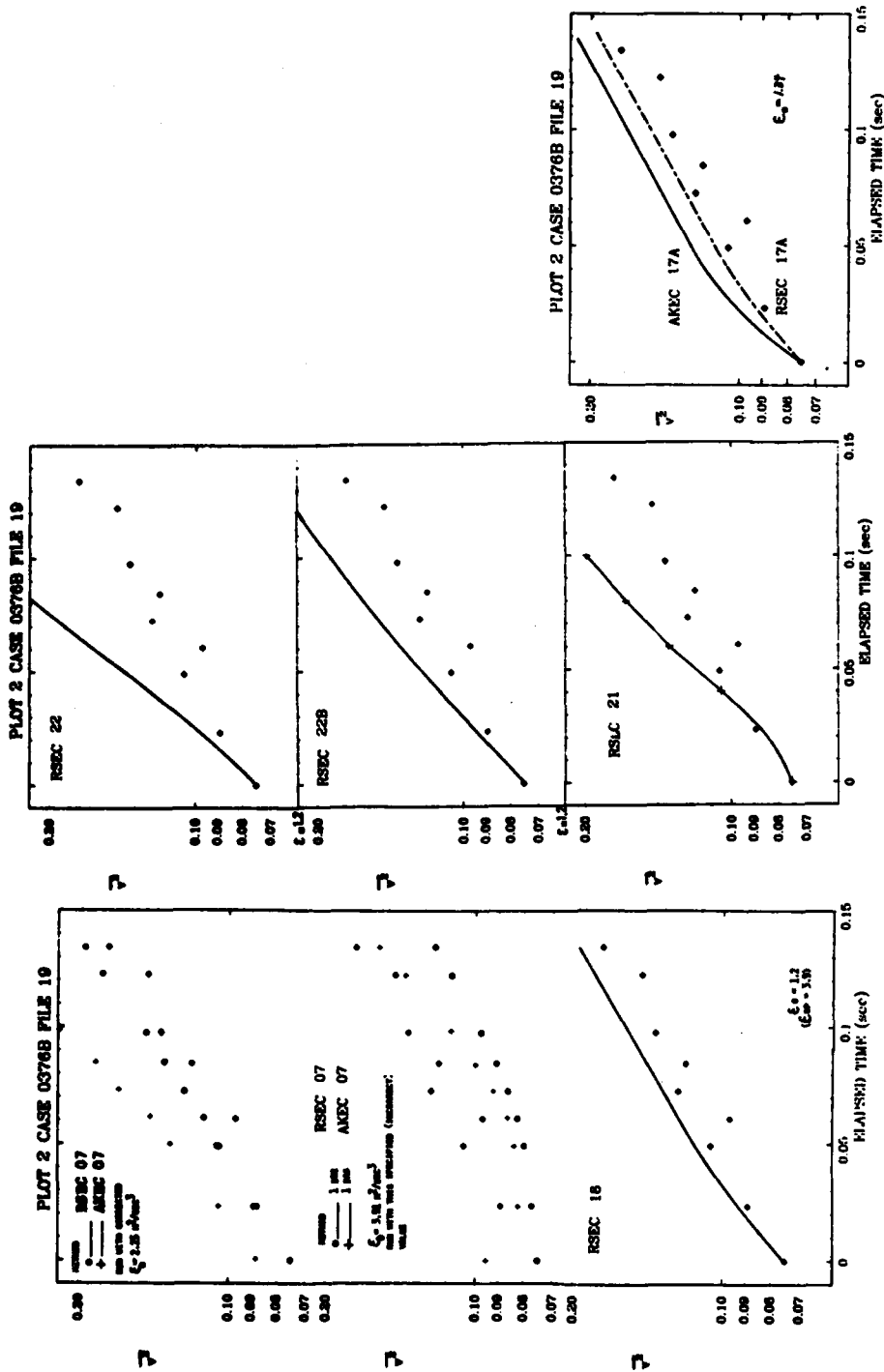
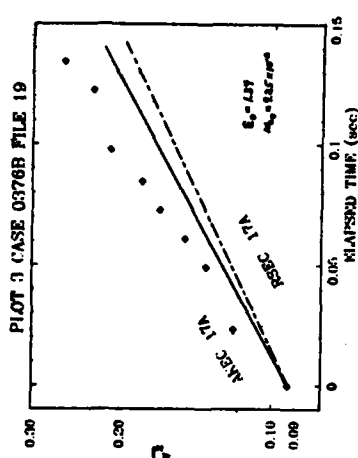
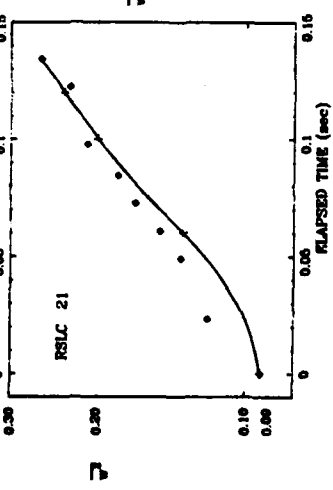
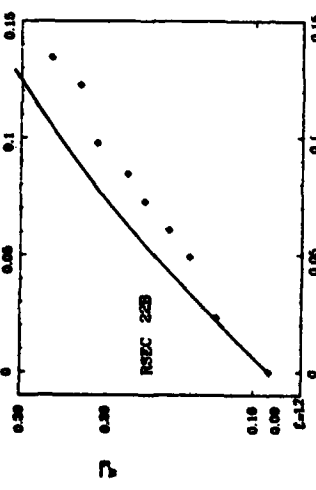
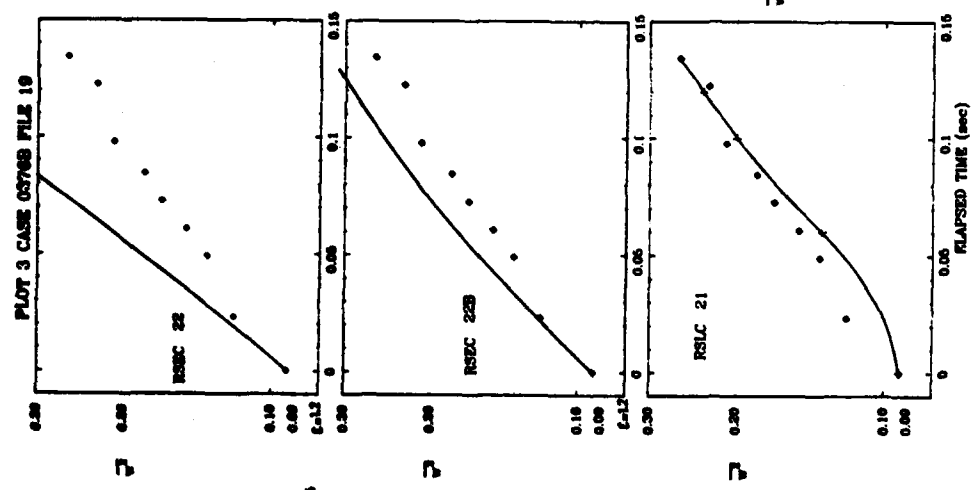
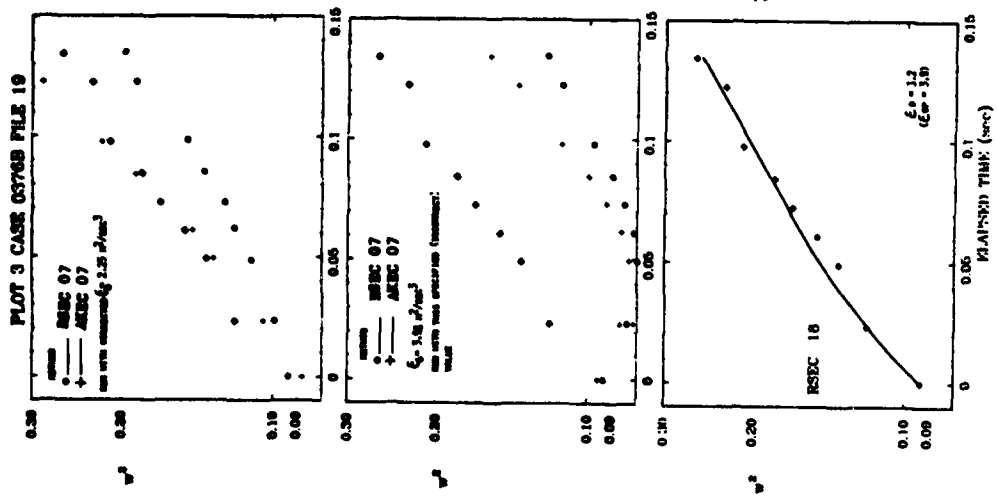


PLATE 93



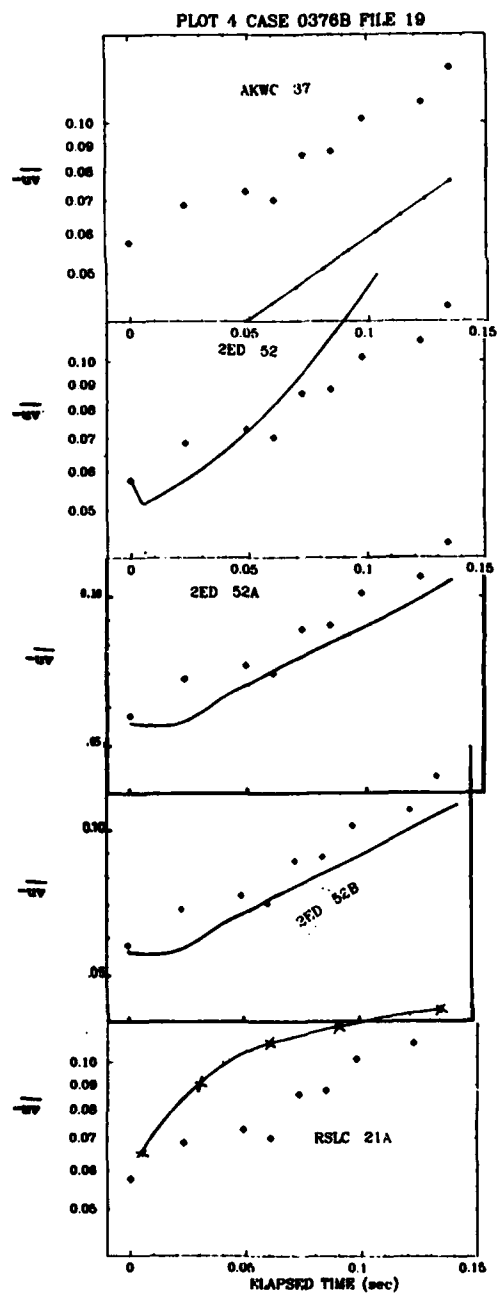
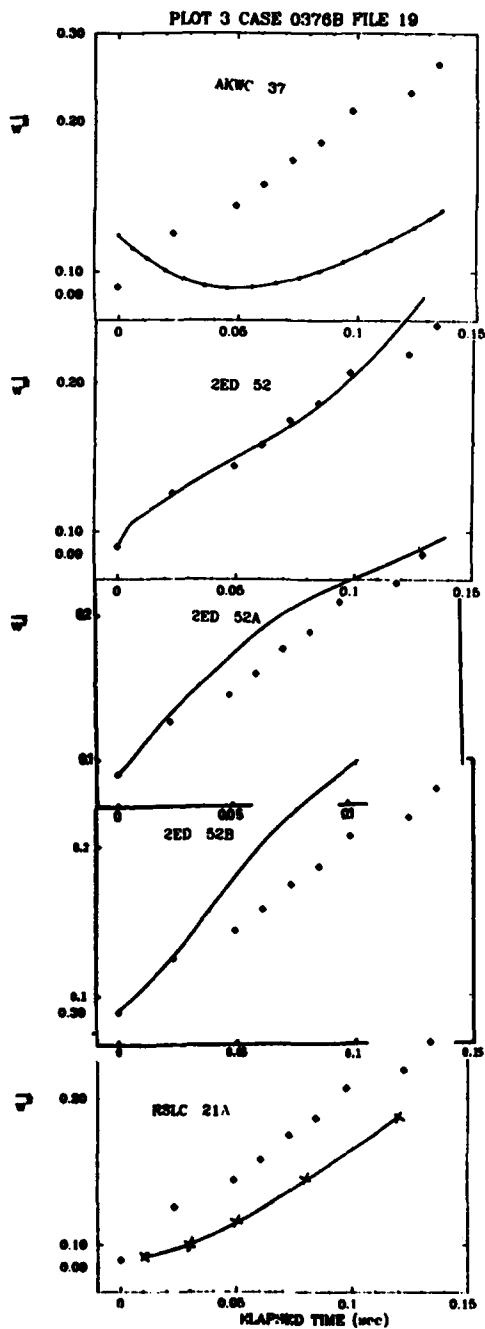
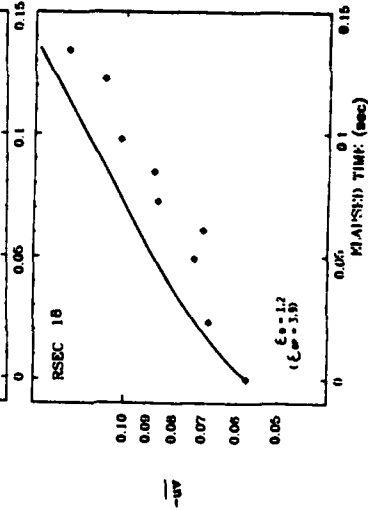
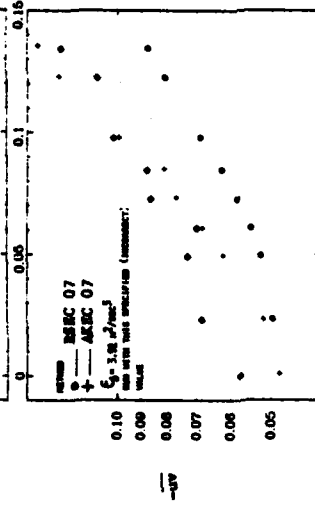
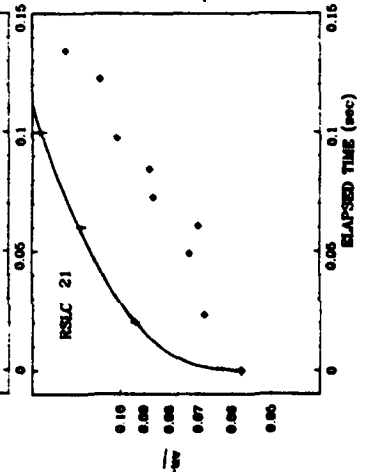
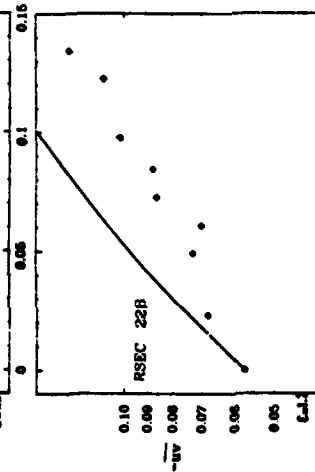
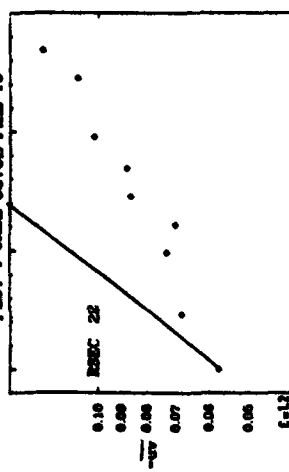


PLATE 95

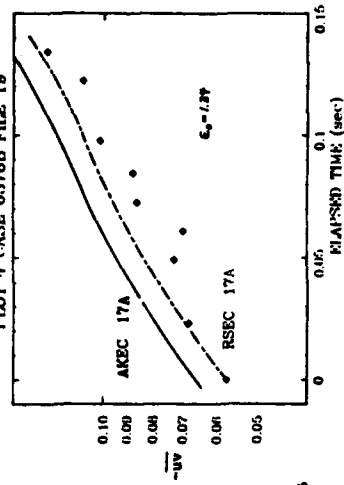
PLOT 4 CASE 03768 FILE 19



PLOT 4 CASE 03768 FILE 19



PLOT 4 CASE 03768 FILE 19



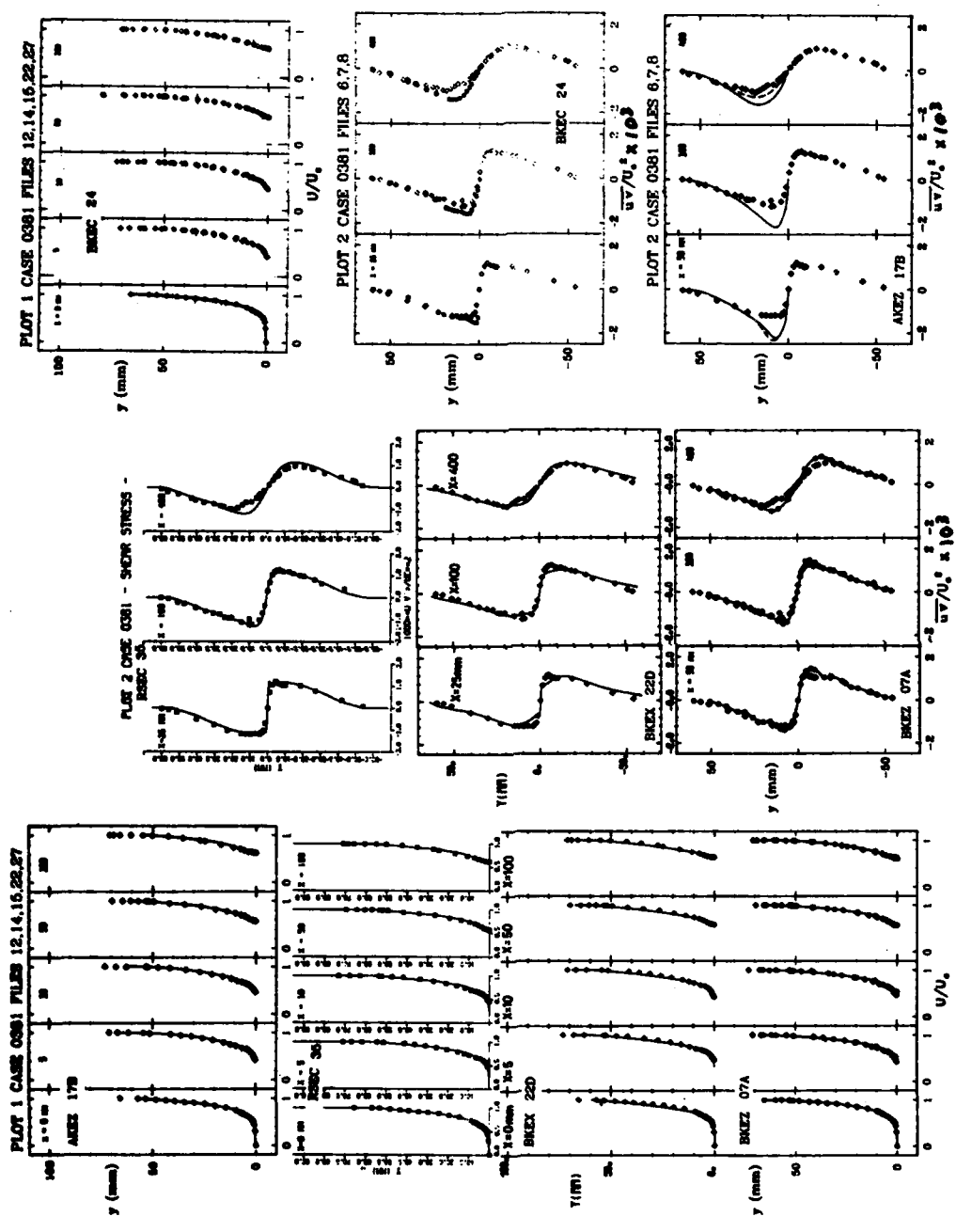


PLATE 97

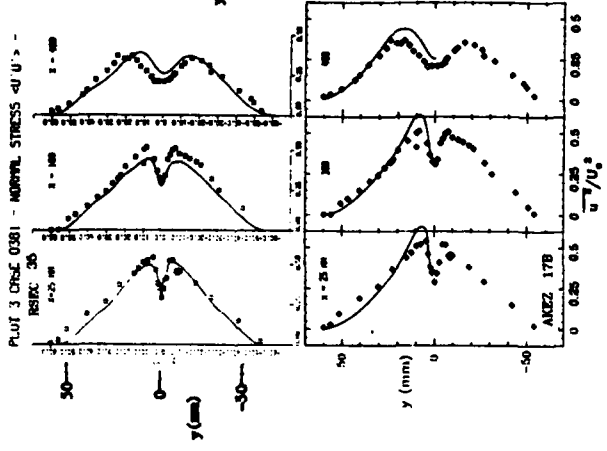
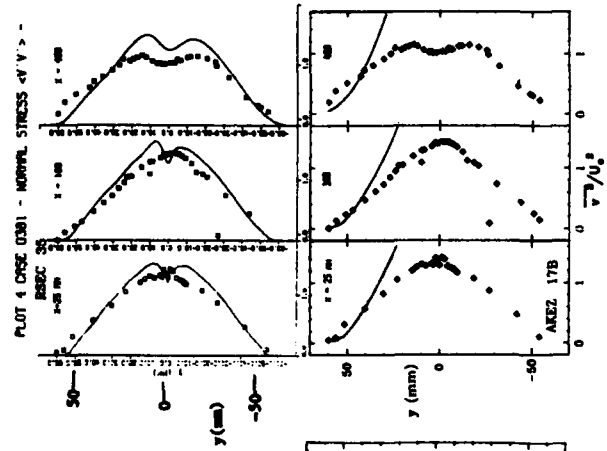
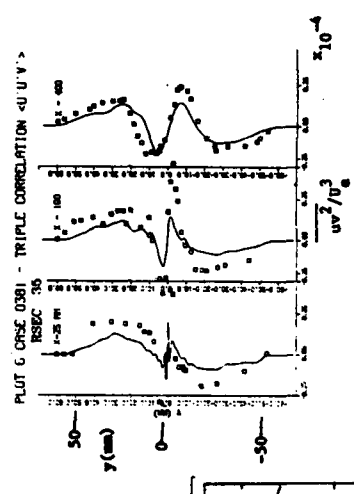
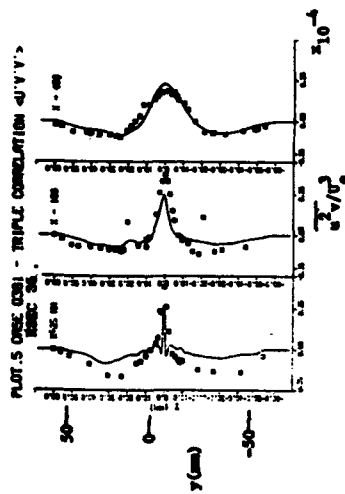
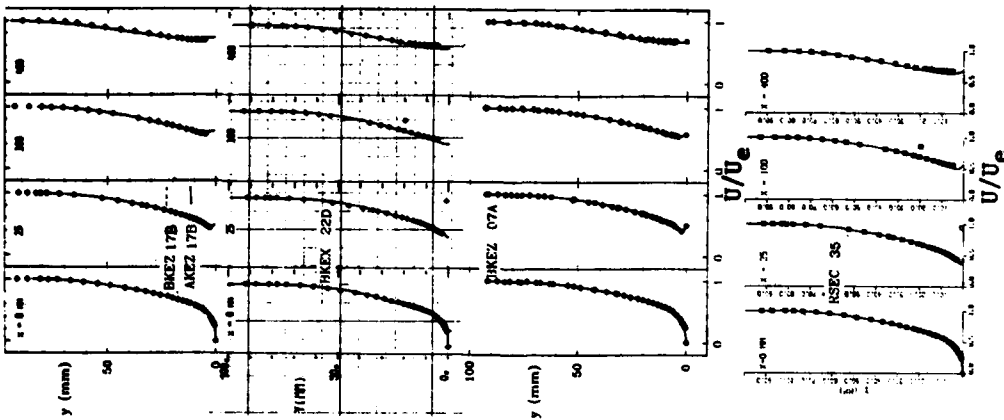
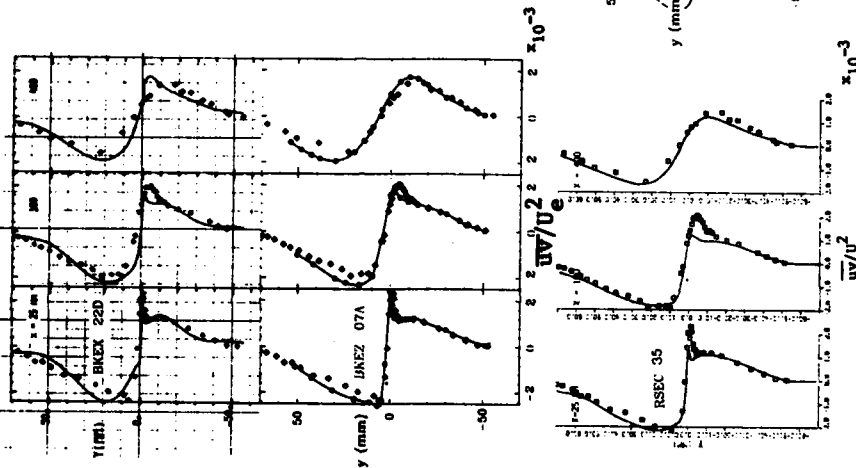


PLATE 98

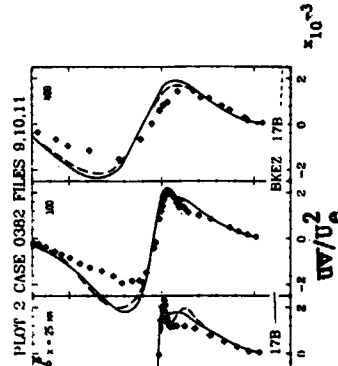
PLOT 1 CASE 0382 FILES 40,42,45,49



PLOT 2 CASE 0382 FILES 9,10,11



PLOT 2 CASE 0382 FILES 9,10,11



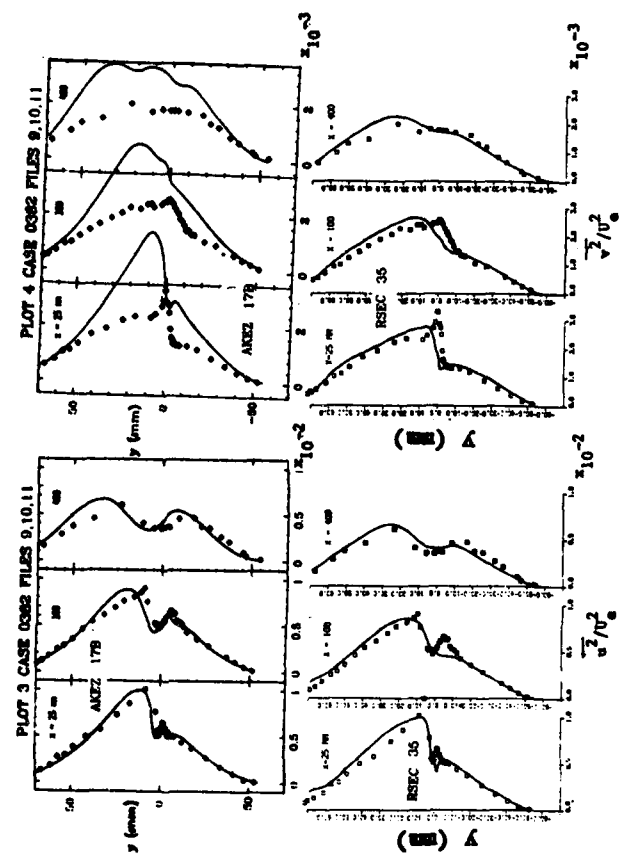
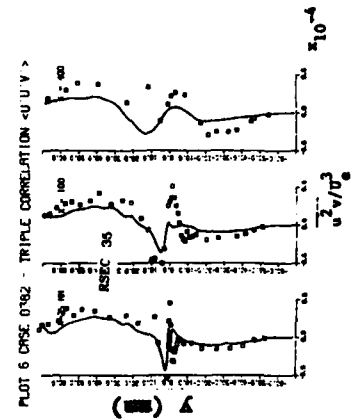
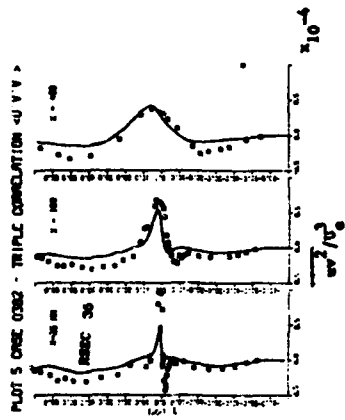


PLATE 100

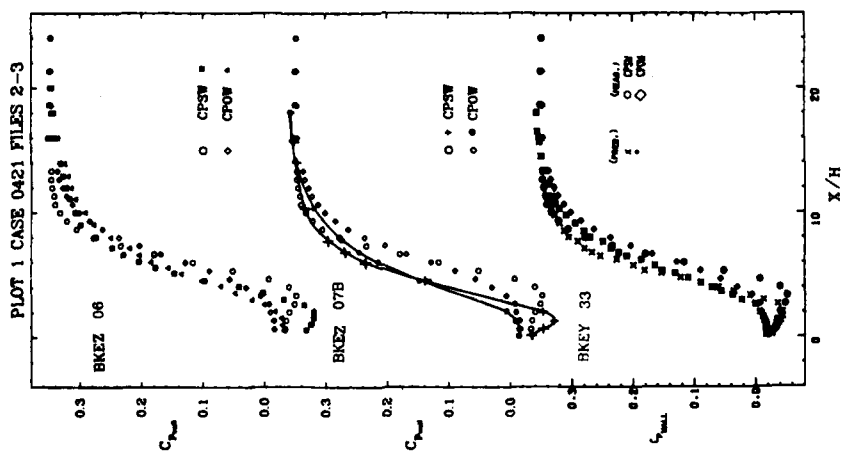
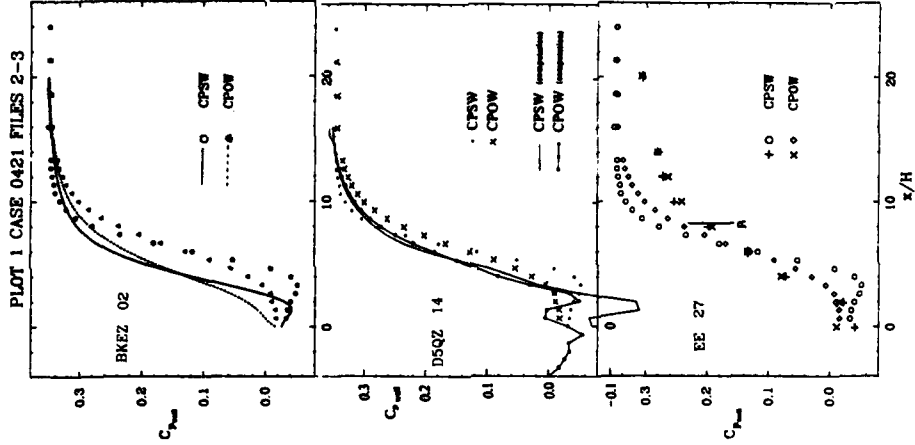
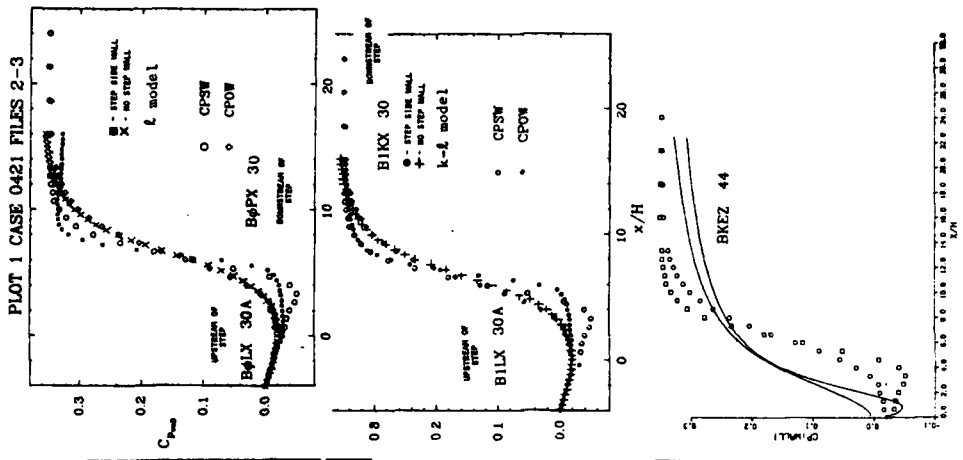


PLATE 101

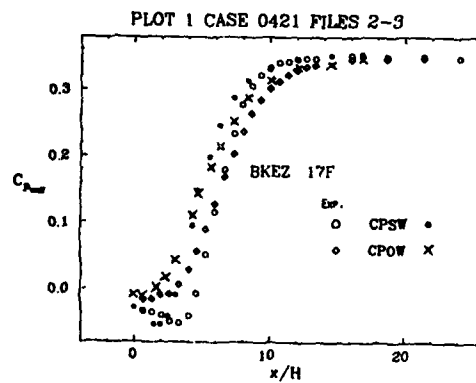
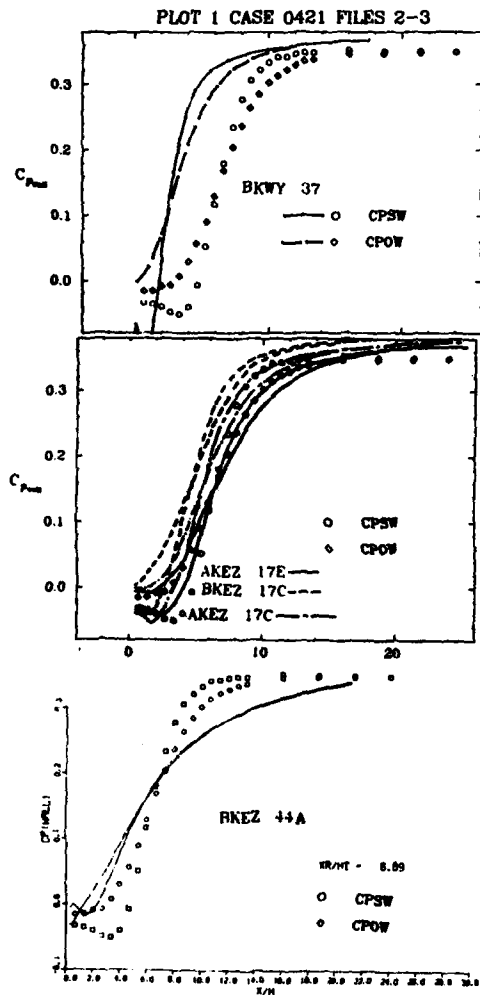
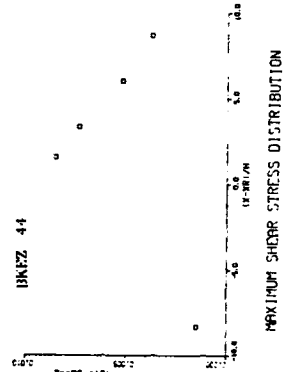
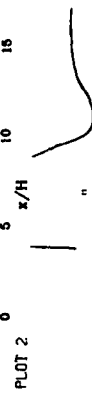
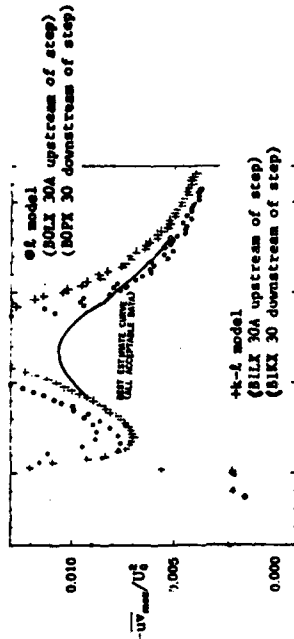
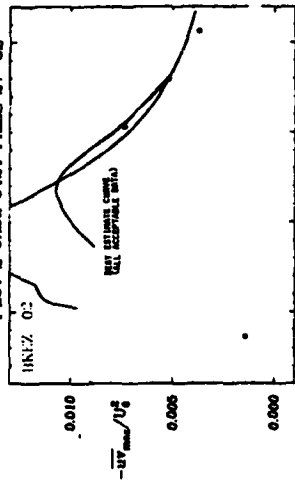
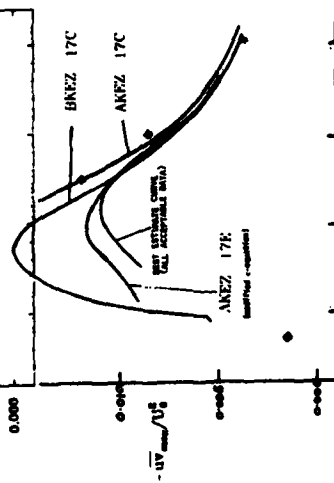
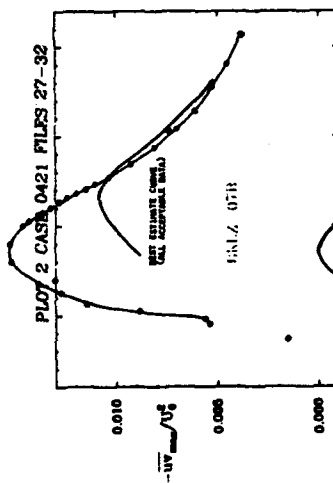


PLATE 102

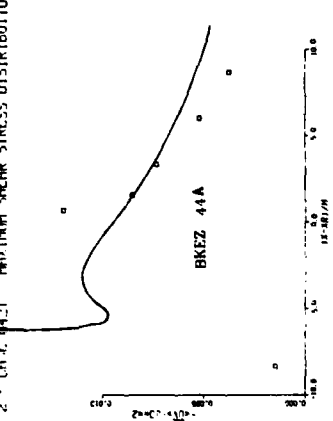
PLOT 2 CASE 0421 FILES 27-32



PLOT 2 CASE 0421 FILES 27-32



PLOT 2 - UVC-0421 MAXIMUM SHEAR STRESS DISTRIBUTION



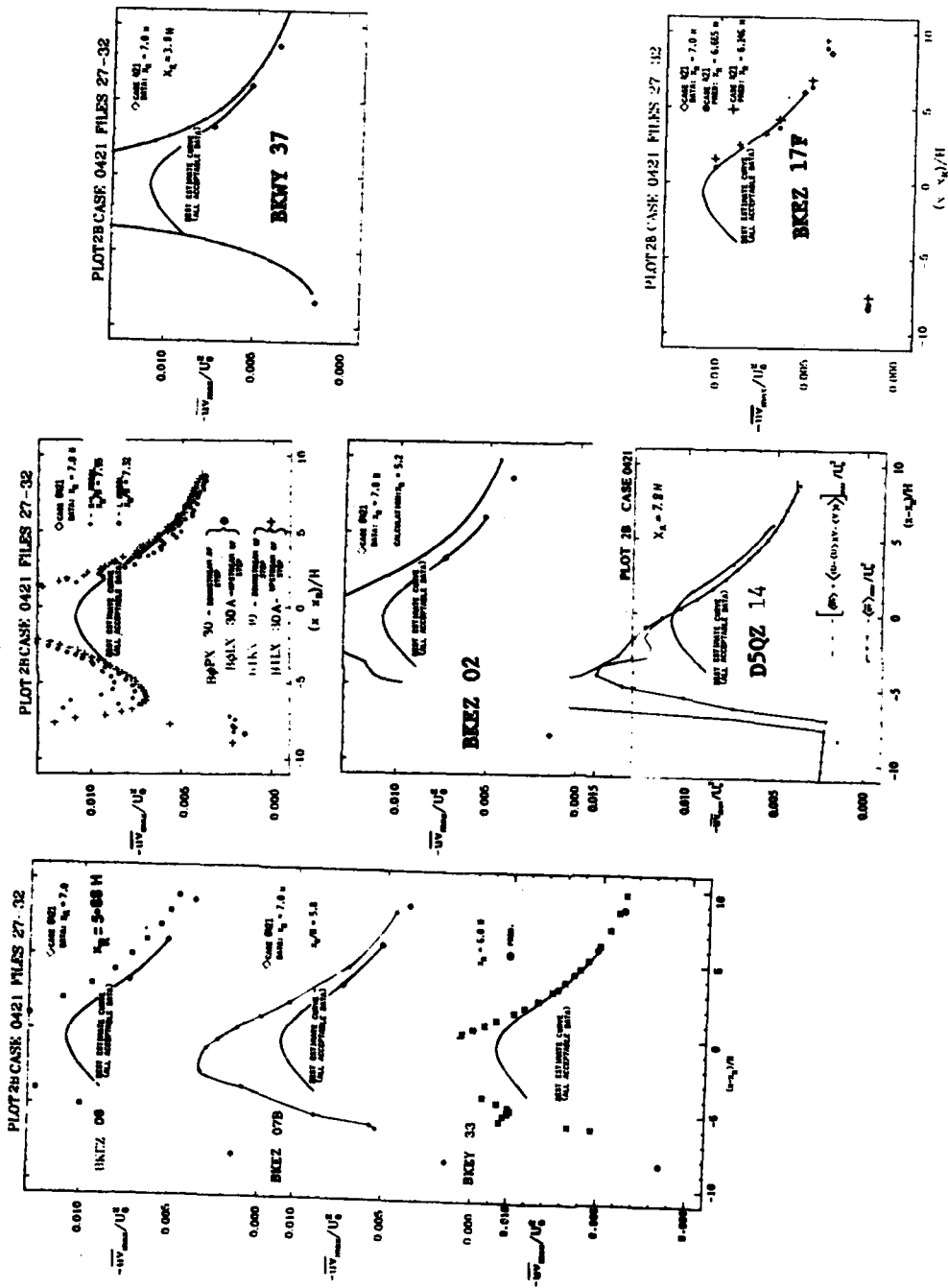


PLATE 104

PLOT 3 CASE 0421 - VELOCITY PROFILES -

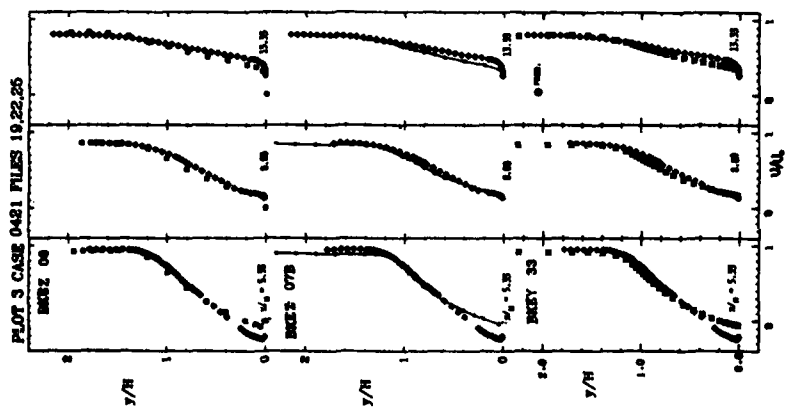
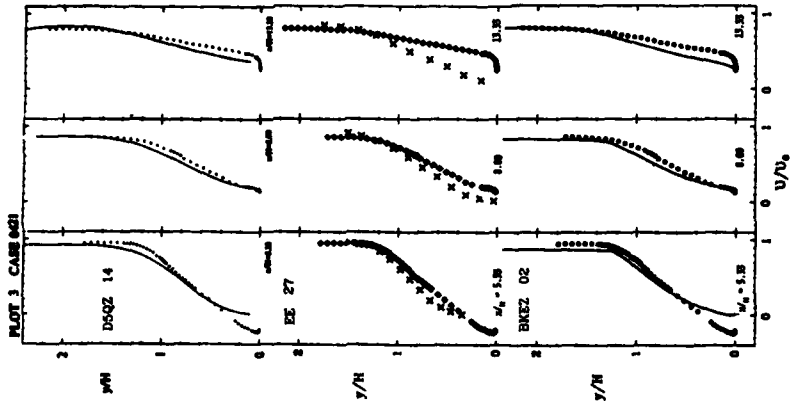
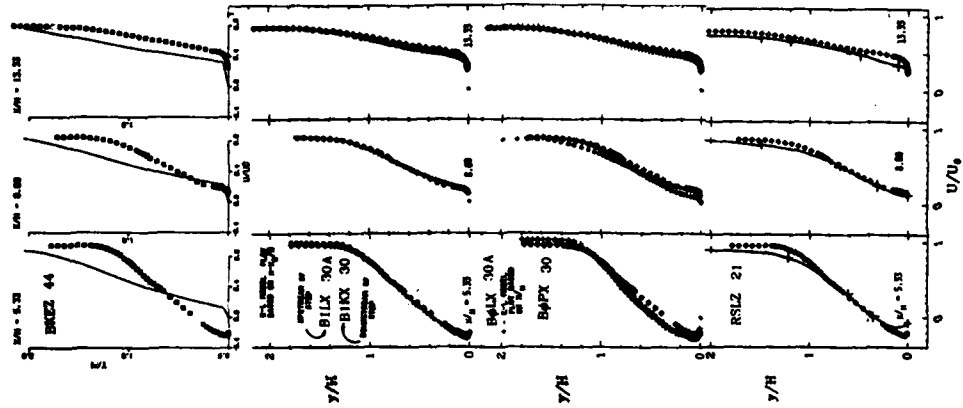
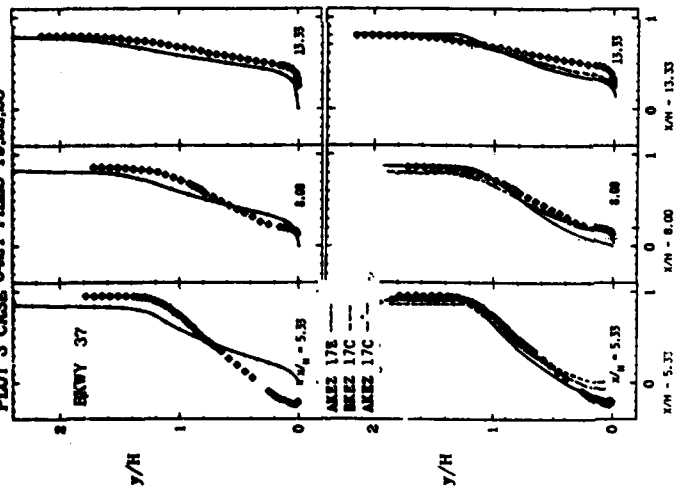


PLATE 105

PLOT 3 CASE 0421 FILES 19.22.25



PLOT 3 CASE 0421 FILES 19.22.25

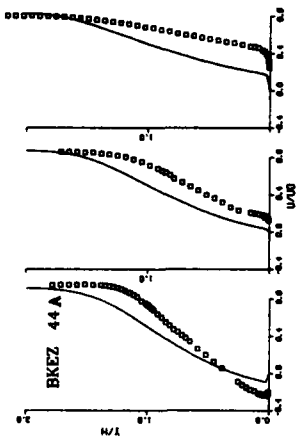
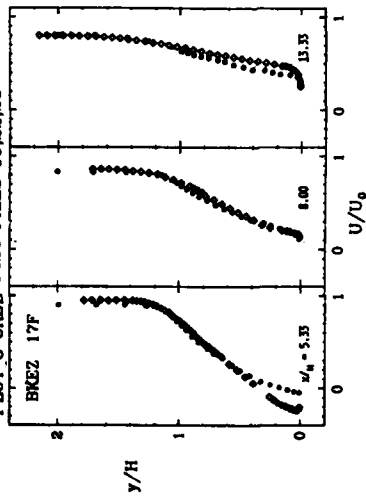
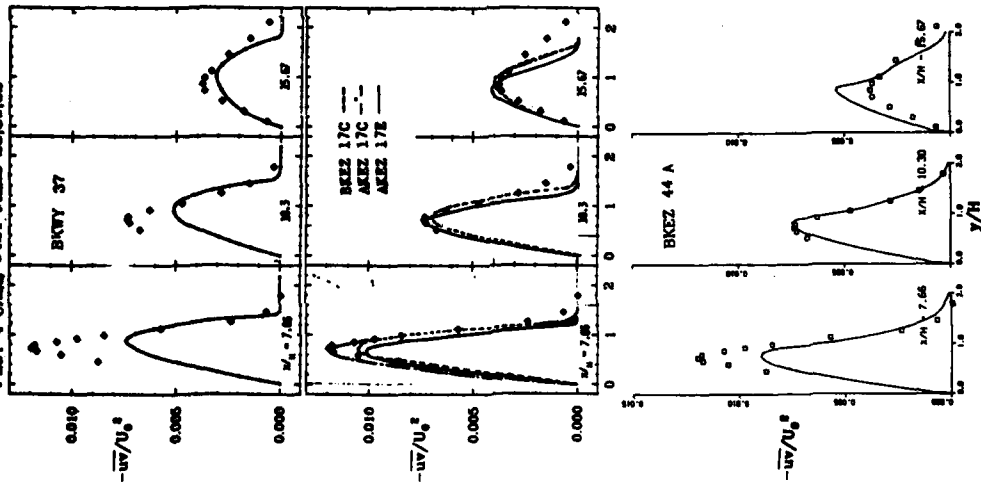


PLATE 106

PLOT 4 CASE 04E1 FILES 26,30,32



PLOT 4 CASE 0421 FILES 26,30,32

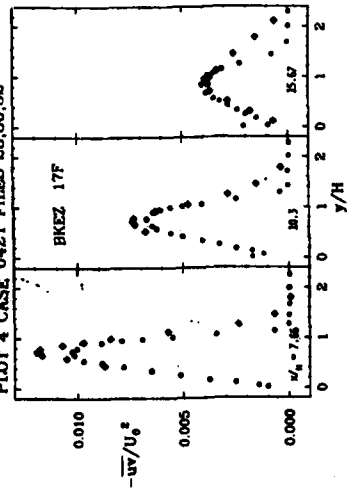


PLATE 107

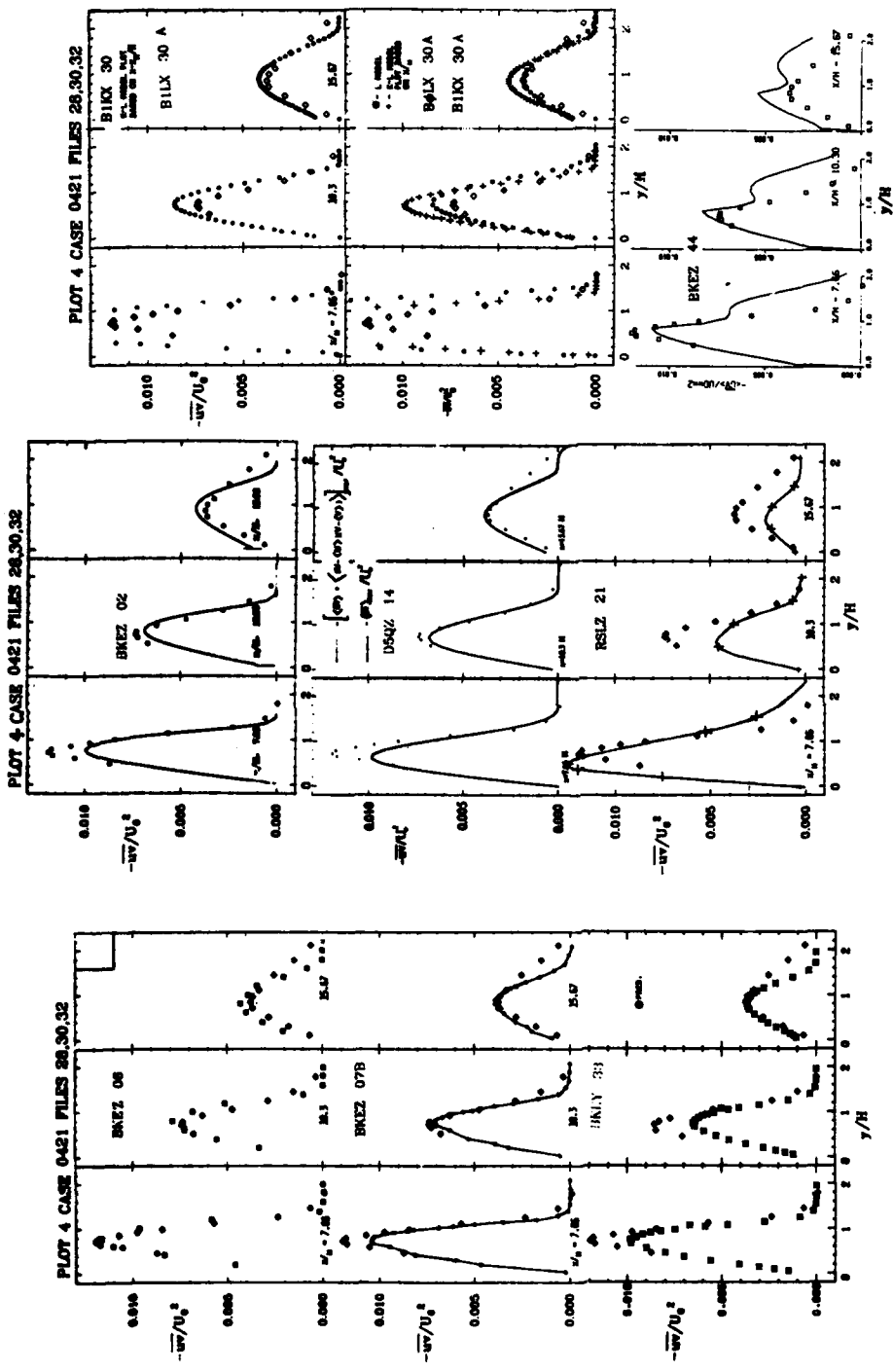


PLATE 108

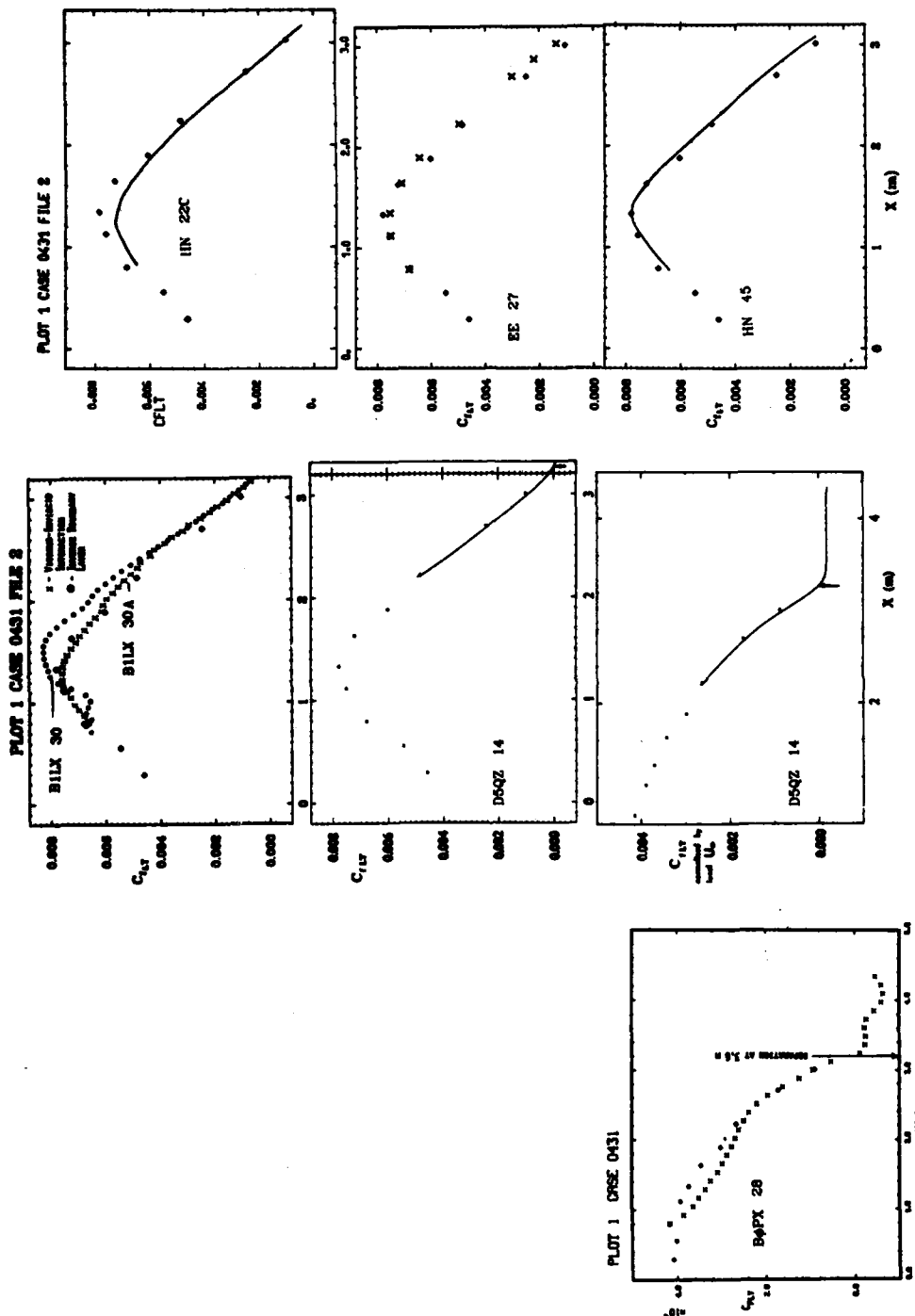
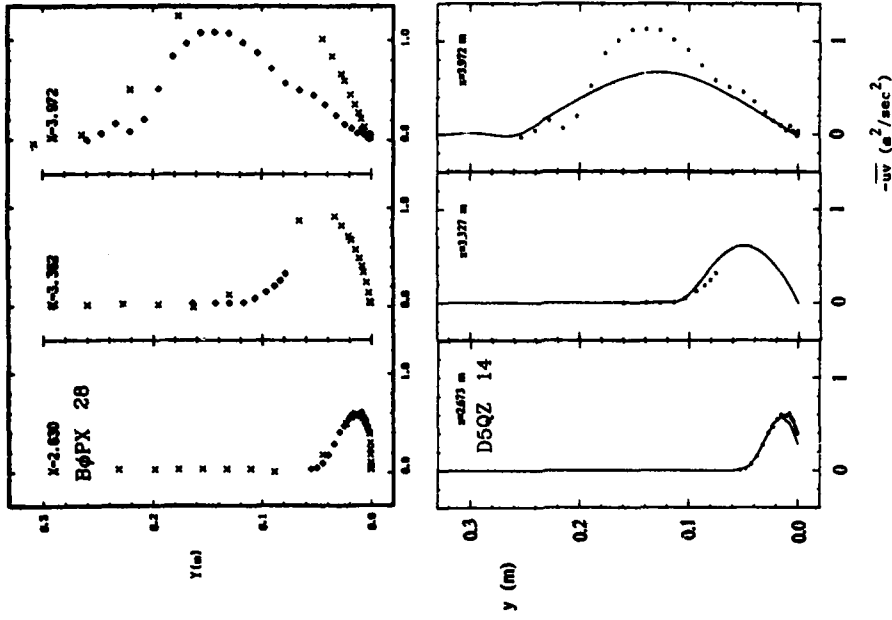


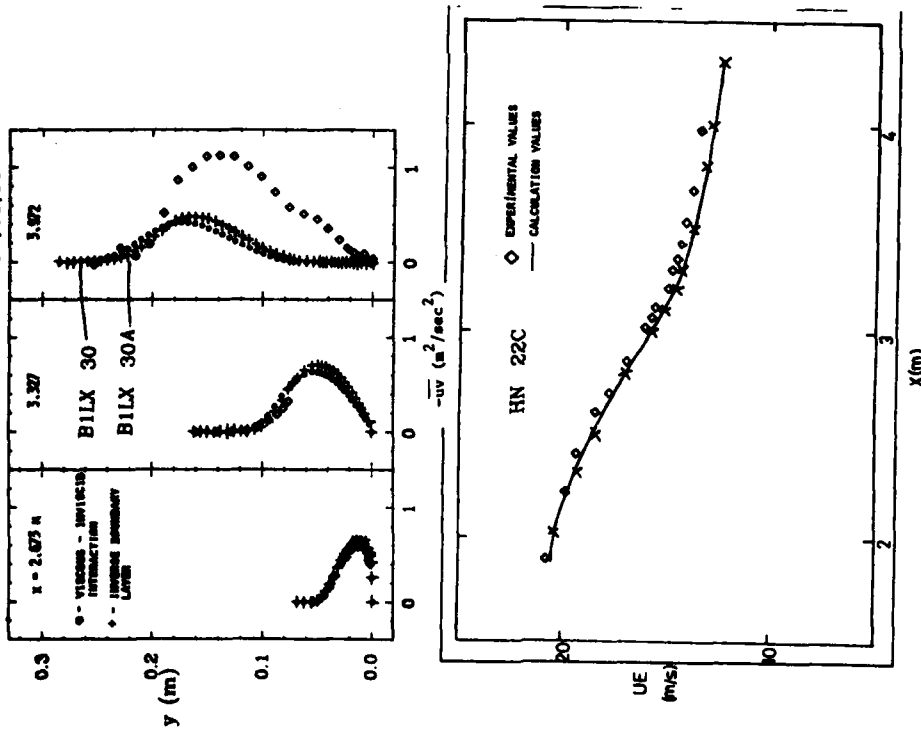
PLATE 109

(Group 28 submitted two sets of output (1) elliptic method (11) parabolic method. There was little difference in the two sets of output and only one set is, therefore, presented here. (See Plates 109-113))

PLOT 2 CASE 0431



PLOT 2 CASE 0431 FILES 18.21.35



This is an additional plot.
See also Plate 113.

PLATE 110

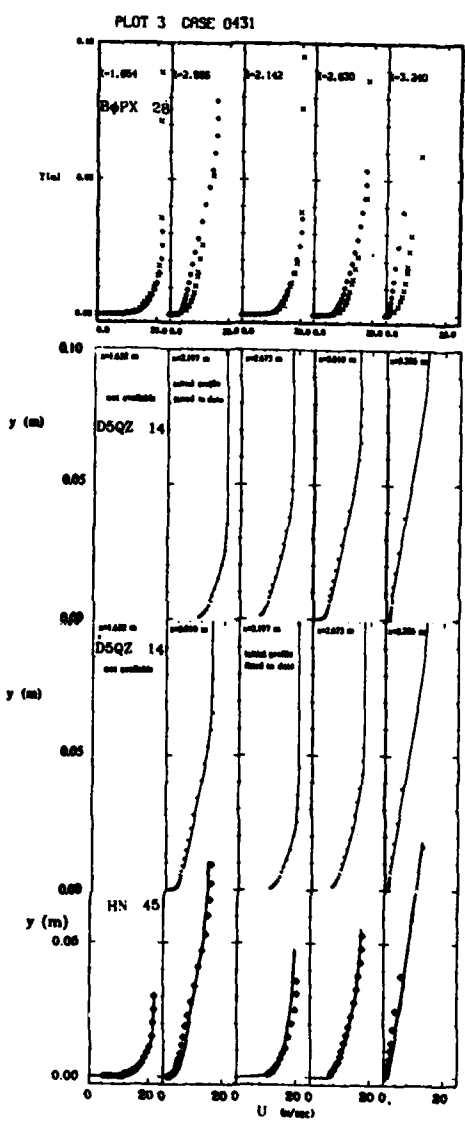
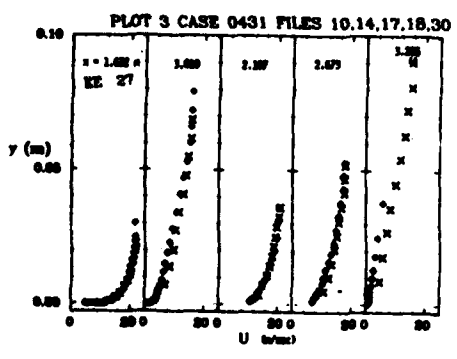
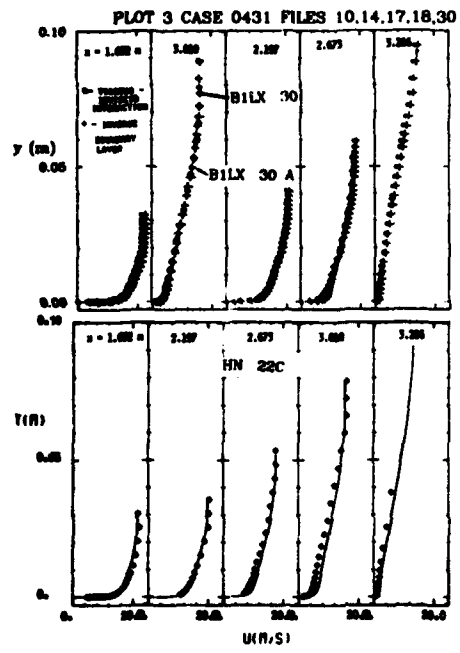
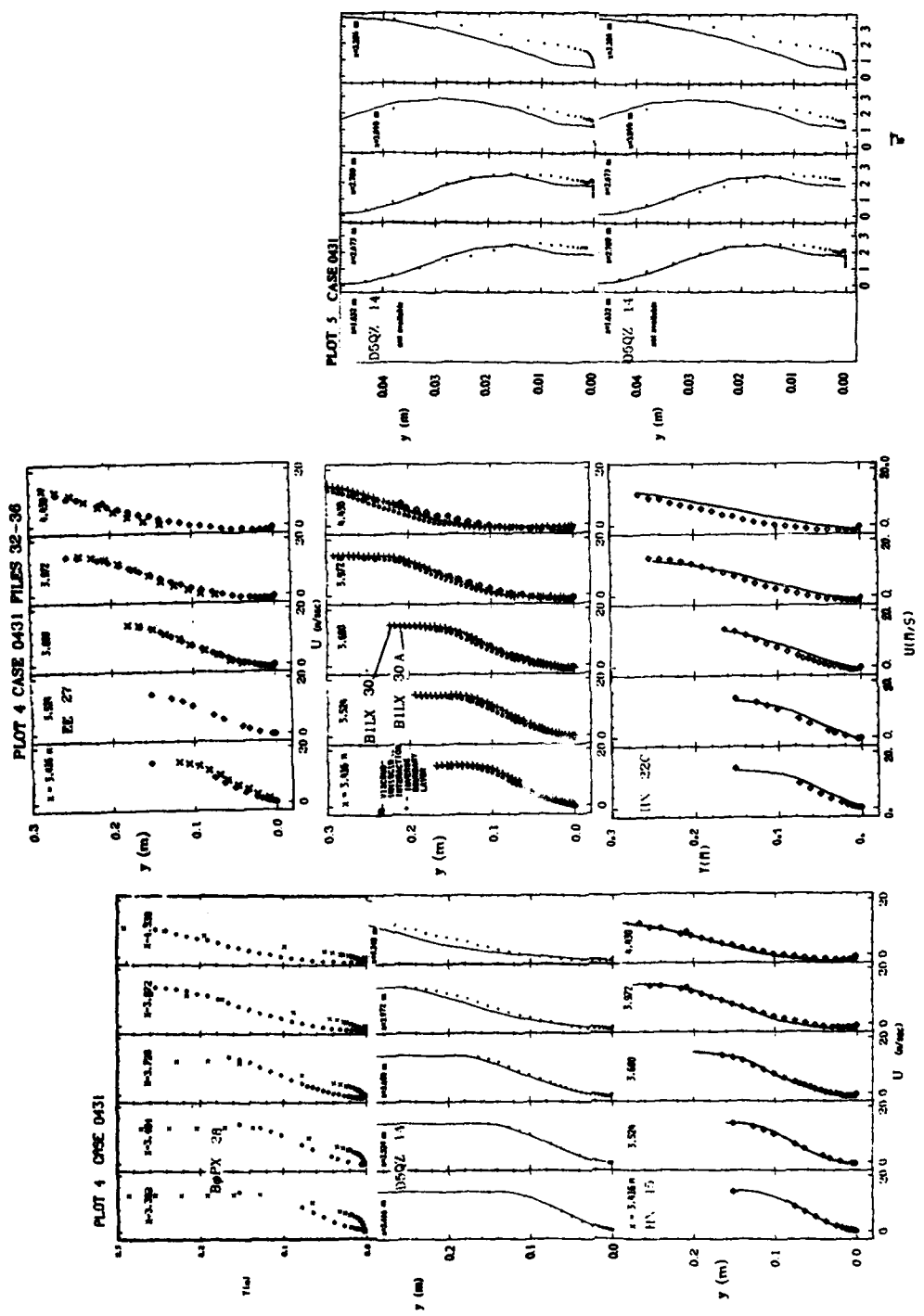


PLATE 111



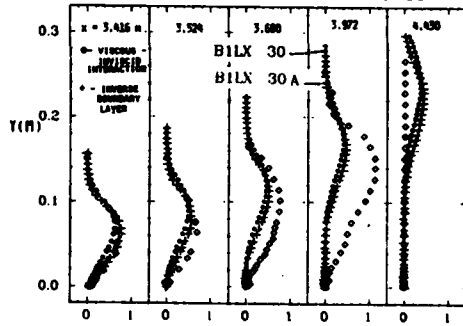
PLOT 4 CASE 0431 PILES 32-36

PLOT 4 CASE 0431

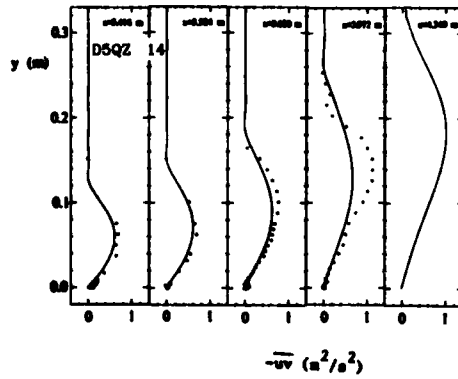
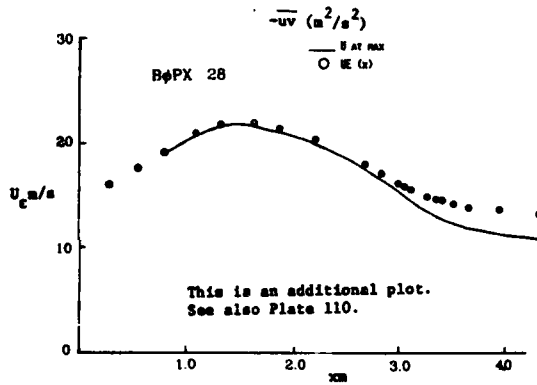
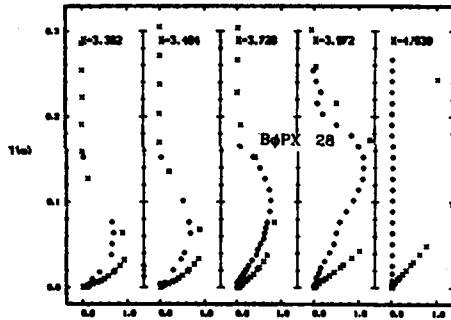
PLOT 5 CASE 0431

PLATE 112

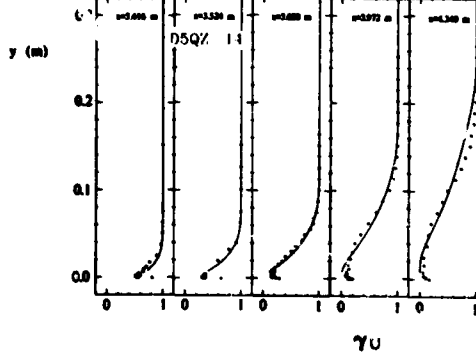
PLOT 6 CASE 0431 FILES 32-36



PLOT 6 CASE 0431



PLOT 7 CASE 0431



AD-A136 034

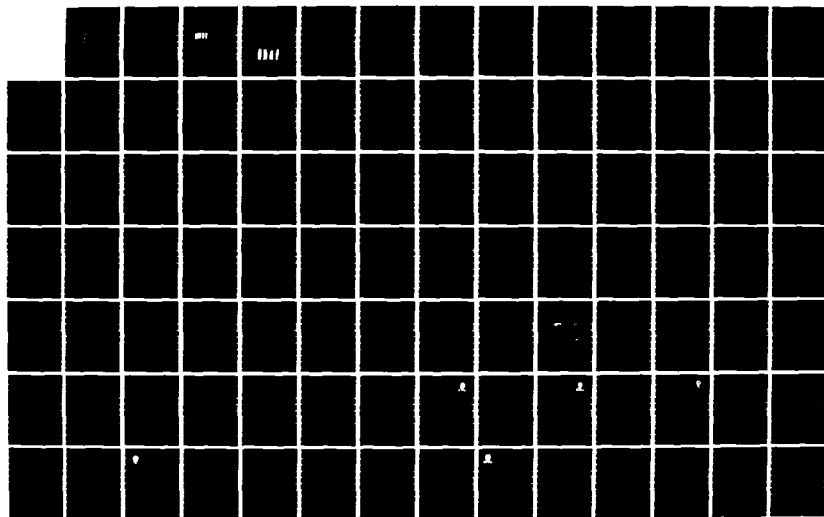
THE 1980-81 AFOSR (AIR FORCE OFFICE OF SCIENTIFIC
RESEARCH)-HTM (HEAT TR. (U) STANFORD UNIV CA DEPT OF
MECHANICAL ENGINEERING S J KLINE ET AL. SEP 81
AFOSR-TR-83-1003 F49620-80-C-0027

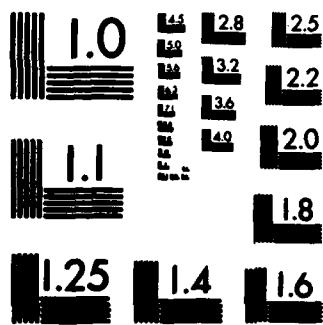
3/6

UNCLASSIFIED

F/G 20/4

NL





MICROCOPY RESOLUTION TEST CHART
NATIONAL BUREAU OF STANDARDS-1963-A

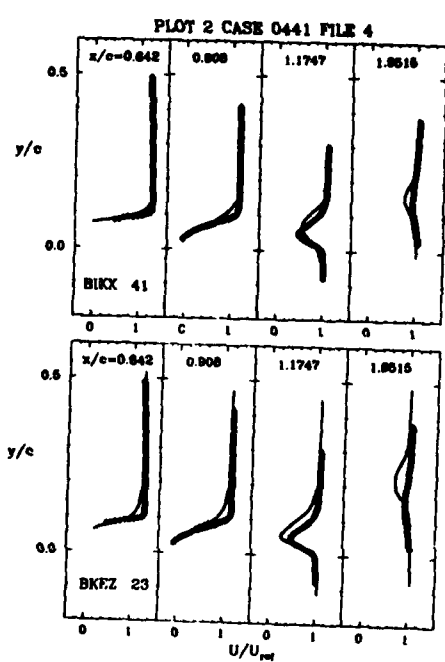
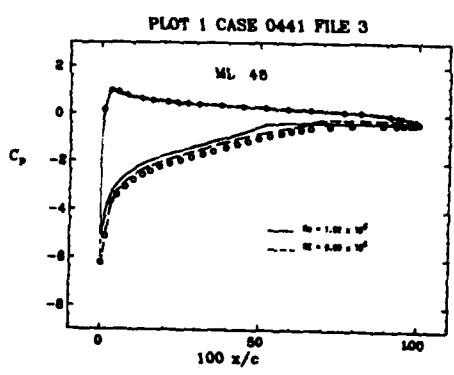
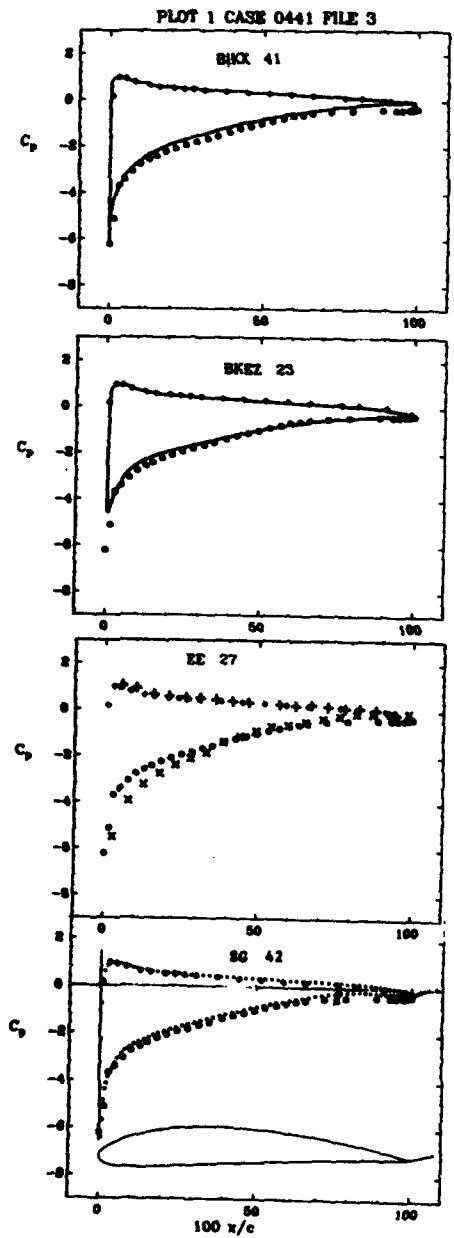


PLATE 114

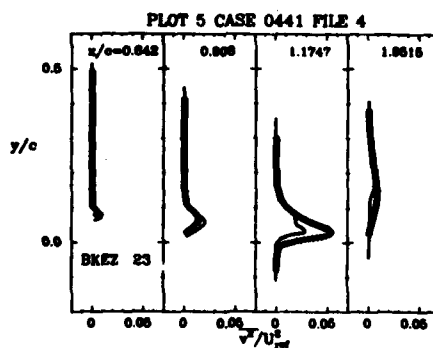
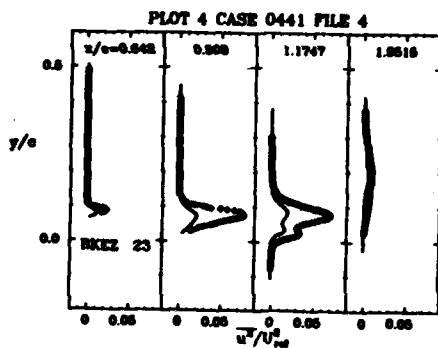
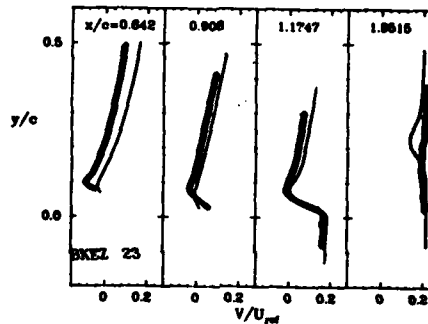
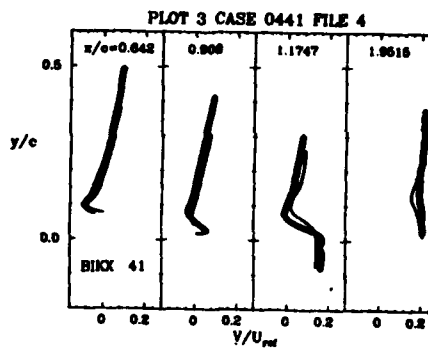
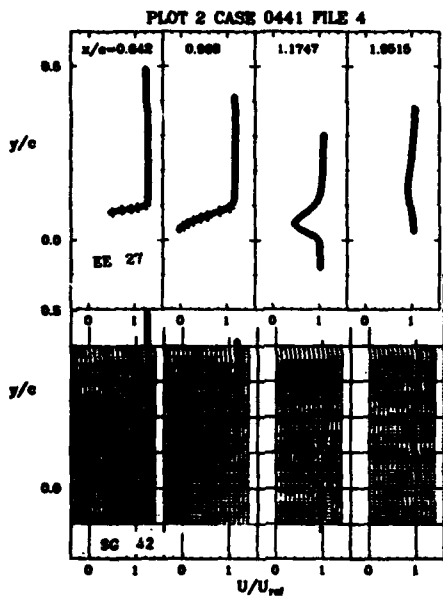


PLATE 115

PLOT 6 CASE 0441 FILE 4

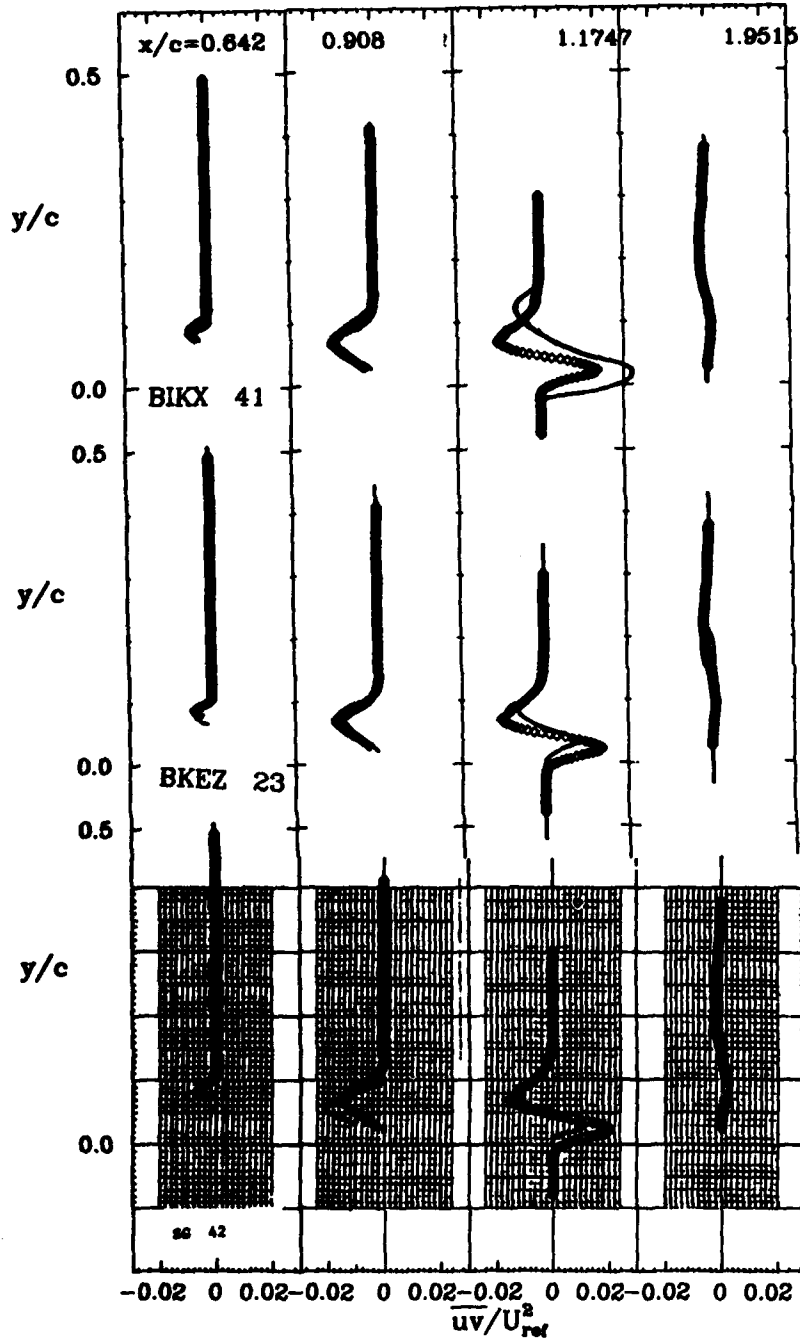
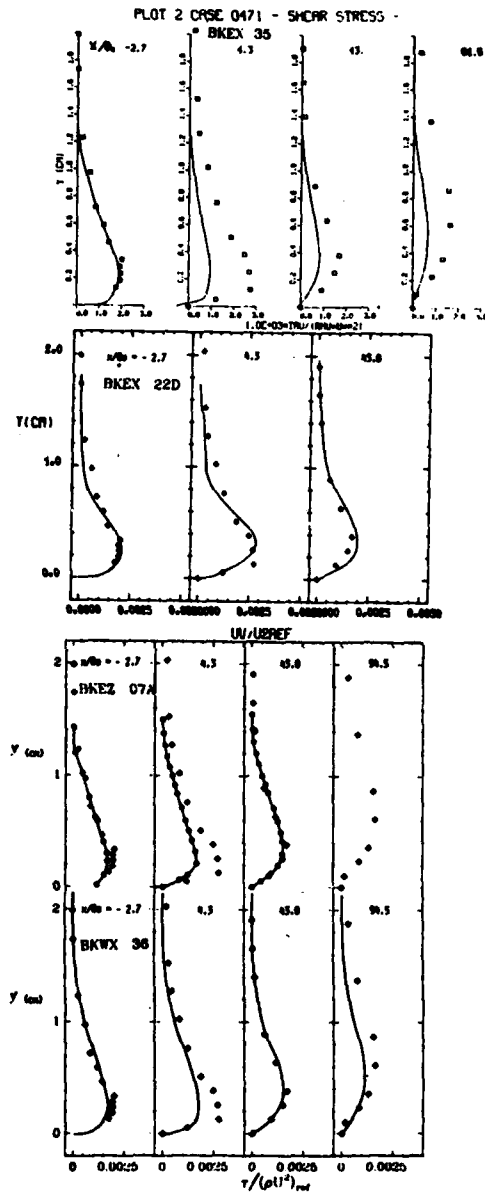
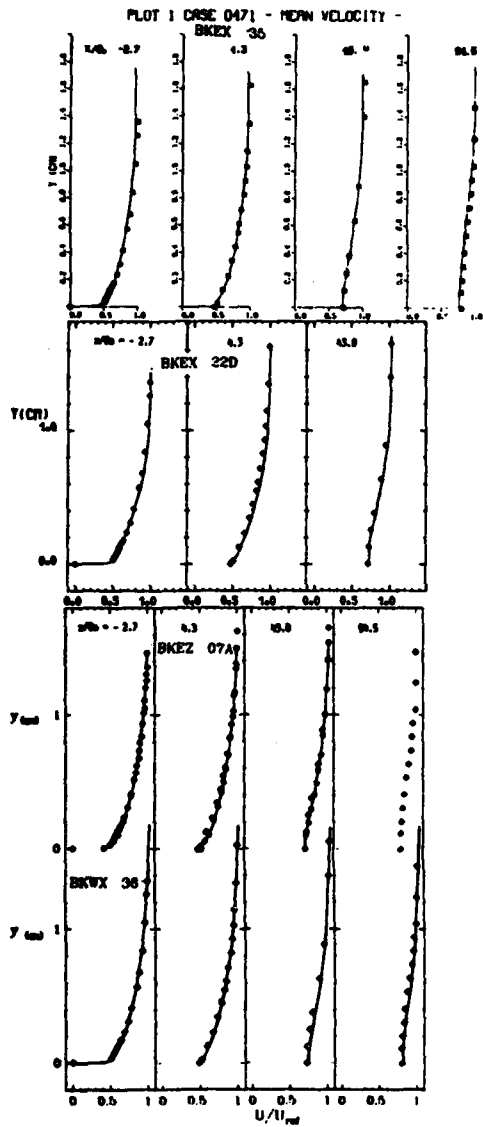


PLATE 116



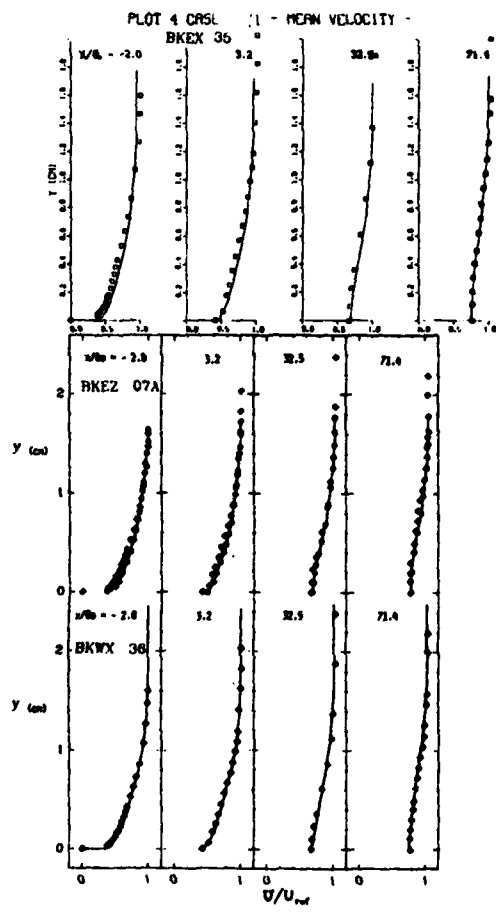
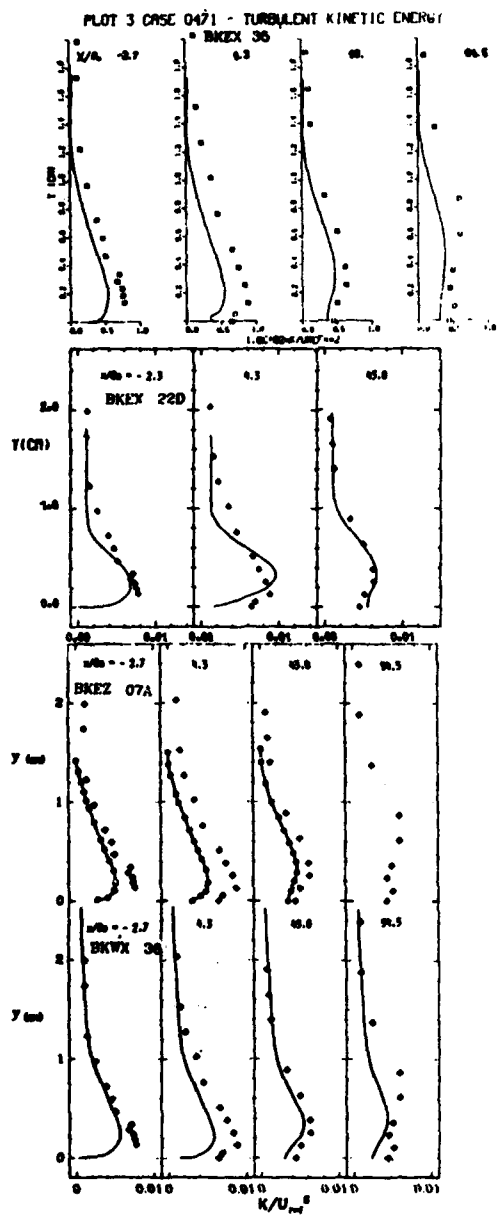


PLATE 118

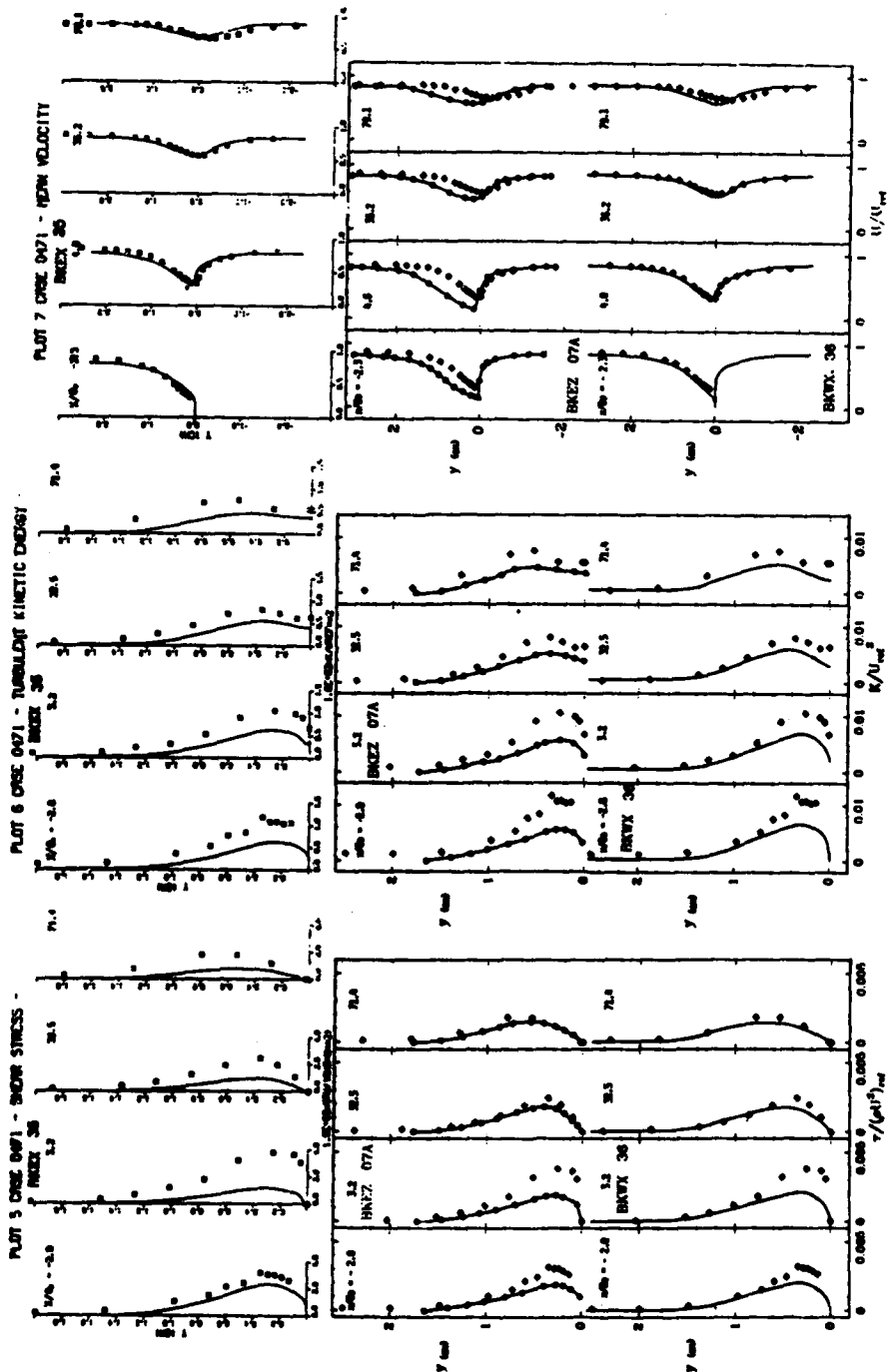


PLATE 119

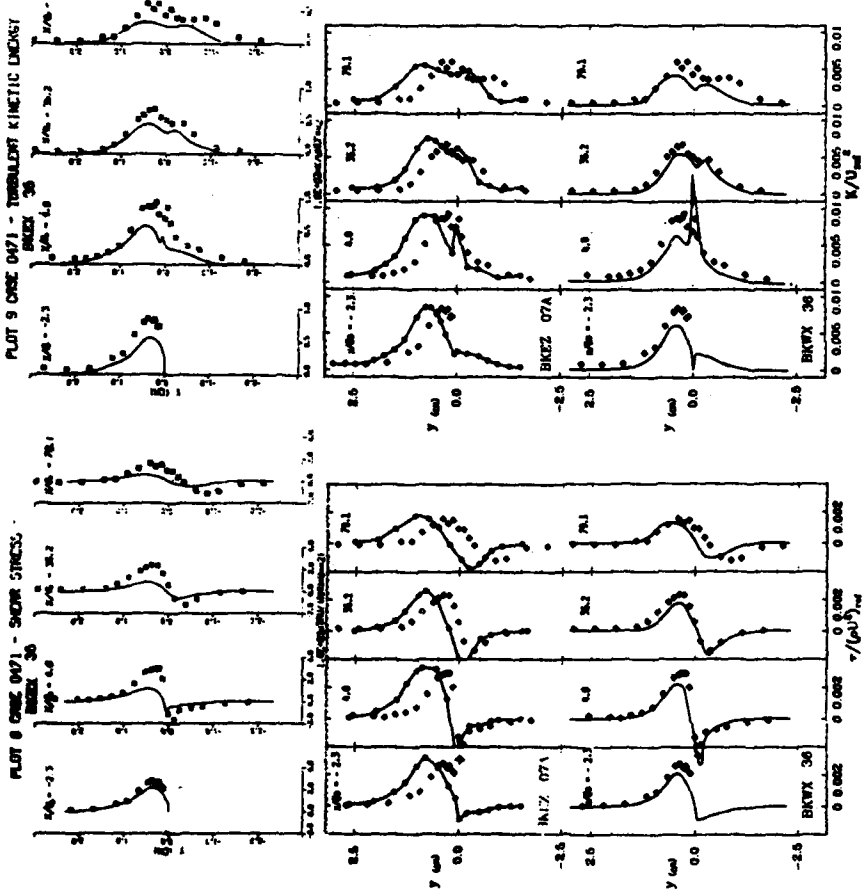
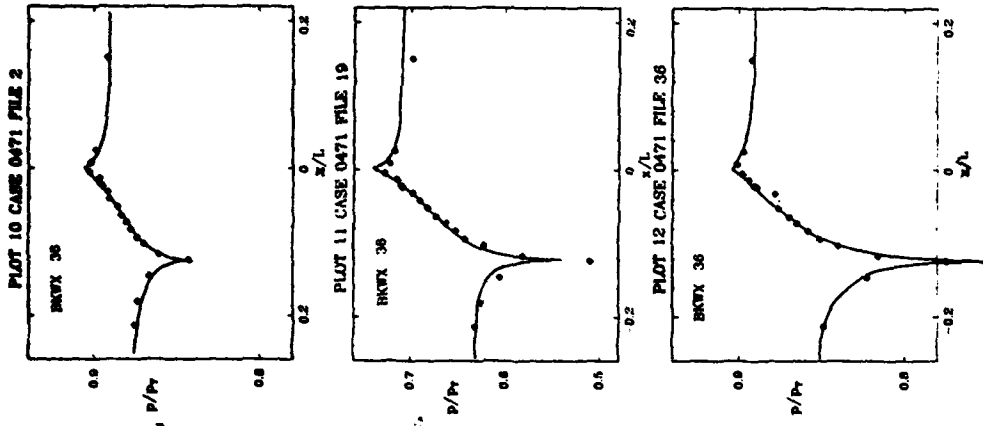


PLATE 120

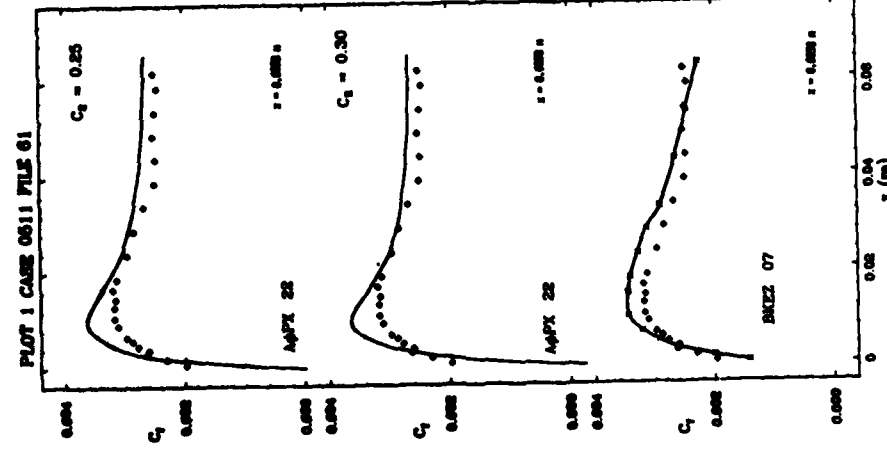
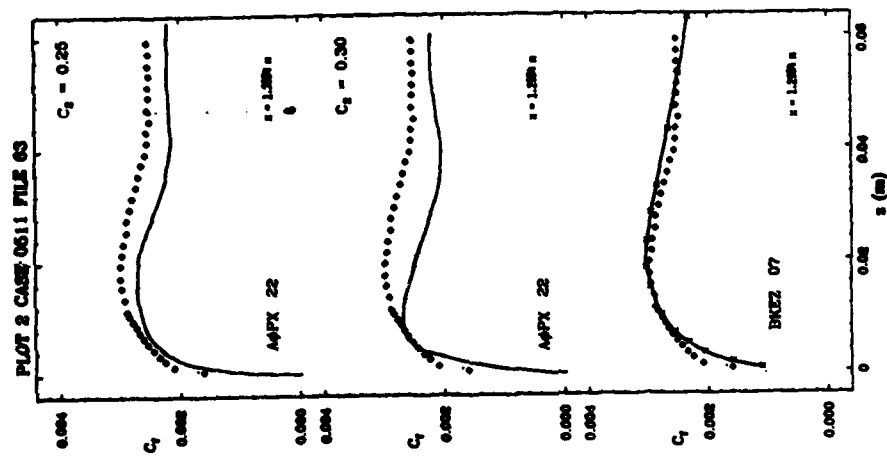
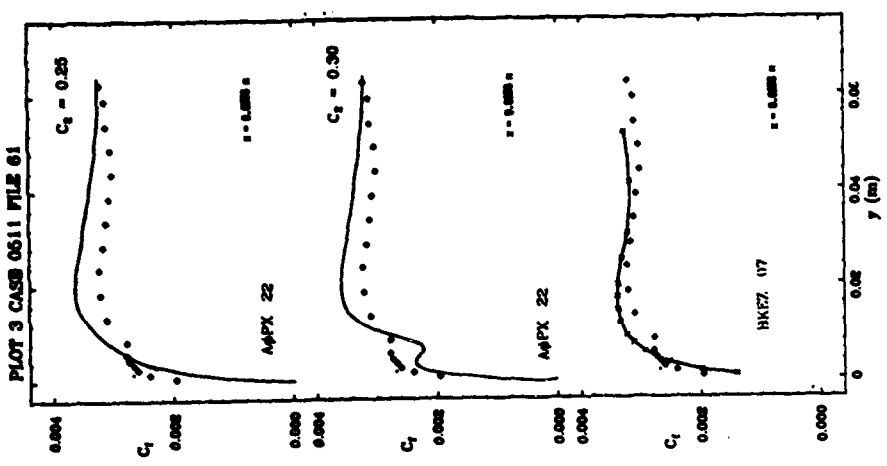


PLATE 121

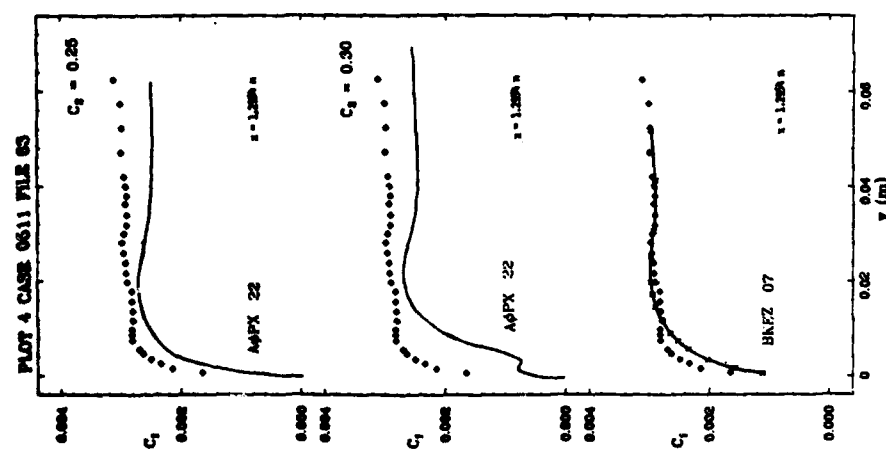
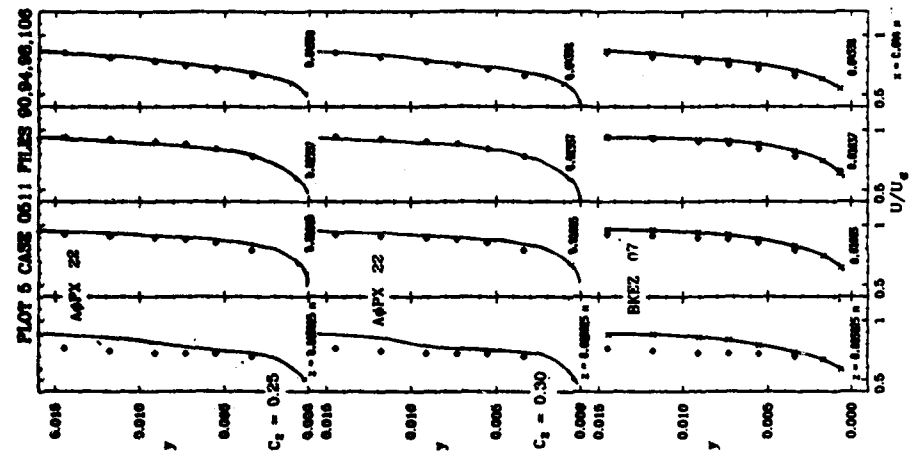
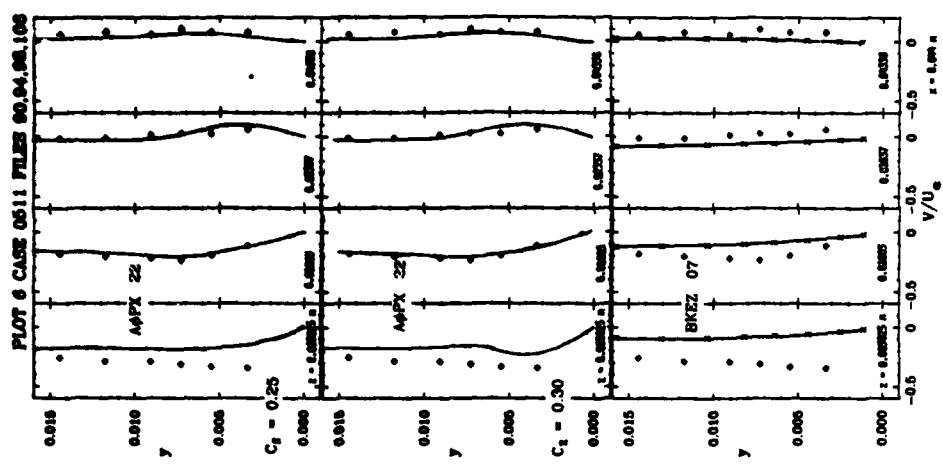


PLATE 123

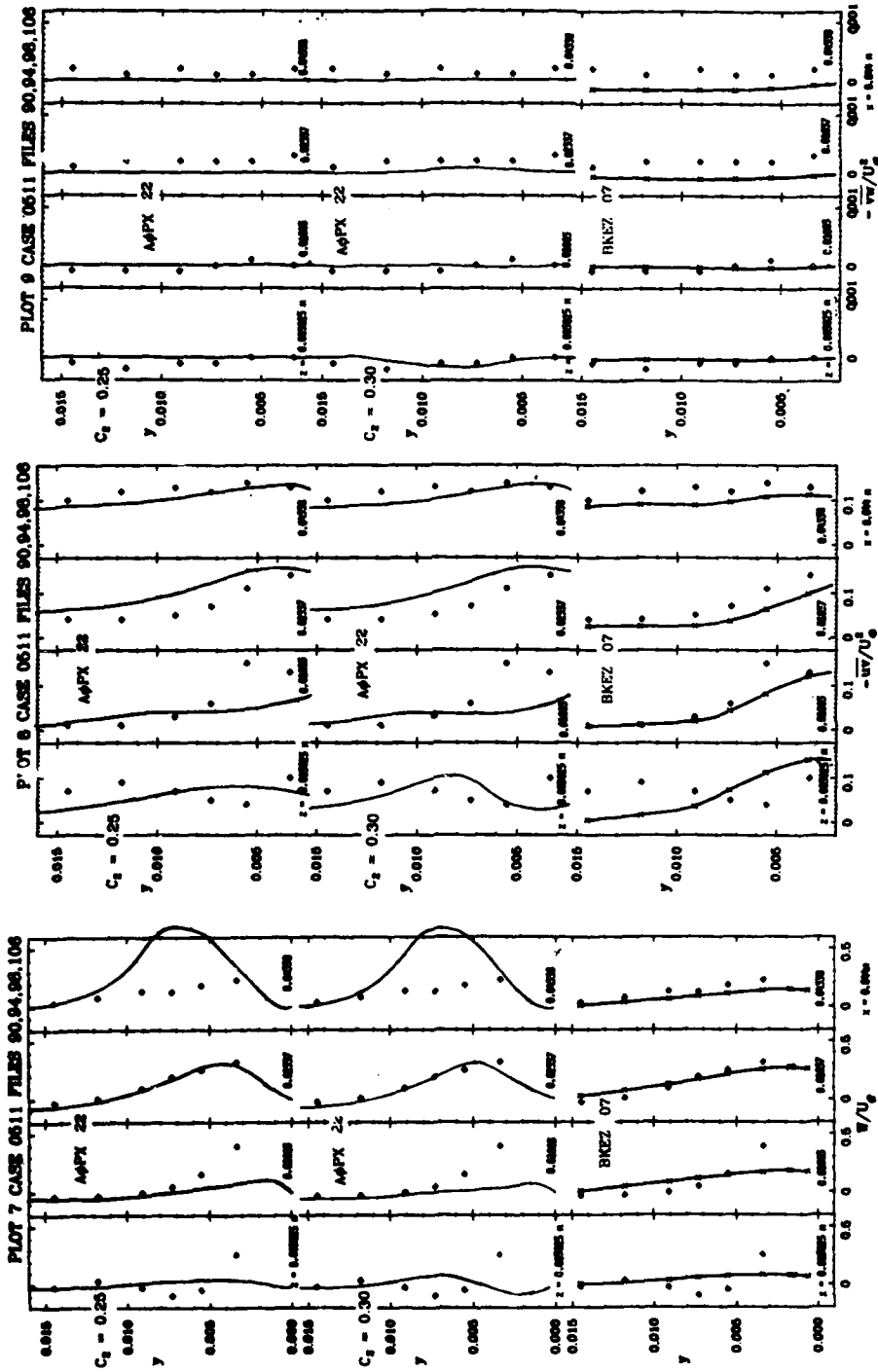


PLATE 123

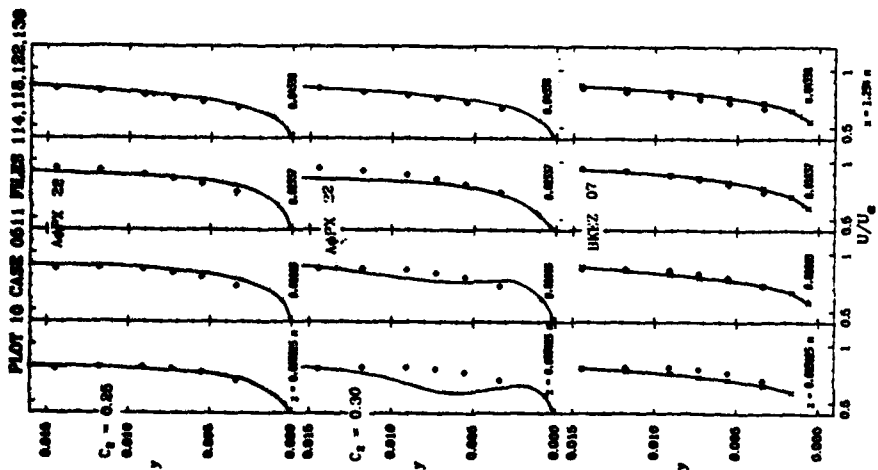
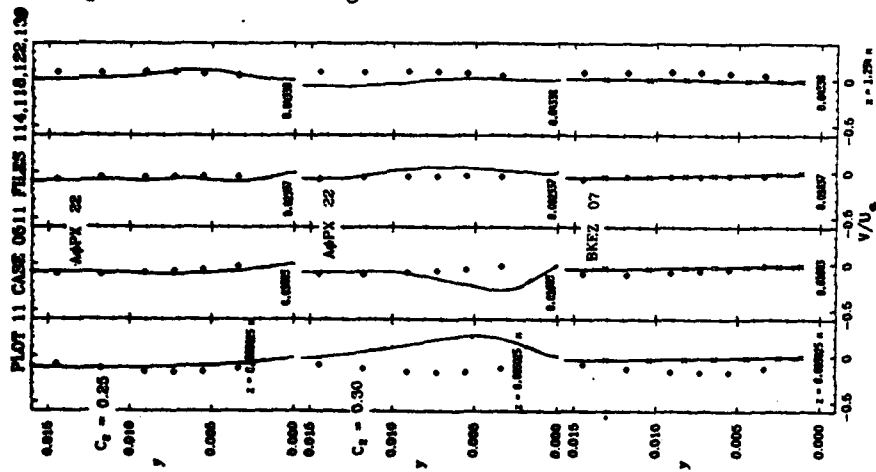
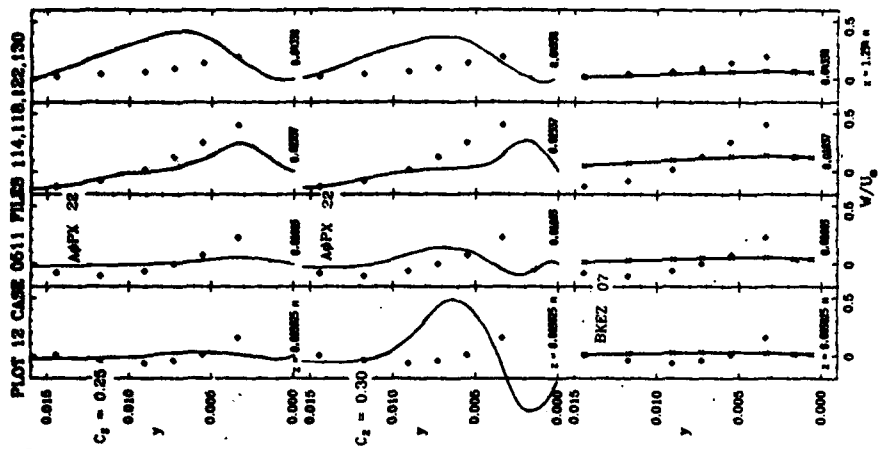
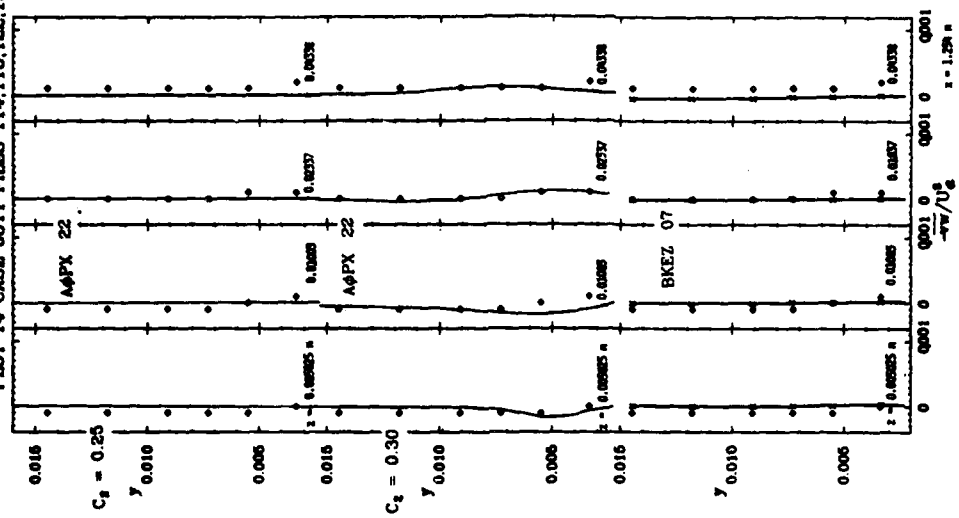
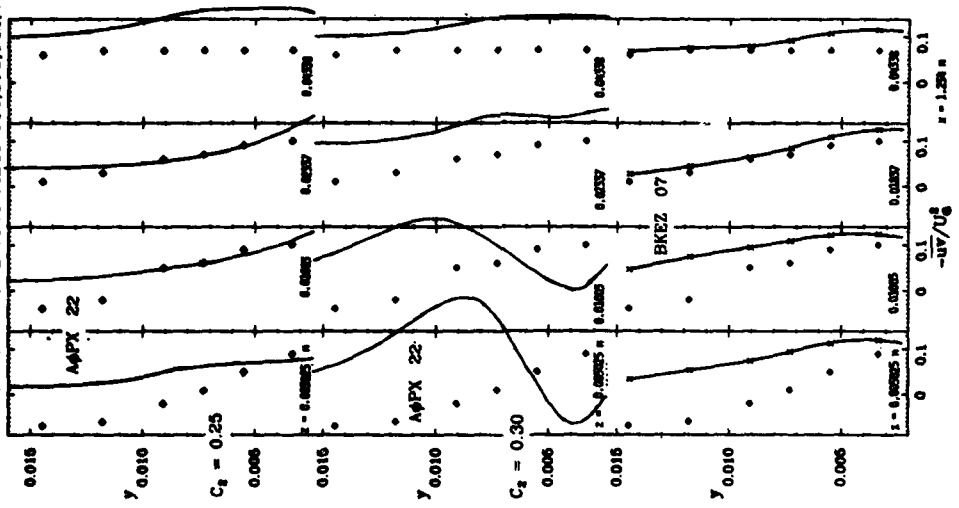


PLATE 124

PLOT 14 CASE 0611 FILES 114,118,122,130



PLOT 13 CASE 0611 FILES 114,118,122,130



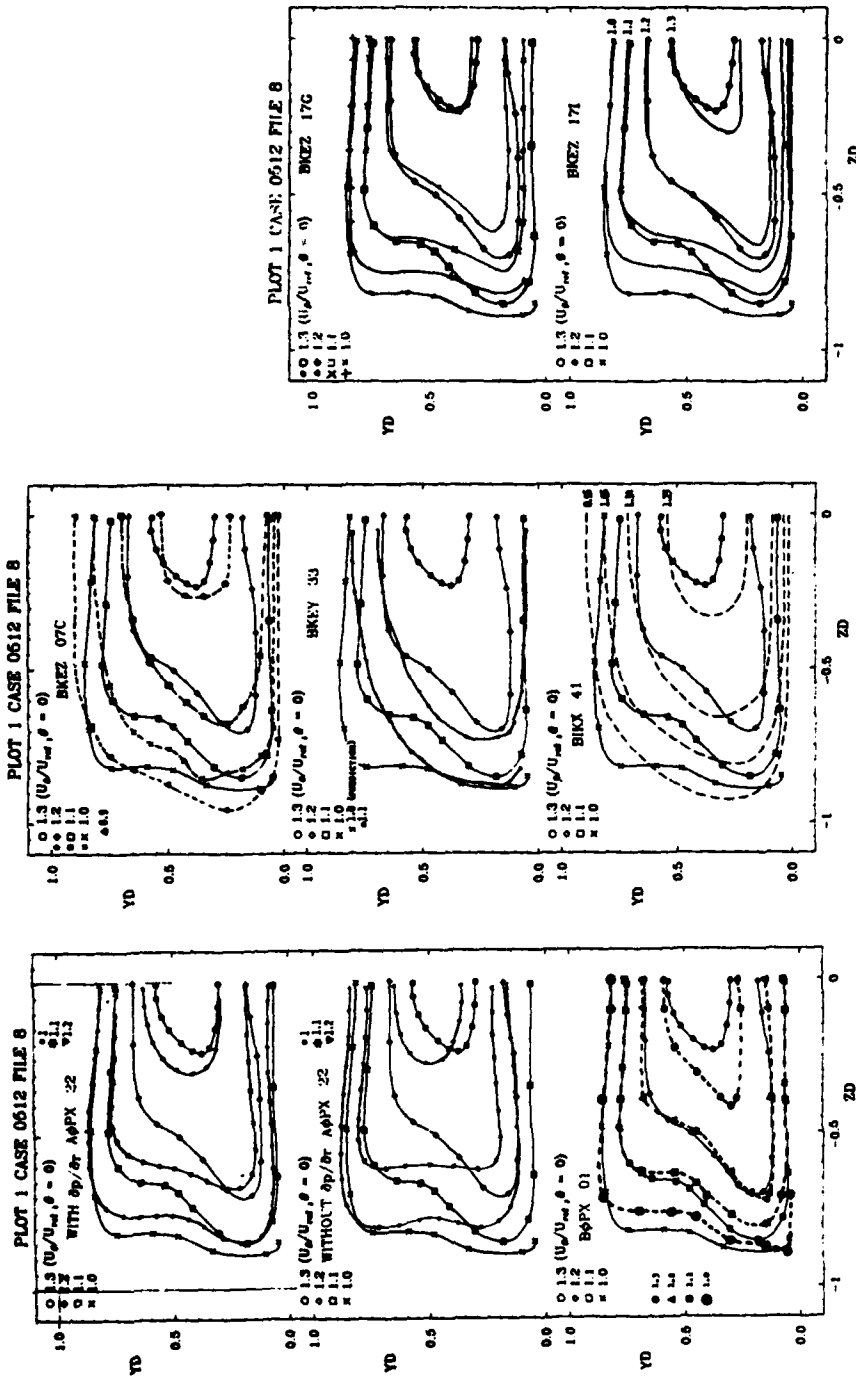


PLATE 126

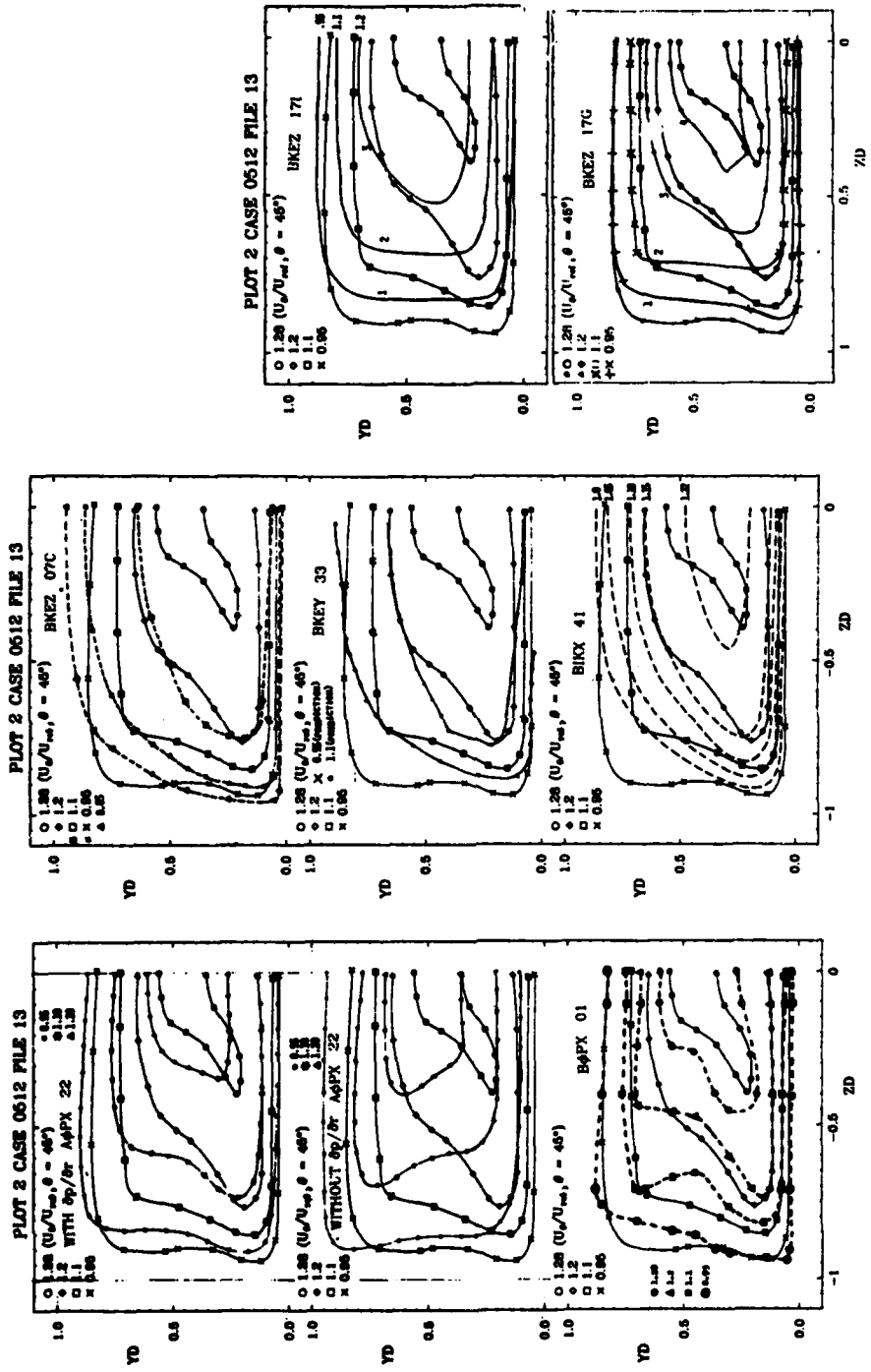


PLATE 127

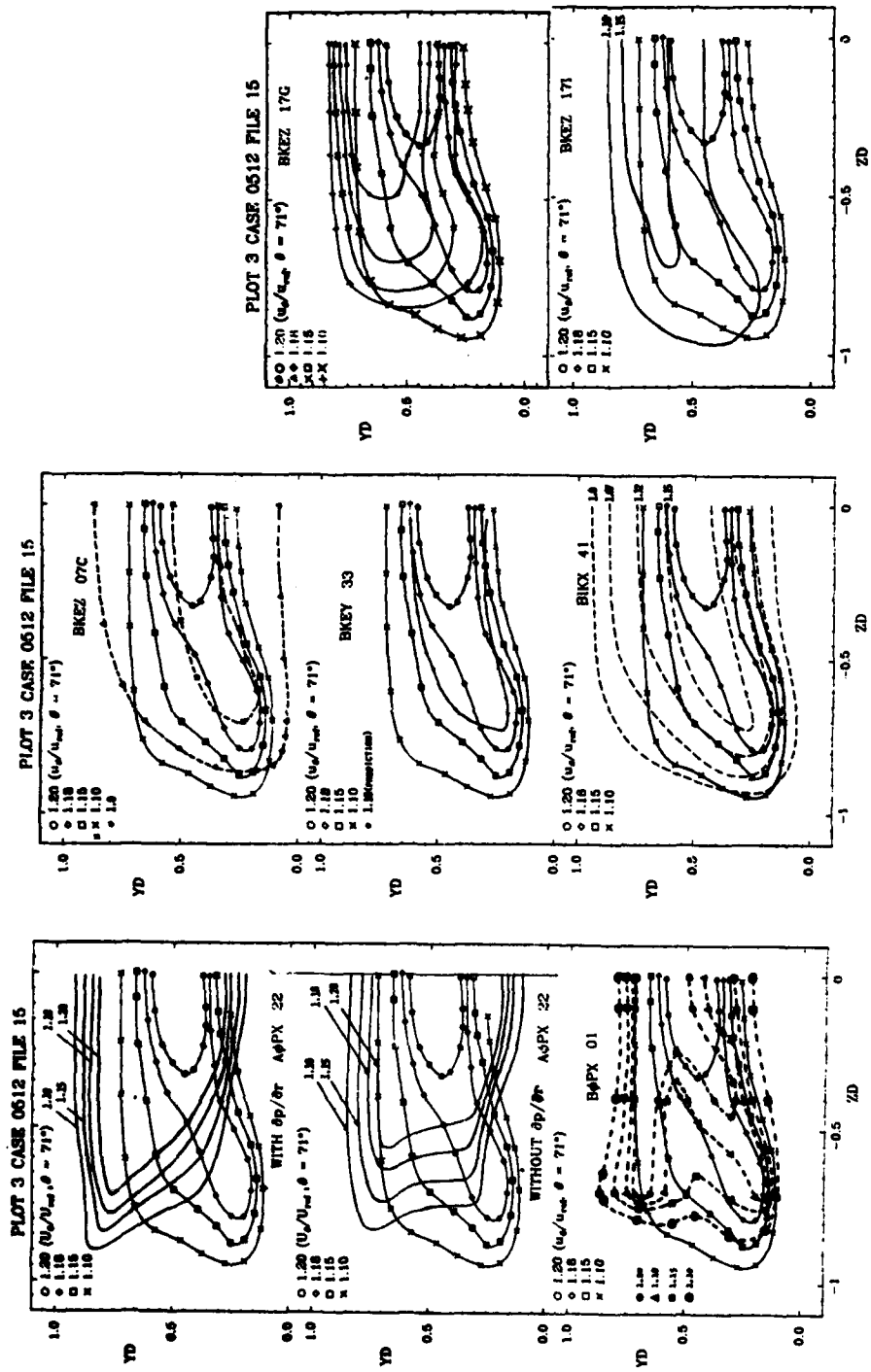


PLATE 128

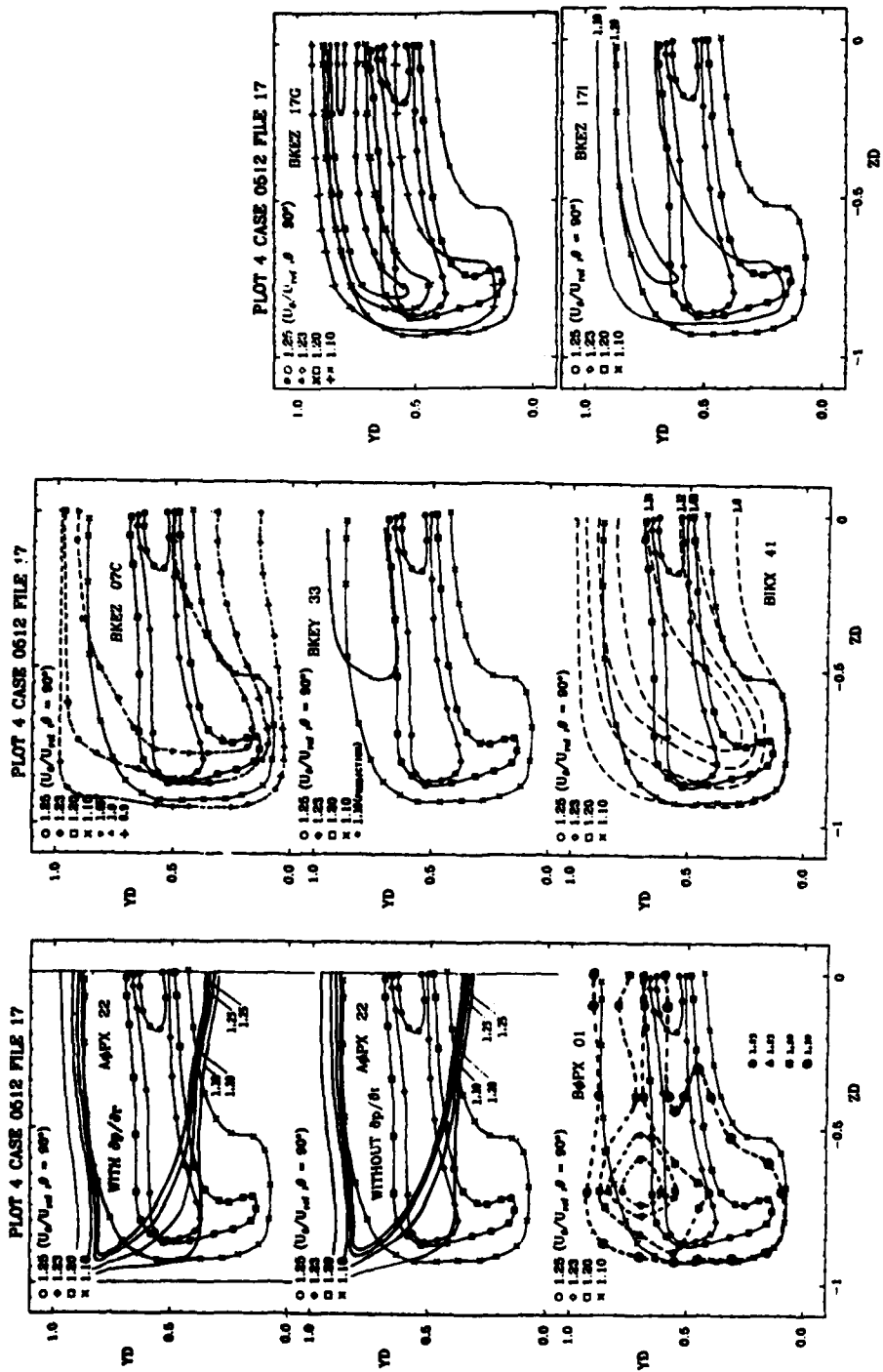


PLATE 129

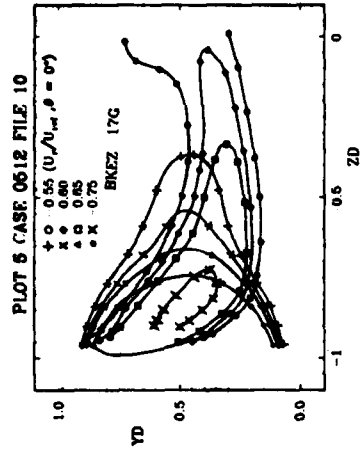
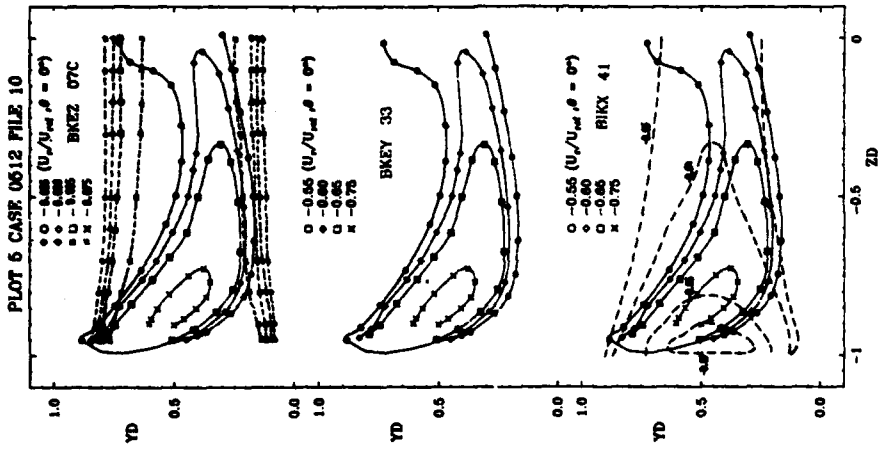
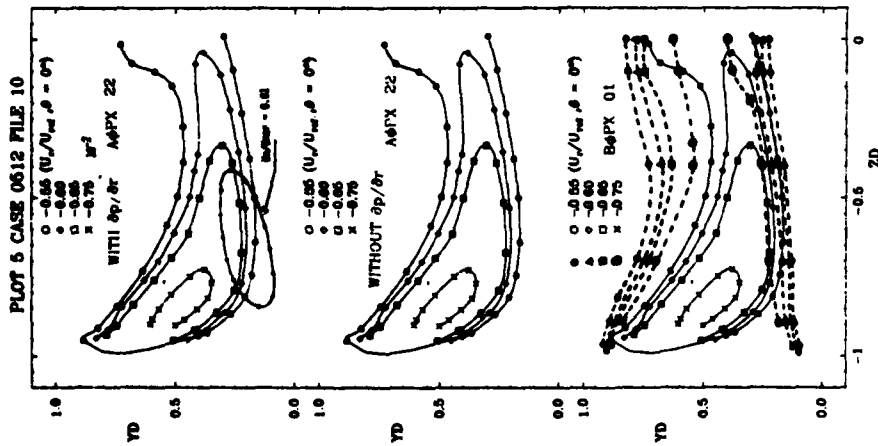


PLATE 130

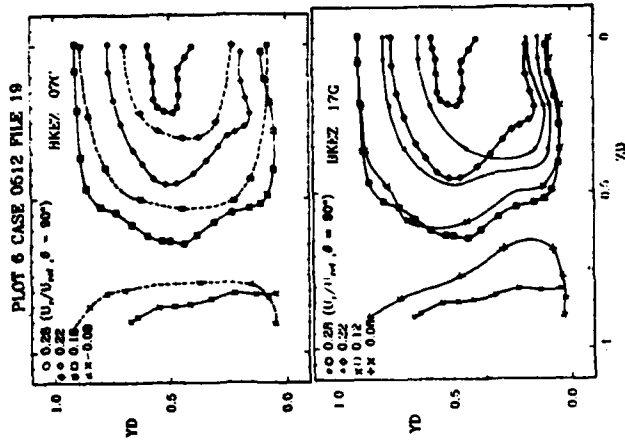
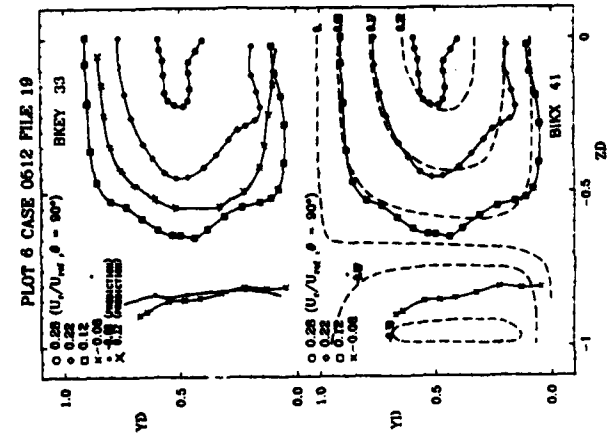
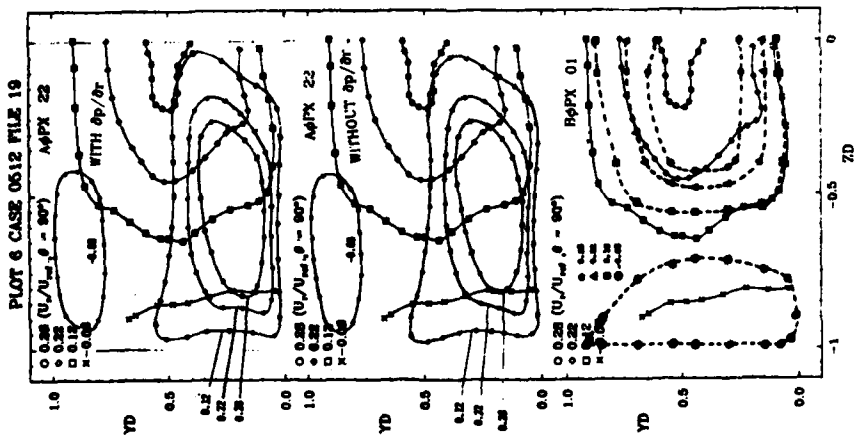


PLATE 131

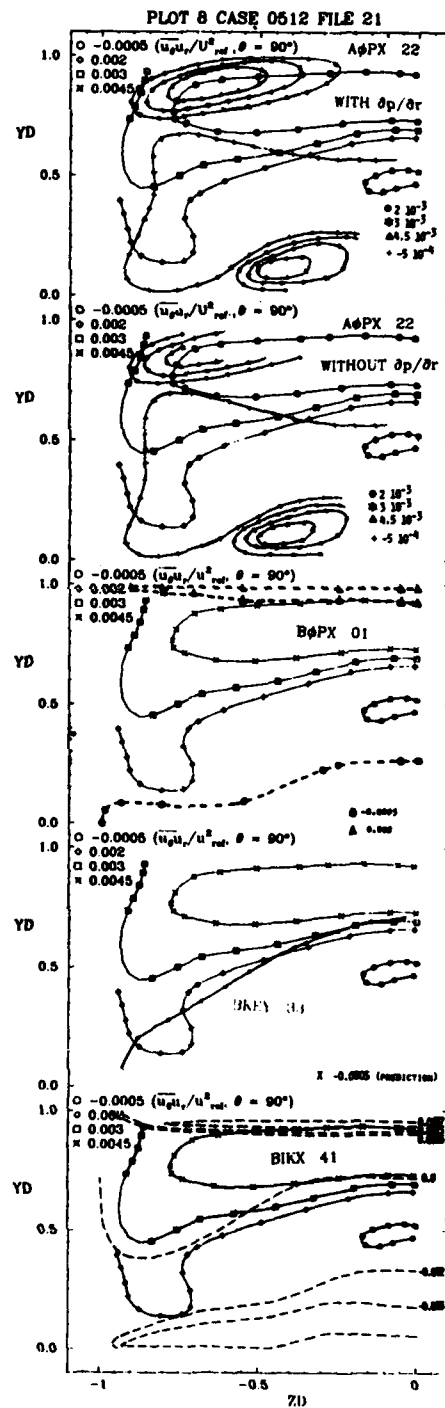
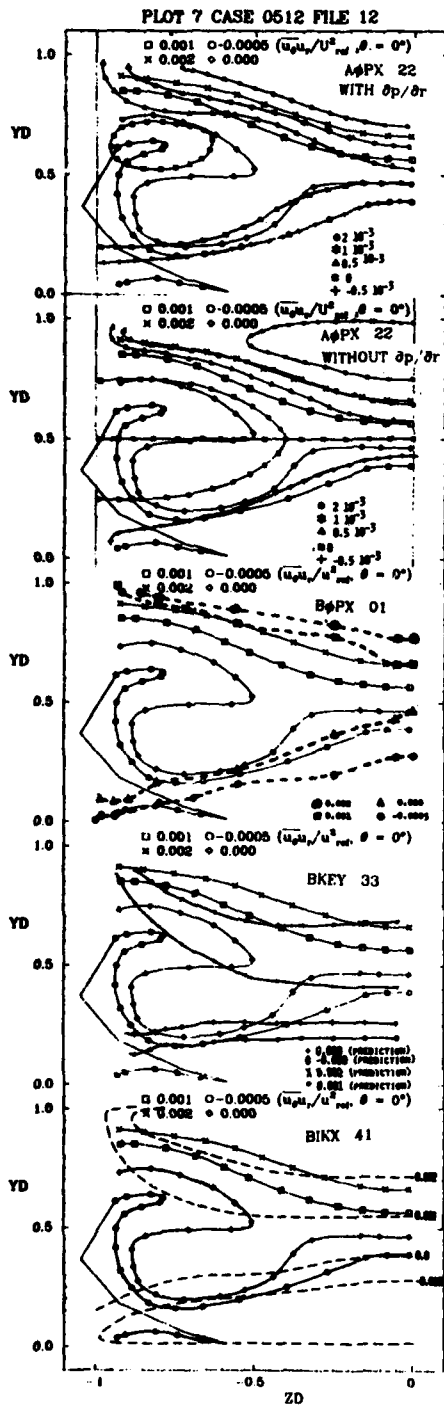
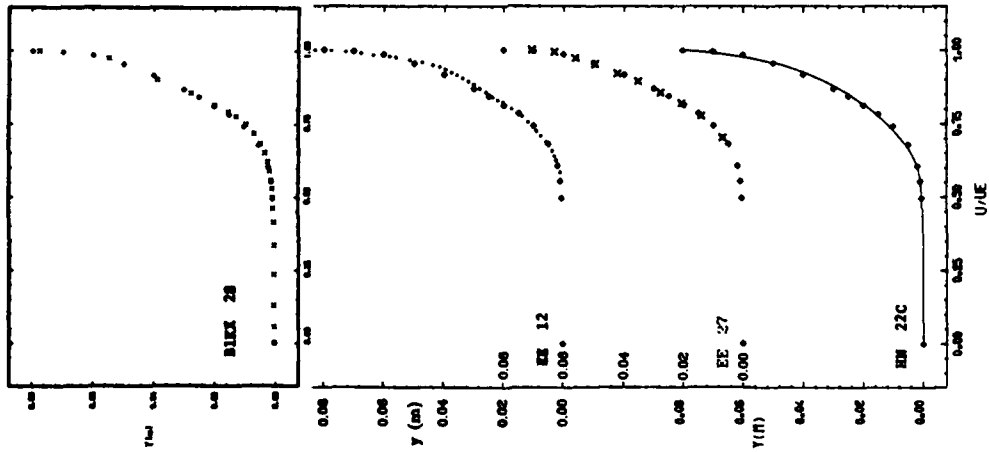
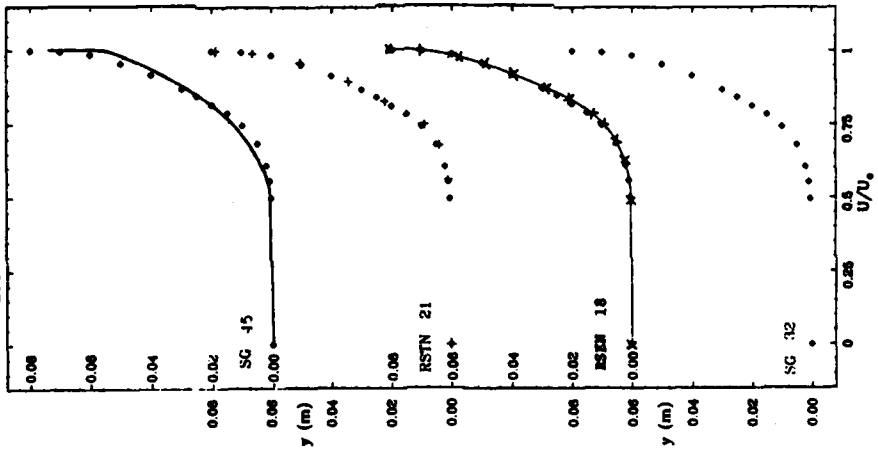


PLATE 132

PLOT 1 CASE 812



PLOT 1 CASE 0612 FILE 25



PLOT 1 CASE 0612 FILE 25

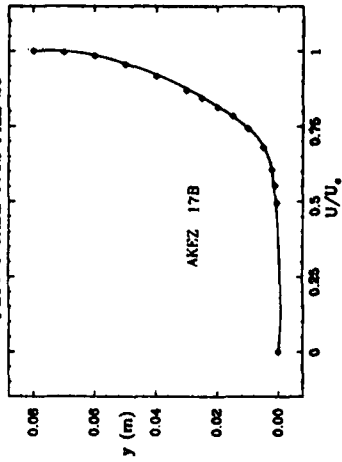


PLATE 133

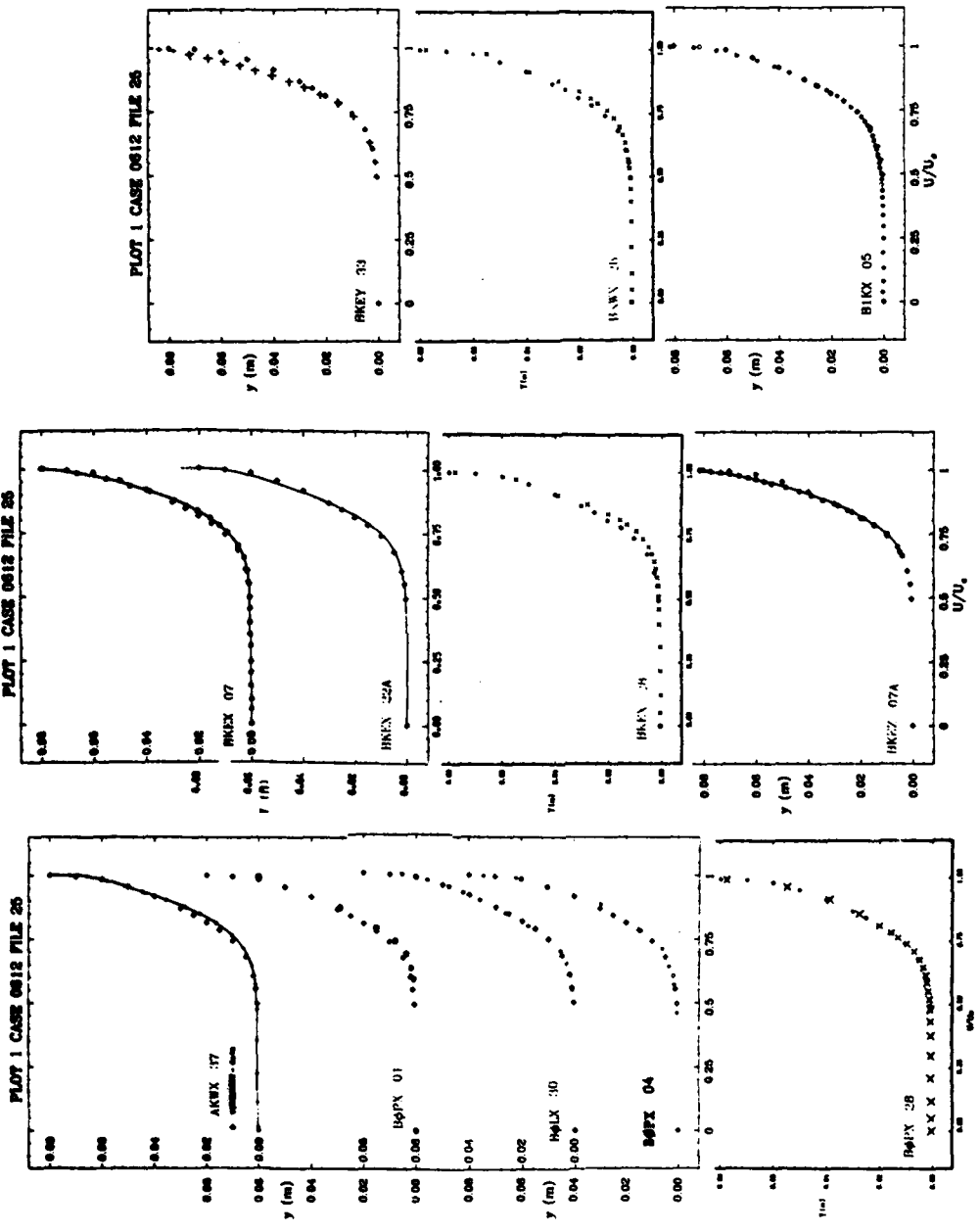


PLATE 134

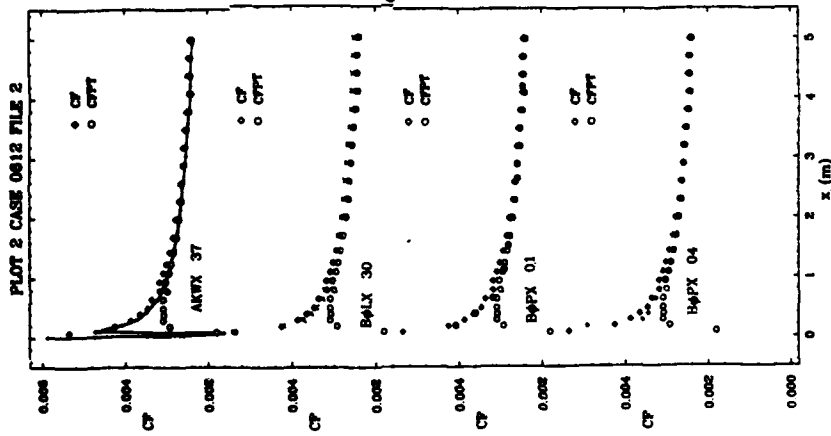
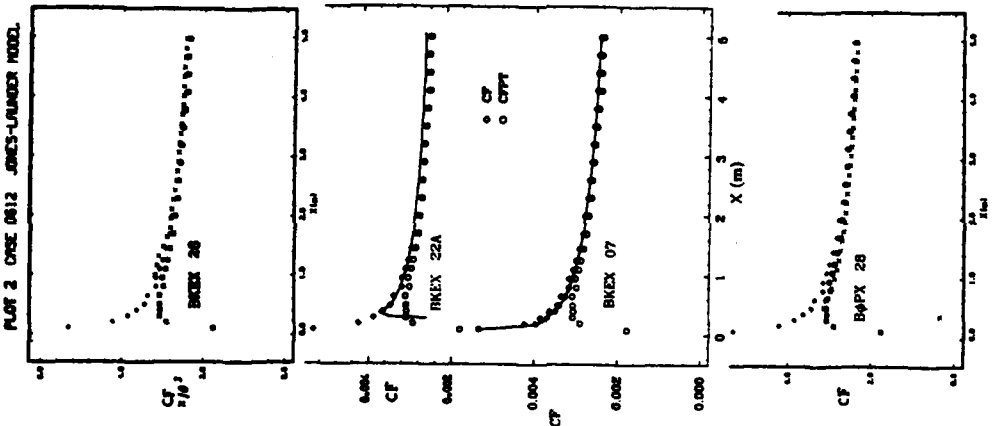
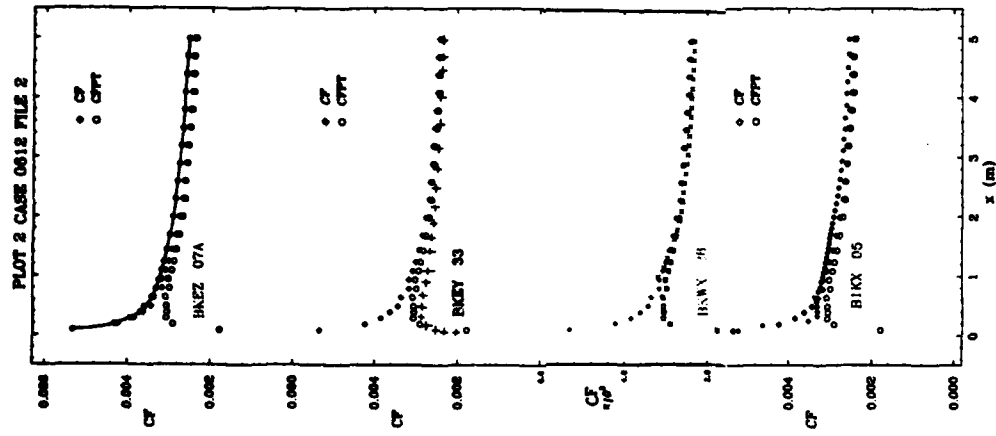
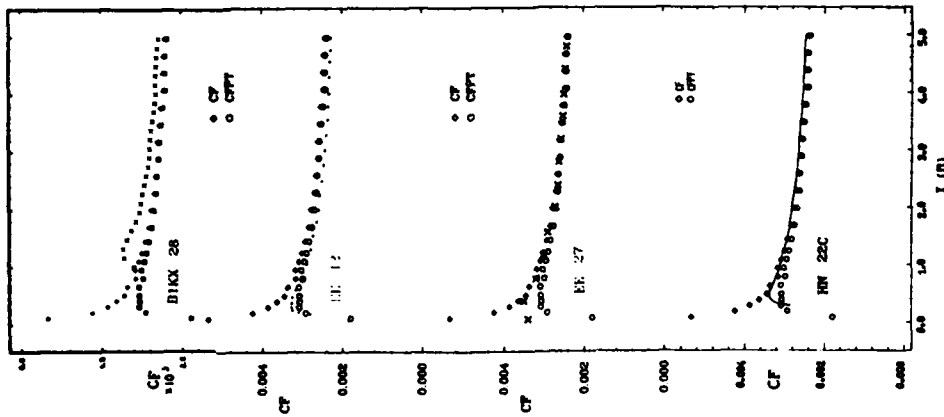
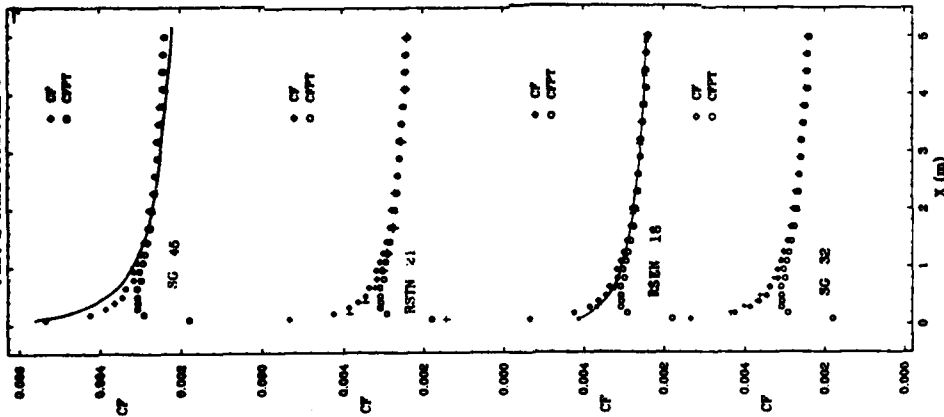


PLATE 135

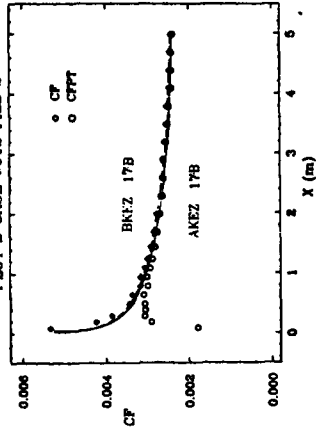
PLOT 2 CASE 0612



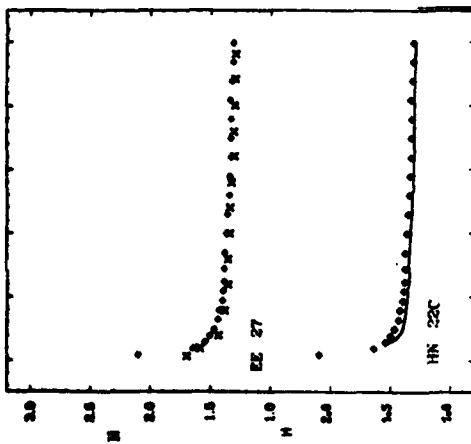
PLOT 2 CASE 0612 FILE 2



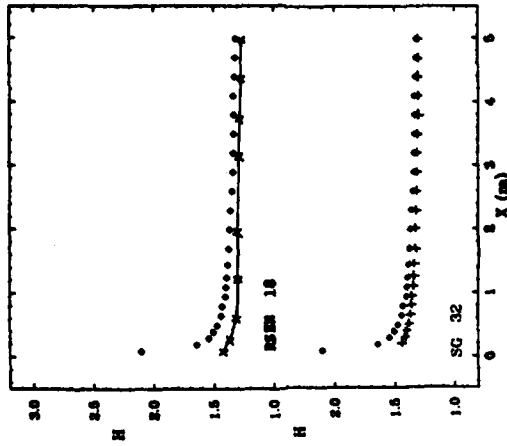
PLOT 2 CASE 0612 FILE 2



PLOT 3 CASE 0612 FILE 2



PLOT 3 CASE 0612 FILE 2



PLOT 3 CASE 0612 FILE 2

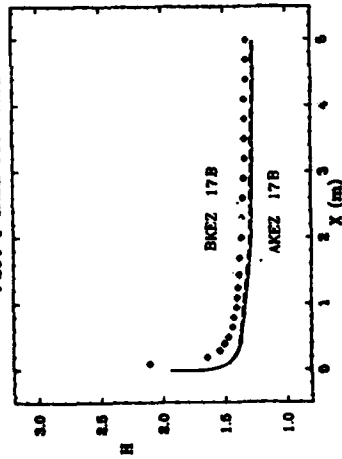
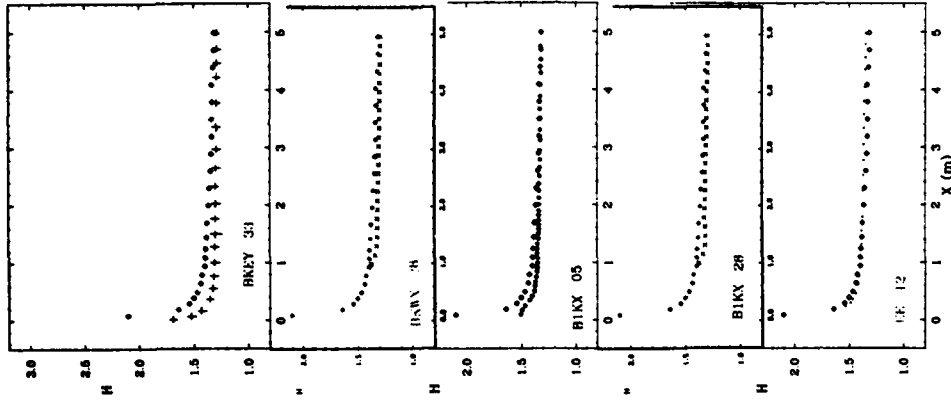
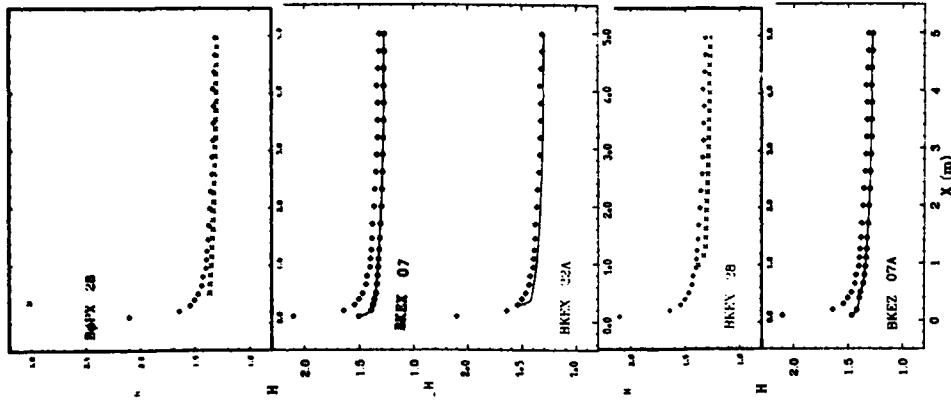


PLATE 137

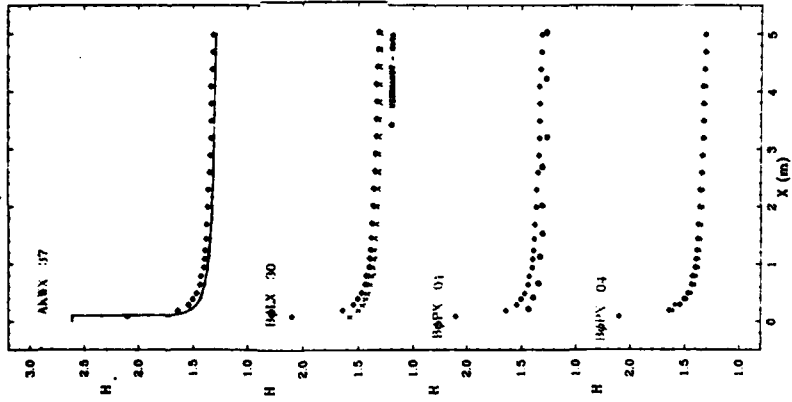
PLOT 3 CASE 0612 FILE 2



PLOT 3 CASE 0612



PLOT 3 CASE 0612 FILE 2



PLOT 1 - CASE 8101 - SKIN FRICTION

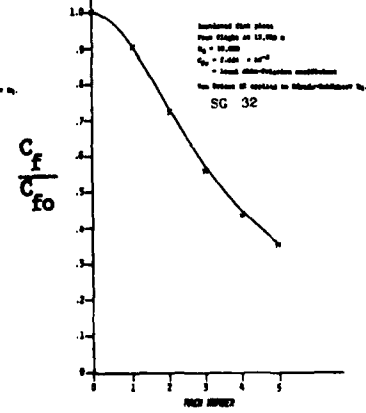
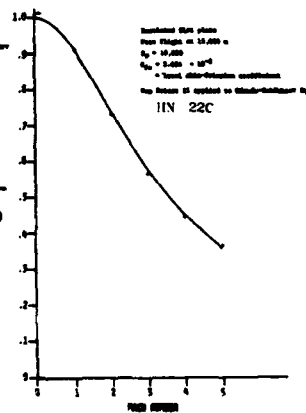
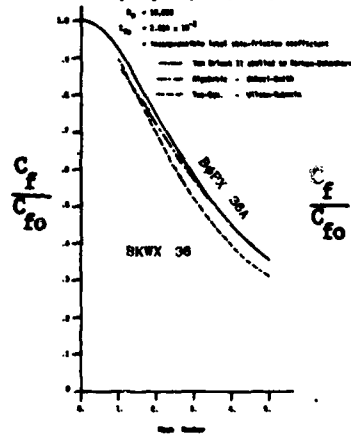
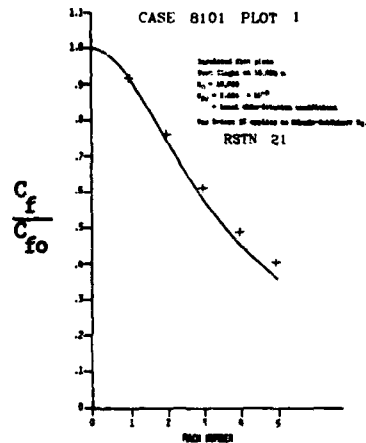
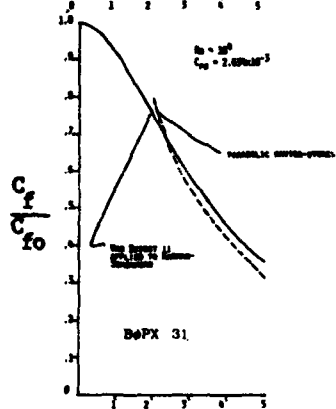
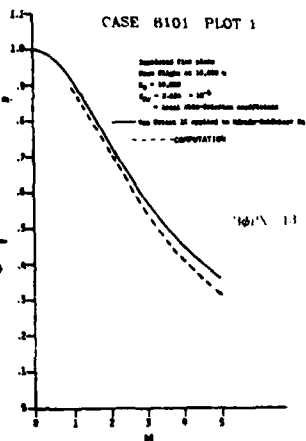
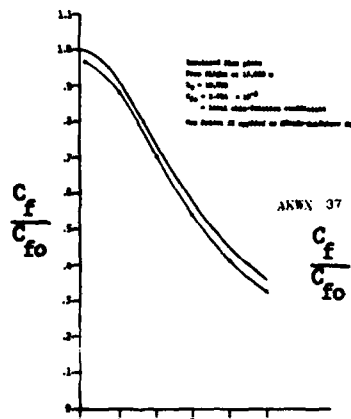
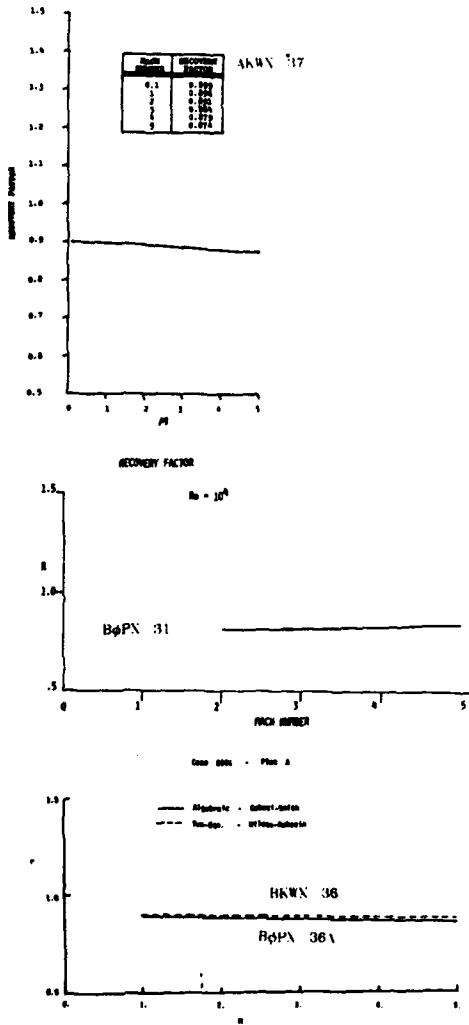
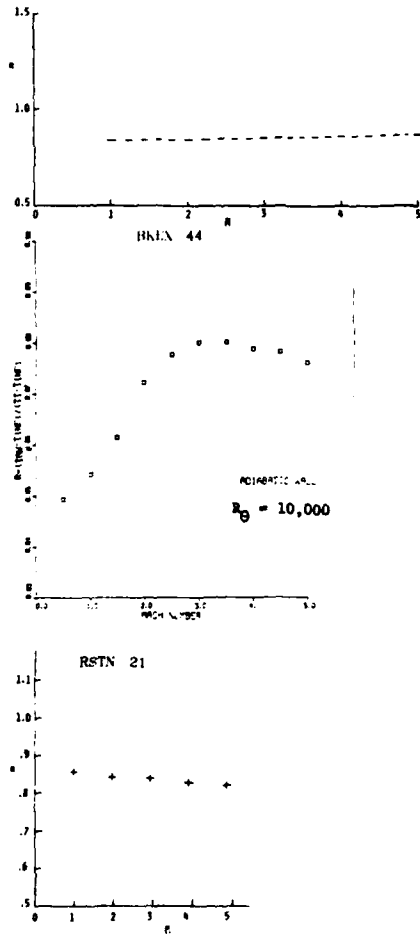


PLATE 139

PLOT 2 - CASE 8101 - RECOVERY FACTOR



CASE 8101 PLOT A
 BOPX 43



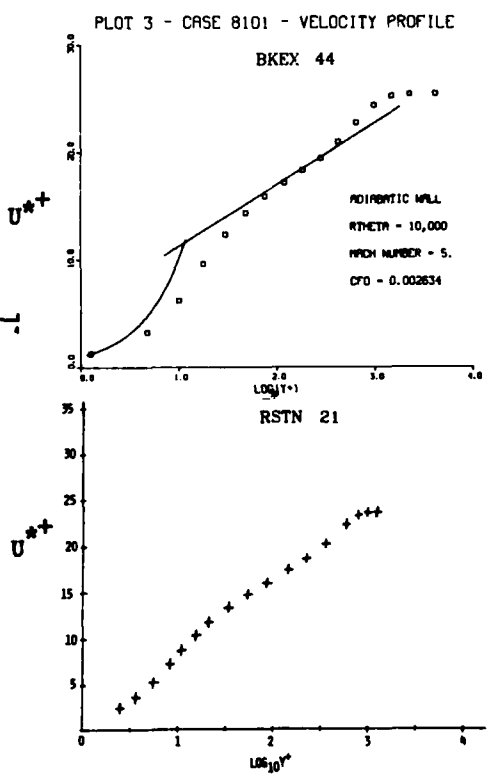
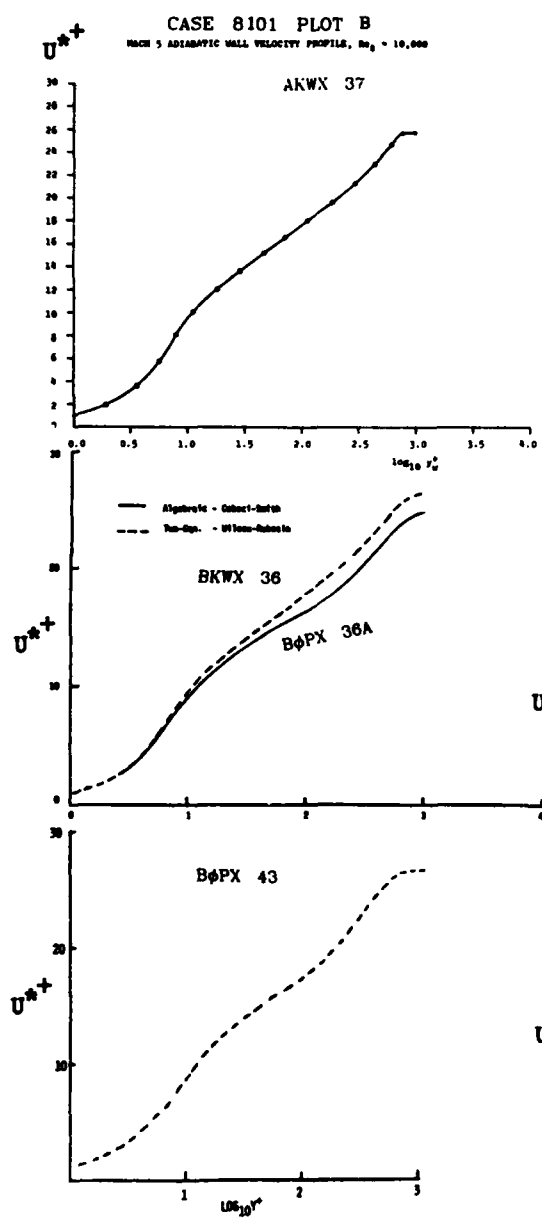
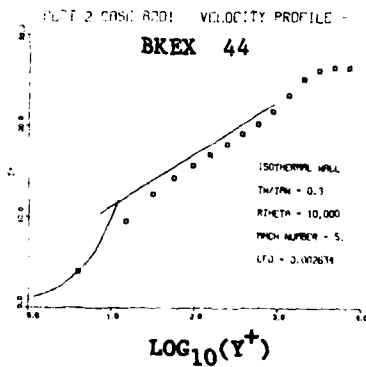
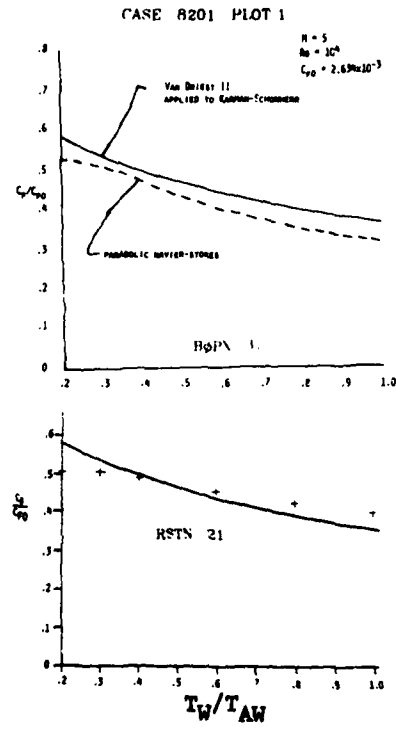
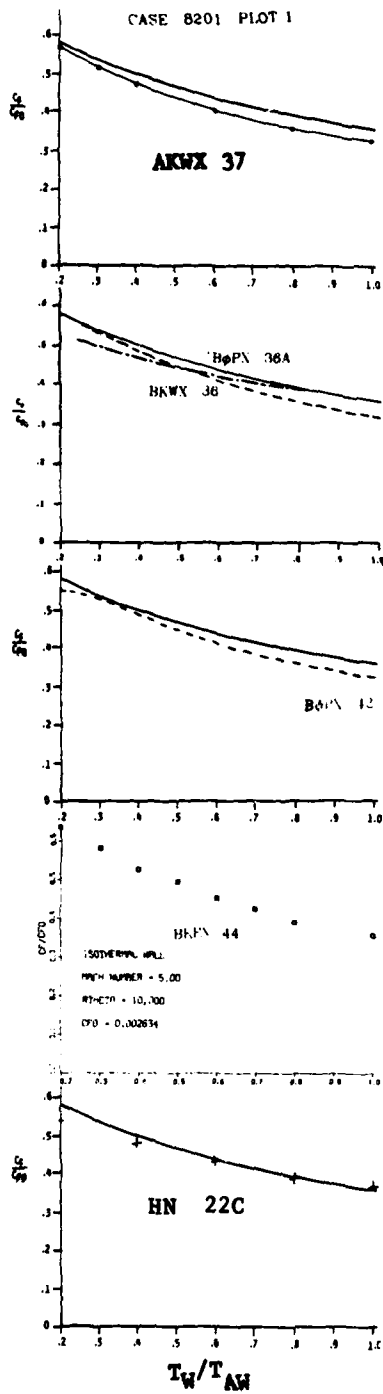


PLATE 141



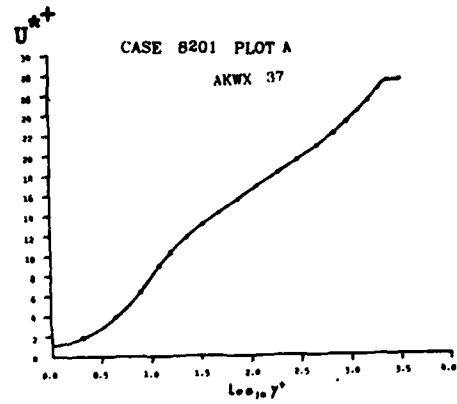
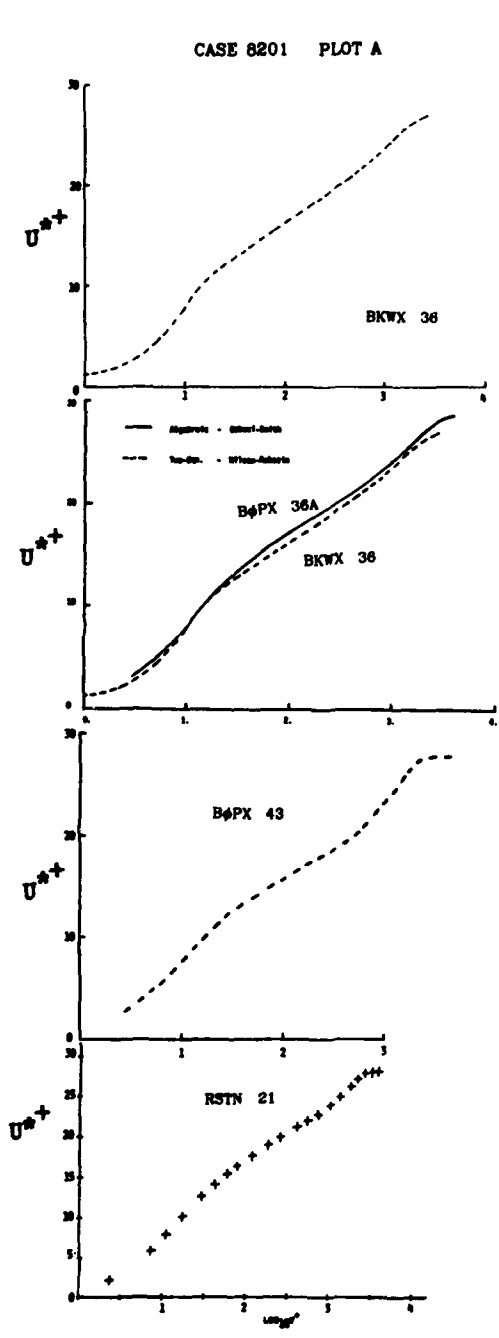


PLATE 143

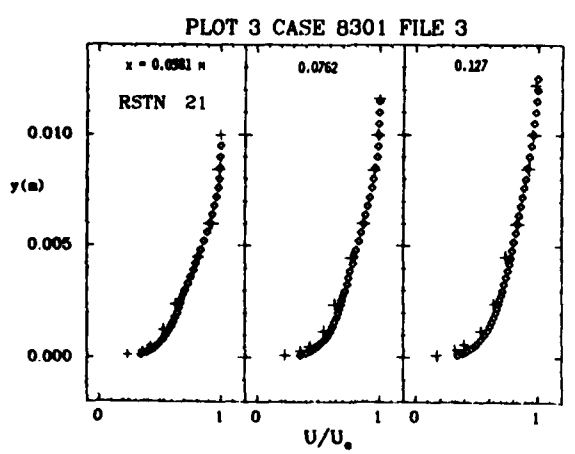
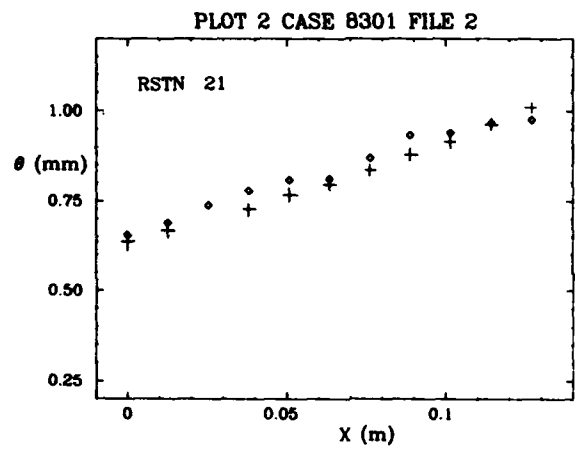
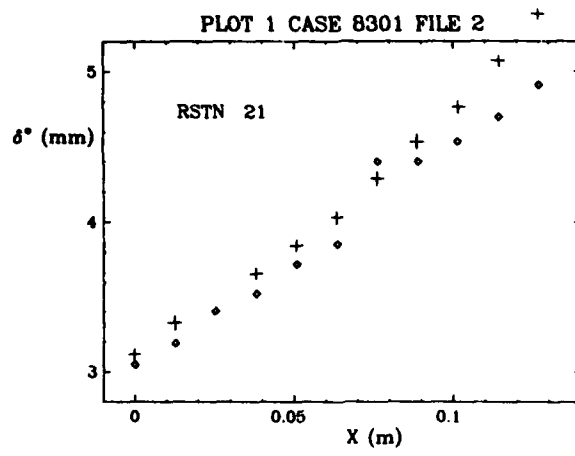


PLATE 144

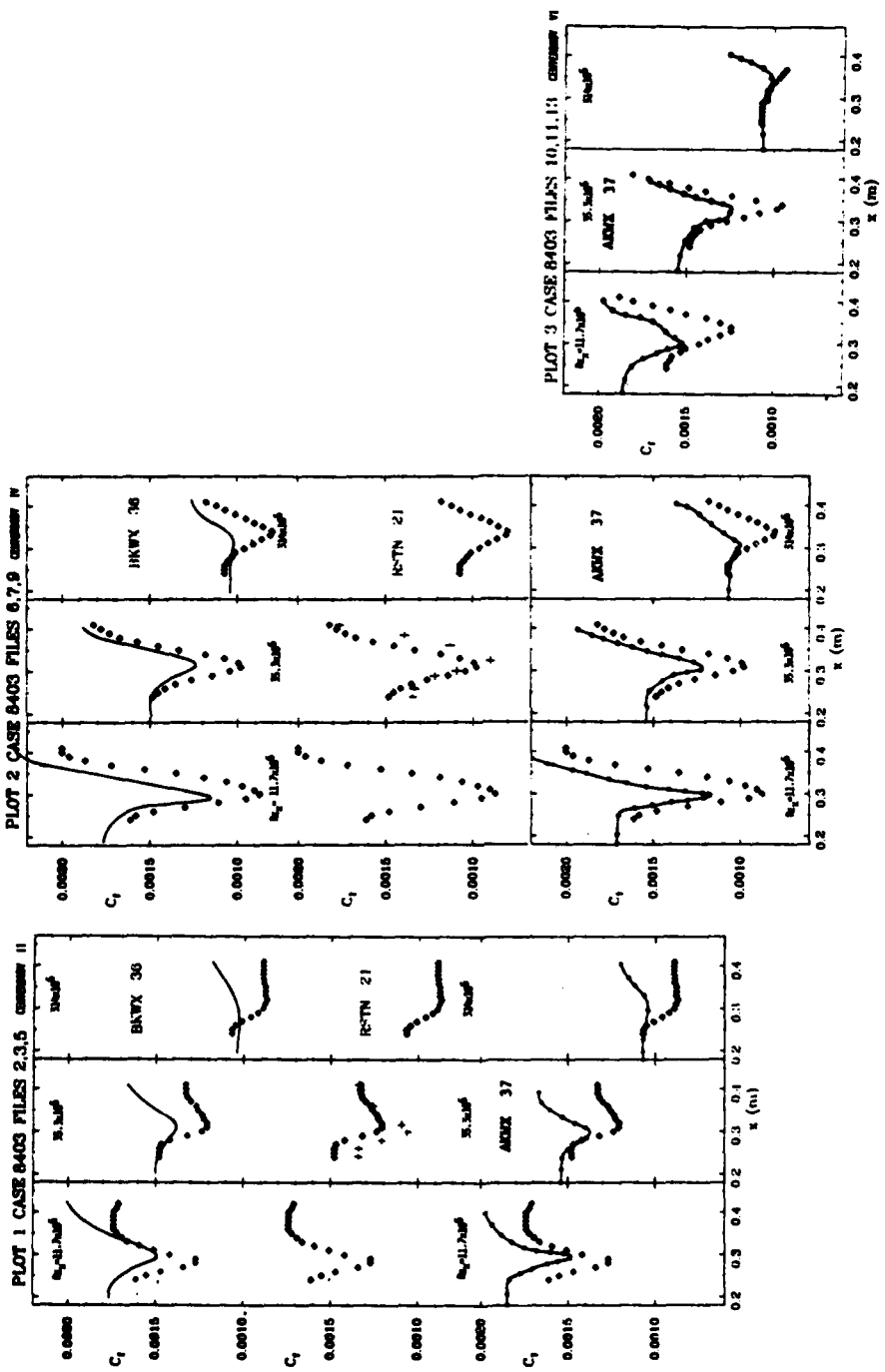
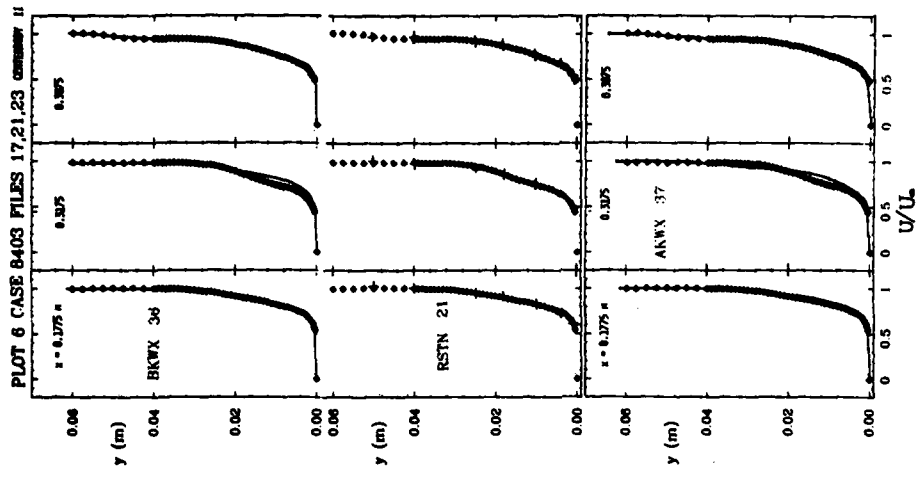
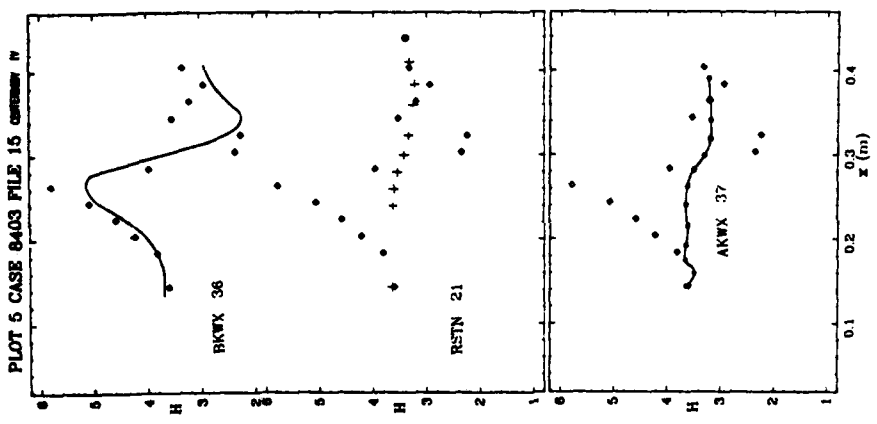
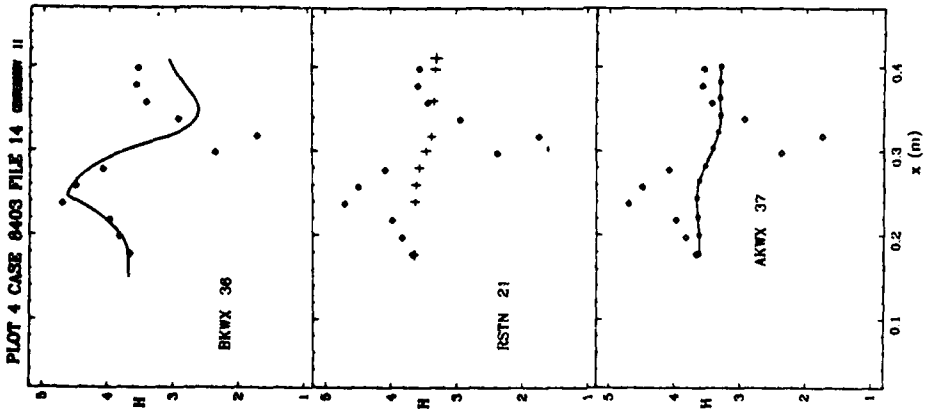


PLATE 145



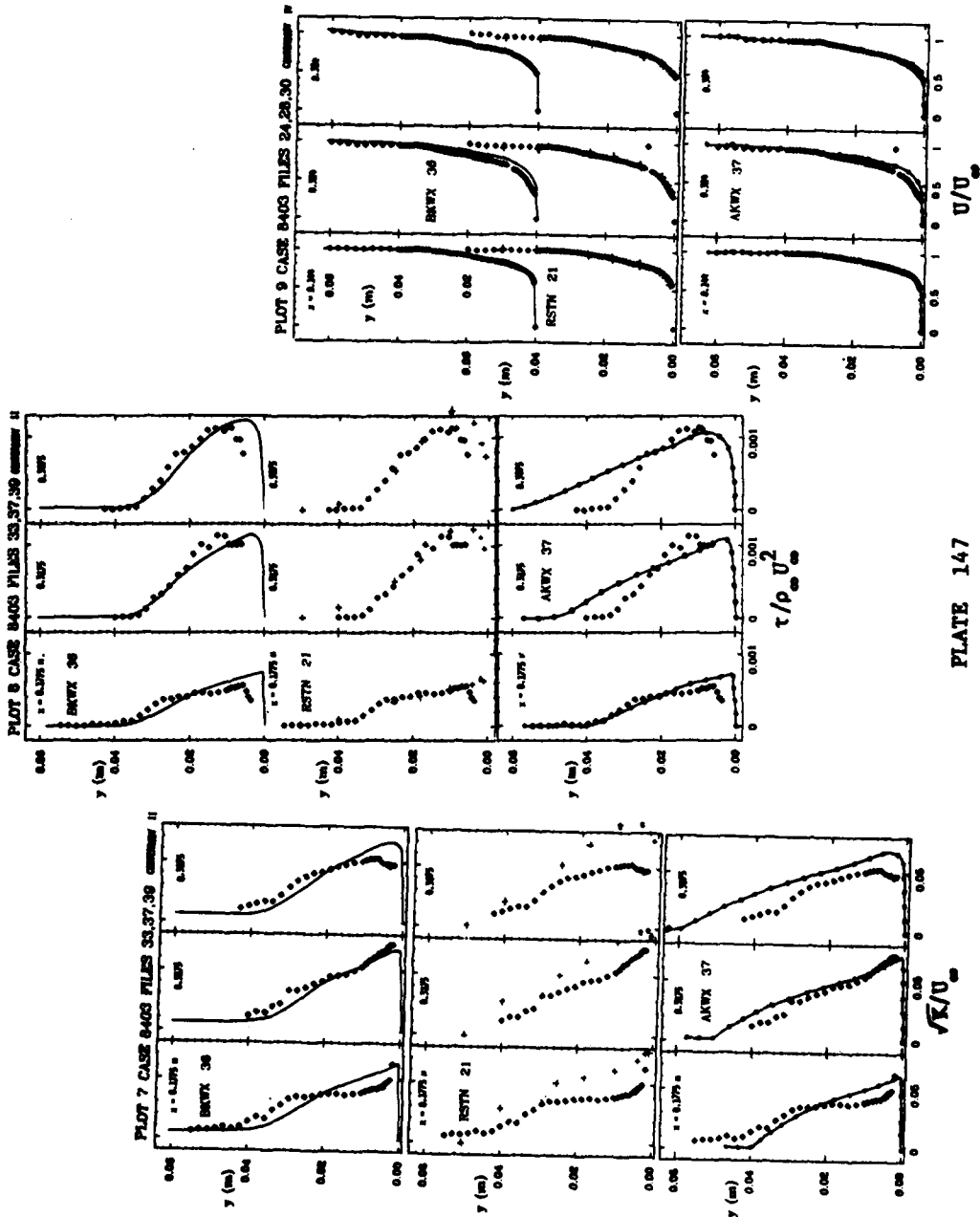
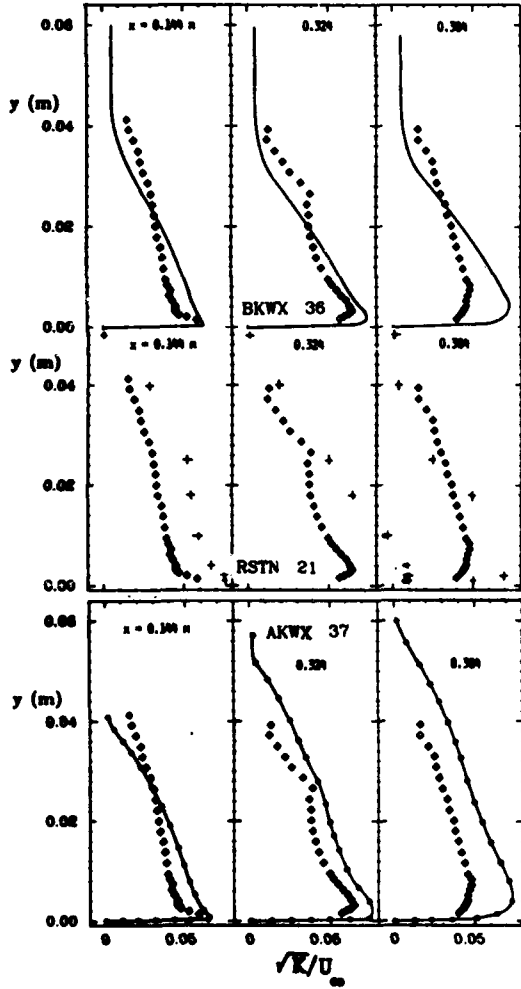
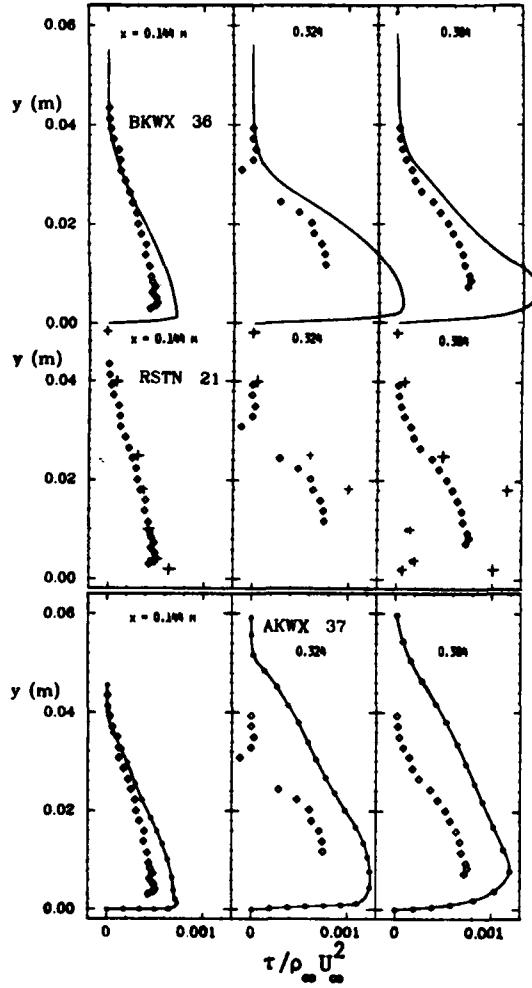


PLATE 147

PLOT 10 CASE 8403 FILES 40,44,46



PLOT 11 CASE 8403 FILES 40,44,46



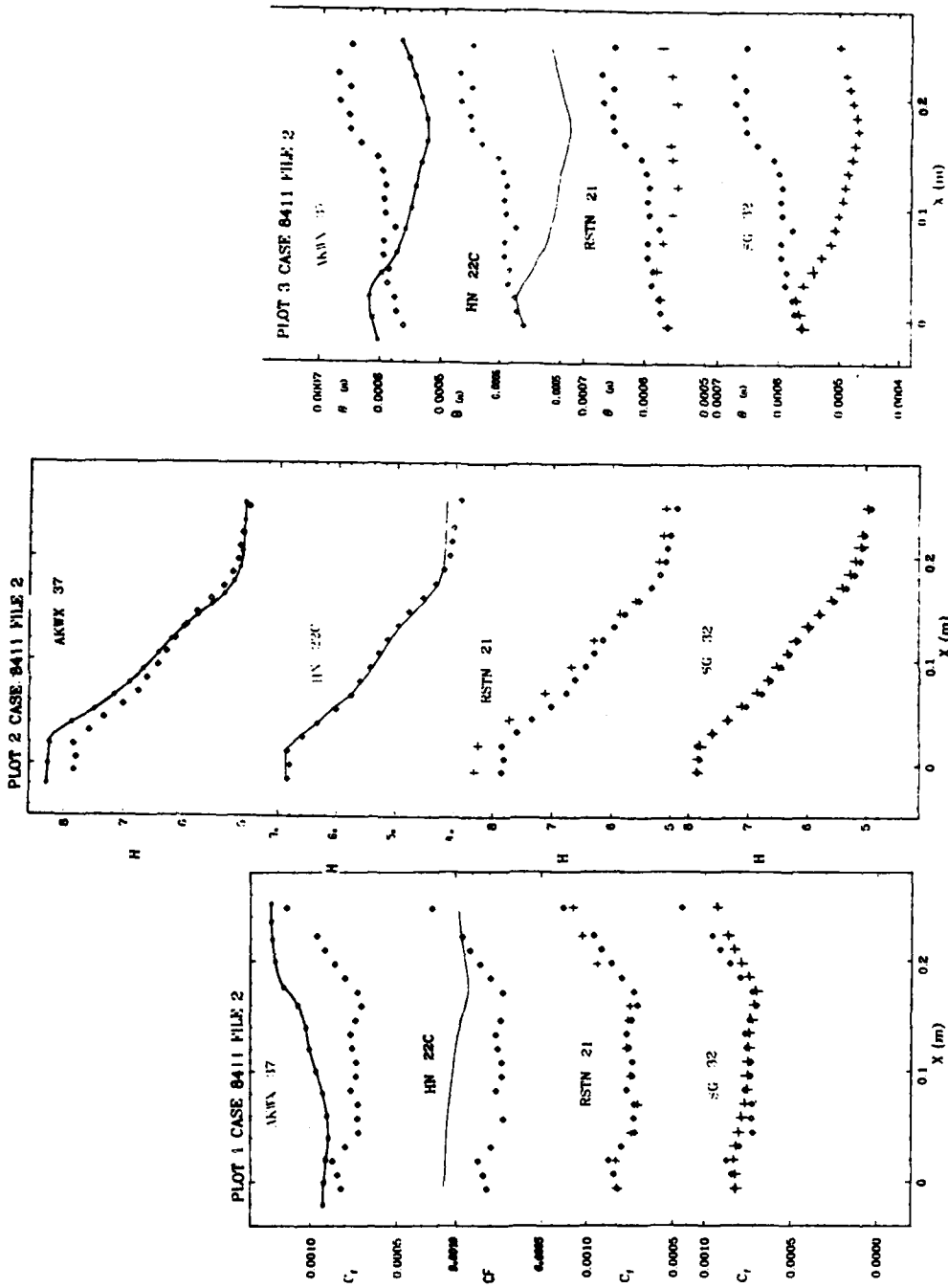


PLATE 149

PLOT 4 CASE 8411 FILES' 3,5,7

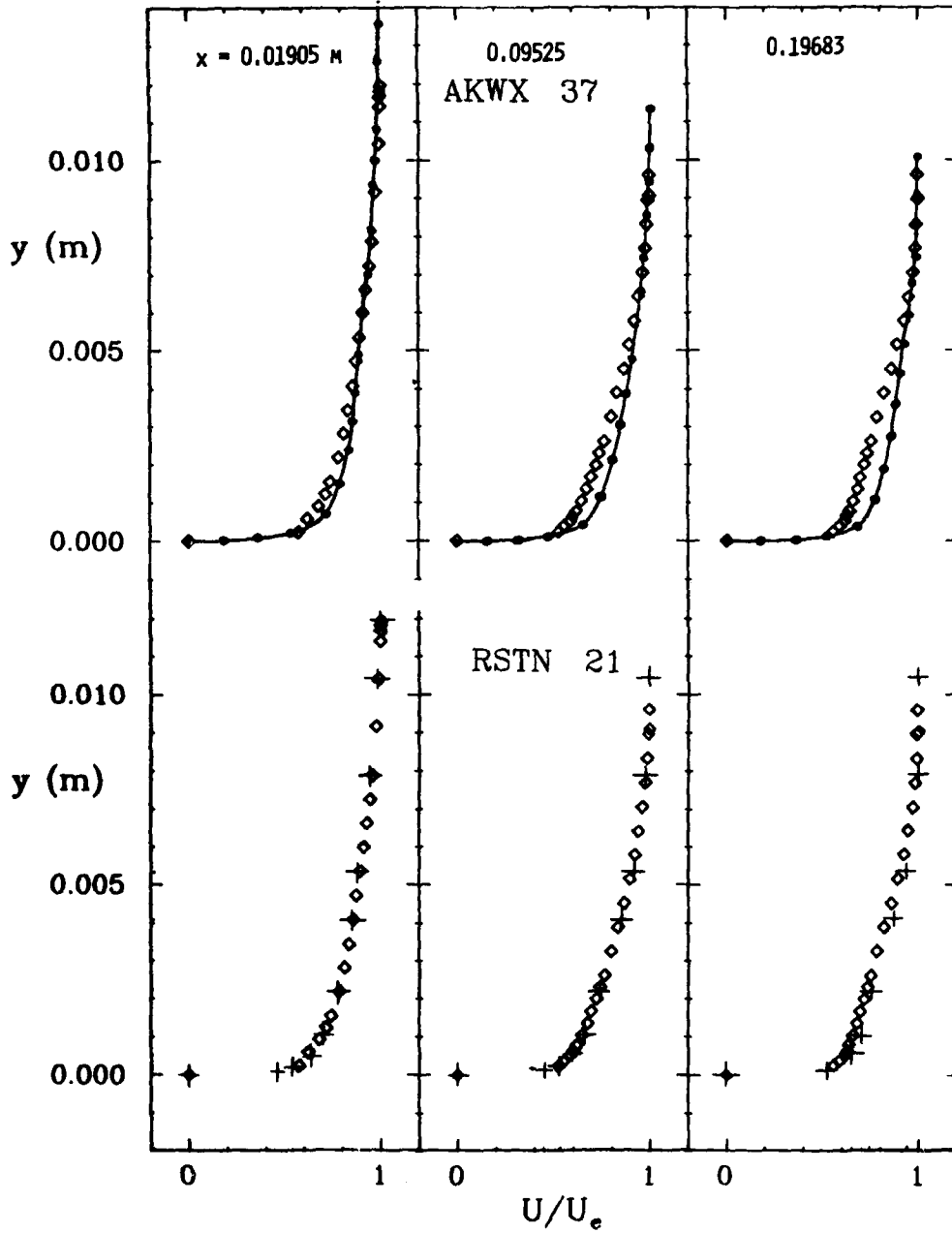
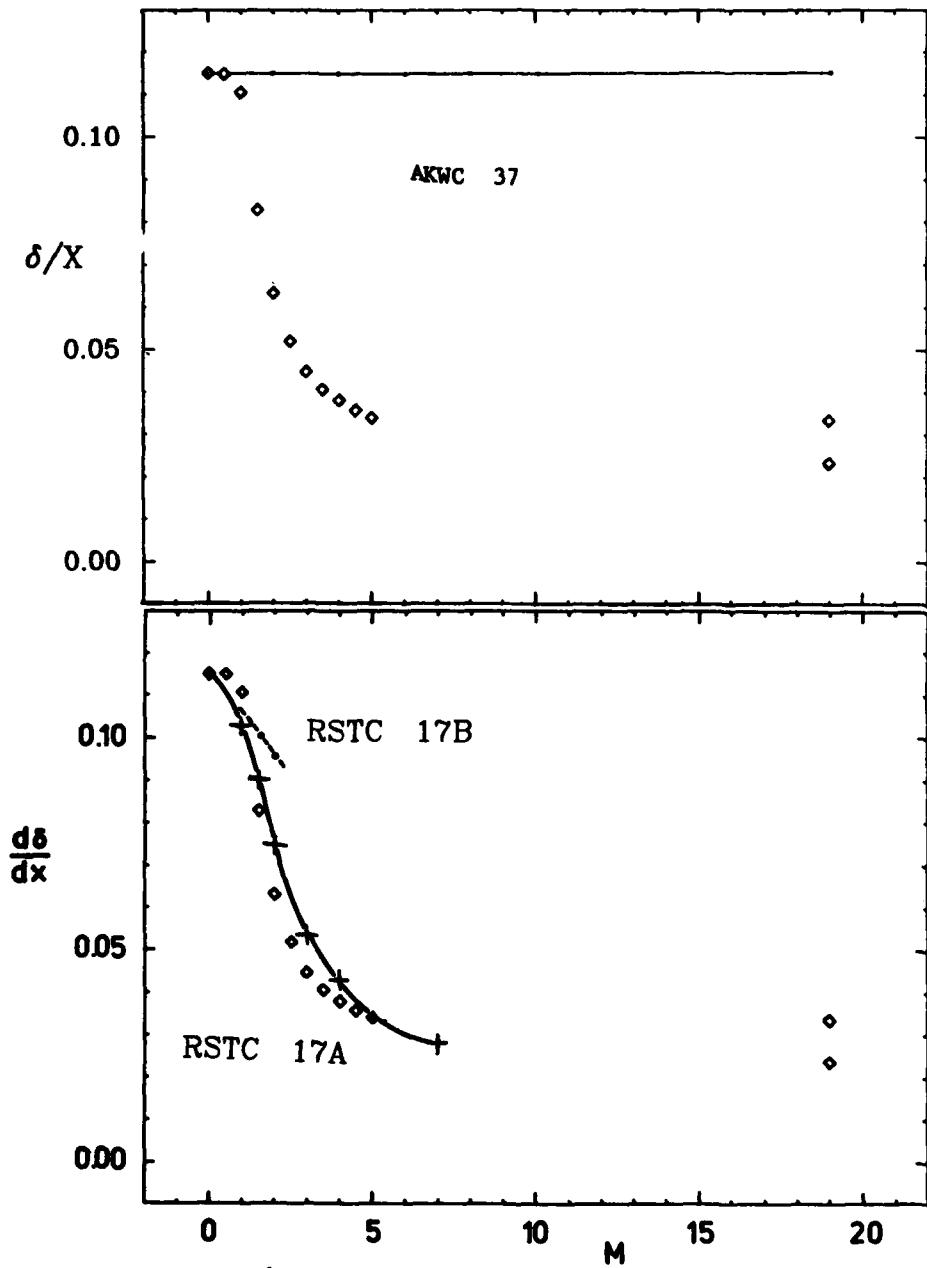
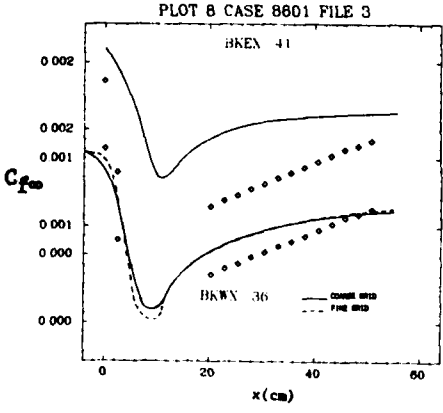
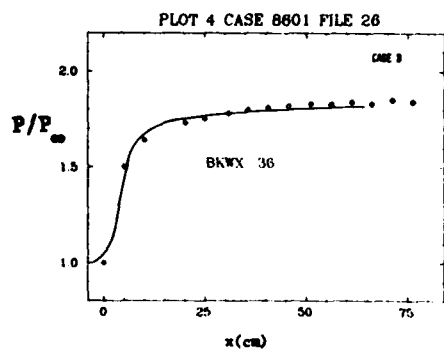
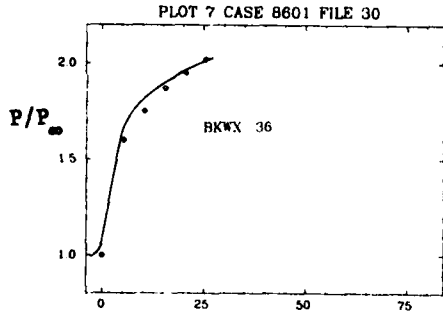
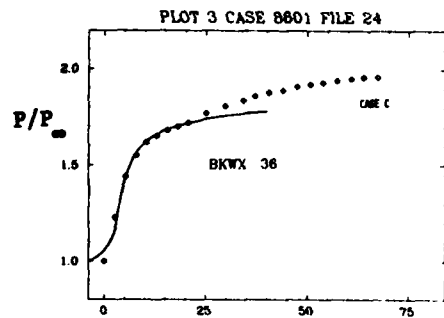
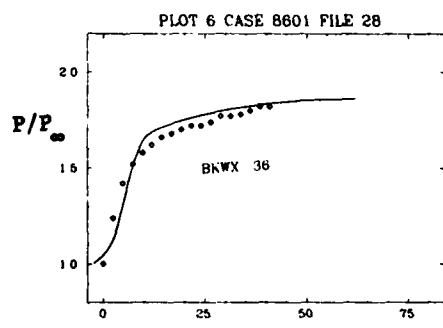
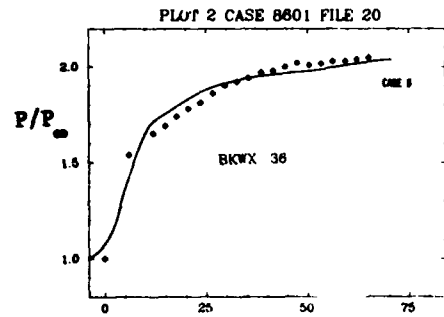
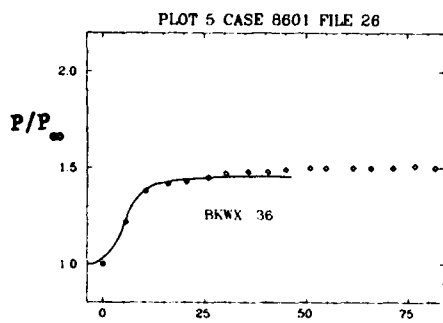
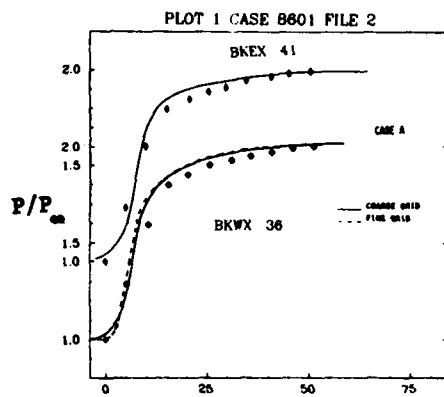


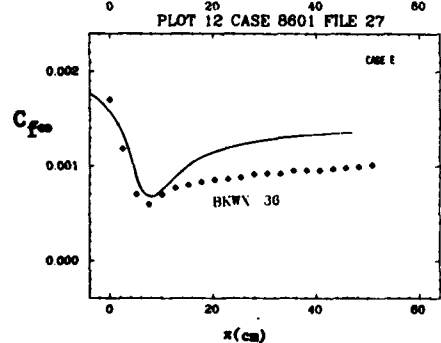
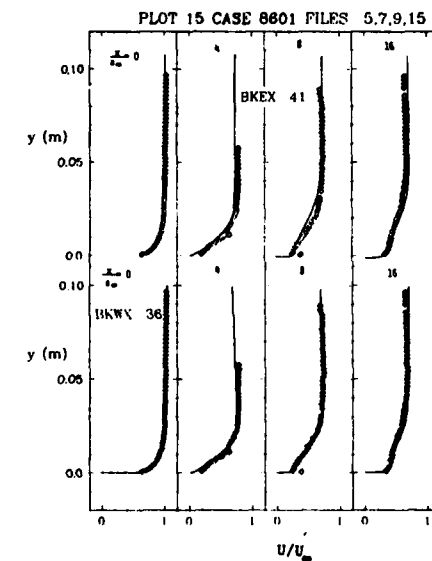
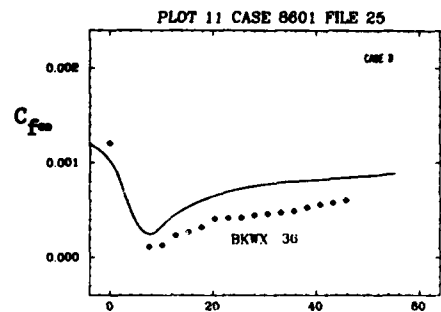
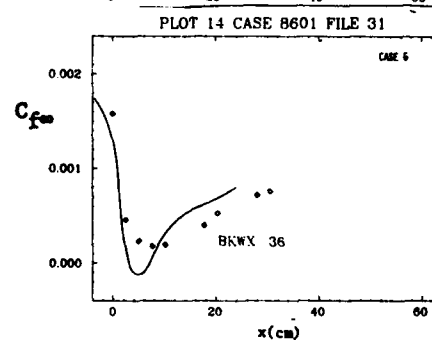
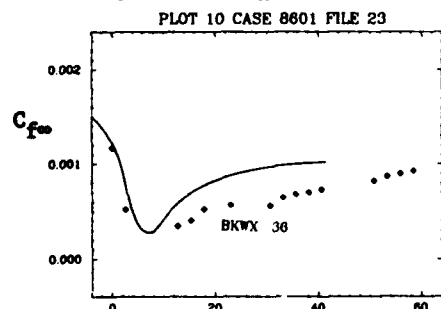
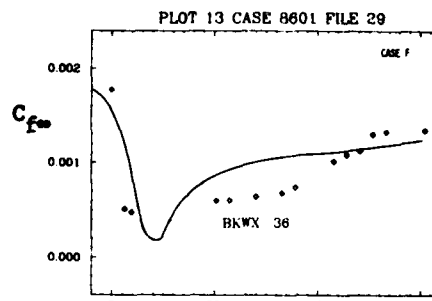
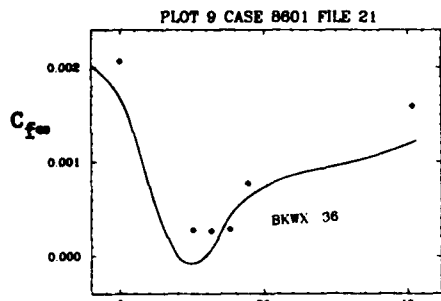
PLATE 150

PLOT 1 CASE 8501 FILE 2



computations $\left\{ \begin{array}{l} \bullet \Phi_{ij,1} \text{ without correction} \\ + \Phi_{ij,1}^* \text{ with correction B (fluctuating mach number)} \end{array} \right.$





PLOT 16 CASE 8601 FILES 6,8,14

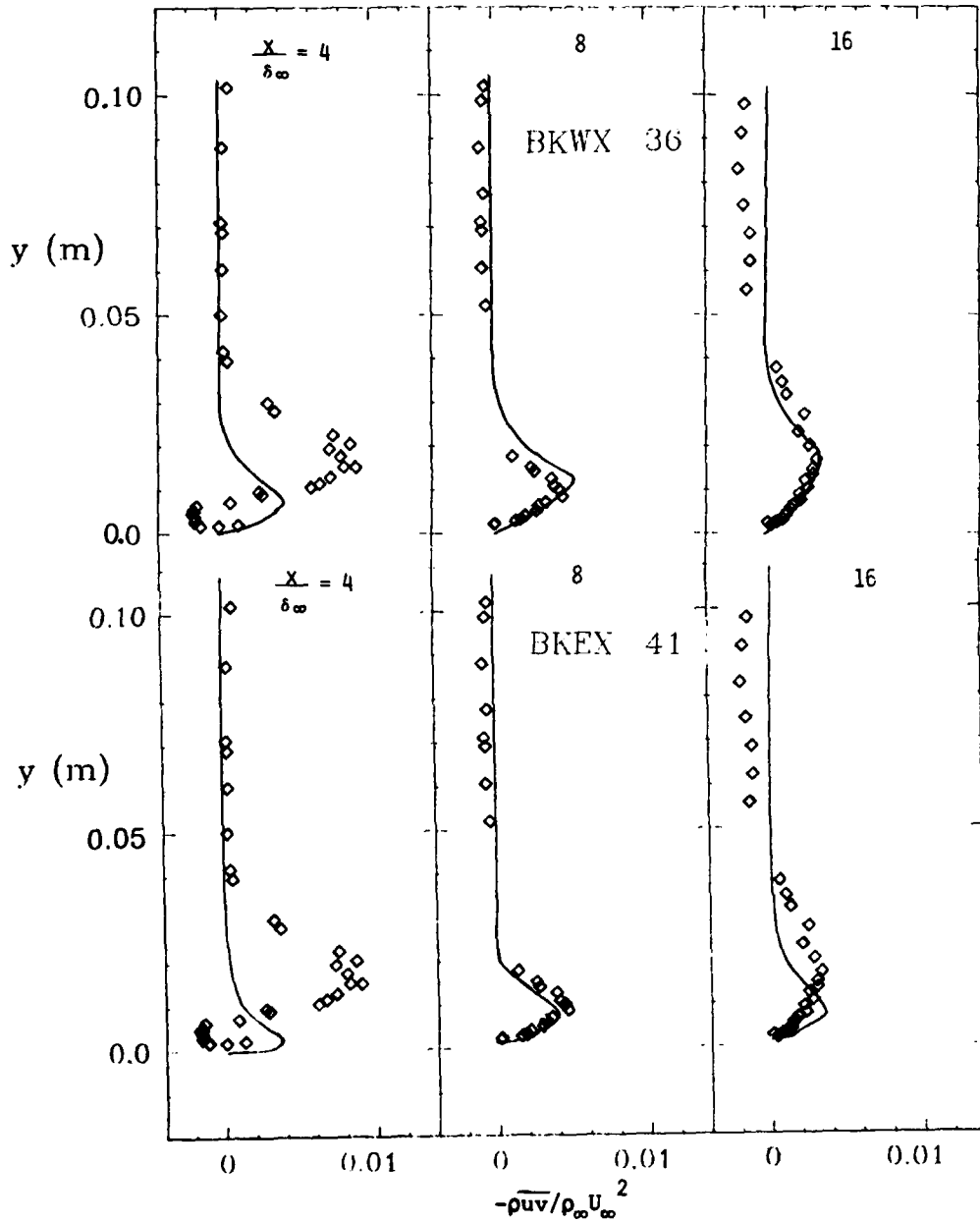
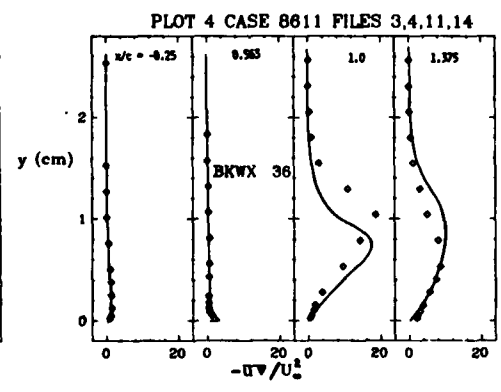
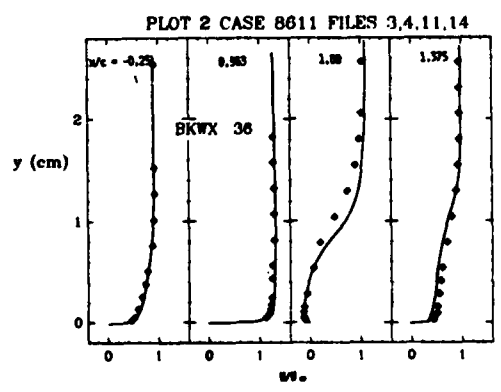
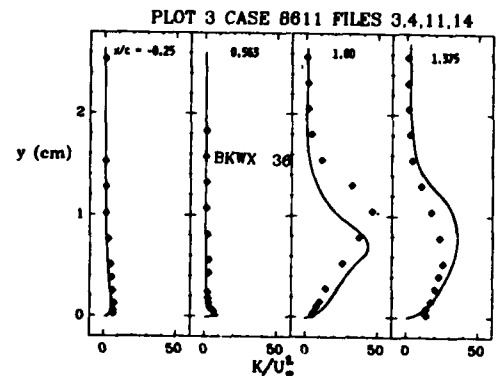
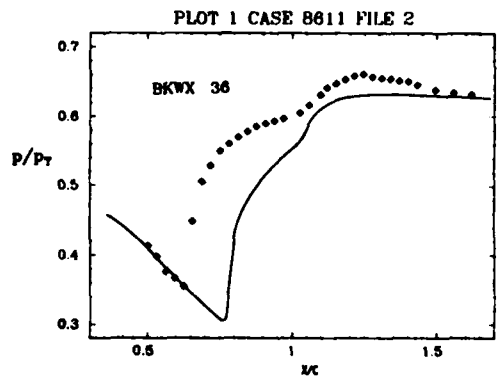


PLATE 154



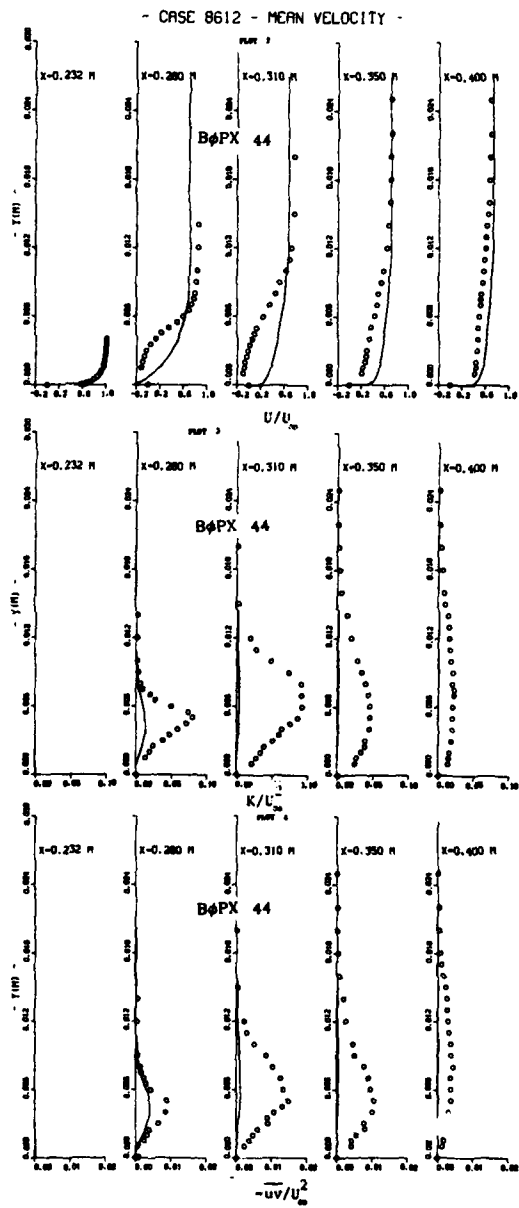
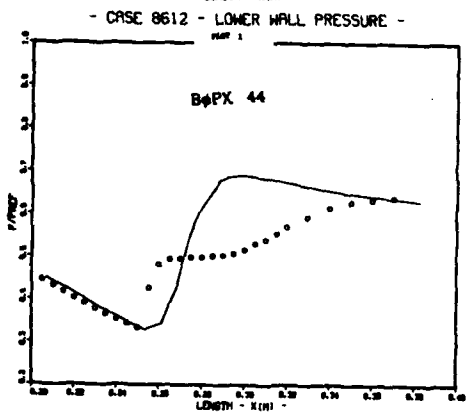
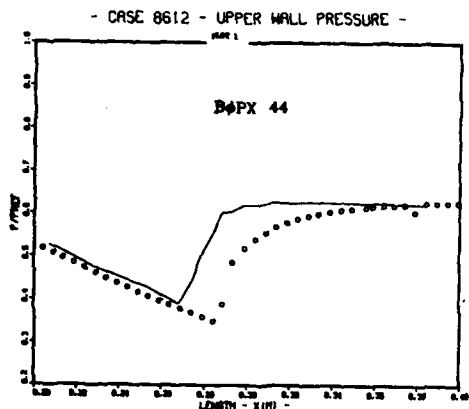


PLATE 156

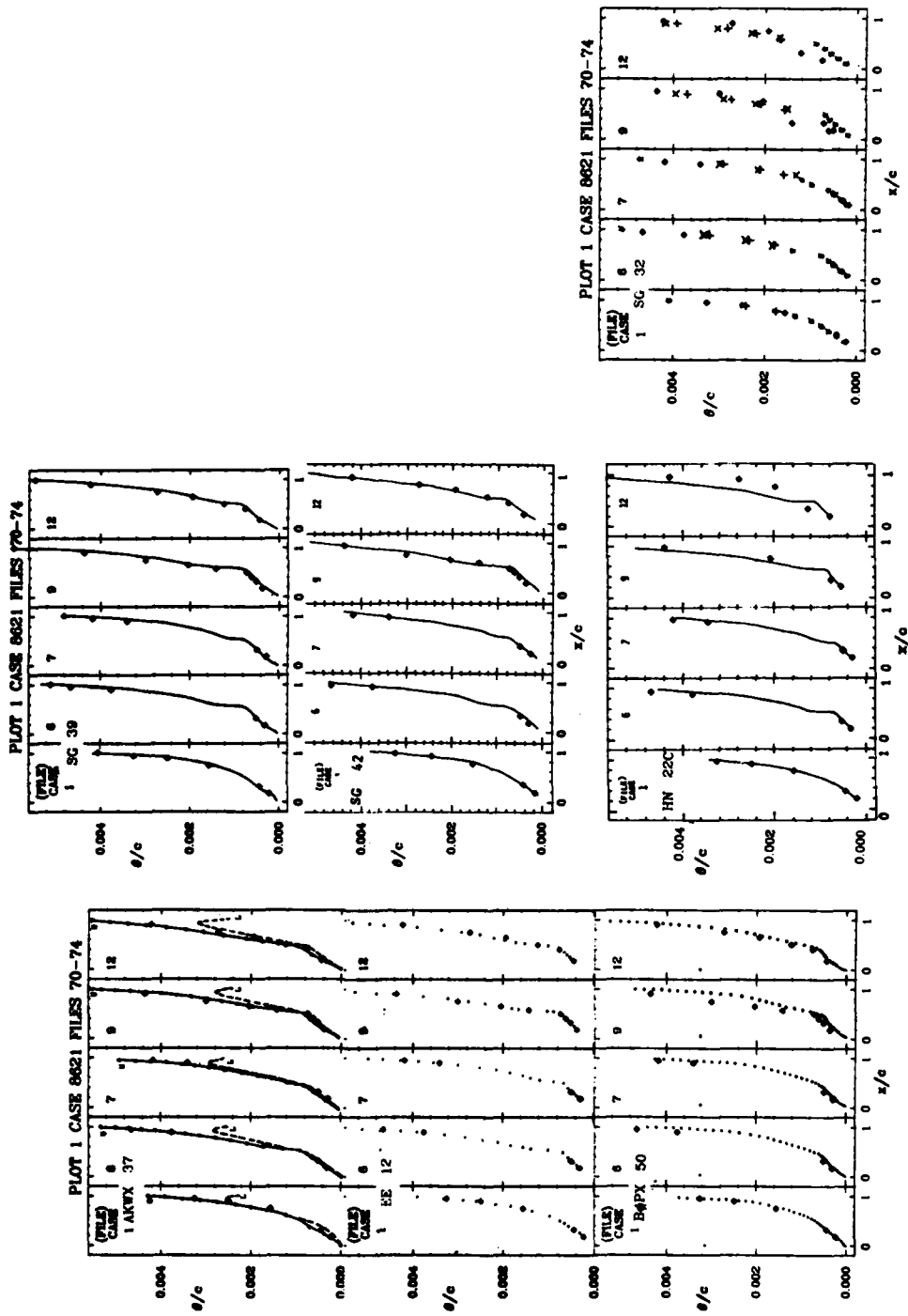
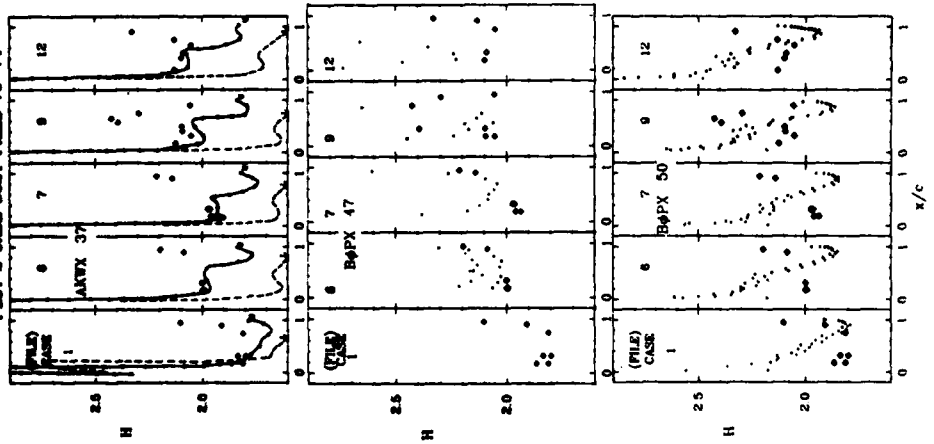
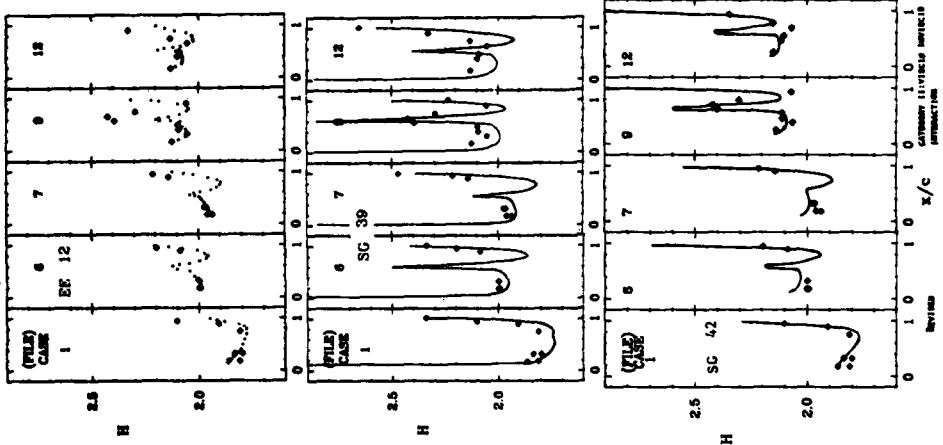


PLATE 157

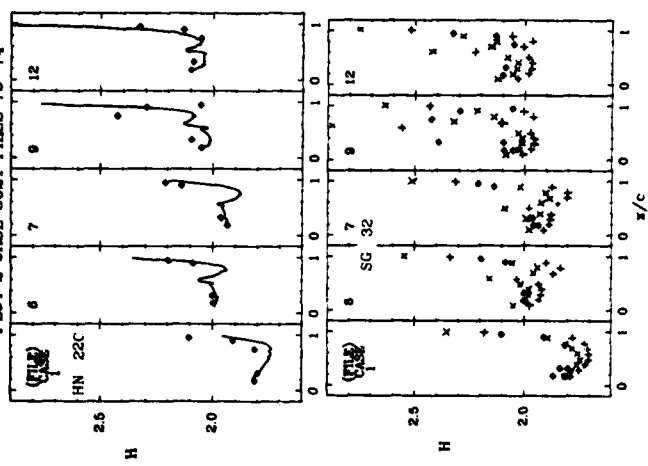
PLOT 2 CASE 8621 FILES 70-74

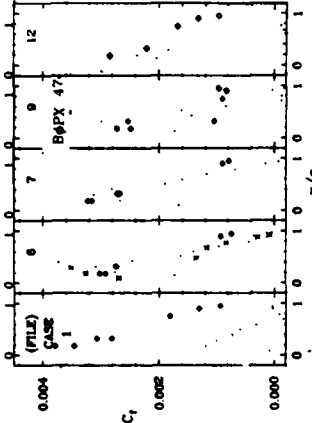
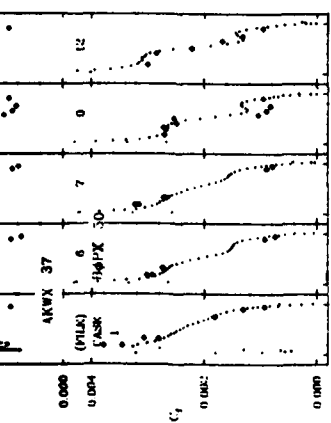
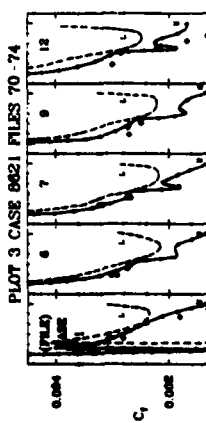
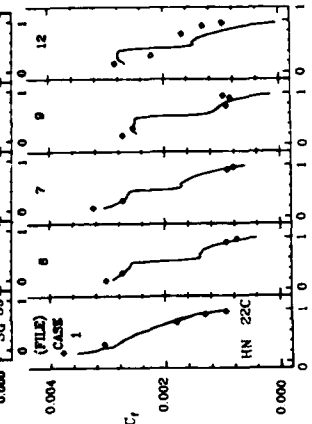
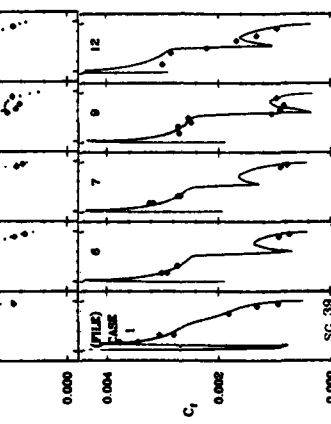
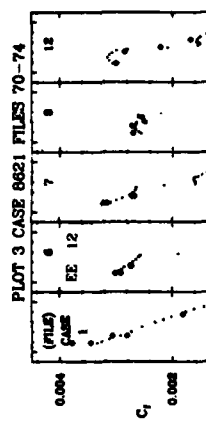
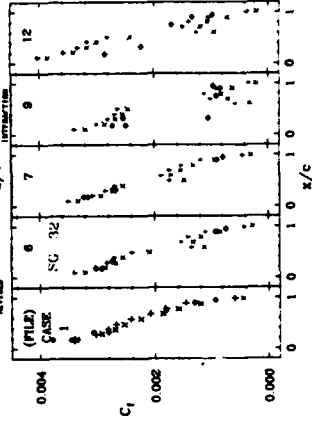
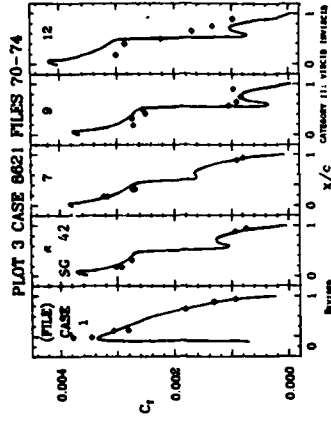
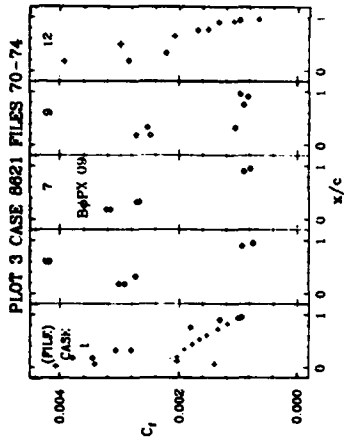


PLOT 2 CASE 8621 FILES 70-74

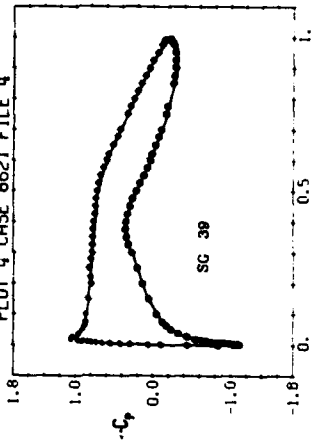


PLOT 2 CASE 8621 FILES 70-74





PLOT 4 CASE 8621 FILE 4

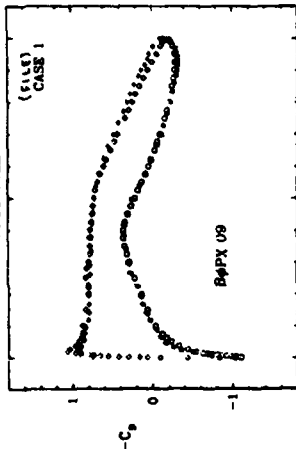


CASE 8621 FILE 4
 SC 39
 REYNOLDS NUMBER: 1.0E+05
 MACH NUMBER: 0.3
 SURFACE: 1.0E+05

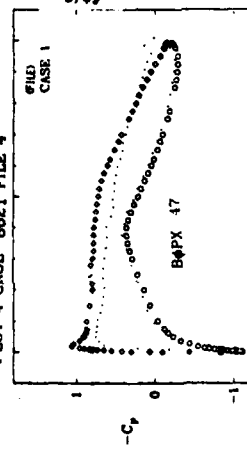
* * *
 * * *
 * * *



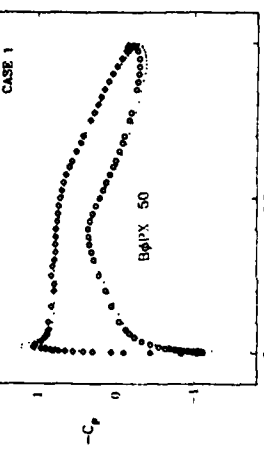
PLOT 4 CASE 8621 FILE 4



PLOT 4 CASE 8621 FILE 4



PLOT 4 CASE 8621 FILE 4



PLOT 4 CASE 8621 FILE 4

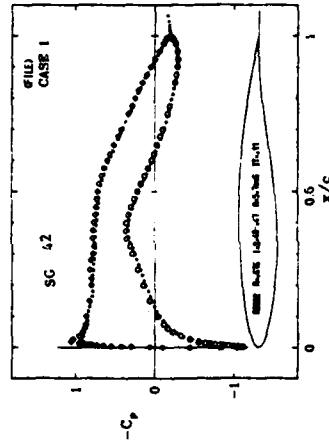
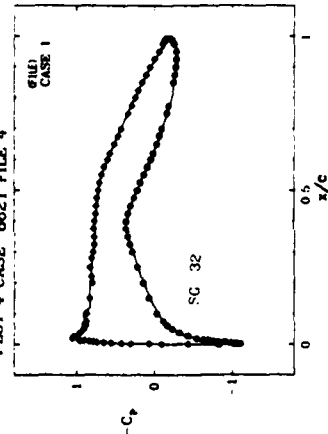
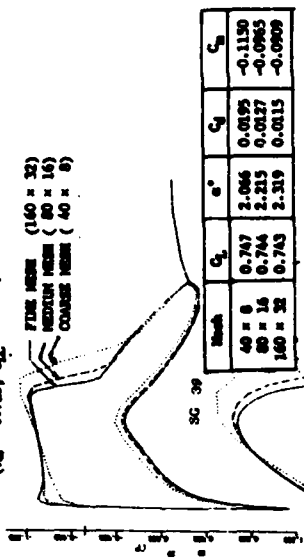


PLATE 160

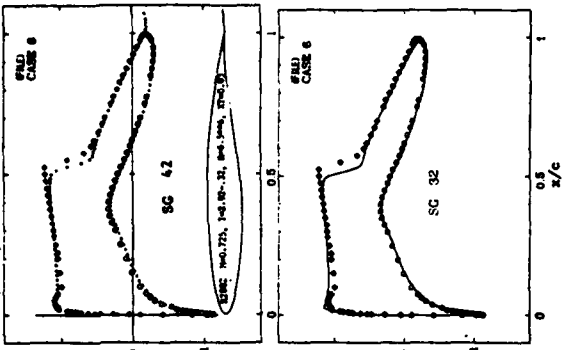
MEMO REFINEMENT STUDY
 CASE 8621 - RAE 2822, FILE/CASE 6
 ($N = 0.725$, $C_L = 0.725$, $M = 6.5 \times 10^4$)



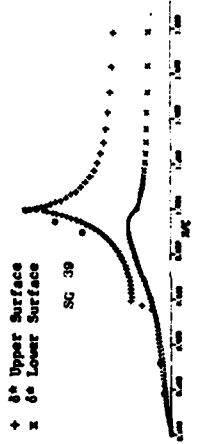
Mesh	C_L	e^*	C_D	C_M
40 x 8	0.747	2.046	0.0195	-0.1130
80 x 16	0.744	2.215	0.0127	-0.0943
160 x 32	0.743	2.319	0.0115	-0.0909

C_L determined from circulation at infinity
 C_D determined from integration of surface pressure

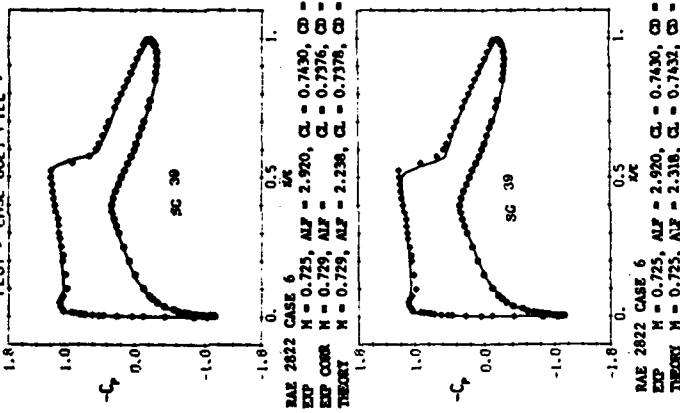
PLOT 5 CASE 8621 FILE 6



DISPLACEMENT THICKNESS
 CASE 8621 - RAE 2822 FILE/CASE 6
 ($N = 0.725$, $M = 0.6500 \times 10^4$, $ALF = 2.238$)



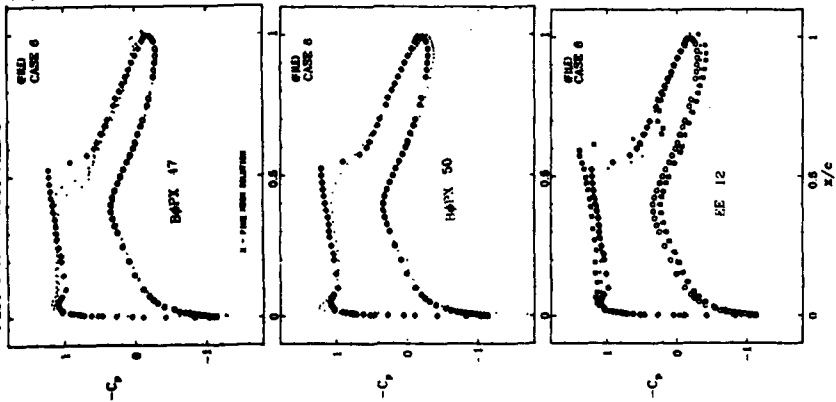
PLOT 5 CASE 8621 FILE 5



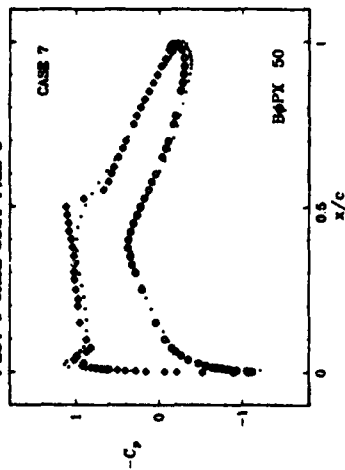
RAE 2822 CASE 6
 $N = 0.725$, $ALF = 2.970$, $C_L = 0.7430$, $C_D = 0.0127$
 EXP CASE $N = 0.725$, $ALF = 2.238$, $C_L = 0.7376$, $C_D = 0.0126$
 THEORY $N = 0.725$, $ALF = 2.238$, $C_L = 0.7378$, $C_D = 0.0122$

RAE 2822 CASE 6
 $N = 0.725$, $ALF = 2.970$, $C_L = 0.7430$, $C_D = 0.0127$
 EXP $N = 0.725$, $ALF = 2.318$, $C_L = 0.7433$, $C_D = 0.0115$
 THEORY $N = 0.725$, $ALF = 2.318$, $C_L = 0.7433$, $C_D = 0.0115$

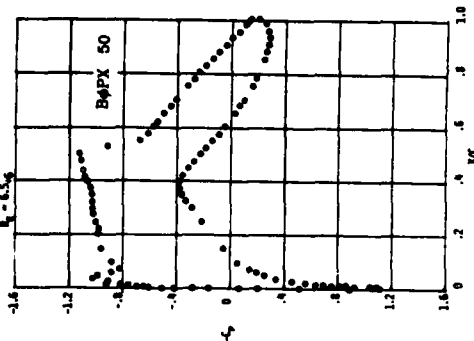
PLOT 5 CASE 8621 FILE 5



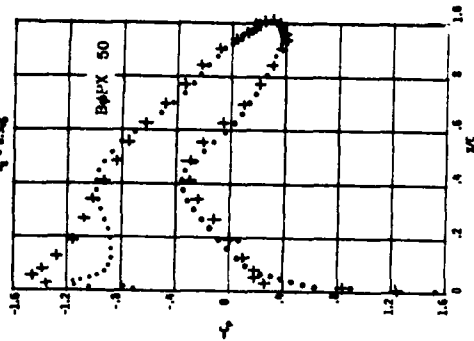
PLOT 6 CASE 0621 FILE 6



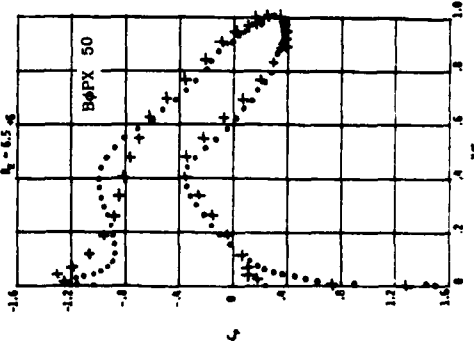
127689
 + 127650
 ME 2022 AIRMAIL (Case 7)
 R = .775
 S = 2.15P
 $\beta_0 = 6.546$



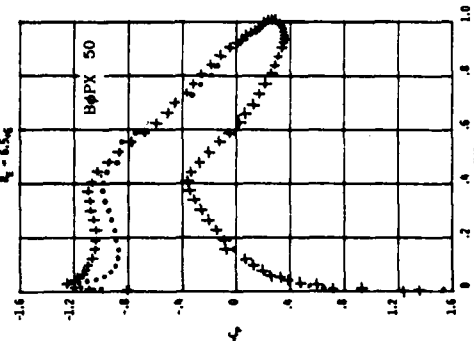
127689
 + 127650
 ME 2022 AIRMAIL (Case 7)
 R = .775
 S = 2.15P
 $\beta_0 = 6.546$



127689
 + 127650
 ME 2022 AIRMAIL (Case 7)
 R = .775
 S = 2.15P
 $\beta_0 = 6.546$



127689
 + 127650
 ME 2022 AIRMAIL (Case 7)
 R = .775
 S = 2.15P
 $\beta_0 = 6.546$



* ONLY IN CASE POINTS REMAIN TO AIRMAIL

* ONLY IN CASE POINTS REMAIN TO AIRMAIL

* ONLY IN CASE POINTS REMAIN TO AIRMAIL

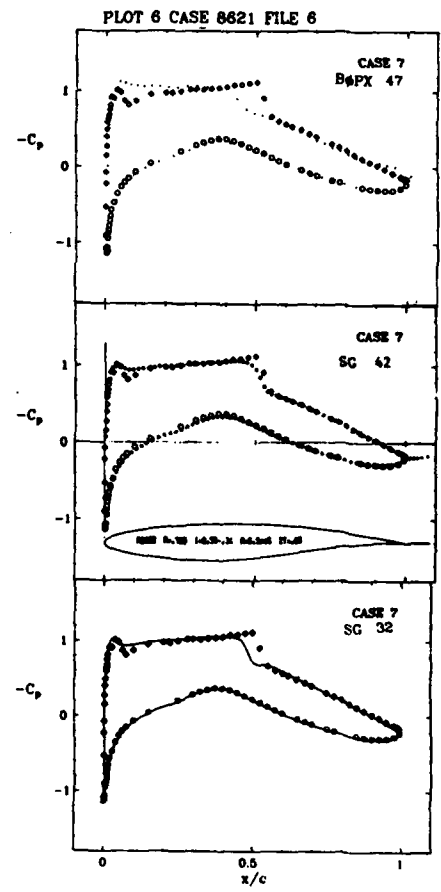
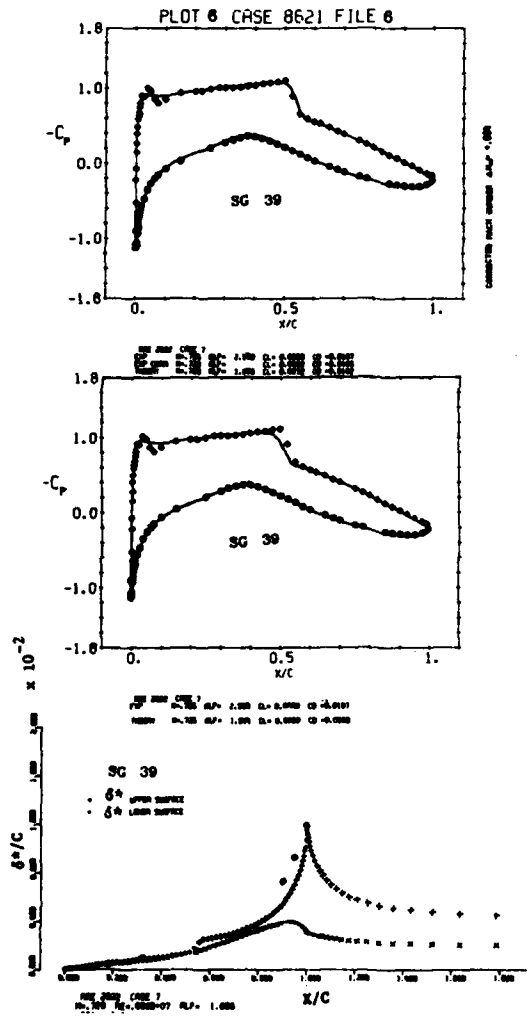
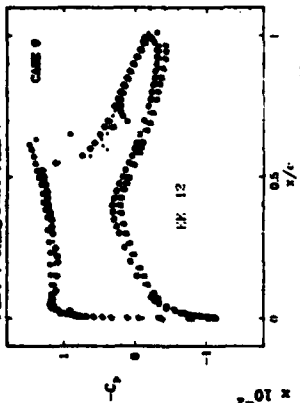


PLATE 163

PLOT 7 CASE 8621 FILE 7

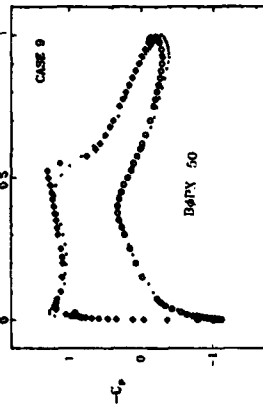
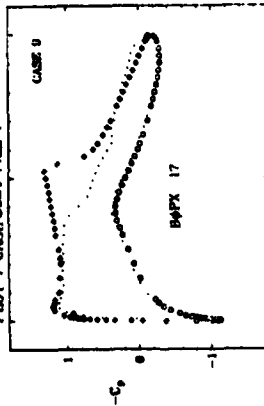


DISPLACEMENT THICKNESS
 CASE 8621 - BAR 2822 FILE/CASE 9
 (M = 0.750, RE = 0.6500 + 07, ALP = 2.537)

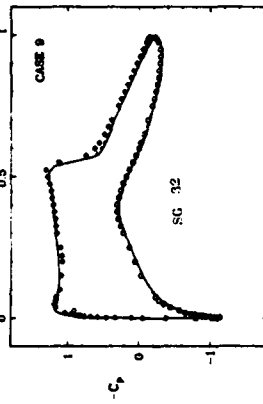
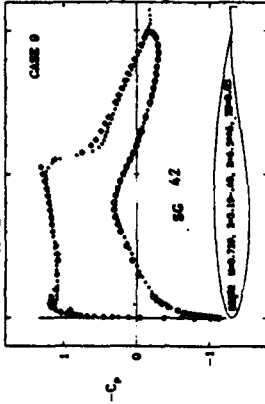
+ δ Upper Surface
 x δ Lower Surface



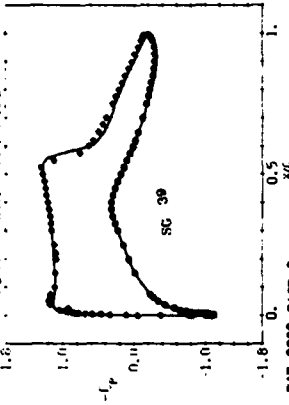
PLOT 7 CASE 8621 FILE 7



PLOT 7 CASE 8621 FILE 7



PLOT 7 CASE 8621 FILE 7



BAR 2822 CASE 9
 EXP H = 0.750, ALP = 3.190, CL = 0.8030, CD = 0.0168
 THEORY H = 0.750, ALP = 2.537, CL = 0.8032, CD = 0.0157

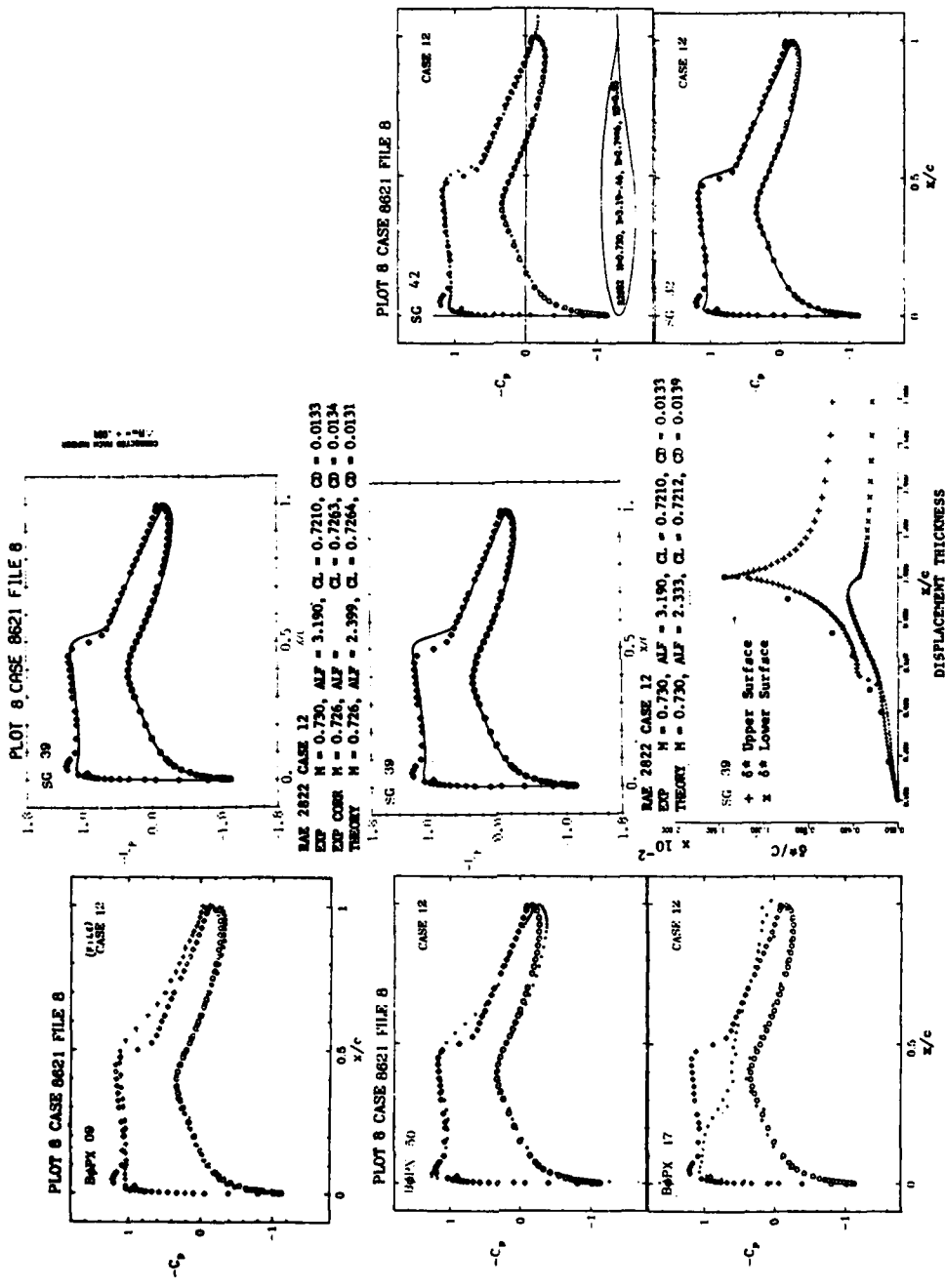


PLATE 165

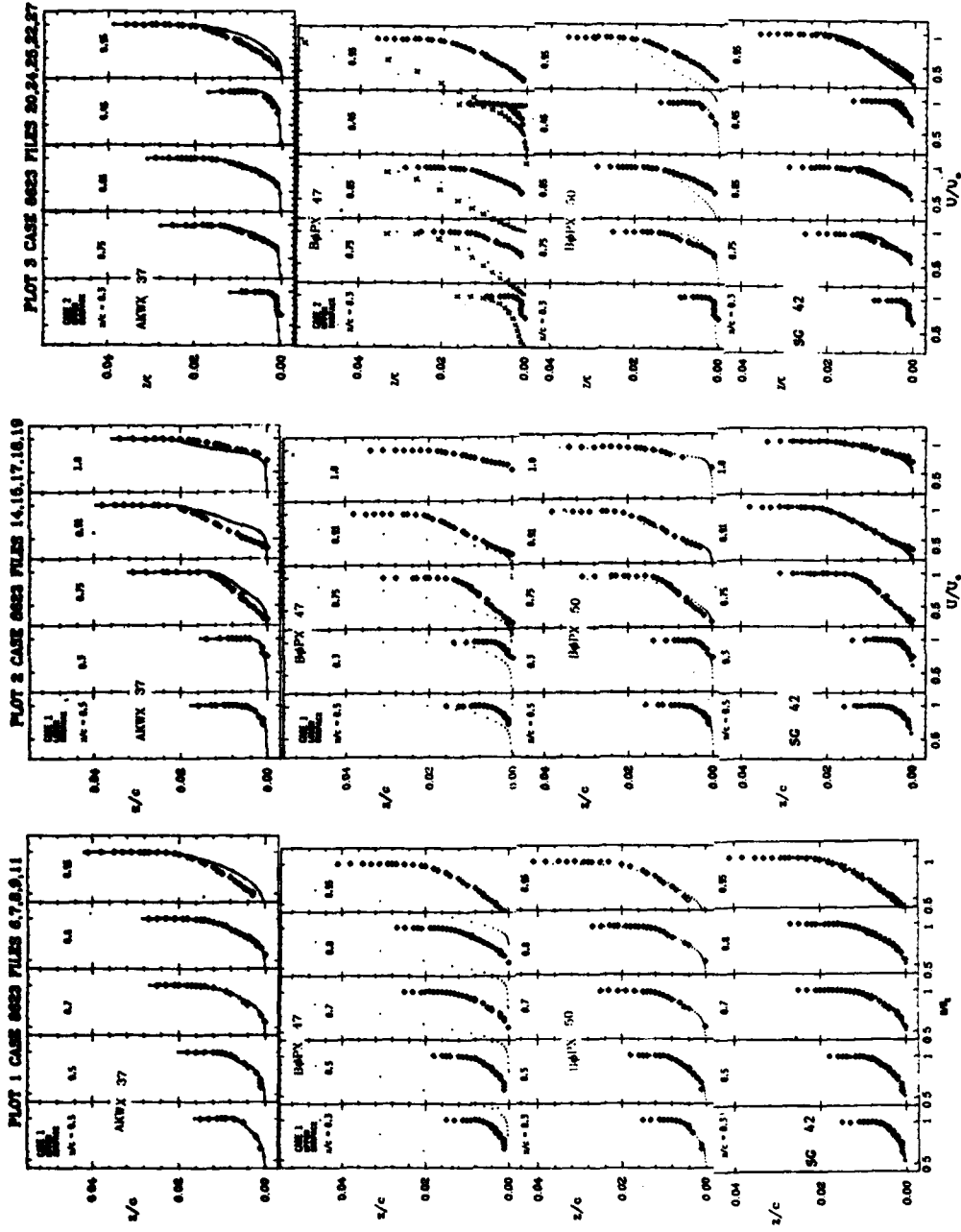


PLATE 166

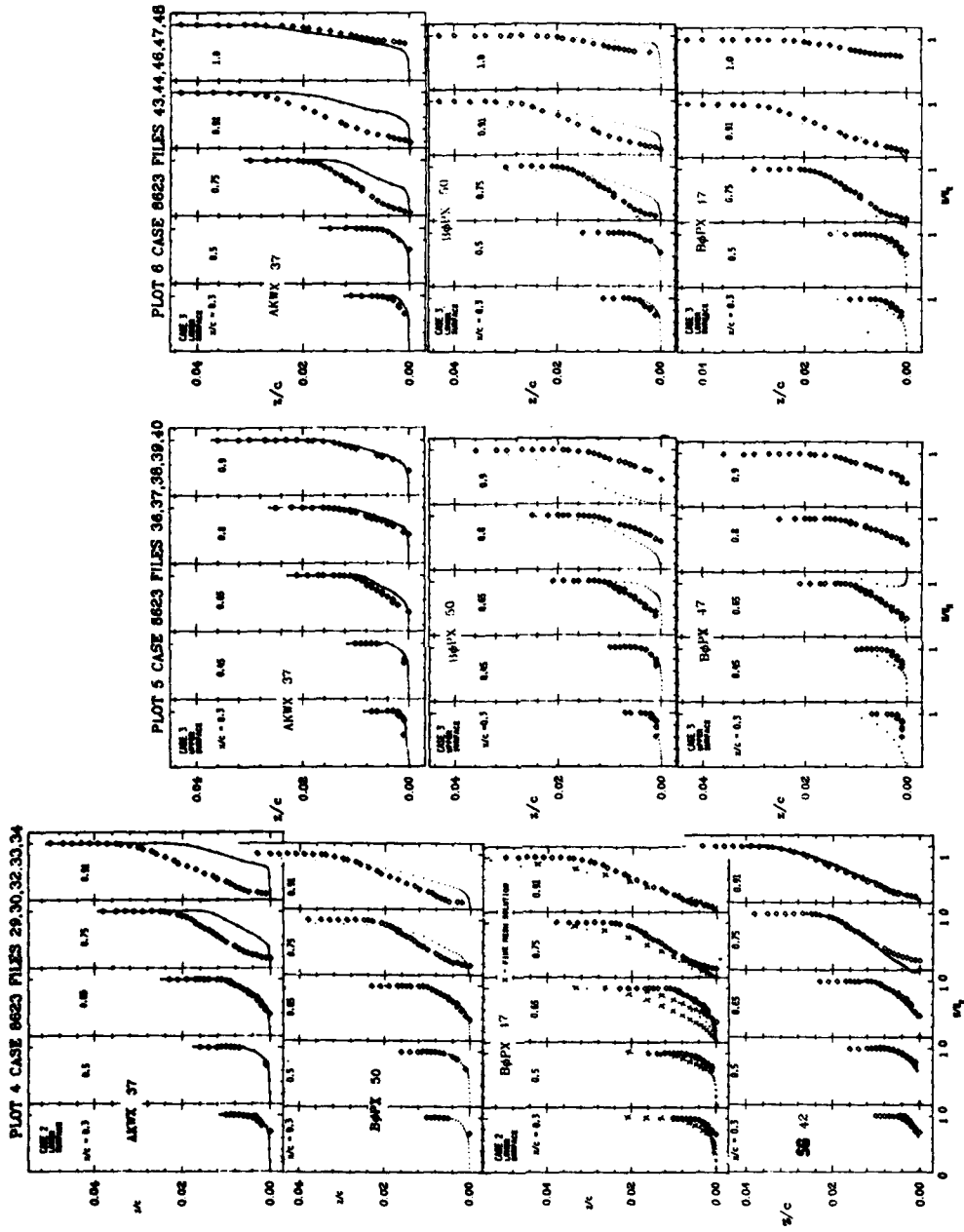


PLATE 167

PLOT 7 CASE 8623 FILE 4

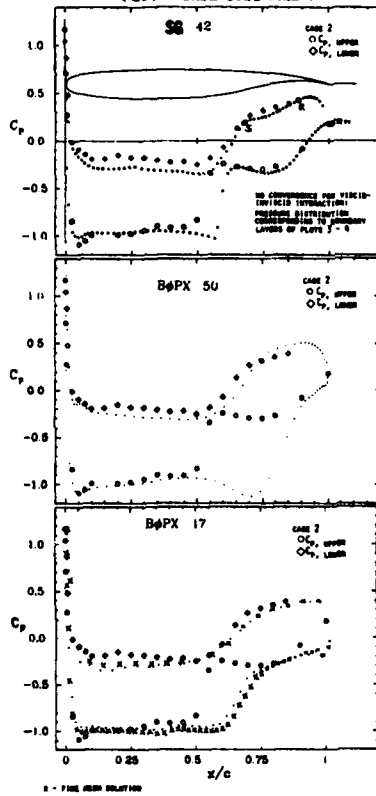
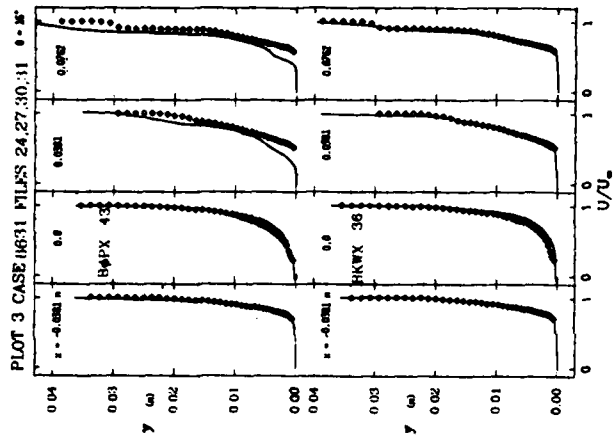
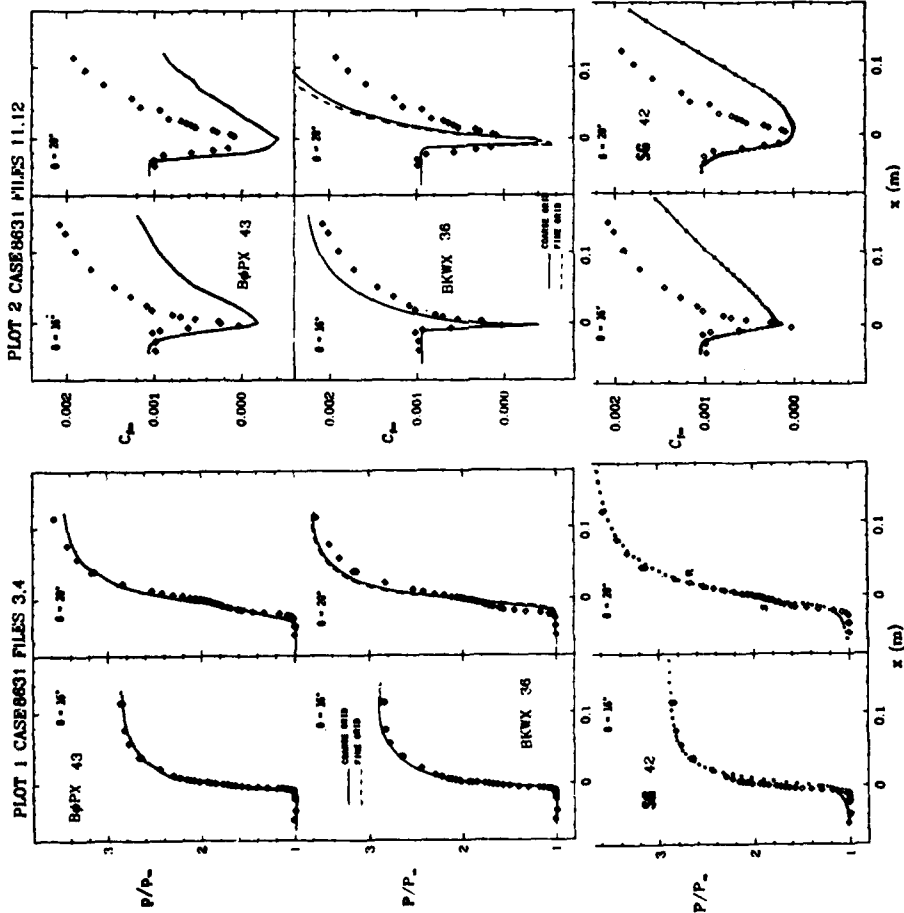


PLATE 168



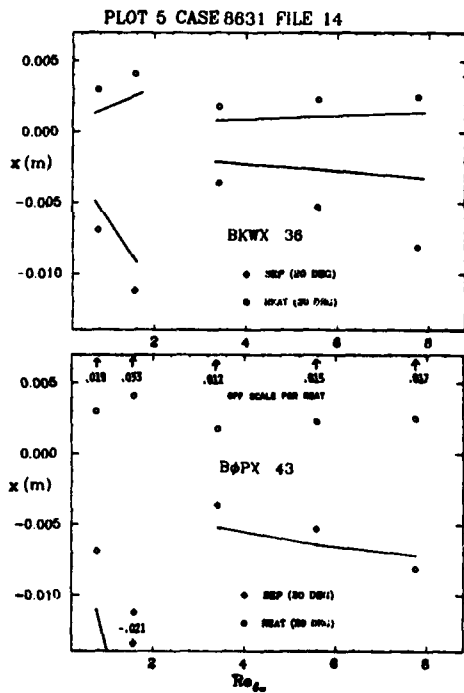
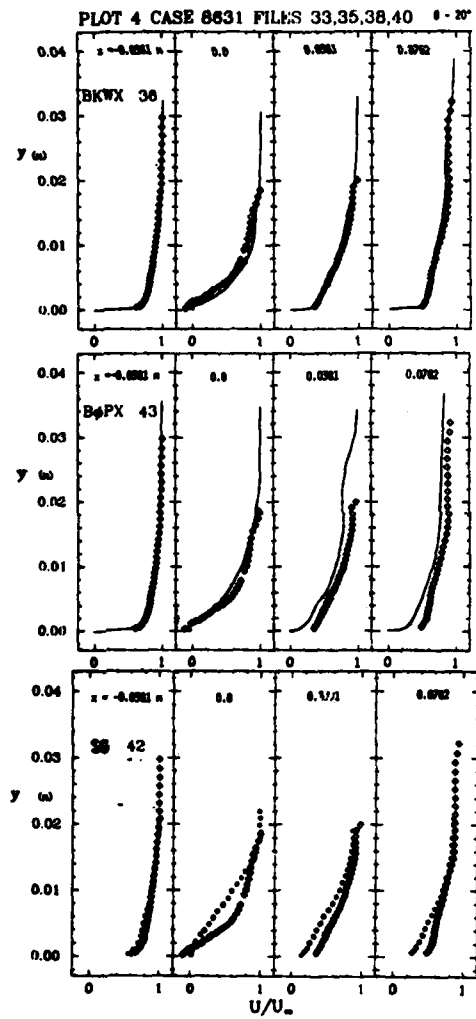
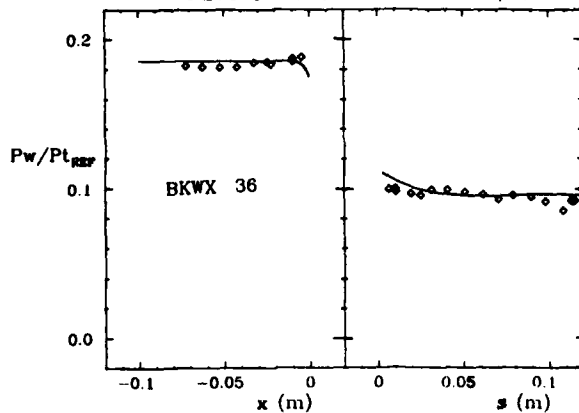
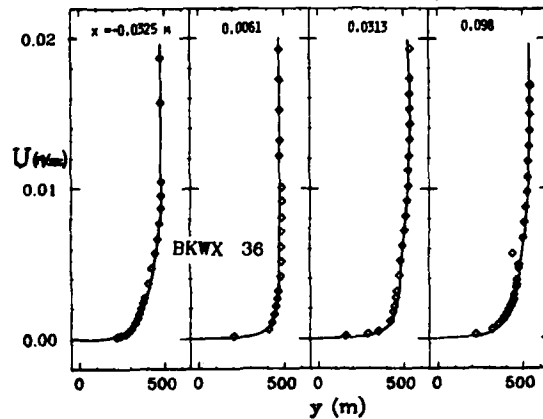


PLATE 170

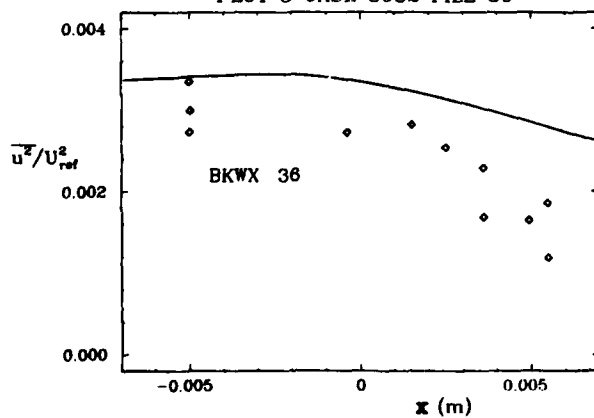
PLOT 1 CASE 8632 FILES 31,32



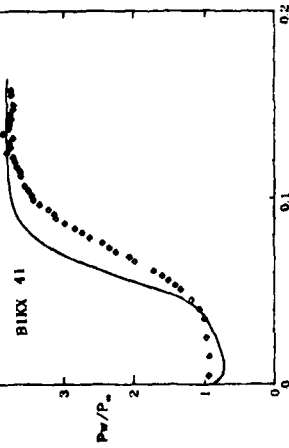
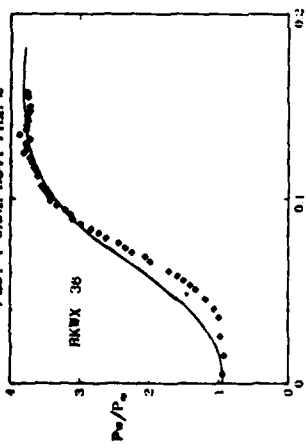
PLOT 2 CASE 8632 FILES 6,13,16,22



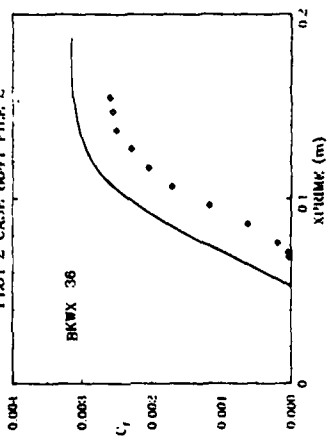
PLOT 3 CASE 8632 FILE 30



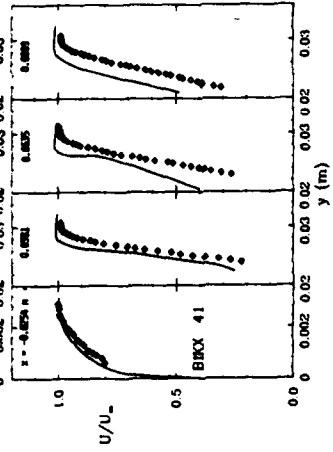
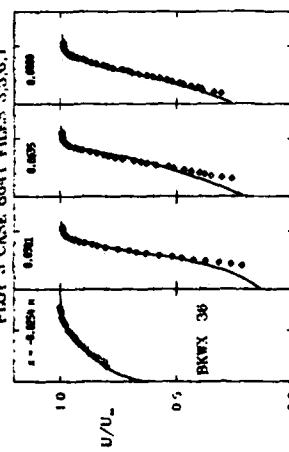
PLOT 1 CASE 8641 FILM 2



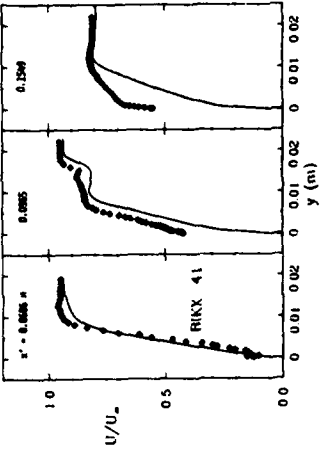
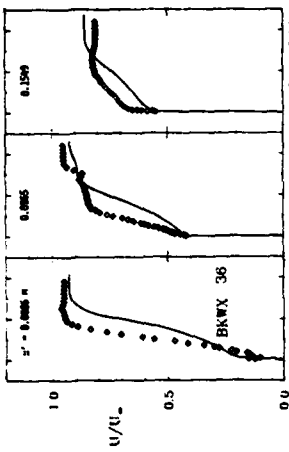
PLOT 2 CASE 8641 FILM 2



PLOT 3 CASE 8641 FILMS 3,5,6,7



PLOT 4 CASE 8641 FILMS 8,10,13



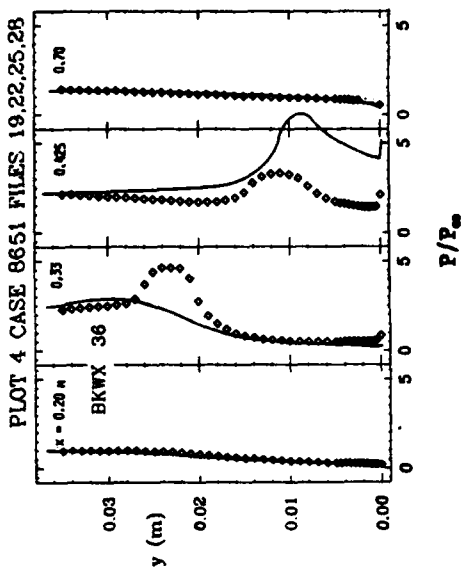
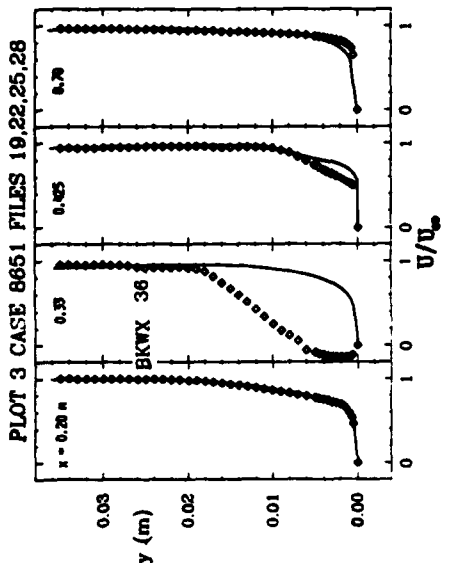
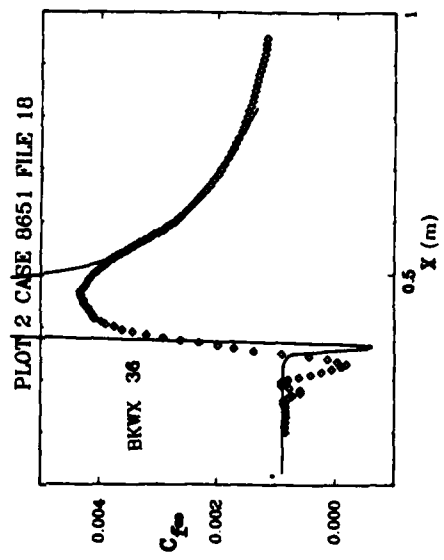
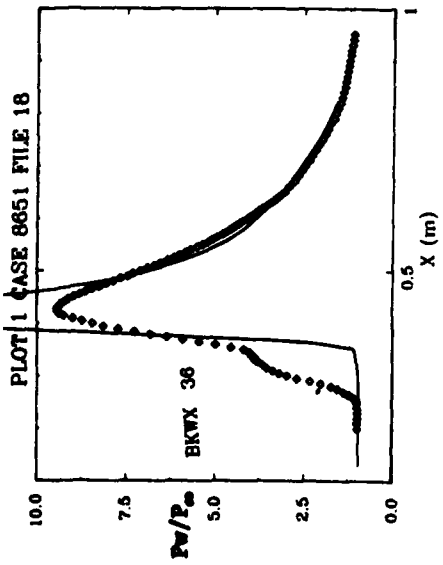
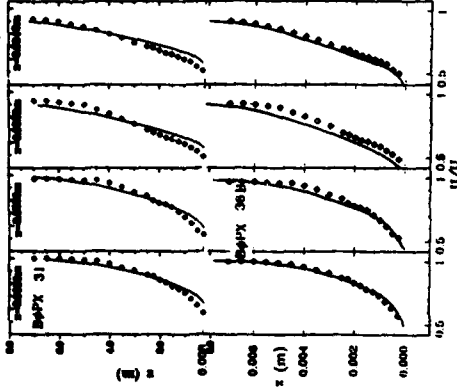
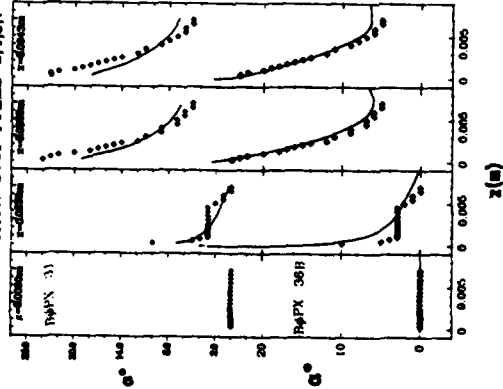


PLATE 173

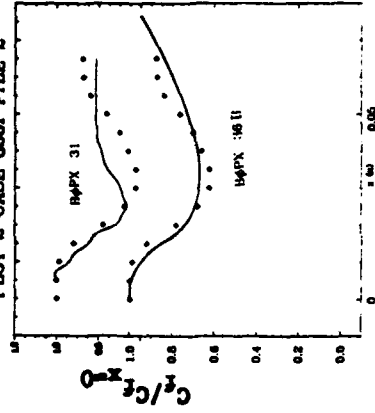
PLOT 4 CASE 8661 FILES 3,4,6,7



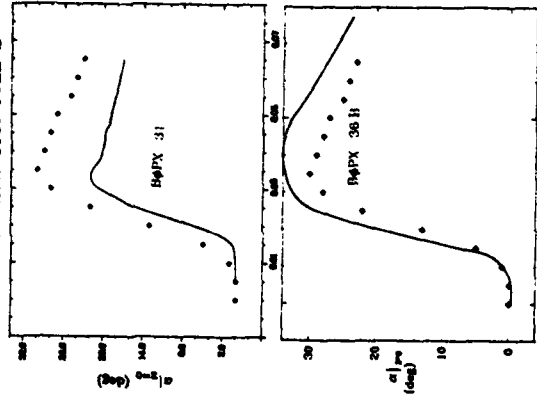
PLOT 5 CASE 8661 FILES 3,4,6,7



PLOT 2 CASE 8661 FILE 2



PLOT 3 CASE 8661 FILE 2



PLOT 1 CASE 8661 FILE 2

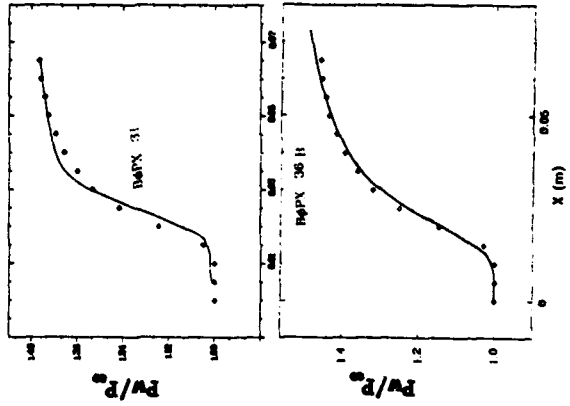


PLATE 174

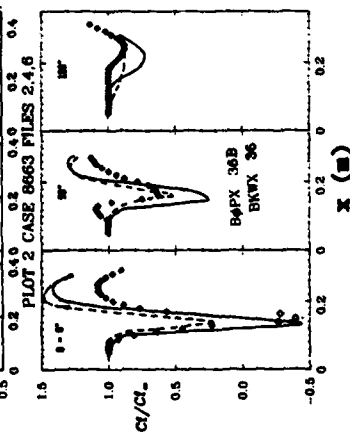
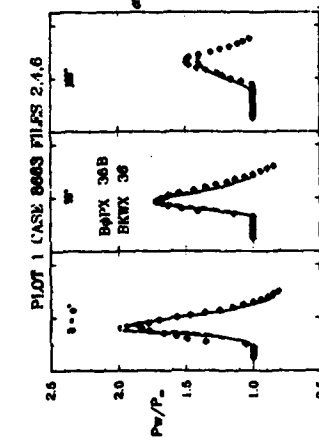
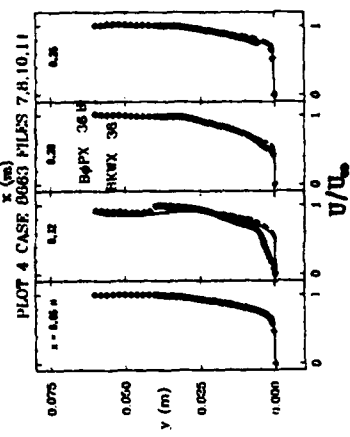
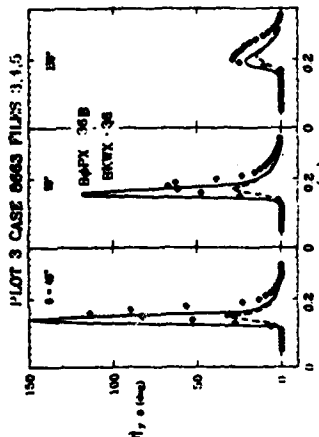
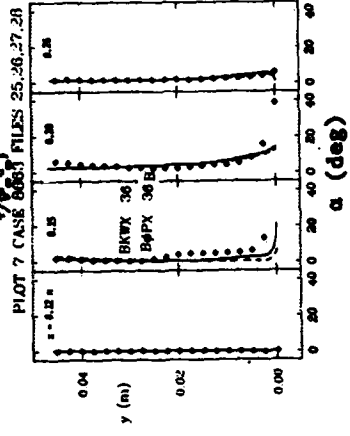
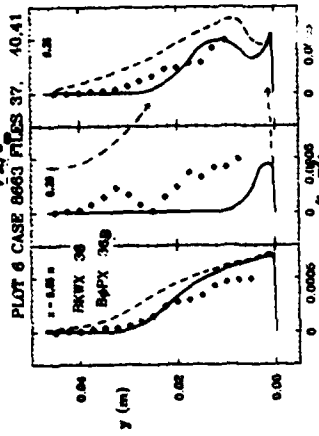
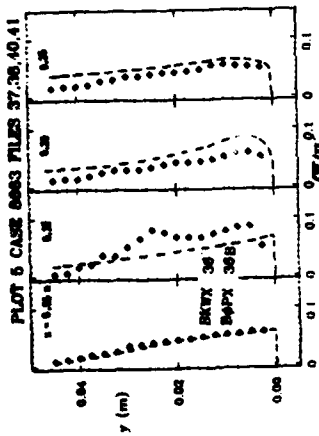
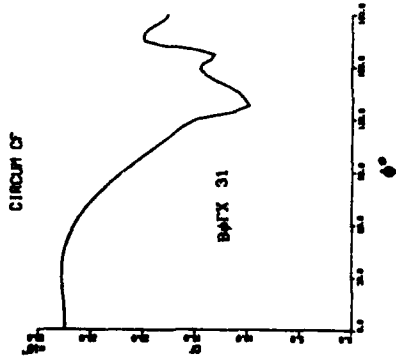
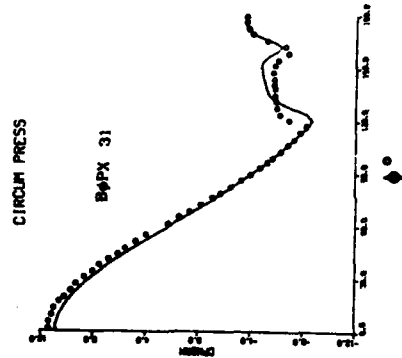


PLATE 175

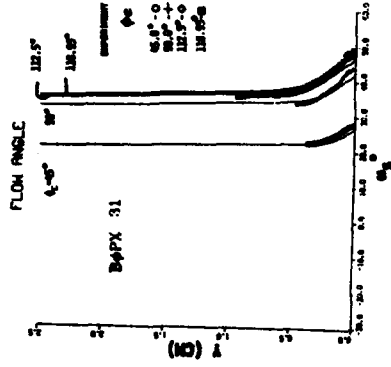
CASE 8671



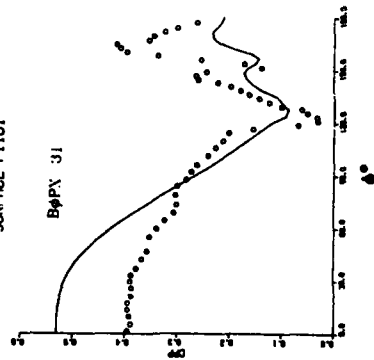
CASE 8671



CASE 8671



CASE 8671



CASE 8671

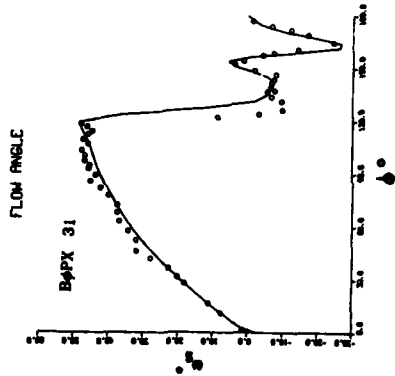
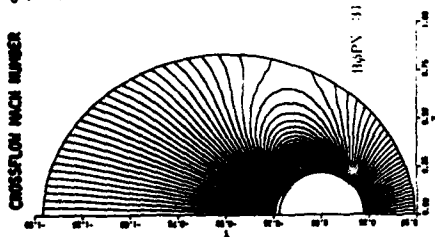


PLATE 176

(Special plots - not in the form requested in Vol. 1)

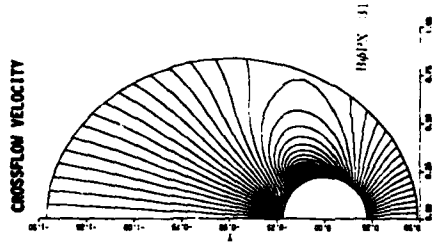
CASE 8671

CROSSFLOW MACH NUMBER
CONTOUR LEVELS
0.2 TO 1.0 IN 0.2
SPACING CONTOUR INTERVALS



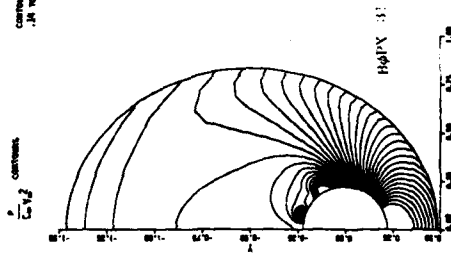
CASE 8671

CROSSFLOW VELOCITY
CONTOUR LEVELS
-2 TO 2 IN 2



CASE 8671

CROSSFLOW VELOCITY
CONTOUR LEVELS
-10 TO 10 IN 10



CASE 8671

ANGLE
CONTOUR LEVELS
150.00 TO 150.00 IN 0.00

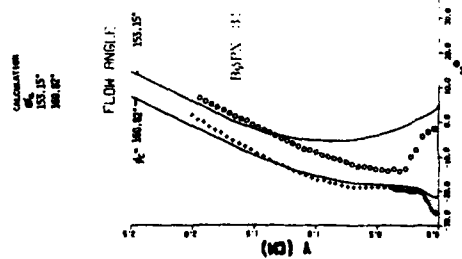
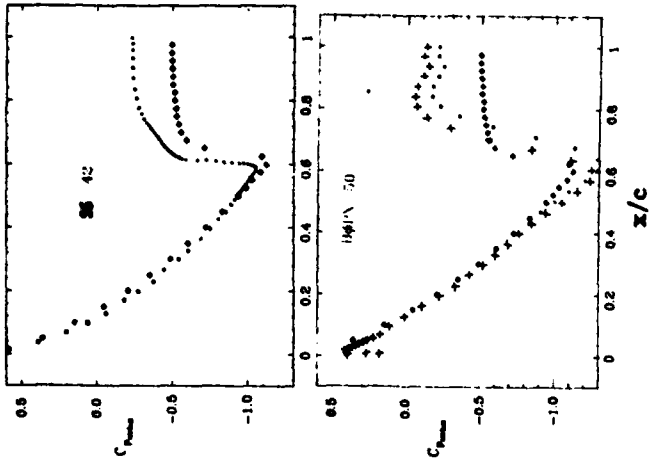


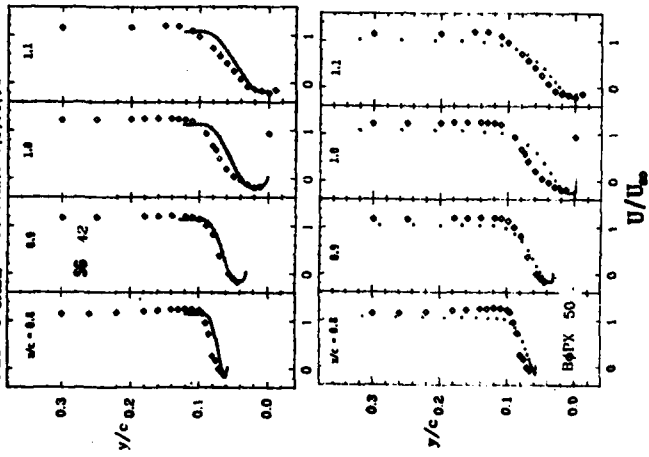
PLATE 177

(Special plots - not in the form requested in Vol. I)

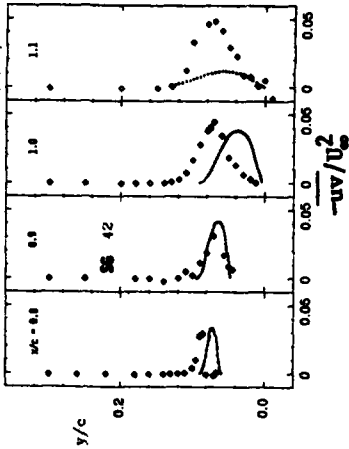
PLOT 1 CASE 8691 FILE 3



PLOT 2 CASE 8691 FILES 7,9,11,13



PLOT 4 CASE 8691 FILES 7,9,11,13



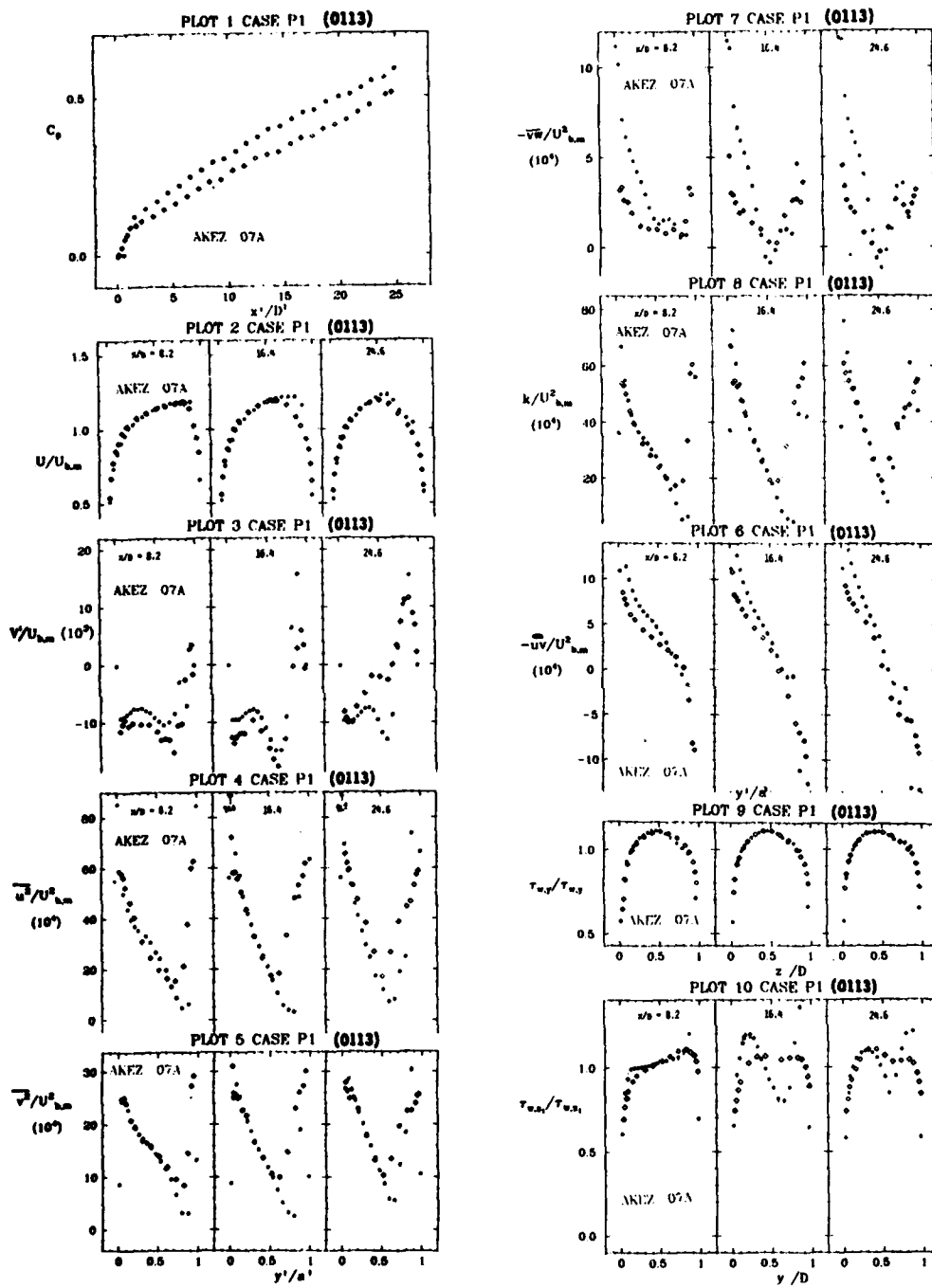


PLATE 179

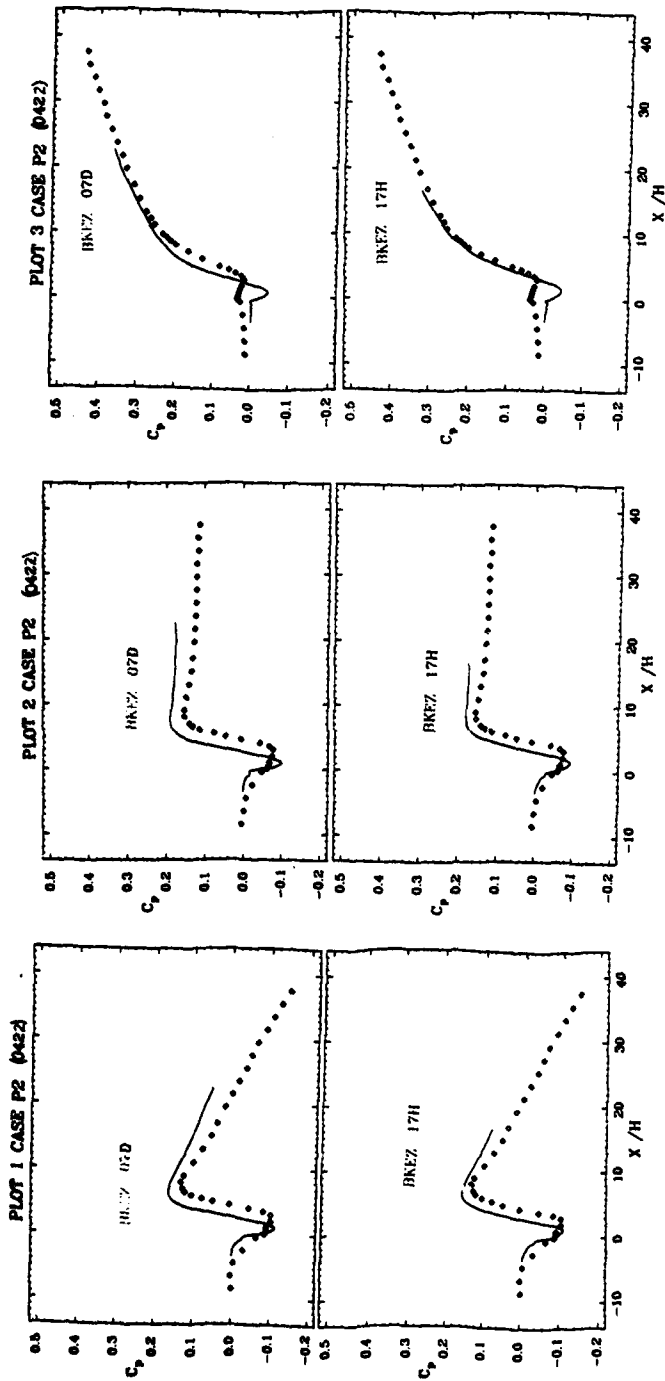


PLATE 180

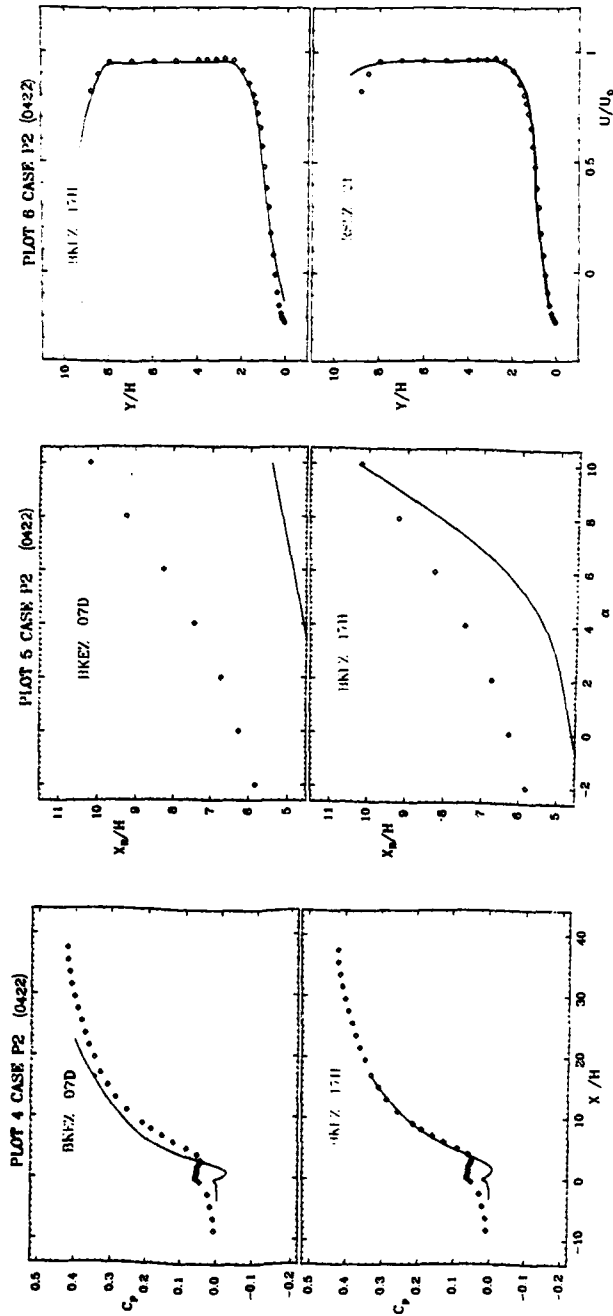


PLATE 181

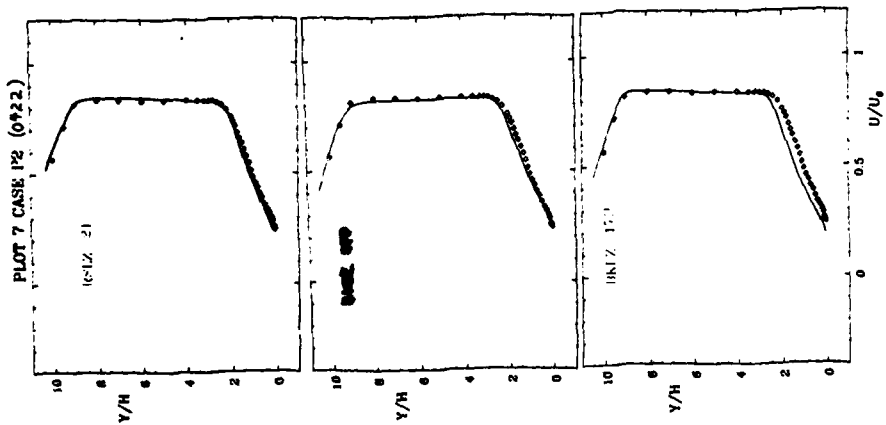
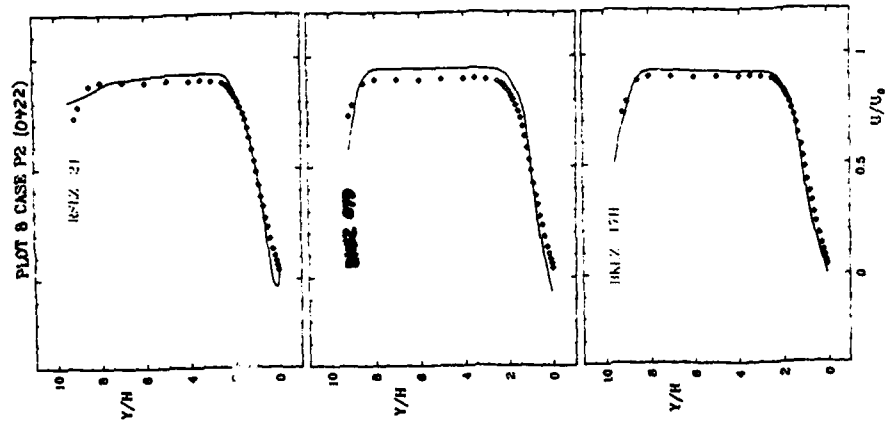
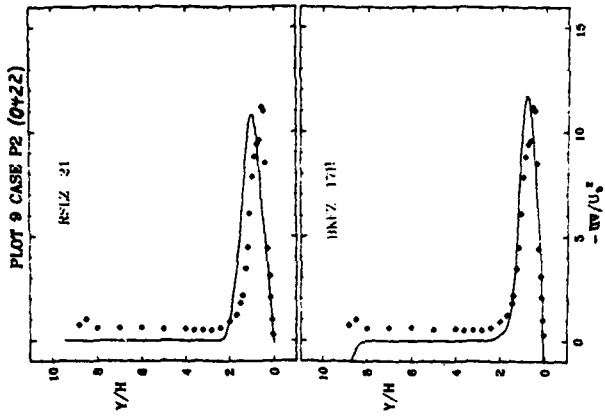
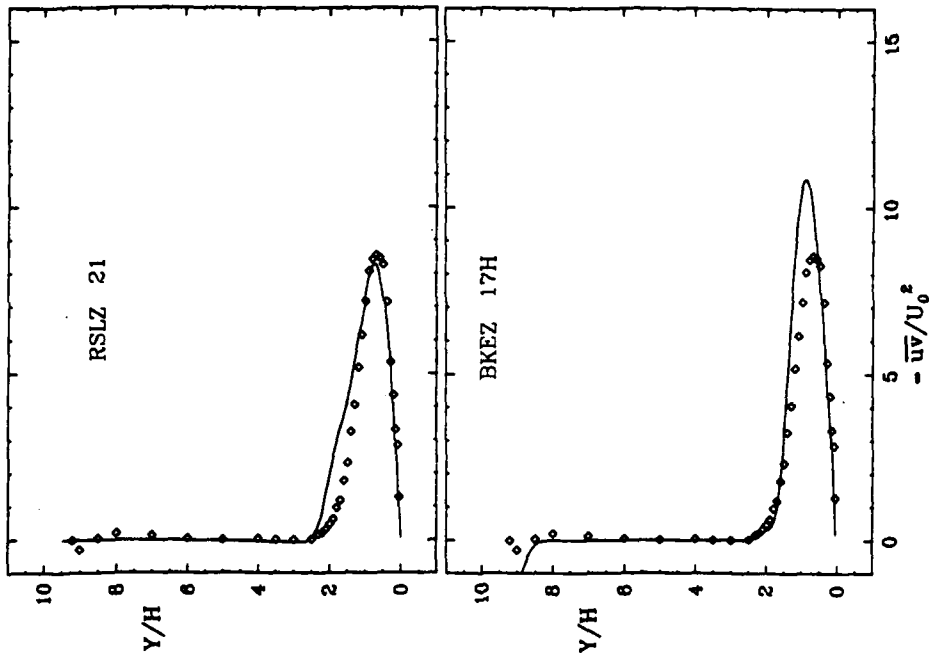


PLATE 182

PLOT 11 CASE P2 (0422)



PLOT 10 CASE P2 (0422)

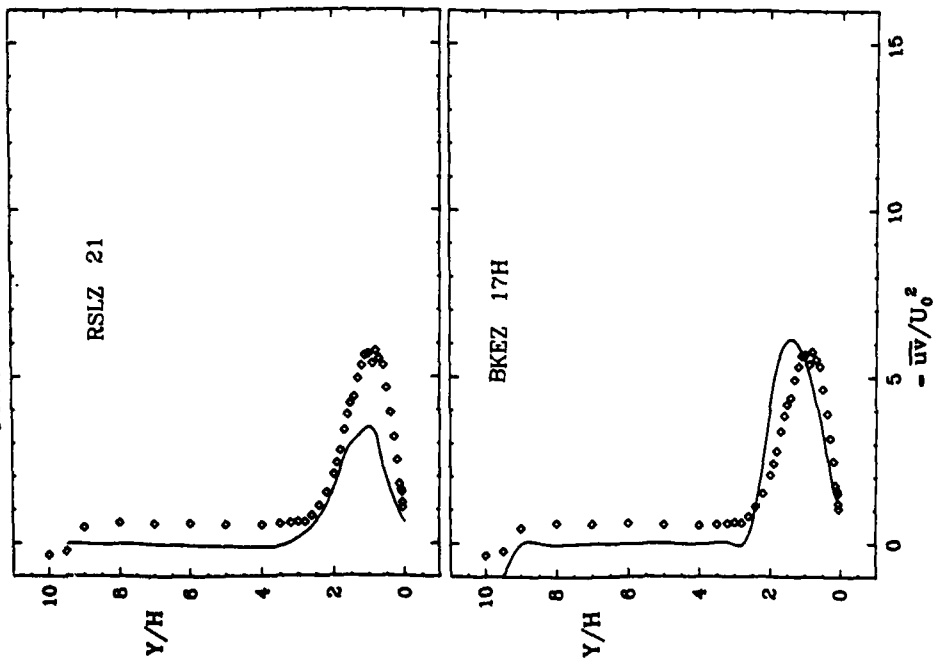


PLATE 183

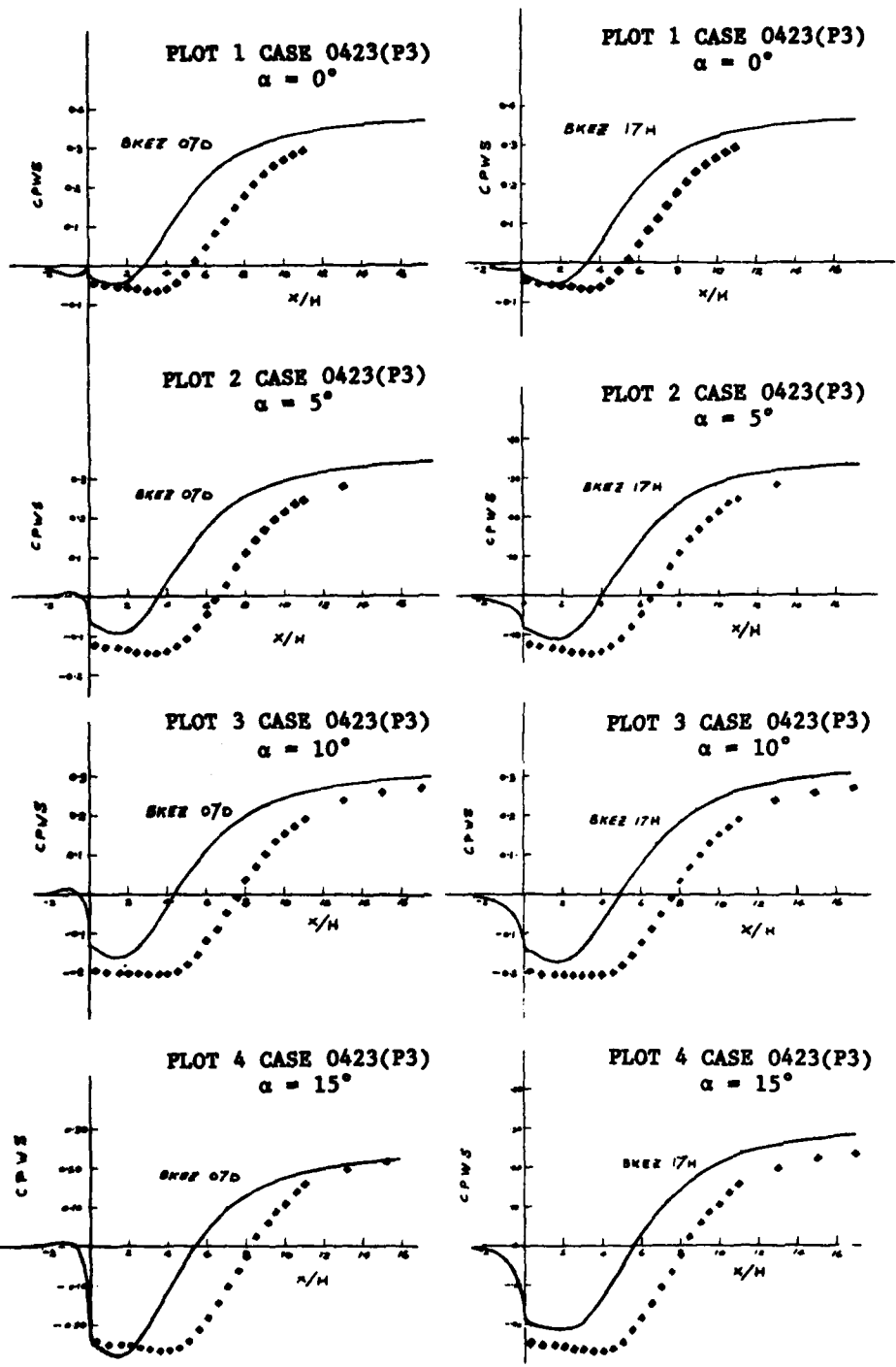


PLATE 184

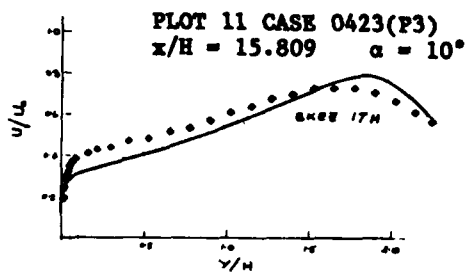
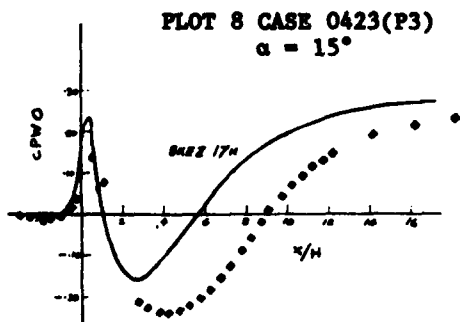
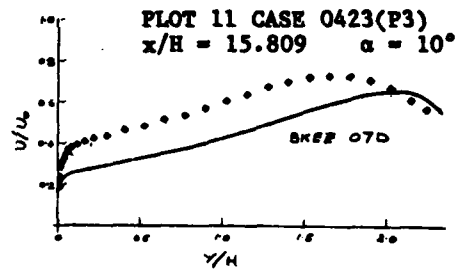
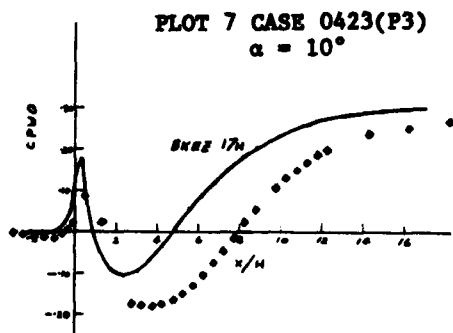
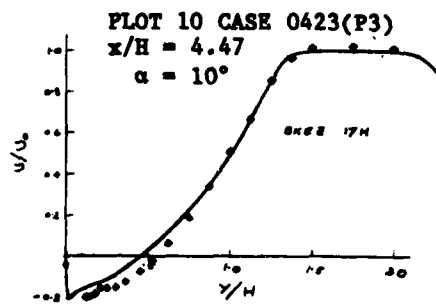
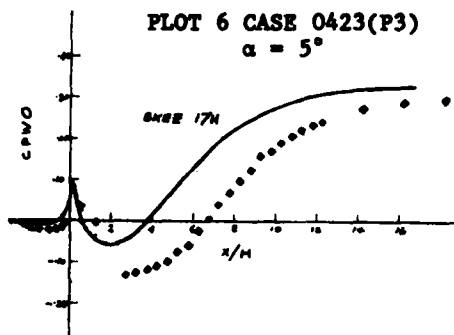
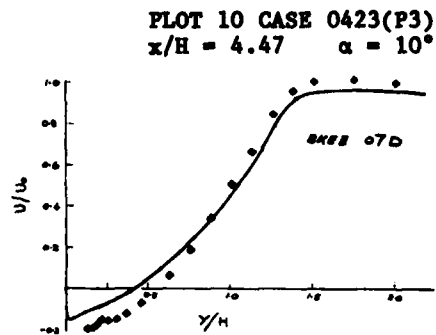
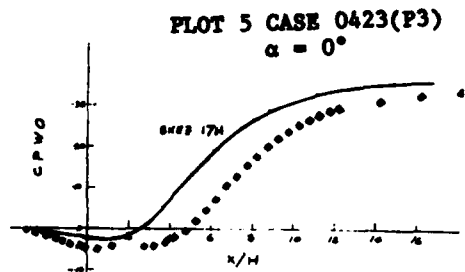


PLATE 185

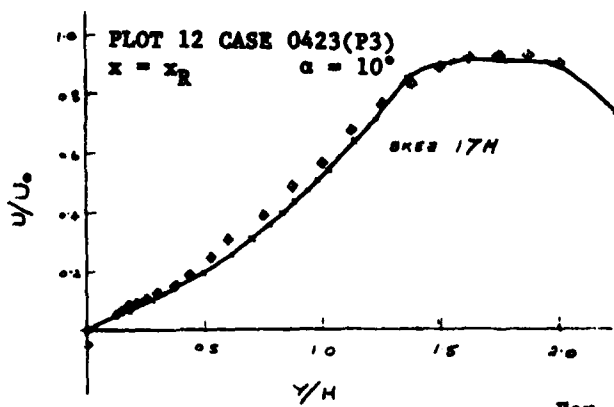
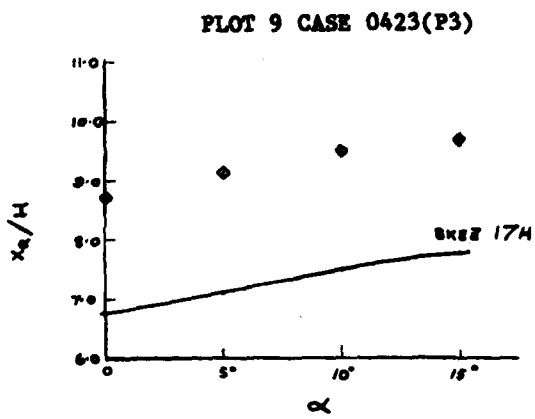
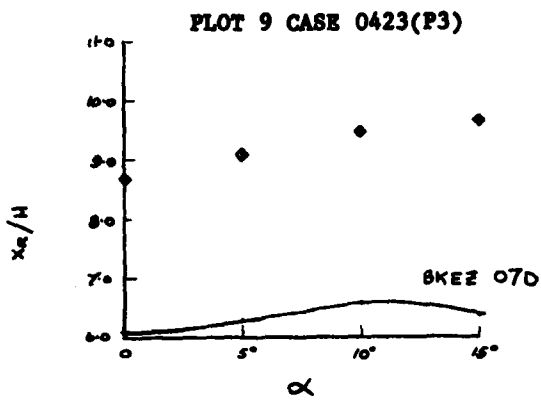
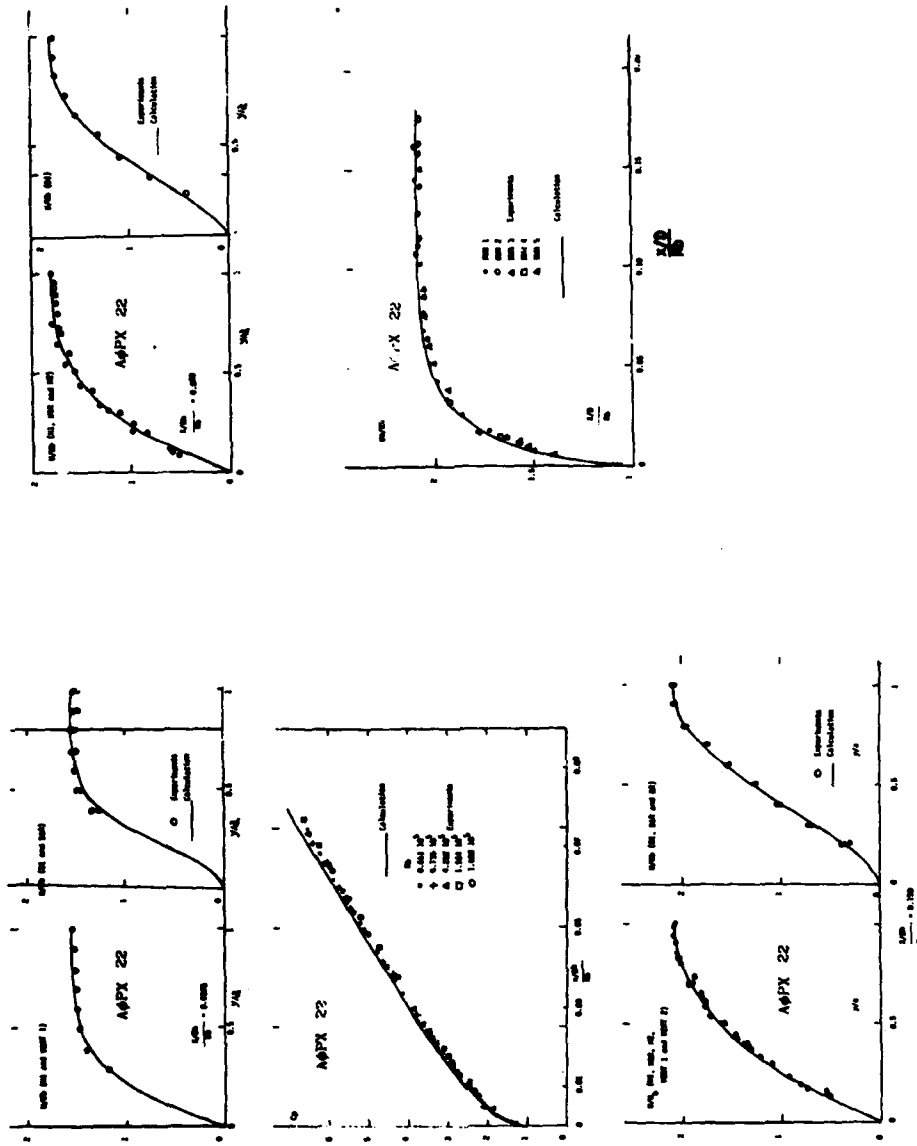


PLATE 186

For some output on Case 0424,
 see page 1390.

SUPPLEMENTARY (LAMINAR) PLOTS
 BY GROUP APOX 22 FOR CASE 0111.



SUMMARY REPORTS
OF COMPUTER GROUPS

COMPARISON OF COMPUTATION WITH EXPERIMENT

Summary Report

by

H.E. Bailey*

Computer Group Number: 50



Cases 8621, 8623, 8691

All of the computations submitted to the Conference were made on the Illiac IV using the method of solution described in detail in Steger (1977). The turbulence model used is fully described in Baldwin and Lomax (1978). Solutions were submitted for Cases 8621, 8623 and 8691. For all cases the smoothing coefficients used were the same with the single exception mentioned below.

For Case 8621 some additional computations were made in an attempt to evaluate the effect of mesh size on the solution. Subcase 7 of Case 8621 was selected for this study. A mesh of 127×59 points was constructed for the RAE 2822 airfoil. This permits the deletion of every other point in either or both of the x and y directions. Plate 162 shows a comparison of the 127×59 mesh solution with the 64×30 mesh solution. The smoothing coefficients for the 64×30 mesh solution have been halved to improve the comparison. Obviously halving the number of mesh points in both directions has seriously affected the solution.

Plate 162 also shows a comparison of solutions on the 127×59 mesh and the 127×30 mesh. Again the smoothing coefficients for the 127×30 mesh have been halved. In this instance the differences in the two solutions are mainly confined to the upper surface on the airfoil. This plate also shows a comparison of the 127×59 mesh solution with the 64×59 mesh solution. There are again severe discrepancies on both the upper and the lower surfaces.

In Plate 162 the experimental results are also shown by themselves. Comparison of experiment with the computation shows that the shock wave clearly evident in the experiment has been smeared out in the numerical solutions with the smearing being greater, the fewer the number of points on the body.

A popular method of comparing transonic test data with numerical solutions which assume no tunnel walls is to make corrections to both the free-stream Mach number and the angle of attack in the numerical solution until the lift coefficients agree. Subcase 3 of Case 8623 was selected to evaluate this procedure for the present code. When the Mach number is increased from $M = 0.8$ to $M = 0.82$ at constant angle of attack, the shock wave position does not move. When the angle of attack is decreased

*NASA-Ames Research Center, Moffett Field, CA 94035

from $\alpha = 2.4^\circ$ to $\alpha = 1.1^\circ$ to get the correct lift coefficients, the shock wave does not move. Thus, in changing both the Mach number and the angle of attack the shock wave remains stationary and is always behind the experimental shock location. This suggests that either the walls should be included in the computation or the scale of the experiment should be changed so that wall effects are reduced.

One final remark concerns Case 8691. This case represents a circular arc airfoil at zero angle of attack. In spite of the fact that the top and bottom pressure distributions should be identical due to symmetry, they are not. During the Conference it was suggested that this difference might be an unsteady effect. No attempt was made during the computation to check for unsteadiness.

References

- Baldwin, B.S., and H. Lomax (1978). "Thin layer approximation and algebraic model for separated turbulent flow," AIAA Paper 78-257.
- Steger, J.L. (1977). "Implicit finite difference simulation of flow about arbitrary geometries with application to airfoils," AIAA Paper 77-665.

COMPARISON OF COMPUTATION WITH EXPERIMENT

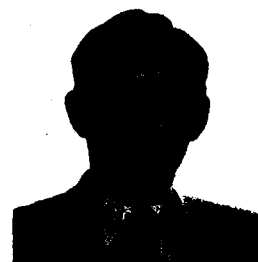
Summary Report

(Calculation of Two Free-Shear Flows)

by

S. F. Birch*

Computer Group Number: 24



Cases 0311, 0381

The computer program used for these calculations solved the boundary-layer version of the 2-D equations of motion together with a two-equation (k-ε) turbulence model. The finite-difference equations were obtained using a finite-volume approach and a hybrid differencing scheme. The equations were solved sequentially using a standard tri-diagonal solver and the solution was iterated between planes. The "v" velocity component was obtained from a direct integration of the continuity equation. The mesh spacing in the "y" direction was variable and the size of the flow domain increased with downstream distance so that most of the mesh points were always within the shear layer. The axial step size also increased with downstream distance and was approximately proportional to the width of the shear layer at all stations.

Turbulence Model

The turbulence model was the standard k-ε model except that the constant in the production term in the dissipation equation was changed from 1.44 to 1.40. This leads to increased mixing rates and improved agreement with data for the calculation of the near field of jets. It is not necessarily an improvement over the standard model for a wider range of flows; it will, for example, increase the error in planar jet calculations.

The Planar Mixing Layer: Case 0311

The initial conditions were selected by running the program for a flat-plate wall boundary-layer flow. Calculated results, independent of initial conditions and for a value of R_0 of 1210, were used as initial conditions for the mixing-layer calculation. For the wall boundary-layer calculation, a wall function was used in the near-wall region. The formula used was:

$$\frac{U}{U_*} = \frac{1}{0.42} \ln \left(\frac{9.0 \rho_w y U_*}{\mu} \right),$$

*Boeing Military Airplane Co., Seattle, WA 98124

where $U_* = (\tau/\rho)_w^{1/2}$ and U, y are evaluated at the near-wall point 'p' where the boundary conditions are applied.

Calculations were run using both 20 and 40 cross-stream points. Both calculations produced almost identical results: those calculated with the mixing layer at $x/\theta = 2000$ changed by only about 1.3%, when the number of mesh points was reduced from 40 to 20. A total of 194 axial steps was used for both calculations. Eight iterations were used between planes. Total run time on a CDC 6600 was 13 sec using 40 mesh points in the y -directions and 6 sec using 20 points.

Symmetric Wake: Case 0381

The initial conditions in this case used the file data for the axial velocity. The turbulence dissipation, ϵ , was obtained as:

$$\epsilon = 0.164 k^{3/2} / l$$

where $l = 0.09\delta$ outer region,

$l = 0.42y$ wall region.

The turbulence kinetic energy, k , was obtained from the values of \overline{uv} supplied using:

$$\overline{uv} = 0.09 \frac{k^2}{\epsilon} \frac{\partial U}{\partial y}$$

The equations were again iterated 8 times between planes for the calculations.

The running time on a CDC 6600 using 40 cross-stream points were:

<u>Distance</u>	<u>No. of Axial Steps</u>	<u>Run Time (sec)</u>
400 mm	93	6
1200 θ_0	265	17

Comments

Our calculations seem to show that the $k-\epsilon$ model will not accurately predict both the near and far field of either the mixing layer or the wake. The prediction is qualitatively in error in the near field of the mixing layer. For the wake, the far field is underpredicted by about 30%.

COMPARISON OF COMPUTATION WITH EXPERIMENT

Summary Report

(Spectral Closure of Homogeneous Turbulence)

by

C. Cambon, J.P. Bertoglio, and D. Jeandel*

Computer Group Number: 52



C. Cambon

Cases 0371, 0372, 0373, 0374, 0375, 0376

Abstract: Two models for describing homogeneous non-isotropic turbulence subjected to mean-velocity gradients are presented. Both methods start from the equations for second-order correlations at two points used in spectral space. An extended eddy-damped, quasi-normal approximation is developed to close the basic equations.

I. Basic Equations

The starting point of the modeling method is the rate equation for the spectral tensor $\phi_{ij}(\vec{k}, t)$:

$$\frac{\partial \phi_{ij}}{\partial t} + 2\nu k^2 \phi_{ij} - \lambda_{lm} k_l \frac{\partial}{\partial k_m} \phi_{ij} + (\delta_{il} - 2 \frac{k_i k_l}{k^2}) \lambda_{lm} \phi_{mj} + (\delta_{jl} - 2 \frac{k_j k_l}{k^2}) \lambda_{lm} \phi_{im} = T_{ij} \quad (1)$$

where

$$T_{ij} = (\delta_{il} - \frac{k_i k_l}{k^2}) t_{lj} + (\delta_{jl} - \frac{k_j k_l}{k^2}) t_{li}^*; \quad \lambda_{ij} = \frac{\partial \bar{u}_i}{\partial x_j}$$

and

$$t_{ij}(\vec{k}, t) = k_l \int_{R^3} \phi_{lji}(\vec{k}, \vec{P}, t) d^3 \vec{P}$$

The equation giving the evolution of the third-order spectral tensor $\phi_{lji}(\vec{k}, \vec{P}, t)$ is closed by splitting into two parts the term governing the fourth-order correlations; the first part is expressed in terms of second-order correlations, in which the rules for evaluating moments of normal distributions are applied. The second one depends linearly on the third-order tensor. Following Orszag (1970) we have then in symbolic form

$$\overline{uuuu} = \int \overline{uu \cdot uu} + \overline{\mu uuu}$$

A single damping coefficient μ appears, given by the expression

$$\mu(\vec{k}, \vec{P}, t) = \eta(k, t) + \eta(P, t) + \eta(Q, t) + \nu(k^2 + P^2 + Q^2); \quad \vec{k} + \vec{P} + \vec{Q} = 0 \quad (2)$$

*Ecole Centrale de Lyon, 69130 Ecully, France

where

$$\eta(k,t) = \lambda \left\{ \int_0^k P^2 E(P,t) dP \right\}^{1/2}$$

is a large-eddy turn-over time scale and λ a given constant. It should be noted that for some rotating flows an attempt to introduce the mean rotation rate in the corrected time scale

$$\eta(k,t) = \lambda \left\{ \int_0^k P^2 E(P,t) dP + \frac{1}{4} (\lambda_{1j} - \lambda_{j1})(\lambda_{1j} - \lambda_{j1}) \right\}^{1/2} \quad (3)$$

has been made (see Method 1).

II. Characterization of the Two Models

Since the resulting closed set of equations is too cumbersome to be handled directly, two different ways have been chosen in order to handle them computationally.

In Method 1, an angular parameterization of $\phi_{ij}(\vec{k},t)$ in the form

$$\phi_{ij}(\vec{k},t) = \frac{E(k,t)}{4\pi k^2} F_{ij}(H_{pq}(k,t); \alpha_n)$$

where

$$H_{ij}(k,t) = \frac{\phi_{ij}(k,t)}{\phi_{\ell\ell}(k,t)} - \frac{\delta_{ij}}{3}; \quad \alpha_n = k_n/k; \quad E(k,t) = \phi_{\ell\ell}(k,t)/2 \quad (4)$$

$$F_{ij}(\underline{H}, \underline{\alpha}) = (\delta_{i\ell} - \alpha_i \alpha_\ell)(\delta_{jn} - \alpha_j \alpha_n) \{ \delta_{\ell n} (1 - (15+7a) H_{pq} \alpha_p \alpha_q) - 2a H_{\ell n} \}$$

is introduced in order to integrate analytically the closed basic equations over a spherical shell of radius k . A final integro-differential equation for the new radial tensor $\phi_{ij}(k,t)$ is deduced.

After comparisons of the model with the analytical solution for the rapid distortion, an explicit expression for the function $a(k,t)$ is found in terms of both \underline{H} and the Lagrangian strain tensor \underline{S} associated with the mean flow.

Method 2 directly retains the basic Eq. (1) but adopts an approximated form of the closed nonlinear term $T_{ij}(\vec{k},t)$. The modeled expression based on an interpolation process, depends on local values computed (using the three-dimensional Extended-Eddy Quasi-Normal Hypothesis Model) for a small set of wave vectors \vec{k} and for a few values of the time.

The detailed basic equations and the two typical methods have been previously described in Cambon et al. (1981) and in Bertoglio (1981).

In both methods only one constant λ , which comes from the eddy-damping rate $\eta(k,t)$, has to be adjusted. The chosen value of λ ($= 0.36$) has been found by Andre and Lesieur (1977) from the test field model for the case of isotropic turbulence.

III. Numerical Procedure and Mesh Requirements

In Method 1, a finite-difference scheme is developed to solve the equations for the components of the radial tensor written in the common form

$$\frac{\partial \phi}{\partial t} + 2\nu k^2 \phi = \psi$$

In order to avoid a limiting stability condition resulting from an explicit viscous term, the following efficient scheme

$$\phi(k, t + \Delta t) = \phi(k, t) e^{-\nu k^2 \Delta t} + \frac{1 - e^{-2\nu k^2 \Delta t}}{2\nu k^2} \psi(k, t)$$

is adopted.

A large constant step in time is used (for the calculated flows the number of time steps is always smaller than one hundred). A fixed logarithmic discretizing in the k-direction of the form

$$k(L) = 5 \times 2^{(L-1)/D}; \quad k(30) = 2 \left(\frac{\nu}{\epsilon} \right)^{1/4}; \quad L = 1.30$$

is chosen.

In Method 2, the final closed equation for $\phi_{ij}(k, t)$ is numerically solved along the characteristic curves corresponding to the whole differential operator. The three-dimensional calculation gives computer values for 18 spherical shells and for 32 directions on each hemisphere.

IV. Generation of Initial Data

Starting from the initial given values for $\overline{u_i u_j}$ and ϵ at $t = t_0$ the spectral computations require spectral data generated by the following successive algorithms:

Algorithm 1 - Generation of the energy spectrum $E(k)$ by the expression

$$E(k) = 1.5 \epsilon^{2/3} L^{5/3} \frac{(kL)^n}{[1+(kL)^2]^{(n+10)/12}} e^{-1.5\gamma(k\xi)^{4/3}}; \quad \xi = \left(\frac{\nu^3}{\epsilon} \right)^{1/4}$$

$$L = \beta \frac{(q^{2/3})^{3/2}}{\epsilon}; \quad \xi = \left(\frac{\nu^3}{\epsilon} \right)^{1/4} \quad \text{for } 3 < n < 4$$

The coefficients β and α are fixed in order to obtain exactly the given values of $\overline{u_i^2}$ and ϵ .

Algorithm 2 - The nonisotropic tensor is deduced from the relation

$$H_{ij}(k, t_0) = \frac{1}{4} \left(5 + \frac{k}{E} \frac{dE}{dK} \right) \left(\frac{\overline{u_i u_j}}{2} - \frac{\delta_{ij}}{3} \right)_{t=t_0}$$

For Method 1, the algorithm is completed by the calculation of

$$s_{ij}(t_0) = \delta_{ij} - \frac{15}{4} \left(\frac{\overline{u_i u_j}}{q^2} - \frac{\delta_{ij}}{3} \right)$$

required to evaluate $a(k, t_0)$.

Algorithm 3 - Generation of $\phi_{ij}(\vec{k}, t_0)$ (required only in Method 2). The isotropic function F_{ij} is used with the results of the previous algorithms. For special cases, more physical initial spectra are deduced at time t_0 with a "precomputation", starting from isotropic conditions at $t = 0$, and applying a suitable mean-velocity gradient.

V. Comparison of Prediction with Experiments

Numerical solutions of Method 1 are presented for all the test cases (Flow 0370), using exactly the given values. This required the generation of spectral data (Algorithms 1 and 2).

With Method 2 only a partial number of cases were computed. Various adjustments of the initial spectra were tested.

For Case 0371, Methods 1 and 2 are basically equivalent to the method initially proposed by Andre and Lesieur (1977). Good agreement is obtained with Method 1, but small discrepancies appear in Method 2 due to the interpolation process used. In Case 0372A, Method 1 overpredicts the magnitude of the decaying kinetic energy. Unfortunately the moderate overestimation will be seen to be of the same order as the small effects of the mean rotation. Indeed, when $\omega = 20$ rad/s or $\omega = 80$ rad/s, the same decaying trends appear; the supplemented points (+ +) correspond to the simplified expression (2) for $n(k)$ and indicate the possible calculated extremes, when the mean rotation is (or is not) introduced in the nonlinear terms. It must be noted that the initial conditions are non-isotropic and consequently the mean rotation is acting simultaneously through both the linear and non-linear terms. In the return-to-isotropy experiment of Uberoi (0373A-D), the decreasing tendency of the radial component v^2 of the stress tensor is correctly predicted but the small streamwise contribution u^2 reverts too quickly towards isotropy. Small discrepancies may be due to a residual contraction at the end of the distorting duct (see Plates 65 and 66, Case 0373C). It should also be noted that the Reynolds-stress components are strongly nonisotropic and Algorithm 2 does not ensure a more isotropic dissipative range. In Case 0373E, two sets of initial spectra were generated (DATA 1 and 2). DATA 1 is found from the standard Algorithms 1 and 2, while DATA 2 takes into account the distortion history (deduced from Method 2). The results underline the strong influence of the initial spectra shapes. Method 2, used with the three-dimensional spectra corresponding to DATA 2, gives similar results to Method 1. In Case 0374A poor agreement occurs especially in the downstream part of the duct. In Method 1 two different energy spectra

were introduced. DATA 1 results from the standard Algorithms 1 and 2. DATA 2 takes into account the shape of a measured spectrum given by Townsend. In Method 2, using DATA 2, some attempts were performed with different mean-velocity gradients in the initial part of the duct arguing a progressive buildup of the mean strain. In Case 0374B, both methods exhibit more satisfactory agreement. The numerical experiments performed by Method 2 correspond to adjustments of initial data of streamwise velocity. Some success is then achieved at the end of the distorting duct. For Case 0375, Method 1 with the standard Algorithms 1 and 2 gives good results.

Concerning shear-flow turbulence, less satisfactory agreement occurs for a large shear rate (Case 0376B) with Method 1. For both cases, it was very difficult to generate spectral information, especially for the non-diagonal component \overline{uv} .

VI. Concluding Remarks

The present methods may be considered as a first attempt to predict nonisotropic homogeneous flows, using the full spectral basic equations. It is also relevant to point out that in both methods, the parameters are optimized once and for all in comparison to other theories (i.e., rapid distortion or the test field model). No adjustment of constants with typical experiments is required. Some improvements of the methods will be made, when some additional spectral data become available. For future developments of such modeling, it seems that the three-dimensional approach would be appropriate to take into account exactly dominant linear processes (see Method 2). Method 1 is less cumbersome to handle and much less expensive in computing time. Flows in which distortion and rotation are acting simultaneously must be considered with special care in the small-wave-numbers range. Extensions of the spectral methods to complex nonhomogeneous turbulent flows will be attempted in the future.

References

- Andre, J. C., and M. Lesieur (1977). "Influence of helicity on the evolution of isotropic turbulence at high Reynolds numbers," J. Fluid Mech., 81, 187.
- Bertoglio, J. P. (1981). (To be published, Proc. 3rd Turbulent Shear Flow Conf., Davis, 1981).
- Cambon, C., D. Jeandel, and J. Mathieu (1981). "Spectral modelling of homogeneous non-isotropic turbulence," J. Fluid Mech., 104, 247.
- Orszag, S. A., (1970). "Analytical theories of turbulence," J. Fluid Mech., 41, 363.



W. L. Chow

COMPARISON OF COMPUTATION WITH EXPERIMENT

Summary Report

(Calculation of the Secondary Flow of the
Second Kind Through a Fully Elliptic Procedure)

by

A. Nakayama, W. L. Chow, and D. Sharma*

Computer Group Number: 23¹

Case 0111

INTRODUCTORY REMARKS

A general fully elliptic calculation scheme has been developed by Nakayama (1981) along with a three-dimensional transformation procedure for arbitrary non-orthogonal coordinate systems, for the purpose of the three-dimensional turbulent separated flows within ducts of arbitrary geometrical configurations. As a sequel to the series of various test flow calculations, this fully elliptic scheme has been employed for the calculation of a three-dimensional developing flow in a square duct with a two-equation ($k-\epsilon$) model coupled to the algebraic stress model. Although the flow of this class may well be treated more economically as a three-dimensional parabolic flow following Patankar and Spalding (1972), it is still worthwhile to solve it as an elliptic problem since all viscous-flow phenomena are governed by the Navier-Stokes equation.

This summary focuses on the results of the calculations for the developing turbulent flow in a square duct. Details of the development of the present elliptic scheme, excluded in this summary, are given by Nakayama (1981), who also presents various results of calculations ranging from fully developed turbulent flow in a trapezoidal duct to three-dimensional turbulent separated flow in a rectangular diffuser.

DESCRIPTION OF THE METHOD

A general form common to all six governing equations, namely, the continuity equation, the u , v , and w time-averaged momentum equations and the transport equations for the turbulent kinetic energy, k , and its rate of dissipation, ϵ , may be written in a Cartesian tensor form as

$$\frac{\partial}{\partial x_i} (u_i \phi - \Gamma_\phi \frac{\partial \phi}{\partial x_i}) = s_\phi \quad (1)$$

*University of Illinois, Urbana-Champaign, IL 61801

where ϕ denotes any one of the dependent variables, Γ_ϕ is the corresponding diffusion coefficient, and the source term is denoted by s_ϕ .

As already indicated, the present scheme employs the transformation procedure for arbitrary non-orthogonal coordinate systems so as to acquire the generality in the application for elliptic flows (for the square duct, the transformation would not be necessary). Through this transformation procedure, Eq. 1 can be transformed into an arbitrary non-orthogonal coordinate system (ξ, η, ζ) as

$$\begin{aligned} & [J(\bar{d}_1 \cdot \bar{v}) \phi - J \Gamma_\phi \bar{d}_1^2 \phi_\xi]_\xi \\ & + [J(\bar{d}_2 \cdot \bar{v}) \phi - J \Gamma_\phi \bar{d}_2^2 \phi_\eta]_\eta \\ & + [J(\bar{d}_3 \cdot \bar{v}) \phi - J \Gamma_\phi \bar{d}_3^2 \phi_\zeta]_\zeta = s_\phi^* \end{aligned} \quad (2a)$$

with

$$s_\phi^* = s_{c\phi} + J s_\phi \quad (2b)$$

$$\bar{d}_1 = (\bar{r}_\eta \times \bar{r}_\zeta)/J, \quad \bar{d}_2 = (\bar{r}_\zeta \times \bar{r}_\xi)/J, \quad \bar{d}_3 = (\bar{r}_\xi \times \bar{r}_\eta)/J \quad (2c)$$

$$J = \bar{r}_\xi \cdot (\bar{r}_\eta \times \bar{r}_\zeta) = [\bar{r}_\xi, \bar{r}_\eta, \bar{r}_\zeta] \quad (2d)$$

and

$$\begin{aligned} s_{c\phi} = & [J \Gamma_\phi (\bar{d}_1 \cdot \bar{d}_2) \phi_\eta]_\xi + [J \Gamma_\phi (\bar{d}_1 \cdot \bar{d}_2) \phi_\xi]_\eta \\ & + [J \Gamma_\phi (\bar{d}_2 \cdot \bar{d}_3) \phi_\zeta]_\eta + [J \Gamma_\phi (\bar{d}_2 \cdot \bar{d}_3) \phi_\eta]_\zeta \\ & + [J \Gamma_\phi (\bar{d}_3 \cdot \bar{d}_1) \phi_\xi]_\zeta + [J \Gamma_\phi (\bar{d}_3 \cdot \bar{d}_1) \phi_\zeta]_\xi \end{aligned} \quad (2e)$$

where the bar indicates vector quantities such as the position vector \bar{r} and the velocity vector \bar{v} , while the subscripts ξ , η , and ζ denote their partial derivatives.

The particular form of Eq. 2a can be justified by the fact that the contribution of $s_{c\phi}$ (see Eq. 2e), is expected to be insignificant for any reasonable coordinate system since the term $s_{c\phi}$ contains only the cross-derivatives (the term vanishes when the coordinates are orthogonal).

The discretization has been performed by integrating Eq. 2a over a volume element in the transformed domain. The resulting finite-difference form is so universal that it can be used for any coordinate by simply specifying the transformation area vectors, \bar{d} 's, either analytically or numerically. For the square duct

$$\bar{d}_1 = \bar{i}, \bar{d}_2 = \bar{j} \text{ and } \bar{d}_3 = \bar{k},$$

Equation 2a naturally reduces to Eq. 1.

ALGEBRAIC STRESS MODEL

The algebraic stress model for the secondary flow of the second kind used for the study on developing flows is essentially the same as the one developed by Launder and Ying (1973) and Gessner et al. (1976). The stress model in Cartesian coordinates prior to the transformation (with x being the primary flow direction), is given by

$$\overline{-u'^2} = 2 v_t u_x - C'_{ko} k \quad (3a)$$

$$\overline{-u'v'} = v_t (u_y + v_x) \quad (3b)$$

$$\overline{-u'w'} = v_t (u_z + w_x) \quad (3c)$$

$$\overline{-v'^2} = (c' C_D k^3 / \epsilon^2) u_y^2 - c'_k k \quad (3d)$$

$$\overline{-w'^2} = (c' C_D k^3 / \epsilon^2) u_z^2 - c'_k k \quad (3e)$$

$$\overline{-v'w'} = (c' C_D k^3 / \epsilon^2) u_y u_z \quad (3f)$$

with

$$v_t = c_D k^2 / \epsilon \quad (3g)$$

where the bar here denotes the time-averaged mean, and the prime indicates the fluctuating component. The subscripts x , y , and z are used for the partial derivatives. As listed above, slightly modified expressions are used for the stress components associated with the primary flow velocity fluctuation

$$\overline{(u'^2, u'v' \text{ and } u'w')}$$

in order to account for the strong acceleration at the inlet region. The inclusion of these axial diffusion terms is possible only for the fully elliptic procedure such as the present one.

The empirical constants (they are linked by two independent constants which can be arbitrarily chosen among themselves) have been set to:

$$C_D = 0.09, c' = 0.0185, c'_k = 0.552, c'_{ko} = 0.915 \quad (4)$$

MISCELLANEOUS MATTERS

A usual near-wall treatment based on the constant stress layer has been employed to preclude the need for fine meshes near the wall. In order to reduce computer execution time, the exit boundary condition has been transformed from the Neumann type to the Dirichlet type. Prior to the full calculation, the values at the exit have been economically provided through the fully developed flow calculation using the two-dimensional version of the present scheme.

Due to symmetry, only one quadrant of the square duct may be taken for the calculation domain. The grid system, $9 \times 9 \times 30$ (30 axial stations) which is highly concentrated toward the inlet and near the wall, has been employed to cover the axial distance of 84 hydraulic diameters. Since the present scheme is based on the fully elliptic procedure, there is essentially no mesh requirement so that the grid system can be constructed faithfully according to the desired distribution of spatial resolution.

Because of the limited available memory field, the grid refinement has been performed only on the cross-sectional plane of a square duct through fully developed flow calculations using the grid systems 9×9 and 15×15 . No significant grid number effects have been observed on the solutions, except that the secondary flow magnitude tends to be somewhat amplified for the finer grid system. The conclusion may be drawn from the comparison (see Fig. 1) that the grid system 9×9 is quite adequate for a quadrant of a square duct.

Prior to the turbulent flow calculations, the present finite-difference scheme has been extensively tested for laminar flows under various geometrical configurations and the numerical accuracy, without the presence of the ambiguity due to imperfection of the turbulence model, has been thoroughly checked. The effects of non-orthogonality of coordinates and those due to the practice of hybrid difference have been found to be insignificant.

COMPARISON WITH THE EXPERIMENT

The overall performance of the algebraic stress model when coupled to the $k-\epsilon$ model is satisfactory in most respects. Some specific features of the model performance under the employment of the present fully elliptic scheme are listed below:

- (a) The predicted pressure drop (the wall-friction coefficient) agrees well with the experiment. The distortion of the wall shear profile over the periphery, however, has been predicted to be more pronounced than the experiment (see Plates 1 to 3).
- (b) The predicted axial variation of the velocity field has been found to be in fairly good accord with the experimental data although the centerline velocity peak is predicted to be about seven hydraulic diameters upstream of the peak observed in the experiment. The velocity level along the wall bisector is in good agreement with experiment, yet the velocity level along the corner bisector has been

underestimated throughout the flow development (see Plates 1, 2, 4 and 5).

- (c) The predicted shear stress opposing the primary flow motion was found to be in good agreement with experiment. The characteristic pattern of the shear stress having the opposite sign has been correctly realized by the prediction toward the fully developed stage (see Plates 5, 6 and 7).
- (d) The degree of bulge toward the corner is underestimated on the kinetic energy contour maps indicating a relatively high kinetic energy field maintained fairly close to the corner. The spreading rate of the kinetic energy boundary layer is overestimated. These failures are, however, consistent with the underprediction of the secondary-flow velocity level along the diagonal in contrast with the overestimation along the wall bisector (see Plates 3, 6 and 7).

Finally, certain suggestions which may lead to possible improvements are listed below.

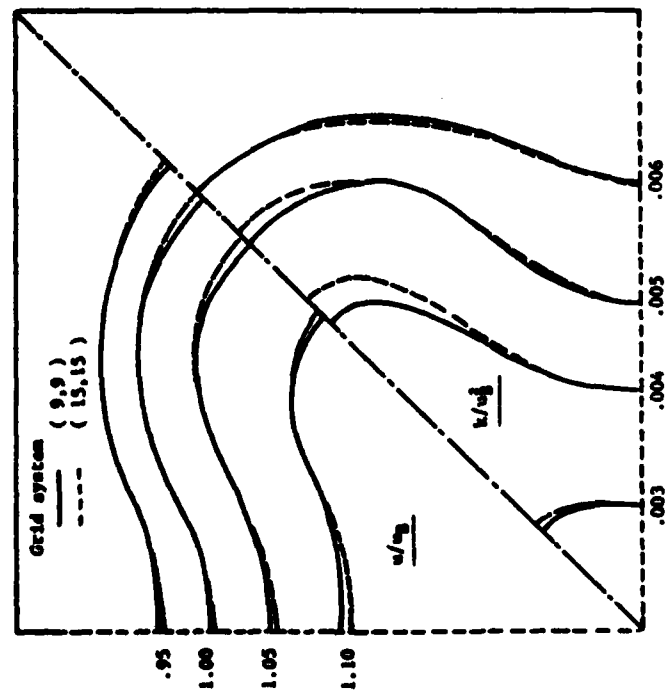
- (a) Increase the Prandtl number for k to delay the diffusion process within the boundary layer (at the same time, C_D may be slightly decreased).
- (b) Extend the calculation domain farther downstream to eliminate "tail-off" behavior observed for the primary flow-velocity field along the wall bisector.

ACKNOWLEDGMENT

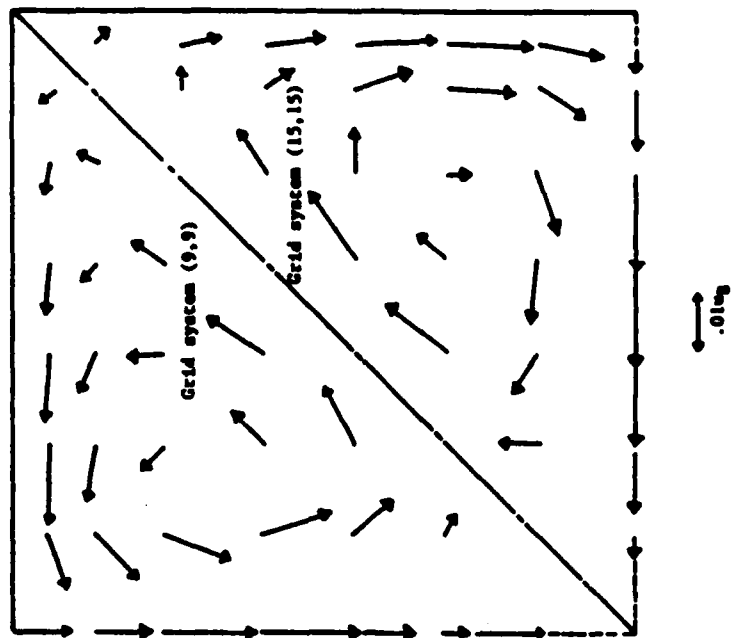
This work was partially supported by U.S. Army Research Office Research Grant DAAG29-79-C-0184.

References

- Gessner, F. B., A. F. Emery, and F. K. Po (1976). "A Reynolds stress model for turbulent corner flows, Part I and Part II, ASME, J. Fluids Engr.
- Launder, B. E., and W. M. Ying (1973). "Prediction of flow and heat transfer in ducts of square cross-section," Heat and Fluid Flow, 3, 2.
- Nakayama, A. (1981). "A three-dimensional flow within conduits of arbitrary geometrical configurations," Ph.D. Thesis, University of Illinois at Urbana-Champaign.
- Patankar, S. V., and D. B. Spalding (1972). "A calculation procedure for heat, mass, and momentum transfer in three-dimensional parabolic flow," Int. J. of Heat and Mass Transfer, 15.

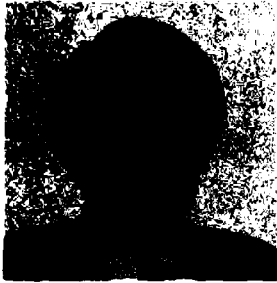


(a) Axial Velocity and Kinetic Energy



(b) Secondary Flow Velocity Vectors

Figure 1. Grid number effects: fully developed flow at $Re = 83,000$.



COMPARISON OF COMPUTATION WITH EXPERIMENT

Summary Report

(A Numerical Study for the Two-Dimensional Stalled Airfoil)

by

C. M. Rhie, W. L. Chow, and D. Sharma*

Computer Group Number: 23²

C. M. Rhie

Case 0441

A finite-difference method has been developed by Rhie (1981) to solve the two-dimensional incompressible, steady, time-averaged Navier-Stokes equations in general curvilinear coordinates for the prediction of the flow over an isolated airfoil with separation. The k - ϵ equation turbulence model is utilized. The present calculation method is an extension and generalization of the procedure of Gosman and Pun (1973). However, a significant modification is introduced to use the ordinary grid arrangement, instead of the usual staggered grid arrangement which is not efficient in the present application. In addition, body-fitted coordinates are generated for the finite-difference computation scheme.

Governing Equations

The continuity equation and the time-averaged Navier-Stokes equations in conjunction with the isotropic turbulent viscosity hypothesis are written in a Cartesian tensor form as

$$\frac{\partial}{\partial x_i} \rho u_i = 0 \quad (1)$$

$$\frac{\partial}{\partial x_i} \rho u_i u_j = - \frac{\partial p}{\partial x_j} + \frac{\partial}{\partial x_i} [(\mu + \mu_t) (\frac{\partial u_i}{\partial x_j} + \frac{\partial u_j}{\partial x_i}) - \frac{2}{3} \rho k \delta_{ij}] \quad (2)$$

where ρ is the mean density, u_j the mean velocity, and p the mean pressure. From the k - ϵ turbulence model (Jones and Launder, 1972), the turbulent viscosity, μ_t , is given by

$$\mu_t = C_\mu \rho k^2 / \epsilon \quad (3)$$

The model thus involves two equations; one for k and another for ϵ as follows:

$$\frac{\partial}{\partial x_i} \rho u_i k = \frac{\partial}{\partial x_i} \left(\frac{\mu_t}{\sigma_k} \frac{\partial k}{\partial x_i} \right) + P - \rho \epsilon \quad (4)$$

*University of Illinois, Urbana-Champaign, IL 61801

$$\frac{\partial}{\partial x_1} \rho u_1 \epsilon = \frac{\partial}{\partial x_1} \left(\frac{\mu_t}{\sigma_\epsilon} \frac{\partial \epsilon}{\partial x_1} \right) + \frac{\epsilon}{k} (C_1 P - C_2 \rho \epsilon) \quad (5)$$

where P is the rate of production of turbulent kinetic energy. This model contains five empirical constants and they are ascribed the following values:

$$C_\mu = 0.09 ; C_1 = 1.45 ; C_2 = 1.90 ; \sigma_k = 1.0 ; \sigma_\epsilon = 1.3 \quad (6)$$

Modeling of a Near Wall

The wall-function method is used to save grid points within the laminar sublayer region. The following functions are used to bridge the near-wall region:

$$\tau_w = (u_p / y_p) [u y_p^+ \kappa / \ln(E y_p^+)] \quad (7)$$

where

$$y_p^+ = \rho (k_p c_\mu^{1/2})^{1/2} y_p / \mu$$

$$\epsilon_p = (c_\mu^{1/2} k_p)^{3/2} / \kappa y_p \quad (8)$$

$$\int_0^{y_p} \epsilon dy = (c_\mu^{1/2} k_p)^{3/2} (1/\kappa) \ln(E y_p^+) \quad (9)$$

$$dk/dy|_w = 0 \quad (10)$$

The subscript p refers to the grid node next to the wall and κ and E are the constants from the law of the wall, with values of 0.4 and 8.8, respectively.

Transformation of the Basic Equations

If new independent variables ξ and η are introduced, the form of the conservation law should be changed according to the general transformation

$$\xi = \xi(x, y), \quad \eta = \eta(x, y)$$

Partial derivatives are transformed through

$$f_x = (y_\eta f_\xi - y_\xi f_\eta) / J, \quad f_y = (-x_\eta f_\xi + x_\xi f_\eta) / J \quad (11)$$

where J is the Jacobian of the transformation, $J = x_\xi y_\eta - x_\eta y_\xi$. Upon introducing definitions of

$$G_1 = u y_\eta - v x_\eta, \quad G_2 = v x_\xi - u y_\xi \quad (12)$$

$$\alpha = x_{\eta}^2 + y_{\eta}^2, \quad \beta = x_{\xi}x_{\eta} + y_{\xi}y_{\eta}, \quad \gamma = x_{\xi}^2 + y_{\xi}^2, \quad (13)$$

the following integral conservation relation is obtained for an arbitrary scalar dependent variable ϕ :

$$\int_B \{ \rho G_1 \phi d\eta - \rho G_2 \phi d\xi \} = \int_B \{ (\Gamma^{\phi}/J)(\alpha\phi_{\xi} - \beta\phi_{\eta}) d\eta - (\Gamma^{\phi}/J)(\gamma\phi_{\eta} - \beta\phi_{\xi}) d\xi \} + \iint_R S^{\phi} J d\xi d\eta \quad (14)$$

where B is the boundary of a region R.

Method of Computation

1. General Transport Equations

In terms of the notation in Fig. 1 for a typical grid node P enclosed in its cell and surrounded by its neighbors N, S, E, and W, a relation between ϕ_p and the neighboring values is obtained through the finite-difference formulation:

$$A_p \phi_p = A_E \phi_E + A_W \phi_W + A_N \phi_N + A_S \phi_S + S^{\phi} J \Delta\xi \Delta\eta - \{ [(\Gamma^{\phi}/J) \beta \phi_{\eta} \Delta\eta]_W^E + [(\Gamma^{\phi}/J) \beta \phi_{\xi} \Delta\xi]_S^N \} \quad (15)$$

where the coefficients A involve the convection, diffusion, area, etc. The terms within the brace in Eq. 15 are the results of cross-derivatives in the diffusion term due to the use of non-orthogonal coordinates. These terms are usually very small and can be combined into the source term and treated as known quantities. ADI is used for the iteration.

2. Pressure Equation

While equations of this kind are used for each of the variables u, v, k, and ϵ for every cell, an equation for the remaining unknown pressure should be obtained by combining the continuity and momentum equations. The preliminary set of velocity components, u^* and v^* , based on the estimated pressure field of p^* will in general not satisfy the continuity equation. Instead, a net mass source m_p is produced for the point P as

$$m_p = (\rho G_1^* \Delta\eta)_e - (\rho G_1^* \Delta\eta)_w + (\rho G_2^* \Delta\xi)_n - (\rho G_2^* \Delta\xi)_s \quad (16)$$

where the superscript * for G_1 and G_2 denotes that they are based on the u^* and v^* . To remove the mass source, m_p , one defines

$$p = p^* + p' \quad (17)$$

where p' is the pressure correction. The corresponding convective components can be

assumed as

$$G_1 = G_1^* + Bp'_\xi \quad \text{and} \quad G_2 = G_2^* + Cp'_\eta \quad (18)$$

where B and C are derived from the momentum finite-difference equations. Upon substituting Eq. 18 into Eq. 16, the finite-difference form for the pressure correction similar to Eq. 15 is obtained. Special treatment was necessary to suppress the oscillations in the pressure field which occurred initially with the ordinary grid arrangement of Rhie (1981). The overall solution procedure is similar to that of Gosman and Pun (1973).

Generation of Coordinate System

The scheme developed by Sorenson and Steger (1977) is adopted for the present application. In their method curvilinear coordinates are generated as a solution of Laplace's equation. A simple clustering method is used for the control of mesh spacing since the grid points derived from the convergent solution of Laplace's equation is seldom adequate. In the present work, minor modifications to the grid generation method is done to avoid the discontinuity in the wake region as is seen in Fig. 2a. The major part of the grid system still remains but the discontinuity is smoothed out by fourth-order polynomials. The resulting grid system is illustrated in Fig. 2b.

Results and Discussion

The numerical accuracy of the present method had been rigorously tested by Rhie (1981) in a variety of laminar flow cases. With this established numerical accuracy, we devoted our efforts to the prediction of the flow past an NACA 4412 airfoil at maximum lift at 13.87° angle of attack. Since the experiment was carried out in the confined wind-tunnel test section, the blockage effect was also simulated in our computations. The computational domain was defined as illustrated in Fig. 3. All the lengths were nondimensionalized by the chord length. The horizontal and vertical Cartesian coordinate axes were used for the computation. As shown in Fig. 3, a fictitious upstream wall boundary was assumed to be composed of convex and concave circular arcs whose centers are located at $x = -3$ and $x = -0.5123$, respectively. The specific geometry was then characterized by the angle θ_1 at the inflection point of the curve. The front outer boundary was defined by half circular arc covering inlet plane at $x = -3$. Uniform approaching free-stream condition was imposed on this circular boundary.

To test the effect of the outer boundaries, several different values of θ_1 and θ_2 were tried. The effect of θ_1 on the flow near the airfoil was almost negligible. However, it changed the reference velocity located at (1.1466, -1.1209) in the experiment. When θ_1 varied from 0 to 10 degrees, the reference velocity, U_{ref} , changed

approximately 2%. Although the flow condition near the airfoil was barely changed, this 2% change in reference velocity, made the computational result vary within a certain range. The diffuser angle, θ_2 , was set to 4° as indicated by Wadcock (1978) and the uniform u-velocity boundary condition was imposed on the rear outer boundary. Wake-profile boundary conditions at the exit plane of the diverging diffuser section was abandoned due to numerical difficulties. The v-velocity component and turbulence quantities were extrapolated from the inner solution. Virtually no influence of this rear outer boundary condition was observed on the inner solution near the airfoil. Wind-tunnel-wall boundary layers were neglected since the displacement effects were expected to be negligible. Instead, slip boundary conditions were imposed on the tunnel walls. While the effect of outer boundary condition was almost negligible, the grid resolution on the airfoil surface was critical. Poor grid spacing in the stream-wise direction near the leading edge could not resolve the sharp variation there, and this altered downstream flow conditions significantly. Therefore, an extremely fine grid near the leading-edge region was necessary.

After all these numerical experiments, the final computation was performed with a 95×31 grid. A total of 63 points were distributed on the airfoil. The grid spacing on the airfoil surface was 0.0015 and 0.009 chords at the leading and trailing edge, respectively. The first grid spacing in η -direction was 0.00125 chords. The converging and diverging sections were defined with $\theta_1 = \theta_2 = 4^\circ$. Reynolds number was based on the reference velocity which was unknown a priori in the computation; hence, the ratio of the reference velocity to the approaching free-stream velocity had to be guessed based on the preliminary results.

Grid dependence was also checked by computing the same conditions with a 95×16 grid. Since additional grid refinement was not possible using CYBER 175 for the present study, the number of grid points in the η -direction was halved, while that in the ξ -direction was kept the same. The pressure, u-velocity, and Reynolds stresses are shown in Fig. 4. It should be mentioned that the u-velocity direction coincides with the airfoil chord line. As is seen in Fig. 4a, the surface-pressure distribution was almost insensitive to the grid change. However, with the coarse grid, a small separation bubble size was produced (Fig. 4b) and smaller magnitude of the Reynolds stresses were predicted in its region (Fig. 4c,d). For the confidence on the computed results, further grid tests by refinements are suggested using a large computer.

The time and storage requirement of the FORTRAN IV computer program were 0.0083 sec/grid node/iteration and 23,440 words plus 37.8 words/grid node. It took approximately 40 min to carry out 1,000 iterations for the convergence in the present problem using the 95×31 grid.

Acknowledgment

This work was partially supported by U.S. Army Research Office through Grant DAAG 29-79-C0184.

References

- Gosman, A. D. and W. M. Pun (1973). "Calculation of recirculating flows," Imperial College, Dept. of Mech. Engr. Rep. HTS/73/2.
- Jones, W. P. and B. E. Launder (1972). "The prediction of laminarization with a two-equation model of turbulence," Int. J. of Heat and Mass Transfer, __, 304-314.
- Rhie, C. M. (1981). "A numerical study of the flow past an isolated airfoil with separation," Ph.D. Thesis, Dept. of Mech. and Ind. Engr., Univ. of Illinois at Urbana-Champaign.
- Sorenson, R. L. and J. L. Steger (1977). "Simplified clustering of nonorthogonal grids generated by elliptic partial differential equations," NASA TM 73252.
- Wadcock, A. J. (1978). "Flying hot-wire study of two-dimensional turbulent separation on an NACA 4412 airfoil at maximum lift," Ph.D. Thesis, Cal. Inst. of Tech., Pasadena, California.

AD-A136 034

THE 1980-81 AFOSR (AIR FORCE OFFICE OF SCIENTIFIC RESEARCH)-HTTM (HEAT TR. (U) STANFORD UNIV CA DEPT OF MECHANICAL ENGINEERING S J KLINE ET AL. SEP 81
AFOSR-TR-83-1003 F49620-80-C-0027

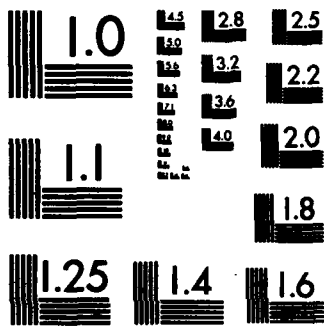
4/6

UNCLASSIFIED

F/G 20/4

NL

			A									
	R					R			A			
			V	P				R	V			
R								V			V	V
											R	V
		P				A					V	



MICROCOPY RESOLUTION TEST CHART
NATIONAL BUREAU OF STANDARDS-1963-A

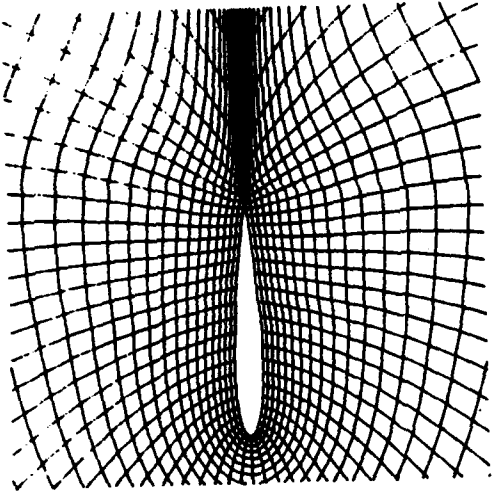
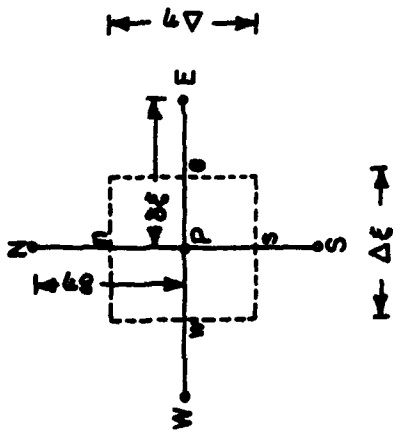


Fig. 2a

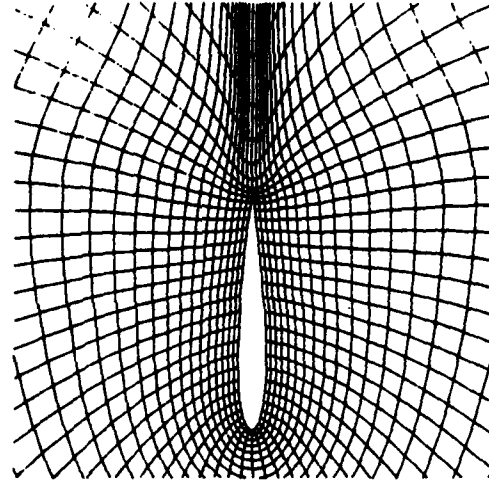
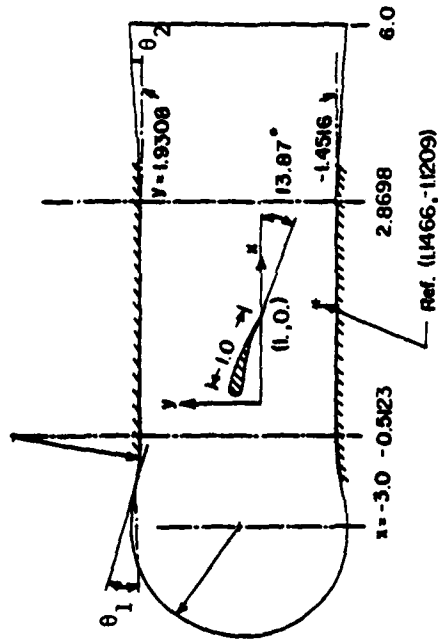


Fig. 2b



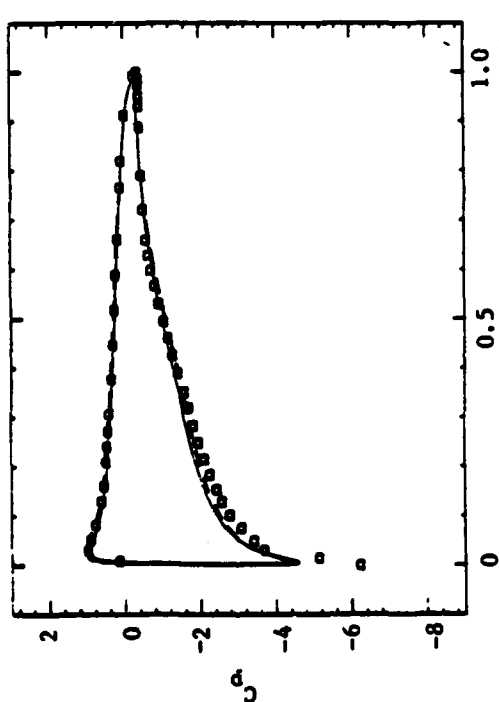


Fig. 4a Surface pressure distribution

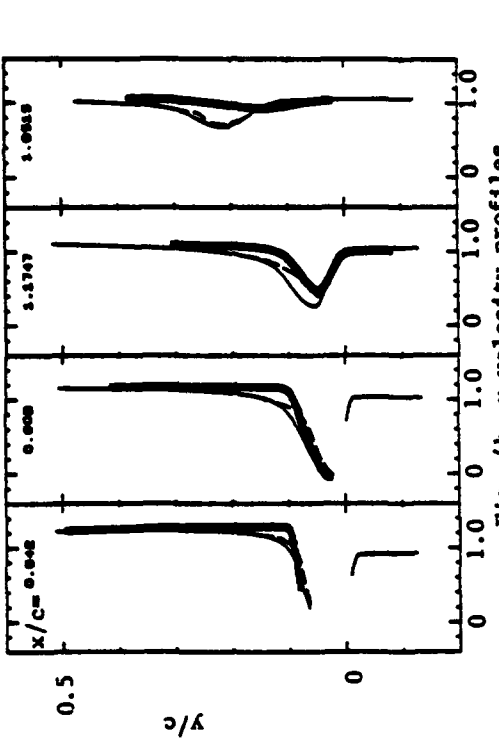


Fig. 4b u-velocity profiles

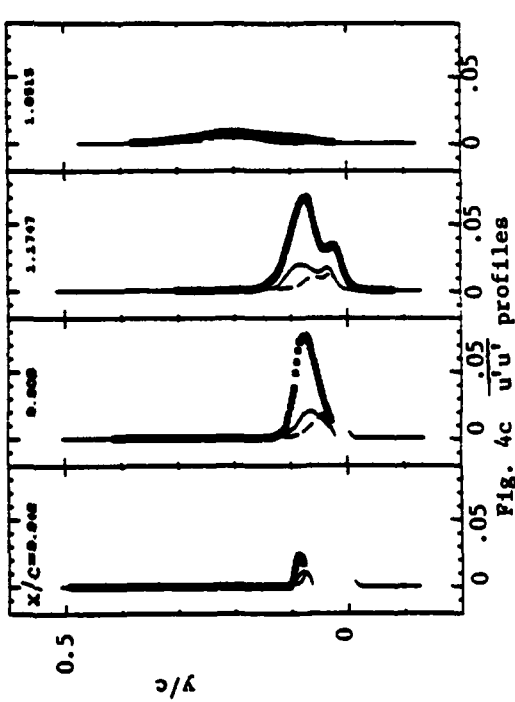


Fig. 4c $u'u'$ profiles

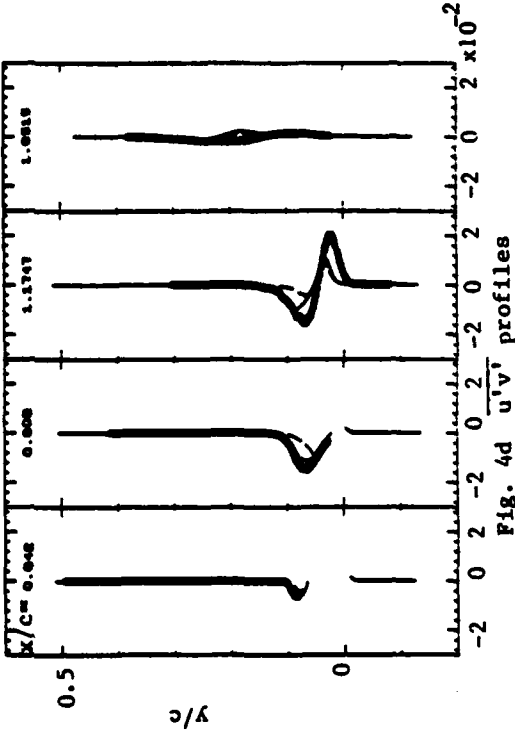


Fig. 4d $u'v'$ profiles

—, present result (95X31); - - -, present result (95X16); □, experiment (ref. 5)



COMPARISON OF COMPUTATION WITH EXPERIMENT

Summary Report

by

J. Cousteix, R. Houdeville, D. Arnal, A. Cler,
P. Berrue, P. Dubois, E. G. Tulapurkara*

Computer Group Number: 22

J. Cousteix

Cases 0111, 0141, 0142, 0143, 0211, 0231, 0232, 0233, 0261, 0381, 0382, 0371, 0374, 0375, 0376, 0431, 0471, 0511, 0512, 0612, 8101, 8201, 8411, 8621

Several methods have been used for computing the test cases. The codes REMI-2D, -2D1, -DIFFU are based on an integral method; ELODIE-KELM, -KELM1, -KELM2, -KEVISC solve the partial differential equations of the boundary layer using a k-ε model; ELODIE-COIN has been developed for corner flows; MULTI solves equations for all components of the Reynolds-stress tensor, and uses the concept of multiple time scales; LRRLW solves the system proposed by Launder-Reece-Rodi, but the constant C_{ϵ_1} of the "production" term in the ε-equation is made a function of the mean rate of strain by comparing the ε-equation with the model of tensorial volume of turbulence developed by Lin and Wolfshtein (1980).

According to the proposed classification, the method descriptors are:

<u>Names of programs</u>	<u>Method descriptor</u>
REMI	
2D, 2D1	HN
DIFFU	HN
ELODIE	
KELM, KELM1, KELM2, KEVISC	BKEX
COIN	AOPX
MULTI	RSEC
LRRLW	RSEC

Description of REMI-2D, -2D1, -DIFFU

The integral method is based on the solution of the global equations (partial differential equations integrated between the wall and the outer edge of the boundary layer): continuity equation, momentum equation and enthalpy equation:

*CERT/DERT, Complexe Aérospatiale, 31055 Toulouse, France

$$C_E = \frac{1}{\rho_e U_e R} \frac{d}{dx} \rho_e U_e R (\delta - \delta_1) ; \quad C_E = \frac{d\delta}{dx} - \frac{V_e}{U_e} \quad (R1)$$

$$\frac{C_f}{2} = \frac{d\theta}{dx} + \theta \left(\frac{H+2}{U_e} \frac{dU_e}{dx} + \frac{1}{\rho_e R} \frac{d}{dx} \rho_e R \right) \quad (R2)$$

$$\frac{\phi_w}{\rho_e U_e h_{1e}} = \frac{1}{\rho_e U_e R} \frac{d}{dx} \rho_e U_e R \Delta \quad (R3)$$

where the following notation is used:

$$\delta_1 = \int_0^\delta \left(1 - \frac{\rho U}{\rho_e U_e} \right) dy ; \quad \theta = \int_0^\delta \frac{\rho U}{\rho_e U_e} \left(1 - \frac{U}{U_e} \right) dy ; \quad H = \frac{\delta_1}{\theta}$$

$$\Delta = \int_0^\delta \frac{\rho U}{\rho_e U_e} \left(\frac{h_1}{h_{1e}} - 1 \right) dy ; \quad \delta_3 = \int_0^\delta \frac{\rho U}{\rho_e U_e} \left(1 - \frac{U^2}{U_e^2} \right) dy$$

h_1 = total enthalpy

R = wall transverse radius (axisymmetric flow)

Subscripts: e = external flow ; w = wall.

Equation R3 is used in compressible flows, but not in incompressible flows.

The basic equations are closed by using the properties of families of velocity and enthalpy profiles, obtained by establishing self-similar solutions. In these solutions, a mixing-length model is employed to solve the resulting self-similar equations as given in Michel et al. (1968).

Analytical formulae have been developed to represent the properties of the self-similar solutions. These constitute the set of closure relationships. Let the index 1 represent incompressible quantities (for example $\delta_{11} = \int_0^\delta (1 - U/U_e) dy$) and let the overbar ($\bar{\quad}$) represent intermediate variables (see Cousteix et al., 1974).

1) The relationships for the integral thicknesses are:

$$\frac{\delta_{11}}{\delta} = \bar{\gamma} F_1(G) ; \quad \frac{\delta_{11}}{\theta_1} = \frac{1}{1 - G\bar{\gamma}} ; \quad \frac{\delta_{31}}{\delta} = \bar{\gamma}^3 F_3(G) - \frac{\delta_{11}}{\delta} + \frac{3\theta_1}{\delta} ; \quad \bar{\gamma} = \left(\frac{\bar{C}_f}{2} \right)^{1/2}$$

$$\frac{\delta_3}{\delta_{31}} = \frac{\theta}{\theta_1} ; \quad \frac{\theta}{\theta_1} = [7.58 + 6.53((\delta - \delta_1)/(\delta - \delta_{11}))^2]^{1/2} - 2.756$$

$$\delta - \delta_{11} = (1 + 0.2M_e^2)\Delta + \delta - \delta_1 + 0.2M_e^2\delta_3$$

F_1 and F_3 , deduced from the self-similar solutions, are represented by:

$$F_1 = 0.613G - (3.6 + 76.86(1/G - 0.154)^2)/G$$

$$F_3 = (0.714 - 0.302/(G - 2.57)^2)G^3$$

II) The skin-friction law is:

$$\frac{1}{\bar{Y}} = \frac{1}{X} \ln \frac{\rho_w U_e \delta_{11}}{\mu_w} + D^*(G, T_w/T_{ad}, M_e) ; \quad X = 0.41$$

D^* is obtained from self-similar solutions:

$$D^* = 2G - a G^{1/2} + b$$

$$a = (0.7945 + 0.296 T_w/T_{ad} - 0.0905 (T_w/T_{ad})^2) (4.2 - 0.143 M_e - 0.0143 M_e^2)$$

$$b = 4.4 T_w/T_{ad} - 2.8 - 0.3 M_e - (0.0678 T_w/T_{ad} + 0.0254) M_e^2$$

$$\frac{\bar{Y}}{Y} = \left(0.76 + \frac{0.296}{0.232 + T_w/T_{ad}} \right) \left(\frac{1 + (0.267 - 0.0955 T_w/T_{ad}) M_e}{1 + (0.267 - 0.0955 T_w/T_{ad}) M_e + 0.11 M_e^2} \right)$$

III) The entrainment coefficient is determined by:

$$C_E = \bar{Y} P(G) ; \quad P(G) = 0.074G - 1.0957/G$$

IV) The law for the wall heat transfer is:

$$\frac{C_f/2}{C_h} = P_t (1 + D_s \bar{Y}) ; \quad C_h = \frac{\phi_w}{\rho_e U_e (h_w - h_{ad})} ; \quad P_t = 0.89$$

$$D_s = [a + 0.035 b \ln((0.07 G^2 + 1)/(0.07 G^2 - 1))] G$$

$$a = -0.0239 M_e - 1.733 ; \quad b = (a_1 T_w/T_{ad} + b_1) / (c_1 T_w/T_{ad} + 1)$$

$$\text{where } a_1 = (-376.2 + 160.4 M_e) / (1 - 8.075 M_e)$$

$$b_1 = (446.9 + 44.89 M_e) / (1 + 2.766 M_e)$$

$$c_1 = (-25.18 + 1.331 M_e) / (1 - 14.43 M_e) .$$

The effects of wall curvature are taken into account in the method. Self-similar solutions have been calculated by using a modified mixing-length model. Mainly, the wall-curvature effects alter the entrainment coefficient which is represented in Cousteix and Houdeville (1977) by,

$$P = - \frac{87.235 X_c + 1.0957}{62.47 X_c + 1} \frac{1}{G} + \frac{-0.37 X_c + 0.074}{15.93 X_c + 1} G$$

where

$$X_c = \frac{F_1 K^+}{G^2} ; \quad K^+ = \frac{\delta}{\bar{Y} R}$$

The effects of free-stream turbulence are also included in the method. Again, self-similar solutions have been calculated by using a modified mixing-length model.

The main effects lie in the entrainment coefficient which is represented in Arnal et al. (1976) by,

$$P = (0.074 f_1 G - 1.0957 f_2 / G) f_3$$

$$f_1 = 1 + 4.054 X_t ; f_2 = 1 - 2.1904 X_t$$

$$f_3 = (G^2 - 1 / (0.0675 + 0.0745 X_t)) / (G^2 - 1 / (0.0675 + 0.078 X_t))$$

$$X_t = \left(\frac{k_e^x}{G^2} \right)^{1/2} ; k_e^x = \frac{k_e}{(\overline{yU_e})^2} ; k_e = (\overline{u_e'^2} + \overline{v_e'^2} + \overline{w_e'^2}) / 2$$

Remarks

I) The method has been extended in Cousteix (1981) to calculate three-dimensional thin boundary layers, unsteady boundary layers and wakes (two- and three-dimensional wakes, symmetric and asymmetric).

II) Possible improvements are being studied. These concern the basic closure relationships in incompressible flows. The set of relationships is modified in an empirical way. The following set has been tried in the REMI-2D1 version of the method:

$$D^* = 1.588G - 2.9G^{1/2} + 1.288 ; P = [1 + 2.273((G/6.13)^2 - 1)] / F_1$$

$$F_1 = [0.613G - (3.6 + 76.86(1/G - 0.154)^2) / G] (1 + 18/G^2)$$

This set of relationships has been tested in the Samuel and Joubert experiment, and also in several test cases of the 1968 Stanford Conference. In all the cases a substantial improvement is obtained. Possibly, the function F_1 needs to be tuned a little bit more.

III) The effects of free-stream turbulence seem to be overestimated, especially at low intensity. The results could be easily improved.

IV) REMI-DIFFU is an extension of REMI-2D for calculating internal axisymmetric flow (diffuser flows). The effects of thick boundary layers are taken into account. The core velocity is calculated from the mass-flow conservation.

V) From the values of H and R_0 which are results of computation, the velocity profiles can be calculated from a velocity profile family (for example, Whitfield's family—see Whitfield et al., 1980).

Description of ELODIE-KELM, -KELM1, -KELM2, -KEVISC

This method solves the partial differential equations (boundary-layer equations), using a $k-\epsilon$ model. Near the wall, the k - and ϵ -equations are replaced by a mixing length model corrected with a damping function.

The basic equations are:

$$\frac{\partial U}{\partial x} + \frac{\partial v}{\partial y} = 0 \quad (E1)$$

$$U \frac{\partial U}{\partial x} + v \frac{\partial U}{\partial y} = -\frac{1}{\rho} \frac{dp}{dx} + \frac{\partial}{\partial y} (-\overline{u'v'}) + \nu \frac{\partial U}{\partial y} \quad (E2)$$

The turbulent shear stress is calculated from a k-ε model:

$$-\overline{u'v'} = \nu_t \frac{\partial U}{\partial y}; \quad \nu_t = C_\mu \frac{k^2}{\epsilon}; \quad C_\mu = 0.09$$

and the k- and ε-equations are:

$$U \frac{\partial k}{\partial x} + v \frac{\partial k}{\partial y} = -\overline{u'v'} \frac{\partial U}{\partial y} - \epsilon + \frac{\partial}{\partial y} \left(\frac{\nu_t}{\sigma_k} \frac{\partial k}{\partial y} \right) \quad (E3)$$

$$U \frac{\partial \epsilon}{\partial x} + v \frac{\partial \epsilon}{\partial y} = -C_{\epsilon_1} \frac{\epsilon}{k} \overline{u'v'} \frac{\partial U}{\partial y} - C_{\epsilon_2} \frac{\epsilon^2}{k} + \frac{\partial}{\partial y} \left(\frac{\nu_t}{\sigma_\epsilon} \frac{\partial \epsilon}{\partial y} \right) \quad (E4)$$

where

$$C_{\epsilon_1} = 1.57, \quad C_{\epsilon_2} = 2, \quad \sigma_k = 1, \quad \sigma_\epsilon = 1.3$$

The above k- and ε-equations are used only in the fully turbulent region of the boundary layer. Near the wall, these equations are not used. In the wall region, the turbulent shear stress is calculated from a mixing-length formula:

$$-\overline{u'v'} = F^2 \ell^2 \left(\frac{\partial U}{\partial y} \right)^2 \quad (E5)$$

where ℓ/δ is a universal function of y/δ :

$$\frac{\ell}{\delta} = 0.085 \tanh\left(\frac{\chi}{0.085} \frac{y}{\delta}\right); \quad \chi = 0.41$$

and F is a damping factor expressed as a function of the total shear stress:

$$F = 1 - \exp\left(-\frac{\ell}{26\chi\mu} (\tau\rho)^{1/2}\right); \quad \tau = \mu \frac{\partial U}{\partial y} - \rho \overline{u'v'}$$

This near-wall procedure is used for $F < 0.99$. The matching (or patching) with the k-ε model is made at the point $y = y_m$, where $F = 0.99$. At this point, the boundary conditions for k and ϵ are given by:

$$k = \tau_m / \rho C_\mu^{1/2}; \quad \epsilon = C_\mu \frac{k^2}{\tau_m / \rho} \left(\frac{\partial U}{\partial y} \right)_m$$

where τ_m and $(\partial U / \partial y)_m$ are values calculated at $y = y_m$ from the wall region procedure.

The wall-curvature effects are taken into account by modifying the ε-equation, as proposed by Launder-Priddin-Sharma. The coefficient C_{ϵ_2} is a function of a Richardson number; see Launder et al. (1977), with

$$C_{\epsilon_2} = C'_{\epsilon_2} \left(1 - \alpha \frac{k^2}{\epsilon^2} \frac{U}{r^2} \frac{\partial r U}{\partial r}\right) \quad (E6)$$

where $\alpha = 0.25$. C'_{ϵ_2} is the value of C_{ϵ_2} when the wall curvature is zero.

For reporting the wall-curvature effects, an alternative procedure used in ELODIE-KELM1 consists of modifying the eddy-viscosity coefficient instead of C_{ϵ_2} ,

$$\overline{u'v'} = C_{\mu} \left(1 - \beta \frac{k^2}{\epsilon^2} \frac{U}{r^2} \frac{\partial r U}{\partial r}\right) \frac{k^2}{\epsilon} \frac{\partial U}{\partial y} \quad (E7)$$

where $\beta = 1.8$.

In the boundary-layer approximation, it is assumed that the $\partial U/\partial x$ terms are small, compared with the $\partial U/\partial y$ terms, but this hypothesis is not always well verified. Hanjalić-Launder have shown that the $\partial U/\partial x$ terms can play a significant role in the ϵ -equation. Accordingly, the ϵ -equation has been modified in ELODIE-KELM2, which is a version of ELODIE-KELM, in which the ϵ -equation is after Hanjalić and Launder (1980),

$$U \frac{\partial \epsilon}{\partial x} + v \frac{\partial \epsilon}{\partial y} = -C_{\epsilon_1} \overline{u'v'} \frac{\partial U}{\partial y} \frac{\epsilon}{k} - C_{\epsilon_2} \frac{\epsilon^2}{k} - C_{\epsilon_3} (\overline{u'^2} - \overline{v'^2}) \frac{\partial U}{\partial x} \frac{\epsilon}{k} + D_{\epsilon} \quad (E8)$$

where

$$\overline{u'^2} - \overline{v'^2} = 0.33k ; C_{\epsilon_1} = 1.44 ; C_{\epsilon_2} = 1.9 ; C_{\epsilon_3} = 4.44$$

In ELODIE-KELM2, the wall treatment is the same as in ELODIE-KELM.

For a few cases, the low Reynolds number turbulent regions have been calculated using the Jones-Launder model. This forms the program ELODIE-KEVISC. The k - and ϵ -equations are according to Jones and Launder (1972):

$$U \frac{\partial k}{\partial x} + v \frac{\partial k}{\partial y} = -\overline{u'v'} \frac{\partial U}{\partial y} - \overline{v'w'} \frac{\partial W}{\partial y} - \epsilon - 2\mu \left(\frac{\partial k}{\partial y}\right)^2 + \frac{\partial}{\partial y} \left[\left(\mu + \frac{\mu_t}{\sigma_k}\right) \frac{\partial k}{\partial y} \right] \quad (E9)$$

$$U \frac{\partial \epsilon}{\partial x} + v \frac{\partial \epsilon}{\partial y} = -C_{\epsilon_1} \frac{\epsilon}{k} \overline{u'v'} \frac{\partial U}{\partial y} - C_{\epsilon_2} f_2 \frac{\epsilon^2}{k} - 2\mu \mu_t \left(\frac{\partial^2 U}{\partial y^2}\right)^2 + \frac{\partial}{\partial y} \left[\left(\mu + \frac{\mu_t}{\sigma_{\epsilon}}\right) \frac{\partial \epsilon}{\partial y} \right] \quad (E10)$$

$$\overline{u'v'} = f_{\mu} C_{\mu} \frac{k}{\epsilon} \frac{\partial U}{\partial y} ; C_{\mu} = 0.09$$

$$f_2 = 1 - 0.3 \exp(-R_t^2) ; f_{\mu} = \exp\left(-\frac{2.5}{(1 + R_t/50)}\right) ; R_t = \frac{k^2}{\nu \epsilon}$$

$$C_{\epsilon_1} = 1.57 ; C_{\epsilon_2} = 2 ; \sigma_k = 1 ; \sigma_{\epsilon} = 1.3$$

Description of MULTI

This model is directly drawn from the multi-scale model of Hanjalić, Launder and Schiestel. It only differs by the values of some coefficients. Four transport equations have been written for the energies k_p , k_T , and the spectral transfer rates ϵ_p and ϵ_T . They have the following form (in homogeneous flows) as given in Hanjalić et al. (1979):

$$\frac{Dk_p}{Dt} = P - \epsilon_p ; \quad \frac{Dk_T}{Dt} = \epsilon_p - \epsilon_T ; \quad P = -\overline{u'_i u'_j} \frac{\partial U_i}{\partial x_j} \quad (M1)$$

$$\frac{D\epsilon_p}{Dt} = C_{p1} P \frac{\epsilon_p}{k_p} - C_{p2} \frac{\epsilon_p^2}{k_p} ; \quad \frac{D\epsilon_T}{Dt} = C_{T1} \epsilon_p \frac{\epsilon_T}{k_T} - C_{T2} \frac{\epsilon_T^2}{k_T} \quad (M2)$$

$$C_{p1} = 1.085 ; \quad C_{p2} = 1.8 - 0.3 \left(\frac{k/k_T - 1}{k_p/k_T + 1} \right) ; \quad C_{T1} = 1.08 \frac{\epsilon_p}{\epsilon_T} ; \quad C_{T2} = 1.15$$

The dissipation rate ϵ is equal to ϵ_T . The total turbulent kinetic energy is $k = k_p + k_T$. The individual Reynolds stresses are computed with the following equation drawn from the Reynolds-stress closure of Launder, Reece and Rodi (1975):

$$\frac{Du'_i u'_j}{Dt} = P_{ij} + \phi_{ij,2} - C_1 \frac{\epsilon_p}{k_p} (\overline{u'_i u'_j} - \frac{2}{3} \delta_{ij} k) - \frac{2}{3} \epsilon \delta_{ij} \quad (M3)$$

The value of the coefficient C_2 of the linear part of the pressure-strain correlation term $\phi_{ij,2}$ is $C_2 = 0.4$.

The value of the coefficient in the return-to-isotropy term is $C_1 = 1.61$. The initial values of the spectral parameters k_p/k_T and ϵ_p/ϵ_T are always taken as:

$$k_p/k_T = 1$$

$$\epsilon_p/\epsilon_T = 0.5$$

Description of LRLW

This model is drawn from the Launder-Reece-Rodi model. In the Reynolds-stress equation, which is written (in homogeneous flows)

$$\frac{Du'_i u'_j}{Dt} = P_{ij} + \phi_{ij,2} - C_1 \frac{\epsilon}{k} (\overline{u'_i u'_j} - \frac{2}{3} \delta_{ij} k) - \frac{2}{3} \epsilon \delta_{ij} \quad (L1)$$

the values of the coefficients are: $C_1 = 1.839$; $C_2 = 0.4$ (coefficient in the linear part of the pressure-strain term $\phi_{ij,2}$).

The turbulent kinetic energy, k , and the dissipation, ϵ , are computed with the following equations:

$$\frac{Dk}{Dt} = P - \epsilon ; \quad P = -\overline{u_i^* u_j^*} \frac{\partial U_i}{\partial x_j} \quad (L2)$$

$$\frac{D\epsilon}{Dt} = C_{\epsilon_1} P \frac{\epsilon}{k} - C_{\epsilon_2} \frac{\epsilon^2}{k} \quad (L3)$$

The only original approach in this model is the determination of the coefficient C_{ϵ_1} . A comparison is made with the tensorial volume of turbulence theory of Lin and Wolfshtein (1980).

These authors have defined a tensorial volume V_{ij} (a symmetric tensor in homogeneous flows). In homogeneous flows, the transport of V_{ij} is given by the following exact equation:

$$\frac{D}{Dt}(kV_{ij}) = -k\left(\frac{\partial U_i}{\partial x_k} V_{kj} + \frac{\partial U_j}{\partial x_k} V_{ik}\right) ; \quad V_{ij}(A) = \int_V \frac{\overline{u_i^*(A)u_j^*(B)}}{\overline{u_l^*(A)u_l^*(A)}/3} dV \quad (L4)$$

A length scale is defined by: $L = (V_{ll})^{1/3}$. After writing that the dissipation rate ϵ is proportional to $k^{3/2}/L$ we obtain:

$$\frac{D}{Dt} \ln\left(\frac{k^{11/6}}{\epsilon}\right) = -\frac{2}{3} \frac{\partial U_l}{\partial x_k} V_{kl}/V_{ll} \quad (L5)$$

The equations for k and ϵ lead to:

$$\frac{D}{Dt} \ln\left(\frac{k^{C_{\epsilon_2}}}{\epsilon}\right) = 2 b_{ij} \frac{\partial U_i}{\partial x_j} (C_{\epsilon_1} - C_{\epsilon_2}) \quad (L6)$$

where b_{ij} is the anisotropy tensor:

$$b_{ij} = \frac{\overline{u_i^* u_j^*}}{2k} - \frac{\delta_{ij}}{3}$$

With $C_{\epsilon_2} = 11/6 = 1.83$, the comparison between Eqs. L5 and L6 gives:

$$C_{\epsilon_1} - C_{\epsilon_2} = -\frac{\frac{V_{kl}}{3} \frac{\partial U_l}{\partial x_k}}{V_{ll} b_{ij} \frac{\partial U_i}{\partial x_j}} \quad (L7)$$

In simple cases, when the derivatives $\partial U_i/\partial x_j$ are known and with an initially isotropic turbulence, it is possible to compute analytically the evolution of the volumes V_{ij} as a function of a dimensionless time τ . For instance, for a constant shear $\partial U/\partial y$ the dimensionless time is written $\tau = st$, where t is the physical time.

In the case where s is not constant, the time $\tau = \int_0^t s dt$ is used. Thus, the coefficient C_{ϵ_1} is a function of the anisotropy and of τ .

For Cases 0376A and 0376B (shear flow), C_{ϵ_1} is computed with the following expression:

$$C_{\epsilon_1} - C_{\epsilon_2} = \frac{2}{3} \frac{\tau}{\tau^2 + 3} / \left(\frac{\overline{u'v'}}{k} \right) \quad (L8)$$

For the irrotational plane strain (Cases 0374A and 0374B), the derivatives of the mean velocity are

$$\frac{\partial U}{\partial x} = 0; \quad \frac{\partial V}{\partial y} = -\lambda; \quad \frac{\partial W}{\partial z} = \lambda$$

The time τ is $\tau = \lambda t$ and C_{ϵ_1} is given by:

$$C_{\epsilon_2} - C_{\epsilon_1} = \frac{4}{3} \frac{\sinh(2\tau)}{1 + 2 \cosh(2\tau)} \frac{1}{(\overline{v'^2}/k - \overline{w'^2}/k)} \quad (L9)$$

For the axisymmetric contractions (Cases 0375B,D,E), the mean-strain rate is given by:

$$\frac{\partial U}{\partial x} = \lambda; \quad \frac{\partial V}{\partial y} = -\frac{\lambda}{2}; \quad \frac{\partial W}{\partial z} = -\frac{\lambda}{2}$$

and τ is given by:

$$\tau = \int_0^t \lambda dt$$

This leads to the following expression for C_{ϵ_1} :

$$C_{\epsilon_2} - C_{\epsilon_1} = \frac{4(e^{3\tau} - 1)}{9(2e^{3\tau} + 1)} \left(\frac{1}{2/3 - \overline{u'^2}/k} \right) \quad (L10)$$

Remark: It should be noted that in our calculations, for both models (MULTI and LRRLW), the initial value of the dissipation in Case 0376B (Harris) was $\epsilon = 1.2$, and not the incorrect datum value $\epsilon = 3.91$.

Description of ELODIE-COIN

The equations to be solved are the following:

$$U \frac{\partial U}{\partial x} + V \frac{\partial U}{\partial y} + W \frac{\partial U}{\partial z} = -\frac{1}{\rho} \frac{dp}{dx} + \frac{\partial}{\partial y} \left(\nu \frac{\partial U}{\partial y} - \overline{u'v'} \right) + \frac{\partial}{\partial z} \left(\nu \frac{\partial U}{\partial z} - \overline{u'w'} \right)$$

$$U \frac{\partial \omega}{\partial x} + V \frac{\partial \omega}{\partial y} + W \frac{\partial \omega}{\partial z} = \omega \frac{\partial U}{\partial x} + \omega_y \frac{\partial U}{\partial y} + \omega_z \frac{\partial U}{\partial z} + \nu \left(\frac{\partial^2 \omega}{\partial y^2} + \frac{\partial^2 \omega}{\partial z^2} \right)$$

$$+ \frac{\partial^2}{\partial y \partial z} (\overline{v'^2} - \overline{w'^2}) + \left(\frac{\partial^2}{\partial z^2} - \frac{\partial^2}{\partial y^2} \right) \overline{v'w'}$$

$$\frac{\partial^2 W}{\partial y^2} + \frac{\partial^2 W}{\partial z^2} = \frac{\partial \omega}{\partial y} - \frac{\partial^2 U}{\partial x \partial z}$$

$$\frac{\partial^2 V}{\partial y^2} + \frac{\partial^2 V}{\partial z^2} = -\frac{\partial \omega}{\partial z} - \frac{\partial^2 U}{\partial x \partial y}$$

where

$$\omega = \frac{\partial W}{\partial y} - \frac{\partial V}{\partial z}; \quad \omega_y = \frac{\partial U}{\partial z} - \frac{\partial W}{\partial x}; \quad \text{and} \quad \omega_z = \frac{\partial V}{\partial x} - \frac{\partial U}{\partial y}$$

The equations are the streamwise momentum equation, the equation for the streamwise component of the vorticity and two Poisson's equations for the secondary velocities V and W. A set of assumptions, which constitutes an extension of the usual boundary-layer hypothesis, leads to a parabolized system in the x-direction (see Arnal and Cousteix, 1981).

The Reynolds shear stresses are expressed as follows:

$$\overline{v'^2} - \overline{w'^2} = \frac{4}{C_1} \left(\frac{4C_2 - 1}{11} \right) \frac{k}{\epsilon} (\overline{u'v'}) \frac{\partial U}{\partial y} - \overline{u'w'} \frac{\partial U}{\partial z}$$

$$\overline{v'w'} = \frac{2}{C_1} \frac{(4C_2 - 1)}{11} \frac{k}{\epsilon} (\overline{u'v'}) \frac{\partial U}{\partial z} + \overline{u'w'} \frac{\partial U}{\partial y}$$

$$-\overline{u'v'} = v_t \frac{\partial U}{\partial y}; \quad -\overline{u'w'} = v_t \frac{\partial U}{\partial z}$$

where

$$v_t = \frac{1}{C} \left(\frac{4}{15} + \frac{-6C_2^2 - 12C_2 + 2}{33C_1} \right) \frac{k^2}{\epsilon_1}$$

Closure relationships:

$$\epsilon = -\overline{u'v'} \frac{\partial U}{\partial y} - \overline{u'w'} \frac{\partial U}{\partial z} \quad (\text{dissipation})$$

$$v_t = F^2 \ell^2 \left[\left(\frac{\partial U}{\partial y} \right)^2 + \left(\frac{\partial U}{\partial z} \right)^2 \right]^{1/2}$$

F is a damping function for the near-wall regions. The expression of the mixing-length ℓ is deduced from Buleev's formulation.

Values of the constants:

$$C_1 = 1.5; \quad C_2 = 0.25 \text{ or } 0.30$$

For Case 0512 (Humphrey), two calculations have been performed:

- the pressure is supposed to be constant in each (r, z) plane: $\partial p / \partial r = 0$,
- the pressure is obtained by a two-dimensional, inviscid calculation ($\partial p / \partial z = 0$, but $\partial p / \partial r \neq 0$); this pressure field is introduced as a datum in ELODIE-COIN. ($C_2 = 0.30$ for Case 0512.)

References

- Arnal, D., and J. Cousteix (1981). "Turbulent flow in unbounded streamwise corners," Symposium on Turbulent Shear Flows, University of California, Davis.
- Arnal, D., J. Cousteix, and R. Michel (1976). "Couche limite se développant avec gradient de pression positif sur un écoulement extérieur turbulent," La Recherche Aéronautique, 1.
- Cousteix, J. (1981). "Turbulence modeling and boundary layer calculation methods," VKI Lecture Series 1981 on Separated Flows in Turbomachinery.
- Cousteix, J., and R. Houdeville (1977). Méthode intégrale de calcul d'une couche limite turbulente sur une paroi courbée longitudinalement," La Recherche Aéronautique, 1.
- Cousteix, J., R. Houdeville, and R. Michel (1974). "Couches limites turbulentes avec transfert de chaleur," La Recherche Aéronautique, 6 (English translation ESA TT-193).
- Hanjalić, K., and B. E. Launder (1980). "Sensitizing the dissipation equation to irrotational strains," Trans. ASME, J. Fluids Eng., 102.
- Hanjalić, K., B. E. Launder, and R. Schiestel (1979). "Multiple time scale concepts in turbulent transport modelling," 2nd Intl. Symp. Turbulent Shear Flows, London.
- Jones, W. P., and B. E. Launder (1972). "The prediction of laminarization with a two-equation model of turbulence," J. Heat and Mass Transfer, 15.
- Launder, B. E., C. H. Priddin, and B. I. Sharma (1977). "The calculation of turbulent boundary layers on spinning and curved surfaces," Trans. ASME, J. Fluid Eng., 99, March.
- Launder, B. E., G. J. Reece, and W. Rodi (1975). "Progress in the development of a Reynolds-stress turbulence closure," J. Fluid Mech., 68, part 3.
- Lin, A., and M. Wolfshtein (1980). "Tensorial volume of turbulence," Phys. Fluids, 23, 3.
- Michel, R., C. Quémard, and R. Durant (1968). "Hypothesis on the mixing length and application to the calculation of the turbulent boundary layer," Proceedings, Computation of Turbulent Boundary Layers--1968 AFOSR-IFP-Stanford Conference, Vol. I, pp. 195-212.
- Whitfield, D. L., T. W. Swafford, and J. L. Jacocks (1980). "Calculation of turbulent boundary layers with separation, reattachment and viscous-inviscid interaction," AIAA Paper 80-1439.

COMPARISON OF COMPUTATION WITH EXPERIMENT

Summary Report

by

G. S. Deiwert*

Computer Group Number: 47



Cases 8621, 8623

Computations are made with the strong conservative form of the time-dependent compressible Navier-Stokes equations by using the MacCormack (1978) finite-volume mixed explicit/implicit/method-of-characteristics algorithm. Written in time-dependent Reynolds-averaged form, the equations are

$$\frac{\partial}{\partial t} \int_{\text{vol}} U \, d(\text{vol}) + \int_{\text{s}} \vec{H} \cdot \vec{n} \, ds = 0$$

where

$$U \equiv \left\{ \begin{array}{c} \rho \\ \rho u \\ \rho v \\ e \end{array} \right\} \quad \vec{H} \equiv \left\{ \begin{array}{c} \rho q \\ \rho u q + \vec{\tau} \cdot \vec{e}_x \\ \rho v q + \vec{\tau} \cdot \vec{e}_y \\ e q + \vec{\tau} \cdot \vec{q} - kVT \end{array} \right\}$$

$$\vec{q} \equiv u\vec{e} + v\vec{e}$$

These equations are written and solved in Cartesian x-y space for computational meshes of arbitrary geometry. An exponentially stretched grid with thickness the order of the shear-layer thickness is used to resolve the viscous-flow regime. Outside this viscous region, a second exponentially stretched grid is used to resolve the inviscid field to distances far from the body surface (typically 15 chord lengths). To facilitate adequate resolution of the near wake, the computational grid is dynamically remeshed during the course of the solution so that the mesh always follows the path of the wake (as defined by the locus of minimum velocity). Solutions are advanced in time until a steady state is reached.

Turbulent transport is incorporated into the molecular-transport stress tensor by adding the scalar eddy-viscosity transport coefficient ϵ , thereby relating turbulent transport directly to gradients of the mean-flow variables. In a Cartesian coordinate system, the two-dimensional molecular stress tensor can be written as

*Ames Research Center, NASA, Moffett Field, CA 94035

$$\tau_l = (p + \sigma_x) \hat{e}_x \hat{e}_x + \tau_{xy} \hat{e}_x \hat{e}_y + \tau_{yx} \hat{e}_y \hat{e}_x + (p + \sigma_y) \hat{e}_y \hat{e}_y \quad (1)$$

where the components are defined by

$$\sigma_x = -2\mu(\partial u/\partial x) - \lambda(\partial u/\partial x + \partial v/\partial y) \quad (2)$$

$$\sigma_y = -2\mu(\partial v/\partial y) - \lambda(\partial u/\partial x + \partial v/\partial y) \quad (3)$$

$$\tau_{xy} = \tau_{yx} = -\mu(\partial u/\partial y + \partial v/\partial x) \quad (4)$$

and

$$\lambda = -2\mu/3$$

The total shear (molecular plus turbulent) is written as

$$\tau = \tau_l + \tau_t = (p + \tilde{\sigma}_x) \hat{e}_x \hat{e}_x + \tilde{\tau}_{xy} \hat{e}_x \hat{e}_y + \tilde{\tau}_{yx} \hat{e}_y \hat{e}_x + (p + \tilde{\sigma}_y) \hat{e}_y \hat{e}_y \quad (5)$$

where

$$\tilde{\sigma}_x = -2(\mu + \rho\varepsilon)(\partial u/\partial x) - \lambda(\partial u/\partial x + \partial v/\partial y) \quad (6)$$

$$\tilde{\sigma}_y = -2(\mu + \rho\varepsilon)(\partial v/\partial y) - \lambda(\partial u/\partial x + \partial v/\partial y) \quad (7)$$

$$\tilde{\tau}_{xy} = \tilde{\tau}_{yx} = -(\mu + \rho\varepsilon)(\partial u/\partial y + \partial v/\partial x) \quad (8)$$

In a similar manner, turbulent heat transport is defined in terms of mean-energy gradients and an eddy-conductivity coefficient k_t so that

$$Q_t = k_t \nabla T \quad (9)$$

The eddy-conductivity coefficient is related to the eddy-viscosity coefficient via a turbulent Prandtl number Pr_t where

$$Pr_t = \rho c_p \varepsilon / k_t \quad (10)$$

An algebraic model of the type suggested by Smith and Cebeci is used where in the boundary layer near the solid surface we have

$$\varepsilon = l^2 [(\partial u/\partial y)^2 + (\partial v/\partial x)^2]^{1/2} \quad (11)$$

$$l = 0.4\eta[1 - \exp(-\eta/\Lambda)] \quad (12)$$

$$\Lambda = 26\mu_w / \sqrt{\rho_w \tau_w} \quad (13)$$

and in the outer part of the boundary layer and in the wake we have

$$\epsilon = 0.0168 \hat{u}_\delta \delta_1^* / \{1 + 5.5[(\eta - \eta_{DS})/\delta]^6\} \quad (14)$$

$$\delta_1^* = \int_{\eta_{DS}}^{\delta} (1 - \hat{u}/\hat{u}_\delta) d\eta \quad (15)$$

To approximate the influence of upstream history a simple relaxation procedure is used such that

$$\epsilon(\xi, \eta) = \alpha \epsilon(\xi - \Delta\xi, \eta) + (1 - \alpha) \epsilon_{eq}(\xi, \eta) \quad (16)$$

where ϵ_{eq} is defined by Eqs. 11 and 14, α is a relaxation parameter with value between zero and one and $\Delta\xi$ is the local streamwise computational mesh spacing. For $\alpha = 0$, there is no relaxation and for $\alpha = 1$, the eddy viscosity is frozen. A value of 0.3 is used for α in the examples. The turbulent Prandtl number is assumed constant at 0.90.

A computational mesh is constructed around the airfoil geometry as follows. First, an orthogonal body-oriented mesh is constructed around the airfoil (with the airfoil surface treated as one mesh line) and extended out a distance sufficient to capture the viscous-dominated flow region (ten percent of the chord length of the airfoil). This mesh is extended downstream from the trailing edge of the airfoil (15 chord lengths) at an angle relative to the mean chord line corresponding to the angle of attack of the airfoil to the oncoming stream. The mesh spacing normal to the airfoil surface is exponentially stretched with the first mesh spacing set equal to 1/12th of the chord length divided by the chord Reynolds number. There are 18 mesh points distributed across this region to the outer edge of the zone. Points are generated (or input) along the airfoil surface and distributed exponentially downstream in the wake to a maximum total of 107 "surface" points in the wake and on the airfoil. Second, a larger and coarser mesh is constructed extending from the outer edge of the viscous mesh to a distance far from the airfoil (typically 15 chord lengths). Again, exponential stretching is used away from the surface and 19 points are distributed across the region. The radial mesh lines are required to be continuous with those in the viscous mesh, but the requirement of orthogonality is relaxed so that mesh lines neither converge (cross) nor diverge too rapidly.

As the flow develops, the position of the viscous wake moves with time. To assure the capture of the wake in the viscous mesh, the mesh downstream from the trailing edge of the airfoil is dynamically adjusted during the course of the solution in a direction normal to the mean chord of the airfoil so that the slope of the wake mesh matches the flow direction in the core of the wake. This dynamic remeshing is initiated sometime after the impulsive start (typically after a dimensionless time

of 1) to allow time for the starting vortex to be shed downstream. Mesh adjustment is realized gradually with the adjustment never exceeding the smallest transverse mesh spacing in any one time step.

The computer code was designed to study unsteady transonic flows where there exist regions of strong viscous/inviscid interactions and large regions of flow separation. Because the method is time dependent and time accurate, fairly long computer times are required to achieve convergence for transonic flows. This time increases directly with the number of mesh points used in the computational grid. In the interest of economy a minimal number of mesh points (37×107) were used in the present computations. This grid permits adequate streamwise resolution except near the trailing edge where clustering should be used to resolve the details of interest. The radial resolution is sufficient for the inviscid region and will support the coupling of the inviscid and viscous regions. However, it is highly unlikely that the boundary-layer details will be adequately resolved. Typically, there are only 5 to 10 mesh points in the boundary layer, except in regions where the viscous region is very thick.

One case was selected to illustrate the influence of grid resolution on the computation of the boundary layer. For the RAE 2822 airfoil, case 6, (Case 8621) ten more points were added to the fine-mesh region in the direction normal to the airfoil-surface. While even this does not provide adequate resolution of the boundary layer, significant improvement in the solution was realized. Previous studies (Baldwin et al., 1975; Deiwert 1975a,b, 1976a,b, 1977, 1979; Deiwert et al., 1975; Deiwert and Bailey, 1979; and McDevitt et al., 1976) indicate that good agreement with experiment can be realized when sufficient grid resolution exists.

For the transonic-airfoil cases considered for this Conference where the viscous/inviscid interactions are not strong and regions of flow separation are essentially non-existent, the present method is not the method of choice. Rather a boundary-layer method (including, perhaps, higher-order effects) would be much more suitable.

References

- Baldwin, B. S., R. W. MacCormack, and G. S. Deiwert (1975). "Numerical techniques for the solution of the compressible Navier-Stokes equations and implementation of turbulence methods," AGARD-LSP-73.
- Deiwert, G. S. (1975a). "High Reynolds number transonic flow simulation," In Lecture Notes in Physics No. 35, Springer-Verlag (edited by R. D. Richtmyer).
- Deiwert, G. S. (1975b). "Numerical simulation of high Reynolds number transonic flows," AIAA Jou., 10.
- Deiwert, G. S. (1976a). "Computation of separated transonic turbulent flows," AIAA Jou., 14:6.

- Deiwert, G. S. (1976b). "Recent computation of viscous effects in transonic flow," In Lecture Notes in Physics No. 59, Springer-Verlag (Edited by A. I. van de Vooren and P. J. Zandbergen).
- Deiwert, G. S. (1977). "On the prediction of viscous phenomena in transonic flows," In Transonic Flow Problems in Turbomachinery, Hemisphere Pub. Corp.
- Deiwert, G. S. (1979). "Computation of turbulent near wakes for asymmetric airfoils," Viscous and Interacting Flow Field Effects, Proc., 4th U.S. Air Force and the Federal Republic of Germany Data Exchange Agreement Meeting, K. H. Gronau and H. U. Meier, eds., BMVg-FBWT 79-31, pp. 455-467. Also NASA TM-78581.
- Deiwert, G. S., and H. E. Bailey (1979). "Prospects for computing airfoil aerodynamics with Reynolds averaged Navier-Stokes codes," NASA CP2045.
- Deiwert, G. S., J. B. McDevitt, and L. L. Levy, (1975). "Simulation of turbulent transonic separated flow over an airfoil," In NASA SP-347 Aerodynamic Analyses Requiring Advanced Computers.
- McCormack, R. W. (1978). "An efficient explicit-implicit-characteristic method for solving the compressible Navier-Stokes equations," SIAM-AMS Proc., XI.
- McDevitt, J. B., L. L. Levy, and G. S. Deiwert (1976). "Transonic flow about a thick circular-arc airfoil," AIAA Jou., 14:5.



COMPARISON OF COMPUTATION WITH EXPERIMENT

Summary Report

(Results from A.R.A.P.'s Second-Order Closure Model)

by

C. duP. Donaldson, B. Quinn, W. S. Lewellen,
R. D. Sullivan, R. I. Sykes, A. K. Varma*

R.D. Sullivan

Computer Group Number: 21

Cases 0141, 0241, 0242, 0244, 0311, 0371, 0373, 0374, 0375,
0376, 0421, 0422, 0612, 8101, 8201, 8301, 8403, 8411

In the course of the last dozen years, A.R.A.P. has frequently been faced with the need to make predictive computations of turbulent flows in regimes for which physical understanding was sketchy. Examples (Donaldson, 1973; Lewellen, 1977) include flows in the atmosphere with temperature and humidity gradients and flows in the ocean with temperature and salinity gradients. Thus we have tried to make a turbulence model as general as possible, without unduly sacrificing simplicity, by using Reynolds-stress closure. Another goal has been to design the model so that it collapses to simpler models for flows that can be adequately treated thereby.

Our codes can be expected to produce accurate results for flows with scales that are not of greatly disparate size in different directions and for which the turbulent spectra are similar and can be described by two parameters, an integral scale and a dissipative scale. Our current research is directed toward developing equations for a tensor of second rank, called the scale tensor, derived from the two-point correlation equations. (If correlations of a scalar with the velocity are also involved in the flow, there is in addition a scale vector to be considered.) We believe that the use of such equations in conjunction with suitably modified Reynolds-stress-closure equations would give results applicable to an even wider class of flows, since such equations contain information about eddy structure.

In making computations for the Stanford Conference we have used operational codes to calculate a variety of turbulent flows in order to demonstrate their generality. The 18 cases represent a compromise between this desire for a broad verification set and the necessity of keeping costs in line. They range from the simple homogeneous flows to the true predictive case of the flow downstream of a backward facing step with the wall opposite the step at a 6° angle. Five of the cases are compressible, the rest incompressible.

We used two main programs for our computations: ARB (Sullivan and Varma, 1978; Sullivan, 1980) and WAKE (Hirsh, 1979). They both use the same Reynolds-stress

*Aeronautical Research Assoc. of Princeton, Inc., P.O. Box 2229, Princeton, NJ 08540

modeling (except that ARB has additional modeling for terms that occur only in compressible flow) with the same values of the coefficients. However, the turbulence scale, λ , is computed differently. ARB uses an algebraic formula, while WAKE uses a differential equation to determine λ . We recognize that any such differential equation with constant coefficients cannot be correct (Donaldson and Sandri, 1981). Nevertheless such equations are more useful than one might expect in much the same way that eddy viscosity is a much more useful concept than one might expect.

As programs, ARB and WAKE differ considerably in that ARB is parabolic with one space dimension and is used only for boundary layers, whereas WAKE is parabolic with two space dimensions and is used for three-dimensional flows or time-dependent two-dimensional flows. Thus WAKE can handle two-dimensional elliptic problems. The boundary layers that ARB computes can be on flat plates or bodies of revolution with an arbitrary distribution of cross-sectional area (the body can be rotating or not). A variation of ARB called RSL has no provision for rotating bodies, but can do unbounded shear layers as well as boundary layers. (RSL also has provision for calculating multi-species reacting flows.) RSL was used in this project only for Case 0311 (mixing layer).

Another difference between the two programs involves wall conditions: ARB computes all the way to the wall with no special provision except that the formula for λ makes it proportional to the distance from the wall when that distance is small, whereas WAKE uses the law of the wall to establish boundary conditions some distance off the wall.

WAKE was used to compute Cases 0421 and 0422(P2). These separated flows have been calculated as elliptic, unsteady flows. The flow is free to develop two-dimensional unsteady eddies which are resolved by the computation. The influence of the smaller three-dimensional turbulence is incorporated by the turbulence closure model.

The homogeneous cases were done by an ordinary differential equation solver using the equations to which the WAKE equations reduce under those conditions.

The method descriptor for ARB is RSTN where the N denotes a no-slip condition at the wall, with no modification of the equations. For RSL the descriptor is RSTC, for WAKE it is RSLZ, and for the ordinary differential equation version of WAKE it is RSLC.

Table 1 lists the cases we did along with the method descriptors, the approximate value of y^+ for the first point off the wall, the approximate number of mesh points, and the approximate CPU computing time on a VAX 11/780.

Many of the cases lacked sufficient data on the initial conditions to show Reynolds-stress modeling to good advantage. Nevertheless the results were generally as good as or better than those submitted by other groups using different methods.

The incompressible boundary layers included cases with blowing, suction, and adverse or zero pressure gradient. The agreement was quite good for the most part.

Specific compressible boundary-layer cases included two with adverse pressure gradient and one with a favorable pressure gradient and blowing. Here we found good results except that velocity correlations were found to be too large by as much as 100%. This is perhaps due to the fact that the extension of our Reynolds-stress modeling to compressible flow introduces new parameters that might be adjusted. No funding has been acquired to accomplish this task, so the coefficients of the new terms have been set equal to the coefficients of similar terms for incompressible flow or set to zero.

Other compressible calculations determined the skin friction of a flat-plate boundary layer as a function of Mach number and as a function of wall temperature. Again the results were reasonably good.

Flows calculated with a differential equation for determining the scale were several homogeneous flows and two flows behind a backward-facing step. Among the homogeneous flows, agreement was generally good for the decay of isotropic turbulence, for plane strain, for axisymmetric strain, and for homogeneous shear. On the other hand, the return to isotropy after distorting strain in axisymmetric flows is much too rapid according to our results. This may be due in part to our neglect of rapid pressure terms which forces a higher coefficient on the Rotta terms. However, some of the flows return so slowly that the inclusion of rapid strain terms would not give good agreement. Furthermore, in the two-dimensional plane strain case, our results are very good indeed. It appears that some account of structure of the eddies is necessary for accurate prediction of these flows; the axisymmetric strain may produce highly elongated vortices aligned with the flow which could be very stable, and hence persist for a long time.

For the backward-facing-step flows we obtained an unsteady two-dimensional solution, i.e., some of the turbulence energy is contained in the two-dimensional eddies. In fact, if the length-scale equation was not modified, most of the energy ended in the resolved eddies. This is unrealistic, since we know there is significant three-dimensional motion, so we applied a lower limit to the length scale, forcing the modeled stresses to contain significant energy. Profiles of turbulence quantities then include both resolved and modeled components, averaged over a time period which covers several flow times through the box. The results for both cases, one of which was predictive, were good.

In summary, we are encouraged by these results. We believe they demonstrate that a wide range of problems can be handled by Reynolds-stress-closure models even with a scale equation that is very primitive. It is our belief that the direction to be taken is the development of tensor- (and vector-) scale equations and the proper

coupling of this information into the Reynolds-stress equations. This view is strengthened by the results of the calculations of return to isotropy mentioned above.

There are really compelling reasons at this time for having predictive capabilities for stratified flows. When one considers turbulence in such flows, it is clear that significant efforts in Reynolds-stress-closure modeling should be expended in the months ahead and, in all probability, for some years to come.*

This work was partially supported by the Air Force Office of Scientific Research, Contract F49620-81-C0057.

References

- Donaldson, C. duP. (1973). "Atmospheric turbulence and the dispersal of atmospheric pollutants," AMS Workshop on Micrometeorology (D. A. Haugen, ed.), Science Press, Boston, pp. 313-390.
- Donaldson, C. duP., and G. Sandri (1981). "On the inclusion of information on eddy structure in second-order closure models of turbulent flows," presented at the AGARD Symposium on Fluid Dynamics of Jets with Applications to V/STOL, Lisbon, Portugal.
- Hirsh, J. E. (1979). "Vortex interactions and decay in aircraft wakes: The WAKE computer program programmer manual," A.R.A.P. Report No. 400.
- Levellan, W. S. (1977). "Use of invariant modeling," in Handbook of Turbulence, (W. Frost and T. H. Moulden, eds.), Plenum Publishing Corporation, Vol. 1, pp. 237-280.
- Sullivan, R. D., and A. K. Varma (1978). "ARB: A program to compute the turbulent boundary layer on an arbitrary body of revolution," A.R.A.P. Report No. 317.
- Sullivan, R. D. (1980). "ARB: A supplementary manual", A.R.A.P. Tech. Memo 80-16.

Table 1

Case	Short Description	Method Descriptor	y^+	Mesh Points	CPU Time
0141	B.L., $\partial p/\partial x > 0$	RSTN	3 30		
0241	B.L., Blowing	RSTN	1 40		
0242	B.L., $\partial p/\partial x > 0$, Suction	RSTN		35	3 min
0244	B.L., Suction	RSTN	2 25		
0311	Mixing Layer	RSTC	- 25		
0371	Homogeneous Isotropic	RSLC	-	-	10 sec
0373	Homogeneous Relaxing	RSLC	-	-	10 sec
0374	Homogeneous Plane Strain	RSLC	-	-	10 sec
0375	Homogeneous Axisymmetric Strain	RSLC	-	-	10 sec
0376	Homogeneous Shear	RSLC	- -		10 sec
0421	Back Step	RSLZ	30	40x60	
0422(P2)	Back Step, Predictive	RSLZ	30	40x60	10 hr
0612	Flat-Plate B.L.	RSTN	1 40		
8101	Compressible B.L., C_f vs M	RSTN	1	35	3 min
8201	Compressible B.L., C_f vs T_w	RSTN	1	35	3 min
8301	Compressible B.L., Blowing $\partial p/\partial x < 0$	RSTN	1	40	3 min
8403	Compressible B.L., $\partial p/\partial x > 0$	RSTN	6	30	3 min
8411	Compressible B.L., $\partial p/\partial x > 0$	RSTN	2	40	3 min

*[Ed.: Two paragraphs here have been moved to consolidate discussion on modeling; see p. 1006 of Vol. II.]



F. A. Dvorak

COMPARISON OF COMPUTATION WITH EXPERIMENT

Summary Report

(The Modeling of Airfoil Separation in Subsonic Flow)

by

F. A. Dvorak and B. Maskew*

Computer Group Number: 46

Case 0441

Abstract

A free-shear-layer model for separation has been developed which enables one to calculate the flow about airfoils up to and beyond the stall. The calculation procedure involves iteration between viscous and inviscid flows. The separation region is modeled in the inviscid flow analysis using free vortex sheets whose shapes are determined by iteration. The outer iteration employs boundary-layer calculations to determine the location of separation. In subsonic flow the inviscid flow field is calculated using a panel method based on linearly varying vortex and source singularities. Viscous effects are introduced via the surface-transpiration approach. The method has been compared with experiment for a wide range of airfoil types. The stall behavior for airfoils with trailing-edge or leading-edge separation is predicted quite well, while thin airfoil or long bubble stall is poorly predicted. The method has been applied at angles of attack through 90° with excellent results.

Introduction

Boundary-layer separation is one of the least understood but most important of fluid-flow phenomena affecting aerodynamic forces and moments. Its accurate modeling is essential to the estimation of airborne vehicle performance. Currently, reliance is placed on wind tunnel tests to determine the consequences of separation, a procedure which is not entirely free of doubt because of Reynolds-number effects. Successful theoretical modeling of separation is limited to a small number of special cases, one of which is two-dimensional turbulent boundary-layer separation from airfoils or diffusers. The first successful model for trailing-edge separation was developed by Jacob (1967). With Jacob's model, the separation region is simulated using source fluid, the distribution of which is chosen to give constant pressure everywhere in the separation region. In general, the method predicts the upstream pressure distribution in a satisfactory manner, although agreement with experiment for base pressure level is not consistent.

*Analytical Methods, Inc., Redmond, WA 98052

Recently a separation model has been developed by Analytical Methods, Inc. which replaces the source distribution in the separation zone by a vortex wake model. This model is described in some detail in Maskew and Dvorak (1977), but is briefly discussed herein for reasons of completeness.

Separation Model

An approximate model of the flow about an airfoil with a region of separation is based on the following:

- (i) The boundary layer and free-shear layers do not have significant thickness and, hence, can be represented as slip surfaces; that is, streamlines across which there exists a jump in velocity.
- (ii) The wake region does not have significant vorticity and has constant total pressure (lower than the free-stream total pressure). It is, therefore, taken to be a potential flow region.

The flow field in the potential flow is obtained using linearly varying vortex singularities distributed on planar panels. The wake is represented by sheets of vorticity shed at the separation points. The mathematical problem is to find the vorticity sheet strength such that the appropriate boundary conditions are met. The position of the vorticity sheet representing the free-shear layer is not known a priori.

Approximations for the Free-Shear Layer

(i) Wake Shape

Initially, the streamlines are not known, and so the shapes of the free-shear layers must be obtained iteratively starting from an initial assumption. Once the wake calculation begins, the initial slope and downstream position of each wake is determined by iteration. The final wake position represents the separating streamline.

(ii) Wake Length

Early calculations indicated that the results were sensitive to the length of the free vortex sheets. Good correlation with experimental results was obtained only with relatively short wakes; i.e., wakes extending $0.1c$ to $0.2c$ beyond the trailing edge. Such a model appears reasonable in the light of experimental evidence: the separated wake does, in fact, close quickly downstream of the trailing edge, as a result of the strong entrainment process brought about by the rotation in the free shear layers (see Seetharam and Wentz, 1975). On the basis of several comparisons with experiment, a simple correlation was obtained for the wake length as a function of the airfoil thickness to chord ratio. This is discussed in detail in (Maskew and Dvorak, 1977).

(iii) Wake Pressure

The approximation of zero static pressure drop across the free-shear layer is used to obtain an expression for the total pressure in the wake in terms of the strength of the free vortex sheets. The jump in total pressure across the shear layer is $\Delta H = -\rho V \gamma_u$.

Once the vorticity strengths of the individual panels representing the airfoil and of the vorticity sheets representing the wake are determined, the velocity at any point in the flow field can be calculated.

The pressures are calculated from the velocities according to the Bernoulli equation which is expressed non-dimensionally as

$$C_p = 1 - \left(\frac{V}{V_\infty}\right)^2 + \frac{\Delta H}{q_\infty}$$

where $C_p = (p - p_\infty)/q_\infty$, $q_\infty = 1/2 \rho V_\infty^2$, and $\Delta H =$ increase in total pressure over that at infinity. Note that $\Delta H = 0$ everywhere except in the wake region.

Boundary-Layer Methods

The laminar boundary-layer development is calculated by the method of Curle (1967), an adaption of the well-known method of Thwaites (1949). The calculation proceeds either to laminar separation or to the end of the airfoil—whichever occurs first. The calculated boundary-layer development is then interrogated to determine if transition, laminar separation, or forced transition (boundary-layer tripping) has taken place. If any of these phenomena has occurred, the downstream flow is assumed to be turbulent.

Methods for the calculation of turbulent boundary layers in two dimensions have been developed by many investigators. A review of these methods was made at the 1968 AFOSR-IFP-Stanford Conference (Kline et al., 1969). One of the methods, an integral method by Nash and Hicks (1969) compared very favorably with the more complex finite-difference methods. Now, several years later, the method remains an excellent approach for application to the current problem, both in terms of accuracy and speed. Separation is predicted when the skin-friction coefficient reaches zero.

Calculation Procedure

The overall calculation procedure involves two separate iteration loops.

(1) Wake Shape Iteration

The iteration loop for wake shape is the inner loop and involves the potential flow analysis only. Within this loop the separation points are fixed. The wake shape is calculated as follows. Using the previous vorticity distribution, velocities are calculated at the panel mid-points on the free vortex sheets. The new wake shape is then determined by piecewise integration starting at the

separation points. The upper and lower sheet downstream end points, which were coincident in the initial wake, are allowed to move independently in subsequent iterations. At each iteration the wake influence coefficients at the surface control points are recalculated, and a new potential flow solution is obtained.

(ii) Viscous/Potential Flow Iteration

This outer iteration loop transfers the potential-flow pressure distribution to the boundary-layer analysis and returns with the separation points and with the boundary-layer source distribution. The source distribution is determined directly from the boundary-layer solution as $\sigma = d/ds(U_e \delta^*)$, where U_e is the streamwise potential flow velocity at the edge of the boundary layer, and δ^* is the displacement thickness. The addition of this source distribution modifies the normal velocity, V_N , at each panel control point. The sources are set to zero in the separated region.

The program generates a new wake shape using the new separation points together with information from the previous iterated wake. A new potential flow situation is then obtained, and so on. The outer iteration is terminated when the change in C_p is below 1%.

Discussion of Results

The comparison with the experimental pressure distribution of Case 0441 is shown on Fig. 1. Two Reynolds-number conditions were evaluated: the nominal test condition, $Re = 1.52 \times 10^6$, and a higher value, $Re = 9.0 \times 10^6$. The calculated pressure distribution at the higher Reynolds number is clearly in better agreement with experiment except in the separated flow region. This raises the question of the effect of a high tunnel turbulence level on the data. A second question arises from the use of a passive flow control system (vortex generators). What local changes occur to the flow field in the airfoil trailing-edge region due to the vortex generators?

Additional calculations were made for comparison with the data of Pinkerton (1938). This data was taken on the same NACA 4412 planform, although the test environment differed considerably from that of Case 0441. Pinkerton used a three-dimensional model with corrections to the angle of attack due to downwash. No wall-boundary-layer control was required. As shown in Fig. 2, a calculated pressure distribution for an effective Reynolds number of 3.4×10^6 (as referenced by Pinkerton) is in excellent agreement with experiment. Figure 3 shows a comparison of the predicted $C_{p,max}$ with Pinkerton's data for a wide range of Reynolds number. The excellent agreement suggests that Program CLMAX correctly predicts the effect of Reynolds number on the maximum lift coefficient. The conclusion remains that some as yet unexplained combination of different

phenomena give rise to the results of Case 0441, which has some characteristics of a high-Reynolds-number flow (high suction peak and delayed separation), while at the same time having a separation pressure level more in line with a lower Reynolds number. NASA Ames Research Center is currently planning a wind tunnel test to explore this airfoil section in greater detail using non-intrusive measuring techniques.

Acknowledgment

The authors gratefully acknowledge the support given by the U.S. Army Research Office, Research Triangle Park, N.C., for this work under Contracts DAAG29-76-C-0019 and DAAG29-79-C-0004.

References

- Curle, N. (1967). "A two-parameter method for calculating the two-dimensional incompressible laminar boundary layer," J. R. Aero. Soc., 71.
- Jacob, K. (1967). "Computation of separated, incompressible flow around airfoils and determination of maximum lift," AVA Report 66, A, 62.
- Kline, S. J., M. V. Morkovin, G. Sovran, and D. J. Cockrell (1969). Computation of Turbulent Boundary Layers, Proc., 1968 AFOSR-IFP-Stanford Conference, Dept. of Mech. Eng., Stanford, California.
- Maskev, B., and F. A. Dvorak (1977). "The prediction of $C_{l_{max}}$ using a separated flow model," Proc., 33rd Annual Forum of the American Helicopter Society, Washington, D.C. Also J. Amer. Hel. Soc., April 1978.
- Nash, J. F., and J. G. Hicks (1969). "An integral method including the effect of upstream history on the turbulent shear stress," in Kline et al. (1969), pp. 37-45.
- Pinkerton, R. N. (1938). "The variation with Reynolds number of pressure distribution over an airfoil section," NACA Report No. 613.
- Seetharam, H. C., and W. H. Wentz (1975). "Experimental studies of flow separation and stalling on a two-dimensional airfoil at low speeds," NASA CR-2560.
- Thwaites, B. (1949). "Approximate calculation of the laminar boundary layer," Aero. Quart., 1.

PLOT 1 CASE 0441 FILE 3

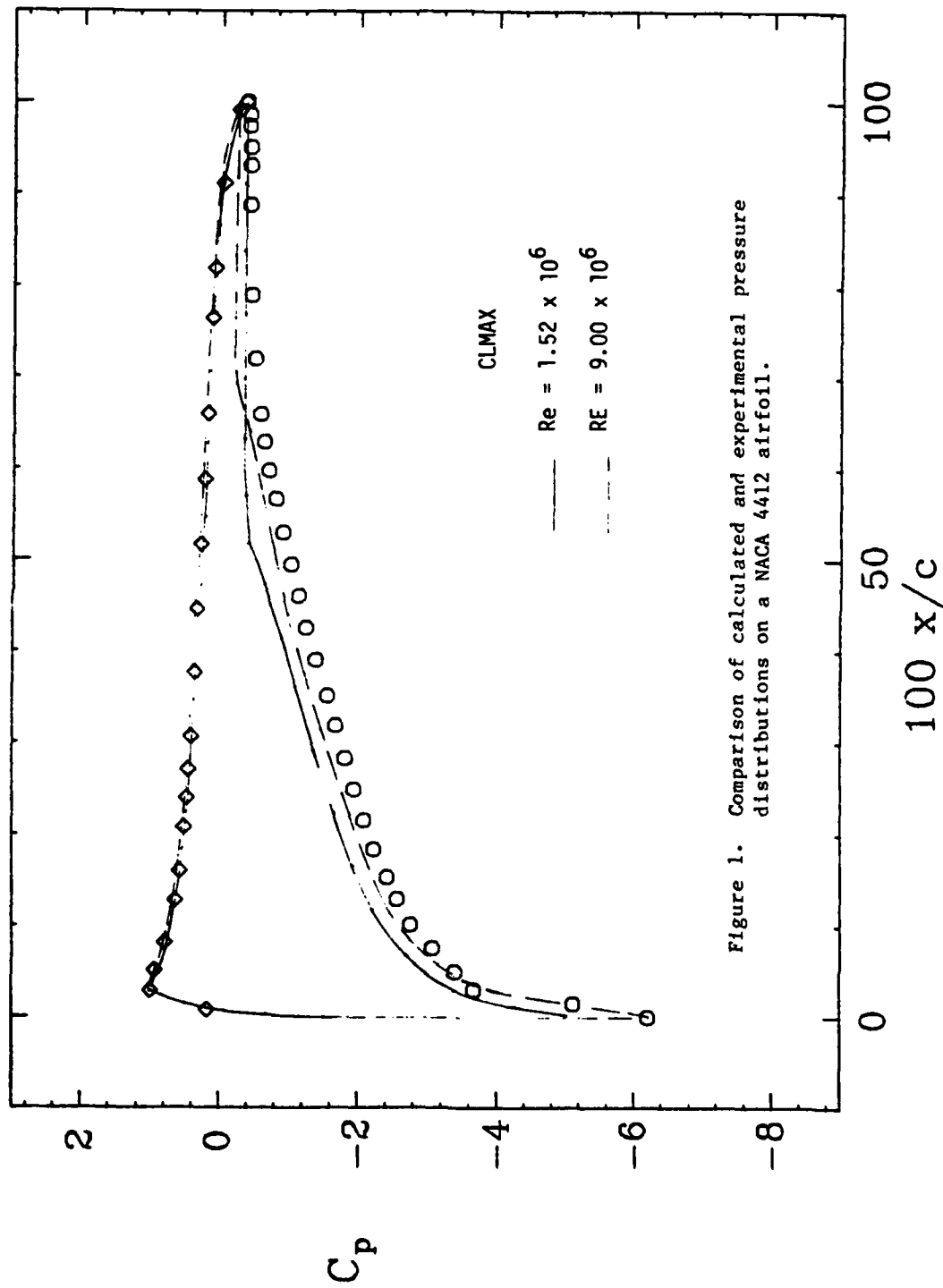


Figure 1. Comparison of calculated and experimental pressure distributions on a NACA 4412 airfoil.

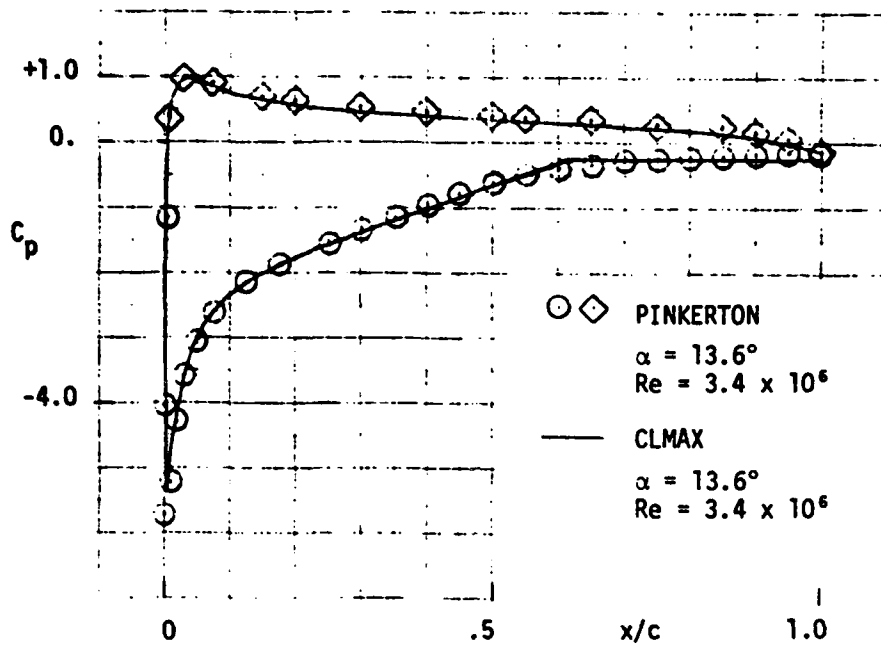


Figure 2. Comparison of calculated and experimental pressure distributions on a NACA 4412 airfoil.

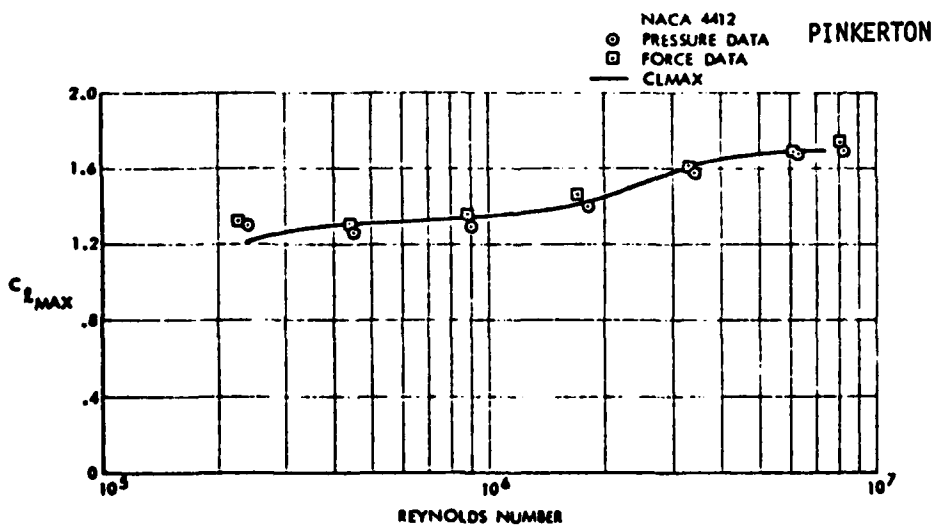


Figure 3. Comparison of calculated and experimental $C_{L_{max}}$ variation with Reynolds number for the NACA 4412.



COMPARISON OF COMPUTATION WITH EXPERIMENT

Summary Report

by

J. H. Ferziger,* J. Bardina,* A. A. Lyrio,*
and R. C. Strawn*

Computer Group Number: 45

J.H. Ferziger

R.C. Strawn

Cases 0141, 0142, 0143, 0431, 0612

Our group at Stanford has developed integral methods for predicting detaching and detached turbulent boundary-layer flows. Variations of one such method have been used to predict five test cases for the 1981 Complex Turbulent Flows Conference. In the following summary, an outline of the relevant equations is presented; more detailed descriptions are contained in Bardina et al. (1981a,b), Childs et al. (1981), Ghose and Kline (1976), and Lyrio et al. (1981).

Finally, a short discussion of each computed test case will be presented.

Summary of Equations

The basic integral methods used in the computations are completely described by Lyrio et al. (1981). They consist of the following equations:

1. Momentum Integral Equation

$$\frac{d\theta}{dx} + (2 + H) \frac{\theta}{U_\infty} \frac{dU_\infty}{dx} = \frac{\bar{c}_f}{2} + \frac{1}{U_\infty^2} \frac{d}{dx} \int_0^\delta (\overline{u'^2} - \overline{v'^2}) dy \quad (1)$$

For detaching flows, the normal stress term is treated by a model due to Ross (1953). According to this model, the last term is modeled as:

$$VN = \frac{A}{U_\infty^2} \frac{d}{dx} (U_\infty^2 \delta^*) \quad (2)$$

A value of $A = 0.023$ was chosen from numerical experiments.

2. Shape Factor and Skin-Friction Correlations

Kline et al. (1981) present the following shape-factor correlation for detaching and detached turbulent boundary layers:

$$h = 1.5\Lambda + 0.179 V_T + 0.321 \frac{V_T^2}{\Lambda} \quad (3)$$

where $h = (H - 1)/H$, $\Lambda = \delta^*/\delta$, and V_T is a nondimensional shear velocity given implicitly by:

*Department of Mech. Eng., Stanford University, Stanford, CA 94305

$$V_T = \frac{1 - 2\Lambda}{\ln\left|\frac{V_T}{\Lambda}\right| + \ln(KRe_{\delta^*}) + 0.05} \quad (4)$$

For ease of computation, we use an explicit approximation to Eq. 4:

$$V_T = 0.44 |1 - 2\Lambda|^{0.885} \left(\frac{\Lambda}{Re_{\delta^*}}\right)^{0.115} \text{sign}(1 - 2\Lambda) \quad (5)$$

Kline et al. (1981) have shown this shape factor relation (3) to correlate a wide range of separating turbulent boundary-layer data.

3. Entrainment Equation

The entrainment rate is defined by:

$$E = \frac{1}{U_{\infty}} \frac{d}{dx} [U_{\infty}(\delta - \delta^*)] \quad (6)$$

Three different correlations for the non-dimensional entrainment rate E were used. All give very similar results for adverse pressure-gradient flows. The use of three correlations rather than one is the result of test cases being computed by different members of our group in various stages of their research and not of selecting a "tuned" correlation for each particular case.

The three entrainment correlations are:

a) A relation between entrainment rate and maximum shear stress in the boundary layer first proposed by Bradshaw et al. (1967):

$$E = \frac{10 \tau_{\max}}{\rho U_{\infty}^2}$$

Details regarding the evaluation of τ_{\max} are given in Ghose and Kline (1976) and Lyrio et al. (1981).

b) A relation between entrainment rate, the integral parameter Λ , and a pressure-gradient parameter Ke :

$$E = 4.24 Ke \left(\frac{\Lambda}{1 - \Lambda}\right)^{0.916} \quad (8)$$

c) For diffuser flows, a simplified entrainment equation is used which requires no lag:

$$E = 0.0083 (1 - \Lambda)^{-2.5} \quad (9)$$

Equations 1 through 9 can be combined to solve prescribed pressure-gradient boundary-layer flows. The system is solved by marching in the downstream direction. For diffuser flows, where the boundary layers and potential core must interact, additional equations are needed.

4. Continuity Equation

In order to couple a potential core flow to the boundary layers in a diffuser flow, a one-dimensional radial source flow is used for the core flow:

$$Q = U_{\infty}(1 - B)W \quad (10)$$

where W is the diffuser width, B is the blockage ($2\delta^*/W$ for symmetric boundary layers), and Q the volumetric flow rate. Equation 10 can be combined with Eqs. 1 through 9. The boundary layers and the core flow are computed simultaneously for internal flows.

5. Diffuser Flows--Limits on Entrainment

For diffuser flows, two physical limits on the entrainment rate are implemented after detachment. These limits are obtained by requiring:

- a) C_p can never decrease in the diffusing section;
- b) \bar{C}_f can never increase in the diffusing section.

These limits complete the system of equations for diffuser flows. Counterparts of the above equations for axisymmetric flow are derived in Lyrio et al. (1981).

Proposed Extensions of the Basic Method

Childs et al. (1981) have already extended the basic integral method to include effects of compressibility up to $M = 0.9$. Lyrio et al. (1981) have extended it to unsteady flows. The extensions to axisymmetric flows have already been mentioned. None of the compressible Conference test cases were calculated, however, due to lack of time and manpower. Proposed extensions of the method would include the effects of boundary-layer suction and blowing and the effects of free-stream turbulence in the correlations referred to above.

Discussion of Results from Computation

1. Case 0612, Zero Pressure-Gradient Boundary-Layer Flow (Wieghardt)

This flow was computed as a prescribed pressure-gradient case using the entrainment correlation given by Eq. 7. Since the initial velocity profile contains only five measured data points, there is probably considerable uncertainty in the starting values of all of the integral parameters including \bar{C}_f . Thus, it was not possible to fit all of the initial data to our correlations. We therefore matched the initial \bar{C}_f , but agreement with the other given inlet parameters is only fair. Trial-and-error tests, using different inlet conditions, could probably produce improved agreement with the data downstream. The velocity profiles were generated using Coles' wall-wake law from which Eqs. 3 and 4 are derived.

2. Case 0141, Adverse Pressure-Gradient Flow (Samuel and Joubert)

This flow was also computed using a prescribed pressure gradient. Results were obtained using the entrainment correlation given by Eq. 8. Velocity profiles for this case were generated using Coles' wall-wake law. Higher-order turbulence quantities such as $\overline{u'v'}$ and $\overline{u'^2}$ are not used in our integral methods so they are not presented in our output plots.

3. Cases 0142 and 0143, High- and Low-Core Turbulence Conical Diffusers (Pozzorini)

These flows were computed by coupling the one-dimensional continuity equation (10) for the core flow to the boundary-layer equations. Results for the low-core-turbulence case (0142) predict pressure recovery quite well, but premature separation is predicted at the diffuser exit plane. Hence, calculated skin-friction and velocity profiles deviate from the data at the diffuser exit.

Results from the high-core-turbulence case indicate the necessity of revising the modeling to account for free-stream turbulence effects.

4. Case 0431, Separating Boundary-Layer Flow (Simpson et al.)

This case was computed as a symmetric diffuser flow. The given streamline near the upper wall surface was used as a line of symmetry, and two identical boundary layers were coupled with a one-dimensional continuity relation to complete the system. The entrainment correlation given by Eq. 9 was used for this case, and velocity profiles were generated using Coles' wall-wake law. Results are quite good for skin-friction and velocity profile prediction, particularly in the vicinity of boundary-layer detachment.

References

- Bardina, J., S. J. Kline, and J. H. Ferziger (1981a). "A prediction method for diffuser flow at low Mach numbers including a new correlation for detachment and reattachment," Report PD-22, Thermosciences Div., Mech. Eng. Dept., Stanford University.
- Bardina, J., A. A. Lyrio, S. J. Kline, J. H. Ferziger and J. P. Johnston (1981b). "A prediction method for planar diffuser flows," Trans. ASME, J. Fluids Eng., 103, 315.
- Bradshaw, P., D. H. Ferriss, and N. P. Atwell (1967). "Calculation of boundary layer development using the turbulent energy equation," J. Fluid Mech., 28, Part 3, 593-616.
- Childs, R., J. H. Ferziger, and S. J. Kline (1981). "A computational method for compressible planar diffusers," Report PD-24, Thermosciences Div., Mech. Eng. Dept., Stanford University.
- Ghose, S., and S. J. Kline (1976). "Prediction of transitory stall in two-dimensional diffusers," Report MD-36, Thermosciences Div., Mech. Eng. Dept., Stanford University. See also Trans. ASME, J. Fluids Eng., Ser. I, 100, 419, 1978.

Kline, S. J., J. Bardina, and R. C. Strawn (1981). "Correlation and computation of turbulent boundary layers on two-dimensional faired surfaces," AIAA Paper 81-1220, presented at AIAA 14th Fluid and Plasma Dynamics Conf., Palo Alto, CA.

Lyrio, A. A., J. H., Ferziger, and S. J. Kline (1981). "An integral method for the computation of steady and unsteady turbulent boundary layer flows, including the transitory stall regime in diffusers," Report PD-23, Thermosciences Div., Mech. Eng. Dept., Stanford University.

Ross, D. (1953). "Evaluation of momentum integral equation for turbulent boundary layers," J. Aero. Sci., 19.



COMPARISON OF COMPUTATION WITH EXPERIMENT

Summary Report

(The Computation of a Highly Curved Mixing Layer with an Algebraic Reynolds-Stress Closure Scheme)

by

C. Hah

C. Hah* and B. Lakshminarayana†

B. Lakshminarayana

Computer Group Number: 19

Case 0331

Abstract

The highly curved mixing layer measured by Castro and Bradshaw (1976) is predicted numerically with an algebraic Reynolds-stress closure scheme. The turbulence closure model is based on the transport equations for the Reynolds stress and the dissipation rate of turbulence kinetic energy. The convection and diffusion terms in the Reynolds-stress transport equation were assumed to be related to the production term. The curvature effect is included in the production of turbulence kinetic energy. The comparison with the experimental data shows that the stabilizing effect of the curvature is well reproduced by the model. However, the experimentally measured rapid rise of turbulence quantities in the straight region downstream of the curved section is not well predicted even though there is good agreement with the qualitative trend.

Coordinate System and Governing Equation

For the calculation of curved mixing layer, a curvilinear coordinate system shown in Fig. 1 was used. r is the distance from the center of curvature, s is the streamwise distance on a specified path, and b is normal to s and r . With this coordinate, the actual streamline of the mixing layer can be closely represented. The detailed characteristics of this coordinate system are given by Hah and Lakshminarayana (1980). The fundamental metric tensor for this coordinate system is

$$g_{ij} = \begin{bmatrix} 1 & -\frac{s}{r} & 0 \\ -\frac{s}{r} & 1 + \frac{s^2}{r^2} & 0 \\ 0 & 0 & 1 \end{bmatrix}; \quad g^{ij} = \begin{bmatrix} 1 + \frac{s^2}{r^2} & \frac{s}{r} & 0 \\ \frac{s}{r} & 1 & 0 \\ 0 & 0 & 1 \end{bmatrix} \quad (1)$$

Christoffel symbols of the second kind are as follows:

*General Electric R&D Center, Schenectady, NY 12345

†Department of Aerospace Engineering, Pennsylvania State University, PA 16802

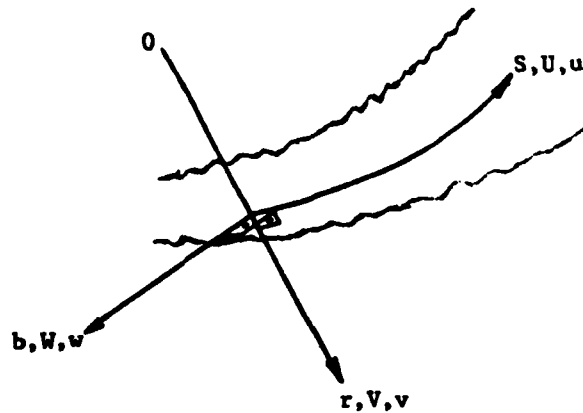


Figure 1. Coordinate System and Notation.

$$\Gamma_{11}^1 = -\frac{s}{r}, \quad \Gamma_{11}^2 = -\frac{1}{r}, \quad \Gamma_{12}^1 = -\Gamma_{22}^2 = \frac{s^2}{r}, \quad \Gamma_{21}^2 = \frac{s}{r}, \quad \Gamma_{22}^1 = -\frac{s^3}{r} \quad (2)$$

All other Christoffel symbols of the second kind are zero.

The above coordinate system is a generalized curvilinear coordinate system and can be converted to either the Cartesian or the s - n coordinate system used by Bradshaw (1973).

Then the governing continuity equation is,

$$\frac{\partial U}{\partial s} + \frac{\partial V}{\partial r} = 0, \quad \frac{\partial u}{\partial s} + \frac{\partial v}{\partial r} = 0 \quad (3)$$

and the mean-momentum-conservation equations for turbulent flow are:

$$U \frac{\partial U}{\partial s} + V \frac{\partial U}{\partial r} + U^2 \Gamma_{11}^1 + V^2 \Gamma_{22}^1 + 2 UV \Gamma_{12}^1 = -\frac{1}{\rho} \left[\frac{s}{r} \frac{\partial p}{\partial r} + \left(1 + \frac{s^2}{r}\right) \frac{\partial p}{\partial s} \right] - \frac{\partial \overline{uv}}{\partial r} - \frac{\partial \overline{u^2}}{\partial s} - u^2 \Gamma_{11}^1 - \overline{uv} \Gamma_{12}^1 - \overline{v^2} \Gamma_{22}^1 \quad (4)$$

$$U \frac{\partial V}{\partial s} + V \frac{\partial V}{\partial r} + U^2 \Gamma_{11}^2 + V^2 \Gamma_{22}^2 + 2 UV \Gamma_{12}^2 = -\frac{1}{\rho} \left[\frac{\partial p}{\partial r} + \frac{s}{r} \frac{\partial p}{\partial s} \right] - \frac{\partial \overline{uv}}{\partial s} - \frac{\partial \overline{v^2}}{\partial r} - \overline{u^2} \Gamma_{11}^2 - \overline{v^2} \Gamma_{22}^2 - \overline{uv} \Gamma_{12}^2 \quad (5)$$

where U and V are contravariant components of mean velocity, u and v are fluctuating components of velocity, and p is the static pressure.

Turbulence-Closure Model

To get closure of the governing equations (3) through (5) for the unknowns U , V , and p , a proper turbulence-closure scheme is required for the description of the correlation of fluctuating velocity components. An algebraic Reynolds-stress closure model is used for the closure of governing equations. With the adopted turbulence-closure model, the diffusion and convection terms are considered collectively and the combined effect of the two terms is assumed to be related to the production term. Then, the Reynolds-stress components can be evaluated if the values of the turbulent kinetic energy, the energy dissipation rate, and the mean shear rates are known at a given location of the flow field.

The two transport equations for the turbulence kinetic energy and the energy dissipation rate are as follows:

$$U^i \frac{\partial k}{\partial x^i} = \frac{\partial}{\partial x^i} \left(\frac{v_{\text{eff}}}{\sigma_k} \frac{\partial k}{\partial x^i} \right) + P - \epsilon \quad (6)$$

$$U^i \frac{\partial \epsilon}{\partial x^i} = \frac{\partial}{\partial x^i} \left(\frac{v_{\text{eff}}}{\sigma_\epsilon} \frac{\partial \epsilon}{\partial x^i} \right) + S - C_{\epsilon_2} \frac{\epsilon^2}{k} \quad (7)$$

where

$$v_{\text{eff}} = C_\mu k^2 / \epsilon ; \quad P = -\overline{u_i u_j} U_{,j}^i ; \quad k = g_{ij} \overline{u^i u^j} / 2$$

and

$$S = C_s \frac{\epsilon^2}{k^3} (\overline{u^i u^j} - 2k\delta_{ij}/3)(\overline{u^j u^i} - 2k\delta_{ij}/3)$$

The Reynolds-stress components are evaluated using the following modeled Reynolds-stress transport equation of Hah and Lakshminarayana (1980a,b):

$$0 = (1+C_1)(-\overline{u_k u^j} U_{,k}^i - \overline{u_k u^i} U_{,k}^j)(1-\gamma) - (2/3)g^{ij}\epsilon(1-\gamma) - C_{\phi 1}(\epsilon/k)(\overline{u^i u^j} - 2g^{ij}k/3) \quad (8)$$

where C_1 relates the collective effects of the convection and diffusion terms to the production terms, and γ is constant related to the pressure-strain correlation due to the presence of mean-strain rate.

The effect of streamline curvature can be qualitatively explained using the following expression:

$$\omega^2 = 2 \frac{U}{r} \frac{d}{dr} (Ur) = 2 \left(\frac{U}{r} \frac{dU}{dr} + \frac{U^2}{r^2} \right) \quad (9)$$

where ω is the corresponding frequency, U circumferential velocity component, and r the radius of curvature. The flow field is stabilized by streamline curvature when ω

has a real value. For most thin shear flows the first term is dominant. To examine the effect of the streamline curvature on the presently used turbulence-closure model, the production term in Eq. 6 is written explicitly. For the coordinate system shown in Fig. 1, the expression for P is given by

$$P = -\overline{u_i u_j u_j^i} = -\overline{u^2} \left(\frac{\partial U}{\partial s} + U \frac{s}{r^2} + v \frac{s^2}{r^3} \right) - \overline{v^2} \left(\frac{\partial V}{\partial r} + U \frac{s}{r^2} - v \frac{s^2}{r^3} \right) - \overline{uv} \left(\frac{\partial U}{\partial r} + \frac{\partial V}{\partial s} - \frac{U}{r} + U \frac{s^2}{r^3} + v \frac{s}{r^2} - v \frac{s^3}{r^4} \right) \quad (10)$$

and if higher-order curvature terms including s/r^2 are neglected,

$$P = -\overline{u^2} \frac{\partial U}{\partial s} - \overline{v^2} \frac{\partial V}{\partial r} - \overline{uv} \left(\frac{\partial U}{\partial r} + \frac{\partial V}{\partial s} - \frac{U}{r} \right)$$

The above expression can be further simplified for the thin shear layer with small pressure gradient in the normal direction and then

$$P = v_{\text{eff}} \left[\left(\frac{\partial U}{\partial r} \right)^2 - \frac{U}{r} \frac{\partial U}{\partial r} \right] \quad (11)$$

The second term of the above expression has the same form as the principal term of Eq. 9 and represents the curvature effect that was discussed qualitatively.

Equation 11 indicates that the production of turbulence kinetic energy is decreased when the flow field is stabilized by the streamline curvature. As the energy dissipation rate is not affected by mean shear rates with the present model, the effective eddy viscosity (k^2/ϵ) behaves properly with regard to the effect of streamline curvature. Many investigators have used the production term P in Eq. 6 as a source term in Eq. 7, and reported poor prediction of curved flows.

When the production term (P) is used as a source term in the energy dissipation equation, the energy dissipation rate is also decreased for the stabilized flow due to streamline curvature. Therefore, the resulting eddy viscosity is almost independent of the effect of streamline curvature. The detailed comparison of numerical predictions with different forms of the source term in the energy dissipation equation is given by Hah and Lakshminaryana (1980b).

Numerical Scheme

The governing equations (3-5) are solved simultaneously with the turbulence-closure equations (6-8). The streamwise diffusion in the governing momentum equations are neglected and the parabolized equations are solved downstream. The curvature of the mixing layer is specified as an input and the calculation was done mainly to examine the performance of the turbulence-closure model for the given flow. Initial conditions are obtained with a preliminary calculation of the straight mixing layer.

The Reynolds stress at $S = 0$ was closely matched with the experimental data by adjusting the energy-dissipation rate. The boundary conditions at the edge of the mixing layer are that the pressure is equal to the atmospheric pressure and the mean velocity is zero. The boundary conditions at the potential flow region is that all the turbulence quantities are zero. The static pressure at the boundary in the potential flow region is obtained by integrating Eq. 5 with the known value of the streamline curvature and the mean velocity at the upstream station. The mean velocity at the boundary in the potential flow region is obtained with the pressure gradient along a streamline using Eq. 4. Approximately 300 forward steps are used in the curved flow region and another 300 forward steps are used in the straight flow region with 61 cross-stream grid points. The computation time on an IBM 370/4033 is approximately 0.2 sec per step.

Comparison with the Experimental Data

The comparison of mean-velocity profiles in Plates 53 and 56 shows good agreement between experiment and prediction. The mean-velocity profiles are very well predicted over the entire flow region. This may partly be due to the fact that the measured value of streamline curvature is used as an input data and the static pressure is estimated from the cross-stream momentum equation.

The comparison for the shear-stress distribution is given in Plates 54 and 57. The shear stress is overpredicted in the initial part of the curved flow, and underpredicted near the end of the curved-flow region and straight-flow region. Rapid rise in shear stress downstream of the curved-flow region is not well predicted. The comparison for the turbulence intensity is given in Plates 55 and 58. The streamwise intensity is overpredicted in the curved-flow region while the turbulence intensity level is substantially underpredicted in the straight-flow region.

Although the mean-velocity profiles are reasonably well predicted, the turbulence quantities are not properly predicted, especially in the region downstream of the severe streamline curvature. However, the stabilizing effect of streamline curvature in the curved-flow region is very well represented with the present turbulence-closure model. The poor agreement between the experimental data and the prediction in the flow region downstream of the curvature may be due to the assumption used for the present turbulence-closure model. Some of the error may be attributed to the experimental data. A full Reynolds-stress-closure scheme which utilizes the convection and diffusion effects individually may improve the prediction. An elliptic Navier-Stokes solution of the full flow field which does not use the streamline curvature as an input may produce more reasonable predictions.

Acknowledgments

The computer program utilized in this investigation was developed under the sponsorship of the National Aeronautics and Space Administration, through Grant NSG-3012, with L. Shaw as the technical monitor.

References

- Bradshaw, P. (1973). "Effects of streamline curvature on turbulent flow," AGARDograph No. 169.
- Castro, I. P. and P. Bradshaw (1976). "The turbulence structure of a highly curved mixing layer," J. Fluid Mech., 73:2, 265-304.
- Hah, C. and B. Lakshminarayana (1980a). "Numerical analysis of turbulent wakes of axial flow turbomachinery rotor blades," J. Fluids Eng., 102, 462-472.
- Hah, C. and B. Lakshminarayana (1980b). "Prediction of two- and three-dimensional asymmetrical turbulent wakes, including curvature and rotation effects," AIAA Jou., 18, 1196-1204.



COMPARISON OF COMPUTATION WITH EXPERIMENT

Summary Report

(Reynolds Stress - Dissipation Method for
High Reynolds Number Turbulent Flows)

by

K. Hanjalić, M. Ivanović, R. Selimović, N. Stosić, and S. Vasić*

Computer Group Number: 18

K. Hanjalić

Cases 0141, 0142, 0143, 0241, 0244, 0371, 0373, 0374, 0375, 0376, 0612

1. Postulations of the Method

Character and origin

The method used for the computations[†] that are discussed below employs the second-order one-point closure scheme, based on modeling the full differential transport equation for each component of the Reynolds-stress tensor $\overline{u_i u_j}$ and, in addition, the differential equation governing the decay rate of the turbulent kinetic energy. The employed modeling scheme is restricted to flows of high turbulence Reynolds number, and, as such, cannot be applied to flows with appreciable viscosity effects without adequate modifications.

Based on some early ideas of several workers, the present method was first shaped in an applicable form and tested extensively by Hanjalić and Launder (1972), and was subsequently refined and extended by Launder et al. (1975). A number of further extensions of the basic model to account for various additional effects, such as variable fluid properties, low-Reynolds-number effects, buoyancy, flow curvature, heat and mass transfer, etc., have been proposed and tested by the above-mentioned and other authors, but in most cases the amendments were proposed in the form of additional terms and functional relationships in such a way that the model remains reducible to the original form when the additional effects are absent.

Because the flow cases considered herein do not require any of the above-mentioned amendments (except, possibly, for the streamline curvature), it is basically the Launder-Reece-Rodi (LRR) form of the model which has been applied, with two modifications, which are briefly described later. They are:

*Masinski Fakultet, Omladinsko Setaliste, 71000 Sarajevo, Yugoslavia

[†]The computations reported here represent a part of the coordinated effort, undertaken jointly with groups from the following institutions: UMIST, Manchester (Prof. B. E. Launder); Imperial College, London (Dr. A. D. Gosman); University of California, Berkeley (Prof. J. A. C. Humphrey) and University of California, Davis. The present report discusses the results of the computations of the above indicated flow cases using the same basic turbulence model as other groups.

- (i) - modification of the modeling of the source term in the dissipation equation
- (ii) - modified treatment of the wall boundary conditions.

Variants of method applied

In its general form the method provides a solution of the full transport equations for all the non-zero components of the Reynolds-stress tensor. However, often simplified forms of these equations have been used for the computation of more complex flows, in particular the flows with recirculation and additional effects, as mentioned earlier. These simpler forms are derived from the full-stress model through either the neglect of the transport terms in the equations for turbulent stresses (Gibson and Launder, 1978), or their modeling by means of the sum of transport terms in the kinetic energy equation as given by Rodi (1976). In both cases the differential equations for the turbulent stresses are reduced to algebraic expressions, while the differential forms are used only for the equations governing the turbulence kinetic energy and its dissipation rate.

The computations reported here have been carried out using the full-stress model for all the above-mentioned cases, except for Cases 0142 and 0143 (axisymmetric diffusers), where the algebraic stress model of Gibson and Launder (1978) was applied (to avoid the computational inconveniences associated with the solution of the shear-stress equation for flows with axisymmetric geometry). For comparison these cases were also solved by means of the simple $k-\epsilon$ method.

Modifications incorporated in the present computations

Because the modifications mentioned earlier were only partially published in the literature so far, a brief summary will be given here (more details will be given in the report by Launder--see Summary Report by Computer Group 17³).

- (i) Almost all models that employ the equation for the dissipation rate as a way of providing the characteristic turbulence scales, use the expression

$$(C_{\epsilon 1} P - C_{\epsilon 2} \epsilon) \frac{\epsilon}{k}$$

to define the source of ϵ . (Here P stands for the production of the kinetic energy due to the mean rate of strain.) In spite of numerous successes in predicting various cases of turbulent flows, there have been notable failures, particularly in the case of rapid evolving flows and those with streamline curvature. The modifications incorporated in the present model replaces $P\epsilon/k$ in the above expression by the term $k(\partial U_i / \partial x_j)^2$. This remedy, as proposed by Hanjalić and

Launder (1981), seems to account, at least partially, for curvature effects. It provides also a somewhat looser coupling (in comparison with previous practice) of the turbulence energy balance in physical space—defined by the kinetic energy equation—and the energy-transfer process in spectral space, supposedly described (at least in gross terms) by the ϵ -equation. Consequently, the new form, satisfying the invariance requirements, seems to yield grounds for a better description of the flow evolution.

(ii) Because the method is not applicable within the viscosity-affected region in the vicinity of the solid wall, the Couette flow analysis is used to specify the boundary conditions in the form of wall functions. In comparison with earlier practice two postulates have been consistently followed here:

- the velocity scale $k^{1/2}$ was used instead of U_T
- characteristic length scale $L = k^{3/2}/\epsilon$ was assumed to vary linearly with the wall distance, ($L \sim C_D y$), with C_D regarded as a universal constant, invariant even under the conditions well removed from local equilibrium.

In addition, a new treatment of the source terms in the stress equations for the first cell next to the wall was applied, as suggested by Chieng and Launder (1980), accounting both for the steep variation of turbulence quantities and their different behavior within the viscosity-affected region and the fully turbulent zone.

2. The Numerical Procedure

The solution of the homogeneous flow cases were obtained by means of a standard Runge-Kutta fourth-order method. Other cases considered here fall into the category of parabolic flows and have been solved by the finite-difference method based on the GENMIX procedure of Patankar and Spalding. The major modification of the original scheme, amenable to the full-stress model, was the use of the staggered grid for turbulence quantities (Samaraweera, 1978). In all cases 30 grid points were used in the direction normal to the flow, slightly squeezed in the wall region, and were proved by the grid optimization studies to be satisfactory.

3. The Modeled Equation Set

Because of space limitations, the equation set will not be given here; the reader is referred to Launder et al. (1975), where the complete set is presented, except for the modifications described earlier. The adjustment of some of the empirical

coefficients is commented on in the discussion below (the same notations is used as in Launder et al. 1975).

4. Discussion of Results

(i) - Homogeneous Flows, Flow 0370

A number of the presently considered homogeneous flow cases have been calculated earlier with the original form of the LRR method, some of them serving as a basis for determining the empirical constants. Consequently the model has already been proven to yield an acceptable quality of agreement with experimental data. The present computation, made with the modified equations and covering a broader range of flows, in line with the Conference propositions, yielded results of similar quality with a slight general improvement, indicating also a need for the readjustment of some of the empirical coefficients. In all cases the calculations were performed using the recommended initial value of ϵ , but if the agreement with the experiments was not achieved, a better value of ϵ was sought. In some cases the adjustment of the initial dissipation rate yielded the same quality of agreement with a different set of coefficients, so the final choice was determined in the light of the experience gained by our group and others in computing more complex flow cases. Care was taken to distinguish the influence of different effects, if they were jointly present in the same flow case, so that the coefficients in various terms of the modeled equations could be optimized separately. So, wherever the stress anisotropy was noticeable, the initial ϵ was chosen to produce the best prediction of kinetic energy, and then the stress-redistribution process was calculated.

Decay of homogeneous isotropic turbulence (Case 0371). For the case of decaying homogeneous isotropic turbulence, the applied turbulence model yielded the solution in form of the power law $k \sim x^{-n}$, with the exponent n directly correlated with the coefficient $C_{\epsilon 2}$ through the relationship $n = (C_{\epsilon 2} - 1)^{-1}$. Because the experiments seem to obey the same power law in the initial period of decay, with the appropriate choice of $C_{\epsilon 2}$ and the initial value of ϵ , the decaying process can be predicted in full agreement with the experiments. Indeed, this case has in the past served as a basis for determining the value of $C_{\epsilon 2}$. As shown on Plate 59, the best agreement with the data of Comte Bellot and Corrsin is achieved with $C_{\epsilon 2} = 1.8$ and with the initial ϵ equal to $18 \text{ m}^2/\text{s}^3$, (which is about 16% higher than the recommended value, and therefore within the accepted $\pm 20\%$ tolerance). However, the value $C_{\epsilon 2} = 1.9$ (corresponding to $n = -1.11$) is more widely used in practice for the computation of more complex flows. The results, obtained with this value, and with the recommended initial dissipation are also presented for comparison. Although this value yields a less

satisfying agreement with experiments, it has been used in all subsequent calculations, in order to stay in accord with the adopted practice.

Return to isotropy (Cases 0373A through E and 0375A and C. These flows serve as a direct test of modeling of the turbulence contribution to the pressure-strain term in stress equations. Here a simple form of Rotta was applied, which presumes that the rate of return to isotropy is linearly proportional to the degree of anisotropy, with a single adjustable constant, and using a single length scale for all stress components. In Case 0373A, which shows a moderate initial degree of anisotropy, with the initial dissipation rate of 33×10^{-4} , instead of the recommended value of $22 \times 10^{-4} \text{ m}^2/\text{s}^3$, the obtained stress components seem to follow closely the experimental points, as seen in Plate 63 for Case 0373A. The same quality of agreement is obtained in Cases 0375A and C, which have smaller initial anisotropy, as shown on Plates 77, 78 and 81, 82, respectively.

Much less satisfactory agreement is achieved in Case 0373B where the contraction ratio is 9:1. Here the experiments show that the stress component u^2 , which is an order of magnitude smaller than v^2 and w^2 , should remain almost constant. This condition would require that C_1 be assigned a value close to 1.0, contrary to findings in most other flow cases. However, because the lateral stress components are much larger, with the reduction of the initial dissipation to a much smaller value (again to obtain the desired kinetic energy decay), the lateral components are predicted reasonably well.

Quite opposite disagreement is obtained in Case 0373E. Here again, with an adjustment of the initial dissipation, the lateral stress components (not equal now) are predicted reasonably well. However, the predicted streamwise component shows considerably slower increase in time in comparison with experiments. To achieve the desired growth rate, the constant C_1 should now be at least twice as large as the adopted value of 1.8.

The experimental data of Cases 0373C and D show another peculiarity: while the lateral stress components (much larger in magnitude), show immediate fall-off, the smallest component u^2 shows a time lag before it begins to increase. Because the present model is incapable of predicting this sort of time delay, much better agreement with experiments is achieved if the initial position of the calculation is shifted back, as shown in Plates 65, 66, and 67, respectively.

If all the experimental data for these cases are to be regarded as trustworthy, even with due account for experimental scatter, the return to isotropy could not be regarded as a simple process governed solely by the degree of anisotropy, as presumed by the present model, but is probably influenced also by the inequality of the scales

in the various direction and also by the spectral transfer, as suggested in the review paper by Ferziger.

One should notice that the major departure from the experiments is produced for the streamwise stress component, which, as smallest in magnitude, should receive the energy from the others. This disagreement is in particular pronounced in cases with large anisotropy. However, it should be noted that the predicted value of $\overline{u^2}$ at the end of the calculation period differs from the experimental value at the most by about 33% (Case 0373B), which could be regarded as acceptable in light of the much better results obtained in all other cases, and accounting for the simplicity of the applied model.

Plane strain (Cases 0374A and B). In the case of plane strain, the predicted results show the acceptable agreements with experiments in all cases except for $\overline{v^2}$ in Case 0374A. It should be noted here that a considerable improvement was achieved with the earlier described modification of the dissipation equation. The present calculations were obtained with the more elaborate form of the mean-strain contribution to the pressure redistribution term $\phi_{ij,2}$ of the stress equation (denoted as Model 1 in the LRR paper). Earlier tests as well as the present ones have shown, that in spite of some criticism of the more elaborate model of $\phi_{ij,2}$ (see Leslie, 1980) and the recent general preference towards the simpler form proposed by Naot et al. (Model 2 in the LRR paper), the more elaborate model as used here yields noticeably better prediction of the plane-strain flows, and has been retained in the present calculations.

Axisymmetric strain. The predictions of Cases 0375B, D, and E show in all cases a consistent deficiency, manifested in a too slow response of the turbulence to the applied strain--the disagreement being more noticeable in Case E with the higher strain (contraction ratio 16:1). This sort of deficiency was noticed earlier and seems to be caused primarily by the inadequate modeling of the spectral energy and dissipation process and the use of a single scale to represent all turbulent interactions. Indeed this type of flow was used by Hanjalić and Launder (1981) as a test case for the improvement of the dissipation equation and the modifications applied here helped to improve the predictions of the same type of flow experimentally investigated by Uberoi. In the cases considered here, the improvement, though noticeable in comparison with the earlier model, does not seem to produce a sufficient effect, and further study is obviously needed. It should be noted that a decrease of the initial dissipation rate may produce better overall agreement, with a slower decay rate at the beginning of the flow section before the strain is applied, but this merely means shifting the curve upwards without changing the overall dynamics of the flow evolution.

Homogeneous shear flows. Both Cases 0376A and B are predicted with acceptable accuracy when account is taken of the experimental uncertainties indicated in the review paper by Ferziger.

(ii) - Plane Boundary Layer at Zero Pressure Gradient, Case 0612

Plates 133, 136, 137 for Case 0612 all show very good agreement between output and experimental data.

(iii) - Diffuser Flows, Cases 0141, 0142 and 0143

The plane diffuser flow, Case 0141, shows both the friction factor and the mean-velocity profiles in very good agreement with the experiments, while the shear-stress profiles show some discrepancies, in particular at the last downstream position. Because the cross-stream distance is not normalized, the agreement depends on the initial conditions and here a trial-and-error routine was applied to guess the appropriate thickness of the boundary layer some distance upstream from the start of the pressure gradient. As mentioned earlier, the flows in axisymmetric diffusers were solved by means of the algebraic stress model as well as with the simple $k-\epsilon$ model. Both models show good prediction of the mean-flow properties, though the algebraic stress model proves to be superior, in particular in Case 0142. In both cases the initial velocity profiles at the pipe entrance were assumed to be almost uniform, the major difference between the two cases being in the prespecified turbulence level, which was one order of magnitude larger in Case 0143.

(iv) - Boundary Layers with Blowing/Suction, Cases 0241, 0244

Cases with blowing and suction were computed with the full-stress model and with the same method used in Cases 0612 and 0141, the only difference being in the modification of the wall function for the momentum equation to account for the lateral transfer of momentum through the wall. The resulting wall function, obtained on the basis on standard Couette-flow analysis, but normalized with the value of the kinetic energy at the edge of the viscous sublayer k_v ,

$$U^+ = [(Ey^+)^{v_w^+/\chi} - 1]/v_w^+,$$

where

$$U^+ = \rho U k_v^{0.5} / \tau_w ; \quad y^+ = y k_v^{0.5} / \nu ; \quad v_w^+ = v_w / k_v^{0.5}$$

(with $E = 5.1$ and $\chi = 0.23$), produced very good agreement with the experimental data in the case of blowing, (0241), but much less satisfactory in the suction cases (0242 and 0244). The supersonic Flow Case 8301 was not considered. It should be pointed out that the applied wall function was derived on the assumption that the variation of the kinetic energy within the first wall grid cell outside the viscous sublayer is

negligible; this assumption is not in accord with the actual situation when a high rate of blowing, and in particular suction, is applied. The case with suction seems to exhibit a much steeper variation of both the kinetic energy and the turbulent shear stress which the model is not able to follow, yielding, in the case of suction, much higher wall shear stress and consequently the higher kinetic energy in the wider part of the wall region. In the authors' opinion, the inadequacy of the wall function is the primary cause of the failure to predict the flow with suction.

5. Conclusion

A judgment on the overall performances of our method is given in the Summary Report of Computer Group 17³ by B. E. Launder (herein) on the basis of the computations performed by all five groups who have used the same basic model. However, the computations reported here, as well as our previous experience which covered a number of other flow cases, give us grounds to believe that the present model is capable of producing results in acceptable agreement with experiments in a large variety of turbulent flows. Some of the weak points indicate an obvious need for further investigation, but in the authors' opinion, with an adequate effort the desired improvements can be achieved.

Acknowledgment

These computations were supported by the Self Governing Community of Interest in Science of Bosnia and Hercegovina.

References

- Chieng, C. C., and B. E. Launder (1980). Num. Heat Transfer, 3.
- Gibson, M. M., and B. E. Launder (1978). J. Fluid Mech., 86.
- Hanjalić, K., and B. E. Launder (1972). J. Fluid Mech., 52.
- Hanjalić, K., and B. E. Launder (1981). To be published.
- Launder, B. E., G. J. Reece, and W. Rodi (1975). J. Fluid Mech., 68.
- Leslie, D. C. (1980). J. Fluid Mech., 98.
- Rodi, W. (1976). Z. Angew Math. Mech., 56.
- Samaraweera, D. S. A. (1978). Ph.D. Thesis, Imperial College, London.



COMPARISON OF COMPUTATION WITH EXPERIMENT

Summary Report

by

C. Hung*

Computer Group Number: 43

Cases 8101, 8201, 8631

A coordinate transformation is employed that maps the body surface onto $\eta = 0$,

$$\xi = \xi(x,y) \quad (1)$$

$$\eta = \eta(x,y) \quad (2)$$

The transformed equations are solved by a time-dependent calculation until a steady state is reached. The approximate Navier-Stokes equations in transformed coordinates are

$$\frac{\partial q}{\partial t} + \frac{\partial E}{\partial \xi} + \frac{\partial F}{\partial \eta} = \frac{1}{R_e} \frac{\partial S}{\partial \eta} \quad (3)$$

where

$$q = J^{-1} \begin{bmatrix} \rho \\ \rho u \\ \rho v \\ e \end{bmatrix}, \quad E = J^{-1} \begin{bmatrix} \rho U \\ \rho u U + p \xi_x \\ \rho u U + p \xi_y \\ (e+p)U \end{bmatrix}, \quad F = J^{-1} \begin{bmatrix} \rho V \\ \rho u V + p \eta_x \\ \rho u V + p \eta_y \\ (e+p)V \end{bmatrix} \quad (4)$$

$$S = J^{-1} \begin{bmatrix} 0 \\ \alpha_1 u_\eta + \alpha_2 v_\eta \\ \alpha_2 u_\eta + \alpha_3 v_\eta \\ \alpha_1 uv_\eta + \alpha_2 (uv)_\eta + \alpha_3 vv_\eta + \alpha(p/\rho)_\eta \end{bmatrix} \quad (5)$$

$$J = \xi_x \eta_y - \xi_y \eta_x \quad (6)$$

$$U = \xi_x u + \xi_y v \quad (7)$$

$$V = \eta_x u + \eta_y v \quad (8)$$

$$\alpha_1 = (\mu + \mu_t) \left(\frac{4}{3} \eta_x^2 + \eta_y^2 \right) \quad (9)$$

*NASA Ames Research Center, Moffett Field, CA 94035

$$\alpha_2 = (\mu + \mu_t) \left(\frac{1}{3} \eta_x \eta_y \right) \quad (10)$$

$$\alpha_3 = (\mu + \mu_t) \left(\eta_x^2 + \frac{4}{3} \eta_y^2 \right) \quad (11)$$

$$\alpha_4 = \frac{\gamma}{\gamma - 1} \left(\frac{\mu}{P_r} + \frac{\mu_t}{P_{rt}} \right) (\eta_x^2 + \eta_y^2) \quad (12)$$

The above expression for S corresponds to the boundary-layer approximation, although that approximation is not used in the inviscid parts of the equations. The terms that have been omitted from S (derivatives with respect to ξ) are not resolved in meshes that are used for numerical solution of the Navier-Stokes equations at high Reynolds numbers. Retention of all inviscid terms (some of which are omitted in the boundary-layer approximation) permits computation of separated flows in which the reversed-flow region remains close to the body surface.

The algebraic turbulence model is based on that of Cebeci with modifications that avoid the necessity for finding the edge of the boundary-layer. The defining relations are

$$\mu_t = \begin{cases} (\mu_t)_{\text{inner}} & y \leq y_{\text{crossover}} \\ (\mu_t)_{\text{outer}} & y > y_{\text{crossover}} \end{cases} \quad (13)$$

where y is the normal distance from the wall and $y_{\text{crossover}}$ is the smallest y at which values from the inner and outer formulas are equal.

The Prandtl-van Driest formulation is used in the inner region

$$(\mu_t)_{\text{inner}} = \rho l^2 |\omega| \quad (14)$$

where

$$l = \kappa y [1 - \exp(-y^+ / A^+)] \quad (15)$$

$$y^+ = \sqrt{\rho_w \tau_w} y / \mu_w \quad (16)$$

and ω is the magnitude of vorticity.

In place of the Clauser formulation, the outer layer formula is

$$(\mu)_{\text{outer}} = K C_{cp} \rho F_{\text{wake}} F_{\text{kleb}}(y) \quad (17)$$

where K is the Clauser constant, C_{cp} is an additional constant and

$$F_{\text{wake}} = \begin{cases} y_{\text{max}} F_{\text{max}} & \text{or} \\ C_{wk} y_{\text{max}} u_{\text{dif}} / F_{\text{max}} \end{cases} \left. \begin{array}{l} \text{The} \\ \text{Smaller} \end{array} \right\} \quad (18)$$

The equations for y_{\max} and F_{\max} are determined from the function

$$F(y) = y \cdot |\omega| \cdot [1 - \exp(-y^+/A^+)] \quad (19)$$

The quantity F_{\max} is the maximum value of $F(y)$ that occurs in a profile and y_{\max} is the value of y at which it occurs. The function $F_{\text{kleb}}(y)$ is the Klebanoff intermittency factor given by

$$F_{\text{kleb}}(y) = [1 + 5.5 \left(\frac{C_{\text{kleb}} \cdot y}{y_{\max}} \right)^6]^{-1} \quad (20)$$

The quantity u_{dif} is the difference between the maximum and minimum total velocity in a profile.

The constants have been determined by requiring agreement with the Cebeci formulation for constant-pressure boundary layers at transonic speeds. The values used are

$$A^+ = 26$$

$$C_{\text{cp}} = 1.6$$

$$C_{\text{kleb}} = 0.3$$

$$C_{\omega k} = 0.25$$

$$\kappa = 0.4$$

$$K = 0.0168$$

$$P_r = 0.72, P_{rt} = 0.9$$

The meshes used in the calculations contain 77×46 mesh points and are stretched in the η direction such that $y^+ \leq 6$ at the first mesh point off the wall. Since the laminar sublayer is thereby resolved, no wall functions are used.

Flat-plate calculations required 13 min per case on a CDC 7600. Calculations for two-dimensional compression corner consumed 26 min per case. The storage required was 86K words.



T. Han

COMPARISON OF COMPUTATION WITH EXPERIMENT

Summary Report

by

S. M. Chang, T. Han and J. A. C. Humphrey^{*†}

Computer Group Number: 17¹



J.A.C. Humphrey

Case 0512

Introduction

The following pages contain a summary of the computational methodology and experience gained at the University of California, Berkeley, in relation to the prediction of Case 0512 (see Humphrey, 1977) for the 1980-1981 AFOSR-HTTM-Stanford Conference on Complex Turbulent Flows. The present contribution is part of a more extensive and coordinated effort aimed at documenting the performance of various (similar or related) turbulence models embodied in a class of numerical procedures familiar to the various collaborating groups. The institutions participating in this collective effort are listed in the computers' summary report presented herein by Launder, Leschziner and Sindir (Computer Group 17³). The computation output appears on the plates in this volume (Methods 17G and 17I).

The contribution summarized here is based on the use of a two-equation (k-ε) model of turbulence as presented in, for example, Launder and Spalding (1974). The numerical algorithm solving finite-difference forms of the transport equations is the Imperial College TEACH-2E code generalized to three-dimensional (3-D) flows by Humphrey (1977, 1978), and subsequently extended as described in Humphrey et al. (1981) to encompass turbulent flows. A "semi-elliptic" version of the numerical procedure, developed along the lines of the work in Prataap (1975), was recently completed by Chang et al. (1982) and includes the use of the QUICK scheme for convective differentiation proposed by Leonard (1979) and tested by Han et al. (1981). The principal results prepared for this conference were calculated using the semi-elliptic version of the 3-D code using the higher-order QUICK scheme for convective differentiation in the cross-stream plane of the flow (Method 17G). Additional predictions of Case 0512 using the HYBRID differencing scheme of the standard TEACH codes have also been made but these are less accurate (Method 17I).

*University of California, Berkeley, California 94720

†Computer Groups 17 were coordinated by B.E. Launder and appear here and in other alphabetic listings under "Launder".

While qualitative features of the 90° curved-duct flow of Case 0512 are well represented by the numerical calculations, these yield poor quantitative agreement with the measurements. The discrepancies are attributed principally to the failure of the two-equation model to account for large-scale anisotropy in the flow.

Equations, Turbulence Model and Boundary Conditions

Time-averaged continuity and momentum equations governing steady, developing, incompressible, isothermal, turbulent flow in cylindrical coordinates, as given by Humphrey et al. (1981) are:

Continuity

$$\frac{\partial U_r}{\partial r} + \frac{1}{r} \frac{\partial U_\theta}{\partial \theta} + \frac{\partial U_z}{\partial z} + \frac{U_r}{r} = 0 \quad (1)$$

Momentum

$$\rho \left[U_r \frac{\partial U_r}{\partial r} + \frac{U_\theta}{r} \frac{\partial U_r}{\partial \theta} + U_z \frac{\partial U_r}{\partial z} - \frac{U_\theta^2}{r} \right] = - \frac{\partial P}{\partial r} + \frac{1}{r} \frac{\partial}{\partial r} \left(\mu_{\text{eff}} r \frac{\partial U_r}{\partial r} \right) + \frac{1}{r} \frac{\partial}{\partial \theta} \left(\mu_{\text{eff}} \frac{\partial U_r}{\partial \theta} \right) + \frac{\partial}{\partial z} \left(\mu_{\text{eff}} \frac{\partial U_r}{\partial z} \right) - \mu_{\text{eff}} \frac{U_r}{r^2} - \frac{2}{r^2} \mu_{\text{eff}} \frac{\partial U_\theta}{\partial \theta} + S_r \quad (2)$$

$$\rho \left[U_r \frac{\partial U_\theta}{\partial r} + \frac{U_\theta}{r} \frac{\partial U_\theta}{\partial \theta} + U_z \frac{\partial U_\theta}{\partial z} + \frac{U_r U_\theta}{r} \right] = - \frac{1}{r} \frac{\partial P}{\partial \theta} + \frac{1}{r} \frac{\partial}{\partial r} \left(\mu_{\text{eff}} r \frac{\partial U_\theta}{\partial r} \right) + \frac{1}{r} \frac{\partial}{\partial \theta} \left(\mu_{\text{eff}} \frac{\partial U_\theta}{\partial \theta} \right) + \frac{\partial}{\partial z} \left(\mu_{\text{eff}} \frac{\partial U_\theta}{\partial z} \right) - \mu_{\text{eff}} \frac{U_\theta}{r^2} + \frac{2}{r^2} \mu_{\text{eff}} \frac{\partial U_r}{\partial \theta} + S_\theta \quad (3)$$

$$\rho \left[U_r \frac{\partial U_z}{\partial r} + \frac{U_\theta}{r} \frac{\partial U_z}{\partial \theta} + U_z \frac{\partial U_z}{\partial z} \right] = - \frac{\partial P}{\partial z} + \frac{1}{r} \frac{\partial}{\partial r} \left(\mu_{\text{eff}} r \frac{\partial U_z}{\partial r} \right) + \frac{1}{r} \frac{\partial}{\partial \theta} \left(\mu_{\text{eff}} \frac{\partial U_z}{\partial \theta} \right) + \frac{\partial}{\partial z} \left(\mu_{\text{eff}} \frac{\partial U_z}{\partial z} \right) + S_z \quad (4)$$

where

$$S_r = \frac{1}{r} \frac{\partial}{\partial \theta} \left(\mu_t r \frac{\partial}{\partial r} \left(\frac{U_\theta}{r} \right) \right) + \frac{1}{r} \frac{\partial}{\partial r} \left(\mu_t r \frac{\partial U_r}{\partial r} \right) + \frac{\partial}{\partial z} \left(\mu_t \frac{\partial U_r}{\partial z} \right) - \mu_t \frac{U_r}{r}$$

$$S_\theta = \frac{1}{r} \frac{\partial}{\partial \theta} \left(\mu_t \left(2 \frac{U_r}{r} \left[\frac{\partial U_\theta}{\partial \theta} \right] \right) \right) + \frac{\partial}{\partial r} \left(\mu_t \left(\frac{\partial U_r}{\partial \theta} - U_\theta \right) \right) + \frac{\partial}{\partial z} \left(\mu_t \frac{\partial U_\theta}{\partial z} \right) + \frac{\mu_t}{r} \left(\frac{\partial U_\theta}{\partial r} - \frac{U_\theta}{r} \right)$$

$$S_z = \frac{1}{r} \frac{\partial}{\partial \theta} \left(\mu_t \frac{\partial U_\theta}{\partial z} \right) + \frac{1}{r} \frac{\partial}{\partial r} \left(\mu_t r \frac{\partial U_r}{\partial z} \right) + \frac{\partial}{\partial z} \left(\mu_t \frac{\partial U_z}{\partial z} \right)$$

and

$$\mu_{\text{eff}} = \mu + \mu_t = \mu_t$$

The turbulent viscosity, μ_t , is assumed to be determined uniquely by the local values of density ρ , turbulent kinetic energy k , and a turbulent length scale l . At high Reynolds numbers l is proportional to $k^{3/2}/\epsilon$, where ϵ is the rate of dissipation of turbulent kinetic energy and as given in Launder and Spalding (1974):

$$\mu_t = C_\mu \rho k^2 / \epsilon \quad (5)$$

where C_μ has the constant value given below. The spatial variation of μ_t is determined by solving transport equations for k and ϵ in cylindrical coordinates, readily derived from the general tensor equations given in Bryant and Humphrey (1976), i.e.:

$$\begin{aligned} \rho \left[U_r \frac{\partial k}{\partial r} + \frac{U_\theta}{r} \frac{\partial k}{\partial \theta} + U_z \frac{\partial k}{\partial z} \right] &= \frac{1}{r} \frac{\partial}{\partial r} \left(\frac{\mu_{\text{eff}}}{\sigma_k} r \frac{\partial k}{\partial r} \right) + \frac{1}{r} \frac{\partial}{\partial \theta} \left(\frac{\mu_{\text{eff}}}{\sigma_k} \frac{\partial k}{\partial \theta} \right) \\ &+ \frac{\partial}{\partial z} \left(\frac{\mu_{\text{eff}}}{\sigma_k} \frac{\partial k}{\partial z} \right) + G - \rho \epsilon \end{aligned} \quad (6)$$

and

$$\begin{aligned} \rho \left[U_r \frac{\partial \epsilon}{\partial r} + \frac{U_\theta}{r} \frac{\partial \epsilon}{\partial \theta} + U_z \frac{\partial \epsilon}{\partial z} \right] &= \frac{1}{r} \frac{\partial}{\partial r} \left(\frac{\mu_{\text{eff}}}{\sigma_\epsilon} r \frac{\partial \epsilon}{\partial r} \right) + \frac{1}{r} \frac{\partial}{\partial \theta} \left(\frac{\mu_{\text{eff}}}{\sigma_\epsilon} \frac{\partial \epsilon}{\partial \theta} \right) \\ &+ \frac{\partial}{\partial z} \left(\frac{\mu_{\text{eff}}}{\sigma_\epsilon} \frac{\partial \epsilon}{\partial z} \right) + C_{\epsilon 1} \frac{\epsilon}{k} G - C_{\epsilon 2} \rho \frac{\epsilon^2}{k} \end{aligned} \quad (7)$$

with

$$\begin{aligned} G &= \mu_t \left\{ 2 \left[\left(\frac{\partial U_r}{\partial r} \right)^2 + \left(\frac{1}{r} \frac{\partial U_\theta}{\partial \theta} \right)^2 + \left(\frac{\partial U_z}{\partial z} \right)^2 - \frac{U_\theta}{r} \left(\frac{1}{r} \frac{\partial U_r}{\partial \theta} + \frac{\partial U_\theta}{\partial r} \right) \right. \right. \\ &+ \frac{U_r}{r} \left(\frac{U_r}{r} + \frac{2}{r} \frac{\partial U_\theta}{\partial \theta} \right) + \frac{1}{r} \left(\frac{\partial U_r}{\partial \theta} \frac{\partial U_\theta}{\partial r} + \frac{\partial U_z}{\partial \theta} \frac{\partial U_\theta}{\partial z} \right) + \frac{\partial U_r}{\partial z} \frac{\partial U_z}{\partial r} \left. \right\} \\ &+ \left\{ \left(\frac{U_\theta}{r} \right)^2 + \left(\frac{\partial U_\theta}{\partial r} \right)^2 + \left(\frac{\partial U_\theta}{\partial z} \right)^2 + \left(\frac{1}{r} \frac{\partial U_r}{\partial \theta} \right)^2 + \left(\frac{\partial U_r}{\partial z} \right)^2 + \left(\frac{\partial U_z}{\partial r} \right)^2 + \left(\frac{1}{r} \frac{\partial U_z}{\partial \theta} \right)^2 \right\} \end{aligned} \quad (8)$$

The constants in these equations were taken as $C_\mu = 0.09$, $C_{\epsilon 1} = 1.47$, $C_{\epsilon 2} = 1.92$, $\sigma_k = 1.0$, and $\sigma_\epsilon = 1.3$, in accordance with the recommendations in Patankar et al. (1975).

In all the above equations capital letters denote mean quantities. Components of the Reynolds-stress tensor in the momentum equations have been modeled according to the Boussinesq approximation, relating stresses to mean-flow gradients through the

turbulent viscosity μ_t . Terms enclosed in boxes were not included in the semi-elliptic numerical procedure.

Equations 1-7 were solved using the boundary conditions summarized in Table 1.

Numerical Procedure

Finite-difference forms of the transport equations were obtained by volume integration over cells discretizing the flow domain as explained in Pratap (1975) to generate a semi-elliptic calculation scheme. In this scheme the neglect of streamwise diffusion in the momentum equations allows a "parabolic" treatment of velocity, requiring two-dimensional storage of velocity components at only two streamwise locations. Elliptic effects are retained in the numerical procedure through three-dimensional storage of pressure. Of course, the use of this scheme precludes the calculation of streamwise flow recirculation.

Further discussion regarding the development and application of the semi-elliptic calculation scheme is available in Pratap (1975) and Chang et al. (1982).

Test Cases

The cases listed in Table 2 were predicted to test the worthiness and accuracy of the numerical procedure. In addition to the laminar flow tests, two turbulent flow calculations were conducted to verify the two-equation turbulence model for conditions where it is known to yield fairly accurate results. The two-dimensional flow cases were predicted by imposing two (streamwise) symmetry plane conditions in the 3-D semi-elliptic calculation scheme.

Remarks on the Prediction of Case 0512

A comparison between measurements and predictions of Case 0512 obtained by us shows that although qualitative agreement has been established, quantitative agreement is rather poor. The calculations were performed on an equally spaced grid of refinement ($r = 14$) \times ($z = 10$) \times ($\theta = 36$) in the curved duct. The grids in the upstream and downstream tangents were ($14 \times 10 \times 37$) and ($14 \times 10 \times 17$), respectively. Computation costs prohibited optimizing the grid distribution. A typical converged run time for these grids was 3.6×10^{-5} CPUs per node visitation and required 135 kg words of storage. The criterion for convergence was that the maximum normalized residual summation should be less than 10^{-3} . A comparison between QUICK-generated and HYBRID-generated* calculations for both laminar and turbulent curved-duct flow showed clearly the superior performance of the former scheme for the same number of equivalently distributed grid nodes.

*The HYBRID scheme employs central differencing when the cell Peclet number is $|Pe| < 2$ and upwind differencing when it is $|Pe| > 2$.

The use of the QUICK scheme in the cross-stream plane of the flow and the stream-wise refinement allowed by the semi-elliptic scheme suggest that it is turbulence model deficiency rather than numerical diffusion which produces the discrepancies observed.

The use of a C_{μ} function (as opposed to a constant value of 0.09) along the lines of Humphrey and Pourahmadi (1981) did not appear to improve the calculated results.

Initially, calculations were performed using the straight-duct developed flow data provided to the Stanford Conference organizers by A. Melling. Calculations using these data revealed an extra pair of small counter-rotating vortices at the outer-radius wall of the curved duct. Calculations using the mass-adjusted data* provided by Melling (1975) in Figure A5.10 of that reference, or performing calculations in which the upstream tangent cross-stream motion was suppressed, did not reveal the second pair of outer-radius wall vortices. Since the measurements corresponding to Case 0512 given by Humphrey (1977) and Humphrey et al. (1981) do not show nor suggest the presence of a second pair of vortices, it is believed that the predictions based on the mass adjusted data are the more accurate of the two. It is also worth noting that differences between sets of calculations with and without mass-adjusted upstream tangent cross-stream flow were not significantly different. This is attributed to the pressure-dominated nature of the flow in the curved duct. To some extent, such a condition relieves the need for a very accurate specification of the cross-stream flow magnitude at the entrance plane.

In our opinion accurate numerical calculations of this case study and similar curved-duct flows as in Buggeln et al. (1980) could probably be started with the entrance plane located nearer to the 0° plane of the curved duct and without a specification of the transverse-flow component (i.e., $U_r|_{inlet} = 0$). Measurements at $x = -2.5$ hydraulic diameters in Humphrey (1977) support this contention as has the subsequent research at Berkeley reported in Chang et al. (1982).

Acknowledgement

The present numerical study was made possible through funding by the Office of Naval Research, Contract No. N00014-80-C-0031. We are particularly grateful to Mr. Keith Ellingsworth for his assistance in obtaining this funding.

*Mass-adjusting had the effect of removing some of the asymmetry in the cross-stream velocity profiles.

References

- Bryant, D. and J. A. C. Humphrey (1976). "Conservation equations for laminar and turbulent flows in general three-dimensional curvilinear coordinates," Imperial College, Mech. Engrg. Rep. No. CHT/76/6.
- Buggeln, R. C., W. R. Briley, and H. McDonald (1980). "Computation of laminar and turbulent flow in curved ducts, channels, and pipes using the Navier-Stokes equations," Final report No. R80-92006-F to the Office of Naval Research.
- Chang, S. M., J. A. C. Humphrey, and A. Modavi (1982). "Developing turbulent flow in a 180° bend and downstream tangent of square cross-sections," Report No. FM-82-1, Mech. Eng. Dept., University of California, Berkeley, CA. Also available as LBL Report No. LBL-14844.
- Gessner, F. B., J. K. Po, and A. F. Emery (1979). "Measurements of developing turbulent flow in a straight duct," Turbulent Shear Flows I, F. Durst, B. E. Launder, F. W. Schmidt, and J. H. Whitelaw (eds.). Springer-Verlag, Berlin.
- Han, T., J. A. C. Humphrey, and B. E. Launder (1981). "A Comparison of hybrid and quadratic-upstream differencing in high Reynolds number elliptic flows," Comp. Meths. Appl. Mech. Eng., 29, 81.
- Humphrey, J. A. C. (1977). "Flow in ducts with curvature and roughness," Ph.D. Thesis, University of London.
- Humphrey, J. A. C. (1978). "Numerical calculation of developing laminar flow in pipes of arbitrary curvature radius," Can. J. Chem. Eng., 56, 151.
- Humphrey, J. A. C., and F. Pourahmadi (1981). "A generalized algebraic relation for predicting developing curved channel flow with a k- ϵ model of turbulence," Paper presented at the Third Symposium on Turbulent Shear Flow, University of California, Davis, Sept. 9-11.
- Humphrey, J. A. C., J. H. Whitelaw, and G. Yee (1981). "Turbulent flow in a square duct with strong curvature," J. Fluid Mech., 103, 443.
- Launder, B. E. and D. B. Spalding (1974). "The numerical computation of turbulent flows," Comp. Meths. Appl. Mech. Engr., 3, 269.
- Leonard, B. P. (1979). "A stable and accurate convective modelling procedure based on quadratic upstream interpolation," Comp. Meths. Appl. Mech. Eng., 19, 59.
- Melling, A. (1975). "Investigation of flow in non-circular ducts and other configurations by laser Doppler anemometry," Ph.D. Thesis, University of London.
- Patankar, S. V., V. S. Pratap, and D. B. Spalding (1975). "Prediction of turbulent flow in curved pipes," J. Fluid Mech., 67, 583.
- Patankar, S. V. and D. B. Spalding (1972). "A calculation procedure for heat, mass and momentum transfer in three-dimensional parabolic flows," Int. J. Heat Mass Transfer, 15, 1787.
- Pratap, V. S. (1975). "Flow and heat transfer in curved ducts," Ph.D. Thesis, University of London.

Table 1. Boundary Conditions for Prediction of Case 0512

Streamwise Location*	Variable
Entrance plane ($x = -7.84$; in upstream tangent)	<p>U_θ taken from A. Melling's data provided by the Stanford Conference organizers.</p> <p>U_r, U_z taken from Fig. A5.10 in Melling (1975).</p> <p>$k \equiv 1/2(\overline{u_1^2} + \overline{u_2^2} + \overline{u_3^2})$; taken from A. Melling's data provided by the Stanford Conference organizers.</p> <p>$\epsilon = k^{3/2}/(0.01 D_H)$.</p>
Exit plane ($x = 2.24$; in downstream tangent)	<p>Pressure at the exit plane is updated every iteration by adding to each node of the preceding (streamwise) plane the calculated average pressure drop which ensures overall mass-flow continuity at the exit plane. This results in values of $\partial p/\partial r$ and $\partial p/\partial z$ at the exit plane being fixed to the values of the preceding plane.</p>
Side walls ("p" denotes node nearest wall)	<p>$U_\theta, U_r,$ and U_z boundary conditions specified by imposing wall shear stress through law-of-the-wall:</p> $\tau_w = \tau_p = \frac{\rho C_\mu^{1/4} k_p^{1/2} U_p}{A \ln\{y_p C_\mu^{1/4} k_p^{1/2} / \nu\}} + B$ <p>$A = 2.39; B = 5.45.$</p> <p>k_p found from transport equation with diffusion neglected and generation according with wall shear stress.</p> <p>ϵ_p determined by requiring that the turbulence length scale vary linearly with distance from wall and assuming local equilibrium:</p> $\epsilon_p = A \frac{C_\mu^{3/4} k_p^{3/2}}{y_p}$

*Flow geometry and notation for Case 0512 are defined in Vol. I, p. 155, of these Proceedings.

Table 2. Predicted Test Cases

Case	Agreement with Experimental, Numerical, or Theoretical Data	Reference for Comparison	Comments
Curved channel (2-D); developing laminar flow	Excellent	BuggeIn et al. (1980)	HYBRID scheme used for calculations on a $(r = 15) \times (\theta = 36)$ grid.
Curved channel (2-D); developing turbulent flow	Very good	BuggeIn et al. (1980)	HYBRID scheme used for calculations on a $(r = 15) \times (\theta = 36)$ grid.
Straight duct (3-D); developing laminar flow	Excellent	Patankar and Spalding (1972)	HYBRID scheme used for calculations on a $31 \times 31 \times 52$ grid. Calculations performed in one quadrant. Results for a $13 \times 13 \times 52$ grid were within 4% of experimental data.
Straight duct (3-D); developing turbulent flow	Very good	Cessner et al. (1979)	HYBRID scheme used for calculations on a $10 \times 10 \times 240$ grid. Discrepancies attributed to inability to predict cross-stream flow. Comparison restricted to maximum centerline velocity and pressure drop coefficient. Calculations performed in one quadrant.
Straight duct (3-D); developing laminar flow; one wall sliding at right angles to main flow	Excellent	Han et al. (1981)	HYBRID and QUICK schemes used for calculations on a $15 \times 15 \times 80$ grid. QUICK calculations were considerably more accurate than corresponding HYBRID results.
90° curved-duct (3-D); developing laminar flow	Very good at bend angles of 0°, 30°, and 90° but discrepancies of order 30% found at 60°	Humphrey (1977)	HYBRID ($z = 15 \times r = 25 \times \theta = 36$) and QUICK ($z = 11 \times r = 17 \times \theta = 36$) schemes used for calculations. Upstream and downstream tangents attached of length -2.6 and 5.4 hydraulic diameters, respectively. Coarse grid QUICK scheme results are as accurate as refined grid HYBRID scheme calculations.

COMPARISON OF COMPUTATION WITH EXPERIMENT

Summary Report
(Some Separated Flow Cases)

by

I. Demirdzic, A. D. Gosman and R. I. Issa^{*†}

Computer Group Number: 17²

Cases 0421, 0422, 0423

1. INTRODUCTION

The present document reports part of a collaborative effort made for the Stanford Conference on Complex Turbulent Flows by five university groups in Europe and the USA; the results appear in the conference volume with the code LHHGM. The participating institutions are: University of California, Davis and UMIST, Manchester (Prof. Launder); University of California, Berkeley (Prof. Humphrey); Masinski Fakultet, Sarajevo (Prof. Hanjalić) and Imperial College (present authors). The computations made at the last-named institution are presented here; the other groups are submitting separate reports. Our collective aim has been to provide computations with the same turbulence model over a sufficiently broad range of flows to allow some general inferences to be drawn about the utility of current particular turbulence closures.

An additional objective of the present effort has been the assessment of a new computational procedure for separated flows in complex geometries, which employs a general non-orthogonal grid system for this purpose. The Conference test cases to which it has been applied comprise the following:

- i) Case 0421: Backward-Facing-Step Flow
- ii) Case 0422(P2): Backward-Facing Step: Variable Opposite-Wall Angle
- iii) Case 0423(P3): Backward-Facing Step: Turned Flow Passage

In what follows, a brief outline is first provided of the mathematical formulations including the equations of the turbulence model employed, and of the numerical solution procedure. Then those features of the predictions for the individual cases are presented which are the focus of attention of the Conference. The report is necessarily brief to comply with Conference requirements, but additional information is available in the references cited and it is anticipated that further details will be provided in later publications.

^{*}Imperial College of Science and Technology, London SW7 2BX, England

[†]Computer Groups 17 were coordinated by B.E. Launder and appear here and in other alphabetic listings under "Launder".

2. MATHEMATICAL MODEL

2.1 Equations of Mean Flow

These are formulated in terms of general curvilinear coordinates x^i and physical velocity components $u(i)$. For a stationary, incompressible, time-averaged turbulent flow obeying a Newtonian stress-strain law, they run as follows, in general tensor notation (see Aris, 1975):

$$\frac{\partial}{\partial x^j} \left\{ \sqrt{\frac{g}{g_{jj}}} [\rho u(j)u(i) - \tau(ij)] \right\} = -\sqrt{g} g_{ii} g^{ij} \frac{\partial}{\partial x^j} \left(p + \frac{2}{3} \rho k \right) - \sqrt{\frac{g g_{ii}}{g_{jj} g_{kk}}} [\rho u(j)u(k) - \tau(jk)] \left[\left\{ \begin{matrix} i \\ j \ k \end{matrix} \right\} - \delta_k^i \frac{g_{ok}}{\sqrt{g_{ii} g_{kk}}} \left\{ \begin{matrix} \alpha \\ j \ k \end{matrix} \right\} \right] \quad (1)$$

$$\frac{\partial}{\partial x^j} \left[\sqrt{\frac{g}{g_{jj}}} \rho u(j) \right] = 0 \quad (2)$$

where ρ and μ_t are respectively the density and turbulent viscosity of the fluid, p is the pressure, k is the turbulent kinetic energy and

$$\tau(ij) = \mu_t [g^{ja} \sqrt{g_{jj}} \nabla_a u(i) + g^{ia} \sqrt{g_{ii}} \nabla_a u(j)] \quad (3)$$

is the turbulent stress tensor. The quantities g_{ij} , g^{ij} and g are respectively the covariant and contravariant components and determinant of the metric tensor, $\left\{ \begin{matrix} i \\ j \ k \end{matrix} \right\}$ is the Christoffel symbol of the second kind and

$$\nabla_j u(i) = \frac{\partial u(i)}{\partial x^j} + \sqrt{\frac{g_{ii}}{g_{\alpha\alpha}}} \left\{ \begin{matrix} i \\ j \ \alpha \end{matrix} \right\} u(\alpha) - \frac{g_{i\alpha}}{g_{ii}} \left\{ \begin{matrix} \alpha \\ i \ j \end{matrix} \right\} u(i) \quad (4)$$

is the covariant derivative of a physical vector.

2.2 Equations of Turbulence Model

We employ the familiar k - ϵ viscosity model as described in Launder and Spalding (1972) but with modifications to the production and diffusion terms in the ϵ -equation as proposed by Launder (private communication). The equations solved for the turbulent kinetic energy k and its dissipation rate ϵ are as follows:

$$\frac{\partial}{\partial x^j} \left[\sqrt{\frac{g}{g_{jj}}} \rho u(j)k - \sqrt{g} g^{ja} \frac{\mu_t}{\sigma_k} \frac{\partial k}{\partial x^a} \right] = \sqrt{g} (G - C_D \rho \epsilon) \quad (5)$$

$$\frac{\partial}{\partial x^j} \left[\sqrt{\frac{g}{g_{jj}}} \rho u(j)\epsilon - \sqrt{g} g^{ja} \frac{\mu_t}{\sigma_\epsilon} \frac{\partial \epsilon}{\partial x^a} \right] = \sqrt{g} (C_1 \frac{\epsilon}{k} G_1 - C_2 \rho \frac{\epsilon^2}{k}) \quad (6)$$

where

$$G = \mu_t \left[g^{j\alpha} g_{i\beta} \frac{1}{\sqrt{g_{\beta\beta}}} \nabla_\alpha u(\beta) + \frac{1}{\sqrt{g_{jj}}} \nabla_i u(j) \right] \frac{1}{\sqrt{g_{ii}}} \nabla_j u(i) \quad (7)$$

$$G_1 = \mu_t g^{j\alpha} g_{i\beta} \frac{1}{\sqrt{g_{\beta\beta}}} \nabla_\alpha u(\beta) \cdot \frac{1}{\sqrt{g_{ii}}} \nabla_j u(i) \quad (8)$$

$$\mu_t = C_\mu \rho k^2 / \epsilon \quad (9)$$

and the various coefficients appearing in the above are defined thus:

$$\sigma_\epsilon = \sigma_{\epsilon 0} (C_2 - C_1) / C_2 - C_1' \quad (10)$$

$$\sigma_{\epsilon 0} = \kappa^2 / (C_2 - C_1) C_\mu^{1/2} \quad (11)$$

$$C_1' = \min(C_1, C_1 G / \rho \epsilon) \quad (12)$$

and

$$C_D = 1, C_1 = 1.44, C_2 = 1.92, C_\mu = 0.09, \sigma_k = 1.0, \kappa = 0.4187$$

2.3 Treatment of Wall Layers

A modified form of the near-wall treatment of Chieng and Launder (1980), proposed by Launder (private communication) is employed; it is based on a one-dimensional model with a two-layer structure comprising viscous and inertial regions, with associated distributions with distance from the wall y of the tangential velocity U , k , and ϵ . These are used in the present finite-volume analysis to modify, and match, the interior numerical solution as follows: the wall shear stress τ_w required in the tangential momentum solution is obtained from:

$$U(\rho k^{1/2} / \tau_w) = \kappa^{*-1} \ln(E^* y k^{1/2} / \nu) \quad (13)$$

evaluated at the matching location y_p . Here $\kappa^* = 0.23$ and $E^* = 5.88$. The turbulence-energy solution is obtained by setting $\partial k / \partial y$ to zero at the wall and calculating the integral production P and dissipation D from:

$$P = \tau_w (U_e - U_v) / y_e \quad (14)$$

$$D = k_p^{3/2} (C_\epsilon^{-1} + 0.381) + C_\epsilon^{-1} \ln(y_e / y_v) \quad (15)$$

where the subscripts v and e refer to the edges of the viscous and inertial layers respectively and $C_\epsilon = 2.55$. The dissipation rate is obtained directly from:

$$\epsilon = C_\mu^{3/4} k^{3/2} / \kappa y \quad (16)$$

in place of the differential equation (6).

Further information about all aspects of the turbulence modeling can be found in the companion paper by Launder for Computer Group 17³.

3. METHOD OF SOLUTION

The finite-volume method employed here to solve the foregoing equations is a further development of an earlier version described by Demirdzic et al. (1980); in view of the availability of this publication and the limited space available for the present description, only a brief outline will be provided. The method employs an arbitrary non-orthogonal computing mesh defined by the physical coordinates of curvilinear quadrilateral cells; scalar quantities, including p , k , and ϵ are calculated at the centers of these cells, while the coordinate-aligned velocities are displaced to the edges, as illustrated in the inset of Fig. 1. Discretized counterparts of Eqs. 1-6 are constructed by integration over contiguous, non-overlapping control volumes centered around the variable in question; in this process convection and diffusion fluxes are approximated by hybrid central/upwind differences, while central differencing is used for other terms. The overall solution algorithm is a form of predictor-corrector method which invokes, in the corrector stage, a pressure equation based on the mass-conservation requirement and especially conditioned to be solvable by iteration.

Systematic grid-refinement tests were performed for Case 0421 and sensibly grid-independent results were obtained with a 28×28 grid arranged as illustrated. Similar grid numbers and distributions were employed for the other two cases but it was not possible in the time available to assess these in the same systematic way. The number of iterations required to reduce the equation residuals to tight tolerance ranged from about 180 to 350 and the corresponding computing times on a CDC 7600 machine were around 45 sec and 90 sec, respectively.

4. PRESENTATION OF RESULTS*

4.1 Case 0421: Backward-Facing Step

The measured inlet conditions for this case were not supplied at a single plane, so the streamwise velocity profiles were linearly interpolated onto the plane $x/H = -1.333$, at which the turbulence information was given. The k -distribution was estimated from the latter with the assumption that $w'^2 = (u'^2 + v'^2)/2$, while the ϵ -distribution was obtained from

$$\epsilon = C_{\mu} k^2 |(du/dy)/\overline{u'v'}|$$

using the measured velocity and $\overline{u'v'}$ profiles. Zero streamwise gradients were imposed on all variables at the outlet plane. The method is referred to as BKEZ 17F.

The dominant feature of the comparison between calculations and experiment is the underprediction of the reattachment length X_R , the respective values being 6.2 H and

*The notation of this section follows, wherever possible, that of the case specifications supplied by the Conference organizers.

7.0 H. The former figure is a modest improvement on the value of 5.6 H obtained using the "standard" $k-\epsilon$ model of Launder and Spalding (1972), but the discrepancy is nonetheless around 11%. Exploration with other wall-function variants revealed that the error is unlikely to stem from this source. The wall-pressure (Plate 102), axial-velocity (Plate 106), and axial-shear-stress (Plate 107) profile comparisons all reflect the effects of the X_R underprediction in the expected way, especially in the separated region. One noteworthy feature is the indication in Plate 107 that the rate of growth of the outer edge of the shear layer is being underestimated. However, the device of plotting the maximum shear stress versus position relative to the reattachment point (Plate 104) does bring the computed results into closer accord with the data.

4.2 Case 0422(P2): Backward-Facing Step, Variable Opposite Wall Angle

For this case the inlet conditions were specified at the plane $x/H = -4$ using the measured values of δ , δ_1 , C_f , and U_0 there (the values of the first three quantities being different for the two walls) and the following relations derived from flat-plate boundary-layer theory (see Launder and Spalding, 1972, and Schlichting, 1968):

$$u = \min[U_0(y/\delta)^{1/n}, U_0], \quad n = \delta/\delta_1 - 1$$

$$k = C_\mu^{-1/2} \ell^2 (du/dy)^2, \quad \ell = \min(\kappa y, 0.09\delta)$$

$$\epsilon = C_\mu k^2 (\ell du/dy)^{-1}, \quad \ell = \min(\kappa y, 0.09\delta)$$

The outlet boundary conditions were treated as in the previous case. The method is referred to as BKEZ 17H.

The results, which would of course also be expected to be subject to errors of the kind exhibited in Case 0421, show the reattachment length X_R as monotonically increasing with wall-divergence angle α , in the range $-2^\circ \leq \alpha \leq 10^\circ$; this is presumably due to the increasingly adverse pressure gradient and decreasing lateral confinement of the separation bubble. That this trend should accelerate is at first sight surprising, in view of the fact that as α becomes large, X_R should asymptotically approach the value for an unbounded flow; however the calculations have not at this stage been carried beyond $\alpha = 10^\circ$. The separation wall pressure profiles (Plates 180 and 181) are consistent with expectations up to $\alpha = 6^\circ$, but the $\alpha = 10^\circ$ result is again curious. The lateral profiles of axial velocity (Plate 182) and axial shear stress (Plate 183) for $\alpha = 6^\circ$ seem reasonable.

4.3 Case 0423(P3): Backward-Facing Step: Turned Flow Passage (Method BKEZ 17H)

The inlet condition treatment here follows that of the previous case, apart from being imposed at $x/H = -3$. The variations in wall pressure along the step and opposite sides are shown in Plates 184 and 185, respectively. These show the expected

trend of increasing initial pressure on the impingement side with increasing α , in the range $0 < \alpha < 15^\circ$, while on the step side the pressure is reduced due to the higher velocity at separation consequent upon the inwards displacement of the flow as it enters the bend. This same acceleration is presumably responsible for the lengthening of the separation zone with increasing α displayed in Plate 186. The velocity profiles shown in Plate 185 are consistent with the above interpretation.

5. DISCUSSION

The final judgment of the outcome of the calculation for two of the three cases just presented must necessarily await the comparison with the measurements. It is, however, nonetheless possible to draw some tentative conclusions: firstly, the errors observed for Case 0421 are almost certainly due to the turbulence modeling and are probably also present to a lesser or greater extent in the predictions for the other two cases; secondly, the wall-layer component of the modeling is not the major error source; and thirdly, on the basis of the experience of our companion group 17³ (see Summary Report of Launder et al. which follows) and other workers, the most likely source is inadequate simulation in the models we have employed of the effects of curvature on the shear-layer development. It is our intention in future work to explore the capabilities of algebraic-stress-model variants of the $k-\epsilon$ approach like that outlined in the Summary Report of Launder et al., which appear better able to simulate the forementioned effects. We intend also to further explore the possibilities for improvements in accuracy and economy through computing mesh optimization afforded by the flexibility of the present computational procedure.

Acknowledgment

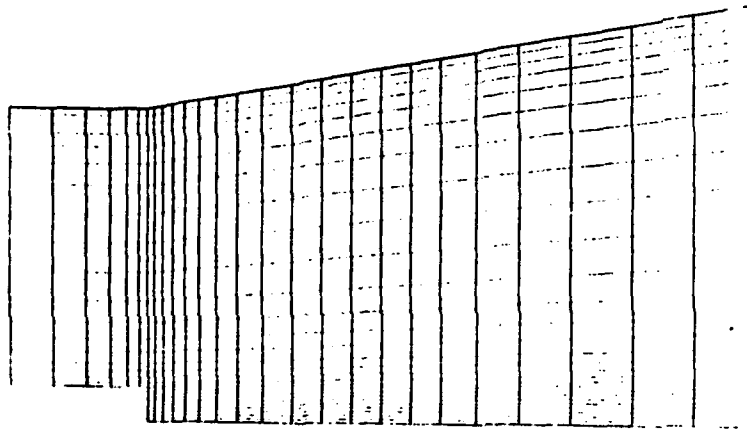
We would like to acknowledge with thanks the cooperation and assistance of Prof. B.E. Launder and Dr. M. Leschziner in connection with this collaborative venture.

References

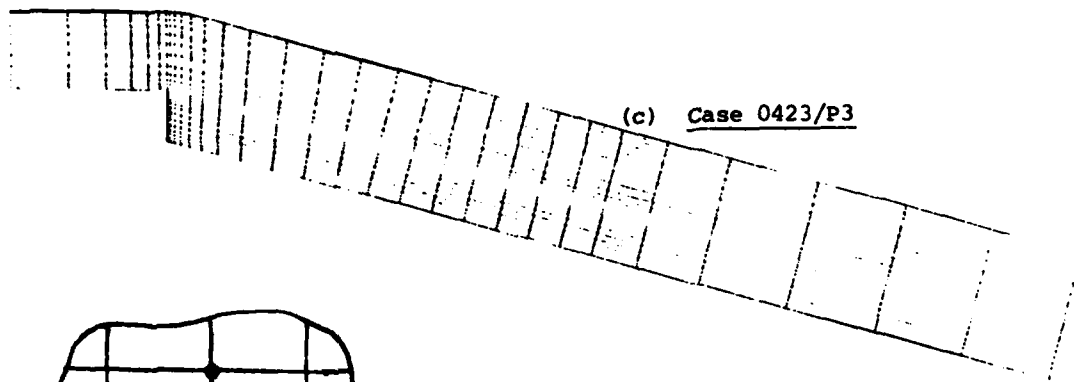
- Aris, R. (1975). Vectors, Tensors and the Basic Equations of Fluid Mechanics. Prentice-Hall, Inc., Englewood Cliffs, N.J.
- Chieng, C. C., and B. E. Launder (1980). "On the calculation of turbulent heat transport downstream from an abrupt pipe expansion," Numer. Heat Transfer, 3, 189.
- Demirdzic, I., A. D. Gosman, and R. I. Issa (1980). "A finite-volume method for the prediction of turbulent flow in arbitrary geometries," Proc., Seventh International Conference on Numerical Methods in Fluid Dynamics. Springer-Verlag, Berlin.
- Launder, B. E., and D. B. Spalding (1972). Mathematical Models of Turbulence. Academic Press, New York.
- Schlichting, H. (1968). Boundary-Layer Theory, 6th Ed. McGraw-Hill, New York.



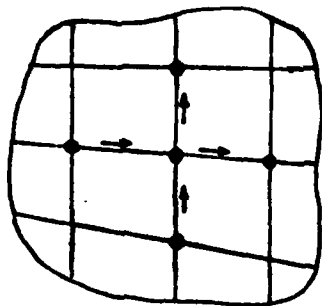
(a) Case 0421



(b) Case 0422/P2



(c) Case 0423/P3



(d) Arrangement of variables

Figure 1. Illustration of computing meshes and location of variables.

COMPARISON OF COMPUTATION WITH EXPERIMENT

Summary Report

by

B. E. Launder,* M. A. Leschziner*, and M. Sindir†

with contributions by

A. Barba, I. M. Ibrahim, R. W. Johnson,
J. M. MacInnes, R. J. Mjolsness, and N. G. Teku*

Computer Group Number: 17³

B.E. Launder

M.A. Leschziner

Cases 0142, 0143, 0211, 0231, 0232, 0233, 0261, 0263, 0311, 0331,
0375, 0376, 0381, 0382, 0421, 0422, 0424, 0612

1. INTRODUCTION

The present document reports part of a collaborative effort made for the Stanford Conference on Complex Turbulent Flows by five university groups in Europe and the USA; the results appear in the Conference volume with the code LHHGM and the participating institutions are Imperial College London (Dr. Gosman), Masinski Fakultet, Sarajevo (Prof. Hanjalić), University of California, Berkeley (Prof. Humphrey), University of California, Davis, and UMIST, Manchester. The computations made at the last two institutions are presented here; the other groups are submitting separate reports.

Our collective aim has been to provide computations with the same turbulence model over a sufficiently broad range of flows to allow some general inferences to be drawn about the utility of current turbulence closures. In common, no doubt, with other groups, the period we have been able to devote to the computations has been brief—a mere four months. Indeed at UMIST the code employed for the two-dimensional thin-shear-flow computations has been written entirely from scratch and so the task of applying the program to the specific test cases has inevitably been intertwined with final debugging of the code itself. The scope of our enquiry has thus necessarily been limited to identifying and understanding the origins of differences between measured and computed behavior. The task of extending the rather modest capabilities of the models examined in the present study is in any event best undertaken outside of the rather hectic period leading up to the Conference itself.

*Univ. of Manchester, Inst. of Science and Technology, Manchester M60 1QD, England

†University of California, Davis, CA 95616. Authors' names appear alphabetically.

2. TURBULENCE MODELS

2.1 Summary and Rationale

The turbulence models tested, save for minor variations, are ones that have been available in the literature for several years, the principal references being Hanjalić and Launder (1972), Launder et al. (1975), Rodi (1972), and Gibson and Launder (1976, 1978). Three levels of closure have been employed (though only two levels have been tested for any single flow):

- (1) Full second-moment closure (referred to as "Reynolds-Stress Transport Models" in this Conference) used for Cases 0375, 0376.
- (2) Algebraic Stress Model (a truncated second-moment closure) based on two transport equations (for k and ϵ). Cases 0142, 0143, 0211, 0231, 0232, 0233, 0311, 0331, 0375, 0376, 0381, 0382, 0421, 0422, 0424.
- (3) Boussinesq Viscosity Model based on two transport equations (again for k and ϵ). Cases 0142, 0143, 0211, 0231, 0232, 0233, 0311, 0331, 0381, 0382, 0421, 0422, 0424.

Our overall philosophy has been to try to provide evidence on what, for a given flow type is the simplest closure level that will give adequate agreement with experiment. The reason for emphasizing simplicity is that most engineering flows (as opposed to laboratory generated flows) are so complex that computer-storage imposes severe constraints on the fineness of computational mesh that can be employed; thus, the simpler one can keep the turbulence model, the better.

2.2 Stress-Strain Connections

(1) Reynolds-Stress Transport Model (RSTM)

The kinematic Reynolds stresses are obtained from solving the differential equations:

$$\frac{D\overline{u_i u_j}}{Dt} = T_{ij} + P_{ij} + \phi_{ij} - \epsilon_{ij} \quad (1)$$

where:

$$\text{Transport, } T_{ij} = C_s \frac{\partial}{\partial x_k} \left(\overline{u_k u_l} \frac{\partial \overline{u_i u_j}}{\partial x_l} \right)$$

$$\text{Production, } P_{ij} = - \left\{ \overline{u_i u_k} \frac{\partial U_j}{\partial x_k} + \overline{u_j u_k} \frac{\partial U_i}{\partial x_k} \right\} \quad \text{- exact}$$

$$\text{Pressure scrambling, } \phi_{ij} = \phi_{ij1} + \phi_{ij2} + \phi_{ijw}$$

$$\text{and } \phi_{ij1} = -C_1 \frac{\epsilon}{k} (\overline{u_i u_j} - \frac{2}{3} \delta_{ij} k) ;$$

$$\phi_{ij2} = -C_2 (P_{ij} - \frac{1}{3} \delta_{ij} P_{kk}) ;$$

wall reflection term,
absent in free flows,

$$\phi_{ijw} = \left\{ C_1^i \frac{\epsilon}{k} (\overline{u_k u_m} n_k n_m \delta_{ij} - \frac{3}{2} \overline{u_k u_i} n_k n_j - \frac{3}{2} \overline{u_k u_j} n_k n_i) \right. \\ \left. + C_2^i (\phi_{km2} n_k n_m \delta_{ij} - \frac{3}{2} \phi_{ik2} n_k n_j - \frac{3}{2} \phi_{jk2} n_k n_i) \right\} \frac{k^{3/2}}{2.5 \epsilon x_n}$$

x_n = normal distance from wall *

$$\text{Dissipation, } \epsilon_{ij} = \frac{2}{3} \delta_{ij} \epsilon$$

(ii) Algebraic Stress Model (ASM)

As Model (i), except the derivatives of stresses are approximated in terms of kinetic energy using the suggestion of Rodi (1972):

$$\left(\frac{D \overline{u_i u_j}}{Dt} - T_{ij} \right) = \frac{\overline{u_i u_j}}{k} \left(\frac{Dk}{Dt} - T_k \right) = \frac{\overline{u_i u_j}}{k} \left(\frac{1}{2} P_{kk} - \epsilon \right) \quad (2)$$

This leads to a system of algebraic rather than differential equations for the $\overline{u_i u_j}$.

(iii) Boussinesq Viscosity Model (BVM)

$$- (\overline{u_i u_j} - \frac{2}{3} \delta_{ij} k) = \frac{C_\mu k^2}{\epsilon} \left(\frac{\partial U_i}{\partial x_j} + \frac{\partial U_j}{\partial x_i} \right) \quad (3)$$

2.3 Transport of Scalar Properties of Turbulence

The kinetic energy dissipation rate ϵ is obtained from the following transport equation:

$$\frac{D\epsilon}{Dt} = T_\epsilon + C_{\epsilon 1} C_\mu k \left(\frac{\partial U_i}{\partial x_j} \right)^2 - C_{\epsilon 2} \frac{\epsilon^2}{k} \quad (4)^\dagger$$

where

$$T_\epsilon = C_\epsilon \frac{\partial}{\partial x_l} \left(\frac{k}{\epsilon} \overline{u_j u_l} \frac{\partial \epsilon}{\partial x_j} \right) \quad \text{for the ASM} \\ = \frac{C_\mu}{\sigma_\epsilon} \frac{\partial}{\partial x_l} \left(\frac{k^2}{\epsilon} \frac{\partial \epsilon}{\partial x_l} \right) \quad \text{for BVM}$$

* In axisymmetric flows (the conical diffusers) an effective wall distance is obtained by integration around the perimeter (see Samaraweera, 1978).

† In many cases the more usual form $1/2 C_{\epsilon 1} \epsilon P_{kk}/k$ has been adopted as the source term in (4) because that was the version embedded in the original coding, and there has proved to be insufficient time to effect a change-over. Except for Cases 0233 and 0331, our experience suggests that the computed behavior would have been negligibly different had the form given in (4) been used.

For the ASM and BVM models* the following equation for k must be solved:

$$\frac{Dk}{Dt} = T_k + \frac{1}{2} P_{kk} - \epsilon \quad (5)$$

where

$$T_k = C_s \frac{\partial}{\partial x_l} \left(\frac{k}{\epsilon} \overline{u_l u_j} \frac{\partial k}{\partial x_j} \right) \quad (\text{ASM})$$

$$= \frac{C}{\sigma_k} \frac{\partial}{\partial x_l} \left(\frac{k^2}{\epsilon} \frac{\partial k}{\partial x_l} \right) \quad (\text{BVM})$$

2.4 Values Assigned to Coefficients

Except where specifically indicated to the contrary the coefficients appearing in the above equations have been assigned the following constant values:

$$\text{RSTM/ASM: } C_1 = 1.8; \quad C_2 = 0.6; \quad C_1' = 0.5; \quad C_2' = 0.3; \quad C_s = 0.22;$$

$$C_{\epsilon 1} = 1.44; \quad C_{\epsilon 2} = 1.92; \quad C_\epsilon = 0.15$$

$$\text{BVM: } \quad C_\mu = 0.09; \quad \sigma_k = 1.0; \quad \sigma_\epsilon = 1.25$$

2.5 Near-Wall Treatment

The principal solution procedures used in the study obtain the set of discretized equations by integration of the transport equations over control volumes surrounding each node. For the wall-adjacent control volumes (with one control volume face coinciding with the wall) special formulae are derived to take, so far as possible, a global account of the effects of the viscous sublayer on the various processes appearing in the turbulence model. The particular formulae used in the present study are reported in Chieng and Launder (1980); space constraints preclude our giving a detailed presentation here. In summary, the square root of kinetic energy at the edge of the viscous sublayer, $k_v^{1/2}$ replaces the friction velocity as the characteristic velocity scale, and for purposes of estimating the mean velocity, and the turbulence-energy generation and dissipation rates, the near-wall region is represented as a viscous (but not laminar) sublayer, whose thickness is equal to $21\nu/k_v^{1/2}$ where turbulent stresses are zero but k and ϵ are not; this abuts a fully turbulent region in which the turbulent length scale is assumed to increase linearly in direct proportion to the distance from the wall.

*For the RSTM the individual $\overline{u_l u_j}$ are found from transport equations and the kinetic energy then obtained as: $k = \overline{u_k u_k} / 2$.

3. NUMERICAL COMPUTATION SCHEMES

3.1 Homogeneous Flows

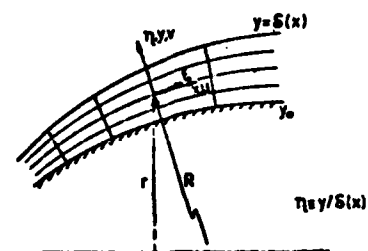
These flows are described by coupled ordinary differential equations in terms of the independent variable x (or t). Separate programs have been written for the two types of flow studied (shear and axisymmetric contraction) employing, for clarity, an Euler first-order solution method. Forward step size was progressively reduced to ensure independence of the solution from this quantity; computation times (~ 0.5 sec CPU time for CDC 7600) were negligible compared with those needed for analyzing the inhomogeneous flows.

3.2 Thin-Shear Flows

Although several general thin-shear-flow codes are available in the literature, it was decided, in the interests of unification, that an entirely new program should be written for the Stanford Conference computations. Our purpose has been to provide a parabolic solution procedure that adopted broadly the same solution methodology as the elliptic flow program outlined in Sec. 3.3 in respect of the choice of independent (and dependent) variables, the discretization scheme and the treatment of boundary conditions. The resultant code PASSABLE* written by Dr. M. A. Leschziner will shortly become available for general use.

Basic Equations: The equations solved are those governing continuity, momentum and the transport of scalars (here k and ϵ). The co-ordinate system and the numerical mesh are sketched in Fig. 1. The independent variables are η , the dimensionless

distance across the shear flow and ξ the (nearly) streamwise co-ordinate (a ξ -directed contour being one connecting point of constant η). The system (ξ, η) is weakly non-orthogonal, but for the flows considered deviations from orthogonality are small enough to permit the approximations



$$\left. \frac{\partial \xi}{\partial x} \right|_y = 1, \quad \left. \frac{\partial \xi}{\partial y} \right|_x = 0 \quad (6)$$

to be introduced in the transformation of the equation from the (x, y) to (ξ, η) plane.

Figure 1. Coordinate system for thin shear-flow program.

*Parabolic Axis-Symmetric Solver Applied to Boundary-Layer Equations.

For plane flows ($r, R \rightarrow \infty$) the resulting equations are:

$$\text{Continuity:} \quad \frac{\delta(\delta U)}{\partial \xi} + \frac{\partial(V-GU)}{\partial \eta} = 0 \quad (7)$$

$$\text{Conservation of } \phi\text{-property:} \quad \frac{\partial(\delta U \phi)}{\partial \xi} + \frac{\partial(V-GU)\phi}{\partial \eta} = \frac{\partial}{\partial \xi} \left(\nu \delta \frac{\partial \phi}{\partial \xi} \right) + \frac{\partial}{\partial \eta} \left(\frac{\nu}{\delta} \frac{\partial \phi}{\partial \eta} \right) + S_\phi \quad (8)$$

where

$$G \equiv \frac{dy_0}{dx} + \eta \frac{d\delta}{dx}$$

and S_ϕ is the variable-dependent source/sink term.

For $\phi = U$,

$$S_U = -\frac{\delta}{\rho} \frac{dP}{dx} + \text{secondary terms}^*$$

while for $\phi = V$,

$$S_V = -\frac{1}{\rho} \frac{\partial P}{\partial \eta} + \text{secondary terms}^*$$

The above thus implies an uncoupling of pressure, i.e., the assumption $\partial P / \partial x \neq f(y)$.

The Solution Code: Discretization was based on the control volume approach. A hybrid, cell-Peclet-number-dependent central/upwind difference scheme is used in the η -direction, and the finite-difference equations are implicit in the ξ -direction. Thus, the discretized form of Eq. 8 is

$$\phi_j^D = A_j^U \phi_j^U + A_{j-1}^D \phi_{j-1}^D + A_{j+1}^D \phi_{j+1}^D + S_\phi^D \quad (9)$$

with U and D denoting upstream and downstream, respectively, and j denoting cross-stream positions.

The solution scheme is a forward-marching one and segregated in variable space. A tri-diagonal matrix algorithm (TDMA) is used to solve linearized sets of the form (9) for all nodal downstream values ϕ_j^E , (i.e., with the A's and S_ϕ evaluated at the upstream plane). Iteration within each forward step is optional if account need be taken of nonlinearity and coupling within a forward step. The V-velocity field is normally obtained by explicitly solving the continuity equation. This, however, requires V to be known at one boundary. An alternative path, involving the solution for V-momentum and pressure $P(y)$ is provided if no boundary V-value is known (as, for example, in the case of the asymmetric wake).

The code is applicable to plane, axially symmetric and plane-curved flows. Adaptation of the mesh to the flow domain is automatic, being controlled by the flow itself on the basis of entrainment. For confined flows, $\partial P / \partial \xi$, appearing in the

* These arise from strain rates not included in the diffusion terms and from the (x,y) - to - (ξ, η) transformation.

ξ -momentum equation, is solved by reference to integral continuity and momentum considerations.

In most flows considered 15-25 n -directed grid lines proved adequate. Typical forward-step numbers were in the range 1000-2000. No attempt was made to economize in this respect. Typical execution times were of the order 50 CPU sec on a CYBER 72 (equivalent to ca. 7 CDC 7600 sec) for 15 n -nodes and 2000 steps covering a plate boundary layer 2 m long.

Turbulence Models: The general forms of the BVM and the algebraic Reynolds-stress model are provided in Section 2. Here, terms associated with $\partial U/\partial x$, $\partial V/\partial y$, V/r , and V/R have been removed, which is consistent with thin-shear-flow assumptions.

3.3 Elliptic Flows

The elliptic flows have been computed with versions of the two-dimensional TEACH-2E computer program of Gosman and Pun. The forms of the code used in the calculations employ a Cartesian mesh so that only an approximate match can be made to a solution domain of complex shape. We retained Cartesian co-ordinates rather than adopting some curvilinear form, because we doubted there would be time to incorporate successfully the ASM treatment into a more generally organized co-ordinate system. The code adopts so-called "primitive" variables and, except as noted below, uses a hybrid upwind/central-difference discretization and a line-by-line iterative solution of the discretized set. For one test case (0331) a "skew" upwind option was introduced into the calculation method. In this scheme, for cell Peclet numbers greater than 2, convection is approximated by applying the usual upwind principle in the direction of the velocity vector. The interpolation involves a 9-point star rather than the 5-point array that results from the conventional upwind scheme. Since the "upwinding" is applied along the velocity vector, artificial diffusion associated with skewness--the major source of error in the hybrid scheme--is largely eliminated.

The basic version of TEACH-2E incorporates a two-equation BVM. In adding the ASM, stresses were, so far as possible, represented as a turbulent viscosity times the relevant velocity gradient; this practice markedly improved stability. The parts of the stress components left over after viscous-type contributions had been removed were incorporated as source/sink terms and treated explicitly.

The backward-step cases employed approximately 40×40 nonuniform grids. A previous study by M. Sindir of a back-step geometry suggested this degree of refinement achieved nearly grid-independent results (the maximum error on reattachment associated with numerical diffusion is estimated at no more than $1/4$ step height). Execution times per computation range from 1.5-12 min CPU for a CDC 7600 according to the test case.

4. THE TEST CASES CONSIDERED

Case 0612: Boundary Layer on a Flat Plate (A. Barba)

Important elements of both the ASM and BVM have been chosen by reference to experiments of this flow, so it is not surprising that very nearly the correct development is obtained, in each case with 15 cross-stream nodes. At low Reynolds numbers, there is some uncertainty as to the effective x origin; this obscures any possible weakness in the model (associated with the wall treatment or viscous effects in the superlayer). The underestimate in H seems mainly due to small integration errors; recent repeat calculations with 20 nodes halved the difference between data and computation with an insignificant effect on C_f .

Case 0211: Effect of Free-Stream Turbulence (N. G. Teku)

The principal results in this case relate to the BVM. Eighteen nodes were used and the computed behavior through which the mean line has been drawn were for momentum thickness Reynolds numbers in the range 3-6,000. It must be said, there was some difficulty in estimating δ_{995} , as the outer-region profile is so flat when the free-stream turbulence is high. The free-stream turbulence was assumed isotropic (no other possibility existed with either the ASM or BVM), and decayed with distance downstream. The BVM seriously underestimates the effects of free-stream turbulence in the middle range of intensities. The ASM curve based on fewer runs is rather better, though here it seems likely that the improvement arises for the wrong reason; this topic is discussed in relation to Case 0143.

Cases 0142, 0143: Axisymmetric Diffuser (N. G. Teku)

Both cases were computed with an 18-node mesh. Experimentally prescribed distributions for U and the Reynolds stresses were adopted at the initial plane. For Case 0142 (Low-Core Turbulence) ϵ was obtained from \overline{uv} , k , and $\partial U/\partial y$ in the shear layers (via the constitutive stress-strain relation), while in the core region $L \equiv k^{3/2}/\epsilon$ was taken as $0.55R$. For Case 0143 $L \equiv \min(2.5y, 0.55R)$ was prescribed. For low-core turbulence the ASM scheme gives nearly the same C_f distribution as that measured, though the stress within the boundary layer is computed too high, which appears to be mainly due to the known tendency of the ϵ -equation to give too large length scales under near-separation conditions.

The BVM does distinctly better for Case 0143 where, due to the high-core turbulence, the wall stress never approaches zero. The ASM does much worse; this result, which initially rather surprised us, is apparently due to the scheme giving much too high levels of effective viscosity in the region near the axis where $P_{kk}/2$ is much less than ϵ . This is a weakness of the particular ASM hypothesis employed (Eq. 2), but not necessarily an intrinsic frailty of this closure type. A very recent proposal

by Launder (1982) appears to avoid the problem, but there has been insufficient time to include the suggestion in the present computations.

Cases 0231, 0232, 0233: Boundary Layers on Curved Surfaces (A. Barba)

All calculations, made with 20 cross-stream nodes, started from a uniform initial U-profile and included the section of plane plate that preceded entry to the curved section. The development length differed somewhat from the actual, however, in order that the correct value of θ be given at the start of curvature in the case of the ASM. For Cases 0231 and 0232 the pressure gradient was applied via a cubic-spline fit to the given $C_p(x)$ (a piecewise linear fit gave very similar results). The convex-wall boundary layer, Case 0231, shows an erratic behavior in the variation of θ and C_f and, after extensive checks for numerical instabilities, we conclude that this is a consequence of the prescribed C_p (the minimum C_f nearly coincides with a change-over of dp/dx from positive to negative). The relative variation of C_f and θ also seems anomalous for, in spite of the presence of a non-negligible variation in streamwise velocity, it is unlikely that a consistently too large value of C_f would produce throughout a too small rate of increase in θ . Qualitatively similar, though less pronounced, differences are seen for the concave wall opposite (Case 0232); here the calculated θ is too large, while the computed C_f is too small. One is led to wonder, whether there may have been weak secondary flow present in the experiment (unlikely, in view of the experience of the data takers), or whether we have misinterpreted the data file.

In any event, inferences about the ability of the turbulence models to reflect the sensitivity of turbulence to streamline curvature are best drawn by reference to Case 0233, where pressure gradients near the convex test surface have been made insignificant. We notice that the ASM treatment produces a rapid diminution in C_f at the start of curvature, while the BVM exhibits none. The mean-velocity and Reynolds-stress profiles are generally in good agreement, though the wall shear stress and near-wall \overline{uv} levels remain somewhat too high. Unfortunately, the source term in the ϵ -equation was based on turbulence energy production $P_{kk}/2$, rather than that given in Eq. 4; this seems to be a case where secondary strains are large enough for the difference between the two forms to be significant (the recommended form produces higher levels of ϵ under stable curvature and, thus, somewhat lower stresses). The benefit of using an ASM in place of a BVM are also evident for Case 0232, though, since the curvature is milder, the differences are less pronounced.

Case 0263:* The Wall Jet on a Logarithmic Spiral (A. Barba)

These computations were made with 20 cross-stream nodes. A roughly wall-jet-like profile was prescribed initially and computations extended downstream until the flow became self-preserving. To assist stability a small external stream velocity ($\approx 4\%$ of maximum velocity at most downstream positions) was prescribed, which we believe has had no significant influence on the computed rate of spread.

At the time of writing only results with the BVM are available, as shown in Fig. 2. These show two anticipated anomalies: (i) the rate of spread is insensitive to the strength of streamline curvature (which is consistent with the boundary-layer results for Cases 0231, 0232, and 0233 above; (ii) the computed rate of spread for the wall jet on a plane surface is 25% too high. The latter weakness arises from the fact that this simple model contains no equivalent of the wall-modification ϕ_{ijw} to the pressure-strain correlation. (That the deficiency is attributable to the absence of ϕ_{ijw} can perhaps best be appreciated by comparing two published RSTM computations. In the first, Hanjalić and Launder (1972), ϕ_{ijw} was omitted with results similar to those here obtained, while in the second, Launder et al. (1975), it was included, resulting virtually in complete agreement with experiment).

Case 0261:* The Equilibrium Wall Jet in an Adverse Pressure Gradient (I. M. Ibrahim)

Time limitations have confined our study to the BVM. A power-law variation of free-stream velocity was applied, $U_E = x^{-m}$, and the shear-flow computations carried downstream until the flow became self-preserving. In fact, only for $m = 0.45$ did the ratio U_M/U_E become strictly uniform though its variation in the other cases was sufficiently slow that a locally prevailing equilibrium could be presumed.[†] As noted above the calculated development of the wall jet in stagnant surroundings is some 25% too high with this model. This overestimate diminishes (Fig. 3), as the velocity ratio increases; indeed at the largest value of U_M/U_E for which computations were made, the rate of spread appears to be seriously too low.

At $U_E/U_M = 0.38$, for which detailed comparisons with Irwin's data are to be made, the computed rate of spread is some 12% higher than measured, which is broadly consistent with the calculated peak shear stress being some 20% below the experimental value (Fig. 5). Figure 4 indicates a satisfactory accord in the mean-velocity profiles, except in the vicinity of the velocity maximum, where the well-known difference in the positions at which the velocity gradient and shear stress vanish, cannot be mimicked with a BVM treatment. The streamwise normal component of the Reynolds stress is shown in Fig. 6.

*Plates for Cases 0261 and 0263 were not prepared in time for the Conference. They are however included as Figs. 2 through 6 herein.

[†]Typically, a 4% variation in U_M/U_E for a doubling of streamwise development length.

Case 0311: Plane Mixing Layer (J. M. MacInnes)

The computed spreading rate is in somewhat less satisfactory agreement with data than expected, principally because the unusual definition for L gives especial prominence to the high velocity edge of the layer. The computed profiles of mean velocity approach the free-stream value too abruptly at the high velocity edge--hence L is too small. The usual definition for length scale (based on distance between the 90% and 10% velocity points) would display much closer accord between the asymptotic slopes of the measured and computed curves.

Cases 0381 and 0382: Near-Field of Plane Wakes (J. M. MacInnes)

These cases highlight some clear weaknesses of the ASM scheme though, even so, the mean profiles are fairly well reproduced. For the symmetric case 18 cross-stream nodes were used, and 44 for the asymmetric case. Mean-velocity profiles obtained with the BVM cannot be clearly distinguished from the ASM results and are therefore omitted. The initial k profile has been set equal to the given u^2 distribution,* while ϵ has been obtained as $k^{3/2}/L$ with $L = \min(2.5y, 0.5\delta)$, which is appropriate to a flat-plate boundary layer. This prescription inevitably gives a too large \overline{uv} (because of the absence of ϕ_{ijw}); the alternative of adjusting ϵ to give the correct initial \overline{uv} profile, while almost certainly leading to better agreement with experiment, is not justifiable. The principal errors in the Reynolds-stress profiles arise from the fact that these are free-shear flows and thus contain no wall effect, ϕ_{ijw} , yet the real flow clearly does retain some wall memory on the relative intensity levels.† The fact that the measured u_{\max}^2 / v_{\max}^2 remains at about 4 throughout the development (compared with about 1.5 in an asymptotic wake) shows how difficult it is to get energy into the highly elongated cigar-like eddies near the wall. This fact translated to the present model would suggest that C_2 and C_1 should diminish under such conditions. Case 0375 allows this idea to be considered further.

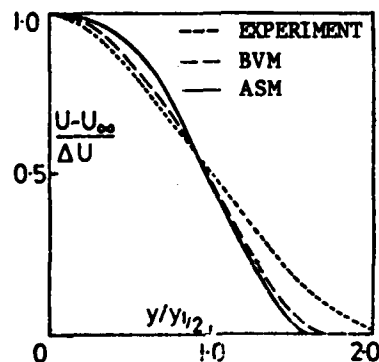
The asymptotic plane wake was computed, as requested, and the results are summarized in Table 1. As is well known, the ASM scheme is more adept than the BVM at coping with both strong and weak shear flows and this is reflected in the higher asymptotic rate of spread; the profile shape is worse, however, because the production of kinetic energy falls to zero on the axis and this feature leads to a sharp increase in the effective viscosity.

*This non-ideal choice, which will give k levels somewhat too high near the wall and somewhat too low in the outer region, is unlikely to have had a significant effect on the computed development.

†The method of Launder et al. (1975) exhibits a similar discrepancy (for the Chevray-Kovassnay wake) though there the error is less because transport equations were solved for the stresses.

Table 1. Spreading Rate in a Plane Wake

	expt	BVM	ASM
$\frac{U_{\infty}}{\Delta U} \frac{dy^2}{dx}$	0.098	0.069	0.090



Case 0331: The Curved Mixing Layer (M. A. Leschziner)

Computations of this flow have used an elliptic solving scheme with a Cartesian mesh, despite the fact that (numerically) more accurate results could have been obtained from a parabolic computation (following the prescribed free streamline) at much less computational effort. We have eschewed use of the parabolic code partly because, in a practical case, one would not know precisely where the flow would go and partly because the thin-shear-flow approximation (with radial equilibrium) becomes an increasingly inexact model of the mean-flow equations as the ratio of shear-layer width: streamline radius of curvature becomes larger. There is thus an endemic problem of confusing errors associated with the model of the mean flow with the model of the turbulence. Our use of the complete Reynolds-stress equations offers in principle a way of avoiding this problem though, in practice, the results reported here all suffer significantly from an inadequately fine mesh.* Nevertheless, these computations are intrinsically relevant to this Conference and for that reason they are included in our presentation.

A 27×31 nonuniform grid was used for all computations with a maximum ratio of 1.2 in the dimensions of neighboring cells. About 400 iterations were required to convergence (somewhat longer with the ASM) with execution times ranging from 1.5 to 4.0 min (CDC 7600), depending on choice of turbulence model and difference scheme (hybrid or skewed). Grids finer than 27×31 have not been used because of computer resource limitations. In the polar-coordinate regions, results are shown only at 0° and 90° , because of the difficulty of interpolation. Moreover the station at $x = 0.708$ lies outside the solution domain covered. The walls have been treated as planes of symmetry and the wall reflection term ϕ_{ijw} has been omitted from the ASM calculations.

*It had originally been hoped that a collaborating group could provide further elliptic computations using a curvilinear mesh, thus allowing a more effective coverage of the shear layer.

The computations obtained with conventional hybrid differencing are, as expected, dominated by false diffusion; the mean velocity profiles at 90° show this clearly with the maximum cross-stream gradient being less than half the measured. The skew-differenced results are much better in this respect, particularly the ASM scheme which, apart from being somewhat displaced towards the high-velocity edge,* exhibits a generally correct profile. The shear stress on Plate 54, and the normal stress u_r^2 on Plate 55, also display the correct maximum level at 90° , albeit distended somewhat on the low velocity side. A comparison of Plates 53, 54, and 55 suggests that the displacement of the stresses towards the low velocity edge at $\theta = 0^\circ$ is incorrectly large, relative to the displacement of the mean U-profile. There are two reasons for this anomaly: first, only two grid points lie within the shear layer at $\theta = 0^\circ$; this results in large errors in the numerical evaluation of the velocity gradient; secondly, the boundary condition $p = 0$ along the entrainment plane $x = 0$ results in strong shear above the jet lip. The shear leads to a large k level which is convected to the $\theta = 0^\circ$ plane. It is the combination of U-profile displacement and a stronger k -profile displacement which contributes to the marked stress-profile displacement. Plate 57 shows that the skew scheme produces excessive shear-stress levels beyond the curved region; this is a manifestation of an excessively fast recovery from curvature effects and is perhaps mainly due to the imperfect accounting of stress transport with the ASM level of closure. Notice that at $x = 0.556$, the computed BVM-upwind (hybrid) velocity is in close accord with measurement, because the computed stresses are too low and the resultant rate of spread is so slow that the measurement "catches up." The agreement is fortuitous but helps to show how apparently satisfactory computations can result with coarse meshes and low-order difference schemes.

Case 0421: Plane Backward-Facing Step (M. Sindir)

Three sets of computations are here included to show the strong effect in this flow of replacing the positive ϵ source given in Eq. 4 by the more conventional form involving the turbulence-energy production. Broadly, ASM leads to longer reattachment lengths than the corresponding BVM with lower stresses in the separated region. The use of $C_\mu k(\partial U_i/\partial x_j)^2$ in place of $P_{kk}/2$ leads to the creation of larger levels of ϵ , hence, lower stresses and, again longer reattachment lengths, (5.3, 5.4 and 6.9 step heights, respectively for BVM, ASM with $P_{kk}/2$ in the ϵ source term and ASM with $C_\mu k(\partial U_i/\partial x_j)^2$, respectively). The recovery region is not particularly well predicted with the ASM scheme giving the longest reattachment length having the slowest downstream growth. It emerges that small differences in stress profiles lead to rather significant variations in the development of the mean-velocity field.

*The displacement occurs close to the jet-exit plane and is thought to be associated with the application of atmospheric pressure along the "stagnant air" boundaries. A constant stagnation pressure condition may alleviate this problem.

Cases 0422, 0424:* Back-Step Variations (M. Sindir)

Computations of these predictive cases have been made with the same models as for Case 0421. The sloping roof has been simulated (rather roughly) by a series of shallow steps, a treatment which we felt would be adequate for small angles of divergence. Computations by Dr. Gosman at Imperial College using body-fitted coordinates will provide an opportunity (with the BVM) of comparing the results of the two numerical treatments. As one would intuitively expect, the increasingly large adverse pressure gradient, whether produced by "tilting the roof" or by providing a larger expansion ratio, has the effect of increasing the length of the reverse-flow region.

Cases 0375, 0376: Homogeneous Strains (A. Barba, R. J. Mjolsness)

These homogeneous flows have employed ASM and RSTM models, one objective being to observe, for two quite different strain fields, how well the algebraic-stress hypothesis, Eq. 2, managed to imitate the development given by the RSTM. A partial answer is: in a shear flow the approximation is fairly successful, even when $P_{kk}/2$ is considerably in excess of ϵ , but where plane-straining is involved and the normal stresses each appear in the generation term of their own transport equation, utterly spurious behavior can result. In several 0375 runs u^2 actually becomes negative.

For the case of axisymmetric strain the standard RSTM fails to reproduce correctly the marked dip in u^2 arising from the acceleration. This defect can be traced to the model of ϕ_{1j2} .[†] In simple terms, the more rapidly turbulence is stretched axially, the less readily can pressure fluctuating "deflect" energy generation to the streamwise component. To help quantify this view, computations are provided where C_2 is reduced from 0.6 to 0.4 at some point in the acceleration. For 0375B this produces too large an effect, for 0375D about the correct modification, and for 0375E an insufficient diminution. These cases represent a progressive increase in the applied strain rates; hence there does appear to be a connection between axial stretching and C_2 . What one is really trying to capture is the modification, by straining, of the shapes of the 2-point velocity correlation iso-correlation surfaces. A first cut at this (appropriate to RSTM closure) is to represent the coefficient(s) in the ϕ_{1j2} model as functions of the local 2nd and 3rd invariants of the Reynolds stress. The second invariant alone (the "anisotropy") is insufficient for this purpose for it does not allow distinction between "cigars" and "saucers".

*The results of Case 0424 are not presented (see Vol. II, p. 886).

[†]Although an error in ϕ_{1j1} appears equally plausible, little effect on the predictions can be achieved by adjusting C_1 . Of course this does not rule out the possibility of a different kind of model having a marked effect.

5. CONCLUDING REMARKS

The study suggests the following conclusions:

- The ASM is decisively superior to the BVM in capturing the effects of streamline curvature (Cases 0232, 0233, 0331).
- The ASM does not infallibly mimic the stress transport processes (Cases 0111, 0381/2, 0375). Although the basic algebraic-stress hypothesis can be improved, an increasing use of RSTM for complex flows can only be advocated.
- The ϵ -equation remains a weak point of all models. The current form produces too large near-wall length scales near separation; for boundary layers in adverse pressure gradients, it is probably safest to prevent L exceeding 2.5 times the distance from the wall. There seem some advantages to using the modified ϵ source advocated herein. For simple shearing, it gives negligibly different behavior than the conventional form, but in flows with strong streamline curvature (0421) or axial stretching (0375), its use appears beneficial.
- Concerning numerics, approximations of convection, such as skew differencing used here (or quadratic upwind employed by Prof. Humphrey), allow numerical diffusion in elliptic flows to be reduced to levels where, even with fairly coarse meshes, the computed mean-velocity field seems principally to reflect the workings of the turbulence model employed.

Acknowledgments

The computations at UC Davis have been strongly supported by the NASA Ames Research Center through Research Grant NSG 2256 and by the personal assistance of J. Marvin and the staff of the Experimental Fluid Mechanics Branch at NASA-Ames. At UMIST some of the work has been supported by the US Office of Naval Research through Grant N00014-80-G-0130 and the SERC through Grant GR/B/33778. We express our sincere thanks to these agencies for their assistance.

References

- Chieng, C. C., and B. E. Launder (1980). Numer. Heat Transfer, 3, 189.
- Gibson, M. M., and B. E. Launder (1976). Trans. ASME, J. Heat Transfer, 98C, 81.
- Gibson, M. M., and B. E. Launder (1978). J. Fluid Mech., 86, 491.
- Hanjalić, K., and B. E. Launder (1972). J. Fluid Mech., 72, 609.
- Launder, B. E. (1982). AIAA Jou., 20, 436.
- Launder, B. E., G. R. Reece, and W. Rodi (1975). J. Fluid Mech., 68, 537.
- Rodi, W. (1972). Ph.D. Thesis, Faculty of Engineering, University of London.
- Samaraweera, D. S. A. (1978). Ph.D. Thesis, Faculty of Engineering, University of London.

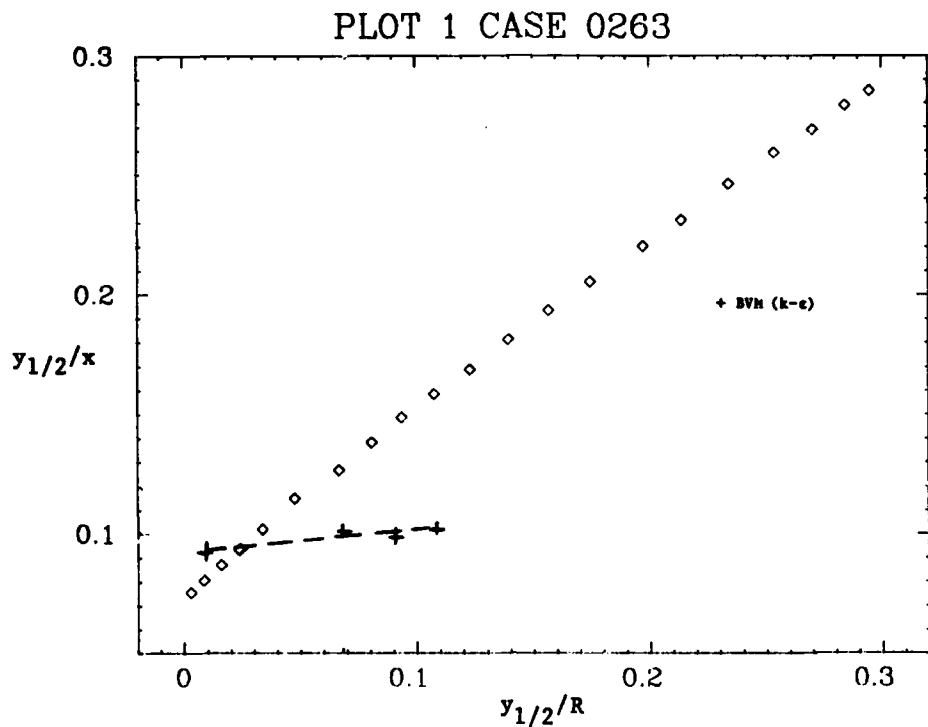


Figure 2. Self-preserving wall jet on a logarithmic spiral.

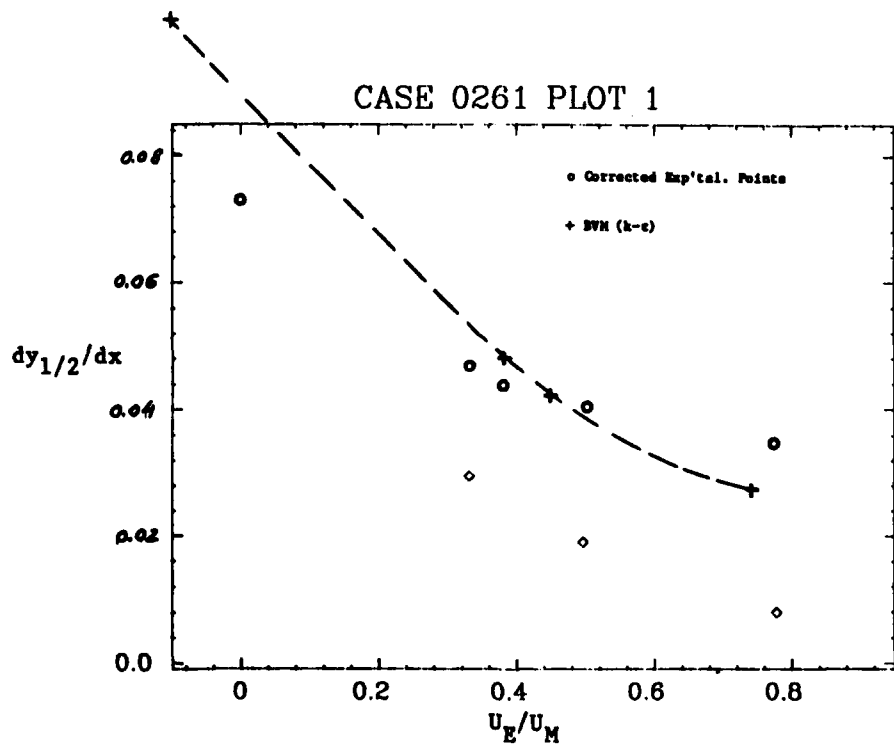


Figure 3. The equilibrium wall jet in an adverse pressure gradient.

CASE 0261 PLOT 3

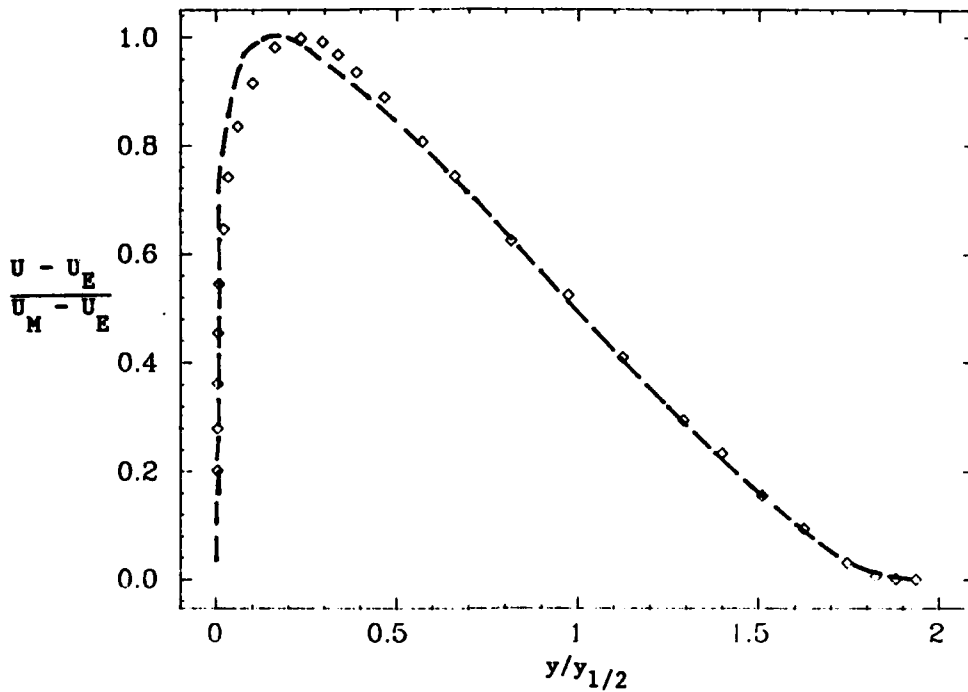


Figure 4.

CASE 0261 PLOT 4

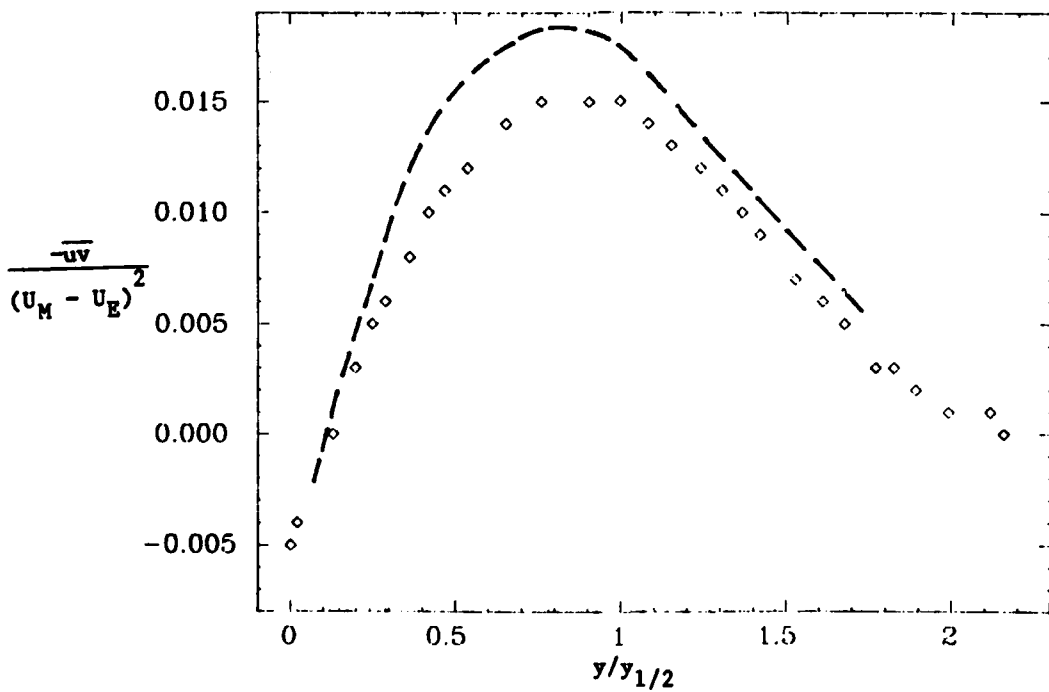


Figure 5.

CASE 0261 PLOT 5

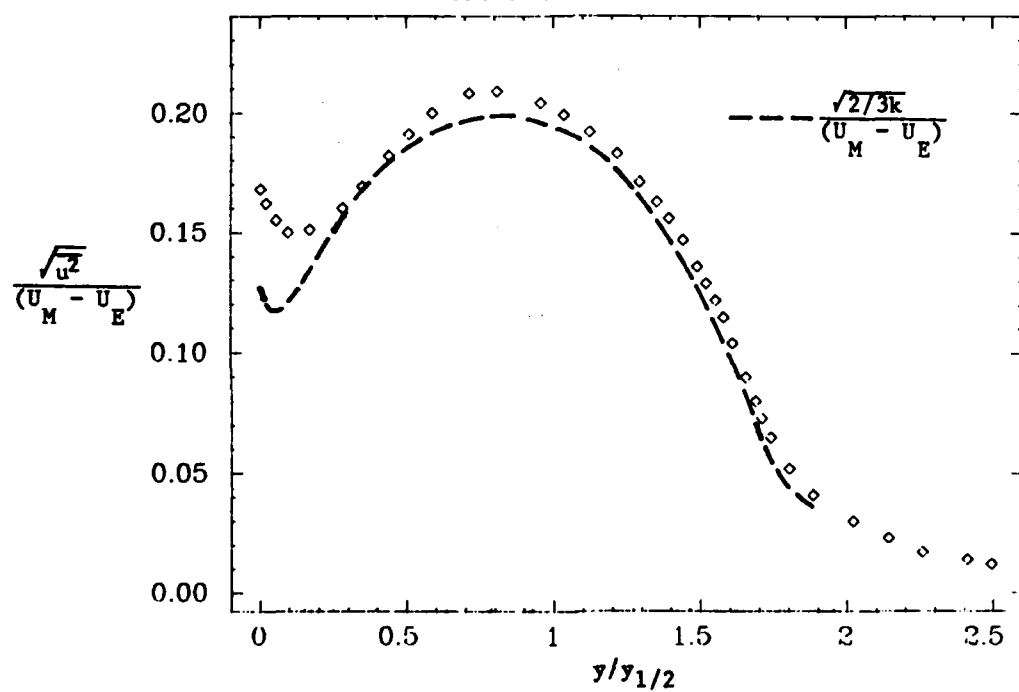


Figure 6.



COMPARISON OF COMPUTATION WITH EXPERIMENT

Summary Report

by

J. P. Bonnet *†

Computer Group Number: 17⁴

Case 8501

The turbulence model used is a second-order closure model directly derived from the "invariant modeling closure" proposed by C. duP. Donaldson (see Varma et al., 1974). Transport equations are written for the quantities U , T , u'^2 , v'^2 , w'^2 , $\overline{u'v'}$, T'^2 , $\overline{T'u'}$, $\overline{T'v'}$ using conventional averages. Some modifications to the model of Varma et al. (1974) have been introduced and are described in Bonnet and Alziary de Roquefort (1977); this model uses a macro-scale Λ defined in this flow as $\Lambda = C_\Lambda \delta$, where $\delta = |y(u_1) - y(u_2)|$ with $u_1 = \sqrt{0.9} u_e$ and $u_2 = \sqrt{0.1} u_e$ (u_e is the supersonic external stream velocity). The dissipation terms are modeled by:

$$\overline{\partial u'_i / \partial x_k \cdot \partial u'_j / \partial x_k} = \delta_{ij} \overline{u'_i u'_i} / \Lambda^2;$$

when the Reynolds number is large, $\Lambda^2 = 2\Lambda/bk$ with $b = 0.125$ and $k = \overline{u'_i u'_i} / 2$. All other closure models follow Donaldson's proposals, except the pressure-strain,

$$P'(\overline{\partial u'_j / \partial x_j} + \overline{\partial u'_j / \partial x_i}) = \phi_{ij,1} + \phi_{ij,2}$$

which is expressed using the following simplified form:

$$\phi_{ij,1} = -C_1 \rho q / \Lambda (\overline{u'_i u'_j} - 2/3 \delta_{ij} k)$$

$$\phi_{ij,2} = -C_2 (P_{ij} - 2/3 \delta_{ij} P)$$

with

$$P_{ij} = -(\overline{u'_i u'_k} \partial \overline{U} / \partial x_k + \overline{u'_j u'_k} \partial \overline{U} / \partial x_k) \text{ and } q^2 = \overline{u'_i u'_i}$$

The equations are integrated by a second-order implicit finite-difference method. The domain is covered by a grid equally spaced in the x- and y-directions; we use 100 mesh points for the initial profiles in y. Discretization of the x derivatives is

* Centre d'Etudes Aérodynamiques et Thermiques, Université de Poitiers, 43 rue de l'Aéronome, 86000 Poitiers, France

† This contribution appears with the Group 17 entries because the work was undertaken by Dr. Bonnet during a period of study leave with Prof. Launder's group at UMIST. It must be emphasized, however, that both the turbulence model and the numerical method are different from those used by the other Group 17 contributors. It appears, as do the other Group 17 contributors, alphabetically under "Launder".

made with second-order, three-point upwind differences. Nonlinearity and coupling of the equations is handled by a Gauss-Seidel iterative scheme at each x step, keeping only one variable as unknown in each equation. A typical running time on CDC 7600 is 0.3 sec per x step for 100 points in y-direction. Convergence is obtained here for a ratio of $u_{e1}/u_{e2} = 0.01$; this ratio seems to not affect the spreading rate (see Rodi, 1975).

As a first step the code has been checked for the incompressible case in order to adjust essentially the constant C_A , using initial profiles given in the review by Rodi (1975). With $C_A = 0.35$ we obtain the correct spreading rate defined as $d\delta/dx$ with $C_1 = 0.575$ and $C_2 = 0.48$. Supersonic flows were then tested with the same version, using as starting profiles for mean and turbulent velocities the experimental results of Lau et al. (1979). The result is a decrease of $d\delta/dx$ when the external Mach number increases, but the evolution is very small compared with the "Langley consensus" data and is essentially the behavior obtained by several authors taking into account only the mean density gradients. This result is also identical to the calculations of Donaldson (see Varma et al., 1974) and is plotted in Plate 151.

The complete form of the Poisson equation for the pressure in steady compressible, two-dimensional thin-shear flows suggests that compressibility affects mainly $\phi_{ij,1}$, via the term:

$$\phi_{ij,1}^C = \frac{1}{4\pi} \int_{\text{vol}} \frac{2(\bar{U}_j)' (\partial^2 \rho' u_i' / \partial x_i \partial x_j)' (\partial u_i' / \partial x_j + \partial u_j' / \partial x_i)}{|\vec{r}|} d \text{vol}$$

In many supersonic flows, two assumptions are generally verified; first, at relatively low Mach numbers ($\text{Mach} \leq 4$ is a value generally adopted as suggested by Kistler, 1959), the pressure fluctuations are small compared to density or temperature: $p'/\bar{p} \ll \rho'/\bar{\rho}$ or T'/\bar{T} , then we can write $\rho'/\bar{\rho} = -T'/\bar{T}$. Secondly, the temperature fluctuations are related to velocity fluctuations, providing there is negligible total-temperature mean gradients and fluctuations (the "Strong Reynolds Analogy", after Morkovin, 1962). This leads to: $T'/\bar{T} = (\gamma - 1)M^2 u'/\bar{U}$ where M is the local mean Mach number and γ the ratio of specific heats. With these two assumptions, we propose the following modification for $\phi_{ij,1} + \phi_{ij,1}^C = \phi_{ij,1}^*$ where,

$$(A) \quad \phi_{ij,1}^* = -C_1 (1 + C_A (\gamma - 1)M^2) \rho q / \Lambda (\overline{u_i' u_j'} - 2/3 \delta_{ij} k)$$

In order to take into account only the high level of the fluctuating Mach number which seems to be one of the most important features of the flows under consideration, we propose an alternative form, purely empirically derived from the form (A):

$$(B) \quad \phi_{ij,1}^* = -C_1 (1 + C_B \overline{u'^2/a^2}) \rho q / \Lambda (\overline{u_i' u_j'} - 2/3 \delta_{ij} k)$$

where a is the local speed of sound.

The use of forms (A) or (B) leads, with $C_A = 1$ or $C_B = 8$, to a rapid decrease of the spreading rate. Form (B) gives slightly better agreement with the data points than (A) but the two calculated spreading rates are very close together. Plate 151 shows the predictions up to Mach number 7, which is the upper limit for the convergence of the model B in its present version. The great sensitivity of the mixing layer to the flow Mach number seems to be well represented either by including a mean Mach number effect, or, better, by including a fluctuating Mach number effect in the first part of the pressure-strain correlation model.

Acknowledgments

This work has been supported by the Royal Society and the French Centre National de la Recherche Scientifique during an European Exchange Program at the Department of Mechanical Engineering of UMIST. We are indebted to Mr. Jordan McInnes for stimulating research discussions and technical assistance.

References

- Bonnet, J. P., and T. Alziary de Roquefort (1977). 1st Symposium on Turbulent Shear Flows, Penn. State University.
- Kistler, A. (1959). Phys. Fluids, 2, 290.
- Lau, J. C., P. J. Morris, and M. J. Fischer (1979). J. Fluid Mech., 93, 1.
- Morkovin, M. V. (1962). In Mécanique de la Turbulence, CNRS (eds.), p. 363.
- Rodi, W. (1975). In Studies in Convection, B. E. Launder (ed.). Academic Press, New York.
- Varma, A. K., R. A. Beddini, R. D. Sullivan, and C. duP. Donaldson (1974). AIAA Paper No. 74-592.

COMPARISON OF COMPUTATION WITH EXPERIMENT

Summary Report

by

J. C. Le Balleur*

Computer Group Number: 42



Cases 0441, 8621, 8623, 8631, 8691

1. GENERAL OUTLINES

The computations performed for the 1980-81 Stanford Conference are based on a viscid-inviscid splitting method, with fully overlaying viscous and inviscid calculation fields.

The inviscid flow has interacting boundary conditions and is presently solved within potential flow assumptions, using relaxation codes. The viscous calculation estimates locally the difference (so-called "defect") between the fictitious inviscid flow and the real flow; it has been reduced to integral equations along the inviscid boundary, through approximations on computing the defect pressure, and through a modeling of the defect velocity profiles given by Le Balleur (1981).

The viscous-defect calculation is then an extension of a boundary-layer integral method, with a capability of computing separated boundary layers or wake flows. Roughly, a single integral method with entrainment closure, interacted with several inviscid codes, has been used to calculate Cases 0441, 8621, 8623, 8631, and 8691. The coupling with the inviscid codes is solved with the same relaxation technique, either "direct" or "semi-inverse", according to whether the boundary layers or wakes are locally attached or separated (see Le Balleur, 1981, and Le Balleur et al., 1980). The switch between the two techniques relies on the shape parameter of the viscous-defect velocity profile, and allows us to use an inverse solution of the viscous equations along the separated-flow regions.

The turbulent entrainment closure is calculated both from the shape parameter of the mean-velocity profile, and from two lag-equations for a non-equilibrium modeling of the kinetic energy and Reynolds-stress levels inside the outer part of the layer. (The method is described as SG42 herein.)

Both improvements of the inviscid calculation, through a solution of the full Euler equations, and improvements of the turbulent integral closure are believed to be possible in the future with the present computational method.

*Aerodynamics Department, ONERA, 92320 Chatillon-sous-Bagneux, France

2. SUMMARY OF EQUATIONS

2.1 Inviscid Part of the Calculations

Cases 0441, 8621, 8623: Full potential equation (conservative scheme).

Case 8631: Prandtl-Meyer relation

Case 8691: Transonic small perturbations to the potential equation (conservative scheme).

The approximations involved in the last two calculations are believed to be restrictive and to be a limitation for the overall viscous-inviscid prediction.

2.2 Viscous Part of the Calculations (see Le Balleur, 1981)

Let us denote by x, o, y the curvilinear intrinsic coordinates measured along the wall or the wake centerline (minimal velocity line), (u, v, P, ρ, h_1) and $(\bar{u}, \bar{v}, \bar{P}, \bar{\rho}, \bar{h}_1)$ being respectively the inviscid and viscous unknowns for the mass-averaged velocity components, pressure, averaged density, and total enthalpy, respectively. If τ is the apparent shear stress and $K^*(x)$ an appropriate y -averaged curvature of the viscous streamlines, the thin-layer time-averaged Navier-Stokes equations are approximated in the following way:

$$\left\{ \begin{array}{l} \frac{\partial(\rho u - \bar{\rho} u)}{\partial x} + \frac{\partial(\rho v - \bar{\rho} v)}{\partial y} = 0 \\ \frac{\partial(\rho u^2 - \bar{\rho} u^2)}{\partial x} + \frac{\partial(\rho u v - \bar{\rho} u v)}{\partial y} = -\frac{\partial(P - \bar{P})}{\partial x} - \frac{\partial \tau}{\partial y} \\ \frac{\partial(P - \bar{P})}{\partial y} = 0 \\ \frac{\partial(h_1 - \bar{h}_1)}{\partial y} = 0 \end{array} \right. \quad \text{First order: compute } \left\{ \begin{array}{l} \bar{\rho}, \bar{u}, \bar{v} \\ \rho, u, v, P \end{array} \right. \quad (1)$$

$$\left. \begin{array}{l} -K^*(x) [\rho u^2 - \bar{\rho} u^2] = -\frac{\partial(P - \bar{P})}{\partial y} \end{array} \right\} \quad \text{Second order: compute } \bar{P}$$

Integral form:

$$\left\{ \begin{array}{l} \left[\frac{d\delta^*}{dx} + \frac{\delta^*}{\rho q} \frac{\partial \rho q}{\partial x} - \frac{\rho v}{\rho q} + \frac{\bar{\rho} v}{\rho q} \right]_{(x,0)} = 0 \\ \left[\frac{d\theta}{dx} + \frac{\delta^* + 2\theta}{q} \frac{\partial q}{\partial x} + \frac{\theta}{\rho} \frac{\partial \rho}{\partial x} - \frac{\bar{\rho} v}{\rho q} \left(1 - \frac{\bar{u}}{q}\right) \right]_{(x,0)} = \frac{C_f}{2} \end{array} \right. \quad \text{First order} \quad (2)$$

$$\left\{ \begin{array}{l} \bar{P}(x, y) = P(x, y) \\ \bar{h}_1(x, y) = h_1(x, y) \\ [P - \bar{P}]_{(x,0)} = -K^*(x) [\delta^* + \theta] [\rho q^2]_{(x,0)} \end{array} \right. \quad \text{Second order}$$

where integral thicknesses are generalized as:

$$\left\{ \begin{array}{l} \delta^*(x) [\rho q]_{(x,0)} = \int_0^{\infty} [\rho u_{(x,y)} - \overline{\rho u}_{(x,y)}] dy \\ [\delta^*(x) + \theta(x)] [\rho q^2]_{(x,0)} = \int_0^{\infty} [\rho u^2_{(x,y)} - \overline{\rho u^2}_{(x,y)}] dy \\ q^2 = u^2 + v^2 \end{array} \right. \quad (3)$$

The previous first-order continuity and x-momentum integral equations are closed with the entrainment equation at the outer edge $y = \delta(x)$ of the layer:

$$\left[\frac{d(\delta - \delta^*)}{dx} + \frac{\delta - \delta^*}{\rho q} \frac{\partial \rho q}{\partial x} - \frac{\overline{\rho v}}{\rho q} \right]_{(x,0)} = \frac{d\delta}{dx} - \left[\frac{\rho v}{\rho u} \right]_{(x,\delta)} = E \quad (4)$$

which is equivalent to the local x-momentum equation at $y = \delta(x)$ if the entrainment rate E is defined as:

$$E = \left\{ \frac{\partial \tau / \partial y}{\rho u [\partial(u - \bar{u}) / \partial y]} \right\}_{(x,\delta)} \quad (5)$$

The final closure of the integral method given by Eqs. 2 and 4 is detailed in Le Balleur (1981). A modeling of the defect-velocity profiles is achieved through an analytical expression with wall and wake components, including separated-flow profiles:

$$\frac{\bar{u}(x,y)}{u(x,y)} = 1 + C_1(x) \log\left[\frac{y}{\delta(x)}\right] - C_2(x) F\left[\frac{y}{\delta(x)}, C_1(x), C_2(x)\right] \quad (6)$$

The wall coefficient C_1 is related to the calculated unknown C_2 in order to match the usual law-of-the-wall, and provides the skin friction. The modeling of the equilibrium entrainment rate $E_{eq}(C_1, C_2)$ (see Le Balleur, 1981), is very similar to what may be deduced from Eqs. 5 and 6 with a mixing-length closure. The final nonequilibrium entrainment rate is deduced from additional lag-equations for y-averaged estimates of the turbulent kinetic energy $k(x)$ and of the Reynolds stresses $\tau(x)$ across the outer part of the layer. The departure from equilibrium values $E_{eq}(x)$, $k_{eq}(x)$, $\tau_{eq}(x)$, is calculated from approximate transport equations:

$$\left\{ \begin{array}{l} \frac{Dk}{Dt} = \frac{1}{l} \left[\frac{\tau}{\tau_{eq}} \left(\frac{k}{k_{eq}} \right)^{1/2} k_{eq} - k \right] \\ \frac{D\tau}{Dt} = \frac{1.5}{l} \left[\left(\frac{k}{k_{eq}} \right)^{1/2} \tau_{eq} - \tau \right] \\ E = \frac{\tau}{\tau_{eq}} E_{eq} \end{array} \right. \quad (7)$$

where E_{eq} , k_{eq} , τ_{eq} are deduced from the velocity profile, the length scale l being also dependent on $k(x)$, $\delta(x)$ (see Le Balleur, 1981).

The asymmetrical wakes are computed by solving Eqs. 2, 4, 6, and 7, both for the upper and lower parts, prescribing the continuity of $\bar{v}(x,0)$, $\bar{u}(x,0)$ across the centerline, and vanishing $C_f(x)$ and $C_l(x)$. The centerline geometry is calculated during the coupling with the interacting inviscid flow.

3. SUMMARY OF COMPUTING CASES

3.1 Case 8621: Transonic Airfoil RAE 2822

Calculation of category II: viscous-inviscid interaction

Inviscid: full potential equation-conservative scheme-relaxation code (factorization, 181×27 grid)

Viscous: laminar + turbulent boundary layers + turbulent asymmetrical wake:

- transition prescribed (continuous θ thickness)
- wake-geometry calculated
- integral method:

}	continuity eq.
	x-momentum eq.
	entrainment eq.
	+ 2 lag-equations ($k - \tau$)
- displacement and curvature effects of the wake
- no special treatment at shock-waves.

Comments: No careful adjustments of Mach number or angle of attack have been performed, but only:

- free-air calculations at the experimental Mach number,
- first runs with the given corrections for the angle of attack,
- a few additional runs with new angles of attack and slightly improved lift predictions (see Table I).

3.2 Case 8623: Transonic Airfoil DSMA 523S

Computing conditions are the same as used for Case 8621 (free-air calculations). They involve no trial for Mach number correction and only corrections for the angle of attack.

Comments:

- fully converged viscid-inviscid solutions are achieved for case 1 (see Plate 166).
- no-convergence for the full viscid-inviscid interaction was possible at the selected flow conditions (Table II) for case 2 or case 3, probably because of an inappropriate mesh resolution of the shock-wave/boundary-layer interaction, or because of a need for Mach number corrections in order to avoid shock-separation.

- However, during the iterations, before the shock-wave will reach an excessively rear position and induce divergence, a valuable estimate of the viscous field including a small bubble on the lower surface may be noticed (Plates 166, 167 and 168), and is roughly in agreement with experiment.

3.3 Case 0441: Stalled Airfoil

Calculation with viscous-inviscid interaction.

- Inviscid: - full potential equation (same as Case 8621)
 - free-air calculation

Viscous: laminar + turbulence boundary layers + turbulent asymmetrical wake:

- transition prescribed (continuous θ thickness)
- wake-geometry calculated
- simplified integral method:

}	continuity eq.
	x-momentum eq.
	entrainment eq.
	equilibrium entrainment closure
- no curvature effect of the wake.

Comments: The selected angle of attack corresponds approximately to the maximum lift prediction (Table III) from the present method (free-air calculation). Fully stalled configurations are not yet allowed from the numerical technique, the selected conditions being at the upper limit for convergence of the present code. For this reason, the influence of wake curvature effects and of non-equilibrium turbulent modeling have not yet been involved.

3.4 Case 8631: Supersonic Ramp

Calculations with viscous-inviscid interaction

Inviscid: potential single-wave approximation (Prandtl-Meyer relation)

- Viscous: integral method:

}	continuity eq.
	x-momentum eq.
	entrainment eq.
	+ 2 lag-equations ($k - \tau$)

The plotted pressure is the viscous pressure, including a "viscous-curvature correction," to the first-order inviscid pressure on the wall. Although second-order, this correction is found to be important (rotational normal pressure gradient).

Comments:

- The Prandtl-Meyer approximation is believed to be a limitation and needs to be changed in the future into an Euler solution.
- A very fine mesh size has been used at the beginning of interaction to eliminate numerical viscosity: $\Delta x = 0.00125$ ($\delta > 10\Delta x$)

- A high sensitivity to the shape parameter of the initial boundary layer has been noticed. More precision on the initial displacement and momentum thicknesses data would be needed.
- In these conditions, a plot of the computed separated length versus Reynolds number at incipient separation ($\theta = 20^\circ$) is not believed to be representative.

3.5 Case 8691: Transonic Shock/Boundary Layer Interaction

Calculations with viscous-inviscid interaction.

Inviscid: potential transonic small-disturbance equation - conservative scheme - relaxation code (SLOR) - symmetrical free-air calculation (Mach = 0.785)

Viscous: integral method: { continuity eq.
 x-momentum eq.
 entrainment eq.
 + 2 lag-equations ($k - \tau$)

Turbulent from leading edge (Reynolds = 10^7 on chord)

Comments:

Transonic small perturbation approximation was used because the available full-potential solvers fail to converge with the fine mesh size required to solve the viscous interaction near the shock-wave. Presently, the local mesh size was approximately such that $\delta > 3 \Delta x$.

References

- Le Balleur, J. C. (1981). "Strong matching method for computing transonic viscous flows including wakes and separation--Lifting Airfoils," La Recherche Aérospatiale, No. 1981-3, pp. 21-45.
- Le Balleur, J. C., R. Peyret, and H. Viviani (1980). "Numerical studies in high Reynolds number aerodynamics," Computers and Fluids, 8:1, 1-30.

Table I. Case 8621 - Category II: Viscid-Inviscid Interaction

RAE 2822 Case	Run	M_∞	α°	R_c	x_t/C	C_L	C_D	C_M	C_D Frict.	C_D Press.	C_D Wake
01	002	0.676	1.93	$5.7 \times 10^{+6}$	0.11	0.566	0.0092	-0.080	0.0056	0.0036	0.0098
06	002	0.725	2.54	$6.5 \times 10^{+6}$	0.03	0.737	0.0136	-0.085	0.0057	0.0079	0.0112
	003	0.725	2.60	$6.5 \times 10^{+6}$	0.03	0.746	0.0137	-0.083	0.0057	0.0080	0.0446
07	002	0.725	2.21	$6.5 \times 10^{+6}$	0.03	0.678	0.0124	-0.085	0.0058	0.0066	0.0109
09	002	0.730	2.79	$6.5 \times 10^{+6}$	0.03	0.787	0.0166	-0.086	0.0055	0.0111	0.0128
	003	0.730	2.85	$6.5 \times 10^{+6}$	0.03	0.800	0.0174	-0.087	0.0055	0.0119	0.0131
12	002	0.730	2.93	$2.7 \times 10^{+6}$	0.03	0.763	0.0168	-0.077	0.0063	0.0105	0.0146
	003	0.730	2.73	$2.7 \times 10^{+6}$	0.03	0.727	0.0162	-0.077	0.0062	0.0100	0.0143

Table II. Case 8623 - Category II: Viscid-Inviscid Interaction

DSMA Case	Run	M_∞	α°	R_c	x_t/C	C_L	C_D	C_M	C_D Frict.	C_D Press.	C_D Wake
01	002	0.600	2.20	$4 \times 10^{+6}$	0.05 0.18	0.732	0.0118	-0.120	0.0059	0.0059	0.0117
02	002	0.800	1.15	$2 \times 10^{+6}$	0.35 0.18				No convergence for viscid-inviscid interaction with these conditions		
03	002	0.800	2.00	$3 \times 10^{+6}$	0.35 0.18				No convergence for viscid-inviscid interaction with these conditions		

Table III. Case 0441 - Two-Dimensional Stalled Airfoil (Free-Air Calculation)

	Run	M_∞	α°	R_c	x_t/C	C_L	C_D	C_M	C_D Frict.	C_D Press.	C_D Wake
NACA 4412 Airfoil	002	0.0778	13.60	$1.5 \times 10^{+6}$	0.025 0.103	1.563	0.0369	-0.056	0.0069	0.0300	0.0368



N.N. Mansour

Cases 0331, 0421

COMPARISON OF COMPUTATION WITH EXPERIMENT

Summary Report

(Computations for a Curved Shear Layer and a Backward-Facing Step Using a k-ε Turbulence Model Comparison)

by

N. N. Mansour* and T. Morel†

Computer Group Number: 02

INTRODUCTION

This summary documents the governing equations and the numerical procedure used to simulate the backward-facing step, Case 0331, and the curved shear layer, Case 0421, entry cases to the Conference. It also includes the boundary conditions used for each case and a summary of checks performed on the code.

The computer code used in these calculations is a derivative of a code MINT developed by Gibeling et al. (1975). It is a Navier-Stokes code for time-dependent three-dimensional compressible flows. The finite-difference scheme utilized has a standard (non-staggered) mesh, central differencing in space, and implicit differencing in time. The resulting difference equations are solved by an alternating direction implicit (ADI) operator splitting in space, and by a non-iterative scheme in time.

GOVERNING EQUATIONS

The equations (in Cartesian tensor notation) governing the statistical properties of the flow are modeled as follows:‡

Continuity

$$\rho_{,t} + (\rho u_j)_{,j} = 0$$

Momentum

$$(\rho u_i)_{,t} + (\rho u_j u_i)_{,j} = -p_{,i} + \tau_{ij,j}$$

where

$$\tau_{ij} = 2(\mu + \mu_T)S_{ij} - \frac{2}{3}(\mu + \mu_T)S_{kk}\delta_{ij} - \frac{2}{3}\rho k\delta_{ij}$$

*General Motors Research Labs. Current address: NASA-Ames Research Center, Moffett Field, CA 94035

†General Motors Research Labs. Current address: Science and Tech. Labs, International Harvester, Hinsdale, IL 60521

‡Mass-weighted (Favre) time-averaging as described in the questionnaire is used. The symbols describing the averaging are dropped for simplicity.

$$S_{ij} = \frac{1}{2}(u_{i,j} + u_{j,i})$$

$$\mu_T = C_\mu \rho k^2 / \epsilon$$

Energy

$$(\rho H)_{,t} + (\rho u_j H)_{,j} = p_{,t} + \phi_{j,j} + u_j p_{,j} + D$$

$$\phi_j = ((\mu + \mu_T) / \sigma_h) H_{,j}$$

$$D = 2\mu S_{ij} S_{ij} - \frac{2}{3} \mu S_{kk}^2 + \rho \epsilon$$

The turbulence kinetic energy (k) and its dissipation rate (ϵ) are computed from the following modeled equations:

k-Equation

$$(\rho k)_{,t} + \frac{1}{2}((\rho u_j k)_{,j} + \rho u_j k_{,j} + k(\rho u_j)_{,j}) = P_k - \rho \epsilon + \left(\frac{\mu_T}{\sigma_k} k_{,j}\right)_{,j}$$

where

$$P_k = 2\mu_T S_{ij} S_{ij} - \frac{2}{3} \mu_T S_{kk}^2 - \frac{2}{3} \rho k S_{kk}$$

ϵ -Equation

$$(\rho \epsilon)_{,t} + \frac{1}{2}((\rho u_j \epsilon)_{,j} + \rho u_j \epsilon_{,j} + \epsilon(\rho u_j)_{,j}) = P_\epsilon - C_2 \frac{\rho \epsilon^2}{k} + \left(\frac{\mu_T}{\sigma_\epsilon} \epsilon_{,j}\right)_{,j}$$

where

$$P_\epsilon = \frac{\epsilon}{k} (C_1' 2\mu_T S_{ij} S_{ij} - C_1' \frac{2}{3} \mu_T S_{kk}^2 - C_1'' \frac{2}{3} \rho k S_{kk})$$

Model Constants

Standard values for the turbulence model constants were used:

$$C_\mu = 0.09 ; C_1 = 1.44 ; C_2 = 1.92 ; \sigma_h = 0.9 ; \sigma_k = 1.0 ; \sigma_\epsilon = 1.3$$

The additional constants C_1' and C_1'' are used only for compressible flows.

The k(ϵ) equation is written in a form that will conserve numerically the integrals of k(ϵ) and $1/2 k^2 (1/2 \epsilon^2)$. If the time derivative is treated as exact and the right-hand side of the equation is set equal to zero, it can be shown by integration (summation) by parts that both the integral of k(ϵ) and $1/2 k^2 (1/2 \epsilon^2)$ over the computational volume are constant with time. The conservation of these integrals is known, as shown in Mansour et al. (1977), to improve the numerical stability of the differenced equations and was found advantageous in some cases.

AD-A136 034

THE 1980-81 AFOSR (AIR FORCE OFFICE OF SCIENTIFIC
RESEARCH)-HTTM (HEAT TR. (U) STANFORD UNIV CA DEPT OF
MECHANICAL ENGINEERING. S J KLINE ET AL. SEP 81

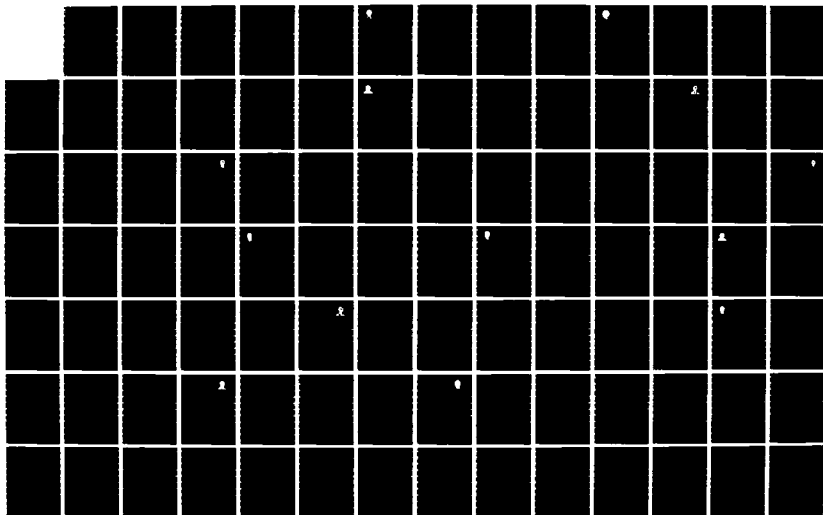
5/6

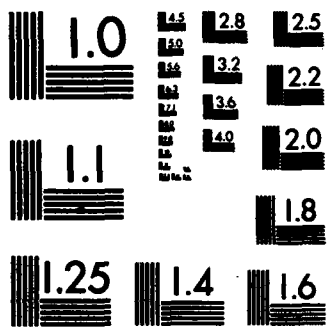
UNCLASSIFIED

AFOSR-TR-83-1003 F49620-80-C-0027

F/G 20/4

NL





MICROCOPY RESOLUTION TEST CHART
NATIONAL BUREAU OF STANDARDS-1963-A

NUMERICAL METHOD

Time-Differencing

The governing equations are finite differenced using backward differencing (fully implicit) in time on all terms except those containing cross-derivatives in space. Terms with cross-derivatives are treated explicitly. The differenced equations are then linearized in time using the technique described in Briley and McDonald (1977). The set of linearized equations is then split in space using the Douglas-Gunn (1964) technique to generate an ADI scheme.

Spatial Differencing

An analytical coordinate transformation is used to distribute the grid in the computational domain. If x is the original coordinate, the transformation is of the form

$$\begin{aligned}ax + b &= \sinh(c\xi + d) \\e\eta + f &= \tanh(g\xi + h)\end{aligned}$$

where η is an equally spaced computational coordinate and a, b, c, \dots are constants. Such a transformation provides grid packing at the boundary of the domain (hyperbolic tangent) and at a region inside the domain (hyperbolic sine). Central differencing is used to evaluate derivatives in the transformed domain.

Boundary Conditions

Near-Wall Submodels at Solid-Walls. At solid-wall boundaries, near-wall submodels were employed to bridge the gap between the wall and the first grid point away from the wall. The same set of submodels was used for all solid walls.

Velocity. The normal-velocity component was set to zero at the wall. The velocity components parallel to the wall were found from the law-of-the-wall applied at the first point away from the wall.

k and ϵ . $\partial k / \partial n = 0$ was used for the k -equation, where n is the direction normal to the wall. The dissipation equation at the first point away from the wall (point 2) was replaced by

$$\epsilon_2 = C_\mu^{3/4} k_2^{3/2} / \ell_2$$

where the dissipation length scale ℓ_2 was obtained by interpolation, assuming that ℓ varies linearly between its value on the wall ($\ell_1 = 0$) and the value at the second grid point away from the wall ($\ell_3 = C_\mu^{3/4} k_3^{3/2} / \epsilon_3$).

H and ρ . Fixed wall temperature $T = T_{ref}$ ($= 300^\circ\text{K}$) was used for the energy equation. The boundary condition for the continuity equation was $\partial(p + 2/3\rho k) / \partial n$ calculated from the momentum equation for the normal-velocity component (at the wall).

Boundary Conditions on Open Boundaries

Exit. At exit openings, the extrapolated boundary condition $\partial/\partial n = 0$ was used on u , v , H , k , and ϵ . A prescribed static pressure ($P_{\text{ambient}} - 2/3\rho k$) along the boundary was used as the boundary condition on the continuity equation.

Inlet. The boundary condition used at an inlet boundary depended on the test case to be simulated.

Case 0421.* Profiles of u and k were obtained from the measured data at the $x = 0$ station. The cross-stream velocity v was set to zero. The dissipation length scale was set to be constant in the bulk of the flow, at $l_c = (0.04)2H$ (where $2H$ is the width of the channel), and was dropped linearly to zero at the wall with a 0.3 slope. The extrapolative boundary condition $\partial(p + 2/3\rho k)/\partial y = 0$ was used as a boundary condition for the continuity equation.

Case 0331.* Profiles of u , v , and k were obtained from the measured profiles at the $\theta = 0^\circ$ station. The dissipation length scale was set to $l_c = 0.00287$ m. $\partial(p + 2/3\rho k)/\partial y = 0$ was used as a boundary condition for the continuity equation.

In the "still" air region, u (u_r in r, θ coordinates) was set to zero and v (u_θ) was obtained using the extrapolative condition $\partial v/\partial y = 0$. The total pressure ($P_0 = p + 2/3\rho k + 1/2\rho v^2$) was taken to be atmospheric. The inlet temperature was set at $T_{\text{ref}} = 300^\circ\text{K}$, the inlet k was set equal to $0.00035U_{\text{ref}}^2$, and the inlet dissipation length scale was set equal to $l_c = 0.00287$ m.

BACKWARD-FACING STEP, FLOW 0420

Case 0421. The numerical procedure was checked by simulating the laminar backward-facing step and comparing the reattachment length to the experimental results of Armaly et al. (1980). Figure 1 shows the reattachment length (defined to be the point where the axial velocity reverses sign) versus Reynolds number. These results suggest that the equations of motion are correctly implemented and that the numerical procedure is trustworthy in such a configuration.

A 39×30 grid layout was used to simulate Case 0421, with the inlet boundary at the dump plane and the length of the domain equal to $L/H = 20$. The simulation predicts a reattachment length equal to $X_R = 5.2$, 26% shorter than the one experimentally observed ($X_R = 7.0$). Several diagnostic runs were carried out, where the length of the simulation domain (L) between the inlet plane and exit plane was varied. The reattachment-length results were found to be independent of L/H . The number of grid points was also changed from 39×30 to 59×30 and to 39×58 . Neither of the changes affected the reattachment length. The inlet turbulence kinetic energy and the inlet dissipation length scale were also varied and found to not affect the

*The coordinate system is the same as indicated in the summary for the test flow case.

reattachment length. Finally, different near-wall submodels were used and in turn they were found to not affect the reattachment length. We are thus satisfied that the results reflect the performance of the present k - ϵ model for this test case. We note that in a simulation of the axisymmetric sudden-expansion case of Chaturvedi (1963), which was not one of the test cases for this conference, this k - ϵ model yielded the correct reattachment length.

CURVED SHEAR LAYER, FLOW 0330

Case 0331. The numerical procedure for this test case was checked by simulating a laminar stagnation flow ($u = cx$, $v = -cy$). The numerical solution reproduced the exact solution. To check the implementation of the terms in the k - and ϵ -equations, a turbulent stagnation flow was simulated. In the ϵ -equation the model constant C_2 was set equal to C_1 ($= 1.44$). The inlet k -level was set to be constant ($= k_0$) and the inlet dissipation length scale was set to yield production equal to dissipation, i.e., $\epsilon = (2C_\mu)^{1/2} \sqrt{S_{ij} S_{ij}} k_0$. Under these conditions the turbulent viscosity throughout the flow field can be shown to be constant. This result was reproduced by the numerical solution.

The results presented at this Conference were obtained using a 50×50 grid layout. They were checked for grid sensitivity by running a 40×40 grid and a 61×59 grid test case. We found that the mean flow was independent of the grid but the turbulence intensity was slightly grid-dependent. Figure 2 shows the turbulence intensity for two grid systems, compared to the experimental data. Finally, the effect of bleed size on the results was investigated. It was found that (Fig. 3) changing the size of the bleed changes the location of the point where $U = 0.5 U_{ref}$. To match the experimental data for $U = 0.5 U_{ref}$, the bleed mass flow would have to be 38% less than the reported experimental value.

CONCLUDING REMARKS

In this short summary we have documented the equations and the numerical method used in simulating the curved-shear-layer and the backward-facing-step test cases. We have included the numerical checks made and our experiences with the code. We believe that the results are representative of the performance of the present k - ϵ model under these flow conditions. Briefly, this k - ϵ model will predict a too-short (with respect to experimental observation) reattachment length for the two-dimensional backward-facing step. In the case of the two-dimensional curved shear layer it predicts a too-large spreading of the shear layer (with respect to that observed experimentally) as it negotiates the curve.

REFERENCES

Arnaly, B. F., F. Durst, and B. Schönung (1980). "Measurements and predictions of flow downstream of a two-dimensional single backward facing step," SFB 80/ET/172, Sonderforschungsbereich 80, Universität Karlsruhe.

Briley, W. R., and H. McDonald (1977). "Solution of multidimensional compressible Navier-Stokes equations by a generalized implicit method," *J. Comp. Phys.*, 24:4, 372.

Chaturvedi, M. C. (1963). "Flow characteristics of axisymmetric expansion," *J. ASCE, Hydraulics Div.*, 89:HY3, 61.

Douglas, J., and J. E. Gunn (1964). "A general formulation of alternating direction methods," *Numerische Math.*, 6, 428.

Gibeling, H. J., H. McDonald, and W. R. Briley (1975). "Development of a three-dimensional combustor flow analysis, Vol. I: Theoretical studies," AFAPL Technical Report AFAPL-TR-75-59.

Mansour, N. N., P. Moin, W. C. Reynolds, and J. H. Ferziger (1979). "Improved methods for large-eddy simulations of turbulence," *Turbulent Shear Flows I*, F. Durst, B. E. Launder, F. W. Schmidt, and J. H. Whitelaw (eds.). Springer-Verlag, Berlin.

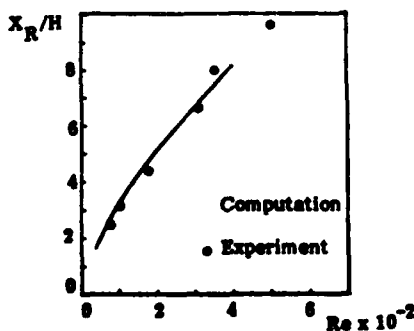


Figure 1. Laminar Flow: Comparison of experimental and numerical results for the reattachment length. $Re = U D/\nu$ where U = the average inlet velocity, D = hydraulic diameter of the inlet channel, and ν = the kinematic viscosity.

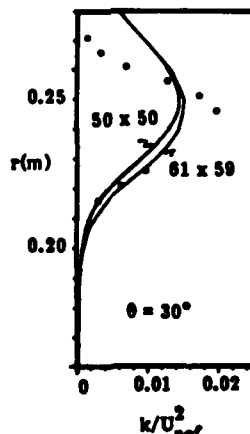


Figure 2. Sensitivity of the Computational Results to Number of Grid Points

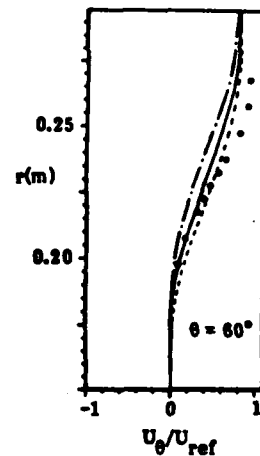


Figure 3. Sensitivity of the Computational Results to Bleed Size
 - - - $m = U_{ref} \times 0.043 \text{ m}$
 — $m = U_{ref} \times 0.035 \text{ m}$
 - · - $m = U_{ref} \times 0.025 \text{ m}$



COMPARISON OF COMPUTATION AND EXPERIMENT

Summary Report

by

H. McDonald*

Computer Group Number: 41

Cases 0441, 0512, 8601, 8641

Case 0441 (BIKX)

The time-averaged Navier Stokes equations were used. The computer code is available from NASA Langley Research Center. The governing equations are given in Shamroth and Gibelung (1980). The code does not include models for roughness effects.

The NACA 4412 airfoil calculation at 13.7° incidence was run with a body-fitted, nonorthogonal constructive mesh which placed coordinate lines on both the airfoil surface and the tunnel walls. The grid used was a "C"-type grid consisting of 141 pseudo-azimuthal grid points and 39 pseudo-radial grid points. The inner "C" loop fell upon the airfoil surface and the wake branch cut; the outer loop fell upon the tunnel walls and the upstream grid boundary. The grid was constructed so as to have continuous metric derivatives through the wake branch cut, thus allowing this line to be treated as a usual type interior line. The grid was highly stretched having very fine streamwise resolution in the leading-edge region so as to allow prediction of the very strong suction peak. At the leading edge the grid spacing was 0.002 chords. The normal (pseudo-radial) grid was also highly stretched so as to obtain grid points in the Heimez layer and the boundary-layer sublayer; the grid spacing at the airfoil surface being 10^{-5} chords. Although conceptually no difficulty would be encountered in resolving the tunnel-wall boundary layers, it was felt that the extra grid points which would be required could be better placed elsewhere and, therefore, slip conditions were placed at these boundaries.

In regard to the calculation itself, although second-order artificial dissipation was used to suppress spurious oscillations, several calculations were run at several artificial dissipation values until a value was resolved where the results became insensitive to further reduction. The calculation was run with total pressure specified at the upstream boundary and static pressure at the downstream boundary; these provide realistic boundary conditions. Finally, the predicted separation point, $x/c = 0.7$, was in good agreement with data.

*Scientific Research Associates, Inc., P. O. Box 498, Glastonbury, CT 06033

Some further details of the calculation are as follows:

- A. Case 0441 was begun from a converged solution at 7.8° incidence. This solution was obtained for the NACA 4412 airfoil immersed in a stream with tunnel walls present. Slip conditions were applied at the tunnel wall. In order to assess the flow development and to obtain a series of calculations, converged solutions were obtained at 10.8° , 12.3° , and 13.7° geometric incidence. Each solution was initiated from the previous converged solution. In general, approximately 120 time steps were required to obtain each solution; based upon previous experience, it is estimated that 150-180 time steps would be required to obtain the 13.7° solution from a "cold start."

Case 0512 (BIKX)

The time-averaged Navier-Stokes equations in fully general orthogonal coordinates were solved together with a $k-l$ turbulence model. The details of the equations used and the method are given in Buggeln et al. (1981). Some further details of the calculations are as follows:

1. The computational grid was chosen to provide resolution of the viscous sublayer region on all duct walls.
2. The coordinate system was constructed to fit both the 90° bend and straight sections both upstream and downstream of the bend. The inflow boundary was located 8.2 duct diameters upstream of the bend, and the axial velocity-profile shape was taken from interpolation of Melling's tabulated values supplied by the Conference. The outflow boundary was located 2.0 duct diameters downstream of the 90° location, to model correctly the elliptic character of this flow at the 90° measuring station.
3. There are very large radial velocities (40% of mean flow) in the region near the end wall within the bend; they terminate in the viscous sublayer. These large radial velocities are an important feature of this flow, but do not appear in the Conference contour plots since measurements were not taken near the end wall.
4. All velocities were normalized by the mean (bulk) velocity as determined by a second-order numerical integration of the computed solution. This calculation also indicated that global mass conservation was satisfied by the solution to within 0.5% at each axial location.

Case 8601 (BKEX)

The $k-\epsilon$ code used for this case is available from the U.S. Army Research Office. It was run with supersonic and subsonic boundary conditions as appropriate on inflow, and subsonic conditions on exit. The grid moved, sensing the shock and tracked it

with a nonuniform packed mesh to give good resolution in the region of the shock. The mesh was 41×31 . An initial uniform velocity field with an axial variation of static pressure was adopted. The inflow supersonic flow was held fixed together with the exit wall static pressure. The shock formed rapidly, was identified and located by the mesh, and the resulting boundary-layer interaction resolved. The transverse mesh resolved the boundary layer, including the viscous sublayer, and although dynamic mesh redistribution was also possible in the transverse direction, it was not necessary. Second-order artificial dissipation was added to keep the cell Reynolds number below 20 (a cell Reynolds number of 2 gives the same truncation error as first-order upwind differencing of the convective terms). A mixing-length calculation was run first, then used to start the two-equation calculation. The calculation proved sensitive to the $k-\epsilon$ relationship assumed in the viscous sublayer. Both the mixing length and the two-equation model predicted the shock to occur in about the correct location in the tube (not discernible from the plotted results by virtue of the choice of axial origin). Only the $k-\epsilon$ results are plotted. Other transonic shock calculations had indicated the moving mesh and high-cell Reynolds number were absolutely necessary for adequate solution numerical accuracy. A small separation bubble formed in the mixing length calculation. This significantly distorted the predicted wall-pressure distribution. For a number of reasons, for example examination of boundary conditions, effect of turbulence model, mesh distribution, etc., no relevant cold-start calculation is available. Based on prior calculations, it is estimated that from a cold start this calculation would converge in approximately 100 time steps. It is observed that the published skin-friction data for this case have changed more than once.

Case 8641 (BIKX)

The time-averaged Navier-Stokes equations were used. The computer program is available from the U.S. Army Research Office. It was run with supersonic inflow and outflow boundary condition, i.e., all variables specified on inflow, none set on outflow. The shock exited the outflow boundary and no-slip was used on the wall. Turbulence was modeled using a mixing-length model as $k-\epsilon$ gave nonphysical turbulent viscosities in the recirculation zone. The mesh was nonorthogonal and body-fitted with 61×41 mesh points. Nonuniform packing was used to define the approach boundary layer including the viscous sublayer, and the shear layer, while the transverse mesh distorted to become aligned with the shock. It is felt that the reattachment near-wall flow is only marginally resolved, but time was not available to construct a better mesh. Second-order artificial dissipation was added to keep the cell Reynolds number below 20. The shock was unacceptably smeared when a cell Reynolds number limit of 2 was used, although the comparison with data was, in fact, better! A cell Reynolds-number limit of 2 gives the same truncation error as first-order one-sided

differencing of the convective term. The mixing length chosen for this case utilized a conventional wall-layer model with sublayer damping and a free-stream mixing length equal to 0.09 of the approach boundary-layer thickness. In the shear layer this maximum mixing length was increased smoothly to a value of 0.05 of a step height.

REFERENCES

- Buggeln, R. C., W. R. Briley, and H. McDonald (1981). "Solution of the Navier-Stokes equations for three-dimensional turbulent flow with viscous sublayer resolution," AIAA Paper 81-1023 (AIAA 5th Computational Fluid Dynamics Conf., Palo Alto, June).
- Shamroth, S. J., and H. J. Gibelg (1980). "Analysis of turbulent flow about an isolated airfoil using a time-dependent Navier-Stokes procedure," AGARD Conference Proceedings No. 296 on 'Boundary Layer Effect on Unsteady Airloads.'



COMPARISON OF COMPUTATION WITH EXPERIMENT

Summary Report

(Some Calculated Elliptical Turbulent Flow Cases,
Cases 0331, 0421, 0431)

by

G. L. Mellor and M. C. Celenligil*

Computer Group Number: 14

M.C. Celenligil

ABSTRACT

A model based on hypotheses of Rotta and Kolmogoroff is here applied to Cases 0421, 0431 and 0331. The model has previously (Mellor and Yamada 1977, 1982; other references are cited in these papers) been shown to yield good simulations of simpler flows; e.g., boundary layers, channel flow, pipe flow and—although required boundary condition and verification data are ambiguous or imprecise—density stratified flows encountered in meteorological and oceanographic problems.

In the present applications, the model has behaved quite well. For some flow regions there are errors, generally associated with inadequate grid resolution, but considering the complex nature of the flows, they do not seem serious overall.

The calculations for Case 0421 (backward-facing step) produced repeating large-scale, two-dimensional, eddy shedding.

THE MODEL EQUATIONS

We define ensemble mean vorticity, ξ , in terms of the mean-stream function, ψ , according to

$$\frac{\partial^2 \psi}{\partial x^2} + \frac{\partial^2 \psi}{\partial y^2} = -\xi \quad (1)$$

The mean vorticity, derived from the curl of the Reynolds-averaged momentum equation, is

$$\frac{D\xi}{Dt} = \frac{\partial^2}{\partial x^2} (-\overline{uv}) - \frac{\partial^2}{\partial x \partial y} (\overline{v^2} - \overline{u^2}) - \frac{\partial^2}{\partial y^2} (-\overline{uv}) \quad (2)$$

The model equations for the Reynolds stresses (Mellor and Yamada, 1977, 1982) are

*Department of Aero./Mech. Sc., Princeton University, Princeton, NJ 08540

$$\begin{aligned}
\frac{D}{Dt} \begin{bmatrix} \overline{u^2} \\ \overline{v^2} \\ \overline{w^2} \\ \overline{uv} \end{bmatrix} &= \frac{\partial}{\partial x} K \begin{bmatrix} 3\overline{u^2}/\partial x \\ \overline{v^2}/\partial x + 2\overline{uv}/\partial y \\ \overline{w^2}/\partial x \\ \overline{u^2}/\partial y + 2\overline{uv}/\partial x \end{bmatrix} + \frac{\partial}{\partial y} K \begin{bmatrix} \overline{u^2}/\partial y + 2\overline{uv}/\partial x \\ 3\overline{v^2}/\partial y \\ \overline{w^2}/\partial y \\ \overline{v^2}/\partial x + 2\overline{uv}/\partial y \end{bmatrix} - \frac{q}{3A_1 \ell} \begin{bmatrix} \overline{u^2} - q^2/3 \\ \overline{v^2} - q^2/3 \\ \overline{w^2} - q^2/3 \\ \overline{uv} \end{bmatrix} \\
&+ C_1 q^2 \begin{bmatrix} 2\partial U/\partial x \\ 2\partial V/\partial y \\ 0 \\ \partial U/\partial y + 2V/\partial x \end{bmatrix} + \begin{bmatrix} -2\overline{u^2} \partial U/\partial x - 2\overline{uv} \partial U/\partial y \\ -2\overline{uv} \partial V/\partial x - 2\overline{v^2} \partial V/\partial y \\ 0 \\ -\overline{u^2} \partial V/\partial x - \overline{v^2} \partial U/\partial y \end{bmatrix} - \frac{2}{3} \frac{q^3}{B_1 \ell} \begin{bmatrix} 1 \\ 1 \\ 1 \\ 0 \end{bmatrix} \quad (3)
\end{aligned}$$

where we define $K \equiv 3\ell S_q/5$; $q^2 = \overline{u^2} + \overline{v^2} + \overline{w^2}$; $A_1 = 0.92$; $B_1 = 16.6$; $C_1 = 0.08$; and $S_q = 0.2$.

The model equation for the master length scale ℓ is

$$\begin{aligned}
\frac{D}{Dt}(q^2 \ell) &= \frac{\partial}{\partial x} [q \ell S_\ell \frac{\partial(q^2 \ell)}{\partial x}] + \frac{\partial}{\partial y} [q \ell S_\ell \frac{\partial(q^2 \ell)}{\partial y}] \\
&+ E_1 \ell [-\overline{uv}(\frac{\partial U}{\partial y} + \frac{\partial V}{\partial x}) - \overline{u^2} \frac{\partial U}{\partial x} - \overline{v^2} \frac{\partial V}{\partial y}] - \frac{q^3}{B_1} \{1 + E_2 (\frac{\ell}{\kappa L})^2\} \quad (4)
\end{aligned}$$

where a wall-proximity length scale, L , is defined according to

$$L^{-1}(\underline{x}) = \frac{1}{\pi} \oint \frac{ds}{|\underline{x} - \underline{x}_0|^2} \quad (5)$$

\underline{x} is any point in the fluid domain bounded by the solid wall at \underline{x}_0 and $ds = |d\underline{x}_0|$. The constants in (5) are $E_1 = 1.8$, $E_2 = 1.33$, and $S_\ell = 0.2$. $\kappa = 0.41$ is von Kármán's constant.

The model is here specialized for two-dimensional mean flow but, in general, need not be.

FINITE-DIFFERENCE EQUATIONS

The computations are done in a rectangular domain with constant Δx and Δy . The differential equations are finite differenced in a conventional way. The transport equations for vorticity, Reynolds stresses and length scale are differenced by an explicit central differencing scheme. The time derivatives and the advective terms are differenced by the leapfrog method, and the diffusion terms are all centrally

differenced. The Laplacian operator in Eq. 1 is centrally differenced, and the stream function is solved by an alternating-direction implicit (ADI) method.

At some intermediate time in the course of calculations, all of the variables from the previous time are known. The values of vorticity, Reynolds stresses and length scale at the next time step are calculated by solving the transport equation explicitly inside the boundaries. Then, the boundary values are evaluated using the boundary conditions cited below. Once the vorticity is known everywhere, Poisson's equation is solved for the stream function.

At time $t = 0$ the flow is set to be irrotational and some small constant initial values are given to Reynolds stresses and length scale. Then, using the algorithm explained above, the transient flow structure is computed by marching forward in time, until the steady state is reached or the flow configuration becomes cyclic in time.

BOUNDARY CONDITIONS

Entrance B.C.

The data are used whenever possible. Assumptions are made for the variables not prescribed by the data.

Case 0331: ($U_0 = 33$ m/sec, $H = 0.127$ m): The velocity profile is flat. $\xi = 0$, $\overline{uv} = 0$. $\overline{v^2}/U_0^2 = 10^{-6}$ (data). We assume $\overline{u^2} = \overline{w^2} = \overline{v^2}/2$ and $l/H = 10^{-3}$.

Case 0421: ($U_0 = 18.2$ m/sec, $H = 0.0381$ m): The data is used for ξ (assuming $\partial\psi/\partial x = 0$) and for ψ . $\overline{u^2}$, $\overline{v^2}$, and \overline{uv} are taken from the data of the nearest station ($x/H = -1.333$). $\overline{w^2}$ is assumed as $\overline{w^2} = \overline{v^2}$. l is obtained assuming an equilibrium turbulent boundary layer.

Case 0431: ($U_0 = 15.06$ m/sec, $H = 0.2$ m): The data is used for ξ (assuming $\partial\psi/\partial x = 0$), ψ , $\overline{u^2}$, $\overline{v^2}$, and \overline{uv} . $\overline{w^2}$ is assumed to be $\overline{w^2} = \overline{v^2}$. l is obtained assuming an equilibrium turbulent boundary layer.

Exit B.C.

Case 0331: $\partial\psi/\partial x = 0$, $\partial\xi/\partial x = 0$, $\partial\overline{u_i u_j}/\partial x = 0$, $\partial q^2 l/\partial x = 0$.

Cases 0421 and 0431: $\partial^2\psi/\partial x^2 = 0$, $\partial\xi/\partial x = 0$, $\partial\overline{u_i u_j}/\partial x = 0$, $\partial q^2 l/\partial x = 0$.

Open B.C.

Case 0331: $\overline{uv} = 0$, $\overline{u^2}/U_0^2 = \overline{v^2}/U_0^2 = \overline{w^2}/U_0^2 = 10^{-6}$, $l/H = 10^{-3}$ are used assuming the flow at the boundary is directed into the calculation domain in the y -direction.

Case 0431: U_0 ($= \partial\psi/\partial y$) data, $\partial\xi/\partial y = 0$, $\partial\overline{u_i u_j}/\partial y = 0$, $\partial q^2 l/\partial y = 0$ are used assuming the top boundary is outside of the boundary layer.

Wall B.C.

Constant values are given to ψ which differ on opposite walls by an amount determined by the volume flow rate. Except at 90° corners, the wall vorticities are not required because in the advective terms they are multiplied by zero normal-wall velocities. At singular 90° corners (Case 0331: $x = 0$, $y = 0.447$ m), (Case 0421: $x = 0$, $y = H$) the vorticities are evaluated using the method given by Briggs et al. (1977) which ensures that the streamlines remain parallel to their original direction after leaving the corner. For the turbulence intensities Neumann boundary conditions are used, $\partial u^2/\partial n = 0$, $\partial v^2/\partial n = 0$, $\partial w^2/\partial n = 0$. At the walls $l = 0$. The turbulent shear stress at the wall is obtained from the turbulent wall layer model (Mellor, 1966) which gives the velocity profile near the wall assuming that the shear stress varies linearly close to the wall. If τ and U are the total shear stress and velocity at the first grid point away from the wall (and $y = \Delta y$), τ_0 is the shear stress at the wall and $u_\tau = |\tau_0/\rho|^{1/2}$, then the equations are:

- i. When τ and τ_0 have the same sign:

$$\frac{U}{u_\tau (\text{sign } \tau)} = B^+ + \frac{1}{\kappa} \ln \left[\frac{y u_\tau}{y} \frac{4}{\{|\tau/\tau_0|^{1/2} + 1\}^2} \right] + \frac{2}{\kappa} [|\tau/\tau_0|^{1/2} - 1]$$

- ii. When τ and τ_0 have opposite signs:

$$\frac{U}{u_\tau (\text{sign } \tau)} = B^+ + \frac{2}{\kappa} [|\tau/\tau_0|^{1/2} + 1] - \frac{1}{\kappa} \ln \left[\frac{y U}{y} \frac{4}{|\tau/\tau_0| + 1} \right] - \frac{2}{\kappa} \tan^{-1} |\tau/\tau_0|$$

where, B^+ depends on the shear-stress gradient ($B^+ = 4.9$ when $\partial\tau/\partial y = 0$).

DISCUSSION

The transport equations are integrated numerically and for Cases 0331 and 0431 a steady-flow structure is obtained after a long time of integration. However, for Case 0421 unsteady vortex shedding is observed and the flow becomes nearly cyclic in time. The non-dimensional cycling time is approximately $\Delta T = 10$. In order to make comparison with the experimental data, the computational results are averaged over the cycles. The averaged quantities are denoted by an angle bracket, e.g. $\langle U \rangle$. Also, one has to add $\langle (U - \langle U \rangle)^2 \rangle$, $\langle (V - \langle V \rangle)^2 \rangle$, $\langle (U - \langle U \rangle)(V - \langle V \rangle) \rangle$ to $\langle u^2 \rangle$, $\langle v^2 \rangle$, $\langle uv \rangle$, respectively, in order to include the effect of mean-velocity fluctuations around $\langle U \rangle$ and $\langle V \rangle$ and obtain the total average values for these variables.

To maintain stability diffusion is added explicitly to the transport equations. This is chosen to be a fraction of the artificial diffusion term inherent in the upwind forward differencing scheme. We used the minimum value for this fraction which maintains stability in each case. The artificial viscosities are of the order of Δx^2 and Δy^2 respectively, and the second-order accuracy of the scheme is preserved (Roache, 1976).

At the wall the various boundary conditions we used for $\overline{u^2}$, $\overline{v^2}$, $\overline{w^2}$ showed almost no effect on the results. In our early computations we used the relations for $\overline{u^2}$, $\overline{v^2}$, $\overline{w^2}$ as proportional to u_τ^2 based on the law-of-the-wall assumption, which does not hold for separated flows.

For the type of time marching, fully elliptic algorithm adopted here, one cannot afford very fine grid resolution and one cannot resolve the viscous sublayer or a large portion of the logarithmic layer. We therefore matched our numerical solution to the wall-layer model. This model, which we used for calculating the turbulent shear stress at the wall, improved the results compared with the law-of-the-wall results.

Case 0331

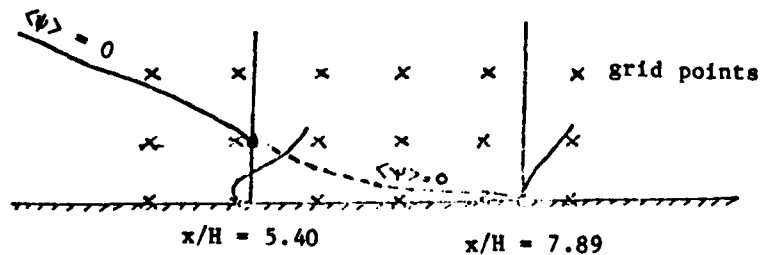
The results, which are from computations done on an 87×23 grid, agree more closely with the experimental data than the results using a 44×44 grid. Finer resolution in the x-direction is needed because the variables change more rapidly in the x-direction than in the y-direction (especially near the entrance).

Various different boundary conditions are applied at the top boundary, and the results are found to be very sensitive to them. The flow configurations for various boundary conditions are shown in Fig. 1. The open boundary conditions which are given in the previous section resulted in a steady flow configuration. When a wall is assumed to be present at the top boundary, however, an unsteady, nearly cyclic vortex shedding is observed and the explicitly calculated unsteady component of the flow dominates the "turbulence" statistics.

Case 0421

The calculations provide repeating, unsteady, streamline flow patterns, as shown in Fig. 2. Figure 3 is the average pattern.

After the unsteady results are averaged, C_p is obtained diagnostically by integrating the momentum equations in the whole calculation domain. $\langle C_f \rangle$ is found to be zero (i.e., the reattachment point) around $x/H = 7.89$, which is a couple of grid points downstream of the location $x/H = 5.40$, where $\langle \psi \rangle$ on the first grid point adjacent to the wall becomes zero:



$$\langle C_f \rangle = 0$$

This is a result of the wall-layer model we are using in our computations. If the law-of-the-wall is used as the wall function, the location where $\langle C_f \rangle$ is zero becomes the same location where $\langle \psi \rangle$ is zero on the first grid point adjacent to the wall.

When we repeated the calculations using half mesh sizes (i.e., using a 61×61 grid instead of 31×31), then $\langle C_f \rangle$ is found to be zero around $x/H = .75$ and $\langle \psi \rangle$ on the first grid point adjacent to the wall becomes zero near $x/H = 5.81$.

Case 0431

The computational domain is between $x = 2.197$ m and $x = 4.34$ m which is about 40% smaller than the one specified in the instructions. Using a 45×45 grid resulted in 4 grid points in the boundary layer at the entrance (instead of 1 grid point, if we started the calculations from $x = 0.805$ m using the same number of grid points with constant mesh spacing). In order to extend the calculation domain to $x = 0.805$ m with good accuracy, one could try using more grid points or a different mesh system with varying mesh size. But considering that the boundary layer grows more than 20 times from $x = 0.805$ m to $x = 4.34$ m it would be necessary to use very small Δy values near the entrance. This requires very small values for Δt , which would increase the computation time considerably. Our computations take about 10 min of computer time with the ASC computer to reach a steady-flow structure.

The height of the computational domain (0.328 m) places the top boundary outside of the boundary layer. Although this is a little larger than the tunnel height near the entrance ($x = 2.197$ m), there should not be any significant error since free-stream flow is stipulated outside of the tunnel height.

The backflow at the exit makes it difficult to apply various exit boundary conditions. Nevertheless, the ones that we used which are less restrictive than the other boundary conditions gave very good results. In some of our computations we tried exit data as the exit boundary condition for the stream function. This gave almost the same results everywhere; however, near the exit $\partial^2 \psi / \partial x^2 = 0$ boundary condition gave better results. When using ψ data as the exit boundary condition, in one of our runs we reduced the backflow velocities at the exit by half, but this did not affect the separation zone. This supports the hypothesis that the backflow is supplied locally by the outer-region large-scale structure and not by the small mean backflow far downstream (Simpson, 1980).

C_f is found to be zero around $x = 3.267$ m and this is the separation point for our results. However, the stream function on the first grid point adjacent to the wall becomes zero near $x = 3.44$ m. This means there is a very small backflow up to the location where C_f is zero which can not be detected from the stream-function results.

The fraction of time the flow moves downstream (γU) is calculated assuming a Gaussian distribution for the u fluctuation.

REFERENCES

- Briggs, M., G. L. Mellor, and T. Yamada (1977). "A second moment turbulence model applied to fully separated flows," Turbulence in Internal Flows, S. M. B. Murthy (ed.). Hemisphere Pub. Corp., pp. 249-276.
- Mellor, G. L. (1966). "The effects of pressure gradients on turbulent flow near a smooth wall," J. Fluid Mech., 24, 255-275.
- Mellor, G. L., and T. Yamada (1977). A turbulence model applied to geophysical fluid problems," Symposium on Turbulent Shear Flows. The Pennsylvania State University.
- Mellor, G. L., and T. Yamada (1982). "Development of a turbulent closure model for geophysical problems," to be published in Rev. Geophys. and Space Physics.
- Roache, P. J. (1976). Computational Fluid Dynamics. Hermosa Publishers.
- Simpson, R. L., Y. T. Chew, and B. G. Shivaprasad (1980). "Measurements of a separating turbulent boundary layer," Technical Report SMU-4-PU, Project Squid. Published for ONR by School of Mechanical Engineering, Purdue University.

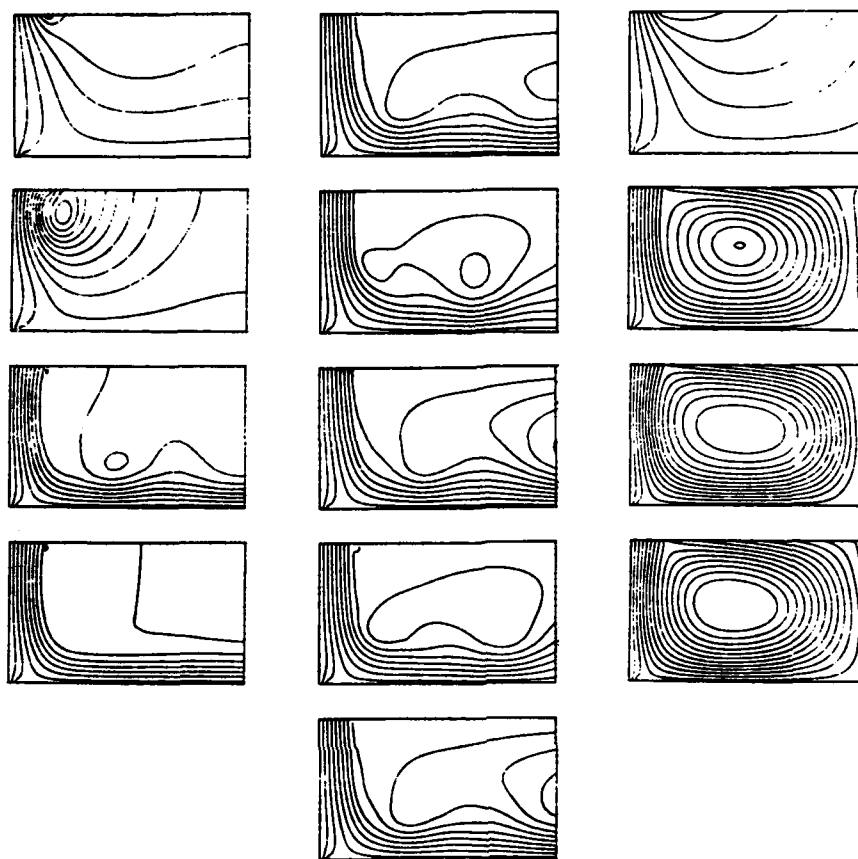


Figure 1. Case 0331. Flow streamlines for various sets of boundary conditions applied at the top portion where flow properties were not known.

1st column: $\partial\psi/\partial y = 0$, $\xi = 0$, $\overline{u^2}/U_0^2 = \overline{v^2}/U_0^2 = \overline{w^2}/U_0^2 = 10^{-8}$, $\overline{uv} = 0$, $l/H = 10^{-3}$.

This is the principal flow calculation detailed elsewhere. The sequence begins at non-dimensional time $T = 0$ and proceeds to a nearly stationary flow at $T = 120$.

2nd column: A wall is assumed to be present at the top boundary. The sequence begins after non-stationary cycling has been established at $T = 180$ and ends at the beginning of a new cycle at $T = 200$.

3rd column: $\partial^2\psi/\partial y^2 = 0$, $\xi = 0$, $\overline{u^2}/U_0^2 = \overline{v^2}/U_0^2 = \overline{w^2}/U_0^2 = 10^{-3}$, $\overline{uv} = 0$, $l/H = 10^{-3}$.

The sequence begins at $T = 0$ and proceeds to a nearly stationary flow at $T = 100$.

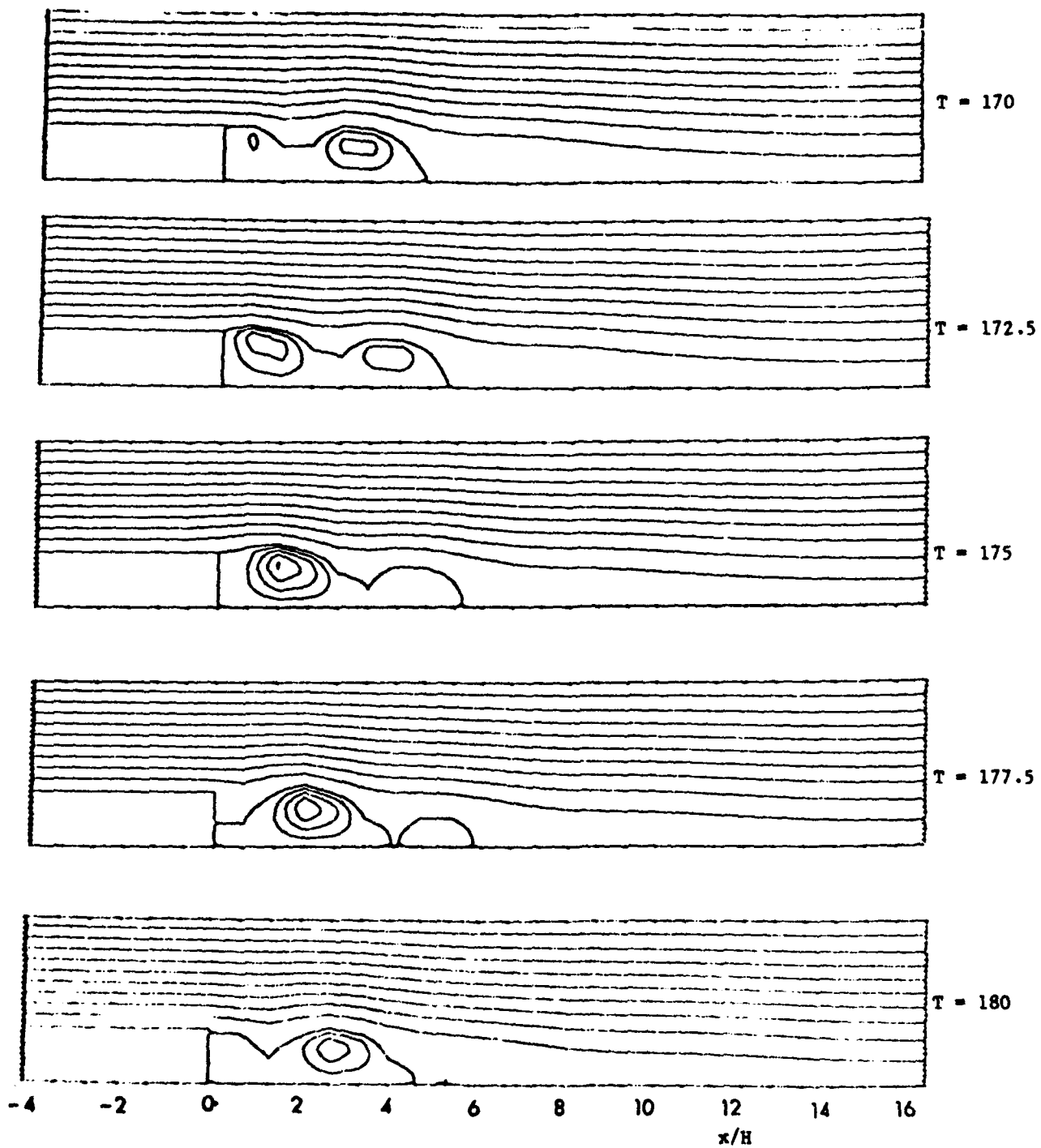
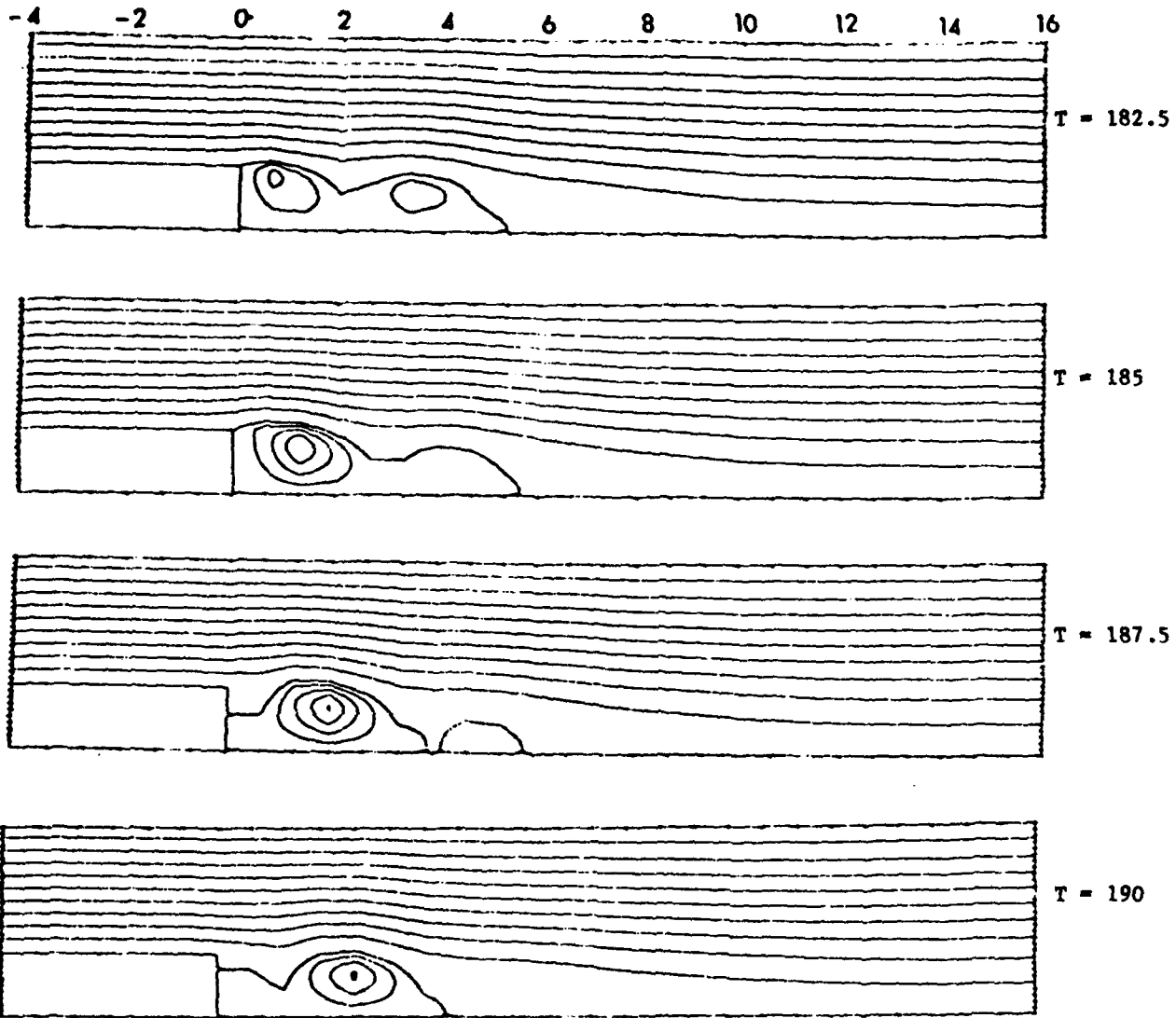


Figure 2. Case 0421. The streamlines of the flow over a backward-facing step. $T = U_0 t/H$ is the non-dimensional time, where U_0 is the free-stream velocity at the entrance and H is the step height.

(Fig. 2 cont.)

(Figure 2 continued)



END Figure 2.

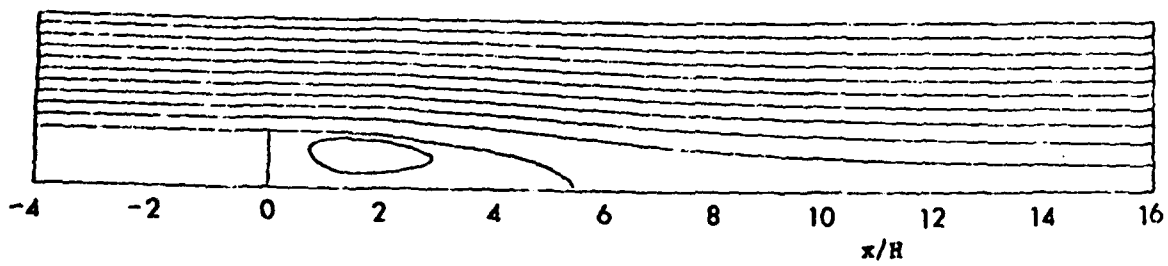


Figure 3. The streamlines after averaging between $T = 170$ and $T = 190$.



R.E. Melnik

COMPARISON OF COMPUTATION WITH EXPERIMENT

Summary Report

(Computation of the Viscous Transonic Flow
over an Airfoil by a Zonal Method)

by

R. E. Melnik^{*}

Computer Group Number: 39

Case 8621

Introduction

Interactive-type calculations were carried out for the transonic airfoil cases (8621) using the zonal method developed by Melnik, Chow, Mead, and Jameson (MCMJ) (Melnik, 1978, 1979, 1980; Melnik et al., 1977, 1981). The MCMJ method employs an iterative procedure to obtain self-consistent solutions of the coupled inviscid and boundary-layer equations. All terms appearing in the matching conditions coupling the inviscid and boundary-layer flows are accounted for in the formulation. Displacement-thickness effects on the airfoil and in the wake are accommodated through an equivalent transpiration velocity form of the matching conditions. The coupling condition associated with the curvature of the wake is accounted for through an equivalent pressure jump across the wake.

It is generally recognized that the boundary-layer approximations fail near strong interaction zones at the trailing edge and at shock waves (see Melnik et al., 1981). The present method employs a local analytic solution to correct the boundary-layer solution for normal pressure-gradient effects at the trailing edge but does nothing special to improve the theoretical modeling of the shock-wave boundary-layer interaction. In its present form, the method is restricted to attached flows or to flows with small regions of separation. A review of recent developments in zonal methods and theories for strong interactions on airfoils is given in Melnik et al. (1981).

Coupling Conditions and Trailing-Edge Corrections

The MCMJ theory uses a local solution to correct the boundary-layer solution for strong interactions at the trailing edge. A solution which is uniformly valid in the entire flow field is formed by adding the boundary-layer and trailing-edge solutions to the inviscid solution and subtracting their "common parts". This results in a standard sum-type composite solution as for the method of matched asymptotic expansions. For example, the representation for the streamwise velocity component is

^{*}Grumman Aerospace Corporation, Bethpage, NY 11714

written in the form,

$$U = U_{INV}(N,S;V_G,[[V]],[[U]]) + [U_{BL}(\eta,S) - \bar{U}_{BL}(\eta,S)] + [U_{TE}(\eta,\xi) - \bar{U}_{TE}(\eta,\xi)] \quad (1)$$

where N,S are curvilinear coordinates normal and tangent to the airfoil and wake streamline, η and ξ are stretched coordinates

$$\eta = N/\epsilon ; \quad \xi = (S - S_{TE})/\epsilon$$

and ϵ is a small scaling parameter of the order of the nondimensional boundary-layer thickness at the trailing edge. The leading term is from the solution of the inviscid equations subject to the coupling conditions, while the second and third group of terms are from the boundary-layer and trailing-edge solutions and their "common parts." The function V_G is the transpiration velocity appearing in the boundary condition at the airfoil surface, and $[[V]]$ and $[[U]]$ are the equivalent jumps in normal and tangential velocity along the wake which are imposed as boundary conditions on the outer inviscid flow.

In the MCMJ theory, "composite" coupling conditions are derived which correct the standard matching conditions of boundary layer theory for strong interaction effects at the trailing edge. The corrected coupling conditions for V_G , $[[V]]$ and $[[U]]$ are written in the form,

$$V_G = \epsilon^2 \left(\frac{d(\rho_e U_e \delta^*)}{\rho_e dS} \right) G_N \quad (2)$$

$$[[U]] = \epsilon^2 [U_e (\delta_w^* + \theta_w)] K G_W \quad (3)$$

$$[[V]] = \epsilon^{3/2} G_S + \epsilon^2 \left(\frac{d\rho_e U_e \delta_w^*}{\rho_e dS} \right) \quad (4)$$

where the subscript "e" denotes surface values of the composite solution, "w" denotes the complete wake thickness, K is the wake curvature and G_N , G_W and G_S are analytic expressions determined from the local trailing-edge solution. Equation (2) specifies the equivalent transpiration velocity leading to the usual displacement effect on the airfoil surface while Eqs. 3 and 4 arise from the wake-curvature and wake-thickness effects, respectively. These relations reduce to the standard coupling conditions of boundary-layer theory for $G_N, G_W = 1$ and $G_S = 0$. The composite solution for the pressure on the airfoil surface and wake centerline, is written in the form

$$P(N = 0, S) = P_{INV}(0, S) - \epsilon^{3/2} \Delta P(S) \quad (5)$$

where the first term is determined from the outer inviscid solution (subject to

coupling conditions) and the second term is a correction to account for pressure changes across the boundary layer and wake near the trailing edge.

Inviscid Flow

It is assumed that total pressure losses across shock waves can be neglected and that the flow in the outer region can be approximated by solutions to the full-potential flow equation. Numerical solutions to the potential equation are obtained with Jameson's, fully conservative, rotated difference scheme. The calculations employ an "O" type grid determined from a conformal transformation of the region exterior to the airfoil to the interior of a circle. The method uses an explicit artificial viscosity in a region that extends slightly beyond the supersonic zone. The artificial viscosity is switched off for local Mach numbers less than M_c , which in the present calculation was set to $M_c = 0.9$. The present calculations employed a fully second-order accurate version of the method.

Boundary-Layer Solution

The boundary-layer equations are solved by a direct method, with the pressure distribution prescribed. A compressible flow version of Thwaites integral method is used to solve for the laminar boundary layer between the stagnation and transition points. In the computations for this Conference, transition is assigned at the location of the roughness strips on the airfoil model. Initial conditions for the turbulent boundary-layer calculations are determined from the assumption that the momentum thickness is continuous and the transformed shape factor experiences a jump, $[[H]] = 1.1$, across the transition point. This initialization procedure leads to good agreement of the computations with the measured turbulent boundary-layer properties just downstream of transition. The calculations of the turbulent boundary layer were carried out with the original version of Green's lag entrainment method (as opposed to the more recent version used by P. D. Smith at this Conference). This is an integral method which makes use of the turbulent-energy equation to derive a lag equation for the entrainment function. The computations were made including terms allowing for the secondary influences of surface curvature and mean dilatation on the turbulence. The wake was treated as two symmetric half-wakes, as in the original method.

Numerics

The inviscid equations were solved on a sequence of three grids (coarse, medium, and fine) employing (40×8) , (80×16) , (160×32) points that were uniformly distributed in the circle plane ("point at infinity" at the origin) with the larger of the two numbers referring to the number of grid points on the airfoil surface. The nonlinear difference equations are solved by hybrid scheme, in which a fast Poisson solver is repeatedly employed after a specified number of SLOR steps in order to

accelerate convergence. The integral boundary-layer equations are integrated with a Runge-Kutta method with automatic error-checking and mesh-halving. This procedure leads to a subgrid embedded in the inviscid mesh to allow for high gradients near the shock wave and trailing edge.

The solution procedure involves two nested iterations, one to solve the nonlinear inviscid-flow equations (with fixed coupling conditions) and the other to solve the inviscid/viscid coupling. The iterative solution of the inviscid equations is interrupted periodically to solve the boundary-layer equations and update the coupling conditions. The coupling condition updates are underrelaxed ($\omega = 0.1$) to assure convergence. The updates are made whenever the maximum residual in the inviscid computations has been reduced by a specified factor, which is typically taken to be equal to 1/5. This results in frequent updates of the coupling conditions, usually about every 20 SLOR cycles. Typical runs for supercritical cases take about 10 min on an IBM 370-168 computer to reduce the maximum residual to below 10^{-5} . The solution on each grid is converged to this level, so that they can be compared to provide an indication of truncation error.

The computer code was organized so that either the incidence or the lift coefficient could be specified. The computations submitted to the Conference were run with C_L set equal to the experimental value (as requested in the specifications to computers). In this mode the incidence is determined as part of the solution by the Kutta condition.

Results

Results were submitted for all runs of the RAE 2822 airfoil (Case 8621) calculated at the experimental Mach number, Reynolds number, and transition point locations. In addition, two cases were submitted with a small blockage correction of $\Delta M_\infty = +0.004$ and one with a correction of $\Delta M_\infty = -0.004$. In these cases, the experimental values of the lift and pressure coefficients were corrected according to formulas given in the specifications. The magnitude of the Mach number corrections were chosen on the basis of comparison between the computations and experiments for the pressure distribution on the lower front part of the airfoil.

Converged solutions comparing the pressure distribution and forces on the coarse, medium and fine meshes were also submitted for the $C_L = 0.743$ case to give some indication of numerical accuracy. These results indicated it was necessary to go to a (160×32) point grid in order to achieve 1% accuracy in the surface pressure distribution and shock location and 5% accuracy in the drag coefficient. The value of the drag coefficients on the three meshes in this case were $C_D = 0.0195, 0.0127,$ and 0.0115 , with an extrapolated zero mesh limit of $C_D = 0.0111$.

Concluding Comments

Although the present method employs only a simple interacting boundary-layer description of the shock-wave boundary-layer interaction, the results indicate that it provides a quantitatively useful prediction of the surface-pressure and displacement-thickness distributions both near and downstream of the shock wave. The main shortcomings of the present code are its relatively long computing times and its inability to handle separated flows. We have recently developed a new version which uses Jameson's multigrid method to solve the inviscid equations. Preliminary computations indicated a factor-of-five reduction in computing time. Extensions to separated flow require improved numerical techniques to handle the viscid/inviscid coupling and improved turbulence modeling.

References

- Melnik, R. E. (1978). "Wake curvature and trailing edge interaction effects in viscous flow over airfoils," Advanced Technology Airfoil Research Conference, CP 2045, Part 1.
- Melnik, R. E. (1979). "Recent developments in a boundary layer theory for computing viscous flows over airfoils," paper presented at 4th USAF/FRG Data Exchange Meeting, Forschungsbericht aus der Wehrtechnig, BMVg-FBWT 79-31, Meersberg, Germany.
- Melnik, R. E. (1980) "Turbulent interactions on airfoils at transonic speeds, recent developments," Paper No. 291 in AGARD Conf. Proc., Computation of Viscous-Inviscid Interactions.
- Melnik, R. E., R. R. Chow, and H. R. Mead (1977). "Theory of viscous transonic flow over airfoils at high Reynolds number," Paper No. 77-680, AIAA 10th Fluid and Plasma Dynamics Conf., Albuquerque, NM.
- Melnik, R. E., R. R. Chow, H. R. Mead, and A. Jameson (1981). "An improved viscid/inviscid interaction procedure for transonic flow over airfoils," NASA CR (to be released).

COMPARISON OF COMPUTATION WITH EXPERIMENT

Summary Report (Complex Turbulent Compressible Flows)

by

Ha Minh Hieu*

D. D. Vandromme† and R. W. MacCormack†

Computer Group Number: 44¹



Ha Minh Hieu

Cases 8101, 8201, 8612

INTRODUCTION

The new MacCormack (1981) explicit-implicit scheme is used to solve the two-dimensional Favre-averaged Navier-Stokes equations. The first two cases concern the flat-plate boundary-layer flows with and without heat transfer across the solid wall. The third case is a more complex flow involving a shock/boundary-layer interaction and an extended flow-separation region in a two-dimensional channel (Delery, 1978). In a first step, all the calculations have been performed with an algebraic formulation for the turbulence correlations (mixing-length theory). In a second step, the Boussinesq approximation is used but the various second-order moments are accessed by the knowledge of two turbulence scales: the turbulent kinetic energy and its dissipation rate (Jones-Launder $k-\epsilon$ turbulence model). All the calculations are started with the algebraic formulation. If the two-equation model is to be used, the switching is done after a small number of iterations.

The Navier-Stokes Equations

Using Favre-averaging, the time-dependent Navier-Stokes equations may be written as:

$$\begin{aligned}\frac{\partial}{\partial t} (\bar{\rho}) + \frac{\partial}{\partial x_k} (\bar{\rho} \tilde{U}_k) &= 0 \\ \frac{\partial}{\partial t} (\bar{\rho} \tilde{U}_i) + \frac{\partial}{\partial x_k} (\bar{\rho} \tilde{U}_i \tilde{U}_k + \overline{\rho u_i'' u_k''} + \bar{\tau}_{ik}) &= 0 \\ \frac{\partial}{\partial t} (\bar{\rho} \tilde{E}) + \frac{\partial}{\partial x_k} (\bar{\rho} \tilde{E} \tilde{U}_k + \overline{\rho u_k'' \tilde{E}''} + \sum_{ik} \bar{\tau}_{ik} \tilde{U}_i + \overline{\sigma_{ik} u_i''}) - \lambda \frac{\partial \tilde{T}}{\partial x_k} &= 0\end{aligned}$$

The closure of the equations is achieved in the first step by the use of a gradient-flux approximation in which the viscosity coefficient is determined algebraically (mixing-length theory). Thus the closed Navier-Stokes equations may be represented by the vector expression:

*Institut de Mécanique des Fluides de Toulouse, 31071 Toulouse, France

†NASA Ames Research Center, Moffett Field, CA 94035

$$\frac{\partial}{\partial t} \vec{U} + \frac{\partial}{\partial x} \vec{F} + \frac{\partial}{\partial y} \vec{G} = 0$$

in which case the vectors \vec{U} , \vec{F} , and \vec{G} are

$$\vec{U} = \begin{Bmatrix} \bar{\rho} \\ \bar{\rho}\tilde{U} \\ \bar{\rho}\tilde{V} \\ \bar{\rho}\tilde{E} \end{Bmatrix}$$

$$\vec{F} = \begin{bmatrix} \bar{\rho}\tilde{U} \\ \bar{\rho}\tilde{U}^2 + \sigma_x \\ \bar{\rho}\tilde{U}\tilde{V} + \tau_{xy} \\ (\bar{\rho}\tilde{E} + \sigma_x)\tilde{U} + \tau_{xy}\tilde{V} - \left(\frac{\mu}{P} + \frac{\mu_t}{P_{rt}}\right)C_v \frac{\partial \tilde{T}}{\partial x} \end{bmatrix} \quad \vec{G} = \begin{bmatrix} \bar{\rho}\tilde{V} \\ \bar{\rho}\tilde{U}\tilde{V} + \tau_{xy} \\ \bar{\rho}\tilde{V}^2 + \sigma_y \\ (\bar{\rho}\tilde{E} + \sigma_y)\tilde{V} + \tau_{xy}\tilde{U} - \left(\frac{\mu}{P} + \frac{\mu_t}{P_{rt}}\right)C_v \frac{\partial \tilde{T}}{\partial y} \end{bmatrix}$$

in which

$$\sigma_x = \bar{P} - (\mu + \mu_t) \left[2 \frac{\partial \tilde{U}}{\partial x} - \frac{2}{3} \left(\frac{\partial \tilde{U}}{\partial x} + \frac{\partial \tilde{V}}{\partial y} \right) \right]$$

$$\sigma_y = \bar{P} - (\mu + \mu_t) \left[2 \frac{\partial \tilde{V}}{\partial y} - \frac{2}{3} \left(\frac{\partial \tilde{U}}{\partial x} + \frac{\partial \tilde{V}}{\partial y} \right) \right]$$

$$\tau_{xy} = \tau_{yx} = -(\mu + \mu_t) \left(\frac{\partial \tilde{U}}{\partial y} + \frac{\partial \tilde{V}}{\partial x} \right)$$

The pressure field is obtained from the equation of state

$$\bar{P} = (\gamma - 1)\bar{\rho}e$$

where

$$\tilde{e} = \tilde{E} - \frac{1}{2} (\tilde{U}^2 + \tilde{V}^2)$$

The turbulent viscosity is

$$\mu_t = \text{Min.} \begin{cases} \mu_t = \bar{\rho} l^2 \left| \frac{\partial \tilde{U}}{\partial y} + \frac{\partial \tilde{V}}{\partial x} \right| \\ \mu_t = 0.0168 \bar{\rho} \tilde{U}_e \delta^* \end{cases}$$

where δ^* is the displacement thickness and the mixing length is defined by

$$l = \chi y \left[1 - \exp \left(-\sqrt{\rho_w \tau_w} y / (A^+ \mu_w) \right) \right]$$

where $\chi = 0.4$ and $A^+ = 26$.

To achieve the closure of the Navier-Stokes equations in the second step, the formulation is slightly different. The Boussinesq approximation is still used but the turbulent viscosity is now determined by two turbulence scales: generally speaking, length and time scales, and, in this model, the turbulent kinetic energy k (related to the turbulent velocity scale) and its dissipation rate, ϵ (related to the length scale). This necessitates the solution of two extra equations, for which a standard form has been given by Jones and Launder (1972). The presence of these two equations breaks the conservative character of the Navier-Stokes equations (which was preserved in spite of averaging in the first step) and yields the pressure terms to be modified by a "turbulent pressure" contribution. The matrix form of the equation is now:

$$\frac{\partial}{\partial t} \vec{U} + \frac{\partial}{\partial x} \vec{F} + \frac{\partial}{\partial y} \vec{G} = \vec{H}$$

$$\vec{U} = \begin{bmatrix} \bar{\rho} \\ \bar{\rho}\tilde{U} \\ \bar{\rho}\tilde{V} \\ \bar{\rho}\tilde{E} \\ \bar{\rho}\tilde{k} \\ \bar{\rho}\tilde{\epsilon} \end{bmatrix} \quad \vec{H} = \begin{bmatrix} 0 \\ 0 \\ 0 \\ 0 \\ P_t - \bar{\rho}\tilde{\epsilon} - 2\mu \left(\frac{\partial\sqrt{\tilde{k}}}{\partial y}\right)^2 - \overline{u''} \frac{\partial\bar{P}}{\partial x} - \overline{v''} \frac{\partial\bar{P}}{\partial y} \\ C_\epsilon^1 \frac{\tilde{\epsilon}}{\tilde{k}} P_t - C_\epsilon^2 f_2 \bar{\rho} \frac{\tilde{\epsilon}^2}{\tilde{k}} + 2\mu_t \frac{\mu}{\rho} \left(\frac{\partial^2\tilde{U}}{\partial y^2}\right)^2 - C_\epsilon^3 \frac{\tilde{\epsilon}}{\tilde{k}} \left(\overline{u''} \frac{\partial\bar{P}}{\partial x} + \overline{v''} \frac{\partial\bar{P}}{\partial y}\right) \end{bmatrix}$$

$$\vec{F} = \begin{bmatrix} \bar{\rho}\tilde{U} \\ \bar{\rho}\tilde{U}^2 + \sigma_x \\ \bar{\rho}\tilde{U}\tilde{V} + \tau_{xy} \\ (\bar{\rho}\tilde{E} + \sigma_x)\tilde{U} + \tau_{yx}\tilde{V} - \left(\frac{\mu}{P} + \frac{\mu_t}{P_{rt}}\right)C_v \frac{\partial\tilde{T}}{\partial x} \\ \bar{\rho}\tilde{U}\tilde{k} + \sigma_{kx} \\ \bar{\rho}\tilde{U}\tilde{\epsilon} + \sigma_{\epsilon x} \end{bmatrix} \quad \vec{G} = \begin{bmatrix} \bar{\rho}\tilde{V} \\ \bar{\rho}\tilde{U}\tilde{V} + \tau_{xy} \\ \bar{\rho}\tilde{V}^2 + \sigma_y \\ (\bar{\rho}\tilde{E} + \sigma_y)\tilde{V} + \tau_{xy}\tilde{U} - \left(\frac{\mu}{P} + \frac{\mu_t}{P_{rt}}\right)C_v \frac{\partial\tilde{T}}{\partial y} \\ \bar{\rho}\tilde{V}\tilde{k} + \sigma_{ky} \\ \bar{\rho}\tilde{V}\tilde{\epsilon} + \sigma_{\epsilon y} \end{bmatrix}$$

in which

$$P_x = 2\mu_t \left[\left(\frac{\partial \tilde{U}}{\partial x} \right)^2 + \left(\frac{\partial \tilde{V}}{\partial y} \right)^2 \right] - \frac{2}{3} \left(\frac{\partial \tilde{U}}{\partial x} + \frac{\partial \tilde{V}}{\partial y} \right) \left[\mu_t \left(\frac{\partial \tilde{U}}{\partial x} + \frac{\partial \tilde{V}}{\partial y} \right) + \overline{\rho k} \right] + \mu_t \left(\frac{\partial \tilde{U}}{\partial y} + \frac{\partial \tilde{V}}{\partial x} \right)^2$$

$$\mu_t = 0.09 e^{-2.5/(1+Ret/50)} \cdot \frac{\overline{\rho k}}{\epsilon} \sim^2$$

$$Ret = \frac{\overline{\rho k}^2}{\mu_t \epsilon} ; f_2 = 1.0 - 0.30 \exp(-Ret)$$

According to Rubesin (1976), the polytropic gas assumption allows us to write

$$\overline{u''} = \mu_t \left[2\tilde{U} \frac{\partial \tilde{U}}{\partial x} + \tilde{V} \left(\frac{\partial \tilde{U}}{\partial y} + \frac{\partial \tilde{V}}{\partial x} \right) - \frac{2}{3} \tilde{U} \left(\frac{\partial \tilde{U}}{\partial x} + \frac{\partial \tilde{V}}{\partial y} \right) - \frac{2}{3} \overline{\rho U k} \right] \frac{\gamma C_v \tilde{T}}{(n-1)}$$

$$\overline{v''} = \mu_t \left[\tilde{U} \left(\frac{\partial \tilde{U}}{\partial y} + \frac{\partial \tilde{V}}{\partial x} \right) + 2\tilde{V} \frac{\partial \tilde{V}}{\partial y} - \frac{2}{3} \tilde{V} \left(\frac{\partial \tilde{U}}{\partial x} + \frac{\partial \tilde{V}}{\partial y} \right) - \frac{2}{3} \overline{\rho V k} \right] \frac{\gamma C_v \tilde{T}}{(n-1)}$$

where $n = 1.2$ is the polytropic coefficient.

$$\sigma_x = \overline{P} + \frac{2}{3} \overline{\rho k} - (\mu + \mu_t) \left[2 \frac{\partial \tilde{U}}{\partial x} - \frac{2}{3} \left(\frac{\partial \tilde{U}}{\partial x} + \frac{\partial \tilde{V}}{\partial y} \right) \right]$$

$$\sigma_y = \overline{P} + \frac{2}{3} \overline{\rho k} - (\mu + \mu_t) \left[2 \frac{\partial \tilde{V}}{\partial y} - \frac{2}{3} \left(\frac{\partial \tilde{U}}{\partial x} + \frac{\partial \tilde{V}}{\partial y} \right) \right]$$

$$\tau_{xy} = \tau_{yx} = -(\mu + \mu_t) \left(\frac{\partial \tilde{U}}{\partial y} + \frac{\partial \tilde{V}}{\partial x} \right)$$

$$\sigma_{kx} = -\left(\mu + \frac{\mu_t}{\sigma_k}\right) \frac{\partial \tilde{k}}{\partial x} ; \sigma_{ky} = -\left(\mu + \frac{\mu_t}{\sigma_k}\right) \frac{\partial \tilde{k}}{\partial y}$$

$$\sigma_{\epsilon x} = -\left(\mu + \frac{\mu_t}{\sigma_\epsilon}\right) \frac{\partial \tilde{\epsilon}}{\partial x} ; \sigma_{\epsilon y} = -\left(\mu + \frac{\mu_t}{\sigma_\epsilon}\right) \frac{\partial \tilde{\epsilon}}{\partial y}$$

The values of the different constants are:

$$C_\epsilon^1 = 1.45; C_\epsilon^2 = 1.94; C_\epsilon^3 = 2.0; \sigma_k = 1; \sigma_\epsilon = 1.30; P_r = 0.72; P_{rt} = 0.9$$

The Numerical Method

The MacCormack (1981) method, which is used here, has the following main characteristics:

- second-order accurate in space and time,
- unconditionally stable,
- no block or scalar tridiagonal matrix inversion,
- allowance of very large CFL numbers (up to 10,000).

The method uses the classical predictor-corrector scheme. The predictor or corrector steps are themselves split into two stages: the first one determines the local change of the solution by explicitly approximating the governing equations. The second stage uses the local solution change with an implicit procedure to determine the actual solution that is to be used to update the solution.

Practical Aspects of the Computations

Computation grid

The grid is made of two parts: the fine mesh has points exponentially stretched in the cross-flow direction which allows a fairly good resolution of the boundary layer in the region close to the solid wall ($y^+ = 1.0$). The coarse grid has a constant spacing in the cross-flow direction. Both grids can be stretched in the streamwise direction to get a better resolution in a specific zone of interest as a shock wave or an interaction region. Most of the calculations have been performed with a 32×32 grid.

Boundary conditions

The boundary-condition problem has been found much easier to handle for Cases 8101 and 8201 than for Case 8612. In the first two cases the flow is supersonic (except close to the wall), and constant or extrapolated boundary values give good results. For the last case, the problem is completely different. Before going into detail in the description of these boundary conditions, it must be emphasized here that one of the goals for this work is to provide a computational tool, which would require as little as possible initial information to describe properly a complex flow pattern, without supplying the main characteristics, such as the shock-wave presence in the initial flow field. Such a computer code should be used like a wind tunnel for which, when the model is set in, it is necessary to adjust only one or two valves to control the whole flow field, the geometries of the model, and the test section governing the flow pattern. Such a requirement is very restrictive on the boundary-condition determination, but it allows us to start the calculation of a given geometry with an arbitrary initial flow field. This allows us also to include a rigid wall as upper boundary and ignore a priori the normal shock position.

At the inlet, the boundary conditions prescribe:

- the normal velocity is equal to zero,
- the input mass flow rate is constant,
- the entropy is constant,
- the density and pressure satisfy a compatibility relation along a characteristic line (see Moretti and Pandolfi, 1981).

At the outlet, the boundary values are given by one-sided difference forms of the continuity, v-momentum, and energy equations, together with a given value for the

pressure. At both boundaries, the turbulence can be obtained by zero-order extrapolation.

For upper and lower boundary conditions, zero values are prescribed for the velocities, and zero gradient for all the other quantities, including k and ϵ . To insure physical behavior of the turbulence quantities in the vicinity of the lower wall, the turbulent viscosity is set to zero. This prescription is not necessary for the upper wall because the mesh points are not close enough to each other to resolve the viscous effects of the upper boundary layer. Nevertheless, the correct choking of the flow is insured and therefore the normal shock position.

The initial flow field

The use of the boundary conditions described in the previous paragraph allows us to start the calculation with a more or less arbitrary constant-flow field and the boundary conditions are sufficient for the equations to completely build the flow field.

For the flat-plate boundary-layer computations, the free-stream values are assumed everywhere, and for the channel-flow calculation, the inlet values are used.

Typical runs

The code has been set up in such a way that whatever the turbulence model is, the computing times are identical.

For a typical flat-plate calculation, the residual error of the skin-friction coefficient is 0.00002 after 128 time steps, which corresponds to 128 sec of CPU time on a CDC7600 computer. For a channel-flow calculation, the program converged after 1000 time steps with the same accuracy.

References

- Delery, J. (1978). "Analyse du décollement résultant d'une interaction choc-couche limite turbulente en transonique," La Recherche Aéronautique, 6, 305-320.
- Jones, W. P., and B. E. Launder (1972). "The prediction of laminarization with a two equation model of turbulence," IJHMT, 15, 310-314.
- MacCormack, R. W. (1981). "A numerical method for solving the equations of compressible viscous flow," AIAA Paper 81-0110, St. Louis, MO.
- Moretti, G., and M. Pandolfi (1981). "Critical study of calculation of subsonic flows in ducts," AIAA Jou., 19:4, 449-457.
- Rubesin, M. W. (1976). "A one equation model of turbulence for use with the compressible Navier-Stokes equations," NASA TM X-73, 128.

COMPARISON OF COMPUTATION WITH EXPERIMENT

Summary Report (Turbulent Recirculating Flows)

by
Ha Minh Hieu, P. Chassaing*
and D. D. Vandromme†
Computer Group Number: 44²



P. Chassaing

Case 0421

INTRODUCTION

A primitive variable method (U,V,P) has been developed to solve the steady time-averaged Navier-Stokes equations for incompressible turbulent recirculating flows. This numerical method is used here to calculate the two-dimensional flow over a backward-facing step. The boundary conditions and the geometry are identical to the experiments of Kim et al. (1978). A two-equation turbulence model is used here, where two transport equations are solved for the turbulence scales: the turbulent kinetic energy, k , and its dissipation rate, ϵ . Two different wall functions are used: the classical one using equilibrium and the Couette flow hypothesis, and the more recent version suggested by Launder (1980). Although the code can be used for variable-density flow calculations, only constant-density calculations are reported here.

The Navier-Stokes Equations

When ensemble-averaging is applied to the Navier-Stokes equations, some new unknown terms appear that make the turbulence-closure problem. The closure of the equations can be achieved by using a gradient-flux approximation in which the diffusivity coefficient (eddy viscosity) is determined either by an algebraic relationship or by some turbulence characteristic scales, such as the turbulent kinetic energy and its dissipation rate. The following equations are included in the numerical procedure:

$$\frac{\partial}{\partial x} \rho \bar{U} + \frac{\partial}{\partial y} \rho \bar{V} = 0$$
$$\frac{\partial}{\partial x} [\rho \overline{UU} - \nu_{\text{eff}} \frac{\partial \bar{U}}{\partial x}] + \frac{\partial}{\partial y} [\rho \overline{UV} - \nu_{\text{eff}} \frac{\partial \bar{U}}{\partial y}] = - \frac{\partial}{\partial x} [\bar{P} + \frac{2}{3} \rho k] + S_u$$
$$\frac{\partial}{\partial x} [\rho \overline{UV} - \nu_{\text{eff}} \frac{\partial \bar{V}}{\partial x}] + \frac{\partial}{\partial y} [\rho \overline{VV} - \nu_{\text{eff}} \frac{\partial \bar{V}}{\partial y}] = - \frac{\partial}{\partial y} [\bar{P} + \frac{2}{3} \rho k] + S_v$$

where

*Institut de Mécanique des Fluides de Toulouse, 31071 Toulouse, France

†NASA Ames Research Center, Moffett Field, CA 94035

$$\mu_{\text{eff}} = \mu_{\text{lam}} + \mu_t ; \quad \mu_t = C_D \rho \frac{k^2}{\epsilon}$$

$$\frac{\partial}{\partial x} \left[\rho \bar{U} k - \left(\mu + \frac{\mu_t}{\sigma_{tk}} \right) \frac{\partial k}{\partial x} \right] + \frac{\partial}{\partial y} \left[\rho \bar{V} k - \left(\mu + \frac{\mu_t}{\sigma_{tk}} \right) \frac{\partial k}{\partial y} \right] = P_k - \rho \epsilon$$

$$\frac{\partial}{\partial x} \left[\rho \bar{U} \epsilon - \left(\mu + \frac{\mu_t}{\sigma_{t\epsilon}} \right) \frac{\partial \epsilon}{\partial x} \right] + \frac{\partial}{\partial y} \left[\rho \bar{V} \epsilon - \left(\mu + \frac{\mu_t}{\sigma_{t\epsilon}} \right) \frac{\partial \epsilon}{\partial y} \right] = C_\epsilon^1 \frac{\epsilon}{k} P_k - \rho C_\epsilon^2 \frac{\epsilon^2}{k}$$

where

$$P_k = \mu_t \left[2 \left(\frac{\partial \bar{U}}{\partial x} \right)^2 + 2 \left(\frac{\partial \bar{V}}{\partial y} \right)^2 + \left(\frac{\partial \bar{U}}{\partial y} + \frac{\partial \bar{V}}{\partial x} \right)^2 \right] \quad (\text{in the incompressible case})$$

and

$$C_D = 0.09 ; \quad C_\epsilon^1 = 1.43 ; \quad C_\epsilon^2 = 1.92 ; \quad \sigma_\epsilon = 1.3 ; \quad \sigma_k = 1.0$$

$$S_u = \frac{\partial}{\partial x} \left[\mu_t \frac{\partial \bar{U}}{\partial x} \right] + \frac{\partial}{\partial y} \left[\mu_t \frac{\partial \bar{V}}{\partial x} \right] ; \quad S_v = \frac{\partial}{\partial x} \left[\mu_t \frac{\partial \bar{V}}{\partial y} \right] + \frac{\partial}{\partial y} \left[\mu_t \frac{\partial \bar{U}}{\partial y} \right]$$

These transport equations can be written with a common form, assuming that ϕ is any transport variable:

$$\text{div} \left[\rho \bar{V} \phi - \left(\mu + \frac{\mu_t}{\sigma_\phi} \right) \text{grad } \phi \right] = S_u(\phi)$$

The Numerical Procedure

All transport equations are integrated over a control volume leading to a relationship between four cardinal nodes surrounding the control volume and the central node. The source terms are calculated by averaging over the control volume while the convective and diffusive terms are determined on the control surface. These relationships are transformed into linear equations solved with a tridiagonal matrix algorithm. The grid is staggered in three different systems, respectively, U, V, and the other dependent variables. Centered and hybrid schemes are used for convective and diffusive terms. The pressure is obtained from a Poisson equation, where the source term plays the role of an artificial compressibility.

Wall Boundary Conditions

Wall function treatments are applied at the wall-adjacent nodes in order to save computing time and storage. Two different approaches are used:

(a) The shear stress is assumed uniform from the wall to the first adjacent grid line. It is obtained from the modified logarithmic law for the smooth flat plate,

$$U^+ = \frac{U}{U_*} = \frac{1}{0.41} \log [9y^+] \quad \text{for } y^+ > 11.5$$

where

$$U_* = \frac{\tau_w}{\rho C_D^{1/4} k^{1/2}} \quad \text{and} \quad y^+ = \rho k^{1/2} y / \mu .$$

τ_w is determined for $y^+ \geq 11.5$ from

$$\tau_w = 0.41 C_D^{1/4} \rho U_P k_P^{1/2} / \log [9 \rho y_P k_P^{1/2} / \mu]$$

where P indicates the adjacent node. A viscous formula is used to calculate ϵ_w if $y^+ < 11.5$. When τ_w is used as a boundary condition for U or V in the wall zone, the average of two shear values on both sides of the control volume is required. In the same way, two different values of the dissipation rate are used: the first (mean value over near-wall cell) is required for the source terms of the turbulence kinetic energy equation, the second value (defined locally) is used for the dissipation equation.

(b) In the second treatment due to Chieng and Launder (see Launder, 1980) the wall shear stress is obtained from the relationship

$$\tau_w = 0.23 \rho U_P k_v^{1/2} / \log [5.0 y_P k_v^{1/2} / \nu]$$

where U_P is the velocity component parallel to the wall at the first near-wall node, y_P is the normal distance from this node to the wall, and k_v is the kinetic energy at the edge of the viscous sublayer obtained by linear extrapolation from the interior to the edge of the sublayer, of which the thickness satisfies

$$y_v k_v^{1/2} / \nu = 20$$

The local value of the dissipation rate is

$$\epsilon_p = 4 k_p^{3/2} / y_p$$

and the mean value used as a source term in the kinetic energy equation is

$$\bar{\epsilon} = \frac{1}{y_e} \left[\frac{2\nu k}{y_v} + k_p^{3/2} \log \left(\frac{y_e}{y_v} \right) \right]$$

where y_e is the nearest node for the velocity.

Flow Boundary Conditions

The upper boundary is a symmetry axis with zero gradient condition on it. The experimental values of Kim et al. (1978) are used as inlet boundary conditions.

Characteristics of the Computations

The computations are made with a 40 x 40 non-uniform grid. The convergence is obtained after 1250 iterations, for which the residual-mass source error over the whole flow field is 0.00097 times the main-mass flow rate.

All the calculations have been performed on a DEC VAX 11/780 computer. This corresponds to 90 min CPU on this class of machine (about 0.0027 sec for 1 grid point/iteration).

REFERENCES

- Kim, J., S. J. Kline, and J. P. Johnston (1978). "Investigation of separation and reattachment of a turbulent shear layer: flow over a backward-facing step," Report MD-37, Stanford University.
- Launder, B. E. (1980). "Treatment of low Reynolds number regions. II. Wall function treatments," VKI LS 1980-3, Belgium.

COMPARISON OF COMPUTATION WITH EXPERIMENT

Summary Report

(Calculation of Five Turbulent Flows Using the Moore Cascade Flow Program)

by

J. Moore and J. G. Moore*

Computer Group Number: 01

Cases 0141, 0142, 0143, 0512, 0612

INTRODUCTION

Calculations have been performed for five of the turbulent flows. The calculations have been used as a basis for evaluating the Moore Cascade Flow Program (Moore and Moore, 1981) and its ability to model boundary-layer and duct flows in relatively simple geometries. The flows considered are a flat-plate boundary layer, a boundary layer in an adverse pressure gradient, flows with high and low inlet turbulence in a conical diffuser, and flow in a 90° bend of constant cross-sectional area. Overall the agreement is good, especially with the measured turbulent shear stresses in the boundary layers and in the diffuser, and with the secondary-flow velocities in the 90° bend.

VISCOSITY MODEL

The mixing-length model for turbulent viscosity uses the following well known relations:

$$l = 0.41y \left[1 - \exp\left(\frac{-y(\rho\tau)^{1/2}}{26\mu_l}\right) \right]$$

$$l = 0.08\delta \quad \text{boundary layer}$$

$$l = 0.08W \quad \text{shear layer}$$

$$\mu_{\text{eff}} = \mu_l + \mu_t = \mu_l + \rho l^2 \frac{du}{dy}$$

In addition, mid-way between the wall and near-wall grid points, the effective viscosity is calculated using the relation

$$\mu_{\text{eff}} = \mu_l^{1/2} (\mu_t + \mu_l)^{1/2}$$

*Virginia Polytechnic Institute and State University, Blacksburg, VA 24061

Case 0612. The Wieghardt Flat-Plate Boundary Layer

The flow was modeled as being on the bottom wall of a rectangular duct whose height was 0.5 m plus the measured displacement thickness, which increased to 0.0092 m. The other three walls were specified as inviscid walls. Since the calculated displacement thicknesses agreed well with the measured values along the plate, this geometry resulted in a calculated free-stream velocity of 33.000 ± 0.001 m/s.

The calculations were started at $x = 0.187$ m, using the measured velocity profile, and were carried out to $x = 4.987$ m.

Grid point locations (relative spacing). Normal to viscous wall: 0, 0.0004, 0.001, 0.002, 0.004, 0.008, 0.016, 0.03, 0.06, 0.12, 0.24, 0.48, 1. In transverse direction: 0.1.

Steps. 35 steps varying in length from 0.02 m initially to 0.4 m finally; these step sizes correspond to between 4 and 6 local boundary-layer thicknesses.

Mixing-length model (0.08 δ). To account for the large change, the boundary-layer thickness δ was calculated at $U/U_e = 0.995$ for use in the expression 0.08 δ used to obtain the mixing length in the outer part of the boundary layer. The free-stream mixing length was set to zero.

Case 0141. Samuel and Joubert, Boundary Layer in Adverse Pressure Gradient

The Samuel and Joubert flow geometry was modeled as a rectangular duct of varying height and 1 m width. The boundary layer was calculated on the flat-bottom wall. The height was calculated using an initial height of 1 m; height variations along the duct were calculated using the measured wall-static pressure coefficient together with Bernoulli's equation for the free stream; these heights were then corrected using the measured displacement thicknesses for the test wall. A no-slip boundary condition was applied at the bottom wall and the other three walls were treated as inviscid.

The marching integration started at $x = 0.85$ m, using the measured velocity profile, and proceeded to $x = 3.4$ m.

Grid point locations (relative spacing). Normal to viscous wall: 0, 0.0003, 0.0012, 0.0048, 0.02, 0.04, 0.06, 0.08, 0.15, 0.3, 1. In transverse direction: 0, 1.

Steps. 14 steps varying in length from 0.05 m initially to 0.25 m finally; the step sizes were approximately twice the local boundary-layer thickness.

Viscosity model. A laminar viscosity of 0.000018 kg/m \cdot s was used together with the mixing-length model for turbulent viscosity. The characteristic length used to define the slope of the total pressure gradient at the edge of the boundary layer was 0.2 m. The free-stream mixing length was set to zero.

Results. The calculated skin-friction coefficients were normalized using a free-stream velocity of 27.0 m/s at $x = 0$. Good agreement with the data from the Clauser

plots and from the Preston tubes was obtained. The calculated values of turbulent shear stress were also in good agreement with the measured values.

Minor improvements to the calculated velocity profile at $x = 3.39$ m could result from a different choice of free-stream velocity distribution, which could be obtained from either measured velocities or by applying turbulence corrections to the static pressure distribution. Because of uncertainties in the experimental data these corrections were not applied.

Case 0142. Pozzorini Diffuser, Low-Core Turbulence

The geometry of the Pozzorini diffuser is such that the conical section is preceded by a straight cylindrical section and there is no rounding of the wall at the beginning of the conical diffuser. Data for starting calculations were given very close to the beginning of the diffuser, only 0.055 m upstream of the end of the cylindrical section. The shape of the velocity profile at this station showed a relatively high velocity near the wall, suggesting that the static pressure was locally low near the wall, due to the curvature of the flow entering the conical section. This also suggests that elliptic pressure calculations may be necessary to obtain improved agreement with the measured boundary-layer development near the beginning of the conical section. However, insufficient data were given upstream of $x = -0.055$ m to allow an elliptic calculation to be started in a region of parabolic flow with uniform static pressure across the inlet section. Such an elliptic calculation was therefore not attempted.

One pass of the marching-integration procedure was performed starting at $x = -0.055$ m and using the measured velocity profile. The static pressure was assumed uniform at this initial station. The parabolic flow calculation then allowed only one-dimensional variations in the pressure field, i.e., $p = p(x)$.

The calculation was performed for a duct with a pie-shaped cross-section. The included angle used was 0.5 radians. Axisymmetric flow was assumed and a viscous-wall boundary condition was applied at the diffuser wall. Inviscid-wall boundary conditions were applied on the two radial walls and on a small inviscid tube of radius 0.001 m along the axis of the diffuser. This geometry was chosen to satisfy the requirements of the Moore Cascade Flow Program, which is written for passages having cross-sections with four corners.

Grid point locations for Cases 0142 and 0143 (relative spacing). Radial direction (inwards from viscous wall): 0, 0.001, 0.0025, 0.005, 0.01, 0.02, 0.04, 0.08, 0.15, 0.3, 0.5, 0.75, 1. Circumferential direction (angle = 0.5 radians): 0, 1.

Mixing length model (0.086). The boundary-layer thickness δ was calculated at $U/U_{r=0} = 0.99$. The free-stream mixing length was set to zero for this low-core turbulence case.

Results. Some improvement in the calculated skin-friction coefficients and turbulent shear-stress distributions could be obtained near the beginning of the diffuser. As discussed above, it is likely that these improvements could have been achieved with an elliptic flow calculation had sufficient information to start an elliptic calculation been provided. It is unlikely that a change in the turbulence model alone could give sufficient improvement.

The static pressure recovery for the diffuser was well calculated by this parabolic calculation. Near the end of the diffuser, at $x = 1.81$ m, the calculated pressure coefficient of 0.74 agrees closely with the measured value of 0.71. The velocity profiles are also in similar good agreement.

Case 0143. Pozzorini Diffuser, High-Core Turbulence

The differences between Case 0142, low-core turbulence calculation and Case 0143, high-core turbulence calculation, are simply in the inlet velocity profile used to start the calculation and in the mixing-length viscosity model. Again the measured velocity distribution was used to start the calculation, but, to model the high-core turbulence, the mixing-length in the outer part of the boundary layer and the core of the flow was set to 0.08 times the local radius of the conical diffuser.

The results show reasonable agreement, but the boundary layer approaches separation more quickly in the calculations than is shown by the measurements. This may be partially explained by the calculated turbulent shear stresses being slightly too low.

Case 0512. Humphrey, 90° Bend with Square Cross-Section

Notes on the changing character of the flow. The specifications for computation call for calculations of the radial component of velocity at the beginning and end of the bend, $\theta = 0^\circ$ and 90° , respectively. These calculations are made complex by the changing character of the three-dimensional flow, which is influenced by at least three flow phenomena. Three major influences are:

- 1) flow redistribution due to elliptic pressure changes;
- 2) generation of streamwise vorticity due to curvature of flow with gradients of total pressure normal to the streamwise direction;
- 3) flow induced by non-isotropic turbulence.

The relative importance of these effects depends on the particular location considered.

Far upstream of the bend, the third influence, due to turbulence, will dominate the development of the three-dimensional flow. In our calculations, we included the influence of non-isotropic turbulence only through the three-dimensional flow which entered the bend. This inlet flow distribution has an effect on the results calculated at the beginning of the bend, but it becomes dominated first by the elliptic flow redistribution and then by the streamwise vorticity generated in the bend. This

streamwise vorticity dominates the three-dimensional flow until the end of the bend, where once again elliptic effects are important. Finally, downstream, the flow becomes parabolic again and turbulence effects grow in a flow still dominated by streamwise vorticity.

Only at the beginning of the bend are all three influences on the three-dimensional flow all significant at the same location. Thus only near this plane, one of those chosen for evaluation of the calculations, must all three effects be well modeled.

3-D partially-parabolic flow calculation. The pressure solution for the flow field was built up using:

- a) three two-dimensional, inviscid-flow passes with a uniform inlet flow;
- b) one three-dimensional, inviscid-flow pass with a distorted inlet flow based on the measured inlet velocity profile;
- c) two three-dimensional, viscous-flow passes using the measured inlet velocity profile.

The final viscous-flow pass was started at $x = -0.024$ m with a uniform static pressure distribution. This location was sufficiently far upstream of the beginning of the bend, that the static pressure variation, over the cross-section, calculated from earlier passes, was less than 10 N/m^2 (i.e., less than 0.03 times the peak pressure difference across the duct, later in the bend). The tabulated data of Melling were used for the u_x component of velocity, and the cross-flow velocity vectors, as given graphically in a supplement by Humphrey, were used for the u_y and u_z components. All the velocity components were adjusted for symmetry by considering 1/8 of the inlet cross-section.

The calculations were performed for half of the duct using a plane of symmetry mid-way between the end walls.

Grid point locations. Grid points were located at $B = 0, 0.003, 0.0125, 0.05, 0.1475, 0.3025, 0.45, 0.55, 0.6975, 0.8525, 0.95, 0.9875, 0.997, 1$; and $C = 0, 0.006, 0.025, 0.1, 0.295, 0.605, 0.9, 1$; where:

$B = 0$ is the suction surface; $B = 1$ is the pressure surface;

$C = 0$ is the end wall; $C = 1$ is the plane of symmetry.

Viscosity model. A laminar viscosity for water of $0.00089 \text{ kg/m}\cdot\text{s}$ was used to be consistent with the flow Reynolds number of 4×10^4 and the bulk mean velocity of 0.89 m/s . The characteristic width for shear-layer gradients was taken to be equal to the duct width of 0.04 m . The free-stream mixing length was set to 0.00008 m .

Turbulent shear stress. The turbulent shear stress $\overline{u_\theta u_r} / U_{\text{ref}}^2$ required for the plots was approximated by the expression $[(\mu_{\text{eff}} - \mu_{\text{lam}}) \partial u_\theta / \partial r] / \rho U_{\text{ref}}^2$.

Results. The mass flow rate corresponding to $U = 0.89$ m/s did not seem consistent with the contours of circumferential velocity given at $\theta = 0^\circ$. For our plots, therefore, we used a reference velocity $U_{ref} = 1.04 \times 0.89$ m/s. This value gave much improved agreement at $\theta = 0^\circ$. Also at this inlet station, the agreement with the measured values of radial velocity was good, indicating that the magnitude and relative importance of the elliptic vorticity, and turbulence effects on the three-dimensional flow were well modeled. The calculated values of turbulent shear stress at $\theta = 0^\circ$ were in reasonable agreement on the suction and pressure side walls. (Note that the plots are presented with a severely distorted scale.)

In the bend, the development of the flow is dominated by the generation of a streamwise component of vorticity and the magnitude of the secondary velocities grows to approximately 50% of the bulk-flow velocity. These high velocities occur near the end walls just upstream of the end of the bend. The data given at $\theta = 90^\circ$ partly reflect the strength of this vorticity by showing the corresponding secondary flow away from the walls. For example, on the plane of symmetry, the radially outward component of velocity is in excess of 28% of the bulk mean-reference velocity. The magnitude of this secondary flow velocity from the calculations is in excellent agreement with the measured value. Also the extent of the flow cross-section influenced by the outward velocities is very well described.

The influence of the streamwise vorticity on the development of the circumferential component of velocity is clearly seen in the data. The thickening of the boundary layer on the suction side near the plane of symmetry is a result of the transport of low momentum fluid by secondary flows and of the unloading of the pressure difference across the duct. This thickening was quite closely modeled. Also the contour shapes are in remarkable good agreement considering the closeness of the contour intervals chosen for the plots.

REFERENCE

Moore, J. and J. G. Moore (1981). "Calculations of three-dimensional, viscous flow and wake development in a centrifugal impeller," ASME, J. Eng. for Power, 103, 367-372.

COMPARISON OF COMPUTATION WITH EXPERIMENT

Summary Report

(Simultaneous Solution of the Turbulent
Boundary Layer and Inviscid Flow)

by

H. L. Moses,^{*} S. B. Thomason, J. M. Hill, and
R. R. Jones, III[†]

Computer Group Number: 27



H.L. Moses

Cases 0141, 0142, 0421, 0431, 0441, 0612

Abstract

A procedure for calculating turbulent boundary layers simultaneously with the inviscid flow is described for two-dimensional, incompressible flow, following the work of Moses (1968) and Moses et al. (1967, 1978, 1979, 1981). The method is intended as an engineering approximation for applications where there is a strong interaction between the boundary layer and an inviscid flow, especially where separation is involved. The stream-function equation is written in finite-difference form for the inviscid flow with integral equations for the boundary layers. At a given longitudinal position, the equations form a linear set with a tridiagonal coefficient matrix. The set is solved simultaneously at each position in a line-relaxation procedure, beginning at the upstream boundary and iterating over the flow field.

Introduction

In many engineering applications there is a need to predict overall performance characteristics, where there is a strong interaction between an essentially inviscid flow and turbulent boundary layers, particularly where separation is involved. Because of the difficulties in analyzing such flows, designers have relied heavily on experimental correlations in the past. However, where a large number of variables are involved, this approach is severely limited. Thus, there is a need for some type of analysis, even if it is essentially an elaborate correlation of experimental data.

The difficulty in predicting flow separation stems from the fact that the boundary-layer equations, with a fixed pressure distribution, exhibit a singular behavior and become unstable. Thus, a straightforward iteration between the boundary layer and inviscid flow is not possible. Only recently has there been a widespread effort to analyze such flows. These efforts generally attempt a solution of some form

^{*}Virginia Polytechnic Institute and State University, Blacksburg, VA

[†]Sverdrop Corp., ARO, Inc., Tullahoma, TN

of the time-averaged equations for the entire flow or a patching solution of the boundary-layer equation with the inviscid flow. In any case, the solutions must be regarded as approximate because of the numerics as well as the turbulence correlations. Furthermore, any two-dimensional, steady model of turbulent separation is an approximation. However, it does appear possible to obtain solutions of separated flows that are acceptable for engineering purposes, although more work is needed.

The purpose of the work described here is to develop a method for approximating flow fields that involve separation. Since the method is fully described in the listed references, only a summary is given here, with a discussion of its application.

Summary of Method

In the work reported here, a simple rectangular grid system (see Fig. 1) was employed, but this simplification is not necessary. For this system, the inviscid-stream-function equations are

$$A \psi_{j,i,j-1} + B \psi_{j,i,j} + C \psi_{j,i,j+1} = D_j \quad (1)$$

where coefficients only depend on the grid spacing, $\psi_{i-1,j}$, and $\psi_{i+1,j}$ for incompressible flow.

For the first grid point away from a solid surface (Fig. 2) the bounding stream function is eliminated from equation 1 by the linear approximation,

$$\psi_{i,1} = \psi_{i,2} - \Delta y_1 U_1 / \left(\frac{ds}{dx} \right)_1 \quad (2)$$

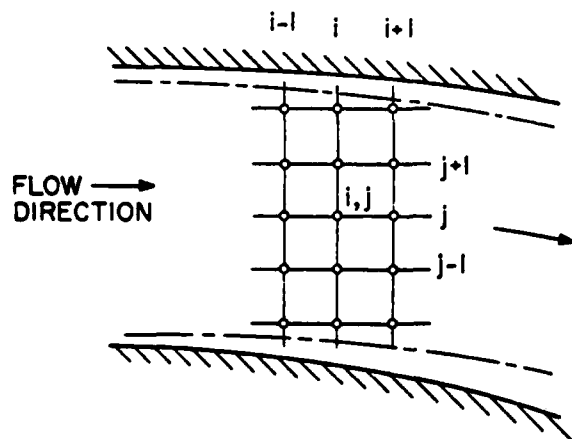


Figure 1. Grid system for inviscid-flow region.

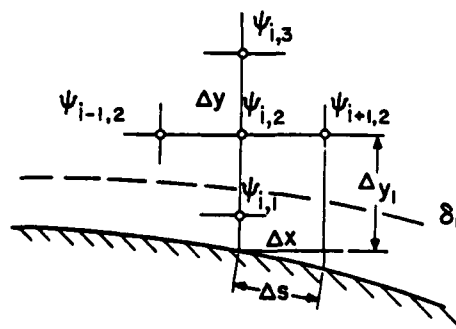


Figure 2. Grid system at boundary layer.

To obtain a relation between the boundary-layer displacement, the edge velocity, and the first calculated stream function, a similar linear relation is employed,

$$U_1 = (\psi_{1,2} - \psi_\delta^*) / [\Delta y_1 (\frac{dx}{ds})_1 - \delta_1^*] \quad (3)$$

where ψ_δ^* is the stream function value on the displaced boundary, which is assumed to be a known constant. (Assuming a constant value for both stream functions results in the one-dimensional pressure assumption.) Equation 3 is differentiated with backward differencing to yield a linear equation of the form,

$$A_3 \delta_1^* + B_3 U_1 + C_3 \psi_{1,2} = D_3 \quad (4)$$

An integral method is employed for the boundary layer, which can be written (again with backward differencing) in the form

$$B_1 H_1 + C_1 \delta_1^* = D_1 \quad (5)$$

and

$$A_2 H_1 + B_2 \delta_1^* + C_2 U_1 = D_2 \quad (6)$$

At any longitudinal position, Eqs. 1, 4, 5, and 6 form a linear set with a tridiagonal coefficient matrix. The set is solved with a line-relaxation procedure, starting at the upstream boundary and iterating over the flow field until convergence is achieved.

It is emphasized that the primary concern here is the approximate solution of the entire flow field where separation is involved. Almost all integral methods can be reduced to the form of Eqs. 5 and 6, so the basic procedure is not restricted to the simple approximations presented here.

In the work presented here, Eqs. 5 and 6 were derived from the momentum and kinetic-energy integral equations. These equations require three correlations for closure: the skin friction, a relation for the second shape factor, and the dissipation integral. If separated flow is included, this condition must be considered in developing the correlations. A number of different approximations have been considered by the authors, and further work is continuing. The correlations given below are the simplest ones that gave acceptable results for all cases considered.

$$H_{32} = \frac{4H}{3H-1} \quad (7)$$

$$C_f = 0.246 R_\theta^{-0.268} 10^{-0.678H} \quad (8)$$

and

$$C_d = 0.004 H/R_\theta^{-0.1667} ; C_d \leq 0.01 \quad (9)$$

If velocity-profile information is desired, the velocity must be related to the integral parameters. In the present work, the usual logarithmic profiles were assumed for

the attached boundary layer. For the separated boundary layer, a wake or free-shear-layer profile was assumed with a region of approximately zero velocity near the surface.

Discussion

The simultaneous solution procedure has been applied to a number of flows with stable and convergent results. However, some of the integral parameter correlations attempted, which seemed quite realistic, did not yield reasonable predictions. Thus, some care must be exercised in selecting these correlations, particularly when large regions of separated flow are included.

Since the method is very approximate, a relatively large grid spacing was used for most of the calculations. A finer mesh did not improve the results within the uncertainty involved with the approximations. The calculations, which were run on an IBM-370, have not been optimized for computational time.

The boundary-layer flows, Cases 0612 and 0141, were calculated with the given pressure distribution. As is typical with integral methods, acceptable results were obtained in a few seconds of computational time.

The unseparated diffuser, Case 0142, was run with the method as described and also with a one-dimensional pressure assumption. Since this flow is nearly parabolic, the overall results were essentially the same. The two-dimensional case, which was run with a grid of 6×100 points, required approximately 50 iterations for convergence and a computational time of 60 sec. The axially symmetric form of the boundary-layer equations was used, but transverse curvature effects were not included.

Since the effective geometry for the separated diffuser, Case 0431, was determined with a one-dimensional pressure assumption, this was also used in the calculations. In this case only one pass was needed, and the calculated results were obtained in a very few seconds.

Although the method was not developed for large regions of separation, such as a backward-facing step, this flow (Case 0421) was included to determine if it could be treated without extensive modifications. This flow was calculated as an 89° diffuser, with the only modification being an extension of the dissipation integral for large values of the shape factor to approximate that for a free-shear layer.

The stalled airfoil, Case 0441, was run with a variable grid spacing and 20 points along the chord. In this case, the boundary layer upstream of the first measured station and on the entire pressure side was not calculated. The wake was approximated by a source, and was not calculated. Iteration on the dividing streamline was required as well as that required to relax the solution. For a convergence criterion of 10^{-5} , a total computational time of approximately 5 min was required.

Conclusions

An approximate procedure for calculating the turbulent boundary layers simultaneously with the inviscid flow has been demonstrated for a number of cases. The primary advantages of the method are short programming and computational times and the ability to calculate separated flows. A single set of boundary-layer correlations have been used for all flow cases with no attempt to optimize them for each case. Although more work is needed on these correlations, acceptable results have been obtained for most applications.

References

- Moses, H. L. (1968). "A strip-integral method for predicting the behavior of turbulent boundary layers," Proceedings, Computation of Turbulent Boundary Layers--1968 AFOSR-IFP-Stanford Conference, Vol. I, Stanford University, Stanford, CA, pp. 76-82.
- Moses, H. L., and J. R. Chappell (1967). "Turbulent boundary layers in diffusers exhibiting partial stall," J. Basic Eng., 89, 655-665.
- Moses, H. L., R. R. Jones, W. F. O'Brien, and R. L. Peterson (1978). "Simultaneous solution of the boundary layer and freestream with separated flow," AIAA Jou., 16:1, 61-66.
- Moses, H. L., J. F. Sparks, and R. R. Jones (1979). "An integral method for the turbulent boundary layer with separated flow," in Turbulent Boundary Layers, H.E. Weber (ed.), ASME.
- Moses, H. L., S. B. Thomason, and R. R. Jones (1981). "Simultaneous solution of the inviscid flow and turbulent boundary layers for compressor cascades, AIAA Paper No. 81-1476.



COMPARISON OF COMPUTATION WITH EXPERIMENT

Summary Report

by

J. D. Murphy*

Computer Group Number: 28

Cases 0141, 0431, 0612

The basic numerical procedure is described in Murphy (1977), and the turbulence models together with parametric studies on nodal spacing and boundary conditions are described in Murphy and Rubesin (1979).

Briefly, the equations considered are the incompressible time-averaged Navier-Stokes equations in stream-function/vorticity variables. These may be written as:

$$\omega = \frac{\partial^2 \psi}{\partial y^2} + \frac{1}{\text{Re}} \frac{\partial^2 \psi}{\partial x^2} \quad (1)$$

$$\frac{\partial \psi}{\partial y} \frac{\partial \omega}{\partial x} - \frac{\partial \psi}{\partial x} \frac{\partial \omega}{\partial y} = \frac{\partial^2 \omega}{\partial y^2} + \frac{1}{\text{Re}} \frac{\partial^2 \omega}{\partial x^2} + \frac{\partial \tau_{xy}}{\partial y} + \frac{1}{\text{Re}} \frac{\partial \tau_{xy}}{\partial x} + \frac{4}{\text{Re}} \frac{\partial^2 \epsilon}{\partial x \partial y} \frac{\partial^2 \psi}{\partial x \partial y} \quad (2)$$

and

$$\tau_{xy} = \frac{\epsilon}{\nu} \left(\omega - \frac{2}{\text{Re}} \frac{\partial^2 \psi}{\partial x^2} \right) \quad (3)$$

The boundary conditions are

$$y = 0, \quad \psi = \frac{\partial \psi}{\partial y} = 0$$

$$y = y_{\max}, \quad \frac{\partial \psi}{\partial y} = \frac{u_e(x)}{u_0}, \quad \omega = 0$$

$$x = x_0, \quad \psi = \psi(x_0, y), \quad \omega = \omega(x_0, y)$$

$$x = x_{\max}, \quad \frac{\partial^2 \psi}{\partial x^2} = \frac{\partial^2 \omega}{\partial x^2} = \frac{\partial^2 \tau_{xy}}{\partial x^2} = \frac{\partial^2 \epsilon}{\partial x \partial y} \frac{\partial^2 \psi}{\partial x \partial y} = 0$$

Splined cubic Taylor's series expansions are used to represent the unknowns and their derivatives. The block tridiagonal system is solved by Newton-Raphson iteration and the solution is fourth-order accurate in y and second-order accurate in x . An additional equation or system of equations is used to define the eddy viscosity. In the present study the several models considered are:

*NASA-Ames Research Center, Moffett Field, CA 94035

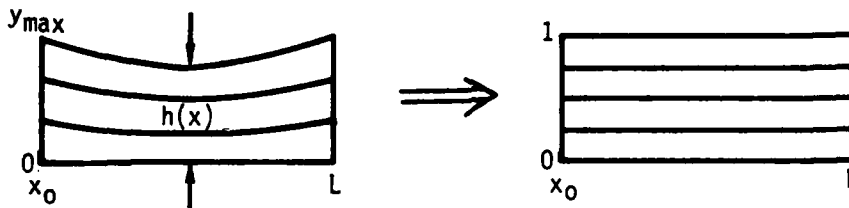
- BOPX - The Cebeci-Smith model (Cebeci, 1970). No intermittency or pressure-gradient correction is made.
- BLKX - The Glushko model (Glushko, 1966). Integration to the wall.
- BKEX - The Jones-Launder model (Jones and Launder, 1973). No wall functions used.
- BKWX - The Wilcox-Rubesin model (Wilcox and Rubesin, 1980). Energy equation is integrated to wall. Specific dissipation varies like $1/y^4$ near the wall and is constrained algebraically for $y^+ \leq 6$.

The Wieghardt flat plate, Case 0612, and the Samuel-Joubert increasing adverse pressure gradient, Case 0141, were solved using each of the above models, as in Murphy and Rubesin (1979).

The last flow considered here is the separating diffuser of Simpson et al., Case 0431. Although a similar case was treated in Murphy and Rubesin (1979), a substantial modification to the code was introduced to treat this case in the present study. In addition to the transformations used in Murphy (1977) and Murphy and Rubesin (1979), the stream-normal coordinate was transformed by the relation

$$\tilde{y} = y/h(x)$$

where $h(x)$ was the streamline trajectory given in the case description. This transformation maps the diffuser shape onto a rectangle. See sketch.



On the upper boundary, $\tilde{y} = 1$, we prescribe a constant stream function. The velocity distribution and skin friction are prescribed at X_0 , and at L all second-derivatives with respect to x are set to zero. In addition, for this case only, the streamwise diffusion is set to zero in the vorticity-transport equation for all x and y . This latter approximation reduces the time averaged Navier-Stokes equations to the so-called thin-layer approximation. Note that the system is still elliptic due to the definition of vorticity. The turbulence model used in these calculations was that proposed by Baldwin and Lomax (1978), which circumvented the problems associated with ill-defined integral parameters in non-boundary-layer methods.

As in Murphy (1977) and Murphy and Rubesin (1979), the initial guess used by the relaxation procedure for the time-averaged Navier-Stokes equations is obtained by a

marching pass through the mesh with all $\partial/\partial x^2$ set to zero, which corresponds to the boundary-layer equations.

Since, in the present case, the stream-function rather than the edge velocity is prescribed, the boundary-layer equations do not encounter a singularity at the separation point and solutions were obtained for the parabolic calculation as well as the elliptic calculation. Although there are differences between the two solutions of a few percent, they are too small to show up to the scale of the plots presented.

The skin-friction-coefficient plots are extended to contain all the data and to show both predicted and experimental separation points. The rather good agreement between predicted and measured skin friction, particularly as regards the separation point, must be regarded as fortuitous, since the predicted velocity gradient is too large by a factor of two in the region of the separation point, see Fig. 1. This figure provides a useful global figure of merit for the turbulence model since the proper growth of the viscous region will automatically provide the correct core velocity. We find that up to some neighborhood of the separation point, say roughly $x = 3$ m, all the parameters are reasonably well predicted, while downstream of this point, all the various parameters degrade progressively.

The machine times and nodal density for the results presented are shown in Table 1.

References

- Baldwin, B. S., and H. Lomax (1978). "Thin layer approximation and algebraic model for separated turbulent flows," AIAA Paper 78-257.
- Cebeci, T. (1970). "Behavior of turbulent flow near a porous wall with pressure gradient, AIAA Jou., 8:12, 2152-2156.
- Glushko, G. S. (1966). "Turbulent boundary layer on a flat plate in an incompressible fluid," NASA TT F-10080.
- Jones, W. A., and B. E. Launder (1973). "The calculation of low Reynolds number phenomena with a two equation model of turbulence," IJHMT, 16, 1119-1130.
- Murphy, J. D. (1977). "An efficient solution procedure for the incompressible Navier-Stokes equations," AIAA Jou., 15:9, 1307-1314.
- Murphy, J. D. and M. W. Rubesin (1979). "A Navier-Stokes fast solver for turbulence modeling applications." In "Turbulent Boundary Layers, Experiment, Theory, and Modeling," AGARD CP 271.
- Wilcox, D. C., and M. W. Rubesin (1980). "Progress in turbulence modeling for complex flow fields, including the effects of compressibility," NASA TP-1517, April 1980.

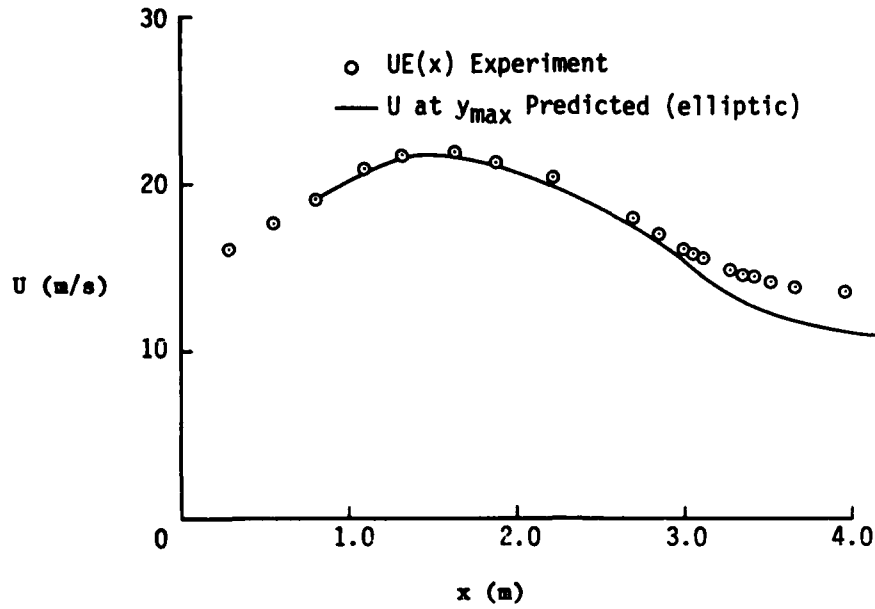


Figure 1. Predicted streamwise velocity distributions.

Table 1

Execution Time	7600 CPU seconds		
	M × N		
	30 × 25	22 × 31	30 × 27
	Wieghardt	Samuel & Joubert	Simpson
Cebeci-Smith	7.68	20.61	16.0* 43.0†
Glushko	13.44	22.01	
Jones-Lauder	15.45	24.33	
Wilcox-Rubesin	20.06	29.96	

*Parabolic Calculation.
†Elliptic Calculation.

COMPARISON OF COMPUTATION WITH EXPERIMENT

Summary Report

by

T. Nagamatsu*

Computer Group Number: 04

Cases 0141, 0231, 0232, 0233, 0612

1. The Governing Equations

For steady-state incompressible two-dimensional flows, the governing boundary-layer equations are (see Cebeci and Smith, 1974; Cebeci and Bradshaw, 1977),

Continuity

$$\frac{\partial}{\partial x}(\rho \bar{u}) + \frac{\partial}{\partial y}(\rho \bar{v}) = 0 \quad (1)$$

Momentum

$$\rho \bar{u} \frac{\partial \bar{u}}{\partial x} + \rho \bar{v} \frac{\partial \bar{u}}{\partial y} = \frac{\partial \bar{p}}{\partial x} + \frac{\partial}{\partial y} \left(\mu \frac{\partial \bar{u}}{\partial y} - \rho \overline{u'v'} \right) \quad (2)$$

The coordinate x denotes the distance along the surface measured from the leading edge. The coordinate y is measured normal to the surface. The velocity components in the x and y directions are u and v , respectively. ρ is the fluid density and μ is the coefficient of viscosity. Bars and primes represent time-averaged and fluctuating quantities, respectively.

The boundary conditions for the preceding equations are given as follows:

$$\begin{aligned} \bar{u}(x, 0) &= 0 \\ \bar{v}(x, 0) &= 0 \\ \bar{u}(x, \delta) &= \bar{u}_e(x) \end{aligned} \quad (3)$$

where δ is boundary-layer thickness.

Boussinesq's eddy-viscosity concepts are used to evaluate the turbulent transport quantity $-\rho \overline{u'v'}$

$$-\rho \overline{u'v'} = \rho \epsilon \frac{\partial \bar{u}}{\partial y} \quad (4)$$

We introduce the Falkner-Skan transformation as

$$\eta = \left(\frac{u_e}{\nu x} \right)^{1/2} y \quad (5)$$

where ν is the kinematic viscosity.

*Mitsubishi Heavy Ind. Ltd., Nagasaki, Japan

If $\Psi(x,y)$ is a stream function such that

$$\frac{\partial \Psi}{\partial y} = \bar{u}, \quad \frac{\partial \Psi}{\partial x} = -\bar{v} \quad (6)$$

then the continuity equation is satisfied. Introducing a dimensionless stream function $f(x,\eta)$ by

$$\Psi(x,y) = u_e \nu x^{1/2} f(x,\eta) \quad (7)$$

and using the new variable of Eq. (5) the momentum equation becomes

$$[(1+\epsilon^+)f'']' + \frac{m+1}{2} ff'' + m[1-(f')^2] = x(f' \frac{\partial f'}{\partial x} - f'' \frac{\partial f}{\partial x}) \quad (8)$$

Here the primes denote differentiation with respect to η .

The boundary conditions (3) now become

$$\begin{aligned} f(x,0) &= 0 \\ f'(x,0) &= 0 \\ f'(x,\delta) &= 1.0 \end{aligned} \quad (9)$$

In Eq. 8, ϵ^+ and m are defined as

$$\epsilon^+ = \frac{\epsilon}{\nu}, \quad m = \frac{x}{u_e} \frac{du_e}{dx} \quad (10)$$

2. Eddy-Viscosity Model

The Cebeci-Smith model is used for calculating two-dimensional turbulent boundary layer.

Inner region:

$$(\epsilon)_i = L^2 \left| \frac{\partial u}{\partial y} \right| \gamma_{tr}, \quad 0 < y < y_c \quad (11)$$

where

$$L = \kappa y [1 - \exp(-\frac{y}{A})], \quad \kappa = 0.40$$

$$A = 26 \frac{\nu}{N} u_\tau^{-1}, \quad u_\tau = \sqrt{\frac{\tau_w}{\rho}}$$

$$N = (1 - 11.8p^+)^{1/2}, \quad p^+ = \frac{\nu u_e}{3} \frac{du_e}{dx}$$

$$\gamma_{tr} = 1 - \exp[-G(x - x_{tr}) \int_{x_{tr}}^x \frac{dx}{u_e}], \quad G = 8.35 \times 10^{-4} \frac{u_e^3}{\nu^2} R_{x_{tr}}^{-1.34}$$

$$R_{x_{tr}} = u_e x_{tr} / \nu, \quad x_{tr} = x \text{ at the location of start of transition}$$

Outer Region:

$$(\epsilon)_0 = \alpha \int_0^{\eta_e} (u_e - \bar{u}) dy | \gamma_{tr}, \quad \gamma_c \leq y \leq \delta \quad (12)$$

where $\alpha = 0.0168$; γ_c is the position where $(\epsilon)_1 = (\epsilon)_0$.

For flow over concave and convex surfaces, the streamwise curvature effect on the eddy viscosity is introduced by multiplying the inner-eddy-viscosity expression by S^2 , where

$$S = \frac{1}{1 + \beta R_1} \quad R_1 = \frac{2\bar{u}}{\lambda} \left(\frac{\partial u}{\partial y} \right)^{-1} \quad (13)$$

where λ is the longitudinal radius of curvature which is positive for a convex surface and negative for a concave surface. The parameter β is taken equal to 7 for a convex surface and 4 for a concave surface.

3. Method for Numerical Calculation

Introducing new dependent variables $q(x, \eta)$ and $w(x, \eta)$,

$$\begin{aligned} f' &= q \\ q' &= w \end{aligned} \quad (14)$$

the momentum equation (8) can be written as

$$[(1 + \epsilon^+)w]' + \frac{m+1}{2} fw + m(1-q)^2 = x \left(q \frac{\partial q}{\partial x} - w \frac{\partial f}{\partial x} \right) \quad (15)$$

The boundary conditions are

$$f(x, 0) = 0, \quad q(x, 0) = 0, \quad q(x, \eta_e) = 1 \quad (16)$$

Let us now consider the grid rectangle and denote the grid points by

$$\begin{aligned} x_0 &= 0, \quad x^n = x^{n-1} + k_n, \quad n = 1, 2, \dots, N \\ \eta_0 &= 0, \quad \eta_j = \eta_{j-1} + h_j, \quad j = 1, 2, \dots, J, \quad \eta_J = \eta_e \end{aligned} \quad (17)$$

Here n and j are sequence numbers.

The quantities (f, q, w) will be approximated at point (x_n, η_j) of the net by net functions denoted by (f_j, q_j, w_j) . We employ the notation g_j^n for points and for any net function:

$$\begin{aligned} x^{n-1/2} &= \frac{1}{2}(x^n + x^{n-1}), \quad \eta_{j-1/2} = (\eta_j + \eta_{j-1}) \\ g_j^{n-1/2} &= \frac{1}{2}(g_j^n + g_j^{n-1}), \quad g_{j-1/2}^n = \frac{1}{2}(g_j^n + g_{j-1}^n) \end{aligned} \quad (18)$$

The finite-difference approximations of Eqs. 14 and 15 can be written by using centered-difference derivatives as follows:

$$\begin{aligned}
h_j^{-1}(f_j^n - f_{j-1}^n) &= q_{j-1/2}^n ; & h_j^{-1}(q_j^n - q_{j-1}^n) &= w_{j-1/2}^n \\
h_j^{-1}(b_j^n w_j^n - b_{j-1}^n w_{j-1}^n) &+ \alpha_1 (f_w)_{j-1/2}^n - \alpha_2 (q^2)_{j-1/2}^n \\
&+ \alpha (w_{j-1/2}^{n-1} f_{j-1/2}^2 - f_{j-1/2}^{n-1} w_{j-1/2}^n) = R_{j-1/2}^{n-1} \quad (19)
\end{aligned}$$

where

$$\begin{aligned}
b &= 1 + \epsilon^+ ; & \alpha &= \frac{\xi^{n-1/2}}{k_n} ; & \alpha_1 &= \frac{m^n + 1}{2} + \alpha ; & \alpha_2 &= m^n + \alpha \\
R_{j-1/2}^{n-1} &= -L_{j-1/2}^{n-1} + \alpha [(f_w)_{j-1/2}^{n-1} - (q^2)_{j-1/2}^{n-1} - m^n \\
L_{j-1/2}^{n-1} &= \{h_j^{-1}(b_j w_j - b_{j-1} w_{j-1}) + \frac{m+1}{2}(f_w)_{j-1/2} + m[1 - (q^2)_{j-1/2}]\}^{n-1}
\end{aligned}$$

The finite-difference equations (19) can be solved by Newton's method.

4. The Net Configuration and Convergence Criterion

The net in the η -direction is a geometric progression having the property that the ratio of length of any two adjacent intervals is constant; that is, $h_j = Kh_{j-1}$. In the present computations, $K = 1.2$ is employed for all cases. No significant difference was found in results calculated using several values of K from 1.1 to 1.5 for the Case 0141.

The step in the x -direction was chosen to be uniform and the values are

$$k_n = 0.3 \text{ m for Case 0612}$$

$$k_n = 0.05 \text{ m for Case 0141}$$

$$k_n = 0.02 \text{ m for Case 0231, 0232 and 0233}$$

In order to obtain a solution of the finite-difference equations (19), iteration was repeated until some convergence criterion was satisfied. We used the wall parameter as the convergence criterion. The iteration was stopped when

$$\left| \frac{w(x,0)^{i+1} - w(x,0)^i}{w(x,0)^i} - \frac{1}{2}(w(x,0)^{i+1} - w(x,0)^i) \right| < 0.02 \quad (20)$$

where i denotes the number of the iteration.

References

- Cebeci, T., and P. Bradshaw (1977). Momentum Transfer in Boundary Layers, McGraw-Hill, New York.
- Cebeci, T., and A. M. O. Smith (1974). Analysis of Turbulent Boundary Layers, Academic Press, New York.



COMPARISON OF COMPUTATION WITH EXPERIMENT

Summary Report

(A One-Equation Turbulence Model

Including the Low Reynolds Number Wall Effect)

by

P. Orlandi*

Computer Group Number: 05

Cases 0141, 0142, 0143, 0231, 0232, 0233, 0241, 0242, 0244, 0612

INTRODUCTION

In order to numerically predict the behavior of turbulent boundary layers incorporating some complexity such as unsteadiness, transpiration, and free-stream pressure gradient, it seems necessary to use a dynamic turbulence model including the near-wall region. An accurate modeling of the wall region involves the simulation of the complex turbulent mechanism occurring in the viscous and buffer regions. In these regions the maxima of turbulence energy production and dissipation occur and the other energy-balance terms are of the same order of magnitude, except the advective term. This latter term shows its influence in the case of high transpiration, and it is predominant near the boundary-layer edge, where it balances the turbulent diffusion. In a previous paper (Orlandi, 1981), the role of the pressure work term in the near-wall region has been emphasized and a first rough model has been introduced, but its behavior, from a quantitative point of view, cannot be proved, due to the lack of experimental measurements. Its introduction, as shown in Orlandi and Reynolds (1979), was intended as a modification of the dissipation term, and allows us to obtain a value of the maximum turbulence energy in very good agreement with the experimental values measured by Klebanoff (1955).

The one-equation model, mentioned above, is satisfactory for numerical investigations on turbulent flows without separation regions. For such flows a length-scale distribution can be easily obtained. In the largest part of the flows calculated for this Conference the mixing-length distribution, strictly valid for the zero-pressure-gradient case, has been found to be satisfactory. The only case presenting some uncertainty is the relaminarizing flow (Case 0281) which needs a deeper investigation. I feel I can affirm that for a large number of non-separated boundary layers, if the near-wall region needs to be modeled, it is not advantageous to use more sophisticated models, such as the two-equation model or the Reynolds-stress model. In these models

*Istituto di Aerodinamica - Universita di Roma, Italy

a larger number of terms appear whose modeling presents large difficulties, especially in the near-wall region; for example, the representation of the pressure-velocity correlations in the two-equation model was found to be impossible, as shown in Orlandi (1980), and the turbulent energy balance in the near-wall region was incorrect. In the case of adverse-pressure-gradient boundary layers a negative turbulent energy was obtained at a distance from the wall of the order of $y^+ \approx 1$.

If Reynolds-averaged turbulence models have to be used for engineering purposes, the code needs to use short CPU calculation times, and hence fast numerical methods have to be developed. The first requirement is based on using implicit methods, in such a way as to avoid stability-condition restrictions. Due to the non-linearity of the equations, implicit schemes need iterative procedures, that can be overcome if efficient linearization schemes are used, as suggested by Warming and Beam (1977). Moreover implicit methods, dealing with turbulent flows, allow us to obtain a fast coupling of the mean-velocity field and the mean-turbulence quantities. Boundary-layer numerical simulation usually employs scaled variables; the major group of methods use the Falkner-Skan type transformation (see Keller, 1978), which is adequate in dealing with laminar boundary layers. If these transformations are used to solve turbulent boundary layers, a continuous check must be conducted to satisfy that the real flow is inside the computational domain. This requires a great programming effort, and if adverse-pressure-gradient cases are considered, where large boundary-layer thickening may occur, a reduction of the streamwise step is necessary. The method employed here scales the normal direction with respect to the unknown boundary-layer thickness $\delta(x,t)$ which is evaluated at the old time step. Whatever steady boundary layer is considered, it is solved as an unsteady boundary layer with the external conditions (free-stream velocity or/and transpiration rate) evolving from a steady flat-plate state to the assigned one. This method allows us to obtain accurate solutions with a reasonable number of time steps and streamwise grid points. In the normal direction a stretching of the scaled variable must be used in order to have some computational points in the viscous region ($y^+ \leq 5$).

GOVERNING EQUATIONS

The momentum and continuity equations for two-dimensional incompressible turbulent boundary layers are

$$\frac{\partial U}{\partial x} + \frac{\partial V}{\partial y} = 0 \quad (1)$$

$$\frac{\partial U}{\partial t} + U \frac{\partial U}{\partial x} + V \frac{\partial U}{\partial y} = \frac{\partial U_e}{\partial t} + U_e \frac{\partial U_e}{\partial x} + \frac{\partial}{\partial y} [(v + v_T) \frac{\partial U}{\partial y}] \quad (2)$$

The velocity time derivatives have been retained because, as previously stated, the steady case has been solved like an unsteady case with the following free-stream velocity distribution

$$U_e(x,t) = 1 + f(t)[U_a(x) - 1] \quad (3)$$

$U_a(x)$ is the desired free-stream velocity distribution and $f(t)$ is a function giving a smooth transition from $t = 0$ to $t = \tau$, where τ is a priori chosen. For $t \geq \tau$ $\partial U_e / \partial t = 0$. It has been checked that the steady solution is not dependent on the assumed value of τ . ν_T is the eddy viscosity, related to the velocity scale, the turbulent kinetic energy, and length scale of the turbulence. The length scale is related to the dimension of the eddies carrying energy in the boundary layer. In the outer region the eddies are of the dimension of the boundary-layer thickness, and in the near-wall region they have dimensions proportional to the distance from the wall. An analytical expression which takes into consideration these physical aspects can be introduced

$$\ell = C_0 \delta (1 - (1 - y/\delta)^{C_1}) \quad (4)$$

A damping factor has been introduced, in the turbulent-viscosity expression, to model the wall suppression of the turbulent transport

$$\nu_T = C_2 Q^{1/2} \ell (1 - e^{-C_6(Q^{1/2}y)/\nu}) \quad (5)$$

More details to support this point of view are reported in previous papers [1,2,7].

The dynamics of the turbulent kinetic energy, $Q = \overline{u^2} + \overline{v^2} + \overline{w^2} = 2k$, is given by a transport equation that under the boundary-layer simplification is written as

$$\frac{\partial Q}{\partial t} + U \frac{\partial Q}{\partial x} + v \frac{\partial Q}{\partial y} = 2\nu_T \left(\frac{\partial U}{\partial y}\right)^2 + \frac{\partial}{\partial y} [(v + \nu_T) \frac{\partial Q}{\partial y}] - 2 \frac{\partial \overline{pv}}{\partial y} - 2D$$

where D is the "isotropic dissipation" to be modeled as a function of the turbulent kinetic energy, mixing length, and laminar viscosity if the near-wall region is considered. By dimensional analysis one obtains the following expression:

$$D = C_3 \frac{Q^{3/2}}{\ell} \left(1 + C_5 \frac{\nu}{Q^{1/2} \ell}\right) \quad (7)$$

The turbulent-kinetic-energy diffusion has been treated by a gradient-diffusion model, in which the pressure-work term has not been included as is usual in one- and two-equation turbulence models. The pressure-work term should play a significant role

mostly in the near-wall region. In Orlandi (1981) a comparison between experimental and numerical results obtained by more sophisticated turbulence models, such as the Large Eddy Simulation Model of Moin et al. (1978), suggested reasons why it is necessary to model explicitly the pressure-work term in the wall region. By dimensional consideration, this term is modeled as

$$-\frac{\partial \overline{pv}}{\partial y} = C_e \frac{Q^{3/2}}{\ell} e^{-\{[(Q^{1/2}\ell)/C_5 v - 1]/C_8\}^2} \quad (8)$$

The values of the constant in Eqs. 4, 5, 7, and 8 can be evaluated following the procedure described by Norris and Reynolds (1975) and by Orlandi and Reynolds (1979). It consists of comparing the experimental data, in wall coordinates, of steady flat-plate turbulent boundary layers at $y^+ = 100$ and in the near-wall region, with the theoretical model. Hence the constants can be evaluated. From the experimental results of adverse-pressure-gradient turbulent boundary layers, with and without transpiration at the wall, it can be seen that the near-wall and logarithmic region up to $y^+ \sim 100$ are not affected by the external pressure gradients; thus the value of the constants, obtained for the zero-pressure-gradient case, have been retained. They are

C_0	C_1	C_2	C_3	C_4	C_5	C_6
0.096	4.16	0.37	0.0425	3.93	0.012	4.5

METHOD OF SOLUTION

A coordinate transformation in the normal direction relative to the boundary-layer thickness is useful to solve the system of continuity, momentum, and turbulent energy-conservation equations. As the boundary-layer thickness is unknown at the new time step, the normal coordinate is normalized with respect to the boundary-layer thickness at the old time step. The independent variables have been transformed according to

$$x = \xi(x_1) ; y = \delta(x, t - \Delta t) \eta(x_2) \quad (9)$$

If the governing equations have to be integrated down to the wall, some computational points have to be inside the viscous layer, extending from $y^+ = 0$ to $y^+ \approx 5$. Since the boundary-layer thickness in wall coordinates is of the order of thousands, a finite-difference scheme with uniform mesh would require an excessive number of grid points. Hence, to avoid enormous computational time, a further coordinate transformation has been introduced,

$$\eta = \eta_w \left(1 - \frac{\tanh(1 - x_2)c}{\tanh(c)} \right) \quad (10)$$

where x_2 is the "new" coordinate with respect to which the governing equations will be discretized. Large values of the transformation parameter c give more computational points near the wall. In order to have the whole boundary layer inside the computational domain, having introduced $\delta(x, t - \Delta t)$ in Eq. 9, a value $\eta_w = 1.25$ has been assumed. The coordinate transformation in the streamwise direction is chosen in order to have more computational points in regions depending on the flow considered.

The continuity equation has been differentiated with respect to the y coordinate for numerical reasons, as given by Orlandi and Ferziger (1981). Then introducing in the continuity, momentum, and turbulent-energy equations the coordinate transformation (9), a system of equations is obtained in which more terms will appear with the derivatives expressed in term of the "new" variables x_1 and x_2 . The transformed equations can be found in Orlandi (1981) and Orlandi and Reynolds (1979). The boundary conditions associated with them are

$$y = 0, \quad U = Q = 0, \quad V = V_0(x, t) \quad (11)$$

$$y = \eta_w \delta, \quad U = U_e(x, t), \quad \frac{\partial V}{\partial y} = - \frac{\partial U}{\partial x} e, \quad \frac{\partial Q}{\partial y} = 0$$

The non-linear system of equations has been solved by an implicit procedure which is useful for two reasons; first to avoid stability conditions on the mesh size in the streamwise direction; second and most important, to have a fast coupling between the velocity field and the turbulent quantities. The system of equations has been linearized along the streamwise direction. All the details of the method, of the finite-difference scheme, and of the methodology of solution of the algebraic system of equations can be found in Orlandi and Ferziger (1981) and Orlandi and Reynolds (1979).

INITIAL CONDITIONS

To solve the system of governing equations described in the previous paragraph initial conditions must be assigned at $x = x_0$ and $t \geq 0$, and at $t = 0$ and $x \geq x_0$. With regard to the velocity profile, usually the experimental velocity data, closer to the wall, lie in the log region. A boundary-layer code, taking into consideration the near-wall region, requires the velocity profile in this region. It can be easily obtained from the profile in wall coordinates if τ_w at $x = x_0$ is known. The turbulent-kinetic-energy profile has been calculated, by an iterative procedure, solving the non-linear turbulent-kinetic-energy conservation equation with the assumption of zero advection. This assumption gives a satisfactory distribution in the inner region, where the advection term is negligible. The same velocity and

turbulent-energy profiles have been assigned as initial conditions ($x = x_0$ and $t > 0$). The initial conditions described above and the further assumption at $x = x_0$ of zero vertical velocity are responsible for the large differences encountered, near the inlet, between the experimental and the numerical data of C_f . The influence of the incorrect initial conditions disappears completely after a few streamwise mesh points.

The initial conditions at $x \geq x_0$ and $t = 0$ have been calculated solving the system of equations with the assumption of steady state and zero pressure gradient. The coordinate transformation in the vertical direction, given in Eq. 9, requires the knowledge of the boundary-layer thickness as a function of x . Only in the case of zero-pressure-gradient turbulent boundary layers does it grow in the streamwise direction with a well-defined law ($\delta \sim x^{4/5}$). Thus the code at $x = x_0$ demands a value for δ .

Each flow considered requires some coefficients in the expression of the streamwise coordinate transformation in order to have more computational points in particular regions. For example the relaminarizing boundary layer (Case 0281) shows very high gradients far away from the inlet, and thus the code was able to run only if more grid points were located in the end region. Almost all the other flows instead require more computational points at the inlet due to the above-mentioned inaccurate assumptions at $x = x_0$. Moreover for the transpired flows (Cases 0241, 0242, 0244), $V_0(x,t) = 0$ has been assumed at $x = x_0$, then $V_0(x,t)$ increases abruptly until it reaches the experimental value of V_0 . This fast growth can be described in a very short streamwise distance only if a refinement of the grid is assumed near $x = x_0$.

COMMENTS AND CONCLUSIONS

The results obtained with this model are in very good agreement with the experimental data for all the flows considered, except for the high-turbulence core diffuser (Case 0143). It appears in this case that a boundary-layer code is not able to describe a flow, where a well-defined potential flow region is not present. To obtain good predictions for such flows a code which includes viscous-inviscid interaction is obviously necessary.

The code has also been modified to calculate boundary layers with streamwise curvature, and attempts were made to solve the Gillis/Johnston boundary layer (Case 0233). In this case the computation started always from a flat-plate boundary layer and a time-dependent curvature radius was assumed. The steady state was not reached, because a negative turbulent kinetic energy was found near the wall at a streamwise position located between the flat and the curved regions, where high streamwise curvature gradients are present. Due to the inability to calculate this flow, the other two boundary layers with curvature (Cases 0231, 0232) were not even considered. Thus

more work needs to be done to take into consideration this kind of boundary layer. The simulation of the effect of free-stream turbulence (Case 0211) will need some small modifications to the code. This will be performed in the near future.

ACKNOWLEDGEMENT

This work was supported by Consiglio Nazionale delle Ricerche.

REFERENCES

- Keller, H. B. (1978). Annual Review of Fluid Mechanics, 10.
- Klebanoff, P. S. (1955). NACA Report 1247.
- Moin, P., W. C. Reynolds, and J. H. Ferziger (1978). Report TF-12, Dept. of Mech. Eng. Stanford University.
- Norris, H. L., and W. C. Reynolds (1975). Report TF-7, Dept. of Mech. Eng. Stanford University.
- Orlandi, P. (1981). "Model of low Reynolds number wall turbulence for Equilibrium Layers," submitted to Trans. ASME, J. Fluids Eng.
- Orlandi, P. (June 1980). Proceedings, VII International Conference on Numerical Methods in Fluids Dynamics, Stanford, U.S.A.
- Orlandi, P., and J. H. Ferziger (1981). "Implicit non-iterative schemes for Unsteady Boundary Layers," to appear in AIAA Jou.
- Orlandi, P., and W. C. Reynolds (1979). "A provisional model for Unsteady Turbulent Boundary Layers," submitted to AIAA Jou.
- Warming, R. F., and R. M. Beam (1977). Symposium on Computational fluid Dynamics, New York. Also SIAM-AMS Proceedings, Vol. 11, 1977.

COMPARISON OF COMPUTATION WITH EXPERIMENT

Summary Report

(Prediction of Some Complex Turbulent Flows
Using the Boundary-Layer Equations
and Viscous-Inviscid Interaction)

by

R. H. Fletcher,* O. K. Kwon†

Computer Group Number: 30



R.H. Fletcher

Cases 0141, 0241, 0242, 0421, 0424, 0431, 0612

INTRODUCTION

Three different computational models and five different turbulence models were used to compute seven cases for the 1980-81 AFOSR-HTTM-Stanford Conference on Complex Turbulent Flows. The cases considered are listed in Table 1. Fully attached flows (Cases 0612, 0141, 0241, and 0242) were computed using an implicit finite-difference procedure (TBL) for solving the turbulent boundary-layer equations. A finite-difference viscous-inviscid interaction procedure (VIS-INVIS) was used to compute flows containing recirculating regions. One separated flow (Case 0431) was also computed by an inverse boundary-layer finite-difference procedure (INVBL). The computational methods and turbulence models employed will be described briefly below.

Table 1. Summary of Cases Computed

Case	Mathematical Model	Turbulence Model
0612, 0141, 0241, 0242	Boundary layer	Model 1
0431	Inverse boundary layer	Model 2
	Viscous-inviscid interaction	Model 2
0421	Viscous-inviscid interaction	l: Model 3 upstream of step; Model 5 downstream
		k-l: Model 2 upstream of step; Model 4 downstream
0424	Viscous-inviscid interaction	k-l: Model 2 upstream of step; Model 4 downstream

*Department of Mechanical Engineering, Iowa State University, Ames, IA 50011

†Present address: Detroit Diesel Allison, Indianapolis, IN

GOVERNING EQUATIONS

The thin-shear-layer (boundary-layer) equations were assumed to govern the viscous flow. The FLARE approximation was introduced to permit marching the solution through regions of reversed flow. For steady, incompressible flow, the equations become:

continuity

$$\frac{\partial U}{\partial x} + \frac{\partial V}{\partial y} = 0 \quad (1)$$

momentum

$$c U \frac{\partial U}{\partial x} + v \frac{\partial U}{\partial y} = U_e \frac{dU_e}{dx} + \frac{1}{\rho} \frac{\partial \tau}{\partial y} \quad (2)$$

where $c = 1.0$, when $U > 0$ and $c = 0$, when $U \leq 0$. The Boussinesq assumption is used to evaluate the shear stress,

$$\tau = \mu \frac{\partial U}{\partial y} - \rho \overline{uv} = (\mu + \mu_T) \frac{\partial U}{\partial y} \quad (3)$$

Equations 1-3 were used in all three computational procedures considered here, although the boundary conditions differed.

For all three methods, the inner boundary conditions were

$$U(x,0) = 0 \quad (4)$$

$$V(x,0) = V_w(x)$$

When the boundary-layer equations were solved in the conventional direct mode, the outer boundary condition used was

$$\lim_{y \rightarrow \infty} U(x,y) = U_e(x) \quad (5)$$

When an inverse procedure was used as in INVBL and VIS-INVIS, the displacement thickness, $\delta^*(x)$ was prescribed. In the iterative viscous-inviscid interaction procedure, an arbitrary initial distribution of $\delta^*(x)$ is assumed, and improved distributions determined as part of the viscous-inviscid matching. The boundary condition is formally that the velocity distribution satisfy the prescribed $\delta^*(x)$:

$$\delta^*(x) = \int_0^{\infty} \left(1 - \frac{U}{U_e}\right) dy \quad (6)$$

A solution for inviscid portions of the flow field is required for the viscous-inviscid interaction calculation procedure. The inviscid flow was assumed to be

two-dimensional, steady and irrotational. Thus, the inviscid flow could be determined from a solution to Laplace's equation for the stream function:

$$\frac{\partial^2 \psi}{\partial x^2} + \frac{\partial^2 \psi}{\partial y^2} = 0 \quad (7)$$

The inviscid calculations for the present Conference were all for two-dimensional channel flows for which the boundary conditions were:

$$\begin{aligned} \psi(x, \delta_L^*) &= 0.0 && \text{(lower)} \\ \psi(x, \delta_u^*) &= \psi_T && \text{(upper)} \\ \psi(0, y) &= U_{e,0} (y - \delta_o^*) && \text{(upstream)} \\ \left. \frac{\partial^2 \psi}{\partial y^2} \right|_{(L,y)} &= 0.0 && \text{(downstream)} \end{aligned} \quad (8)$$

where ψ_T is the total volume flow rate per unit width.

TURBULENCE MODELS

Model 1. All flows remaining fully attached were predicted using the one-half equation model designated as Model D in Pletcher (1979), supplemented by the sublayer modification for blowing and suction presented in Pletcher (1974). The model utilizes the concept of a mixing length whereby $\mu_T = \rho l^2 \left| \frac{\partial U}{\partial y} \right|$ with l given in the inner region by

$$l_1 = 0.41 D y \quad (9)$$

with $D = 1 - e^{-z}$, where z is given by equation 15 of Pletcher (1974) and includes a modification for blowing and suction. The mixing length in the outer region is given by

$$l_0 = 0.12 L \quad (10)$$

where L is given by the solution of the one-dimensional transport equation

$$U_e \frac{dL}{dX} = 1.25 |\bar{u}_\tau| \left[\left(\frac{L}{\delta} \right) - \left(\frac{L}{\delta} \right)^2 \right] \quad (11)$$

The quantity $|\bar{u}_\tau|$ is a representative velocity of turbulence taken to be $(|\tau_{FT}|/\rho)^{1/2}$, where τ_{FT} is the characteristic fully turbulent stress given by equation 20 of Pletcher (1974). The parameter δ is the boundary-layer thickness. The value of τ_{FT} becomes equal to τ_w for flows without blowing or suction. Details on the development of Eq. (11) can be found in Pletcher (1979).

Model 2. For several flows, improved predictions were noted when the turbulence kinetic energy was utilized in the modeling for the outer region. The form of the turbulence kinetic-energy equation utilized was

$$\rho U \frac{\partial k}{\partial x} + \rho V \frac{\partial k}{\partial y} = \frac{\partial}{\partial y} \left[\left(\mu + \frac{\mu_T}{Pr_T} \right) \frac{\partial k}{\partial y} \right] + \mu_T \left(\frac{\partial U}{\partial y} \right)^2 - C_D \rho k^{3/2} / \ell_0 \quad (12)$$

where $C_D = 0.164$ and $Pr_T = 1.0$. The turbulence kinetic-energy equation was solved subject to boundary conditions given as equations 15 and 16 of Fletcher (1979). The turbulent viscosity was again evaluated according to $\mu_T = \rho \ell^2 \left| \frac{\partial U}{\partial y} \right|$ in the inner region with $\ell = \ell_1$ where ℓ_1 was evaluated as

$$\ell_1 = 0.41 \left(\tau_{\max} / \tau_w \right)^{1/2} Dy \quad (13)$$

Here, D was represented as

$$D = 1 - \exp \left[\left(\frac{1}{v} \left| \frac{\partial U}{\partial y} \right|_{\max} \right)^{1/2} \frac{y}{26} \right] \quad (14)$$

In the outer region, the turbulent viscosity was evaluated by $\mu_T = 0.548 \rho k^{1/2} \ell_0$, where ℓ_0 was determined as indicated for Model 1. The switch point from inner to outer model was made at the y location, where ℓ_1 first became equal to or greater than ℓ_0 . This one-and-a-half-equation model was used for Case 0431 and upstream of the step for some of the results presented for Cases 0421 and 0424.

Model 3. This model evaluates μ_T in the inner region exactly as given for Model 2. The turbulence kinetic-energy equation is not used for μ_T in the outer region; instead the formulation of Model 1 is used. For attached flows in mild pressure gradients without blowing or suction, this model becomes indistinguishable from Model 1. Model 3 was used upstream of the step for some of the results presented for Case 0421.

Model 4. This model and Model 5 described below were developed to obtain improved predictions downstream of rearward-facing steps. Attempts to extend Models 2 and 3 in applicability to this region showed promise, but overall, the best predictions to date were obtained by specifying ℓ_0 algebraically downstream of the step. Model 4 differs from Model 2 only in the determination of ℓ_0 . The turbulence kinetic-energy equation is used as indicated for Model 2. In Model 4, ℓ_0 is taken as the smaller value obtained from the following two expressions:

$$\ell_0 = 0.1 \left(\frac{\delta}{\delta^*} \right) \delta \quad (15)$$

$$\ell_0 = 0.08 \left(1 + c \frac{x}{\delta} \right) (\delta - y_D) \quad (16)$$

where

$$\delta' = \{0.5 [y_{T_{\max}}^2 + (\delta - y_{T_{\max}})^2]\}^{1/2} \quad (17)$$

and

$$C = \begin{cases} 0.3 & \text{if } h/H \leq 0.3 \\ h/H & \text{if } h/H > 0.3 \end{cases} \quad (18)$$

In the above, x is the distance downstream of the step, h is the step height, H is the channel height downstream of the step, y_D is the height of the dividing streamline downstream of the step and $y_{T_{\max}}$ is the height of maximum shear stress. All heights are measured from the wall on which the step occurs. Motivation for the above formulation is discussed in Kwon and Pletcher (1981).

Model 5. This model is a version of Model 4 in which the turbulence kinetic energy equation is not used; instead, $\mu_T = \rho l_o^2 \left| \frac{\partial U}{\partial y} \right|$ in the outer region. The inner-region modeling is the same as for Model 2 and l_o is evaluated as indicated for Model 4.

SOME COMPUTATIONAL DETAILS

A stretching transformation $\eta = (y/x) (Re_x)^{1/2}$, $\xi = x$, was utilized in the TBL procedure to remove the leading-edge singularity and to provide a more gradual growth of the boundary layer in the transformed coordinates. The difference procedure was fully implicit and formally second-order accurate. A three-point representation was used for the streamwise first derivatives and linearization of coefficients was achieved by a second-order accurate extrapolation. No iterations were required. Unequal grid spacing in the normal direction was implemented by a geometric progression, such that the ratio of two adjacent normal coordinate increments was a constant, K . Case 0612 was computed as a turbulent flow from the leading edge with no matching required. The starting length for Cases 0141 and 0241 was adjusted to match the experimental δ^* at the first measurement station. Difficulty in matching the first δ^* was observed for Case 0242 using the reported pressure gradient and suction rate. The $\Delta\xi$, $\Delta\eta$, and K parameters were refined several times until changes in the solution were negligible. After grid refinement, streamwise sizes were typically $\approx 0.3\delta$, $K = 1.05$, and about 90 grid points were used across the flow.

In the INVBL procedure, the thin-shear-layer equations were solved in a coupled manner in physical coordinates using an implicit finite-difference scheme with Newton linearization. The pressure gradient was treated as an unknown in the numerical formulation. Coupling was facilitated by the introduction of the streamfunction. The algebraic equations were solved by a block tridiagonal elimination scheme. The use of the FLARE approximation permitted the calculation to proceed smoothly through separated regions. Details are provided in Kwon and Pletcher (1981). The INVBL scheme can also be used in the direct mode with $U_o(x)$ specified and this procedure was followed

in Case 0431 from the channel entrance up to $x = 0.6$ m, where the calculation switched to the inverse mode with $\delta^*(x)$ specified. Only two Newton iterations were generally required at each streamwise station to achieve convergence to a relative tolerance of 0.0005 on the U and ψ variables. For Case 0431, the number of grid points across the flow varied from 35 near the channel entrance to 110 at the end of the channel. The computational region for the inverse calculation was spanned by 298 streamwise steps. Calculations made with a significantly finer grid showed no significant changes.

The VIS-INVIS procedure employed the INVBL scheme to compute the viscous portion of the flow. The inviscid flow domain was transformed to a rectangle by an independent variable transformation given in Kwon and Pletcher (1981) prior to solution by an ADI finite-difference procedure using successive overrelaxation. To start the calculation, an arbitrary distribution of $\delta^*(x)$ was assumed. After the boundary-layer and inviscid-flow solutions had been determined with the assumed $\delta^*(x)$, an improved distribution was obtained from

$$\delta_{n+1}^* = \delta_n^* \left(\frac{U_{e,BL}}{U_{e,INV n}} \right) \quad (19)$$

No under-relaxation was needed in the application of Eq. 19 for Case 0431, but was required for the lower (step-side) wall for step flows (Cases 0421, 0424). The required value of the under-relaxation factor seemed to be a strong function of the ratio of δ^* before the step to the step height. When δ^* at the step was larger than the step height, under-relaxation was not necessary. In the worst case (0421), an under-relaxation factor of 0.1 was used. The calculation proceeded iteratively until the solutions gave identical distributions of $U_e(x)$ within a prescribed tolerance,

$$\frac{|U_{e,BL} - U_{e,INV}|}{U_{e,INV}} = \leq \epsilon \quad (20)$$

at all calculation points in the interaction zone. The values used for ϵ were 0.0125 for Cases 0421 and 0424 and 0.005 for Case 0431. Thirty-eight global iterations were required for Case 0421 and 9 iterations for Case 0431. The interaction zone extended from $x = 0.805$ m to the last data station for Case 0431 and from four step heights upstream of the step to 16 step heights downstream for Cases 0421 and 0424. The boundary layer was computed on both channel walls for Cases 0421 and 0424. The grid used for the viscous region for Case 0431 was as indicated above for the INVBL procedure. A 48×51 grid was used in the inviscid region for Case 0431. For the step cases, approximately 130 unequally spaced grid points were used across the viscous portion of the flow and 104 streamwise steps were used to span the interaction zone. A 51×51 grid was used for the inviscid region. Preliminary calculations (not to

complete convergence) were made using various grid sizes in order to establish the adequacy of the grid used for the final calculations. The step cases (0421 and 0424; see table below) required the largest amount of computer time, approximately 9.7 sec per global iteration on the NAS AS/6 computer.

CLOSING COMMENTS

Cases 0242 (suction) and 0421 (rearward-facing step) were the most challenging. The results for Case 0242 are especially puzzling in light of the relatively good success achieved with Model 1 for the blowing case (0241). Assuming that the experimental data have been interpreted properly and the case set up correctly for computation, some interesting further work on turbulence modeling is indicated.

The viscous-inviscid interaction mathematical model used for the step flows does not account for normal pressure gradients in the viscous region. Prior to doing the turbulent-flow calculations, this mathematical model was evaluated for laminar flows as given in Kwon and Pletcher (1981). Good agreement was observed between predictions of the VIS-INVIS procedure and experimental measurements for laminar flow. Inadequacies in turbulence modeling are believed to be the major cause of discrepancies between the predictions and measurements for the rearward-facing step flows, rather than shortcomings in the mathematical model. The reattachment length was predicted more accurately without use of turbulence kinetic energy in the model (Model 5) but the Reynolds stresses were predicted more accurately with Model 4. Clearly more work is called for on this class of flow.

ACKNOWLEDGMENT

This material is based upon work supported by the National Science Foundation under Grant ENG-7812901.

REFERENCES

- Kwon, O. K., and R. H. Pletcher (1981). "Prediction of the incompressible flow over a rearward-facing step," Technical Report HTL-26, CFD-4, ISU-ERI-AMES-82019.
- Pletcher, R. H. (1974). "Prediction of transpired turbulent boundary layers," ASME, J. Heat Transfer, 96, 89-94.
- Pletcher, R. H. (1979). "Prediction of incompressible turbulent separating flow," ASME, J. Fluids Eng., 100, 427-433.

Table of Output: Four Area Ratios, Case 0424(P4)

Area Ratio A_1/A_2	Reattachment Length X_R/H	Step Height H_{step} (mm)
0.6667	7.95	0.0381
0.750	7.28	0.0254
0.8333	6.58	0.0152
0.9091	5.79	0.00762

[Ed.: This is the only output received for Case 0424(P4).
It is worth note that it is a zonal method.]



COMPARISON OF COMPUTATION WITH EXPERIMENT

Summary Report

(Flow over a Backward-Facing Step)

by

A. Pollard*

Computer Group Number: 06

Case 0421

INTRODUCTION

A summary is provided of the turbulent two-dimensional, isothermal flow over a backward-facing step (Case 0421) computed via a general three-dimensional finite-difference computer code. This computer code has been adapted for two dimensions by considering only three planes in the step spanwise direction, and calculates the distributions of two velocity components, pressure and two turbulence quantities (i.e., $k-\epsilon$) only on the mid-plane. The links between this center-plane and its two neighbors have been severed.

The summary is laid out in the following manner: first, the time-averaged equations (supposedly) governing the flow are stated; these equations introduce the effective turbulent viscosity as an unknown. To effect closure, this effective viscosity is calculated from two additional transport equations; namely, one for turbulent kinetic energy and one for its dissipation rate. The boundary conditions applied to all equations are then stated. This is followed by a brief summary of the method used to solve this set of equations and their boundary conditions. Numerical details then follow. A comparison of the computed results with the supplied experimental data is then provided. Generally reasonable agreement is noted between the calculations and data. Finally, some conclusions are drawn from the present work.

THE EQUATIONS

The time-averaged equations governing the flow situation are:

$$\frac{\partial}{\partial y}(\rho V) + \frac{\partial}{\partial x}(\rho U) = 0, \quad (1)$$

$$\frac{\partial}{\partial y}(\rho V^2) + \frac{\partial}{\partial x}(\rho VU) = \frac{\partial}{\partial y}(\mu_e \frac{\partial V}{\partial y}) + \frac{\partial}{\partial x}(\mu_e \frac{\partial V}{\partial x}) + \frac{\partial}{\partial x}(\mu_e \frac{\partial U}{\partial y}) + \frac{\partial}{\partial y}(\mu_e \frac{\partial V}{\partial x}) - \frac{\partial p}{\partial y}, \quad (2)$$

$$\frac{\partial}{\partial y}(\rho VU) + \frac{\partial}{\partial x}(\rho U^2) = \frac{\partial}{\partial y}(\mu_e \frac{\partial U}{\partial y}) + \frac{\partial}{\partial x}(\mu_e \frac{\partial U}{\partial x}) + \frac{\partial}{\partial x}(\mu_e \frac{\partial U}{\partial x}) + \frac{\partial}{\partial y}(\mu_e \frac{\partial V}{\partial x}) - \frac{\partial p}{\partial x}; \quad (3)$$

where V , U are the time-averaged velocities in the y , x coordinate directions respectively; ρ is the density which is here considered a constant, although there is no

*Dept. of Mech. Engr., Queen's University, Kingston, Ontario, Canada K7L 3N6

real need to have it so in the program; p is the local pressure. μ_e is the effective viscosity; the viscosity is obtained, and the equations closed by the introduction of a two-equation model of turbulence, namely the k - ϵ model in the form given by Launder and Spalding (1974). The equations are:

$$\mu_e = \mu + \rho C_\mu k^2 / \epsilon, \quad (4)$$

$$\frac{\partial}{\partial y}(\rho V k) + \frac{\partial}{\partial x}(\rho U k) = \frac{\partial}{\partial y}(\Gamma_k \frac{\partial k}{\partial y}) + \frac{\partial}{\partial x}(\Gamma_k \frac{\partial k}{\partial x}) + G_k - \rho \epsilon, \quad (5)$$

$$\frac{\partial}{\partial y}(\rho V \epsilon) + \frac{\partial}{\partial x}(\rho U \epsilon) = \frac{\partial}{\partial y}(\Gamma_\epsilon \frac{\partial \epsilon}{\partial y}) + \frac{\partial}{\partial x}(\Gamma_\epsilon \frac{\partial \epsilon}{\partial x}) + \frac{\epsilon}{k} [C_1 G_k - C_2 \rho \epsilon]; \quad (6)$$

where C_μ , C_1 , C_2 are constants ($= 0.09$, 1.44 , 1.92 , respectively), $\Gamma_k = \mu_e / \sigma_k$, $\Gamma_\epsilon = \mu_e / \sigma_\epsilon$, and $\sigma_k = 1.0$, $\sigma_\epsilon = 1.3$, with σ signifying the turbulent Prandtl number. G_k is the volumetric generation rate; it is given by:

$$G_k = \mu_e [2 \{ (\frac{\partial U}{\partial x})^2 + (\frac{\partial V}{\partial y})^2 \} + \{ \frac{\partial V}{\partial x} + \frac{\partial U}{\partial y} \}^2].$$

BOUNDARY CONDITIONS

The geometry used is as stipulated by the organizers of the Conference; the boundary conditions used were as follows:

EQUATION:	U	V	k	ϵ
$\frac{X}{H} = -4$	As Provided	0	$0.0015 U_o^2$	$C_\mu k^{1.5} / 0.18H$
$\frac{X}{H} = 20$	$\frac{\partial U}{\partial x} = 0$	0	$\frac{\partial k}{\partial x} = 0$	$\frac{\partial \epsilon}{\partial x} = 0$
$\frac{Y}{H} = 0$	WF	0	WF	WF
$\frac{Y}{H} = 3$	WF	0	WF	WF

In the above, the term "WF" denotes that the wall functions of Launder and Spalding (1974) are employed; these are given below. Note that since the inlet conditions that would enable μ_t or ϵ to be prescribed at $X/H = -4$ were not provided by the organizers, the value of ϵ at this location has been estimated using a fixed length scale. These inlet conditions have not been varied.

The wall functions (WF) employed to link the near wall grid node to the wall are as follows:

$$\begin{aligned}
 \text{Momentum:} \quad \tau_w &= \frac{\rho u C_\mu^{1/4} k^{1/2}}{\log_e(Ey^+)} \\
 \epsilon\text{-Equation:} \quad \epsilon &= \frac{k^{3/2} C_\mu^{3/4}}{\kappa y} \\
 k\text{-Equation:} \quad G_k &= \tau_w \frac{\delta v}{\delta s}
 \end{aligned} \tag{7}$$

where u is the velocity parallel to the wall, $\kappa = 0.4$, $E = 9.0$, $\delta v/\delta s$ is the gradient of velocities parallel to the wall, a distance δs from the wall.

SOLUTION METHOD

The solution to the afore-mentioned equations and their boundary conditions is effected by a modified version of the code described by Pollard (1979) which incorporates hybrid-differencing (Spalding, 1972) and the well-known SIMPLE algorithm of Patankar and Spalding (1972). A very brief summary of the sequence of steps followed by this code are:

- 1) Pressure is assigned a guessed value over all grid nodes superposed non-uniformly over the physical domain; a staggered orthogonal grid is used.
- 2) The U , V , and "pressure-correction" equations are solved (via TDMA) sequentially over the whole domain.
- 3) An overall mass-balance is performed and, if necessary, the volume outflow is altered such that outflow equals the known inflow.
- 4) Auxiliary equations are solved (e.g., k, ϵ).
- 5) Repeat steps 2-4 until satisfactory convergence is obtained; steps 2-4 constitute one iteration.

CONVERGENCE, COST, AND STORAGE REQUIREMENTS

The calculations were performed using 3 finite-difference grid densities: 24×34 , 24×58 , and 38×87 in the transverse (y) and axial (x) co-ordinate direction. The program was set up for a maximum grid of 40×100 ; this required 731,154 words of storage (36 bit/word) using double precision. Since care in eliminating redundant arrays (enthalpy, density, and third velocity component) has not been exercised, together with the use of 3 planes of grid nodes in the spanwise direction (as noted in the introduction), the storage requirements used here are somewhat exorbitant. Furthermore, the use of double precision is not necessary but was maintained for reasons of minimum program changes. By removing double precision, considering only one plane of grid nodes, and removing redundant arrays, the present

program would use only 89,000 words of storage; this may be lowered even further by careful restructuring of the program.

Convergence was checked in two ways: first, the absolute sum of each equation's residuals, summed over all calculation grid nodes and suitably normalized by the influx of the variable, must be below 0.01 (always ϵ -equation limited); secondly, values of the variables must not change more than 0.1% between the last 25 iterations. The following table illustrates the number of iterations and the CPU time required to achieve this level of convergence:

GRID (Y x X)*	No. ITER.	CPU†
24 x 34	269	10188
24 x 58	271	16260
38 x 87	400	66720

From the above, it is noted that the CPU times are very large; for the finest grid, the quoted CPU times (= 18 hrs!) is, according to computer specialists, approximately equal to 50 min on a CDC 7600 computer.‡

Note that, to ensure a smooth rate of convergence of the equations, an under-relaxation factor of 0.4 was applied to all equations; this is not necessarily the optimum value; higher values have not been tried.

OTHER COMMENTS

The results provided are from the 38 x 87 grid although the 24 x 58 grid results varied little from these.

The physical situation under consideration contains a step. In the computations, the step is aligned with the grid cell lines. The velocity cell's faces, adjoining the step, have been appropriately modified by reducing the cell face areas over which the shear stress acts.

The Reynolds stress ($-\overline{u'v'}$) calculations were performed after obtaining the solution to the other equations; where $-\overline{u'v'} = \mu_t(dU/dy + dV/dx)$.

COMPARISON WITH EXPERIMENTAL DATA

The results of the computations are shown in Plates 101, 104, 105 and 108. It is seen that the mean flow results (i.e., pressure and velocity) are in reasonable agreement with the "accepted" data. The calculations for cross-stream Reynolds stresses

*Grid non-uniformly distributed; details are available.

†CPU, in seconds on a Honeywell series 6600 operating under Multics; FORTRAN compiler release 6 with standard optimization.

‡Using FTN 4.2, opt = 2.

are also in reasonable agreement; however, the axial variation of the maximum Reynolds stress is poorly calculated in the reattachment region. The reattachment length is calculated here to be at 5.88 H downstream of the step (as compared to the "accepted" value of 7 H), where H is the step height.

CONCLUSIONS

In the author's opinion, the foregoing study that uses a numerical procedure which employs hybrid differencing and embodies the k- ϵ model of turbulence, provides:

- predictions that are in reasonable agreement with the mean-flow data;
- predictions that are in reasonable agreement with the cross-stream Reynolds-stress data;
- predictions that are not in general accord with the axial variation of the maximum Reynolds-stress data;
- predictions in computation times that should be interpreted carefully before comparing with other schemes.

ACKNOWLEDGMENT

The author is glad to acknowledge the financial support of the Natural Science and Engineering Research Council of Canada. Thanks go to the University of Calgary for providing the resources for the preparation of this contribution while the author was a member of the staff.

REFERENCES

- Launder, B. E., and D. B. Spalding (1974). "The numerical computation of turbulent flows," Computer Methods Applied Mechanics Engineering, 3, 269.
- Patankar, W. B., and D. B. Spalding (1972). "A calculation procedure for heat, mass and momentum transfer in three-dimensional parabolic flows," IJHMT, 15, 1787.
- Pollard, A. (1979). "Numerical calculation of partially elliptic flows," J. Numer. Heat Transfer, 2, 267.
- Spalding, D. B. (1972). "Novel finite difference formulation for differential schemes involving both first and second derivatives," IJNME, 4, 551.

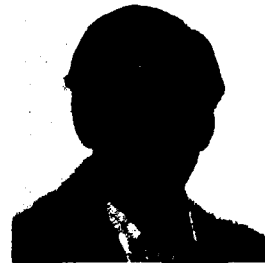
COMPARISON OF COMPUTATION WITH EXPERIMENT

Summary Report

by

J. V. Rakich, J. C. Tannehill, and I. K. Tree*

Computer Group Number: 31



J.V. Rakich

Cases 8101, 8201, 8661, 8671

INTRODUCTION

The present work employs the Parabolic Navier-Stokes (PNS) approximation for solving the steady Navier-Stokes and energy equations for compressible flows in which the inviscid part of the flow is supersonic. The full equations, which are elliptic, are simplified by neglecting the derivatives of the shear stress in the marching direction, thus reducing the equation to a parabolic form. The complete viscous and inviscid flow field is computed at once, including the coupling between the two regions. It has been applied primarily to three-dimensional steady flows over bodies and wings at angle of attack and to two-dimensional boundary-layer-like test cases.

COMPUTATION METHOD

The method is fully described in Vigneron et al. (1978a,b) and Rakich et al. (1979). Here we outline the equations and boundary conditions used for the present study. The governing equations are:

$$(\partial E^*/\partial \xi) + (\partial F/\partial \eta) + (\partial G/\partial \zeta) = -(\partial P/\partial \xi) \quad (1)$$

where:

$$E^* = (x^2/D) \bar{E}^*$$

$$F = (x/D)[A_1(\bar{E}-\bar{E}_v) + A_2(\bar{F}-\bar{F}_v) + A_3(\bar{G}-\bar{G}_v)] \quad (2)$$

$$G = (x/D)[B_1(\bar{E}-\bar{E}_v) + B_2(\bar{F}-\bar{F}_v) + B_3(\bar{G}-\bar{G}_v)]$$

$$P = (x^2/D) \bar{P}$$

Here, the notation $(\bar{\quad})$ is used to signify the basic conservation-law quantities for a Cartesian (x,y,z) coordinate system and D is the Jacobian of the transformation to ξ,η,ζ coordinates, which are aligned with the body and shock surfaces.

Thus, denoting column vectors with braces, one can write

*NASA-Ames Research Center, Moffett Field, CA 94035

$$\begin{aligned}
\bar{E}^* &= \{\rho u, \rho u^2 + \omega p, \rho uv, \rho uw, (\rho e_T + p)u\} \\
\bar{E} &= \{\rho u, \rho u^2 + p, \rho uv, \rho uw, (\rho e_T + p)u\} \\
\bar{F} &= \{\rho v, \rho uv, \rho v^2 + p, \rho vw, (\rho e_T + p)v\} \\
\bar{G} &= \{\rho w, \rho uw, \rho vw, \rho w^2 + p, (\rho e_T + p)w\} \\
\bar{P} &= \{0, (1 - \omega)p, 0, 0, 0\}
\end{aligned}
\tag{3}$$

The subscript v in Eq. 2 identifies the viscous terms:

$$\begin{aligned}
\bar{E}_v &= \{0, \sigma_{xx}, \tau_{xy}, \tau_{xz}, (u\sigma_{xx} + v\tau_{xy} + w\tau_{xz} + q_x)\} \\
\bar{F}_v &= \{0, \tau_{xy}, \sigma_{yy}, \tau_{yz}, (u\tau_{xy} + v\sigma_{yy} + w\tau_{yz} + q_y)\} \\
\bar{G}_v &= \{0, \tau_{xz}, \tau_{yz}, \sigma_{zz}, (u\tau_{xz} + v\tau_{yz} + w\sigma_{zz} + q_z)\}
\end{aligned}
\tag{4}$$

where x, y, z are Cartesian coordinates. The total internal energy is designated by

$$e_T = e + 0.5(u^2 + v^2 + w^2) \tag{5}$$

and the equation of state is

$$p = (\gamma - 1)\rho e \tag{6}$$

The parameter ω is introduced to control the fraction of pressure that is included on the left side of the equation; the remaining part $(1 - \omega)$ is included in the forcing term P. This is discussed in Vigneron et al. (1978a,b) and Rakich et al. (1979), as are the details of the geometric transformation.

TURBULENCE MODEL

The turbulent eddy viscosity is given by a two-layer mixing-length model.

In the inner region:

$$\mu_{T1} = \rho \ell^2 |u_\eta| \quad 0 < \eta < \eta_1 \tag{7}$$

where

$$\ell = 0.4\eta[1 - \exp(-\eta/A)]$$

$$A = 26u_w/\rho_w(|\tau_w|/\rho_w)^{-1/2}$$

In the outer region:

$$\mu_{T0} = 0.0168\rho_w \delta^* / [1 + 5.5(\eta/\delta)^6], \quad \eta_1 \leq \eta \leq \eta_2 \tag{8}$$

where

$$\delta^* = \int_0^{\eta_e} [1 - (u/u_e)] d\eta$$

Here, τ_w is the wall shear stress and μ_w is the molecular viscosity given by Sutherland's formula.

The approximate factorization method of Beam and Warming was used for this code because it eliminates the need for costly iterations. The system is solved by two one-dimensional sweeps of block tridiagonal matrices, using the routine described by Steger. The present code solves the following form of the equations

$$\left[\frac{\partial E^*}{\partial U} + \Delta\xi \frac{\partial}{\partial \zeta} \left(\frac{\partial G}{\partial U} \right) \right] \left(\frac{\partial E^*}{\partial U} \right)^{-1} \left[\left(\frac{\partial E^*}{\partial U} \right) + \Delta\xi \frac{\partial}{\partial \eta} \left(\frac{\partial F}{\partial U} \right) \right] \Delta^i U = -\Delta\xi \left(\frac{\partial F}{\partial \eta} + \frac{\partial G}{\partial \zeta} \right) - \Delta^{i-1} P \quad (9)$$

where

$$U = \{ \rho, \rho u, \rho v, \rho w, \rho e_T \}$$

and P is the pressure gradient term which is usually neglected. The Jacobians $(\partial G/\partial U)$ and $(\partial F/\partial U)$ are complicated expressions which have previously been given in Vigneron et al. (1978b). This method requires the use of artificial damping terms, in some cases, to control oscillatory solutions.

INITIAL AND BOUNDARY CONDITIONS

Two-Dimensional Test Flows

For the flat-plate test cases, a two-dimensional version of the code was developed with the outer computational boundary in the inviscid region outside the wall boundary layer. The pressure is specified on the outer boundary; total enthalpy and entropy are used to calculate the outflow (v) velocity on the outer boundary, subject to the specified pressure. At the wall, $u = v = 0$, and T_w or $\partial T/\partial y = 0$ is specified, as appropriate for the problem.

Initial conditions are specified at a starting x , which is much smaller than the plate length L , and the solution is marched from x_g to L . If $x_g \ll L$, the initial values have little effect on the solution at L , so approximate initial values can be used. For the present computations, the boundary-layer thickness was estimated at x_g , and a $1/7$ power velocity profile was used, together with a temperature distribution based on Crocco's integral for the energy equation.

Cone Flow

For this type of flow, the computational domain is bounded by the cone and the outer shock surfaces; the shock location is determined in the course of the solution. The Rankine-Hugoniot jump conditions are applied at the shock, and no-slip and temperature conditions at the cone surface. Symmetry conditions permit computation of only half of the complete field. The grid consisted of 50 unevenly spaced points between the body and shock, and 47 points circumferentially.

Initial conditions are based on an approximate laminar flow at a starting location, $x_s \ll L$, and on estimated shock angles on the windward and leeward sides. The turbulent viscosity is turned on after the laminar flow has developed. The final turbulent calculation was started at $x = 0.1 L$.

Three-Dimensional Shock-Impingement Flow

This flow was bounded by a flat plate as the lower surface ($z = 0$) and an inclined plate on the left side ($y = 0$) which generates a shock wave perpendicular to the lower plate. Zero slip conditions were applied on the solid boundaries; however, a coarse grid was used on the left boundary and, therefore, the boundary layer was not properly resolved there or in the corner region. On the left boundary, the Mach number was greater than unity at the first point off the wall. On the lower boundary, the stretched grid resulted in a y^+ less than 3. Zero-gradient conditions were applied over most of the upper and right-side boundaries. On the upper boundary, to the right of the shock, free-stream values of p , ρ , u , v were applied, while on the right boundary the free-stream p was used.

The grid expanded in the z direction with increasing x , so as to capture the shock growing out from the left wall. Forty-five unequally spaced points were used normal to the viscous plate, and thirty points in the transverse, y , direction.

Initial data were obtained from a two-dimensional turbulent boundary-layer computation, and applied at $x = x_s$, for all values of y . The two-dimensional shock pressure, and shock position were set at x_s . As the solution was marched in the x -direction, the captured shock was allowed to seek its own position.

MARCHING SOLUTION

The parabolic equations are marched downstream once in the x -direction from the initial station $x = x_s$, to the final location $x = L$, where the specified Reynolds number is achieved. The step size in the x -direction is governed by numerical stability constraints, which are empirically determined. The only limitations of the present codes are that the x component of Mach number, in the inviscid region, must be supersonic and the u velocity must be greater than zero. Flow reversal in the cross-plane is allowed and fully accounted for.

References

- Rakich, J. V., Y. C. Vigneron, and R. Agarwal (1979). "Computation of supersonic viscous flows over Ogive-cylinders at angle of attack," AIAA Paper 79-0131 17th Aerospace Sciences Meeting.
- Vigneron, Y. C., J. V. Rakich, and J. C. Tannehill (1978a). "Calculation of supersonic flow over Delta wings with sharp subsonic leading edges," NASA TM 78500.
- Vigneron, Y. C., J. V. Rakich, and J. C. Tannehill (1978b). "Calculation of supersonic viscous flow over Delta wings with sharp subsonic leading edges," AIAA Paper 78-1137, 11th Fluid and Plasma Dynamics Conference.

COMPARISON OF COMPUTATION WITH EXPERIMENT

Summary Report

by

W. Rodi^{1,*}, I. Celik,² A. O. Demuren,³ G. Scheuerer,⁴
E. Shirani,⁵ M. A. Leschziner,^{6,†} and A. K. Rastogi^{7,‡}

Computer Group Number: 07



W. Rodi

Cases 0111, 0112, 0113, 0141, 0142, 0143, 0211, 0231, 0232, 0233, 0241,
0242, 0244, 0261, 0263, 0281, 0311, 0331, 0371, 0372, 0373, 0374, 0375,
0376, 0381, 0382 0421, 0422, 0423, 0471, 0511, 0512, 0612

INTRODUCTION

The computer group identified above has submitted results for 33 test cases, all of which are for incompressible flows. Eleven different methods have been used to obtain these results; some cases have been calculated with several methods. Table 1 below summarizes the main features of the individual methods and relates them to the taxonomy issued by the organizers of the Stanford Conference. The methods differ by the numerical solution procedure as well as by the turbulence model employed. In what follows, the essence of the individual methods is presented in as compact a form as is possible with separate sections on the mean-flow equations solved, the turbulence models and the numerical schemes. For lack of space, the equations cannot always be given in all the coordinate systems used so that in some cases reference has to be made to the literature. Subsequent to the description of the methods, the choice of an individual method for a particular test case will be discussed. In the second

*University of Karlsruhe, Karlsruhe, Germany

†University of Manchester Institute of Technology, Manchester, England

‡Det norske Veritas, Hovik, Oslo, Norway

¹Co-ordinator.

²Cases 0142, 0143.

³Cases 0111, 0112, 0113, 0511, 0512.

⁴Cases 0141, 0211, 0231, 0232, 0233, 0241, 0242, 0244, 0261, 0263, 0281, 0311, 0331, 0381, 0382, 0471, 0612.

⁵Cases 0371, 0372, 0373, 0374, 0375, 0376.

⁶Cases 0422, 0423.

⁷Case 0421.

major part of this summary paper, the present computers comment on their results for the individual test cases, report on any special experiences, and discuss briefly the successes or failures of their methods.

Table 1. Summary of Calculation Methods

	Method	Stanford Code	Turbulence Model	Numerical Scheme	
1D	1DSE	RSTC	stress-eq. model	Simple Euler method, no mean-flow equations solved.	
	1DAS	AKEC	ASM*		
2D	2DPHR	BKEZ	standard k-ε	GENMIX code Implicit marching-forward integration procedure of Patankar and Spalding (1970) for 2D boundary-layer-type flows. Automatic grid expansion as layer grows.	
	2DPHRA	AKEZ	ASM		
	2DPLR	BKEX	low Re k-ε		
	2DPLRA	AKEZ	low Re ASM		
		2DETHY	BKEZ	standard k-ε	TEACH code of Gosman et al. (1974) for 2D-steady, elliptic flows with rectangular geometry, iterative, pressure correction scheme, hybrid differencing.
		2DEV	BKEZ	standard k-ε	Transient boundary-fitted method of Leschziner (1980) for variable geometry, implicit ADI, otherwise similar to 2DETHY.
3D	3DFP	BKEZ	standard k-ε	Marching-forward scheme of Patankar and Spalding (1972) for 3D parabolic flows, 2D storage of all variables, pressure correction scheme, hybrid differencing.	
	3DFPA	AKEZ	ASM		
		3DPP	BKEZ	standard k-ε	As 3DFP, but 3D storage for pressure and several downstream sweeps, each time updating pressure field, as given by Pratap and Spalding (1976).

* ASM = algebraic stress model

MEAN-FLOW EQUATIONS

For incompressible, statistically steady flows the continuity and momentum equations read:

$$\frac{\partial U}{\partial x} + \frac{\partial V}{\partial y} + \frac{\partial W}{\partial z} = 0 \quad (1)$$

$$U \frac{\partial U}{\partial x} + V \frac{\partial U}{\partial y} + W \frac{\partial U}{\partial z} = -\frac{1}{\rho} \frac{\partial P}{\partial x} + \frac{\partial}{\partial x} (\nu \frac{\partial U}{\partial x} - \overline{u^2}) + \frac{\partial}{\partial y} (\nu \frac{\partial U}{\partial y} - \overline{uv}) + \frac{\partial}{\partial z} (\nu \frac{\partial U}{\partial z} - \overline{uw}) \quad (2)$$

$$U \frac{\partial V}{\partial x} + \underline{v \frac{\partial V}{\partial y}} + \underline{w \frac{\partial V}{\partial z}} = - \frac{1}{\rho} \frac{\partial P}{\partial y} + \frac{\partial}{\partial x} (\underline{v \frac{\partial V}{\partial x}} - \overline{uv}) + \frac{\partial}{\partial y} (\underline{v \frac{\partial V}{\partial y}} - \overline{v^2}) + \frac{\partial}{\partial z} (\underline{v \frac{\partial V}{\partial z}} - \overline{vw}) \quad (3)$$

$$U \frac{\partial W}{\partial x} + \underline{v \frac{\partial W}{\partial y}} + \underline{w \frac{\partial W}{\partial z}} = - \frac{1}{\rho} \frac{\partial P}{\partial z} + \frac{\partial}{\partial x} (\underline{v \frac{\partial W}{\partial x}} - \overline{uw}) + \frac{\partial}{\partial y} (\underline{v \frac{\partial W}{\partial y}} - \overline{vw}) + \frac{\partial}{\partial z} (\underline{v \frac{\partial W}{\partial z}} - \overline{w^2}) \quad (4)$$

where here, and in the remainder of the paper, capital and small letters indicate respectively mean and fluctuating quantities. This general form of the equations is not used in any of the methods, but the various simplified versions can be obtained easily from Eqs. 1 through 4.

In all 3D-methods, the terms with dotted lines underneath are neglected which means that the streamwise diffusion of momentum is neglected, as is permissible for situations without reverse flow in the x-direction. Method 3DPP uses the equations with these terms neglected, although when applied to Case 0512 (curved channel flow) the equations were written in polar coordinates as given in Leschziner and Rodi (1979). Methods 3DFP and 3DFPA further assume that the streamwise pressure gradient $\partial P/\partial x$ is constant over any cross-section and can be replaced by the average pressure gradient dP/dx . This decoupling of the streamwise pressure gradient from the pressure distribution over the cross-section makes the equations fully parabolic in the x-direction.

In two-dimensional flows, all derivatives with respect to z are zero. Therefore, all 2D-methods solve equations with the fully underlined terms omitted and also the momentum equation (4) omitted. In 2D shear-layer flows, the momentum equation (3) need not be solved as a differential equation but yields the lateral pressure distribution, as given for curved shear layers below. For shear layers without longitudinal curvature, the lateral pressure variation is zero and the longitudinal pressure gradient $\partial P/\partial x$ in the streamwise momentum equation (2) is equal to the known pressure gradient in the free stream or can be calculated in duct flows with a one-dimensional treatment as described in Patankar and Spalding (1970). Further, in 2D shear layers the longitudinal diffusion of momentum is negligible so that in all methods starting with 2DP the term with the dotted line in equation (2) is omitted. For curved shear layers, the equations are written in the curvilinear coordinate system defined in Fig. 1.

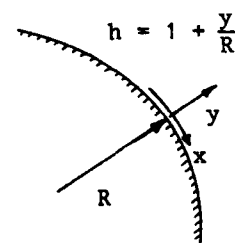


Fig. 1: Curvilinear coordinate system

$$\frac{\partial U}{\partial x} + \frac{\partial hV}{\partial y} = 0 \quad (5)$$

$$U \frac{\partial U}{\partial x} + hV \frac{\partial U}{\partial y} + \frac{UV}{R} = - \frac{1}{\rho} \frac{\partial P}{\partial x} + v \left(h \frac{\partial^2 U}{\partial y^2} + \frac{1}{R} \frac{\partial U}{\partial y} - \frac{U}{R^2 h} \right) - h \frac{\partial \overline{uv}}{\partial y} - 2 \frac{\overline{uv}}{R} \quad (6)$$

The longitudinal pressure gradient is obtained by integrating the lateral momentum equation to yield:

$$\frac{\partial P}{\partial x} = \left(\frac{\partial P}{\partial x}\right)_{y=0} + \frac{d}{dx} \left[\frac{1}{R} \int_0^y \frac{\rho U^2}{h} dy \right] \quad (7)$$

These equations are used in methods 2DPHRA and 2DPLRA whenever longitudinal curvature is present.

In all the methods except 2DPLR and 2DPLRA, the above equations are not integrated to the wall, but the viscous sublayer is bridged by wall functions. In these methods therefore the viscous stresses, that is all terms involving v are omitted. The velocities at the first grid point away from the wall are related to the wall shear stress by the logarithmic law of the wall, which in the 3D-methods is applied to both velocity components parallel to the wall:

$$\frac{U_{R,1}}{U_{\tau R}} = \frac{1}{\kappa} \ln (E y_1^+) \quad (8)$$

where $U_{R,1}$ is the resultant velocity at the first grid point and $U_{\tau R}$ is the resultant friction velocity, y_1^+ is the dimensionless wall distance $U_{\tau R} y_1 / \nu$, κ is the von Karman constant ($= 0.435$) and E is a friction parameter (here for smooth walls $E = 9$). According to equation (8), the ratio of the wall shear stresses in 3D-flows is determined by the ratio of the velocities at the first grid point. In calculations with method 3DPP of case 0512 (curved channel flow) it was found that, due to the relatively coarse grid used, the maximum of the secondary velocity components occurred between the first grid point and the wall so that the log-law (8) is not realistic and the direction of the resultant velocity changes significantly between the first grid point and the wall so that the resultant shear stress can no longer be assumed to be in the same direction as the resultant velocity at point 1. To correct for this, the shear stress obtained from (8) for the secondary velocities was enhanced by the factor f_i .

$$f_i = \exp(-c_i y_1), \quad \text{with } c_i = \frac{\ln\left(\frac{U_{1,1}}{U_{1,2}} \frac{U_2}{U_1}\right)}{y_1 - y_2} \quad (9)$$

where the indices 1 and 2 related to values at the first and second grid point and the index i relates to the secondary velocity component in question (either V or W). This procedure was applied only in method 3DPP for the calculation of the case 0512 (curved channel flow) where the secondary velocities are fairly large.

TURBULENCE MODELS

Altogether four different turbulence models or model variants were used in the calculations, and these will now be described briefly.

a) Standard k-ε model (BKEZ)

The standard k-ε model, as described in detail in Launder and Spalding (1974) and Rodi (1980) was used in methods 2DPHR, 2DETHY, 2DEV, 3DFP, 3DPP. The model is based on the Boussinesq viscosity concept, relates the eddy viscosity ν_t to the kinetic energy k and the dissipation rate ϵ , and determines these two quantities from transport equations. The model is given in tensor notation by Eqs. 10 through 13:

$$\overline{-u_i u_j} = \nu_t \left(\frac{\partial U_i}{\partial x_j} + \frac{\partial U_j}{\partial x_i} \right) - \frac{2}{3} \delta_{ij} k \quad (10)$$

$$\nu_t = c_\mu \frac{k^2}{\epsilon} \quad (11)$$

$$U_i \frac{\partial k}{\partial x_i} = \frac{\partial}{\partial x_i} \left(\frac{\nu_t}{\sigma_k} \frac{\partial k}{\partial x_i} \right) + \nu_t \left(\frac{\partial U_i}{\partial x_j} + \frac{\partial U_j}{\partial x_i} \right) \frac{\partial U_i}{\partial x_j} - \epsilon \quad (12)$$

$$U_i \frac{\partial \epsilon}{\partial x_i} = \frac{\partial}{\partial x_i} \left(\frac{\nu_t}{\sigma_\epsilon} \frac{\partial \epsilon}{\partial x_i} \right) + c_{\epsilon 1} \frac{\epsilon}{k} \nu_t \left(\frac{\partial U_i}{\partial x_j} + \frac{\partial U_j}{\partial x_i} \right) \frac{\partial U_i}{\partial x_j} - c_{\epsilon 2} \frac{\epsilon^2}{k} \quad (13)$$

In the 3D-methods, all gradients with respect to the streamwise direction x were neglected on the right-hand side of (12) and (13), while in all 2D-methods all the gradients with respect to the third coordinate z are zero. Additionally in method 2DPHR, gradients with respect to x on the right-hand side were also neglected. The following standard constants cited in Launder and Spalding (1974) and Rodi (1980) were employed:

$$c_\mu = 0.09, c_{\epsilon 1} = 1.44, c_{\epsilon 2} = 1.92, \sigma_k = 1.0, \sigma_\epsilon = 1.3$$

The above turbulence model is valid only for regions with high values of the local Reynolds number $R_T = \nu_t/\nu$ and therefore cannot be applied very near walls. Hence, boundary conditions are specified at the first grid point y_1 which is located outside the viscous sublayer in the log-law region. With the assumption of local equilibrium and the log-law, k and ϵ take the following values at this point:

$$k_1 = \frac{U_\tau^2}{\sqrt{c_\mu}}, \quad \epsilon_1 = \frac{U_\tau^3}{\kappa y_1} \quad (14)$$

In three-dimensional situations, U_τ is the resultant friction velocity. The condition (14) for ϵ at grid point 1 is used in all the methods employing the standard k-ε model but the relation for k only in method 2DPHR. The other methods determine k

at the first grid point from the k-balance for a control volume adjacent to the wall, with diffusive and convective transport through the wall set zero. Under local-equilibrium conditions, this yields the k-relation given in (14).

b) Low Reynolds number version of the k-ε model (BKEX)

A low Reynolds number version of the k-ε model that can be used also in the viscous sublayer was employed only in shear-layer calculations with 2DP-methods. The model was suggested by Lam and Bremhorst (1978) and has the following form:

$$-\overline{uv} = v_t \frac{\partial U}{\partial y}; \quad v_t = c_\mu f_\mu \frac{k^2}{\epsilon} \quad (15)$$

with

$$f_\mu = (1 - e^{-A_\mu R_y})^2 \left(1 + \frac{A_t}{R_t}\right) \quad (16)$$

where

$$R_y = \frac{\sqrt{k} y}{\nu}, \quad R_t = \frac{k^2}{\nu \epsilon}$$

$$U \frac{\partial k}{\partial x} + v \frac{\partial k}{\partial y} = \frac{\partial}{\partial y} \left[\left(\nu + \frac{v_t}{\sigma_k} \right) \frac{\partial k}{\partial y} \right] + v_t \left(\frac{\partial U}{\partial y} \right)^2 - \epsilon \quad (17)$$

$$U \frac{\partial \epsilon}{\partial x} + v \frac{\partial \epsilon}{\partial y} = \frac{\partial}{\partial y} \left[\left(\nu + \frac{v_t}{\sigma_k} \right) \frac{\partial \epsilon}{\partial y} \right] + c_{\epsilon 1} f_1 \frac{\epsilon}{k} v_t \left(\frac{\partial U}{\partial y} \right)^2 - c_{\epsilon 2} f_2 \frac{\epsilon^2}{k} \quad (18)$$

with

$$f_1 = 1 + \left(\frac{A_{c1}}{f_\mu} \right)^3; \quad f_2 = 1 - e^{-R_t^2} \quad (19)$$

The following boundary conditions are specified at the wall:

$$k = 0, \quad \frac{\partial \epsilon}{\partial y} = 0 \quad (20)$$

The additional constants not appearing in the standard k-ε model take the following values. They are slightly different from those given in Lam and Bremhorst (1978):

$$A_\mu = 0.016, \quad A_t = 19.5, \quad A_{c1} = 0.06$$

All the other constants are the same as listed above for the standard k-ε model. For high local Reynolds numbers R_t (e.g. outside the viscous sublayer) the model reduces to the standard k-ε model presented above.

c) Reynolds-stress equation model (RSTC)

Here model 2 of Launder, Reece and Rodi (1975) was adopted, but with the wall-proximity correction to the pressure-strain term proposed by Gibson and Launder (1978). The modeled form of the Reynolds stress transport equation reads:

$$\begin{aligned} \frac{D\overline{u_i u_j}}{Dt} = & \text{Diff} \frac{\overline{u_i u_j}}{u_i u_j} + P_{ij} - c_1 \frac{\epsilon}{k} (\overline{u_i u_j} - \frac{2}{3} \delta_{ij} k) \\ & + c_1' \frac{\epsilon}{k} (\overline{u_n^2} \delta_{ij} - \frac{3}{2} \overline{u_n u_i} \delta_{nj} - \frac{3}{2} \overline{u_n u_j} \delta_{ni}) f\left(\frac{L}{x_n}\right) \\ & + \pi_{ij} + c_2' (\pi_{nn} \delta_{ij} - \frac{3}{2} \pi_{ni} \delta_{nj} - \frac{3}{2} \pi_{nj} \delta_{ni}) f\left(\frac{L}{x_n}\right) - \frac{2}{3} \epsilon \delta_{ij} \end{aligned} \quad (21)$$

where

$$P_{ij} = -\overline{u_i u_l} \frac{\partial u_j}{\partial x_l} - \overline{u_j u_l} \frac{\partial u_i}{\partial x_l}, \quad F = \frac{1}{2} P_{ii} = -\overline{u_i u_j} \frac{\partial u_i}{\partial x_j} \quad (22)$$

$$\pi_{ij} = -c_2 (P_{ij} - \frac{2}{3} \delta_{ij} P) \quad (23)$$

The model for the diffusion term is not given in explicit form as it is not needed here. The terms with the wall-damping function f are the wall-proximity corrections, in which the index n denotes the direction normal to the wall.

The function f will be given below in the section on algebraic stress models; it is not needed here because Eq. 21 was used only in method 1DSE for homogeneous flows where there is no wall effect. The wall-proximity corrections are included in (21) because this forms the basis for the algebraic-stress model to be discussed shortly. The dissipation rate ϵ appearing in (21) is determined from (here without diffusion term as used in method 1DSE):

$$\frac{D\epsilon}{Dt} = c_{\epsilon 1} \frac{\epsilon}{k} P - c_{\epsilon 2} \frac{\epsilon^2}{k} \quad (24)$$

The empirical constants were taken from Gibson and Launder (1978):

$$c_1 = 1.8, \quad c_2 = 0.6, \quad c_1' = 0.5, \quad c_2' = 0.3$$

d) Algebraic stress models

Two versions of algebraic-stress models were used for the calculations, one in methods 1DAS, 2DPHRA and 2DPLRA and the other one in method 3DFPA for the calculation of turbulence-driven secondary motions in channel flow. The two versions are very similar, but there are distinct differences that need to be reported.

(i) Algebraic-Stress Model in Methods 1DAS, 2DPHRA and 2DPLRA

This model follows directly from the Reynolds-stress equation (21) with the following assumption:

$$\frac{D\overline{u_i u_j}}{Dt} - \text{Diff} \frac{\overline{u_i u_j}}{u_i u_j} = \delta_{ij} \frac{\overline{u_i u_j}}{k} \left(\frac{Dk}{Dt} - \text{Diff}_k \right) = \delta_{ij} \frac{\overline{u_i u_j}}{k} (P - \epsilon) \quad (25)$$

in which the summation convention does not apply. Equation 25 relates the transport of normal stresses to the transport of k and neglects the transport of shear stresses. The transport of shear stresses could of course also be related to the transport of k , and this did in fact give better results for Case 0376 (homogeneous shear flow) but proved detrimental in other flow situations like buoyant jets (see Hossain, 1980) and was hence not adopted here.

With (25), the differential equation (21) can be reduced to an algebraic expression for $\overline{u_i u_j}$. When the wall proximity terms involving f are retained, this expression is rather complex and is not given here. For calculating homogeneous flows, these terms can be omitted, and the following expression is used in model 1DAS:

$$\overline{u_i u_j} = k \left[\frac{2}{3} \delta_{ij} + \frac{(1-c_2) \left(\frac{P}{\epsilon} \delta_{ij} - \frac{2}{3} \delta_{ij} \frac{P}{\epsilon} \right)}{c_1 + \delta_{ij} \left(\frac{P}{\epsilon} - 1 \right)} \right] \quad (26)$$

c appearing in this expression is determined from Eq. 24 and k from the corresponding k -equation.

The algebraic-stress model will now be given in a form suitable for two-dimensional shear layers with longitudinal curvature and wall-proximity effects. The derivation of this form starts from Eq. 21 written in the curvilinear coordinate system sketched in Fig. 1 (the transformed equations are given in Gibson and Rodi, 1981). With (25), these equations yield the following algebraic expressions for the stresses of interest in 2D-shear layers:

$$\frac{\overline{v^2}}{k} = \frac{2}{3} \frac{1 - P/\epsilon \phi_2}{1 + 2\phi_5} - \frac{4R_f}{1-R_f} \frac{\phi_2}{1+2\phi_5} \frac{P}{\epsilon} \quad (27)$$

$$\frac{\overline{u^2}}{k} = \frac{2}{3} \left(1 + \frac{P}{\epsilon} \phi_4 \right) + \phi_5 \frac{\overline{v^2}}{k} + \frac{4R_f}{1-R_f} \frac{P}{\epsilon} \phi_3 \quad (28)$$

$$-\overline{uv} = \underbrace{\phi \left[1 - \left(\frac{2\overline{u^2}}{\overline{v^2}} - 1 \right) R_f \right]}_{c_\mu^*} \frac{\overline{v^2}}{k} \frac{h}{1-R_f} \frac{k}{\epsilon} \frac{\partial U}{\partial y} (1 - R_f) \quad (29)$$

The important parameters expressing the influence of longitudinal curvature and wall proximity are

$$\text{the curvature Richardson number } R_f = \frac{U/Rh}{\partial U / \partial y}, \quad (30)$$

$$\text{the wall damping function } f = \frac{c_\mu^{3/4}}{\kappa} \frac{k^{3/2}}{\epsilon y} \quad (31)$$

Further:

$$\phi_2 = \frac{1 - c_2 + 2c_2'c_2f}{\delta}, \quad \phi_5 = \frac{c_1'f}{\delta}, \quad \delta = c_1 + \frac{P}{\epsilon} - 1 \quad (32)$$

$$\phi_4 = \frac{2 - 2c_2 + c_2'c_2f}{\delta}, \quad \phi_3 = \frac{1 - c_2 + c_2'c_2f}{\delta}, \quad \phi = \frac{1 - c_2 + 1.5c_2c_2'f}{c_1 + 1.5c_1'f}$$

The shear-stress relation can be seen to be basically the same as in the standard k- ϵ model, but the constant c_μ is now replaced by the function c_μ^* given above. However, in the absence of curvature and wall-proximity effects ($R_f = 0$, $f = 0$) this function does not give 0.09 used for c_μ in the standard model. To make the algebraic model reduce to the standard model for $R_f = 0$ and $f = 0$ the following c_μ -function is used:

$$c_\mu = 0.09 \frac{c_\mu^*}{c_\mu^*} (R_f = 0, f = 0) \quad (33)$$

k and ϵ appearing in the algebraic-stress relation are determined from the following k- and ϵ -equations in the curvilinear coordinate system:

$$U \frac{\partial k}{\partial x} + Vh \frac{\partial k}{\partial y} = \frac{\partial}{\partial y} \left(\frac{v_t}{\sigma_k} h \frac{\partial k}{\partial y} \right) + v_t h \left(\frac{\partial U}{\partial y} \right)^2 (1 - R_f)^2 - h\epsilon \quad (34)$$

$$U \frac{\partial \epsilon}{\partial x} + Vh \frac{\partial \epsilon}{\partial y} = \frac{\partial}{\partial y} \left(\frac{v_t}{\sigma_\epsilon} h \frac{\partial \epsilon}{\partial y} \right) + c_{\epsilon 1} \frac{\epsilon}{k} v_t h \left(\frac{\partial U}{\partial y} \right)^2 (1 - R_f)^2 - c_{\epsilon 2} h \frac{\epsilon^2}{k} \quad (35)$$

where v_t is calculated from Eq. 11. The constants were introduced already in the section on Reynolds-stress equations and on the standard k- ϵ model. For flows without curvature and wall-proximity effects ($R_f = 0$, $f = 0$) the model is identical to the standard k- ϵ model.

(11) Algebraic-Stress Model in Method 3DFPA

This algebraic-stress model is based on model 1 of Launder, Reece and Rodi (1975) for the stress equations, which differs from Eq. 21 in that the wall-proximity terms involving f are absent, two additional terms involving the constants β and γ are present in the mean-strain part of the pressure-strain term, and wall-proximity effects are now simulated by making the empirical coefficient dependent on the wall-damping function f . In the present model, convective and diffusive transport of $\overline{u_i u_j}$ are neglected entirely, and the production P of k is set equal to ϵ in the resulting algebraic equations. These can then be written to yield the following general expression for $\overline{u_i u_j}$:

$$\overline{u_i u_j} = \frac{k}{c_1} \left[\frac{2}{3} \delta_{ij} (c_2 + \beta + c_1 - 1) + (1 - c_2) \frac{P_{ij}}{\epsilon} - \beta \frac{D_{ij}}{\epsilon} - \gamma \frac{k}{\epsilon} \left(\frac{\partial u_i}{\partial x_j} + \frac{\partial u_j}{\partial x_i} \right) \right] \quad (36)$$

where

$$D_{ij} = -\overline{u_i u_l} \frac{\partial U_l}{\partial x_j} - \overline{u_j u_l} \frac{\partial U_l}{\partial x_i} \quad (37)$$

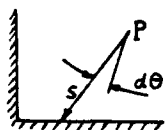
This algebraic-stress equation is applied only to the stresses $\overline{v^2}$, $\overline{w^2}$ and \overline{vw} appearing in the momentum equations for the secondary motions in channel flow. The primary shear stresses \overline{uv} and \overline{uw} appearing in the streamwise momentum equation are determined from the standard k-ε model given above. In the algebraic equations for $\overline{v^2}$, $\overline{w^2}$, and \overline{vw} , the gradients of the secondary velocities are retained, as it was found that the inclusion of these terms, particularly in the \overline{vw} expression, had a significant influence on the magnitude of the secondary motion. The coefficients in (36) were calculated from:

$$c_1 = 1.5 - 0.5f, \quad c_2 = 0.7636 - 0.06f, \quad \beta = 0.1091 + 0.06f, \quad \gamma = 0.182 \quad (38)$$

as suggested by Launder, Reece and Rodi. These authors used a linear wall-damping function $f = L/y^*$, where L is the local length scale of turbulence and y^* is a characteristic wall distance. Here a quadratic function is used as suggested by Naot and Rodi (1981):

$$f = \frac{L^2}{y^{*2}} \quad \text{with} \quad L = \frac{c_\mu^{3/4}}{\kappa} \frac{k^{3/2}}{\epsilon} \quad (39)$$

where $c_\mu = 0.09$ as in the k-ε model and $\kappa = 0.42$. The characteristic wall distance y^* is determined from the following integration:



$$\frac{1}{y^{*2}} = \frac{2}{\pi} \int_0^{2\pi} \frac{d\theta}{s} \quad (40)$$

The resulting expression for a duct is rather complex and can be found in Naot and Rodi (1981).

It was intended first to bring this algebraic-stress model in line with the other model described above, but this could not be done in the time available.

NUMERICAL SOLUTION PROCEDURES

All methods employ finite-difference procedures, and, apart from method 2DEV, these procedures were well tested before the calculations for the Stanford Conference. A few common features of the various schemes will be described first. The finite-difference equations were derived by integrating the differential equations over control volumes so that the schemes are all conservative. The finite-difference equations are brought into tridiagonal matrix form and are solved with efficient

recursion formulae. Finally, all the schemes use hybrid differencing for the discretization of the convective terms (central differencing for grid Peclet numbers $Pe \leq 2$ and upwind differencing for $Pe > 2$), except for the streamwise convection in parabolic situations when no discretization assumption is necessary.

2DP-Methods

The fully implicit, marching-forward procedure of Patankar and Spalding (1970) is used which is suitable for 2D shear layers that are parabolic in the x-direction. This scheme requires 1D-storage, and the pressure is either prescribed or, for duct flows, determined from 1D-forms of the momentum and continuity equations. Because of small lateral velocities, Pe is usually below 2 so that mainly central differencing is used and numerical diffusion is not a problem. The method uses a dimensionless stream function as lateral coordinate which causes the grid to expand automatically as the shear layer grows.

2DETHY

This method uses the iterative code of Gosman et al. (1974) for steady, 2D recirculating flows employing a rectangular staggered grid and requiring 2D-storage. At each iteration, the momentum equations are solved first with a guessed pressure field from the previous iteration, and a Poisson-type pressure correction is then solved to obtain corrected values for pressure and velocities that then satisfy the continuity equation. In recirculation areas, the upwind differencing may cause significant numerical diffusion when the grid is not very fine.

2DEV

This method solves the equations with the recently developed code of Leschziner (1980) for unsteady 2D-elliptic flows. A boundary-fitted, quasi-orthogonal grid is used that allows slopes of top and bottom of up to about 20° . A two-step, three time level ADI-method is used that is implicit in time. Otherwise, the scheme is the same as that of 2DETHY.

3DFP-Methods

The implicit marching-forward procedure of Patankar and Spalding (1972) is used which is suitable for 3D flows that are fully parabolic in x-direction. 2D-storage is required for all variables. The solution at each cross-section is the same as that in the 2D-elliptic scheme 2DETHY; at each step the pressure-correction equation is solved iteratively until mass is conserved.

3DFP

The partially parabolic procedure of Pratap and Spalding (1976) is used that allows upstream pressure effects, but no other upstream effects (e.g. no reverse flow). Basically the procedure is the same as in 3DFP, but now with 3D-storage for

the pressure (still 2D-storage for other variables) and repeated application of the fully parabolic 3DFP-method, where at each sweep the pressure field is updated until convergence is achieved. A rectangular grid is used in the y-z-cross-section, but the streamwise coordinate x can be curved.

CHOICE OF METHOD FOR THE INDIVIDUAL TEST CASES

The first choice was according to the dimensionality of the problem: one-dimensional, two-dimensional and three-dimensional problems were calculated with 1D, 2D and 3D methods respectively. All 2D-shear-layer cases were calculated with the parabolic 2DP-methods, and all 2D-situations with separation with the elliptic 2DE-methods. In the latter cases, situations with rectangular geometry were treated with 2DEHY and those with non-rectangular geometry with 2DEV. All three-dimensional cases where upstream pressure effects were negligible were calculated with the fully parabolic methods starting with 3DFP, while cases with significant upstream pressure effects (here only 0512) were calculated with the partially parabolic method 3DPP.

In addition to the choice of the solution procedure, different turbulence models can be chosen in connection with some of the procedures. The standard k- ϵ was used whenever this appeared possible. In some cases, the low Reynolds number version of this model was also employed for comparison purposes; in boundary layers with relaminarization and with blowing or suction only the low Reynolds number version could be applied. The standard k- ϵ model is also not suitable to account for longitudinal curvature effects on the turbulence such as occurring in curved shear layers, wall-proximity effects that are of importance in wall jets, and secondary motion of the second kind prevailing in straight ducts. In these cases, an algebraic-stress model was used. In Cases 0511 and 0512, where the secondary motion is pressure dominated, the standard model was thought to be sufficiently accurate.

DISCUSSION OF THE RESULTS AND COMMENTS ON INDIVIDUAL CASES

a) One-dimensional homogeneous turbulent flows (methods 1DSE, 1DAS)

Case 0371 (isotropic grid turbulence)

In the model, the decay of q^2 ($= 2k$) is determined entirely by the constant $c_{\epsilon 2}$ in the ϵ -equation. The present constant $c_{\epsilon 2} = 1.92$ yields $q^2 \propto t^{-1.087}$. A value of 1.83 would be needed to get the faster decay of the data. However, $c_{\epsilon 2} = 1.92$ is the more suitable value for many other flows.

Case 0372 (rotating turbulence)

Rotation can have no influence in the present model when the shear stresses are zero as was approximately the case in this experiment. Hence, the calculations are the same as for the previous case, but with different initial conditions. In the

experiment, the decay rate decreased with increasing rotation, and this brings the experimental decay curves closer to the predicted ones. The ratio of the fluctuations $\sqrt{u^2}/\sqrt{v^2}$ is predicted to approach unity quite rapidly while in the experiment this ratio remains constant or even increases. Hence, the pressure-strain model employed cannot simulate this observed behavior.

Case 0373 (return to isotropy)

The return to isotropy is generally fairly well simulated by the model of Rotta (1972) (term involving c_1 in the $\overline{u_i u_j}$ -equation (21)). A smaller value for the constant c_1 would have given better quantitative agreement, but the value 1.8 adopted here gives generally better results for shear flows than the value 1.5 recommended in Launder et al. (1975). Further, when the isotropy is approached, the model appears to overpredict the return to isotropy. Concerning Case 0373B, it is strange that u^2 should have remained constant in the experiment as it was almost a factor of 10 smaller than v^2 .

Case 0374 (plane strain distortion)

In the previous cases without production the algebraic-stress model 1DAS predicts isotropic turbulence according to Eq. 26. This is the first case with production and hence 1DAS can be used to simulate the development of the individual stress-components, and results are therefore now included also with this model. The stress-equation model simulates the distortion under the influence of plane strain fairly well, the algebraic-stress model predicts u^2 and w^2 correctly but v^2 is from the beginning too high.

Case 0375 (axisymmetric strain)

Here results with the 1DAS-model are included only for contraction ratios of 1 because for larger ratios negative u^2 -values resulted, so that the model is not really applicable in such situations of fairly strong negative production. The observed dip in u^2 and the rise of v^2 towards the end of the contraction are underpredicted by the stress-equation model, but this is exaggerated by the plots; the discrepancies are only up to about 30%.

Case 0376 (homogeneous shear flow)

In case A, all the stress components are predicted too low so that the kinetic energy is also too low. This is primarily the consequence of the shear stress \overline{uv} being predicted too low which then gives too low production of kinetic energy. It is interesting to note that in Launder et al. (1975) the shear stress was predicted correctly with the same model, but with somewhat different constants. The difference between the model 1DSE and 1DAS is not very significant in this case. In case B where a much stronger shear was applied, an incorrect initial value of ϵ was

provided by the organizers, and only the the results obtained with the corrected value should be compared with the data. When this is done, model 1DSE can be seen to describe the development of the individual stress components fairly well, but it should be mentioned here that much better agreement was achieved when the transport of \overline{uv} was not neglected but was also related to the transport of k according to Eq. 25 (effectively δ_{ij} was removed in the denominator of (26)). In this case the ratio of production of k to dissipation, P/ϵ , is of the order of 2, so that the term $(P/\epsilon-1)$ in the denominator of (26) has a significant influence.

b) 2D-shear-layer flows

These flows were calculated with the 2DP-methods, using 40 grid points across the layer and forward steps of one momentum thickness for boundary layers and typically 0.05 layer widths in free shear flows in the 2DPHR-methods, and 100 cross-stream grid points and forward steps of 0.25 momentum thickness in the 2DPLR-methods using a low-Reynolds-number turbulence model. Grid-refinement tests were carried out, and the grid density quoted were found to be more than sufficient for the results to be grid-independent.

Case 0612 (flat-plate boundary layer) Methods 2DPHR, 2DPRA

The calculations were started at a momentum thickness Reynolds number of 450 with turbulent conditions. The initial velocity profile was fitted carefully, but this yielded a shape parameter H of only 1.5, compared with the given value of 2.2. Because of the few experimental points across the layer for $x < 1m$, the measured integral parameters are probably not very reliable in this range. Further downstream, method 2DPHR predicts c_f too high by 5% and H too low by 3%, while method 2DPLR gives c_f somewhat better but H slightly worse. Method 2DPHR predicts the velocity profile in the log-law region very well at the last station (the matching point in the log-law was at $y^+ = 300$) but in the outer part the velocity is slightly low. On the other hand, the method 2DPLR predicts the velocity slightly high in the log-law region, as is typical for the Lam-Bremhorst (1978) turbulence model. A calculation was also carried out with method 2DPHRA, in which c_{μ} is reduced near the wall due to the wall-proximity correction, and the results are very similar to those with 2DPHR, c_f being lower by 1.2% and H higher by 0.4%, so that the agreement with the data is slightly improved.

Case 0141 (boundary layer with $dP/dx > 0$) Methods 2DPHR, 2DPLR

Both methods predict the wall shear stress and the shear-stress distribution in the initial region of positive pressure gradient fairly well, but overpredict the shear stress as separation is approached. Associated with the high shear stress are too high velocities near the wall. It appears that the turbulence model must be blamed for this, as the Navier-Stokes solution of Murphy and Rubesin (1979) gave no

better results than the boundary-layer calculation. It is mainly the ϵ -equation that must be blamed, because it yields a length-scale that lies above the universal experimental variation $l_m = \kappa y$.

Cases 0142, 0143 (conical diffuser) Method 2DPHR

Calculations were started at the initial plane ($x = -0.055m$) with measured profiles of U and k . In Case 0142, the initial ϵ -distribution was determined from measurements of \overline{uv} , k , and $\partial U/\partial y$ via (11). For Case 0143 the same procedure was applied near the wall, but calculations were carried out with two different values of ϵ in the core region ($r \leq 0.8R$). The first value ($\epsilon R/U_{CL}^3 = 0.0034$) was chosen to give approximately the correct decay of k along the diffuser axis and the second value ($\epsilon R/U_{CL}^3 = 0.0106$) corresponds to a reasonable choice of the length scale $l = k^{3/2}/\epsilon = 0.55R$ in pipe flow and was used also by the group of Launder et al. The results for Case 0143 can be seen to be quite sensitive for the initial ϵ , the higher value yielding generally much closer agreement with experiments for c_f , U , and \overline{uv} , but at the same time producing a decay of k along the axis (not shown here) which is considerably faster than the measured one. As in Case 0141, the friction factor c_f is overpredicted also in Case 0142 and the velocity is too high near the wall (and too low at the center), only that the agreement is even worse here because the adverse pressure gradient is higher. The worse agreement in c_f is also due to the fact that the wall friction is made dimensionless with the square of the local centerline velocity, and this is underpredicted (at the last station by 10%). In Case 0143 the adverse pressure gradient is smaller, and hence the better predictions with the higher initial ϵ -value are consistent with the results for Case 0142.

Case 0211 (boundary layer with free-stream turbulence) Methods 2DPHR, 2DPLR

Calculations were started with free-stream turbulence of various intensities and length scales, and the various runs produced a correlation between the increase in skin friction and the free-stream turbulence parameters similar to the measured one, but there is considerable scatter. For method 2DPHR there is no clear influence of the initial turbulence conditions, while for method 2DPLR the high intensity calculation with low length scale reacts faster to the rapid decay of free-stream turbulence due to a large dissipation connected with the small length scale and produces only a small increase in skin friction. It is interesting to note that in the range of practical interest (value of the abscissa of about 1) the correlation of the different runs is fairly good. It should be mentioned that the Δc_f plotted is very sensitive to small changes in actual c_f values, so that the scatter and the differences between measurements and calculations are blown up. The parabolic increase in Δc_f at small intensities is predicted correctly. On the whole the results on the plot submitted indicate that Δc_f is predicted about 30% too low. Simulations of individual

experimental runs of Hancock (1980) and a direct comparison with his results yielded much better agreement.

Case 0281 (relaminarizing boundary layer) Method 2DPLR

Calculated θ , H , and the velocity profiles are in good agreement with the data. The calculated c_f is very sensitive to the specification of the free-stream velocity (here the data points were interpolated by cubic splines), as small irregularities in the pressure gradient produced the large irregularities occurring in the present results. Further there were difficulties in fitting representative initial profiles for the turbulence variables, which leads to the sharp initial drop of c_f .

Cases 0241, 0242, 0244 (boundary layers with blowing and suction) Method 2DPLR

In Case 0241 of constant blowing under zero pressure gradient, the trend of a sharp reduction of c_f by the blowing is predicted correctly, but not to the same extent as shown by the data. The momentum thickness θ is predicted well, while the displacement thickness δ^* is too low. In Case 0242 with constant suction under adverse pressure gradient, the method predicts correctly that c_f is constant, but the value is 5% below the data. The velocity profiles and hence the shape factor are well predicted but both momentum and displacement thickness are too high, indicating that the calculations settle at a somewhat different equilibrium than the measurements. In Case 0244 with constant suction at zero pressure gradient the velocity profiles are very well predicted and also the shear-stress profiles for small negative F -values, while the shear stress is somewhat overpredicted for higher negative F -values, although the shape of the \overline{uv} -profile agrees well.

Cases 0231, 0232, 0233 (curved boundary layers) Methods 2DPHRA, 2DPLRA

For these cases, the high-Reynolds-number and the low-Reynolds-number algebraic-stress models yield approximately the same results. In Case 0231 with weak convex curvature, momentum thickness and shape parameter are predicted well, while c_f is too high, although this is exaggerated in the plot; at the last station the discrepancy is about 10%. The reduction of the stresses v^2 and \overline{uv} by the curvature is underpredicted. In summary, the models do not respond sufficiently to weak curvature. For Case 0232 with weak concave curvature, c_f , θ , H and the velocity profiles are fairly well predicted. At the last station, $x_g = 1.123$, the destabilizing influence of concave curvature on v^2 and \overline{uv} is underpredicted, indicating again that the models do not respond sufficiently to weak curvature. Case 0233 with strong convex curvature and subsequent recovery is predicted well in the curved section but not so well in the recovery section. The models predict a fairly fast recovery, and while the measurements also show fast recovery in the turbulence quantities, the mean velocity field and the friction factor show only very slow recovery. For experiments in a similar apparatus, doubts have been expressed previously (Gibson et al., 1981) about the

two-dimensionality of the measurements in the recovery section. Finally, the stresses $\overline{u^2}$, $\overline{v^2}$ and \overline{uv} are fairly well predicted except for the overshooting of $\overline{u^2}$ and \overline{uv} at the end of the curvature. Finally, it should be mentioned that calculations with the standard k- ϵ model have underpredicted the influence of curvature in this case significantly.

Case 0261 (equilibrium plane wall jet) Method 2DPHRA

The dependence of the half-width spreading on the velocity ratio U_E/U_M is predicted correctly by the algebraic-stress model within the experimental accuracy. It should be mentioned that the standard k- ϵ model yields a half-width spreading 0.09 for the situation with zero free-stream velocity ($U_E = 0$). The influence of the velocity ratio on the location of maximum velocity y_m is also predicted correctly, but the velocity maximum is consistently too close to the wall, which can be seen also from the velocity profile. This is a consequence of the use of an eddy-viscosity model which does not allow a separation between the point of maximum velocity and the point of zero shear stress. The latter is predicted correctly and so are the profiles of \overline{uv} and $\overline{v^2}$ for the velocity ratio $U_E/U_M = 0.38$. The calculated c_f -values are about 5 to 10% above the Bradshaw-Gee curve, but they are still within the experimental range given in the evaluation report. These results show that wall-proximity effects are well simulated by the present algebraic-stress model.

Case 0263 (wall jet on log-spiral) Method 2DPHRA

While the spreading rate is slightly overpredicted for a plane wall jet, it is underpredicted increasingly as the curvature (characterized by $K = x/R$) increases. For $K = 2/3$ the agreement in the asymptotic spreading rate is still very close and consequently the shear stress is also predicted reasonably well. The turbulent kinetic energy shows larger deviations from the data because it is not as directly affected by the algebraic model as is the shear stress.

Case 0311 (plane mixing layer) Method 2DPHR

The calculation was started with the measured velocity profile and with profiles for k and ϵ as in developed turbulent boundary layers. For small x/θ_1 -values, there is fairly good agreement with the data, but the asymptotic spreading rate is underpredicted by about 7%.

Case 0331 (curved mixing layer) Method 2DPHRA

The calculations were started at the nozzle exit with similarity profiles and a layer thickness of 3mm. The shear-layer calculations were carried out in a (s,n)-coordinate system where s follows the curved centerline of the mixing layer given in Castro and Bradshaw (1976) and n is perpendicular to s . The pressure was assumed atmospheric at the zero-velocity edge and was calculated in the layer according to

Eq. 7. The resulting velocity on the high-velocity side agrees well with measurements. The development of the shear-layer width is predicted well, but the location of the profiles in the curved region is not in agreement with the data provided by the organizers. It is likely, however, that these data are not correct, and should be shifted to the left. The model produces the reduction of the shear stress by the curvature. The recovery of the shear stress after the curvature is too fast, as the predicted values overshoot the plane-mixing-layer values, and approach these only further downstream. The reduction of the lateral fluctuations is also produced (and again somewhat overpredicted at 60°), and here the recovery is in fairly good agreement with the data. The mean velocity profiles in the recovery region are also in accord with the measurements.

Cases 0381, 0382, 0471 (2D-wakes) Method 2DPHR

The symmetric (0381) and asymmetric (0382) wakes of Andreopoulos are calculated very well, including the development of the shear-stress peaks in the asymmetric case. The velocity profiles in the symmetric trailing-edge flows of Case 0471 (I and II) are also fairly well predicted. The shear stress in case I agrees with the data in the boundary-layer region and again far downstream in the wake, but is too low in the immediate vicinity of the trailing edge. The measured shear stress is probably high in this region because of the finite trailing-edge width. A similar shear-stress behavior can be observed for case II, only that here the calculated shear stress is already low in the boundary layer. In both cases I and II, the turbulent kinetic energy is also predicted low in the vicinity of the trailing edge but agrees fairly well with the measurements further downstream in the wake. The data points indicate that there was significant free-stream turbulence, and this may have caused high k -levels. In case III of an asymmetric trailing-edge flow, the boundary-layer calculation on the upper surface ($y > 0$) is rather poor because separation is approached. The initial disagreement is carried down to $x/\theta_0 = 70$, so that history effects are particularly important in this flow. The vastly different levels of shear stress on the two sides of the trailing edge are predicted correctly, but the maximum on the near-separation side is shifted towards the outer edge of the flow. This shift is also retained as the flow develops downstream.

c) 2D-Flows with separation regions

Case 0421 (backward-facing step) Method 2DETHY

Thirty-two grid points were used in both x - and y -direction with a concentration in the shear layer springing off the corner. Much finer grids could not be used, so that the solution obtained with the hybrid differencing scheme is probably not entirely grid-independent. The results portray the often observed fact that the method underpredicts the length of the recirculation zone; the reattachment length

x_R/H is 5.8 compared with a measured value of 7. As a consequence, the velocity profile at $x/H = 5.33$ is not well predicted. Further downstream, the predicted profiles are better, but the recovery ($x/H = 13.33$) is also not too well described. This is somewhat strange in view of the good agreement of the shear stress in the downstream region. The shear stress is fairly well predicted also in the immediate vicinity of the step, but assumes too high values in the curved shear layer bordering the recirculation zone. Here, the standard $k-\epsilon$ model does not account properly for the stabilizing effect of the curvature. Further weak points of the method when applied to recirculating flows are the ϵ -equation in its present form, the wall functions which are suitable really only for shear layers, and the hybrid differencing scheme that may introduce a fair amount of numerical diffusion.

Cases 0422 and 0423 (sudden expansion with inclined duct walls) Method 2DEV

These predictive cases were calculated with 35 grid points in the x -direction and 23 in the y -direction and the results are again not entirely grid-independent. In Case 0422 where only the top wall is inclined, the pressure coefficient increases with the angle α as expected. It is interesting to note that there is little difference between $\alpha = 6^\circ$ and 10° , indicating a deterioration in diffuser performance. The reattachment length x_R increases with α (as was to be expected), but as in Case 0421, this length is probably underpredicted significantly for the same reasons as given above. In Case 0423 with both top and bottom walls inclined at the same angle (constant area), the difference between the maximum and minimum value of $c_{p,w}$ at a given α is constant which appears correct for a constant-area duct. The lowering of the pressure in the recirculation region with increasing α also seems reasonable as the deflection of the streamlines must set up a lateral pressure gradient. The reattachment length x_R is influenced little by the angle α and this may be due to the following counteracting phenomena. First, it may be expected that the stagnation streamline would take a larger distance to meet the lower wall as the slope is increased, but on the other hand the lower pressure generated in the recirculation zone acts to pull the shear layer down. Again the reattachment length is very likely to be underpredicted. It appears that for this kind of recirculating flows a more accurate differencing scheme is necessary, but also a refined turbulence model as well as refined wall functions.

d) Three-dimensional flows

In the three-dimensional calculations, only relatively coarse grids could be used (15-20 grid points in y - and z -direction) and the results are probably not grid-independent. However, for Cases 0111, 0112, 0113 and 0511 where the secondary velocities are relatively small, numerical diffusion is not a serious problem; it may be more severe in Case 0512.

Case 0511 (Wing-body junction) Method 3DFP

According to Shabaka and Bradshaw (1981), there are large regions of negative eddy-viscosity in this flow so that method 3DFP should fail badly. However the friction coefficient and the longitudinal velocity distribution appear to be not too sensitive to locally wrong assumptions so that they are surprisingly well predicted. There are larger discrepancies on the secondary velocity components, particularly in the corner region. There, the eddy-viscosity assumption breaks down and the shear stress \overline{uv} is also poorly predicted. On the whole however, the results are better than expected.

Case 0512 (flow in curved rectangular channel) Method 2DPP

The calculations were carried out with a 14×17 grid in the cross-sectional planes (covering half the channel) 20 grid planes before and after the straight section, and 30 grid planes in the curved part of the channel. The change in shape of the velocity contours due to the secondary motion is generally predicted well, but the velocity levels in the center-portion of the channel are consistently lower than in the measurements so that certain measured isovels do not exist in the calculations. This is particularly true for $\theta = 90^\circ$, where the smallest velocity for which an experimental isovel was given is $U_0/U_{ref} = 1.1$, while the maximum calculated velocity was 1.08. Isovels for lower velocities are included in Plate 129 to show that the shapes of the velocity contours are similar to the measured ones. The low longitudinal velocities in calculations are probably due to an overprediction of the secondary motion which causes a transport of low momentum fluid from the wall regions to the center. Plate 130 shows that already at $\theta = 0^\circ$, the secondary motion is larger than measured (maximum value is 0.11) and this continues as the flow goes around the bend. At 90° , the agreement of predicted and measured radial velocity is quite reasonable according to Plate 131, but it should be mentioned that near the bottom wall much larger negative velocities appear in the calculations than have been observed. Since other strongly curved channel flows have been calculated successfully with the same method by Leschziner and Rodi (1979), the reasons for the poor agreement in the present case are not clear.

Cases 0111, 0112, 0113 (duct flows with turbulence-driven secondary motion)

Method 3DFPA

In Case 0111 of flow developing in a duct from a uniform inlet profile the secondary velocity is underpredicted by almost a factor of 2 whence the bulging of the longitudinal velocity and k -contours towards the corners is by far not as strong as in the experiments, and the streamwise velocity development is predicted rather poorly along the corner bisector. It should be reported that the influence of the terms involving gradients of the secondary velocities in the algebraic-stress model was

found very strong. In fact when these terms were omitted, as was done in most calculations of this flow reported in the literature, such a strong secondary motion developed that the calculations became unstable. In many of the previous calculations mentioned, this problem was avoided by omitting the source terms producing the secondary motion at the first grid points near the wall. In Case 0112 of a rectangular channel with partially rough walls, the longitudinal velocity contours are predicted fairly well, even though the secondary motion is again underpredicted by a factor of almost 2. The longitudinal velocity and the fluctuating components $\overline{u^2}$, $\overline{v^2}$, and $\overline{w^2}$ along the plane of symmetry agree reasonably well with the data, while the shear stress has a maximum near the wall that is not present in the experiments. Plausible results were obtained for the predictive case (0113) of flow developing from non-uniform inlet profiles in a duct produced by subdividing a larger square duct with the aid of a cruciform, although the bulging of the velocity contours in the cruciform corner and the corresponding secondary motion towards this corner are probably somewhat too large at the initial stations.

CONCLUDING REMARKS

Many of the test cases, and in particular most of the 2D-shear-layer situations, were calculated with satisfactory accuracy with the k- ϵ model and its low-Reynolds-number and algebraic-stress variants. It should be emphasized that these variants reduce to the standard parent model when low-Reynolds-number, longitudinal-curvature and wall-proximity effects are absent. It should also be emphasized that all the calculations were carried out with the same set of empirical constants. Problems were noted in the application to shear layers in adverse pressure gradients and to recirculating flows, where also the hybrid differencing scheme used in the present work is probably not accurate enough. Lastly, for three-dimensional flows the calculations generally show the correct trends, but the accuracy on the details is sometimes poor; in particular the turbulence-driven secondary motion is underpredicted significantly by the present model.

ACKNOWLEDGEMENTS

The work reported here was sponsored mainly by the Deutsche Forschungsgemeinschaft through the Sonderforschungsbereich 80 and by the Forschungsvereinigung Verbrennungskraftmaschinen. The calculations were carried out on the UNIVAC 1108 and BURROUGHS B7700 computers of the University of Karlsruhe. The authors are grateful to Prof. V. C. Patel for his advice on the calculations and to Gaby Bartman for the efficient typing of the original manuscript.

AD-A136 034

THE 1980-81 AFOSR (AIR FORCE OFFICE OF SCIENTIFIC
RESEARCH)-HTM (HEAT TR. (U) STANFORD UNIV CA DEPT OF
MECHANICAL ENGINEERING S J KLINE ET AL. SEP 81
AFOSR-TR-83-1003 F49620-80-C-0027

6/6

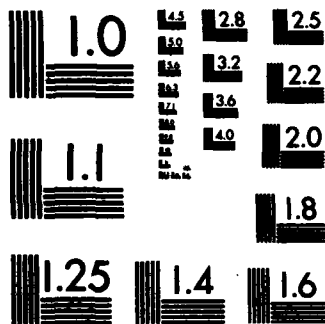
UNCLASSIFIED

F/G 20/4

NL

END

FILED
184
DTIC



MICROCOPY RESOLUTION TEST CHART
NATIONAL BUREAU OF STANDARDS-1963-A

REFERENCES

- Castro, I. P., and P. Bradshaw (1976). "The turbulence structure of a highly curved mixing layer," J. Fluid Mech., 73, 265-304.
- Gibson, M. M., and B. E. Launder (1978). "Ground effects on pressure fluctuations in the atmospheric boundary layer," J. Fluid Mech., 86, 491.
- Gibson, M. M., W. P. Jones, and B. A. Younis (1981). "Calculation of turbulent boundary layers on curved surfaces," Phys. of Fluids, 24, 386-395.
- Gibson, M. M., and W. Rodi (1981). "A Reynolds-stress closure model of turbulence applied to the calculation of a highly curved mixing layer," J. Fluid Mech., 103, 161-182.
- Gosman, A. D., and W. M. Pun (1974). "Calculation of recirculating flows," Imperial College London, Report No. HTS/74/2.
- Hancock, D. E. (1980). "The effect of free-stream turbulence on turbulent boundary layer," Ph.D. Thesis, Univ. of London.
- Hossain, M. S. (1980). "Mathematische Simulierung turbulenter Auftriebsströmungen," Ph.D. Thesis, University of Karlsruhe.
- Lam, C. K. G., and K. A. Bremhorst (1978). "Modified form of the k- ϵ model for predicting wall turbulence," Univ. of Queensland, Dept. Mech. Eng., Res.-Rept. 3/78.
- Launder, B. E., and D. B. Spalding (1974). "The numerical computation of turbulent flow," Comp. Meth. in Appl. Mech. and Eng., 3, 269.
- Launder, B. E., G. J. Reece, and W. Rodi (1975). "Progress in the development of a Reynolds stress turbulence closure," J. Fluid Mech., 68, 537-566.
- Leschziner, M. A. (1980). "A numerical scheme for simulating the vertical structure of time-dependent natural water flows," Report SFB 80/T/168, University of Karlsruhe.
- Leschziner, M. A., and W. Rodi (1979). "Calculation of strongly curved open channel flow," ASCE, J. Hydraulics Div., 105:HY10, 1297-1314.
- Murphy, J. D., and M. W. Rubesin (1979). "A Navier-Stokes fast solver for turbulence modelling applications," AGARD-CP 271, 12-1-12-16.
- Neot, D., and W. Rodi (1981). "Numerical simulation of secondary currents in open channel flow with an algebraic stress turbulence model," Rept. SFB80/T/187, University of Karlsruhe.
- Patankar, S. V., and D. B. Spalding (1970). Heat and Mass Transfer in Boundary Layers, 2nd ed. Intertext, London.
- Patankar, S. V., and D. B. Spalding (1972). "A calculation procedure for heat, mass and momentum transfer in three-dimensional parabolic flows," IJHMT, 15, 1787.
- Patel, V. C., W. Rodi, and G. Scheuerer (1981). "Evaluation of turbulence models for near-wall and low-Reynolds number flows," Proc., 3rd Symposium on Turbulent Shear Flows, Davis, Calif.
- Pratap, V. S., and D. B. Spalding (1976). "Fluid flow and heat transfer in three-dimensional duct flows," IJHMT, 19, 1183.
- Rodi, W. (1980). Turbulence Models and Their Application in Hydraulics - A State-of-the-Art Review. International Association for Hydraulic Research Book Publication, Delft.
- Rotta, J. C. (1972). Turbulent Strömungen. B. G. Teubner, Stuttgart.
- Shabaka, I. M. M. A., and P. Bradshaw (1981). "Turbulent flow measurements in an idealized wing-body junction," AIAA Jou., 19, 131-132.

COMPARISON OF COMPUTATION WITH EXPERIMENT

Summary Report

(Lag Entrainment, Viscous Garabedian and Korn and
Advanced Viscous Garabedian and Korn Methods)

by

P. D. Smith*

Computer Group Number: 32



Cases 0141, 0231, 0232, 0233, 0612, 8101, 8411, 8621

The calculations which have been made for this Conference are of two types: (a) flows involving boundary-layer calculations for a prescribed external flow (Cases 0141, 0231, 0232, 0233, 0612, 8101 and 8411) and (b) flows involving an interactive calculation between the viscous and inviscid parts of the flow field (Case 8621).

Type (a) calculations were made with the lag-entrainment method of Green et al. (1973). This method, which is fully described in the previous reference, uses the momentum integral equation, the entrainment equation and an equation for the stream-wise rate of change of the entrainment coefficient. This last equation, developed from the equation for shear stress, which Bradshaw, Ferriss and Atwell (1967) derived from the turbulent kinetic-energy equation, allows account to be taken of the influence of the upstream flow history on the turbulent stresses. The method also allows for the effects of secondary influences, such as longitudinal surface curvature (Cases 0231, 0232 and 0233), upon the turbulence structure to be taken into account.

Type (b), interactive, calculations have been made with the viscous Garabedian and Korn method developed by Collyer and Lock (1978, 1979). For the inviscid part of the flow the method is based on the work of Garabedian and Korn (1971) and Bauer, Garabedian and Korn (1972). The development of a satisfactory solution, when shock waves of appreciable strength are present, is obtained by the use of a "partially conservative" finite-difference scheme in the inviscid method. This approach is based upon an empirical scheme (involving a variable λ here taken to be 0.4), which ensures that the pressure jump at a shock wave provides a reasonable approximation to the true Rankine-Hugoniot shock jump. For the calculation of the boundary-layer development a laminar boundary layer, calculated by the Thwaites method modified for compressibility proposed by Curle (1962), is assumed to occur from the stagnation point to a specified transition point. At transition, continuity of momentum thickness is assumed. The turbulent boundary layer and the wake downstream of the airfoil are calculated by the lag-entrainment method of Green et al. (1973) described above.

*RAE, Bedford, England

An iterative procedure is employed to obtain consistent solutions for the inviscid flow and the boundary layer. After every few iterations of the inviscid scheme the current pressure is calculated on the airfoil surface and along the wake. This is used to determine the current values of the boundary layer and wake displacement and momentum thicknesses. The boundary conditions for the inviscid scheme are modified to take account of the viscous effects by means of the "equivalent source" or "surface transpiration" model. Under-relaxation is used in applying the boundary conditions. An allowance for curvature effects of the boundary layer on the pressures on the airfoil and in the wake is included in these boundary conditions.

In addition to the calculations for Case 8621 with the standard viscous Garabedian and Korn method, calculations have also been made with what is termed here the Advanced Viscous Garabedian and Korn method in which the boundary-layer method has been improved to make allowances for the effects of pressure gradients normal to the surface and the effects of the turbulent normal stresses. These improvements have been detailed elsewhere (in East, 1981; Lock and Firmin, 1981), but as both these references are very recent, some details are given below.

The method uses a curvilinear coordinate system s, n with s along the wall and n normal to it. The wall curvature is denoted by k_w (taken positive if the wall is concave upwards). The concept of the equivalent inviscid flow is introduced as an analytic continuation of the inviscid flow outside the shear layer right down to the surface. Values appropriate to the equivalent inviscid flow are denoted by the subscript i , wall values by the subscript w . In terms of the difference between the real viscous flow and the equivalent inviscid flow the equation of continuity may be written

$$\frac{\partial}{\partial s} (\rho_i u_i - \rho u) + \frac{\partial}{\partial n} [(1 - k_w n)(\rho_i v_i - \rho v)] = 0 \quad (1)$$

which when integrated from $n = 0$ to $n = \delta$ yields

$$\rho_i v_{iw} = \frac{d}{ds} \int_0^{\delta} (\rho_i u_i - \rho u) dn \quad (2)$$

We may define a displacement thickness $\bar{\delta}$ as

$$\bar{\delta} = \frac{1}{\rho_{iw} u_{iw}} \int_0^{\delta} (\rho_i u_i - \rho u) dn \quad (3)$$

so that the transpiration velocity v_{iw} required in the matching process is given by

$$v_{iw} = \frac{1}{\rho_{iw}} \frac{d}{ds} (\rho_{iw} u_{iw} \bar{\delta}) \quad (4)$$

The usual displacement thickness δ^* is defined by the equivalence of mass flows

$$\int_{\delta^*}^{\delta} \rho_1 u_1 dn = \int_0^{\delta} \rho u dn \quad (5)$$

or

$$\int_0^{\delta^*} \rho_1 u_1 dn = \rho_{1w} u_{1w} \bar{\delta} \quad (6)$$

Note that if $\rho_1 u_1$ is invariant with n , then $\bar{\delta}$ and δ^* are identical.

Similarly we may derive a streamwise momentum integral equation for the differences between the real viscous and the equivalent inviscid flows. After the neglect of two higher-order terms related to the wall curvature, this reads

$$\frac{1}{\rho_{1w} u_{1w}} \frac{d}{ds} (\rho_{1w} u_{1w}^2 \theta) + \frac{\bar{\delta}}{u_{1w}} \frac{du_{1w}}{ds} - \frac{C_f}{2} = \frac{1}{\rho_{1w} u_{1w}} \frac{d}{ds} \left[- \int_0^{\delta} (p_1 - p) dn + \int_0^{\delta} \overline{\rho u'^2} dn \right] \quad (7)$$

where the momentum thickness $\bar{\theta}$ is defined by

$$\rho_{1w} u_{1w}^2 (\bar{\theta} + \bar{\delta}) = \int_0^{\delta} (\rho_1 u_1^2 - \rho u^2) dn$$

so that

$$\bar{\theta} = \frac{1}{\rho_{1w} u_{1w}^2} \int_0^{\delta} [\rho u (u_{1w} - u) + \rho_1 u_1 (u_1 - u_{1w})] dn \quad (8)$$

If the terms on the right-hand side of Eq. 7 are neglected and U_1 is set equal to U_{1w} , the ordinary first-order momentum integral equation is recovered.

From consideration of the momentum equation in the direction normal to the surface and from experimental evidence East (1981) has shown that the terms on the right-hand side of Eq. 7 may be approximated as

$$\int_0^{\delta} (p_1 - p) dn = \frac{1}{2} \rho_{1w} u_{1w}^2 K^* (\bar{\theta} + \bar{\delta})^2 + \int_0^{\delta} \overline{\rho v'^2} dn \quad (9)$$

where $K^* = K_w + \frac{d^2 \bar{\theta}}{ds^2}$

and

$$\int_0^{\delta} (\overline{\rho u'^2} - \overline{\rho v'^2}) dn = 0.072 \rho_{1w} u_{1w}^2 \bar{\theta} \frac{(\bar{H} - 1)}{\bar{H}} \frac{C_T}{C_{T_{eq}}} \quad (10)$$

where $H + 1 = (\bar{H} + 1)(1 + 0.2 M_{1w}^2)$, $H = \bar{\delta}/\bar{\theta}$ and C_T and $C_{T_{eq}}$ are parameters (actually maximum shear-stress coefficients) occurring in the lag-entrainment equation.

The result of an interactive calculation is the velocity distribution over the airfoil, U_{1w} , or its equivalent, the pressure distribution, P_{1w} . The required result

is the pressure distribution in the viscous flow, P_w , and this is found to be given by

$$\frac{P_{1w} - P_w}{2 \rho_{1w} u_{1w}} = K^* (\bar{\theta} + \bar{\delta}) \quad (11)$$

Two additional modifications have also been made to the boundary-layer calculation method when used in the "Advanced Viscous Garabedian and Korn" calculations. First, the skin-friction law has been modified to include a low-Reynolds-number effect; and second, in evaluating the effects of curvature upon the turbulence structure, a lag equation with a lag length of ten boundary-layer thicknesses has been introduced.

REFERENCES

- Bauer, F., P. R. Garabedian, and D. G. Korn (1972). "Supercritical wing sections," Lecture notes in Economic and Mathematical Systems No. 66, Springer-Verlag, Berlin.
- Bradshaw, P., D. H. Ferriss, and N. P. Atwell (1967). "Calculation of boundary-layer development using the turbulent energy equation," J. Fluid Mech., 28:3, 593-616.
- Collyer, M. R., and R. C. Lock (1978). "Improvement to the viscous Garabedian and Korn (VGK) method for calculating transonic flow past an aerofoil," RAE TR 78039.
- Collyer, M. R., and R. C. Lock (1979). "Prediction of viscous effects in steady transonic flow past an aerofoil," Aero. Quart., 30, 485.
- Curle, N. (1962). "The laminar boundary layer equations," Oxford Mathematical Monograph.
- East, L. F. (1981). "A representation of second order boundary layer effects in the momentum integral equation and in viscous-inviscid interactions," RAE TR 81002.
- Garabedian, P. R., and D. G. Korn (1971). "Analysis of transonic aerofoils," Comm. Pure Appl. Maths, 24, 841-851.
- Green, J. E., D. G. Weeks, and J. W. F. Brooman (1973). "Prediction of turbulent boundary layers and wakes in compressible flows by a lag-entrainment method," ARC R & M, 3791.
- Lock, R. C., and M. C. P. Firmin (1981). "Survey of techniques for estimating viscous effects in external aerodynamics," Proceedings, IMA Conference on Numerical Methods in Aeronautical Fluid Dynamics Reading University 30 March - 1 April 1981. Also RAE TM 1900.

COMPARISON OF COMPUTATION WITH EXPERIMENT

Summary Report

(Prediction of Complex Turbulent Flows using the PHOENICS Computer Code)

by

A. M. Abdelmeguid, S. Y. Goh, J. Ilegbusi, D. B. Spalding*

Computer Group Number: 33

Cases 0141, 0142, 0143, 0421, 0512, 0612

INTRODUCTION

PHOENICS is a flow-simulating computer code developed for the solution of fluid-flow problems; these may be transient or steady, compressible or incompressible, laminar or turbulent, and one-, two-, or three-dimensional. This summary describes the calculations performed on six of the Stanford Conference test cases which are steady and incompressible (Cases 0612, 0141, 0142, 0143, 0421, and 0512).

THE GOVERNING EQUATIONS

The full three-dimensional governing equations for the present calculations are as given in Appendix A. The conservation equations of the velocities, turbulence energy and turbulence dissipation may be expressed in the form of a single equation for a generic fluid variable ϕ , in vector notation, as:

$$\frac{\partial}{\partial t} (\rho\phi) + \text{div}(\rho\vec{u}\phi + \vec{J}_\phi) = S_\phi \quad (1)$$

where ρ is the fluid density, \vec{u} is the velocity vector, \vec{J}_ϕ is the diffusive-flux vector, and S_ϕ is the source of ϕ per unit volume. The source term S_ϕ includes the pressure-gradient term and the viscous and body-force terms. The diffusive flux is assumed to obey the following relationship:

$$\vec{J}_\phi = -\Gamma_\phi \text{grad } \phi$$

where Γ_ϕ denotes the exchange coefficients. The exchange coefficient of the momentum equations, the eddy viscosity, is calculated from the k- ϵ turbulence model described by Launder and Spalding (1974). The equation set (1), together with a pressure-correction equation derived from the continuity equation, are expressed in their finite-difference form. The solution procedure for these finite-difference equations is a development of that first reported by Patankar and Spalding (1972).

*Imperial College of Science and Technology, Department of Mechanical Engineering, Exhibition Road, London SW7, England

A SPECIAL FEATURE OF THE PHOENICS CODE

An important feature of the computer code is that it allows to the user to switch the solution procedure to that appropriate to solve economically (both in terms of computer time and storage) the equations of the particular type of flow. One of the following options may be activated by the user:

- (a) the whole-field solution of the pressure-correction equation, for flows which exhibit strong elliptic effects;
- (b) the repeated-march slab-by-slab solution of the pressure-correction equation, for flows in which the elliptic effects are small; and
- (c) the single-march slab-by-slab solution of the pressure-correction equation, for flows which are parabolic in nature.

DETAILS OF CALCULATIONS

Flows of a Parabolic Nature (Cases 0612, 0141, 0142, 0143)

The governing equations of the above-indicated cases reduce to those of the two-dimensional (plane or axisymmetric) boundary layer. The variables solved in each of these cases were pressure p , the two components of velocity U and V , the turbulence energy k , the turbulence dissipation ϵ , and the pressure correction p' . The grid was expanded to fit the flow domain of interest and the solution was obtained by marching integration in the longitudinal direction. For the half-grid cell element next to the wall, a "wall function" modified to account for pressure gradient, as proposed by Spalding (1977), was employed. The constants for the log law of the wall suggested by Coles and Hirst (1968) were adopted.

(a) Flat-plate boundary layers (Cases 0612 and 0141)

For these two flat-plate cases, the grid was made to expand with the boundary-layer growth so that the cross-stream width of the grid was proportional to $x^{0.8}$ where x was the longitudinal distance. The initial grid width was taken as 0.012 m and the flow was assumed to be turbulent from the start. A grid-independent solution was obtained with 87 forward steps of a size equal to the grid width, 21 cross-stream grid points, and 5 iterations of the solution of all variables at each forward step. This was checked by halving the forward-step size, and by increasing the number of cross-stream grid points to 25 and the number of iterations to 8 in turn, without significant change in the predicted results.

In Case 0612, the predicted results of the skin-friction coefficient C_f and the shape factor H , for x less than 1 m, were found to be sensitive to the initial velocity-profile specification. To procure better agreement of the predictions of the shape factor for x less than 1 m, the power of the initial velocity profile was increased from 1/7 to 3/4. This change in the velocity-profile did not affect the predicted results of C_f or H for x greater than 1 m.

The initial profile for k was obtained by fitting a cubic polynomial between the free-stream and the near-wall values of k as proposed by Ng (1971). The initial

values of dissipation ϵ were deduced from k and l_m where l_m was obtained from Escudier's formula (see Spalding, 1980).

The computer time per cell per forward step per variable was 0.0349 sec and the total time of the run was 319 sec on the Perkin-Elmer 7-32 computer.

Case 0141 was computed in the same manner as Case 0612, except that the velocity in the free stream was calculated from the given measurements of the pressure coefficient by assuming that Bernoulli's equation applies in the free stream. It was found necessary to assume an initial free-stream velocity of 26.2 m/s to obtain a solution of the free-stream velocity which matched the measured value of 26.0 m/s at $x = 1.04$ m.

A further check of grid independence of the solution was made by putting 5 extra cross-stream grid points between the first and the fifth grid points near the wall, without any significant change in the results. The computer time per cell per forward step per variable was 0.0363 sec and the total time of the run with 75 forward steps was 286 sec on the Perkin-Elmer 7-32 computer.

(b) Conical diffusers (Cases 0142 and 0143)

The grid for these two axisymmetric cases was made to fit the whole of the diffuser. The computations were started upstream of the divergent section and the initial velocity U and turbulence energy k were assumed uniform across the duct. The magnitude of the initial U and k were chosen so as to provide solutions of U and k at the symmetry axis which matched the following measured values at $x = -0.055$ m:

Case	0142	0143	
U	43.8	20.7	m/s
k	0.0219	13.9	m^2/s^2

The starting distance x_0 and the pressure coefficient C_{pw} were assumed as follows:

Case	0142	0143	
x_0	-0.9	-0.5	m
C_{pw}	0	-10.03	

The solutions presented are for a forward step size of 0.125 times the local duct radius, 29 cross-stream grid points and 5 iterations of all variables at each forward step. By arranging the cross-stream grid points to be closer to one another near the wall, grid-independent solutions may be obtained with 25 cross-stream grid points. Halving the step size did not have any significant effect on the predicted results.

It may be observed in Plates 22 and 26 for Cases 0142 and 0143, respectively, that the predictions of $\overline{u'v'}/U_\infty^2$ at $x = 1.813$ m were approximately twice as large as the measured values. (Note that at $x = 1.813$ m, $\overline{u'v'}/U_\infty^2$ plotted on twice the scale of the measured values.) This is surprising considering that the predictions of pressure coefficient, the skin-friction coefficient, and velocity distribution are in fair agreement with the measured values.

For Case 0142, the computer time per cell per forward step per variable was 0.0449 sec and the total time of the run with 176 forward steps was 987 sec on the Perkin-Elmer 7-32 computer. The corresponding values for Case 0143 were 0.0430 sec and 774 sec (144 forward steps), respectively.

The Backward-Facing Step (Case 0421)

For this case, the two-dimensional governing equations for continuity, the velocity components U and V , the turbulence energy k , the turbulence dissipation ϵ , and the pressure correction p' were solved. A Cartesian coordinate system was employed. The grid was made to fit the duct and step. A wall function derived from a $1/7$ -power velocity profile was used for the half-cell elements next to all walls. The calculations were started at $x/H = -4$ using a velocity profile generated from the given measured data at this station. The boundary-layer thickness at the north wall was assumed to be the same as that at the south wall. The initial value for k was assumed uniform across the duct and equal to $1.00 \text{ m}^2/\text{s}$. The turbulence dissipation ϵ was deduced from k and l_m as in Case 0612.

The grid lines were distributed non-uniformly over the flow domain with a larger number of grid points in the mixing layer just off the corner of the step. Grid-independence checks on the solution were performed up to a grid specification of 30 grid lines in the transverse direction and 50 grid lines in the main flow direction. Although the trend in the results showed that the predictions approached in the direction of the measurements with greater grid refinement, a grid-independent solution had not been reached. Further work is currently being carried out to refine the grid.

The computer time per cell per sweep over the flow domain per variable was 0.00152 sec and the total time of the run (for a total of 140 sweeps) was 1600 sec on a CDC 6600 computer.

The Curved Rectangular Duct (Case 0512)

Except for the transient terms and the Reynolds normal-stress terms, the full three-dimensional governing equations were solved in this problem. The curvature effects were introduced by way of the centrifugal force term $\rho U^2/R$ and the "Coriolis" term $\rho VU/R$ in the respective momentum equations. A Cartesian coordinate system was used with the stretching of the distances, areas, and volumes of the cell elements in the curved section of the duct accounted for by multiplying with "stretching factors," which are functions of the radius of curvature. The given continuity-corrected data of initial values were used. Errors arising out of interpolation between the measured velocity data to obtain values at the grid nodes were corrected by multiplying the interpolated velocity with a correction factor to ensure that the bulk velocity remained unchanged. A print-out of the mass flow calculated at each section confirmed that mass conservation was satisfied. The initial values of k and ϵ were calculated

from the measured data. A wall-function similar to that of Case 0421 was used for the half-cell element next to all walls.

A grid-independent solution was obtained for a grid with 34 grid points in the main flow direction, 20 grid points in the direction of the curvature and 16 grid points in the lateral direction. This was checked with reference to solutions obtained for coarser and finer grids. Further, the use of two different procedures (the arithmetic mean and the harmonic mean) for calculating the mean values between two grid points in the solution procedure produced substantially the same results.

The predictions showed only qualitative agreement with the measured data up to 71° of the bend. It should be noted that the additional terms resulting from the curvature of the duct in the U, V, W, k, and ϵ equations, as given by Pratap (1975), as well as the Reynolds normal-stress terms $\overline{u'^2}$, $\overline{v'^2}$ and $\overline{w'^2}$ in the momentum equations had been neglected in the calculations. Until further calculations with these terms included in the appropriate equations are completed, it is not known how they will affect the predicted results.

The computer time per cell per sweep per variable was 0.00142 sec and the total time of the run (for a total of 100 sweeps) was 9272 sec on a CDC 6600 computer.

CONCLUSION

A single flow-simulating computer code has been used to predict six steady and incompressible turbulent flows, including flows which are two-dimensional parabolic, two-dimensional elliptic, and three-dimensional partially parabolic. No attempt has been made to adjust the "constants" in the standard high-Reynolds number k- ϵ turbulence model incorporated in the computer code. The agreement with measured data was good for the four boundary layers, moderate for the duct flow and uncertain for the sudden enlargement.

References

- Coles, D., and E. Hirst (1968). "Memorandum on data selection," Proc., 1968-AFOSR-IFP-Stanford Conference on Turbulent Boundary Layers, Vol. II, Stanford Univ., CA.
- Launder, B. E., and D. B. Spalding (1974). "The numerical computation of turbulent flows," Computer Methods in Appl. Mech. and Eng., 3, 269-289.
- Ng, K. H. (1971). "Predictions of turbulent boundary layer developments using a two-equation model of turbulence," Ph.D. Thesis, University of London.
- Patankar, S. V., and D. B. Spalding (1972). "A calculation procedure for heat, mass and momentum in three-dimensional parabolic flows," IJHMT, 15, 1787-1806.
- Pratap, V. S. (1975). "Flow and heat transfer in curved ducts," Imperial College Heat Transfer Section Report No. HTS/75/25.
- Spalding, D. B. (1977). GENMIX - A General Computer Program for Two-Dimensional Parabolic Phenomena. Pergamon Press, New York.
- Spalding, D. B. (1980). "Turbulence models," Imperial College Heat Transfer Section Report No. HTS/80/2.

Appendix A:

Reynolds Momentum Equations (Time-Averaged Navier-Stokes):

$$\begin{aligned} \frac{\partial(\bar{\rho})}{\partial t} + \frac{\partial(\bar{\rho}\bar{u})}{\partial x} + \frac{\partial(\bar{\rho}\bar{v})}{\partial y} + \frac{\partial(\bar{\rho}\bar{w})}{\partial z} &= -\frac{\partial\bar{p}}{\partial x} + \frac{\partial(\bar{\tau}_{xy} - \bar{\rho}\overline{u'v'})}{\partial y} + \frac{\partial(\bar{\tau}_{xz} - \bar{\rho}\overline{u'w'})}{\partial z} - \frac{\bar{\rho}\bar{u}}{R} \\ \frac{\partial(\bar{\rho}\bar{v})}{\partial t} + \frac{\partial(\bar{\rho}\bar{v}\bar{u})}{\partial x} + \frac{\partial(\bar{\rho}\bar{v}\bar{v})}{\partial y} + \frac{\partial(\bar{\rho}\bar{v}\bar{w})}{\partial z} &= -\frac{\partial\bar{p}}{\partial y} + \frac{\partial(\bar{\tau}_{yz} - \bar{\rho}\overline{v'v'})}{\partial z} + \frac{\partial(\bar{\tau}_{yx} - \bar{\rho}\overline{v'u'})}{\partial x} - \frac{\bar{\rho}\bar{v}}{R} \\ \frac{\partial(\bar{\rho}\bar{w})}{\partial t} + \frac{\partial(\bar{\rho}\bar{w}\bar{u})}{\partial x} + \frac{\partial(\bar{\rho}\bar{w}\bar{v})}{\partial y} + \frac{\partial(\bar{\rho}\bar{w}\bar{w})}{\partial z} &= -\frac{\partial\bar{p}}{\partial z} + \frac{\partial(\bar{\tau}_{zx} - \bar{\rho}\overline{w'u'})}{\partial x} + \frac{\partial(\bar{\tau}_{zy} - \bar{\rho}\overline{w'v'})}{\partial y} + \frac{\bar{\rho}\bar{w}}{R} \end{aligned}$$

Continuity:

$$\frac{\partial\bar{\rho}}{\partial t} + \frac{\partial(\bar{\rho}\bar{u})}{\partial x} + \frac{\partial(\bar{\rho}\bar{v})}{\partial y} + \frac{\partial(\bar{\rho}\bar{w})}{\partial z} = 0$$

$$-\bar{\rho}\overline{u'_j u'_j} = \mu_t \left\{ \frac{\partial\bar{u}_j}{\partial x_j} + \frac{\partial\bar{u}}{\partial x_1} \right\}, \quad \bar{\tau}_{ij} = \mu \left(\frac{\partial\bar{u}_i}{\partial x_j} + \frac{\partial\bar{u}_j}{\partial x_i} \right),$$

$\mu_t = C_\mu \bar{\rho} \frac{k^2}{\epsilon}, \quad \mu = \text{laminar viscosity}$

Turbulence Kinetic Energy Equation:

$$\begin{aligned} \frac{\partial}{\partial t} (\bar{\rho}k) + \frac{\partial}{\partial x} (\bar{\rho}k\bar{u}) + \frac{\partial}{\partial y} (\bar{\rho}k\bar{v}) + \frac{\partial}{\partial z} (\bar{\rho}k\bar{w}) &= \frac{\partial}{\partial x} \left[\left(\mu + \frac{\mu_t}{\sigma_{t,k}} \right) \frac{\partial k}{\partial x} \right] + \frac{\partial}{\partial y} \left[\left(\mu + \frac{\mu_t}{\sigma_{t,k}} \right) \frac{\partial k}{\partial y} \right] + \frac{\partial}{\partial z} \left[\left(\mu + \frac{\mu_t}{\sigma_{t,k}} \right) \frac{\partial k}{\partial z} \right] + \rho(P-\epsilon) \\ P &= \frac{\mu_t}{\bar{\rho}} \left\{ 2 \left[\left(\frac{\partial\bar{u}}{\partial x} \right)^2 + \left(\frac{\partial\bar{v}}{\partial y} \right)^2 + \left(\frac{\partial\bar{w}}{\partial z} \right)^2 \right] + \left[\frac{\partial\bar{u}}{\partial z} + \frac{\partial\bar{w}}{\partial x} \right]^2 + \left[\frac{\partial\bar{v}}{\partial y} + \frac{\partial\bar{w}}{\partial z} \right]^2 \right\} \end{aligned}$$

Turbulence Dissipation Equation:

$$\frac{\partial}{\partial t} (\bar{\rho}\epsilon) + \frac{\partial}{\partial x} (\bar{\rho}\epsilon\bar{u}) + \frac{\partial}{\partial y} (\bar{\rho}\epsilon\bar{v}) + \frac{\partial}{\partial z} (\bar{\rho}\epsilon\bar{w}) = \frac{\partial}{\partial x} \left[\left(\mu + \frac{\mu_t}{\sigma_{t,\epsilon}} \right) \frac{\partial \epsilon}{\partial x} \right] + \frac{\partial}{\partial y} \left[\left(\mu + \frac{\mu_t}{\sigma_{t,\epsilon}} \right) \frac{\partial \epsilon}{\partial y} \right] + \frac{\partial}{\partial z} \left[\left(\mu + \frac{\mu_t}{\sigma_{t,\epsilon}} \right) \frac{\partial \epsilon}{\partial z} \right] + C_1 \frac{\bar{\rho}k^2}{R} - C_2 \frac{\bar{\rho}k^2}{R}$$

Law of the Wall:

$$R_e \geq 132.25, \quad \bar{s} = \left[\frac{K}{2\pi} (\text{ER}_e \bar{s}^2) \right]^2 \quad \text{where } \bar{s} = s + M/(1+b) + \frac{1}{2}P$$

$$R_e < 132.25, \quad s = \frac{M \left[1 - \exp(-MR_e) \right] - 1 - MR_e}{\exp(MR_e) - 1} F / (M R_e)$$

$S \equiv \tau_B / (\bar{\rho}\bar{u}^2) C$
 $M \equiv (\bar{u}_B^2 / \bar{\rho}\bar{u}) C \frac{d\bar{p}}{dx}$
 $P \equiv (y / \bar{\rho}\bar{u}^2) C \frac{d\bar{p}}{dx}$
 $Re \equiv (\bar{\rho}\bar{u}y / \mu) C$

Constants: $C_\mu = 0.09, C_1 = 1.44, C_2 = 1.92, \sigma_{t,k} = 1.0, \sigma_{t,\epsilon} = 1.314, K = 0.410, b = 7.768.$

COMPARISON OF COMPUTATION WITH EXPERIMENT

Summary Report

by

Y. Tassa*

Computer Group Number: 09

Case 8621

SUMMARY

The unsteady compressible Reynolds time-averaged Navier-Stokes equations which include an algebraic turbulence model, have been applied to the RAE 2822 airfoil for subcritical and supercritical flow conditions. The program has also the option of using $k-\epsilon$, but it was not used in our present results. The governing equations are written in conservation form in a body-fitted coordinate system and solved numerically using an Alternating Direction Implicit (ADI) procedure. In the following sections an outline is first given of the mathematical formulation, then the grid generation and the numerical procedure. The boundary conditions and turbulence model are discussed. Finally, the numerical results and outcomes of our experience with the present method for calculating complex flow problems are summarized.

MATHEMATICAL FORMULATION

The two-dimensional unsteady compressible Navier-Stokes equations may be written in a strong conservation form in a general non-orthogonal curvilinear coordinate system as

$$\frac{\partial}{\partial \tau} \{\hat{q}\} + \frac{\partial}{\partial \xi} \{\hat{F}\} + \frac{\partial}{\partial \eta} \{\hat{G}\} = 0 \quad (1)$$

where ξ , η , and τ are the independent variables, subject to the general transformation

$$\xi = \xi(x, y, t); \quad \eta = \eta(x, y, t); \quad \tau = t \quad (2)$$

and

$$\{\hat{q}\} = \frac{1}{J} \{\hat{q}^*\}; \quad \{\hat{F}\} = \frac{1}{J} \{\xi_t \hat{q}^* + \xi_x \hat{F}^* + \xi_y \hat{G}^*\}; \quad \{\hat{G}\} = \frac{1}{J} \{\eta_t \hat{q}^* + \eta_x \hat{F}^* + \eta_y \hat{G}^*\} \quad (3)$$

where:

$$\hat{q} = \begin{Bmatrix} \rho \\ \rho u \\ \rho v \\ \rho \left(e + \frac{u^2 + v^2}{2} \right) \end{Bmatrix}; \quad \hat{F} = \begin{Bmatrix} \rho u \\ \rho u^2 + p - \tau \\ \rho uv - \tau_{xy} \\ \rho u \left(\gamma e + \frac{u^2 + v^2}{2} \right) - \beta_x \end{Bmatrix}; \quad \hat{G} = \begin{Bmatrix} \rho v \\ \rho uv - \tau \\ \rho v + \tau_{yy} \\ \rho v \left(\gamma e + \frac{u^2 + v^2}{2} \right) - \beta_y \end{Bmatrix} \quad (4)$$

*Lockheed Georgia Co., Dept. 72-74, Zone 404, Marietta, GA 30063

$$J = \xi_x \eta_y - \xi_y \eta_x \quad (5)$$

$$\mu_T = \mu + \mu_t \quad (6)$$

where p is the pressure, ρ is the density, e the specific internal energy, and λ is taken as $-2/3\mu_T$ according to the Stokes' hypothesis. Here x_T and y_T are the Cartesian velocities of the grid point (x,y) . In the present calculation the airfoil is stationary; therefore, x_T and y_T are taken to be zero. In the above equations all distances are normalized with respect to the airfoil chord c , the velocities are normalized with respect to free-stream velocity V_∞ , the density is normalized with respect to free-stream density ρ_∞ , and the specific internal energy is normalized with respect to V_∞^2 . R_e and P_R are the Reynolds number and Prandtl number, respectively, and μ_T is the total viscosity.

GRID GENERATION

The main advantage of a generalized curvilinear coordinate system is that boundary surfaces in the physical plane are mapped onto rectangular surfaces in the transformed plane and boundary conditions may be treated more accurately. Also grid points may be clustered in regions where rapid changes in the flow field gradients occur. The grid generation used in the present work is based on the Thompson method that solves two Poisson equations. An "O"-type grid has been used in the present work, since it gives the best airfoil resolution for the same number of grid points. In the present calculation the first grid point is placed 0.0001 chords from the airfoil surface, and 35 grid points are placed in the η direction. The airfoil surface is represented by 81 grid points and the outer boundary is placed at 16 chord lengths from the airfoil surface for the subcritical case and 24 chord lengths for the supercritical case.

NUMERICAL PROCEDURE

The numerical procedure used to solve the governing equations is a modified form of the Briley-McDonald ADI procedure. It is also closely related to the Warming-Beam algorithm. The method can be outlined as follows: The governing equations are parabolic with respect to time. Assuming the flow field is known at a time level t_n , the ADI procedure is used to advance the solution to a new time level $t_n + 1$ using a fairly large time step. The metric terms ξ_x , ξ_y , etc., are evaluated numerically at an intermediate time level $t_n + 1/2$. The mixed derivatives that arise from terms such as $(\xi_x u_{r_{xx}})\xi$ etc. are lagged one time step. The flow quantities ρ , u , v , and e at the new time level are written in terms of their values at the known time level and incremental quantities. For example,

$$\rho^{n+1} = \rho^n + \Delta\rho \quad (7)$$

Terms involving non-linearities at the time level $t_n + 1$ are linearized by a Taylor expansion about the solution at known time level t_n . The time derivative $\partial q / \partial t$ is written as a two-point backward difference formula at the new time level. Performing these operations and taking all the quantities at the known time level to the right-hand side, one obtains a linear matrix equation for the incremental quantities at each grid point in the computational plane, except at grid points on the boundaries. The matrix equation may be written as:

$$[A]\{\Delta q\} + \frac{\partial}{\partial \xi} [B]\{\Delta q\} + \frac{\partial}{\partial \eta} [C]\{\Delta q\} = \{R\}^n \quad (8)$$

The Douglas-Gunn procedure for generating an alternating-direction implicit scheme is introduced now to solve the above system of equations by approximately splitting Eq. 8 into two equations, where each involves only a one-dimensional operator:

$$[A]\{\Delta q\}^* + \frac{\partial}{\partial \xi} [B]\{\Delta q\}^* = \{R\}^n \quad (9)$$

$$[A]\{\Delta q\} + \frac{\partial}{\partial \eta} [C]\{\Delta q\} = [A]\{\Delta q\}^* \quad (10)$$

Note that

$$\{\Delta q\} = \{\Delta \rho, \Delta u, \Delta v, \Delta e\}^T \quad (11)$$

Equations 9 and 10 are discretized using second-order accurate central-difference formulas for the spatial derivatives. This technique leads to a system of block tri-diagonal matrix structure which may be solved efficiently by a standard block-elimination procedure. One needs to provide boundary conditions for the unknown $\{\Delta q\}$, as well as for $\{\Delta q\}^*$ at the boundaries. Once $\{\Delta q\}$ is obtained, the flow-field variables at the new time level is explicitly known. In the present application fourth-order artificial dissipation terms have been added explicitly to the right-hand side in the manner suggested by Steger to suppress the high-frequency components associated with numerical instability that appear in high-Reynolds-number problems. The conservation of mass momentum and energy is inherent in the equations and no specific check is done in the program.

BOUNDARY CONDITIONS

The present procedure requires boundary conditions to be set on the solid boundary $\eta = \eta_{\min}$, the far-field boundary $\eta = \eta_{\max}$, and at the fictitious cuts $\xi = \xi_{\min}$ and $\xi = \xi_{\max}$. At the solid boundary the condition of no slip requires the fluid velocity to be the same as that of the solid; the solid motion is known. Also, the adiabatic flow condition ($\partial e / \partial \eta = 0$) has been applied on the solid surface. The density at the surface may be evaluated in various ways; in the present calculation we

used a two-point extrapolation of the form

$$\rho_{i,1} = \frac{4}{3} \rho_{i,2} - \frac{1}{3} \rho_{i,3} \quad (12)$$

For the far-field boundary, $\eta = \eta_{\max}$, the free-stream values have been used since the boundary is reasonably far from the airfoil.

ALGEBRAIC TURBULENCE MODEL

In the present work, the effects of turbulence are simulated using an algebraic eddy-viscosity model. Recently, progress has been made in using multi-equation turbulence models in conjunction with Navier-Stokes equations to simulate the behavior of separated turbulent flows. Yet numerical results using multi-equation turbulence models for separated flows are not completely satisfactory. For this reason the simpler, algebraic model was chosen. The algebraic turbulence model used in the present work is that of Baldwin-Lomax, who modified the Cebeci turbulence model; this model is more suitable for use in Navier-Stokes solvers.

NUMERICAL RESULTS

The numerical results reported here include the subcritical and supercritical flow conditions over the RAE 2822 supercritical airfoil tested experimentally by Cook et al. (Case 8621). The test cases calculated are referenced in Cook et al. as test case (1) and test case (12). The flow conditions are:

	Test Case 1	Test Case 12
M_∞	0.676	0.730
α [deg]	2.40	3.19
$R_\infty/c * 10^{-6}$	5.7	2.7
Transition trip x/c	0.11	0.03

As suggested by Cook et al. the angle of attack must be corrected according to the formula

$$\Delta\alpha = \frac{cC_L}{h} \delta_0 + \frac{c^2}{\beta h^2} \delta_1 \left(\frac{1}{4} C_L + C_m \right) \quad [\text{radian}] \quad (13)$$

The corrected angles of attack for case (1) and case (12) are 1.787° and 2.734° , respectively. In the present calculations no Mach-number corrections have been tried and the free-stream values were used as recommended by Cook et al. The physical plane, which is "O"-type mesh, is transformed into a rectangular domain using the Thompson et al. method for grid generation with 81 grid points over the airfoil surface and 35 points in the η -direction.

The first grid spacing is $\Delta y = 0.0001 c$ away from the surface and is exponentially stretched to the outer boundary which is 16 chords away for case (1) and 24 chords away for case (12). The pressure distribution and skin-friction distribution for both cases are shown in Plates 160-165 and 159, respectively. Convergence has been obtained in about 2000 iterations using impulsive start. The time steps used start with relatively low, about 2-5 CFL, and increase up to about 100 after the transient motion has been relaxed.

An interesting experience occurs due to the effect of the outer boundary conditions; when the outer boundary is about 8 chords away, non-reflecting boundary conditions must be used to cancel reflected waves from outflow boundary which otherwise tend to affect the pressure flow field. In the present results the outer boundary is far enough away not to cause any meaningful changes of the results before steady state has been reached. This in turn slows down the convergence and requires more time steps to reach convergence. It seems important to use non-reflecting boundary conditions for an outflow region, particularly for supercritical cases when the outer boundary is of the order of 8-10 chords away. If the free-stream condition was used when the outer boundary is about 6 chords away, the reflected waves from the boundary affected the results very adversely, and the calculations became unstable after a certain time. The results were obtained using a VAX 11/780.

COMPARISON OF COMPUTATION WITH EXPERIMENT

Summary Report (Computation of Turbulent Wakes)

by

D. D. Vandromme*

Computer Group Number: 35

Cases, 0381, 0382, 0471

INTRODUCTION

The first two cases are the prediction of turbulence quantities for incompressible symmetric and asymmetric wake flows behind a flat plate. The experimental data were obtained by Andreopoulos (1978). The asymmetry of the second case (0382) is induced by a thickening of the boundary layer on one side with sandpaper; the free-stream conditions are identical. The requirements are the prediction of the mean-velocity and turbulence correlations up to the third order.

The third case corresponds to higher-speed wakes. Within this case, three flow conditions are considered

- Symmetric wake, Mach number M = 0.4
- Symmetric wake, Mach number M = 0.7
- Asymmetric wake, Mach number M = 0.4

Instead of a thin flat plate, the body has a finite thickness and is terminated by a 12°-angle wedge. This induces strong pressure variations both in the streamwise and in the cross-flow directions. The requirements for this case are the prediction of the mean-velocity and Reynolds stresses (shear stress and turbulent kinetic energy).

For all cases, the same numerical scheme is used. The method is a modified version of the original Patankar-Spalding marching procedure (1970).

The Navier-Stokes Equations for Two-Dimensional Parabolic Flow

The basic approximation for these calculations is to use the boundary-layer form of the Favre-averaged Navier-Stokes equations. For a two-dimensional steady flow without heat transfer, the Navier-Stokes equations are reduced to the continuity equation and one momentum equation for the streamwise velocity component:

$$\frac{\partial}{\partial x} (\overline{\rho U}) + \frac{\partial}{\partial y} (\overline{\rho V}) = 0$$
$$\frac{\partial}{\partial x} (\overline{\rho U^2}) + \frac{\partial}{\partial y} (\overline{\rho UV}) = - \frac{\partial \overline{P}}{\partial x} + \frac{\partial}{\partial y} \left[\mu \frac{\partial \overline{U}}{\partial y} - \overline{\rho u''v''} \right]$$

* NASA Ames Research Center, Moffett Field, CA 94035

In order to remove the closure problem, two different turbulence models have been used. As triple velocity correlations are required for Cases 0381 and 0382, a second-order closure model (Launder-Reece-Rodi) is used. The transport equations for the four Reynolds-stress components and their dissipation rate are obtained by transforming the Navier-Stokes equations and all modeling assumptions as explained in Launder et al. (1975). The solution of these equations provides the values of the second-order moments and the triple velocity correlations can easily be approximated by a product of Reynolds stress with their derivatives (see Launder et al., 1975). The calculation of the third case was not done with this model. A simpler k-ε turbulence model (Jones and Launder, 1972) has been used to predict only the mean velocity, the Reynolds stress, and the turbulent kinetic energy. The standard form of the model with no pressure-gradient term is coupled with the Navier-Stokes equations. Any pressure gradient is taken into account only through the body-force term of the longitudinal momentum equation.

The Numerical Method

The equations, which are to be solved by the marching procedure, are written under a common form,

$$\frac{\partial \phi}{\partial x} + [A + B\omega] \frac{\partial \phi}{\partial \omega} = \frac{\partial}{\partial \omega} \left[C \frac{\partial \phi}{\partial \omega} \right] + S_1 \phi + S_{NL}$$

where (x,ω) are the transformed coordinates:

$$x = x ; \quad \omega = \frac{\psi - \psi_I}{\psi_E - \psi_I} ; \quad \psi = \int_0^y \rho \tilde{U} dy$$

The equations are then discretized and integrated over an elementary cell, through a tridiagonal matrix inversion. The equations are solved successively, starting with the momentum equation. Experience (see Vandromme, 1980) has shown that no iteration is necessary at each step, provided that the marching step is small enough.

Practical Aspects of the Computations

Computation grid

In the cross-flow direction, 200 points are distributed for which the spacing decreases in the regions of the velocity gradients. For the boundary-layer calculations (Case 0471, x < 0) only 100 points are used in each single layer but starting from the trailing edge, the two separate grids join each other to make the 200 point wake grid. The marching step size is calculated at each step as a fraction of a characteristic thickness (usually the half-velocity width).

Boundary conditions

The boundary conditions are chosen to be as simple as possible. We used Dirichlet-type for the longitudinal velocity and Neumann-type (zero gradient) for the Reynolds-stress components and the dissipation rate.

The initial profiles are given by the experiments at the trailing edge (Cases 0381, 0382).

For Case 0471, a boundary-layer calculation is started 1 m ahead of the trailing edge, with equilibrium turbulent boundary-layer profiles. The initial boundary-layer thickness is adjusted to match the measured data before the trailing edge. At the trailing edge, the two grids are put together, the low turbulent Reynolds-number corrections are shut off, and the wake calculation starts.

The longitudinal pressure-gradient value is given by the experiments and the boundary values of the longitudinal velocity are determined accordingly.

Typical runs

All calculations were performed on a DEC-VAX 11/780 computer, on which the average time for the wake calculation was 30 min of CPU time.

REFERENCES

- Andreopoulos, J. (1978). "Symmetric and asymmetric near wake of a flat plate," Ph.D. thesis. Imperial College, London.
- Jones, W. P., and B. E. Launder (1972). "The prediction of laminarization with a two equation model of turbulence," IJHMT, 15, 301-314.
- Launder, B. E., G. J. Reece, and W. Rodi (1975). "Progress in the development of a Reynolds stress turbulence closure," J. Fluid Mech., 68:3, 537-566.
- Patankar, S. V., and D. B. Spalding (1970). Heat and Mass Transfer in Boundary Layers. Intertext, London.
- Vandromme, D. D. (1980). "Turbulence modelling in variable density flow," Ph.D. thesis. Brussels University, Belgium.



J. Viegas

COMPARISON OF COMPUTATION WITH EXPERIMENT

Summary Report

by

J. Viegas, C. C. Horstman and C. Hung*

Computer Group Number: 36



C.C. Horstman

Cases 0471, 8101, 8201, 8403, 8601, 8611, 8631, 8632, 8641, 8651, 8661, 8663

The V-H-H group solved an incompressible free-shear flow (Case 0471), five transonic flows (Cases 8101, 8201, 8403, 8601, 8611), and six supersonic flows (Cases 8631, 8632, 8641, 8651, 8661, 8663) with two- and three-dimensional versions of a single numerical method using three different turbulence models.

The numerical method used here is the basic second-order, predictor-corrector, finite-difference, time-splitting method of MacCormack modified by his recently developed efficient explicit-implicit-characteristic algorithm. These modifications apply near a surface and result from replacing the basic explicit operator that accounts for the effects of flux normal to the wall with a combination of more efficient operators. This hybrid method is described in detail in MacCormack (1976) and Coakley and Viegas (1977).

The differential equations used to describe the mean flow for this study are the time-dependent, mass-averaged Navier-Stokes equations for a compressible fluid. Turbulent transport is included through an eddy-viscosity hypothesis. Zero bulk viscosity is assumed. The resulting equations in double subscript notation and in terms of mass-averaged variables can be written as

∂ρ / ∂t + ∂ / ∂x_i (ρu_i) = 0 (1)

∂ / ∂t (ρu_i) + ∂ / ∂x_j (ρu_j u_i) = - ∂p / ∂x_i + ∂ / ∂x_j (τ_ij^T) (2)

∂ / ∂t (ρh) + ∂ / ∂x_j (ρu_j h) = ∂p / ∂t + u_i ∂p / ∂x_i - ∂q_i^T / ∂x_i + τ_ij^T ∂u_i / ∂x_j (3)

The quantities q_i^T and τ_ij^T are the total (laminar plus turbulent) heat-flux vector and the total stress tensor, respectively.

*NASA-Ames Research Center, Moffett Field, CA 94035

They are defined by

$$q_i^T = -\frac{\mu}{Pr} \frac{\partial h}{\partial x_i} - \langle \rho u_i \tilde{h} \rangle = -\left(\frac{\mu}{Pr} + \frac{\mu_t}{Pr_t}\right) \frac{\partial h}{\partial x_i}$$

$$\tau_{ij}^T = \tau_{ij} - \langle \rho u_i \tilde{u}_j \rangle$$

where

$$\tau_{ij} = \mu \left(\frac{\partial u_i}{\partial x_j} + \frac{\partial u_j}{\partial x_i} - \frac{2}{3} \frac{\partial u_k}{\partial x_k} \delta_{ij} \right)$$

and where μ is the molecular viscosity given by the Sutherland viscosity law, μ_t is the turbulent eddy viscosity, and Pr and Pr_t are the molecular and turbulent Prandtl numbers, taken as 0.72 and 0.9, respectively. Two algebraic models and a two-equation model were used for the turbulence in this study. The expressions used for the Reynolds stress $-\langle \rho u_i \tilde{u}_j \rangle$ and the turbulent eddy viscosity μ_t in these models are outlined in the next few paragraphs.

Turbulence Model 1

In this model, the Reynolds stress is defined by $-\langle \rho u_i \tilde{u}_j \rangle \equiv (\mu_t/\mu)\tau_{ij}$. The turbulent eddy viscosity is expressed in terms of an inner and outer eddy-viscosity function as

$$\mu_t = \begin{cases} \mu_{t_{inner}} = \rho l^2 \left| \frac{\partial u}{\partial y} + \frac{\partial v}{\partial x} \right|; & \text{if } y < y_c \\ \mu_{t_{outer}} = \frac{0.0168 \rho u_e \delta^*}{[1 + 5.5(y/\delta)]^6}; & \text{if } y > y_c \end{cases}$$

where y_c is the first point at which $\mu_{t_{inner}}$ exceeds $\mu_{t_{outer}}$. The function l is the Prandtl mixing length modified by the van Driest damping factor and

$$l = \kappa y \left[1 - \exp\left(-\sqrt{\rho_w |\tau_w|} \frac{y}{A^+ \mu_w}\right) \right]$$

where $\kappa = 0.4$, $A^+ = 26$ are the von Karman and van Driest constants, respectively. The boundary-layer edge velocity u_e is set to the maximum value of u for $y < y_{max}$, y_{max} being chosen slightly outside the boundary layer. δ^* is the kinematic displacement thickness, and δ is the boundary-layer thickness.

Turbulence Model 2

In this model the Reynolds stress is also given by $(\mu_t/\mu)\tau_{ij}$. The turbulent eddy viscosity is based on the model of Escudier,

$$\mu_t = \rho (D\hat{l})^2 \hat{\omega}$$

where D is the van Driest damping factor. $\hat{\omega}$ is the absolute magnitude of the vorticity:

$$\hat{\omega} = |\nabla \times \mathbf{v}| = \left[\left(\frac{\partial w}{\partial y} - \frac{\partial v}{\partial z} \right)^2 + \left(\frac{\partial u}{\partial z} - \frac{\partial w}{\partial x} \right)^2 + \left(\frac{\partial v}{\partial x} - \frac{\partial u}{\partial y} \right)^2 \right]^{1/2}$$

\hat{l} is a mixing-length scale:

$$\hat{l} = \lambda \delta \tanh(0.41d/\lambda\delta)$$

and d is a "modified distance":

$$d = 2yz / \left[(y+z) + \sqrt{y^2 + z^2} \right]$$

Here δ is the value of d at the edge of the boundary layer, λ is a constant, and τ_w , ρ_w , μ_w are the values of shear stress, density, and molecular viscosity on the wall, respectively. y and z are coordinates normal to the flow direction x . The constant λ is taken as 0.08.

Turbulence Model 3

This model is known as the Wilcox-Rubesin two-equation model. Here the eddy viscosity is given by

$$\mu_t = \gamma^* \rho k / \omega \quad (\text{note, all quantities are mass-weighted averages})$$

The rate equations describing the kinetic energy of the turbulence k and the turbulent dissipation rate ω (ω is the turbulent dissipation rate per unit of kinetic energy) are

$$\frac{\partial}{\partial t} (\rho k) + \frac{\partial}{\partial x_j} (\rho u_j k) = \tau_{ij}^* \frac{\partial u_i}{\partial x_j} - \beta^* \rho \omega k + \frac{\partial}{\partial x_j} \left[(\mu + \sigma^* \mu_t) \frac{\partial k}{\partial x_j} \right]$$

$$\frac{\partial}{\partial t} (\rho \omega^2) + \frac{\partial}{\partial x_j} (\rho u_j \omega^2) = \gamma \frac{\omega^2}{k} \tau_{ij}^* \frac{\partial u_i}{\partial x_j} - [\beta + 2\sigma \left(\frac{\partial L}{\partial x_k} \right)^2] \rho \omega^3 + \frac{\partial}{\partial x_j} \left[(\mu + \sigma \mu_t) \frac{\partial \omega^2}{\partial x_j} \right]$$

where

$$\tau_{ij}^* = -\frac{2}{3} \rho k \delta_{ij} + \frac{\mu_t}{\mu} \tau_{ij}$$

and the length scale L is given by

$$L = \sqrt{k} / \omega$$

Modeling closure coefficients employed are:

$$\gamma^* = [1 - (1 - \lambda^2) \exp(-R_{e_T} / R_k)] ; \quad \gamma = \gamma_w [1 - (1 - \lambda^2) \exp(-R_{e_T} / R_w)] \gamma^*$$

$$\beta^* = 0.09 ; \quad \beta = 0.15 ; \quad \sigma^* = 1/2 ; \quad \sigma = 1/2$$

$$R_k = 1 ; \quad R_w = 2 ; \quad \lambda = 1/11 ; \quad \gamma_w = 0.9$$

The stress tensor for this model is given by

$$-\langle \rho u_i u_j \rangle = -\frac{2}{3} \rho k \delta_{ij} + \frac{\mu_t}{\mu} \tau_{ij} + Ck \frac{(S_{im} \Omega_{mj} + S_{jm} \Omega_{mi})}{(\beta^* \omega^2 + 2 S_{mn} S_{nm})}$$

where

$$S_{ij} = \frac{1}{2} \left(\frac{\partial u_i}{\partial x_j} + \frac{\partial u_j}{\partial x_i} \right); \quad \Omega_{ij} = \frac{1}{2} \left(\frac{\partial u_i}{\partial x_j} - \frac{\partial u_j}{\partial x_i} \right),$$

and C, the coefficient of the anisotropic terms, is 8/9.

For more details on the analysis or models, see Viegas and Horstman (1979) and Hung and MacCormack (1978).

Application of the numerical procedure to each of the flows studied was conceptually similar. The computational domain is divided into a two-mesh system. An exponentially stretched fine mesh is used near the wall to resolve that part of the flow where viscous effects are important; the outer flow, which is predominantly inviscid, is described using a uniform coarse mesh. A uniform mesh is also used in the flow direction and in the cross-flow direction for three-dimensional flows. The number of mesh points used and the minimum spacing near the wall varied with the problem and the turbulence model. Generally, the first mesh point adjacent to the wall is selected such that moving it any closer to the wall would not significantly alter the solutions. For the algebraic models the first mesh point from the wall is taken within the viscous sublayer ($y_{\min}^+ \leq 4$); for the two-equation model, the minimum y^+ required was smaller by a factor of 10 or 20. In the flow direction, a grid spacing of from 0.16 to δ has been successfully applied to various flows, however; typically $\Delta x \sim 0.5\delta$ seems to give grid-independent results. In the cross-flow direction, although computer-storage limitations have prevented mesh-refinement studies, the results obtained for three-dimensional flows look reasonable in spite of the relatively coarse mesh used. Typical grid sizes were 100×40 for two-dimensional flows and $20 \times 30 \times 30$ for three-dimensional flows. Mesh-refinement studies were done for Cases 8403, 8601, 8611, and 8631. These had negligible effect on the results. Results are presented for the different grids used for Cases 8601 and 8631.

Other remarks on the calculated results of V-H-H group follow:

1. Turbulence model 3, the two-equation model, was used for all flows except the three-dimensional corner, Case 8661.
2. Although two turbulence models (Model 1 and Model 3) have been applied by V-H-H to Cases 8403, 8601, 8611, 8631, and 8651, we have only presented the two-equation (Model 3) results. In all cases Model 3 gave better results than did Model 1 for these flows.

3. The skin-friction results obtained for the adverse pressure-gradient flow, Case 8403, are inferior to some previously obtained from boundary-layer calculations by Horstman and Hung (1979). This appears to result because the time-averaged Navier-Stokes code, which solves the entire flow field, did not exactly match the given wall-pressure distribution.
4. Turbulence model 2 was the only model we tried on the three-dimensional swept shock flow (8661). This was because of its relative ease of applicability and its simple length-scale definition. It appears to have worked well.
5. Two turbulence models were tried for the three-dimensional flow, Case 8663. This is one of the few cases in which an algebraic model predicted separated flow results better than a two-equation model.
6. We tried to calculate the free-shear-layer flow (8501). It was found that the spreading rate was a function of the boundary conditions on the low-speed side. We did not finish calculating this flow.

In conclusion, we have presented mesh-independent solutions of a single numerical method (MacCormick's Hybrid Scheme) over a variety of flow conditions for three turbulence models. This method seems to reproduce the overall physics of the flows accurately for these complex flows. For the cases examined the two-equation $k-\omega$ turbulence model works well for shock/boundary-layer interactions with very little separation. For flows with large separation regions, the models tested do not have enough forward influence. Special turbulence models are needed for flows with separation.

References

- Coakley, T. J., and J. R. Viegas (1977). Symposium on Turbulent Shear Flows, University Park, PA.
- Horstman, C. C. and C. M. Hung (1979). AIAA Paper 79-0002, New Orleans, LA.
- Hung, C. M., & R. W. MacCormack (1978). AIAA Jou., 16, 1090.
- MacCormack, R. W. (1976). "Computing in Applied Mechanics," AMD, 18.
- Viegas, J. R., and C. C. Horstman (1979). AIAA Jou., 17, 811.



COMPARISON OF COMPUTATION WITH EXPERIMENT

Summary Report

by

D. Whitfield,* A. Jameson,[†] and W. Schmidt[‡]

Computer Group Number: 12

D. Whitfield

Cases 0141, 0612, 8621

Boundary-layer computations were performed using both a direct and an inverse compressible, turbulent, mean-flow kinetic-energy integral method; and, transonic viscous-inviscid interaction calculations were performed using a finite-volume Euler equation method coupled with the inverse boundary-layer method. The direct boundary-layer-calculation method was used to compute Cases 0612 and 0141. The inverse boundary-layer-calculation method was used to compute the upper surface boundary-layer for all five cases of Case 8621. The viscous-inviscid interaction calculation method was used to compute two cases (cases 6 and 9) of Case 8621. Each calculation method is summarized below.

Direct Boundary-Layer Method

The direct boundary-layer method is the mean-flow kinetic-energy integral method described in detail in Whitfield (1978). A distinguishing feature of this integral method is the use of a three-parameter family of analytical velocity profiles that describe the boundary layer over the entire domain $0 \leq y < \infty$. The dissipation integral is integrated using the analytical velocity profile at each streamwise location, Prandtl's mixing-length theory for the middle region of the boundary layer, and Clauser's eddy viscosity for the outer region of the boundary layer. The inner-region portion of the dissipation integral is integrated analytically using results stemming from the development of the velocity profile as explained in Whitfield (1978). Initial conditions of boundary-layer momentum thickness and shape factor are used to start the calculations. The equations are solved numerically using a predictor-corrector scheme.

Inverse Boundary-Layer Method

The inverse boundary-layer method is described in Whitfield et al. (1980). It is based on an extension of the attached-flow analytical boundary-layer velocity profile

*Mississippi State University, Mississippi State, MS 39762

[†]Princeton University, Princeton, NJ 08544

[‡]Dornier GmbH, D-7990 Friedrichshafen, West Germany

of Whitfield (1978) to separated flow. The velocity-profile expression used describes either attached or separated flow, depending on whether the shear stress at the surface is positive or negative.

In an inverse boundary-layer method, pressure (or velocity at the edge of the boundary layer) is a dependent variable, and in this particular inverse method the displacement-thickness (δ^*) distribution is specified. The method used to provide a rational, a priori, specification of the δ^* distribution is the method of Carter (1979). Carter's method can be written as

$$\delta^{*(m+1)} = \delta^{*(m)} + \omega \delta^{*(m)} \left(\frac{u_{e,v}}{|\vec{q}|_{w,i}} - 1 \right) \quad (1)$$

where $\delta^{*(m+1)}$ is the new displacement thickness at a streamwise location, $\delta^{*(m)}$ is the displacement thickness from the previous iteration, $u_{e,v}$ is the local velocity at the edge of the boundary layer obtained from the last boundary-layer solution, $|\vec{q}|_{w,i}$ is the magnitude of the local velocity vector obtained from the last Euler-equation solution, and ω is the relaxation parameter.

Equation 1 can be used with the inverse method to solve a conventional boundary-layer problem with known pressure distribution. For such a problem, the known pressure distribution is used to determine the velocity distribution which corresponds to $|\vec{q}|_{w,i}$ in Eq. 1. In this case the $|\vec{q}|_{w,i}$ distribution remains fixed and Eq. 1, with $u_{e,v}$ updated after each inverse boundary-layer solution, is used to obtain the converged δ^* distribution. This method was used to solve for the boundary-layer on the upper surface of the airfoil in Case 8621 using the measured pressure distributions. The initial δ^* distribution was assumed to be that corresponding to a flat plate. A comparison between direct and inverse solutions for Case 0141 is given in Schmidt et al. (1981). After four iterations, with $\omega = 2$, the difference between the inverse and direct solutions is not discernible in Figure of Schmidt et al. (1981). The inverse solutions for Case 8621 were obtained using $\omega = 2$. The numerical method used to solve the inverse boundary-layer equations was a fourth-order Runge-Kutta scheme.

Viscous-Inviscid Interaction Method

The viscous-inviscid interaction method is described in Schmidt et al. (1981). It consists of coupling the inverse boundary-layer method with a finite-volume Euler-equation method using the surface source model. The surface-source model has an advantage over the effective-displacement-surface approach in that a surface-source mass flux is imposed as a boundary condition in the inviscid calculation at the physical body surface and in the wake, and hence mesh adjustment during the iteration process is not required. The surface-source mass flux, $(\rho v)_n$, imposed at the physical surface is given by

$$(\rho v)_n = \frac{d(\rho_e u_e \delta^*)}{dx} \quad (2)$$

where $(\rho v)_n$ is the local mass flux normal to the surface. The right-hand side of Eq. 2 is evaluated after each inverse boundary-layer solution to determine $(\rho v)_n$ for subsequent inviscid calculations.

The viscous-inviscid interaction calculation scheme proceeds in the following steps:

1. The Euler-equation solution is advanced 50 cycles with $(\rho v)_n \equiv 0$.
2. An inverse boundary-layer solution is obtained with $\delta^{*(1)}$ given by Eq. 1, where $\delta^{*(0)}$ is a flat-plate distribution, $u_{e,v}$ is constant at the free-stream value (u_∞), and $|\vec{q}|_{w,1}$ is obtained from the last cycle of the Euler-equation solution.
3. The Euler-equation solution is advanced 50 cycles with $(\rho v)_n$ held fixed at the value given by Eq. 2.
4. An inverse boundary-layer solution is obtained with $\delta^{*(m+1)}$ given by Eq. 1.
5. Steps 3 and 4 are repeated until convergence on δ^* or c_p (surface-pressure coefficient) is obtained.

Viscous-inviscid interaction solutions were obtained for cases 6 and 9 of Case 8621 using $\omega = 1$. A 121×30 C-type mesh was used with 85 points on the airfoil. The solutions were started impulsively and the boundary layer was started turbulent near 15% chord. A free-stream Mach-number correction of 0.004 was used, as that was the value used by Lock (1980).

This code is operational on the CRAY-1 and the CYBER 203 computers. However, no significant optimizations have yet been performed to fully utilize either machine, hence current computation times represent an upper bound and mean very little. Currently one cycle per mesh point requires 4.2×10^{-5} sec on the CRAY-1 and the CYBER 203 requires about twice this much time. Reasonably converged inviscid solutions require 1000 cycles, although good engineering answers are obtained in 500 to 800 cycles. The viscous-inviscid interaction solutions for Case 8621 are the result of 2000 cycles.

References

- Carter, J. E. (1979). "A new boundary-layer inviscid iteration technique for separated flow," AIAA Paper No. 79-1450.
- Lock, R. L. (1980). "A review of methods for predicting viscous effects on aerofoils and wings at transonic speeds," AGARD-CP-291.

Schmidt, W., A. Jameson, and D. Whitfield (1981). "Finite volume solution for the Euler equation for transonic flow over airfoils and wings including viscous effects," AIAA Paper No. 81-1265.

Whitfield, D. L. (1978). "Integral solution of compressible turbulent boundary layers using improved velocity profiles," AEDC-TR-78-42, Arnold Air Force Station, TN.

Whitfield, D. L., T. W. Swafford, and J. L. Jacocks (1980). "Calculation of turbulent boundary layers with separation, reattachment and viscous-inviscid interaction," AIAA Paper No. 80-1439.



COMPARISON OF COMPUTATION WITH EXPERIMENT

Summary Report

(Two-Equation Model of Turbulence)

by

D. C. Wilcox*

Computer Group Number: 37

Cases 0141, 0142, 0143, 0241, 0242, 0244, 0311, 0371, 0372, 0374,
0376, 0421, 0612, 8101, 8201, 8403, 8411, 8501, 8621, 8623

The objective of our participation in this Conference has been to use a single method to compute as wide a range of flows included in the Conference as possible. By so doing, it has been our hope that we can objectively assess progress made to date in developing a universally applicable engineering model of turbulence. To accomplish this objective we have computed 20 flows with a total of 62 separate computations. The flows we have computed are listed in Table 1.

Table 1. Summary of Flows Computed

<u>Case Number</u>	<u>Description</u>	<u>No. of Tests</u>
0141/Simple	Incompressible B.L. in Adverse Pressure Gradient	1
0142/Entry	Pozzorini Low-Core Turbulent Diffuser	1
0143/Entry	Pozzorini High-Core Turbulent Diffuser	1
0241/Entry	Boundary Layer with Blowing	1
0242/Entry	Boundary Layer with Suction	1
0244/Entry	Boundary Layers with Suction	5
0311/Entry	Mixing-Layer Development	1
0371/Simple	Homogeneous Isotropic Turbulence	1
0372/Simple	Homogeneous Rotating Turbulence	3
0374/Simple	Homogeneous Plane Strain	2
0376/Simple	Homogeneous Shear	2
0421/Entry	Backward-Facing Step	1
0612/Simple	Constant-Pressure Boundary Layer	1
8101/Simple	Mach No. Effects on Boundary Layer	6
8201/Simple	Wall-Temperature Effects on Boundary Layer	6
8403/Simple	Compressible B.L. in Adverse Pressure Gradient	9
8411/Simple	Compressible B.L. in Adverse Pressure Gradient	1
8501/Simple	Mach No. Effects on Mixing Layer	3
8621/Entry	RAE 2822 Transonic Airfoil	10
8623/Entry	DSMA 523s Transonic Airfoil	6

All 62 computations were done using the two-equation model of turbulence devised by Wilcox and Rubesin (1980) with some minor "fine-tuning" of the closure coefficients. Computational tools used to solve the equations of motion were (a) a fourth-

*DCW Industries, Inc., Studio City, CA 91604

order accurate Runge-Kutta integration scheme for the 8 homogeneous turbulent flows (Cases 0371, 0372, 0374 and 0376), (b) a fully elliptic incompressible program named EDDYNSI for the backward-facing step (Case 0421) and a compressible/incompressible boundary-layer program named EDDYBL for the other 53 computations.

In the following sections, we present in detail the equations of motion and boundary conditions employed. We then give a brief description of the numerical tools used followed by a discussion of the various numerical checks made during the course of the many computations. Finally, we summarize results obtained and outline possible future avenues of research.

EQUATIONS OF MOTION

The equations of motion used in all of our computations are those devised by Wilcox and Rubesin. The model is of the two-equation variety in which the Reynolds-stress tensor τ_{ij} is assumed proportional to the mean-strain-rate tensor S_{ij} according to

$$\tau_{ij} = 2\rho\epsilon(S_{ij} - \frac{1}{3} \frac{\partial u_k}{\partial x_k} \delta_{ij}) - \frac{2}{3} \rho e \delta_{ij} \quad (1)$$

where ϵ is the eddy diffusivity, e is the turbulent mixing energy, ρ is the mass density, u_i is the mean velocity vector, x_i is the position vector, and δ_{ij} is the Kronecker delta. The mean equations of motion are thus written as follows:

$$\frac{\partial \rho u_i}{\partial x_i} = 0 \quad (2)$$

$$\frac{\partial \rho u_j u_i}{\partial x_j} = - \frac{\partial p}{\partial x_i} + \frac{\partial}{\partial x_j} [2\mu(S_{ij} - \frac{1}{3} \frac{\partial u_k}{\partial x_k} \delta_{ij}) + \tau_{ij}] \quad (3)$$

$$\frac{\partial \rho u_j h}{\partial x_j} = u_i \frac{\partial p}{\partial x_i} + \beta^* \rho \omega e + [2\mu(S_{ij} - \frac{1}{3} \frac{\partial u_k}{\partial x_k} \delta_{ij})] \frac{\partial u_i}{\partial x_j} + \frac{\partial}{\partial x_j} (\frac{\mu}{Pr_L} + \frac{\rho\epsilon}{Pr_T}) \frac{\partial h}{\partial x_j} \quad (4)$$

In Eqs. 2-4 p is mean pressure, h is mean enthalpy, μ is viscosity, Pr_L and Pr_T are laminar and turbulent Prandtl numbers, ω is turbulent dissipation rate per unit of kinetic energy and β^* is a closure coefficient which will be defined below. Before introducing the two turbulence model equations it is instructive to note that the mean energy equation (4) appears to find the conventional work term $\tau_{ij} \partial u_i / \partial x_j$ replaced by $\beta^* \rho \omega e$. This is not an ad-hoc closure approximation, but rather a closure approximation consistent with those made below in the turbulent energy equation. The correctness of Eq. 4 becomes obvious when the resultant equation for total energy, viz., $[h + (u_i u_i)/2 + e]$ is formed.

To complete our set of equations, we compute the eddy diffusivity in terms of e and ω from:

$$\epsilon = \gamma^* e / \omega \quad (5)$$

where γ^* is a closure coefficient given below in Eqs. 8. The equations governing the evolution of e and ω are

$$\frac{\partial \rho u_j e}{\partial x_j} = \tau_{ij} \frac{\partial u_i}{\partial x_j} - \beta^* \rho \omega e + \frac{\partial}{\partial x_j} \left(\mu + \sigma^* \rho \epsilon \frac{\partial e}{\partial x_j} \right) \quad (6)$$

$$\frac{\partial}{\partial x_j} (\rho u_j \omega^2) = \gamma \gamma^* \frac{\omega^2}{e} \tau_{ij} \frac{\partial u_i}{\partial x_j} - \left[\beta + 2\sigma \left(\frac{\partial l}{\partial x_k} \right)^2 \right] \rho \omega^3 + \frac{\partial}{\partial x_j} \left(\mu + \sigma \rho \epsilon \frac{\partial \omega^2}{\partial x_j} \right) \quad (7)$$

where l is a turbulent length scale defined as $e^{1/2}/\omega$. In Eqs. 5-7 there are several closure coefficients whose values are given in Eqs. 8.

$$\gamma^* = 1 - (1 - \lambda^2) \exp(-Re_T)$$

$$\gamma \gamma^* = 25/27 [1 - (1 - \lambda^2) \exp(-Re_T/1.5)] \quad (8)$$

$$\lambda = 1/11 ; \quad \beta = 3/20 ; \quad \beta^* = 9/100 ; \quad \sigma = 2/3 ; \quad \sigma^* = 2/3$$

Note that $Re_T = \rho e / \omega \mu$ is the turbulent Reynolds number.

In performing the homogeneous turbulent flow calculations, we used the nonlinear stress/strain-rate constitutive relation devised by Wilcox and Rubesin (1980) which, for the high Re_T , incompressible cases considered becomes:

$$\frac{\tau_{ij}}{\rho} = 2\epsilon S_{ij} - \frac{2}{3} \epsilon \delta_{ij} + \frac{4e(S_{im}\Omega_{mj} + S_{jm}\Omega_{mi})}{9\beta^* (\omega^2 + 2S_{mn}S_{nm})} \quad (9)$$

where $\Omega_{ij} = 1/2(\partial u_i/\partial x_j - \partial u_j/\partial x_i)$. Additionally, for the rotating homogeneous flow, Case 0372, we added the Wilcox-Chambers (1977) rotation term to the equation for e , or,

$$\frac{\partial e}{\partial t} = \tau_{ij} \frac{\partial u_i}{\partial x_j} + 9\Omega \langle -u'v' \rangle - \beta^* \omega e \quad (10)$$

where t is time and Ω is rotation rate. Finally, for the transonic airfoil, Cases 8621 and 8623, we used the Wilcox-Chambers (1977) streamline curvature term, or,

$$\frac{\partial \rho u_j e}{\partial x_j} = \langle -u'v' \rangle \frac{\partial u}{\partial y} - 4.5 \langle -u'v' \rangle \frac{u}{R} + \dots \quad (11)$$

where R is surface radius of curvature (positive for convex, negative for concave).

BOUNDARY CONDITIONS

For all but the 8 homogeneous cases, solid boundaries were present and surface boundary conditions must be specified. With the exception of the backward-facing step, all computations integrated all the way to the surface, $y = 0$. Surface boundary conditions were as follows:

$$u = 0 ; \quad T = T \text{ or } \partial T / \partial y = 0 ; \quad e = 0 ; \quad \omega = S \mu_{\tau}^2 / (\beta^{*1/2} \nu) \quad (12)$$

where T is temperature and subscript w denotes surface. For the dissipation rate, the quantity S is a universal function of surface roughness and mass injection rate defined by Wilcox-Traci (1976):

$$S = (S_B + S_R) ; \quad S_B = 6 / [v_w^+ (1 + v_w^+)] ; \quad S_R = (36/k^+)^2 + (8/k^+)^{1/2} \quad (13)$$

where $v_w^+ = v_w / u_{\tau}$ is the nondimensional injection rate and $k^+ = k u_{\tau} / \nu$ is the non-dimensional roughness height. Note that for suction ($v_w < 0$) we take $S_B = 0$ and in the limit of zero roughness and injection the near-surface behavior of ω is:

$$\omega \rightarrow 20\nu / (\beta y^2) \text{ as } y \rightarrow 0 \quad (14)$$

where ν is the kinematic viscosity.

For the backward-facing step we used boundary conditions consistent with the law-of-the-wall, with:

$$u / u_{\tau} \rightarrow (1/0.41) \log(u_{\tau} y / \nu) + 5.0 ; \quad \omega \rightarrow u_{\tau} / (0.41 \beta^{*1/2} y) ; \quad e \rightarrow u_{\tau}^2 / \beta^{*1/2} \quad (15)$$

While more accurate boundary conditions (also known as wall functions) are available for our equations, limited time and funds precluded their use for this Conference.

COMPUTATIONAL TOOLS

Because of their inherent simplicity, we solved the equations of motion for the 8 homogeneous turbulent flows with a straightforward fourth-order accurate Runge-Kutta integration scheme and, for obvious reasons, the program requires no further description.

The lion's share of our computations were done with the same program, namely our two-dimensional/axisymmetric compressible/incompressible boundary-layer/shear-layer program known as EDDYBL which is described in Wilcox (1976). In performing the calculations all compressible cases were done on a UNIVAC 1108 and all incompressible cases on a TRS-80 Microcomputer. The latter cases were actually done with a version of EDDYBL in which all of the compressibility terms were eliminated. The program is a parabolic marching code which is second-order accurate in both streamwise and normal directions.

The backward-facing step case was done with an incompressible, elliptic program known as EDDYNSI. The program is a modified version of the TEACH-2E Code described by Gosman and Ideriah (1976); it is also second-order accurate in streamwise and normal directions.

NUMERICAL CHECKS

We performed many numerical accuracy tests on a more or less random sampling of the many cases we computed. In general we tested the effect of total mesh point number, location of mesh point nearest the surface, and size of streamwise steps taken. For all of the boundary-layer cases we found 80-100 mesh points normal to the surface with the value of y^+ for the point nearest the surface less than unity to be quite satisfactory. Except for the very strong adverse pressure-gradient cases there is virtually no loss in accuracy in taking streamwise steps up to about one boundary-layer thickness. In some of our compressible boundary-layer runs we used as many as 280 points normal to the surface with y^+ nearest the surface as small as 0.09. The difference in computed integral properties over a 100-point calculation was never found to be more than 2%.

For the backward-facing step case we used meshes which had a total of 196, 529, and 870 mesh points. The total number of mesh points had very little effect on predicted reattachment length, even though local flow properties varied substantially with the number of points used.

SUMMARY AND OBSERVATIONS

The model employed in our computations predicts flow properties in quite close agreement with experimental data for the constant-pressure boundary layer, the incompressible mixing layer and for flows with surface mass transfer. Additionally, predicted effects of Mach number and surface cooling on a constant-pressure boundary layer are close to measured effects.

For flows with strong adverse pressure gradient, most notably the backward-facing step, the model's predictions differ substantially from corresponding measurements. As an almost uniform trend, the model responds much more rapidly to an adverse pressure gradient than has been measured (e.g., Cases 0141, 0142, 0143, 0421) and, upon removal of the gradient, returns to equilibrium more rapidly than measured (e.g., Cases 0142, 0143, 8621, 8623).

Our success with the flows with suction and blowing is in part due to the careful research which has gone into developing appropriate surface boundary conditions for such flows. This success is perhaps an argument in favor of integrating to the surface (as opposed to using wall functions) for this type of flow.

Our relative lack of success in computing flows with strong adverse pressure gradient is less easy to explain. Perhaps we should expect to do poorly when the flow departs even slightly from equilibrium upon observing the gross discrepancies between computed and measured Reynolds-stress development for the homogeneous cases. Yet, this would be too easy an explanation as the primary culprit is the eddy-viscosity approximation in the homogeneous case. More plausibly, with a two-equation turbulence model, we may be attempting to describe too much with too little in the turbulent boundary layer. That is, the near-wall portion of the boundary layer responds on a grossly different scale from that of the defect layer. Yet, we attempt, from a single equation (the equation for ω), to deduce the scales on which the entire boundary layer will respond and change. This problem could actually be partly accommodated by using wall functions! A more satisfactory approach, however, might be to use more than a single dissipation rate. In this way we could concentrate more of the physics of the boundary layer into the equations of motion.

ACKNOWLEDGMENT

I would like to thank the Air Force of Scientific Research and the NASA Lewis Research Center for providing special funds to make this contribution to the Conference possible.

REFERENCES

- Gosman, A. D., and F. J. K. Ideriah (1976). "TEACH-2E: A general computer program for two-dimensional, turbulent, recirculating flows."
- Wilcox, D. C. (1976). "User's guide for the EDDYBL computer program," DCW Industries Report DCW-R-14-02.
- Wilcox, D. C., and T. L. Chambers (1977). "Streamline curvature effects on turbulent boundary layers," AIAA Jou., 15, 574-580.
- Wilcox, D. C., and M. W. Rubesin (1980). "Progress in turbulence modeling for complex flow fields including effects of compressibility," NASA TP 1517.
- Wilcox, D. C., and R. M. Traci (1976). "A complete model of turbulence," AIAA Paper 76-351.

COMPUTOR GROUP MEMBERS IN ALPHABETIC ORDER

<u>Name</u>	<u>Group No.</u>	<u>Page</u>	<u>Name</u>	<u>Group No.</u>	<u>Page</u>
Abdelmaguid, A.M.	33	1521	MacCormack, R.W.	44 ¹	1443
Arnal, D.	22	1326	MacInnes, J.M.	17 ³	1390
Bailey, H.E.	50	1303	Mansour, N.N.	02	1418
Barba, A.	17 ³	1390	Maskew, B.	46	1346
Bardina, J.	45	1353	McDonald, H.	41	1424
Berrue, P.	22	1326	Mellor, G.L.	14	1428
Bertoglio, J.P.	52	1307	Melnik, R.E.	39	1438
Birch, S.F.	24	1305	Ha Minh, H.	44 ¹	1443
Bonnet, J.P.	17 ⁴	1408	"	44 ²	1449
Cambon, C.	52	1307	Mjolsness, R.J.	17 ³	1390
Celenligil, M.C.	14	1428	Moore, J.	01	1453
Celik, I.	07	1495	Moore, J.G.	01	1453
Chang, S.M.	17 ¹	1375	Morel, T.	02	1418
Chassaing, P.	44 ²	1449	Moses, H.L.	27	1459
Chow, W.L.	23 ¹	1312	Murphy, J.D.	28	1464
"	23 ²	1318	Nagamatsu, T.	04	1468
Cler, A.	22	1326	Nakayama, A.	23 ¹	1312
Cousteix, J.	22	1326	Orlandi, P.	05	1472
Daiwert, G.S.	47	1337	Pletcher, R.H.	30	1479
Demirdzic, I.	17 ²	1383	Pollard, A.	06	1486
Demuren, A.O.	07	1495	Quinn, B.	21	1342
Donaldson, C.duP.	21	1342	Rakich, J.V.	31	1491
Dubois, P.	22	1326	Rastogi, A.K.	07	1495
Dvorak, F.A.	46	1346	Rhie, C.M.	23 ²	1318
Ferziger, J.H.	45	1353	Rodi, W.	07	1495
Goh, S.Y.	33	1521	Scheuerer, G.	07	1495
Gosman, A.D.	17 ²	1383	Schmidt, W.	12	1540
Hah, C.	19	1358	Selimović, R.	18	1364
Han, T.	17 ¹	1375	Sharma, D.	23 ¹	1312
Hanjalić, K.	18	1364	"	23 ²	1318
Hill, J.M.	27	1459	Shirani, E.	07	1495
Horstman, C.C.	36	1535	Sindir, M.	17 ³	1390
Houdeville, R.	22	1326	Smith, P.D.	32	1517
Humphrey, J.A.C.	17 ¹	1375	Spalding, D.B.	33	1521
Hung, C.	43	1372	Stosić, N.	18	1364
"	36	1535	Strawn, R.C.	45	1353
Ibrahim, I.M.	17 ³	1390	Sullivan, R.D.	21	1342
Ilegbusi, J.	33	1521	Sykes, R.I.	21	1342
Issa, R.I.	17 ²	1383	Tannehill, J.C.	31	1491
Ivanović, M.	18	1364	Tassa, Y.	09	1527
Jameson, A.	12	1540	Teku, N.G.	17 ³	1390
Jeandel, D.	52	1307	Thomason, S.B.	27	1459
Johnson, R.W.	17 ³	1390	Tree, I.K.	31	1491
Jones, III, R.R.	27	1459	Tulapurkara, E.G.	22	1326
Kwon, O.K.	30	1479	Vandromme, D.D.	44 ¹	1443
Lakshminarayana, B.	19	1358	"	44 ²	1449
Lauder, B.E.	17 ³	1390	"	35	1532
Le Balleur, J.C.	42	1411	Varma, A.K.	21	1342
Leschsiner, M.A.	17 ³	1390	Vasić, S.	18	1364
"	07	1495	Viegas, J.	36	1535
Lowallen, W.S.	21	1342	Whitfield, D.	12	1540
Lyrio, A.A.	45	1353	Wilcox, D.C.	37	1544

**LOCATION OF THE CONCLUSIONS
AND GENERAL COMMENTS IN THESE PROCEEDINGS**

The 1980-81 AFOSR-HTTM-Stanford Conference on Complex Turbulent Flows includes two major elements:

1. Completion of data sets, and test cases based on the data, for use in formulating models and testing output of computations.
2. Extensive comparison of the output of computations with the data sets.

Considerable effort has been expended to make the work complete in both Part 1 and Part 2 by provision of: position papers; reporters' summaries; evaluations; and extensive discussions of both details and more general underlying questions. These elements have been prepared with the active cooperation of the international research community in order to provide the best collective opinions on the state of the art. As a result conclusions and comments of a general nature appear at a number of places in these Proceedings as indicated in the remainder of this section. Considerable cross-referencing and indexing is also provided to aid the reader.

The general conclusions regarding data appear at the end of Volume I, p. 605. The four position papers at the beginning of Volume I were intended to set the stage for the work of the Conference and provide underlying comments about data needs and uses that have not been available previously. Discussions of several important questions of experimental technique and accuracy appear in the reports of the ad-hoc committees in Volume I; these reports incorporate the ideas of an unusually large group of able, experienced experimenters.

The general conclusions about computations appear in three places in Volume II. First, in three documents at the end of Volume II: (a) Report of the Evaluation Committee, p. 979; (b) an OPINION by the leading Editor on the strategy of turbulence modeling with comments and closure, p. 991; (c) the Editors' Concluding Remarks, p. 1022. Second, in the Reporters' Summaries for various flow classes throughout Volume II; see Table of Contents. Third, in the discussions of individual sessions and in the concluding discussions, p. 1017.

Other documents that may assist readers in finding particular elements include:

- (i) Taxonomies of flows, turbulence models, and numerics in the beginning of both Volumes II and III;
- (ii) A Reader's Guide to Volumes II and III, p. xx of Vol. II;
- (iii) Several cross indexes of Cases, Computer Groups, and output at the beginning of Volume III;
- (iv) An index of individual computers on the preceding page.

END

FILMED

1-84

DTIC